Local Dynamics
and Spatiotemporal Chaos

The Kuramoto-Sivashinsky Equation:
A Case Study

Ralf Werner Wittenberg

Abstract

The nature of spatiotemporal chaos in extended continuous systems is not yet well-understood. In this thesis, a model partial differential equation, the Kuramoto-Sivashinsky (KS) equation

$$u_t + u_{xxxx} + u_{xx} + uu_x = 0$$

on a large one-dimensional periodic domain, is studied analytically, numerically, and through modeling to obtain a more detailed understanding of the observed spatiotemporally complex dynamics. In particular, with the aid of a wavelet decomposition, the relevant dynamical interactions are shown to be localized in space and scale. Motivated by these results, and by the idea that the attractor on a large domain may be understood via attractors on smaller domains, a spatially localized low-dimensional model for a minimal chaotic box is proposed.

A (de)stabilized extension of the KS equation has recently attracted increased interest; for this situation, dissipativity and analyticity are proven, and an explicit shock-like solution is constructed which sheds light on the difficulties in obtaining optimal bounds for the KS equation. For the usual KS equation, the spatiotemporally chaotic state is carefully characterized in real, Fourier and wavelet space. The wavelet decomposition provides good scale separation which isolates the three characteristic regions of the dynamics: large scales of slow Gaussian fluctuations, active scales containing localized interactions of coherent structures, and small scales. Space localization is shown through a comparison of various correlation lengths and a numerical experiment in which different modes are uncoupled to estimate a dynamic interaction length.

A detailed picture of the contributions of different scales to the spatiotemporally complex dynamics is obtained via a Galerkin projection of the KS equation onto the wavelet basis, and an extensive series of numerical experiments in which different combinations of wavelet levels are eliminated or forced. These results, and a formalism to derive an effective equation for periodized subsystems externally forced from a larger system, motivate various models for spatially localized forced systems. There is convincing evidence that short periodized systems, internally forced at the largest scales, form a minimal model for the observed extensively chaotic dynamics in larger domains.

Contents

List of Figures

Chapter 1

The Kuramoto-Sivashinsky Equation

1.1 Introduction

There has been much recent interest in the complex spatiotemporal behavior of extended systems with many degrees of freedom, described by partial differential equations (PDEs) [CH93]. For relatively low-dimensional (highly constrained) systems, dynamical systems methods have clarified some of the intricate bifurcation sequences leading to chaos; for larger systems, much effort has gone into obtaining effective equations accounting for the statistical behavior at large length and long time scales (the thermodynamic limit). An important goal is to account for the dynamics of the energetically active modes in a spatiotemporally chaotic system, which occur at *intermediate* length and time scales, and to relate them to the dynamics observed and understood in lower-dimensional systems.

In the light of the analytic and numerical complexities of nonlinear PDEs in two and three dimensions, such as the equations of fluid mechanics, one studies simpler model equations which nevertheless display complex spatiotemporal dynamics ("weak turbulence"), and hence serve as a testing ground for theories and techniques for infinite-dimensional dynamical systems and real fluid turbulence. Motivated by successes in the context of turbulence, one also attempts to extract relatively low-dimensional models capturing the most energetic and dynamically relevant modes, together with appropriate modeling of the neglected modes, with the hope of obtaining a simplified description amenable to more detailed understanding.

In this thesis, we implement part of the above program, focusing on one particular popular model equation, the *Kuramoto-Sivashinsky (KS)* equation. This Chapter provides necessary background material by introducing the KS model and reviewing major relevant properties; a reader familiar with the KS equation may wish to proceed directly to Sec. 1.5, where we outline the remaining Chapters and the contributions of this thesis.

1.1.1 The Kuramoto-Sivashinsky equation

Real space formulation

We work only in one space dimension, on a domain of length L, in which the equation reads

$$u_t + u_{xxxx} + u_{xx} + uu_x = 0, \qquad x \in [0, L]. \tag{1.1}$$

Here $u_t \stackrel{\text{def}}{=} \partial u/\partial t$, $u_x \stackrel{\text{def}}{=} \partial u/\partial x$, and after rescaling the only control (bifurcation) parameter is L. By analogy with fluids, we will sometimes refer to u as the velocity field.

The literature contains several equivalent formulations of the KS equation, with the parameter introduced as a coefficient of some of the terms (for instance as a viscosity), rather than in the domain size. We have included a summary of some of the alternative forms, and their relations to (1.1), in App. A. We find (1.1) particularly useful, as it emphasizes the role of the space variable x and of the length of the domain. In particular, we shall see below that the linear instability mechanism introduces a characteristic intrinsic length scale l_0 into the system, so that the effect of increasing domain size may be interpreted in terms of the "aspect ratio" L/l_0. In this scaling, the idea of extracting "short subsystems" of a "long system" is reasonable, and will be the focus of much of this thesis.

Unless otherwise stated (see Sec. 4.3.1 and App. B.1.3) we shall restrict ourselves to *periodic boundary conditions*. In this way we enforce spatial homogeneity; however, our results are largely independent of boundary effects, apart from excessive constraints imposed by periodicity on short systems.

To complete the mathematical formulation of (1.1), we need to specify initial conditions $u(x,0) = u_0(x)$ in some appropriate function space. We shall see later that the smoothing properties of the equation are such that $u_0 \in L^2[0,L]$ is sufficient.[†] We shall always let $u_0(x)$ be "arbitrary" and generic; that is, we claim, and often check, that our results are independent of initial data. The only caveat is that u_0 is not an unstable fixed point or orbit in phase space. However, our numerical method of direct integration effectively excludes this possibility.

Conservation of the mean   A straightforward, but fundamental, consequence of periodicity is the conservation of the mean,

$$\frac{dm}{dt} = 0, \quad \text{where} \quad m(t) \overset{\text{def}}{=} \int_0^L u(x',t)\,dx';$$
(1.2)

this result is readily confirmed by use of (1.1) and application of the periodic boundary conditions. We will typically set the conserved mean to zero, especially as u may often be interpreted as the derivative of a periodic function h (see below); however, we note here already that the connection between the (local) mean and drift will be important later in this thesis (see Secs. 1.2.1 and 5.4.2).

Integral form of the KS equation   The formulation (1.1) is sometimes referred to as the "derivative", or conservation, form of the KS equation, as it may be rewritten:

$$\frac{\partial}{\partial t}u + \frac{\partial}{\partial x}\left(u_{xxx} + u_x + \tfrac{1}{2}u^2\right) = 0.$$

This form contrasts with another important formulation, the "integral" equation for $h(x,t) \overset{\text{def}}{=} \int_0^x u(x',t)\,dx'$ (that is, $u = h_x$):

$$h_t + h_{xxxx} + h_{xx} + \tfrac{1}{2}h_x^2 = 0.$$
(1.3)

Here h can be interpreted as an interface height. In contrast with the formulation (1.1), in (1.3) the mean is not conserved, and typically grows without bound, unless it is explicitly subtracted, as in (A.3). While this may be "troubling behavior" [Dan95] for some analytical and numerical purposes, the growth of the mean is reasonable if $h(x,t)$ is thought of as a local position of a front.

[†]Since we are on a bounded domain, this condition is equivalent to "finite almost everywhere"; we have the luxury of choosing almost any initial data we like!

Fourier space formulation

The Fourier space formulation of (1.1) is basic to the understanding of the KS equation. Our scaling for the Fourier transform is

$$u(x,t) \stackrel{\text{def}}{=} \mathrm{i} \sum_q \hat{u}_q(t) \mathrm{e}^{\mathrm{i}qx}, \qquad \hat{u}_q(t) \stackrel{\text{def}}{=} -\frac{\mathrm{i}}{L} \int_0^L u(x',t) \mathrm{e}^{-\mathrm{i}qx'}\, dx' \tag{1.4}$$

(the factor of $\mathrm{i} = \sqrt{-1}$ in the definition is for convenience, to avoid an i in (1.5)). Here $q \stackrel{\text{def}}{=} 2\pi n/L$, $n \in \mathbb{Z}$, and we use q for the Fourier wave number throughout this thesis to avoid confusion with the index k in the wavelet decomposition (3.9). The reality condition for u from (1.4) is $\hat{u}_q = -\hat{u}_{-q}^*$.

Substituting (1.4) into (1.1), the evolution equation for the complex Fourier modes $\hat{u}_q$ is

$$\begin{aligned}
\frac{d}{dt}\hat{u}_q &= (q^2 - q^4)\hat{u}_q + \sum_{q'} q' \hat{u}_{q'} \hat{u}_{q-q'} \\
&= (q^2 - q^4)\hat{u}_q + q \sum_{q'} \hat{u}_{q'} \hat{u}_{q-q'}.
\end{aligned} \tag{1.5}$$

Note that conservation of the mean translates to $\hat{u}_0 = \text{constant}$. In Sec. 3.2.1 we shall write down a third formulation of the KS equation, in terms of wavelets, after introducing some preliminaries about the wavelet basis.

Fundamental features of the KS equation From (1.5) we may read off the linear dispersion relation, $\omega(q) \stackrel{\text{def}}{=} q^2 - q^4 = (2\pi n/L)^2 \big(1 - (2\pi n/L)^2\big)$. From this, we immediately see that the uniform zero solution becomes unstable to the mode $n = 1$ at $L = 2\pi$. As L increases, all Fourier modes with $q < 1$ successively become linearly unstable, so that the number of (complex) unstable modes $\lfloor L/2\pi \rfloor$ is proportional to L. The most unstable (fastest growing) mode is at $q_0 \stackrel{\text{def}}{=} 1/\sqrt{2}$, or $n_0 \in \mathbb{Z}$ near $L/2\pi\sqrt{2}$, corresponding to a wavelength $l_0 \stackrel{\text{def}}{=} 2\pi/q_0 = 2\pi\sqrt{2}$.

For L sufficiently large, we thus have many unstable modes, interacting through the nonlinear term. For instance, for the length we study in the most detail in this thesis, $L = 100$, we have $L/2\pi \approx 16$, so that the center-unstable manifold of the zero state is 32-dimensional. We thus have a very high-dimensional dynamical system for reasonably large bifurcation parameter, to which standard techniques of low-dimensional dynamical systems [GH83] are not easily applied. One of the goals of this thesis is to investigate the possibility of reducing the dimensionality to a tractable size, while retaining the dynamics observed at large L.

The forms (1.1) and (1.5) reveal the contributions of the different terms to the overall dynamics. The u_{xx} term is responsible for the instability at large scales (low q, where q^2 dominates), while the dissipative u_{xxxx} term provides damping at small scales (high q, where $q^4 > q^2$). The nonlinear term uu_x, which has the same form as that in the Burgers or one-dimensional Navier-Stokes equations, stabilizes by transferring energy between large and small scales.

The scope of this thesis The KS equation is a popular prototypical example for many ideas and techniques in the study of infinite-dimensional dynamical systems. Many of the issues that arise in the KS equation also arise in other nonlinear, dissipative evolution equations, such as the Swift-Hohenberg equation, the (complex) Ginzburg-Landau equation, and reaction-diffusion equations (see [CH93]), as well as in interface growth and roughening equations, and even in turbulence. However, instead of seeking the most general results, we have opted for investigating this system

(1.1) in more depth. As will be apparent from Ch. 5 and 6, even for a single equation with fixed parameters, we have been unable to exhaust the range of experiments that provide a detailed understanding of the nature of spatiotemporal chaos in this system. Unless otherwise stated, therefore, in this thesis we restrict our investigations to the one-dimensional Kuramoto-Sivashinsky equation (1.1) or (1.3).

1.1.2   Notes on the derivation and physical relevance of the KS equation

Equations (1.1) and (1.3) have been derived independently in several different contexts, where physical systems are driven far from equilibrium by intrinsic long-wave instabilities. Since the equation is by now very well-established in the literature, we shall not repeat any of the derivations here, instead contenting ourselves with a partial summary of those of which we are aware.

Among the numerous and diverse origins claimed for the KS equation, an early derivation occurred in the context of trapped-ion mode instabilities in plasmas by LaQuey *et al.* [LMRT75], and extended in [CKTR76]. Similar equations had also been derived in the context of fluids. The equation was named, however, after early investigators who well appreciated its significance.

Kuramoto and Tsuzuki, in studying instabilities just beyond a Hopf bifurcation in reaction-diffusion systems (motivated by the Brusselator) derived a complex Ginzburg-Landau equation for a slowly varying complex amplitude [KT75]; they then found that under some conditions the phase of this complex solution could be described by an equation equivalent to (1.1) [KT76]. The remarkable nature of this description of (chemical) "phase turbulence" was rapidly appreciated in numerical [KY76, YK76, Kur78] and analytical [FY77] studies. Kuramoto [Kur80] also realized that transverse instabilities of planar wavefronts in multi-dimensional reaction-diffusion systems obeyed a similar equation; see [Kur84] for a review.

In independent work performed approximately simultaneously, Sivashinsky [Siv77] derived an integrodifferential equation for small diffusive instabilities in a planar flame front, which reduces to (1.3) in a simple limit. In numerical simulations, spatiotemporally irregular solutions with sensitive dependence to initial conditions were observed and studied [MS77]. Subsequent work [Siv79] led to a similar description for a perturbed spherical flame front.

The equations describing long-wave instabilities for thin liquid films flowing down an incline [Ben66] also have the form (1.1), a fact which was appreciated by Sivashinsky and Michelson [SM80]; here u describes modulations in the film thickness. Instabilities at the interface between two viscous fluid similarly satisfy (1.1) [HG85]. A clear derivation of the KS equation in the context of fluids, based on work by Chang [Cha86], appears in the thesis of Brown [Bro92].

Such general applicability to a wide range of ostensibly disparate fields suggests a deeper underlying principle, and Misbah and Valance [MV94] have pointed out that the KS equation is a generic amplitude equation, or normal form, in the vicinity of long-wavelength primary instabilities in the presence of appropriate symmetries. Specifically, assuming parity and Galilean invariance (see below), and an instability at $q = 0$, the KS equation (1.1) provides an appropriate description. Alternatively, (1.3) is relevant for an interface with left-right symmetry and invariance with respect to the zero position of the front. Given its status as a generic amplitude equation, it is hardly surprising that the KS equation appears in such a diverse range of fields. (See also Sec. 2.3.4 for applications of the damped KS equation (2.2) and other extensions of (1.1).)

4

1.2 Notes on symmetries, analysis and bifurcations

1.2.1 Symmetries of the KS equation

We have just observed that the KS equation is the simplest equation obeying certain symmetries and with large scale instabilities, and is thus relevant for physical systems which satisfy those symmetries. We shall see later in Sec. 1.2.3 and throughout this thesis, that the symmetries are also fundamental to the dynamics and bifurcation structure. Writing $\mathcal{S}$ for the set of solutions to (1.1), the symmetries are (see also [Fri95, Sec. 2.2]):

1. Invariance under translation in time:

$$u(x,t) \in \mathcal{S} \Rightarrow u(x, t + \delta t) \in \mathcal{S}, \qquad \delta t \in \mathbb{R}. \tag{1.6}$$

2. Invariance under space translations:

$$u(x,t) \in \mathcal{S} \Rightarrow u(x + \delta x, t) \in \mathcal{S}, \qquad \delta x \in [0, L] \tag{1.7}$$

   (and hence for $\delta x \in \mathbb{R}$). This symmetry holds on an unbounded domain and for periodic boundary conditions; it is broken for fixed (for example, Dirichlet or mixed) boundary conditions, although it is approximately restored in the interior of such domains for large L (see Sec. 4.3.1).

3. Parity invariance:
$$u(x,t) \in \mathcal{S} \Rightarrow -u(-x, t) \in \mathcal{S}. \tag{1.8}$$

   Together with periodicity, $u(x,t) = u(x+L, t)$, this corresponds to invariance under reflection through $L/2$.

4. Galilean invariance:
$$u(x,t) \in \mathcal{S} \Rightarrow u(x - ct, t) + c \in \mathcal{S}. \tag{1.9}$$

   If u is interpreted as a velocity, then this important symmetry reflects the fact that the laws of physics are unchanged when viewed from a coordinate system moving at constant velocity. We can generalize this symmetry to $u(x,t) \to u(x - c(t), t) + \dot{c}(t)$ [Dan95].

We can translate these symmetries to the integrated KS equation (1.3) with periodic boundary conditions, interpreting h as an interface position (see also [BS95, Sec. 5.2]):

$1'$. Time translation invariance, as in 1.:

$$h(x,t) \in \mathcal{S} \Rightarrow h(x, t + \delta t) \in \mathcal{S}, \qquad \delta t \in \mathbb{R}. \tag{1.6$'$}$$

$2'$. Space translation invariance, as in 2.:

$$h(x,t) \in \mathcal{S} \Rightarrow h(x + \delta x, t) \in \mathcal{S}, \qquad \delta x \in [0, L] \tag{1.7$'$}$$

$3'$. Left-right symmetry (space inversion):

$$h(x,t) \in \mathcal{S} \Rightarrow h(-x, t) \in \mathcal{S}. \tag{1.8$'$}$$

$4'$. (a) Symmetry with respect to arbitrary shifts of the front:

$$h(x,t) \in \mathcal{S} \Rightarrow h(x,t) + \delta h \in \mathcal{S}, \qquad \delta h \in \mathbb{R}. \tag{1.9'a}$$

If h is an interface position, this invariance along the growth direction states that the equation is independent of where we defined the zero of h.

(b) Tilt invariance (see [RK95]):

$$h(x,t) \in \mathcal{S} \Rightarrow h(x - ct, t) - cx + \tfrac{1}{2}c^2 t \in \mathcal{S}. \tag{1.9'b}$$

Note that, ignoring physical applications for now, the sign of the nonlinear term in (1.1) or (1.3) is irrelevant; changing its sign merely corresponds to the rescaling $u \to -u$ or $h \to -h$, keeping everything else fixed.

The above symmetries are essential to the understanding of the bifurcation structure of the KS equation. Most important is the translation and inversion symmetry of (1.3), (1.7′) and (1.8′) (or its equivalent for (1.1)), which corresponds to rotations and reflections for the complex Fourier coefficients, that is, equivariance with respect to the group $O(2)$ [AGH89, KNS90]. The translation symmetry (1.7′) alone corresponds to the group $SO(2)$.

The invariance with respect to arbitrary translations (1.7) (or (1.7′)) implies symmetry under discrete translations L/k, where $k \in \mathbb{Z}$. In Fourier space, this implies $\mathbb{Z}_k$ symmetry, with respect to rotations $2\pi/k$. Combining $\mathbb{Z}_k$ and reflection symmetry, we get the dihedral group D_k. Much of the generic bifurcation behavior under $O(2)$ symmetry [AGH88] persists when we weaken the symmetry to D_k (see [CH92] for D_4). The symmetry under discrete translations is relevant to the wavelet formulation of the KS equation (see [MHEB95] and Sec. 3.2.2), and the symmetry groups $\mathbb{Z}_k$ and D_k play an important role in organising the dynamics (see for instance [Joh98]).

Invariant subspaces Fundamental to understanding the effect of the symmetries is the fact that they correspond to invariant subspaces of the KS dynamics. That is, the fixed point subspaces of the symmetry groups are invariant under the evolution (1.5). We highlight two examples which are relevant to our discussion:

- The space of odd solutions, $u(x,t) = -u(-x,t)$ is invariant under (1.1) (see (1.8) above). This space is spanned by sine functions, $\{\sin(2\pi nx/L)\}$. It turns out that analytical results are often more readily obtainable for this subspace than for the general periodic case; see for instance Sec. 2.1, or [NST85].

- Another subspace preserved by the dynamics is the fixed point subspace of $\mathbb{Z}_k$, that is, the space of L/k-periodic functions invariant under discrete translations, $u(x,t) = u(x + L/k, t)$. This fact is most readily seen in the Fourier representation: $u \in \mathrm{Fix}(\mathbb{Z}_k)$ if its only nonzero Fourier modes are multiples of the kth mode; that is, $\hat{u}_q = 0$ except if $q = nq_k \overset{\mathrm{def}}{=} n \cdot 2\pi k/L$, $n \in \mathbb{Z}$. From the structure of the nonlinear term in (1.5), this property is maintained by the KS evolution. For $k = 2^{j_0}$, we rederive this fact in the wavelet representation in Sec. 3.3.

Galilean invariance: Correspondence between the mean and drift A fact which will be very important to us later, for instance in Sec. 5.4.2, is the Galilean invariance (1.9). We interpret this as *"a variation in the mean corresponds to a drift"*: From (1.2) we know that the mean is conserved. The symmetry (1.9) then implies that a solution of (1.1) with mean $m \neq 0$ is just the sum of m and a mean zero solution, seen from a reference frame moving with speed m and direction

6

determined by the sign of m (the drift is to the right, towards increasing x, for positive mean). Hence, without loss of generality, we need only study mean zero solutions of the KS equation (1.1).

In Sec. 4.3 we will argue that for large enough length L, the KS dynamics is locally determined over a distance l_c of order a few characteristic wavelengths. One can then heuristically conclude that a nonzero *local* mean, averaged over a region of order l_c, induces a local drift with traveling structures. Such behavior is indeed observed (Sec. 5.4.2).

We have summarized some consequences of symmetry in the KS equation. Of course, individual solutions (see Fig. 1.2 below) break these symmetries, and the simple attractors known for small L, such as fixed points, or standing or (modulated) traveling waves, lose some or all of these symmetries. However, on the spatiotemporally chaotic attractor, considerable numerical evidence indicates that the symmetries are restored in a statistical sense. For instance, we have confirmed that $u(x_0, t)$, for arbitrary x_0, possesses the same pointwise statistics as those obtained from averaging over x; that is, for increasing L, the attractor undergoes symmetry-increasing bifurcations [CG88, DGN94].

1.2.2 Summary of analytical results

With the exception of some results in Ch. 2, we concentrate here on numerical investigations rather than rigorous analysis of the PDE. Thus we shall not state any theorems in this Section, let alone present their proofs. Instead, we briefly outline some highlights in the analytical study of the KS equation. We shall rigorously state and extend some of these results in Ch. 2, as needed. Many of the earlier results described here are reviewed in detail in the book by Temam [Tem97].

The well-posedness of (1.1), and the existence and uniqueness of solutions on an arbitrarily long interval, was shown using standard energy [NS84] or fixed point [Tad86] methods. See also [Tem97], where an appropriate functional setting is also given. Strictly speaking, the KS equation is well-posed with weak solutions in the Sobolev space H^2; classical solutions should be four times differentiable. The powerful smoothing action of the linear operator is such that initial data in L^2 immediately obtains arbitrarily high differentiability properties, as will be noted below, so the appropriate smoothness of solutions is not an issue.

Dissipativity, regularity and inertial manifolds

More interesting is the dissipativity of the dynamics (see Secs. 2.1–2.2). It was shown, initially for odd initial data only, that solutions are attracted to an absorbing ball in L^2, with an L-dependent radius; similar absorbing balls exist in higher Sobolev spaces [NST84, NST85]. The extension to general L-periodic initial conditions was provided later in [Il'92, CEES93a, Goo94]. Nicolaenko, Scheurer and Temam [NST85] used the dissipativity to show that the system has a finite number of determining *modes* and a compact global attractor with finite fractal and Hausdorff dimension, thus demonstrating the finite-dimensionality of the dynamics. While this result demonstrated that the asymptotic behavior is completely specified by a finite number of Fourier modes, an analogous real space result has more recently been obtained: solutions are asymptotically determined by their values at four sufficiently nearby points [FK95] (see also [FT91]). That is, there are finitely many determining *nodes*.

Finite-dimensionality of the dynamics While the attractor can have very complex and perhaps pathological structure, an even stronger result was obtained: the existence of a finite-dimensional inertial manifold (IM), invariant under the dynamics, exponentially absorbing and

containing the attractor [FNST85, FNST88] (see also [Nic86, HN86, Tem97] for reviews). On restricting the PDE to the inertial manifold one obtains an ODE (the inertial form), which completely describes the long-time dynamics; this is a global version of the local center manifold method. Thus the KS evolution is rigorously equivalent to a finite-dimensional dynamical system. An improved construction of the inertial manifold using different techniques was described in [CFNT89a, CFNT89b].

The demonstration of the existence of an inertial manifold does not provide an explicit construction, and various approximation schemes have been introduced to facilitate computational investigation. Jolly *et al.* [JKT90] have shown that one can construct approximate inertial manifolds (AIMs) so that all trajectories of the KS equation approach a small neighborhood of the AIM at an exponential rate; this result was extended in [Liu91], and some further analyses concerning AIMs are found in [FJKT94, FJ95, WS95].

Regularity   The smoothing properties of the linear operator in the KS equation are such that one can deduce strong regularity conditions by using the dissipativity in L^2, and interpolating between the L^2 norm and a suitably defined analyticity norm, the Gevrey norm. This lets one deduce regularity in the Gevrey class, which gives exponential decay of the high Fourier modes and analyticity in a strip around the real axis [Liu91, CEES93b] (see also Sec. 2.3.1). In this way, one can obtain bounds for all Sobolev norms (L^2 norms on the spatial derivatives) simultaneously, eliminating the need for successive estimation of these bounds by "bootstrapping". More recently, a method has been introduced which allows estimates of the analyticity radius in terms of the L^p (including L^∞) norm of the initial data [GK98].

In addition to being analytic in space, solutions of the KS equation are also time analytic, and again the radius of analyticity may be estimated in terms of L^2 [JKT90] or L^∞ [GK97] bounds.

In every sense, solutions of the KS equation (1.1) are thus "nice", sufficiently smooth and well-behaved for any purpose. For the remainder of this thesis, we use these results as justification not to worry about convergence or smoothness in space and time of our numerical results. In particular, provided we retain sufficiently many modes in our numerical integrations, the small scales are well-behaved; this is extensively borne out by our numerical experiments.

Estimation of bounds

An important aspect of many of the above studies is the explicit estimation of the scaling of bounds—for the radius of the absorbing ball in L^2 or various Sobolev spaces, for the dimension of the attractor or the inertial manifold, for the number of determining modes, for the radius of the strip of analyticity—in terms of the bifurcation parameter L. This is especially interesting because theory has not yet caught up with experiment in this case; numerical evidence makes a definite prediction for the scaling, but the best theoretical estimates give worse bounds.

We recall that the number of linearly unstable Fourier modes is proportional to L. Since the attractor (and hence the inertial manifold) must contain the unstable manifold of the zero solution, the attractor and inertial manifold dimensions cannot be less than $\mathcal{O}(L)$. This linear scaling is conjectured to hold. For instance, Manneville [Man85] has numerically computed the fractal dimension of the dynamics for some large values of L, and found it to be proportional to L (see also Sec. 4.3.2).

More generally, for large L the dynamics appears to be *extensive* (see Sec. 1.3.1 below): its local properties are asymptotically independent of L. We shall discuss and present much numerical evidence for this in Ch. 4. The simplest property is probably a bound on $|u(x,t)|$; all analytically

approximated and numerically computed solutions are uniformly bounded independent of L (see Fig. 4.1). However, a uniform L^∞ bound has not yet been proved in general, although some special cases have been shown, such as a uniform bound for all stationary solutions [Mic86] and for solutions on the attractor near stationary solutions [Gru00].

An L-independent bound $\|u\|_\infty$ for the amplitude of u implies that the L^2 norm (or energy), defined by

$$\|u(\cdot, t)\|^2 \stackrel{\text{def}}{=} \int_0^L u^2(x', t) \, dx', \tag{1.10}$$

is proportional to L; or equivalently, it implies the existence of a finite energy density $\varepsilon(t) \stackrel{\text{def}}{=} E(t)/L \stackrel{\text{def}}{=} (1/L) \int_0^L u^2(x', t) \, dx'$ in the large system limit. The radius ρ_0 of the absorbing ball in L^2 turns out to be the most fundamental bound, as the others may be derived from it; so the most attention has been devoted to improving this bound to its "optimal" value of $\mathcal{O}(L^{1/2})$.[†] The earliest results of Nicolaenko *et al.* [NST85], which were valid only for odd solutions, gave the scaling $\rho_0 = \mathcal{O}(L^{5/2})$, which implied bounds on the dimension of the attractor, and an inertial manifold of dimension $\mathcal{O}(L^{7/2})$ [FNST88]. The restriction to odd solutions has been lifted [Il'92, CEES93a, Goo94], and Collet *et al.* [CEES93a] were able to improve the bound to $\rho_0 = \mathcal{O}(L^{8/5})$.

Based on this improvement, better estimates for the size of inertial manifolds in various Sobolev spaces have been obtained [Rob94, TW94]. The best estimate we know of for inertial manifolds in L^2 currently stands at $\mathcal{O}(L^{1.64}(\ln L)^{0.2})$ [TW94], some way from the expected optimal value of $\mathcal{O}(L)$. The $\mathcal{O}(L^{51/40})$ estimate for the attractor dimension [CEES93a], currently the best available, is somewhat closer to the optimal $\mathcal{O}(L)$ scaling. A similar situation pertains to the radius of the strip of analyticity, or the rate of exponential decay of Fourier modes; it is conjectured, but not yet proved rigorously, that this decay is L-independent [CEES93b]; see also [GK98, Gru00] and Sec. 2.3.1.

The above discussion summarizes some highlights concerning the analysis of the general KS equation (1.1) for periodic boundary conditions (some similar results hold for Dirichlet conditions [NST85]).[‡] With the exception of the analysis in Ch. 2, we shall largely take these results as background material for this thesis, without using them explicitly.

1.2.3 Notes on bifurcations and special solutions

The KS equation for relatively small lengths L and few linearly unstable modes displays a complex and fascinating bifurcation behavior. At $L = n \cdot 2\pi$, the nth Fourier mode $\hat{u}_q$, $q = 2\pi n/L$ bifurcates from the trivial zero solution in a pitchfork bifurcation. As n increases, these modes interact through the nonlinear term to give rise to an intricate sequence of secondary bifurcations. These were first described systematically by Hyman *et al.* [HN86, HNZ86], and have since been subject to detailed studies. What early investigators found particularly striking was the apparent low-dimensionality of the behavior of the PDE: many of the observed bifurcations strongly resembled those seen in (low) finite-dimensional dynamical systems. This motivated the work on inertial manifolds mentioned above, by which the KS dynamics was, in fact, shown to be rigorously finite-dimensional.

Instead of reviewing the observed bifurcation sequence, we briefly highlight a few of the main themes of the research, and then mention some of the fundamental "simple" solutions observed for

---

[†]For this reason, the L^2 bound is the main focus of our attention when we consider the damped KS equation in Ch. 2.

[‡]There are many other analytical results which we do not review here, including more detailed analyses of special families of solutions (for instance [Mic86]), and Painlevé-type analyses of the integrability of the KS equation.

small L. Some aspects which have received attention, with some pertinent references, include:[†]

- The importance of symmetries, especially equivariance with respect to $O(2)$ and its subgroups, in producing the observed bifurcation behavior [KNS90, AGH89, AGL92, ALT93, AL93, SK93, MHEB95].

- The sensitivity of the details of the bifurcation diagram, especially the order of occurrence of some bifurcations near each other, on the specific computational scheme [JKT90, ALT93].

- The use of scaling relations to predict parts of the bifurcation structure [SKN88, Bro92].

- The development of numerical algorithms and software to facilitate computational investigation of details of the bifurcation picture, including visualization of manifolds [FJKT94, FJ95, WS95, Joh98].

The following classes of elementary solutions are particularly important for the understanding of the KS dynamics:

1. **Stationary solutions:** The most basic solutions are the time-independent spatial patterns, $u(x,t) = u(x)$; observe that for each spatial structure $u(x)$, there is a whole circle of such steady states $u(x + \delta x)$ which one finds by acting on a representative $u(x)$ by the symmetry group $O(2)$. Fundamental studies, showing that this family of solutions is remarkably complicated, include the analytical and numerical work of Michelson [Mic86], and the extensive study of the bifurcating branches in [GK88].

   The *cellular*, or *roll*, solutions (Fig. 1.1(a)) form the backbone to the spatial structure of KS solutions (see also Sec. 1.3.1 below). The *N-modal* or *N-cell* state consists of solutions with periodicity L/N, which lie on the branch bifurcating from the trivial solution at $L = N \cdot 2\pi$, and which live in the invariant subspace of the dynamics $\mathbb{Z}_N$ mentioned previously. These cellular solutions $U_N(x)$ typically have most of their energy concentrated in the Nth Fourier mode, and their Fourier expansions consist only of multiples of wave number $q_N \overset{\text{def}}{=} 2\pi N/L$, with exponentially decaying amplitude [HNZ86]; up to a translation in x, these solutions may be written as

   $$U_N(x) = a_1 \cos(q_N x) + \varepsilon a_2 \cos(2q_N x) + \varepsilon^2 a_3 \cos(3q_N x) + \ldots$$
   $$= \sum_k a_k \varepsilon^{k-1} \cos\left(\frac{2\pi N k}{L}\right). \tag{1.11}$$

   The most stable N-modal states are those with N near $L/2\pi\sqrt{2}$, which corresponds to maintaining a preferred separation between peaks as close as possible to $l_0 = 2\pi\sqrt{2}$. We shall see later that the complex dynamics for large L is related to persistent creation and annihilation of cells to maintain this characteristic spacing. The stability of these N-cell states to large wavelength perturbations has been studied extensively using multiscale homogenization methods by Frisch, She and Thual [SFT85, FST86]; work extended recently in [EW96].

   Another interesting stationary solution is the *strange fixed point* [HNZ86] (or *giant state* [GK88]). In fact, there are several of these, a "zoo of strange hyperbolic fixed points" [HNZ86]. Their distinguishing feature is that unlike the cellular states they do not have

---

[†]Of course, most of the analytical and numerical concepts and techniques relevant to the KS equation were first developed in the context of other systems; we review here only works specifically on the KS equation.
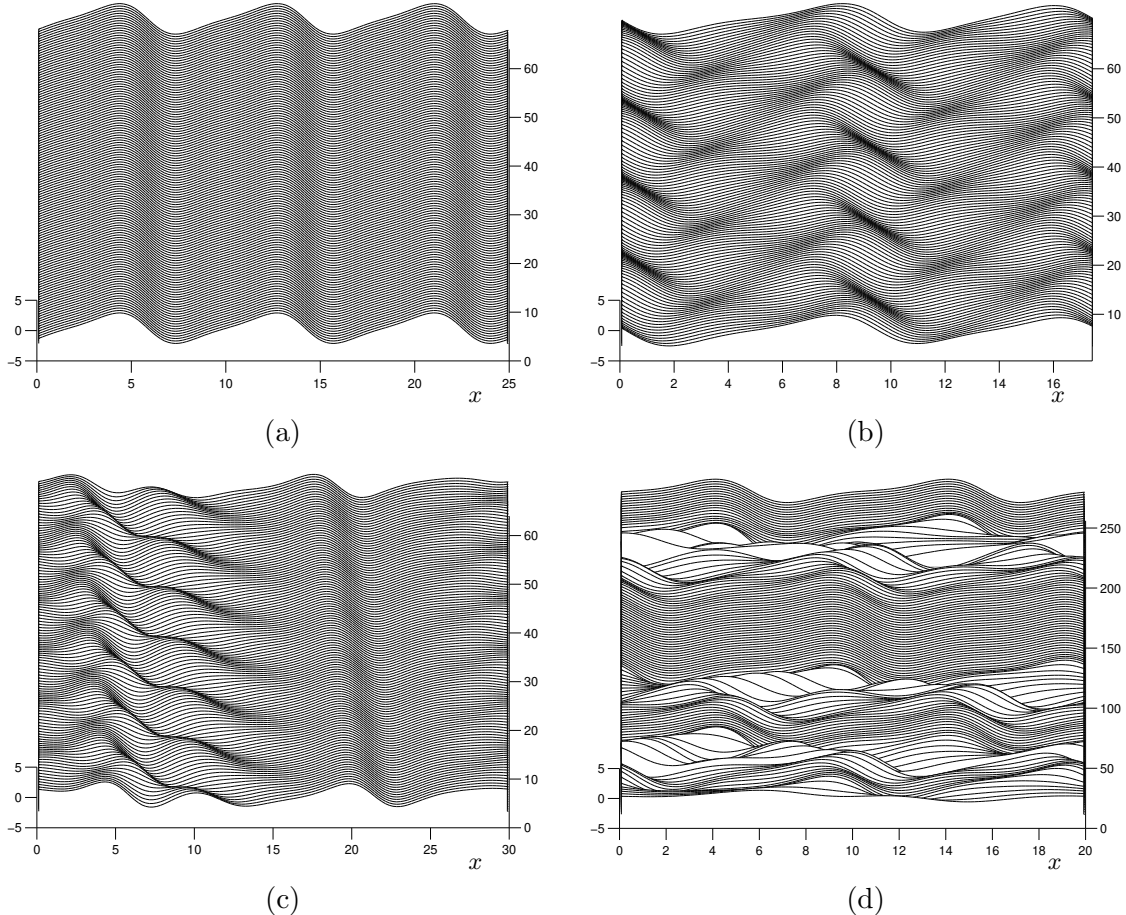
Figure 1.1: Elementary solutions observed in small systems; compare the gray-scale visualizations of Fig. 6.7 and Fig. 6.8 (containing four copies of each of these systems). (a) Cellular stationary solution for $L = 25$. (b) Time-periodic standing wave for $L = 17.5$. (c) Modulated traveling wave bifurcating from the strange fixed point, for $L = 30$. (d) Heteroclinic cycle for $L = 20$.

a dominant Fourier mode, instead having a broad energy spectrum with significant amplitudes in all unstable Fourier modes. This characteristic has made them popular as a test case for alternatives to Fourier methods for capturing dynamical and bifurcation behavior in a low-dimensional system; see [KA92, CS97] and Sec. 1.4.1 below. Fig. 1.1(c) shows a modulated traveling wave which has bifurcated off the first strange fixed point, and carries the same spatial structure.[†]

2. **Time-periodic solutions:** Solutions which vary periodically in time, $u(x,t) = u(x, t + T)$, can be divided into two kinds [KA92].

   By spatial periodicity, *traveling waves* (or *rotating waves* [KNS90]) satisfying $u(x,t) = u(x - ct)$ have period $T = L/c$. These solutions translate through the domain at constant speed with an invariant spatial shape, and may arise from a steady state via a Hopf bifurcation to a drift along the group orbit of $SO(2)$, the translational symmetry group. By the Galilean

---

[†]The cross-section of Fig. 1.1(c) is in fact the spatial derivative of the strange fixed point profile frequently seen in the literature (for example [HNZ86, GK88, KA92, SK93]), which is that appropriate to (1.3).

invariance (1.9), they may be interpreted as a steady state with nonzero mean, in a frame moving at constant velocity. Thus they are frequently studied along with the steady states [Mic86, GK88], and extensive bifurcation studies show a range of interesting behaviors [KE92].

Standing waves are solutions in which the spatial pattern varies periodically in time. Again, these limit cycles are not isolated solutions, but form part of a family related by the translational symmetry $SO(2)$. A standing wave for $L = 17.5$ is seen in Fig. 1.1(b). On the basis of ideas that unstable periodic orbits form a skeleton for chaotic dynamics, and that solutions traverse the attractor, successively approaching such orbits closely (see [CAMV98]), many standing wave solutions have been computed for relatively large L [CCP97]; see also [ZG98].

3. **Modulated traveling waves:** These solutions, satisfying $u(x,t) = u(x+cT, t+T)$, combine the previous two types; they can be interpreted as a standing wave in a drifting frame, and form (a special class of) tori in phase space. The existence of modulated traveling wave solutions, due to a Hopf bifurcation from a branch of traveling waves, has been proved in the vicinity of $L = 4\pi$ by using center manifold techniques [AGH88, AGH89]. Their computation requires special techniques, and their bifurcation behavior in conjunction with the other elementary solutions leads to highly intricate bifurcation diagrams [Bro92, BK96]. Fig. 1.1(c) shows a modulated traveling wave formed via a secondary Hopf bifurcation from a strange fixed point.

4. **Heteroclinic cycles:** Such solutions consist of a connection in phase space between two saddles, in the simplest case between two symmetry-related cellular solutions. The evolution of such *pulsing waves* [KNS90] involves much time spent near one saddle solution, before a rapid transit to the neighborhood of the other; an example is shown in Fig. 1.1(d). *Homoclinic connections*, in which the system undergoes an excursion in phase space before returning to the same saddle state, are also possible. Heteroclinic cycles, which are generically unstable [GH83], are stabilized by the presence of $O(2)$ symmetry [AGH88]. For the KS equation with $L \approx 4\pi$, stable heteroclinic cycles connecting diametrically opposite points on a circle of equilibria have been shown to exist due to the symmetry [AGH89, KNS90]. The bifurcations of heteroclinic connections have recently been studied in more detail [PDM97, Joh98].

There are many other features of the KS bifurcation picture, some previously unobserved elsewhere, which have been studied in great depth; this system has proved to be a treasure trove for interesting bifurcations. They include strong numerical evidence for various routes to chaos and dynamics associated with chaos [GH83], including a Feigenbaum period doubling cascade [SP91, SP96], Šil'nikov connections and their associated intricate dynamics [KE92, Joh98], and crises of chaos [HNZ86].

1.3 Spatiotemporal chaos

After passing through a succession of ordered and more complex states as L increases, including various intermediate chaotic attractors which destabilize after a window of stability, eventually we reach a state of persistent disorder for (almost) all L [HNZ86]. For sufficiently large L (beyond about $L = 50$ or 60) there is strong numerical evidence that the "simple" solutions all become unstable to an (apparently unique) spatiotemporally chaotic attractor.

In this thesis, we are mainly interested in this regime of *spatiotemporal chaos* (STC). There has been much recent interest in understanding and characterizing this state in different systems, and it has been the subject of numerous theoretical, numerical and mathematical studies. Examples of

systems that have been investigated include the complex Ginzburg-Landau and Swift-Hohenberg partial differential equations, which are closely related to the KS equation; spatially discrete models such as coupled map lattices; and experimental systems including Rayleigh-Bénard convection and the Faraday experiment. The goals of the investigations include understanding the observed patterns and the bifurcations leading to the STC state, deducing relevant diagnostics such as length scales, and obtaining a theoretical understanding using techniques such as those of statistical mechanics. In Ch. 4 we discuss many of these issues in the context of characterizing the STC state for the KS equation. We shall not review the general case further here, referring to reviews such as the earlier ones of Manneville [Man90] and Cross and Hohenberg [CH93], and the more recent discussion of Greenside [Gre98].

Relation to fluid turbulence The common alternative designation of "weak turbulence" for spatiotemporal chaos indicates a popular motivation for these studies, apart from their intrinsic interest; namely the desire for a deeper understanding of fluid turbulence (see [Fri95] for a recent introduction), through the study of simpler model systems. Indeed, many of the techniques used for the study of the Navier-Stokes equations have also been applied to the KS equation. However, one should note the distinction between "weak" or "soft" turbulence, involving spatiotemporally complex behavior in which there are no major excursions from space and time averages, and "strong" or "hard" turbulence, subject to large intermittent excursions from the average behavior. In this context, the "phase turbulence" in the KS equation corresponds to soft, or weak turbulence, in contrast to the situation for the Navier-Stokes equation. This point has been clarified in the context of the complex Ginzburg-Landau equation, in which both types of turbulence are expected to occur [BCDGG90]. While understanding of the KS equation may provide new techniques or insights, one should therefore not expect direct relevance of results on the KS equation for true turbulence.

1.3.1 STC for the KS equation

The main focus of this thesis is the study of the KS equation in the STC regime, where the chaotic behavior is indicated by, for instance, a finite density of positive Lyapunov exponents [Man85]. For most of our investigations, we choose for our bifurcation parameter the length $L = 100$, for which a typical evolution is shown in Fig. 1.2. In (a) we show cross-sections at different times for a solution of the KS equation (1.1) on the STC attractor; the gray-scale view in (b) shows the same evolution, highlighting features of the dynamics more clearly. Lighter shades of gray represent larger (more positive) pointwise values of $u(x,t)$, and the lightest regions represent the "peaks"; the shading is chosen so that white and black indicate the limits of $u = +3.5$ and $u = -3.5$, respectively, as solutions are observed to remain within these bounds for all x and t (see Fig. 4.1(a)). We shall use the representation of Fig. 1.2(b) throughout this thesis to show the space-time evolution of our models.

The transition to STC The transition to the STC state in the KS equation is not well-characterized yet.[†] As discussed above, detailed information is known about the complicated bifurcation structure (see for instance [BK96]); while indicating many of the special solutions which are known to exist, the bifurcation analyses do not provide much transparently useful information about the eventual STC attractor, and indeed, the multiplicity of concurrent complex dynamical phenomena tends to obscure the essential issues.

[†]In fact, there may be more than one transition, if additional parameters are permitted; for instance, inclusion of a damping term as in Ch. 2 leads to a postulated route to STC via "spatiotemporal intermittency" [CM87].

(a)   (b)
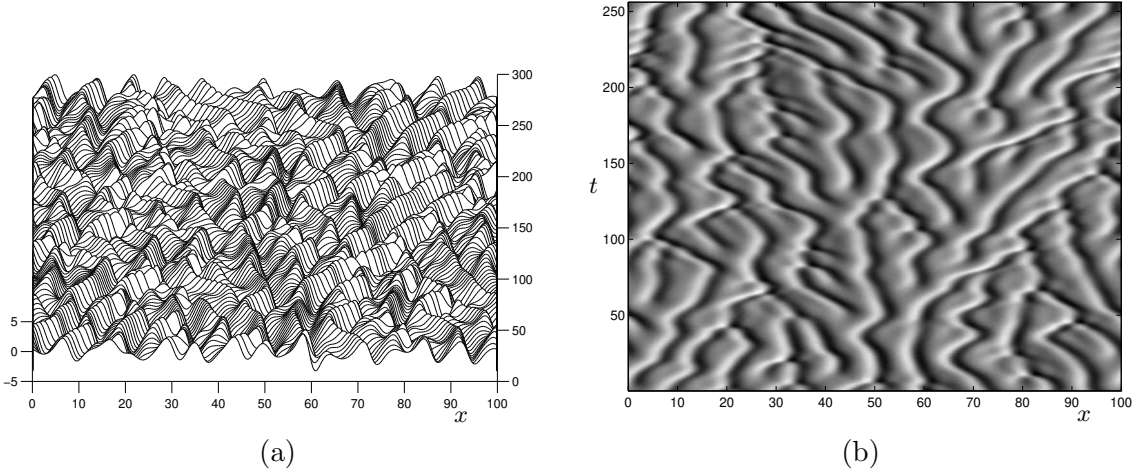
Figure 1.2: (a) A solution of the KS equation (1.1) on the spatiotemporally chaotic attractor, for $L = 100$, and covering 256 time units separated by $\Delta t = 1$ (beginning at $t \approx 1.0 \times 10^5$). (b) Grayscale view of the evolution in (a), clearly showing the typical cellular structure, traveling cells, and creation and annihilation of peaks.

To overcome this problem, recently the transition to STC was discussed in detail by Goren *et al.* [GEP98] for a simpler model. They chose their system to retain the essential symmetries of the KS equation, but to have a much simpler linear part (with only two unstable modes), so that it could be more fully described. They were able to use a symbolic language to characterize stationary solutions, including spatially chaotic solutions; these stationary states organize the dynamics. The space-time chaos is then understood qualitatively in terms of orbits in function space that successively visit different words in the language, in a random fashion. Unfortunately, due to the complexity of the bifurcation diagram, the prospect of a similar description for the KS equation with increasing L appears unlikely.

The STC attractor   Well within the STC regime for the KS equation, consistent with previous studies and with our numerical findings, we assume the existence of a unique topologically transitive attractor. We obtain our statistical results by invoking ergodicity to replace averages on the attractor by time averages on a single solution trajectory—taking care, of course, to confirm that our results are independent of initial conditions, and that the integration time is long enough for the statistics to converge acceptably.[†] Because of sensitive dependence on initial conditions, comparison of individual solutions for different initial data—or even (after sufficiently long time) different integration schemes or parameters—yields little that is useful; we mainly seek qualitative and statistical information.

The thermodynamic limit   Visual inspection, and numerically obtained statistics discussed in depth in Ch. 4 and also (partially) obtained by other workers, strongly suggest that the local dynamics is invariant under changes in system size, for sufficiently large L. For example, one may compare the integration of the KS equation (1.1) for $L = 400$ shown in Fig. 1.3 with Fig. 1.2(b).

[†]For our numerical experiments of Sec. 4.3.3, Ch. 5 and Ch. 6, while taking care to avoid special initial data, we invoke ergodicity to justify the examination of only one or a few simulations for each model to deduce their qualitative behavior and estimates of their statistics.
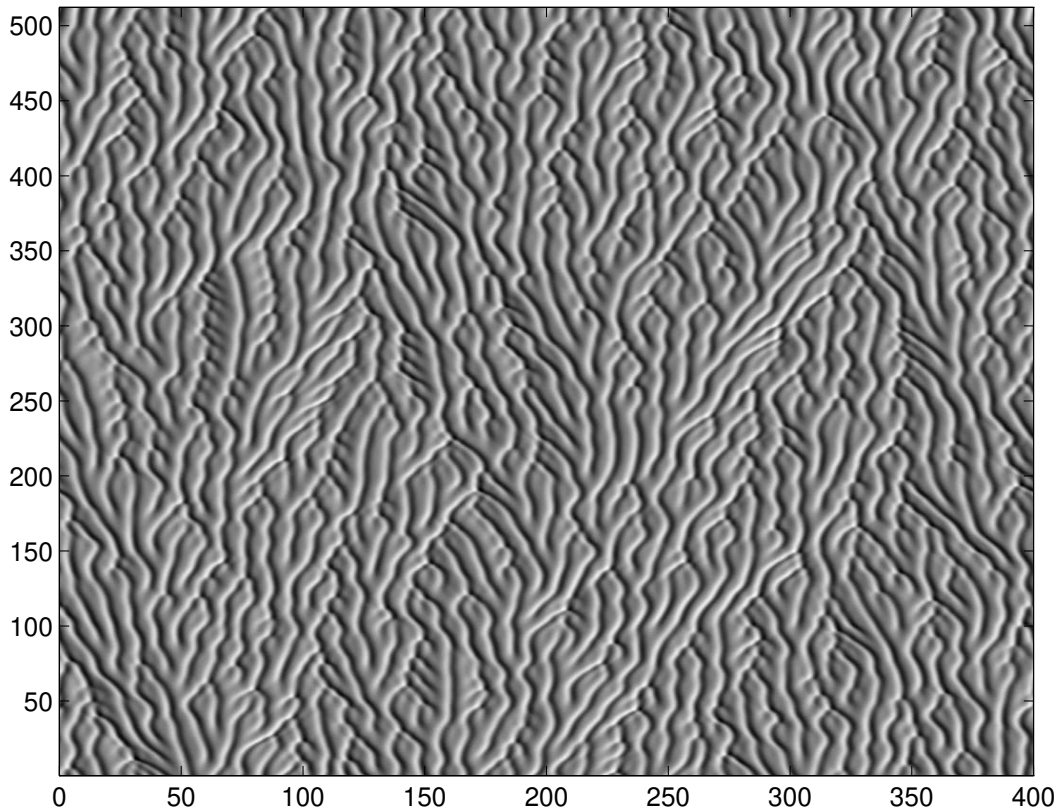
Figure 1.3: Visualization of space-time structure of a solution to the KS equation (1.1) for $L = 400$.

This motivates the study of the *"thermodynamic limit"* for infinitely large system size [CH93, Gre98], with the hope of applying some appropriate tools from thermodynamics and statistical mechanics to this problem [HS89]. In the thermodynamic interpretation, it is natural to consider two kinds of quantities [Gre98]: namely *extensive* quantities (such as the energy) whose values are (asymptotically) proportional to L, and *intensive* (or local) quantities (for instance, densities of extensive quantities) whose values are independent of the system size. A common interpretation of the thermodynamic limit [LL80] sees the large system as being composed of interacting subsystems; in this view, extensive (proportional to the number of subsystems) and intensive (characteristic of a subsystem) quantities arise if interactions are *spatially localized*, so that the subsystems may be considered statistically independent, and approximately uncorrelated for short enough times.

This interpretation is standard and unsurprising in thermodynamics. However, the prevalence and significance of intensive and extensive properties in a nonequilibrium system displaying spatiotemporal (deterministic) chaos is by no means well-established [Gre98]. In particular, as we have seen above in Sec. 1.2.2, certain analytical results on extensive and intensive properties which might seem rigorously provable have so far remained elusive. For instance, the uniform L^∞ bound on the solution values $u(x,t)$, or the existence of a finite energy density—that is, that the bound ρ_0 on the L^2 norm is expected to be proportional to $L^{1/2}$—have not yet been shown in general.

15
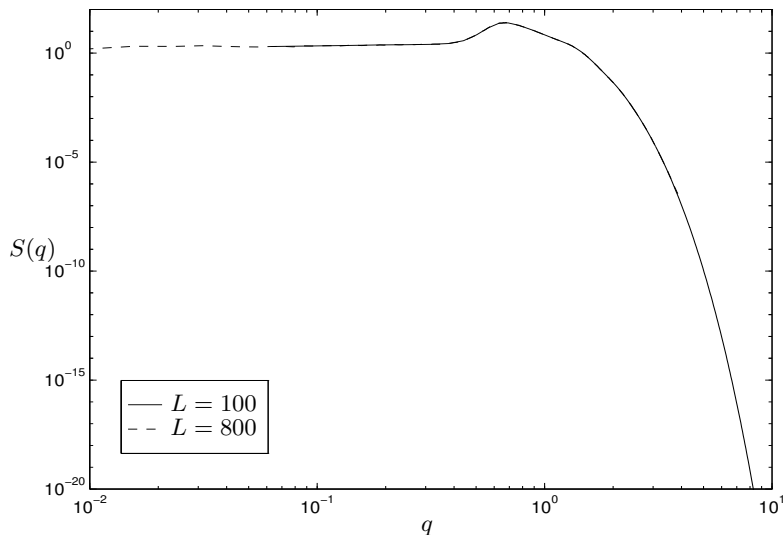
Figure 1.4: Rescaled power spectrum $S(q)$, for $L = 100$ and $L = 800$.

The power spectrum in the STC regime

The conjectured existence of a finite energy density is consistent with the calculated energy (or power) spectrum (Fig. 1.4), which is well known [FY77, PPP84, Toh87]. Here, we define the normalized spectral density by

$$S(q) \stackrel{\text{def}}{=} L\langle |\hat{u}_q|^2 \rangle, \tag{1.12}$$

where the ensemble average $\langle \cdot \rangle \stackrel{\text{def}}{=} \langle \cdot \rangle_t$ is computed via a time average for a long-time integration on the STC attractor, invoking ergodicity. As is apparent in Fig. 1.4, $S(q)$ appears to be independent of L in the complex regime, indicating an invariant distribution of energy among the Fourier modes in the thermodynamic limit.

The power spectrum contains the most basic features for the understanding of the KS statistics and dynamics in the STC state, and we shall frequently refer to it throughout this thesis. Many of its properties have been accounted for [PPP84], and its general shape modeled [Toh87]; here is a brief summary: The exponential tail is due to the strong dissipation at small scales, corresponding to the exponential decay of the Fourier modes of an analytic function. There is a pronounced peak near $q = q_0 = 1/\sqrt{2}$, corresponding to a characteristic length $l_m \approx l_0 = 2\pi\sqrt{2} \approx 8.886$; that is, it turns out that the most linearly unstable mode *approximately* coincides with the peak of the energy spectrum in the nonlinear system (but see Sec. 4.1.2). For low q, there is a shoulder which flattens out as $q \to 0$, reminiscent of a thermodynamic regime with equipartition of energy. We shall give a more detailed characterization and discussion of the different regions of the spectrum in Sec. 4.1.2; see Fig. 4.7 below.

1.3.2 "Typical" local dynamics

In the gray-scale representation of the KS dynamics in Fig. 1.2 we observe structures at the characteristic scale $\sim l_0$, with spatially localized dynamics. It is difficult to give an unequivocal quantitative characterization of these structures, but their existence is strongly suggested by

the visualization, and we shall frequently refer to these structures—*peaks*, or *cells*, or *coherent structures*—throughout this thesis.

It has been argued that the understanding of the spatiotemporal complexity, and in particular the large-scale stochasticity, should be addressed in terms of the interactions of cells [FST86, Shr86, HS89, RK95, CH95]. Visual inspection, as well as the power spectrum, indicates that *locally*, the system is in a cellular state most of the time; there is fairly well-defined structure at scales of order l_0, approximately at the typical wavelength. Decorrelations and disorder occur only at much larger scales. One can draw such conclusions by writing down and studying equations for the slow evolution of symmetry-breaking perturbations from the cellular state [Shr86].

Persistent cell dynamics lead to STC A heuristic explanation for the persistent distortions of the cellular state is straightforward [CH95]: Locally, cells are stretched or compressed relative to their preferred wavelength. Too much stretching, and there is room for a new cell to form, to compensate for the growth in the local wavelength; similarly, too much compression, and adjacent peaks collide to give a cell coalescence event. Cell creation and annihilation form space-time *topological defects*, corresponding to a discontinuous jump in the local phase of the cellular state.

For a large enough system, this leads to constant frustration; as collision or birth of coherent structures compensates for deviations of the local wavelength from its ideal value at one location, it becomes distorted more elsewhere. This gives a qualitative account of the persistent spatiotemporal chaos. A hydrodynamic theory for how these local cell interactions at the scale of the characteristic wavelength lead to large-scale stabilization has been implemented by Chow and Hwa [CH95]; and the effective dynamics at large scales is discussed further in Sec. 4.2.2 below. Note that the cell dynamics is an "emergent property", in that it arises from the interplay between the linear instability and the nonlinearity in a nontrivial way [RK95].

Spatially localized cell interactions For the purposes of the later discussion of this thesis, it is significant to notice that these *"typical events"* (motion and interaction of peaks, including cell creation and annihilation) occurring near a point x depend on only small spatial neighborhood of x, and appear to be affected by distant events only after a finite propagation time; such space localization will be discussed at length in Sec. 4.3. In addition, the typical events resemble those observed in the dynamics of small length systems (see Sec. 1.2.3). In addition to cellular states (Fig. 1.1(a)), the two small-L solutions whose space-time image recurs locally throughout the STC regime are

- local (modulated) traveling waves, in which the local wavelength is approximately maintained, for instance near $x = 40$, $t = 250$ of Fig. 1.2(b);

- local heteroclinic "events": cell creation and annihilation events, such as those near $x = 50$, $t = 130$ of Fig. 1.2(b), resemble the heteroclinic cycle of Fig. 1.1(d).

These observed similarities between local dynamics of the full system in the STC state, and the dynamics observed in some small systems, motivates the search for a short-length, low-dimensional description of local dynamics in the STC regime.

1.4 Low-dimensional models

There has been much effort in the last decade or so at understanding the dynamics and statistics of certain systems with complex spatiotemporal dynamics, including some fluid turbulent systems,

through the extraction of low-dimensional models which capture the most energetic and dynamically relevant modes, together with appropriate modeling of the neglected modes. We shall not attempt to review this work here, referring instead for an introduction and references to Berkooz *et al.* [BHL93], to the book by Holmes, Lumley and Berkooz [HLB96], or for a briefer introduction, to our review article [HLBMW97].

Identification of coherent structures For a variety of turbulent fluid flows, including incompressible boundary layers, circular jets, mixing layers, and the flow in a cylinder wake, flow visualizations or direct numerical simulations often indicate that a large fraction of the energy is contained in *coherent structures*, which may undergo complicated temporal interactions. For example, in the turbulent boundary layer, one observes streamwise vortices and low speed streaks. The idea of the *proper orthogonal decomposition* (POD), also known as the Karhunen-Loève (KL) decomposition, or principal component analysis, is to provide an unbiased estimator for these most energetic modes:

Given a, preferably large, data set of realizations of the flow, obtained via experiment or simulation, one extracts a set of basis functions (the POD or KL eigenmodes, or *empirical eigenfunctions*) successively by minimizing the average error, with respect to some chosen norm, between the data and its projection on a finite set of eigenmodes. In practice, this corresponds to finding the eigenvectors of the ensemble-averaged autocovariance matrix, the corresponding eigenvalues being the energy of the empirical eigenfunctions. This procedure gives rise to an orthonormal basis, and one can show that it is *optimal* in the sense that, relative to all other orthonormal bases for the same Hilbert space, for a given number of basis functions the POD modes capture the most energy, on average; see [BHL93, HLB96].

The empirical eigenfunctions efficiently capture the spatial structure of "typical" velocity fields, and thus provide a way to identify the "backbone" of a complex flow; they reveal the fundamental components whose interactions largely drive the turbulent dynamics. Applied in this manner, the POD is useful for *identification* of the major contributors to the flow.

Extraction of low-dimensional models Moreover, one can project the governing partial differential equations onto the POD eigenmodes to derive a *finite-dimensional model* for the dynamics. Having extracted a low-dimensional dynamical system, one can bring appropriate tools of dynamical systems theory to investigate the system, for instance to detect bifurcations, or the presence of various stationary or oscillatory solutions and their interactions. These methods are related to the (approximate) inertial manifold techniques mentioned earlier, but they are often practically applied in situations where the inertial manifold is not (yet) rigorously known to exist. This thus provides a systematic way of extracting *empirical* models in the absence of a complete theory.

As an example, in the study by Aubry *et al.* [AHLS88] in which this approach was introduced, POD modes for the turbulent boundary layer were extracted. A Galerkin projection of the Navier-Stokes equations onto these eigenfunctions, coupled with modeling of the neglected modes—including a Heisenberg eddy viscosity model and a noisy pressure forcing term to account for a missing boundary condition—yielded a low-dimensional dynamical system. Simulation and analysis of this dynamical system reproduced key features of the boundary layer dynamics; in particular, it led to an understanding of the burst/sweep cycle of the coherent structures in terms of heteroclinic connections stabilized by symmetry. Since this original study, many related investigations have occurred for fluid and other systems; some of these are summarized in [HLB96, HLBMW97].

1.4.1 The POD and related approaches in the KS equation

As discussed previously in Sec. 1.3.1, the observation of localized interactions of cells in the KS equation (Fig. 1.2) motivates the search for localized low-dimensional models in this case. Indeed, many of the previously reported low-dimensional analyses of the KS equation were motivated by the desire to test some of the ideas which arose in the fluid POD models in a simpler, one-dimensional system, which nevertheless displays complex spatiotemporal dynamics. These investigations included the examination of the effects of $(O(2))$ symmetry on bifurcations [AGH88], which led to the demonstration of the existence of modulated traveling waves and heteroclinic cycles for $L \approx 4\pi$ [AGH89].

Translation invariance: POD modes are Fourier modes   A fundamental fact in the application of the POD to the KS equation is that for periodic boundary conditions, *spatial homogeneity implies that the empirical eigenfunctions are Fourier modes*; for the straightforward derivation, see for instance [HLB96, HLBMW97]. The potential difficulty with this is that the Fourier basis is not spatially localized; each Fourier basis function (sine or cosine) is evenly supported on the entire domain, and so does not enable us to extract aspects of the dynamics which are due to spatially localized interactions. This is not a problem for low-dimensional studies for small parameter, when L is of the same order as l_0, in which case there are few interacting modes [AGH89]; Fourier modes succeed well in capturing the elementary cellular solutions, traveling and modulated traveling waves and heteroclinic cycles.

However, the Fourier basis does not do too well for more complex shapes at larger L; these include, in particular, the strange fixed point discussed earlier (see Fig. 1.1(c)), which has a broad power spectrum. This state and its associated bifurcations—a Hopf bifurcation to a standing wave, followed by another to a modulated traveling wave—have therefore been very popular for testing various ideas concerning the construction of low-dimensional localized models using modes other than the Fourier basis.

There have been a few attempts at obtaining appropriate spatially localized modes for the translationally invariant KS equation:

- For a *particular* bifurcation, one can extract POD eigenmodes in a neighborhood of the bifurcation point. If necessary, for traveling waves one can extend the POD via a template matching procedure to give a maximum fit at each time step, so that the eigenmodes travel with the wave. Comparison of the modes thus obtained then gives an indication of which eigenmode became unstable, and yields some insight into the bifurcation behavior. This approach has been implemented for understanding Hopf bifurcations near the strange fixed point [KAG91, KA92]. In these situations, of course, except for the traveling wave, the flow is non-ergodic in the direction of translational invariance; that is, of the whole group orbit of attractors equivalent by symmetry, a unique one is chosen at every realization.

- One can perform the POD analysis using a different norm to minimize the error (or maximize the "energy"), for example, an appropriately chosen weighted Sobolev norm. To obtain spatial localization, the procedure must again be implemented for a particular realization of a symmetry-breaking state. Such a method can sometimes allow one to reconstruct dynamics using fewer eigenmodes—for instance, the limit cycle at the strange fixed point required 19 POD eigenmodes for a stable simulation, but only seven Sobolev POD modes when weights were adjusted for optimum performance [Kir92]. This construction appears rather *ad hoc*, however, and eigenfunctions computed in the vicinity of a particular bifurcation do a poor job of capturing the behavior as the bifurcation parameter is varied [SK93].

- Another approach that has been proposed to extract the dominant features of the flow—and again, mainly tested on dynamics in the vicinity of the strange fixed point in the KS case—is the use of archetypes [SC96a, SC96b, CS97]. Given a data set, archetypes characterize its convex hull; each point in the data set is represented as a superposition of archetypes. Since this method is sensitive to outliers in the data, it is useful for the characterization of intermittent events. However, archetypes do not form an orthogonal basis, and hence they do not lend themselves to mathematical analysis, as one cannot systematically derive dynamical equations by projecting onto a set of archetypes. Due to this restriction, at present it seems that archetypes are mainly a descriptive tool for identifying characteristic structures in numerical or experimental data.

- It appears from the aforegoing that any basis which is optimized for the ergodic, hence translationally invariant, STC state of the KS equation must itself be translationally invariant, and hence not spatially localized. An alternative approach is thus to choose a basis, which has no *a priori* connection to the KS equation, but which breaks the symmetry and is localized as desired. This motivates the use of an orthonormal wavelet basis, introduced for the study of the KS equation in [BEH92, EBH93, MHEB95, EBH96]. After an analytical interlude in Ch. 2, this approach will form the basis for the remainder of this thesis; the wavelet method will be introduced with a discussion of some theoretical implications in Ch. 3, and form the foundation of the numerical studies and experiments of Ch. 4–6.

1.5   The contents and contributions of this thesis

In this thesis we develop methods to characterize and model spatiotemporal chaos, using the Kuramoto-Sivashinsky equation (1.1) as our test case and example. In this introductory Chapter, we have reviewed relevant previous work on the KS equation; we now give a brief outline of the remainder of this thesis, and highlight its major contributions. In summary, we employ analytical techniques, statistical analysis of long-time computations and experimental manipulation of the KS equation to obtain a detailed structural understanding of spatiotemporal chaos, and use our insights to motivate the construction of spatially localized models reproducing the dynamics of the full system.

In Ch. 2 we study some analytical issues for a generalized system, the "damped KS equation" (2.2), in which the Galilean invariance is broken by an additional linear term; this system has recently attracted increasing interest, as outlined in Sec. 2.3.4. We use the techniques of Collet *et al.* [CEES93a, CEES93b] to establish the important properties of dissipativity of the dynamics and analyticity of the solutions, for both odd and general periodic initial data; while the results of Sec. 2.1.1 have been obtained elsewhere [Zie95], the others are new. In the case where the additional term is destabilizing, we discover numerically and construct asymptotically a new explicit shock-like solution in Sec. 2.3.3, which has interesting implications for the search for a proof of extensivity in the KS equation. With the exception of the shock solution, whose form recurs in other contexts in some experiments of later Chapters, Ch. 2 is essentially independent of the rest of this thesis.

In Ch. 3, we establish the theoretical framework for much of the remainder. After reviewing relevant aspects of the wavelet decomposition and introducing our notation in Sec. 3.1, we recall fundamental aspects of the wavelet Galerkin projection of the KS equation in Sec. 3.2. Having established this necessary background, in Sec. 3.2.2 we continue with a thorough review of previous work by Elezgaray, Berkooz, Holmes and coworkers, who pioneered the use of wavelets for the study of the KS equation. This Section also serves as a preview for later Chapters, showing in detail how the investigations of this thesis relate to and extend previous studies. In Sec. 3.3, we

provide a theoretical foundation for many of our studies, and some previous ones, by considering the consequences of models constructed from spatially localized subsystems of the full wavelet hierarchy, and we systematically derive an effective equation for a local periodic model as a subsystem of a larger system. This theoretical Section may be read in conjunction with Ch. 6, as here the theory stimulated the experiments and *vice versa*.

We begin our numerical investigations in Ch. 4, with a statistical characterization of the STC state through data analysis of long-time computations. With these computations we obtain an improved understanding of the STC state, and establish a benchmark of "correct" statistics with which we can compare our experimental manipulations of Chs. 5 and 6. In Sec. 4.1, we review and extend known results on real and Fourier space properties, providing a detailed characterization of distributions, spectra and correlation times, as well as a reinterpretation of some previously published results. In Sec. 4.2, we find that a representation in a wavelet basis significantly clarifies the scale separation of the KS dynamics, in which we can clearly distinguish between the contributions of large, active and small scales. In particular, a review of previous work on an effective description for large-scale dynamics, in Sec. 4.2.2, motivates our introduction in Sec. 4.2.3 of a simplified stochastic model which simulates the large-scale behavior particularly well, and which we use in later experiments. In the last part of this Chapter, Sec. 4.3, we show how KS dynamics is localized in space, by discussing correlation lengths, including some new results, and the effects of boundary conditions. We then introduce an experiment in Sec. 4.3.3 in which we explicitly use the wavelet projection of the equation to cut interactions and estimate a dynamical interaction length.

Motivated by the resulting detailed characterization of the STC regime and the statistical distinctions between scales, in Ch. 5 we perform a novel and extensive series of experiments in which we manipulate the interactions between different wavelet levels, by eliminating modes, or imposing different kinds of forcing. Using this approach, which might profitably be extended to the investigation of other systems, we are able to obtain a fairly complete qualitative picture of how the spatiotemporally complex dynamics is built up, how different levels interact and how the system responds to disruptions such as variations in driving amplitude or time scale. In Sec. 5.3 we also obtain some interesting results concerning the possibility of synchronization or tracking.

Based on these understandings of characteristic interaction lengths and the relative contributions of different scales to the overall dynamics, in Ch. 6 we construct spatially localized models of relatively low dimension with the hope of robustly reproducing typical spatiotemporally complex behavior in a small system. Although the range of models studied is much more extensive than those of previous attempts, we still frequently observe behavior inconsistent with the full KS equation, also seen by previous investigators. However, we are able to harness the results of Chs. 4 and 5 to clarify qualitatively the reasons for these atypical dynamics. Armed with this understanding and with the theory of Sec. 3.3, we finally propose a low-dimensional periodic model with large-scale forcing which appears to reproduce the behavior of the STC regime very well, and suggest that further study of this model may be profitable to understand some of the origins of spatiotemporal chaos.

We conclude by reviewing our results and suggesting possible directions for future research. Some details are relegated to the Appendices: in App. A we review alternative formulations of the KS equation which have been used in the literature, while in App. B we describe our numerical techniques and derive some appropriate algorithms.

Chapter 2

The Damped KS Equation

This Chapter is somewhat different from the remainder of this thesis, both in the problem studied and in the approach. We consider possibly the simplest generalization of the KS equation (1.1), containing an additional linear term. For this system we show dissipativity and analyticity. The result is a straightforward generalization of work by Collet *et al.*, and parts have been previously derived by Ziegra. However, some aspects are quite interesting, and shed light on the difficulties that have been found in attempts to show extensivity of the KS equation—see Sec. 1.2.2. Furthermore, our results may be interpreted in terms of the effect of excessive or insufficient energy in the largest scales, which ties in with subsequent experimental results on disrupting the energy budget by modifying the KS equation in various ways.

While we show some results rigorously in other chapters as well, this Chapter is the only one in which we explicitly state theorems. We shall include discussion and a context for this problem in the light of recent work in Sec. 2.3.4 after deriving our results; we shall also speculate somewhat on implications for the KS equation. We shall not show the calculations in complete detail, as they are very similar to previous computations.

The stabilized KS equation

In this Chapter (only)[†], we write the KS equation in a rescaled form (A.11), which explicitly isolates the negative definite linear operator:

$$u_t = -(\partial_x^2 + 1)^2 u + \alpha u - u u_x; \qquad \alpha = 1.$$

In this form, we see immediately that the αu term on the right-hand-side is the source of the linear instability, at those modes for which it dominates the first, stable term. This provides an easy way to strengthen or weaken the instability, by modifying α. For $\alpha < 0$, one readily sees from the Fourier space formulation or energy estimates that the trivial zero solution is attractive, and $\limsup_{t \to \infty} \|u\| = 0$. We thus emphasize $\alpha \geq 0$ by setting $\alpha = \varepsilon^2$, so that our generalized KS equation is

$$u_t = -(\partial_x^2 + 1)^2 u + \varepsilon^2 u - u u_x; \tag{2.1}$$

or alternatively, for correspondence with (1.1),

$$u_t + u_{xxxx} + 2u_{xx} + (1 - \varepsilon^2)u + u u_x = 0. \tag{2.1'}$$

[†]We caution the reader that some of the notation in this Chapter is somewhat different from that used in the remainder of the thesis, for consistency with previous works we are using heavily, especially [CEES93a]. Any modifications will be announced as needed, and notation reverts back to that introduced in Ch. 1 at the end of this Chapter.

In concordance with previous works [EGG97, PE97], we shall refer to (2.1) as the *damped Kuramoto-Sivashinsky equation* (DKS equation), or alternatively, as the stabilized KS equation [MV94, BPRdlR98]. This nomenclature refers to the fact that, for $\varepsilon^2 < 1$, we have added an additional linear damping, or stabilizing, term to the KS equation. However, our notation and nomenclature may be misleading; for we impose no requirement on ε to be small, or even less than one. In fact, some of our most interesting results arise for $\varepsilon^2 > 1$ (see Sec. 2.3.3), in which case we have added a *destabilizing* term, or negative damping. Nevertheless, for convenience we shall continue to refer to (2.1′) as the DKS equation, for general ε.

To simplify notation, we introduce here the linear operators

$$\mathcal{L}_0 \stackrel{\text{def}}{=} -\partial_x^4 - 2\partial_x^2, \qquad \mathcal{L} \stackrel{\text{def}}{=} \mathcal{L}_0 - (1 - \varepsilon^2) = -\partial_x^4 - 2\partial_x^2 - (1 - \varepsilon^2),$$

so that in this notation the DKS equation is

$$\partial_t u = \mathcal{L}u - u\partial_x u. \tag{2.2}$$

We impose periodic boundary conditions on a domain of length L; to simplify the analysis, it is convenient to work in this Chapter on the interval $\Omega \stackrel{\text{def}}{=} [-L/2, L/2]$, instead of on $[0, L]$ as in the remainder of this thesis; in particular, all integrals are over $[-L/2, L/2]$, unless otherwise stated. We define $\|\cdot\|$ to be the norm on $L^2(\Omega) = L^2([-L/2, L/2])$.[†]

Fourier formulation   We write the Fourier decomposition here as

$$u(x, t) \stackrel{\text{def}}{=} \mathrm{i} \sum_n u_n(t)\mathrm{e}^{\mathrm{i}n\bar{q}x}, \tag{2.3}$$

where $\bar{q} \stackrel{\text{def}}{=} 2\pi/L$, and by comparison with the previous notation introduced in (1.4), we have $u_n = \hat{u}_q$ for $q = n\bar{q}$ (modulo the rescaling needed from (1.1) to (2.1′)). We shall assume throughout that $L \geq 2\pi$, that is, $\bar{q} \geq 1$, since otherwise all modes are damped and all initial data converge to zero (in the space L^2). Writing (2.2) in Fourier space (compare (1.5)), we readily find the linear dispersion relation $\omega(q) = \varepsilon^2 - (1 - q^2)^2$, or $\omega(n\bar{q}) = \varepsilon^2 - 1 + 2(n\bar{q})^2 - (n\bar{q})^4$. In particular, the mean $m(t) \stackrel{\text{def}}{=} \int_{-L/2}^{L/2} u(x', t)\,dx'$ evolves as (see (1.2))

$$\frac{dm}{dt} = (\varepsilon^2 - 1)m. \tag{2.4}$$

That is, for $\varepsilon^2 < 1$ the mean decays, for the pure KS equation $\varepsilon^2 = 1$ it is conserved, and for $\varepsilon^2 > 1$ the mean grows exponentially. *A priori*, therefore, we can only expect to get an absorbing ball in L^2 for $\varepsilon^2 < 1$ [MS95]. However, by (2.4) the damped KS equation conserves the property of vanishing mean, so provided we only consider initial conditions $u_0(x)$ with mean zero,[‡] then we need not fear blowup of the mean even for $\varepsilon^2 > 1$. Henceforth, therefore, we restrict ourselves

---

[†]At this point, we warn the reader about a potential source of confusion in our nomenclature which is particularly apparent here, namely the use of L to refer both to the Hilbert space L^2 of (mean zero) square-integrable functions, and to the length L of the spatial domain on which we are solving the KS or DKS equation. However, which of these two meanings is appropriate is always clear from the context, and we shall retain this notation without fear of ambiguity.

[‡]We have used u_0 in two senses: By the notation of (2.3), u_0 can refer to the zeroth Fourier mode, or mean. However, we set the mean to zero for the remainder of this Chapter (indeed, throughout the thesis), and without fear of confusion use $u_0(x)$ to indicate the initial data.

to zero mean functions only, and consider solutions in the class of real, L-periodic functions with vanishing mean,

$$\mathcal{P}_L^0 \stackrel{\text{def}}{=} L_{per}^2([-L/2, L/2]) \stackrel{\text{def}}{=} \left\{ u : u(x + L) = u(x), \int_{-L/2}^{L/2} u(x)\, dx = 0 \right\}.$$

2.1 Dissipativity: The antisymmetric case

In this Section and the next, we establish the dissipativity of the DKS equation. This is a rather straightforward extension of the results for the "pure" KS equation, $\varepsilon^2 = 1$, reported in the important paper of Collet, Eckmann, Epstein and Stubbe [CEES93a]. We retain their notation, with some minor obvious deviations, and also retain the main features and order of their proof, there being little reason to modify it. Thus we do not give all details of the calculation here, instead referring the reader to [CEES93a] as needed.

We note that the dissipativity for the DKS equation for $\varepsilon^2 \in (0, \frac{1}{4})$ and odd $u(x, t)$ has previously shown by Ziegra [Zie95]. Our computations in Sec. 2.1.1 concerning the antisymmetric case for $\varepsilon^2 \leq 1$ are based on his, with minor changes, mainly to ensure that the bounds are uniformly valid over the entire range $\varepsilon^2 \in (0, 1]$. Thus we also refer the reader to [Zie95] to fill in missing details. The extensions to $\varepsilon^2 \geq 1$ in Sec. 2.1.2, and to general periodic (asymmetric) solutions in Sec. 2.2, have not previously been reported.

Evolution equation for the antisymmetric case

We consider first the space of odd periodic functions on $[-L/2, L/2]$:

$$\mathcal{A}_L \stackrel{\text{def}}{=} \{ u : u(x + L) = u(x), u(x) = -u(-x) \}.$$

Note that these functions automatically have vanishing mean, so $\mathcal{A}_L \subset \mathcal{P}_L^0$; also, $\mathcal{A}_L$ is invariant under the evolution (2.2)—see (1.8). For $u(x, t) \in \mathcal{A}_L$, we set

$$u(x, t) = v(x, t) + \phi(x), \qquad v, \ \phi \in \mathcal{A}_L.$$

This expression defines the *comparison function* $\phi(x)$: It was a fundamental realization of Nicolaenko, Scheurer and Temam [NST85] that while standard energy methods to establish dissipativity appear to fail, one can show the existence of a suitably chosen function ϕ, itself bounded, so that the L^2 norm of the difference v between u and ϕ remains bounded. Our construction of the comparison function is based on that of Collet *et al.* [CEES93a] (see also [Joh98] for a discussion of both approaches for a slightly different problem).

As in [CEES93a, Zie95], it is straightforward to write down an equation for $\partial_t v$; multiplying this by v and integrating by parts, we obtain an evolution equation for the L^2 norm $\|v\|^2 \stackrel{\text{def}}{=} \int v^2$ (we recall that all integrals are over $[-L/2, L/2]$; $\int V \stackrel{\text{def}}{=} \int_{-L/2}^{L/2} V(x', \cdot)\, dx'$):

$$\frac{1}{2} \partial_t \|v\|^2 = -(v, v)_{\phi/2} - (v, \phi)_\phi. \tag{2.5}$$

Here the bilinear form $(\cdot, \cdot)_{\gamma\phi}$ is defined, for sufficiently smooth $v_1,\ v_2$ (for instance, in the Sobolev space $H_{per}^2(\Omega)$) as

$$(v_1, v_2)_{\gamma\phi} \stackrel{\text{def}}{=} \int v_1'' v_2'' - 2 \int v_1' v_2' + (1 - \varepsilon^2) \int v_1 v_2 + \gamma \int v_1 v_2 \phi', \qquad \gamma \in \mathbb{R};$$

for functions in H_{per}^4, this definition is equivalent to

$$(v_1, v_2)_{\gamma\phi} = -\int v_1(\mathcal{L} - \gamma\phi')v_2.$$

We also note for later reference that the bilinear form $(\cdot, \cdot)_{\gamma\phi}$ defines an inner product and satisfies the Cauchy-Schwarz inequality, from which we may deduce a Young's inequality,[†]

$$(v_1, v_2)_{\gamma\phi} \le \frac{\epsilon}{2}(v_1, v_1)_{\gamma\phi} + \frac{1}{2\epsilon}(v_2, v_2)_{\gamma\phi}, \quad \epsilon > 0. \tag{2.6}$$

Since the subsequent treatments for $\varepsilon^2 \le 1$ and $\varepsilon^2 \ge 1$ are slightly different, we consider them separately. In both cases, our results reduce to those of Collet *et al.* [CEES93a] for the "pure KS equation" for $\varepsilon^2 = 1$. We observe that, in the search for the best bounds, for $\varepsilon^2 \le 1$ we would prefer more powers of ε in the final bound, while for $\varepsilon^2 \ge 1$ we prefer fewer; this motivates our computations.

2.1.1 The stabilized odd case, $\varepsilon^2 \le 1$

Following [CEES93a], we define the quadratic forms[‡]

$$R_{\gamma\phi}(u) \stackrel{\text{def}}{=} (u, u)_{\gamma\phi} = \int (u'')^2 - 2\int (u')^2 + (1 - \varepsilon^2)\int u^2 + \gamma\int u^2\phi', \tag{2.7}$$

$$Q(u) \stackrel{\text{def}}{=} \frac{\varepsilon^2}{4}\left(\int (u'')^2 + \int u^2\right), \tag{2.8}$$

and observe that $R_{\gamma\phi}(\phi) = R_0(\phi)$. This allows us to obtain the result [Zie95]:

Proposition 1 *There are constants c_1, c_2 so that the following holds for all $L > 0$: There is a function $\phi = \phi(L, \varepsilon) \in \mathcal{A}_L$ so that for all $0 < \varepsilon \le 1$, all $\gamma \in [1/4, 1]$ and all $v \in \mathcal{A}_L$,*

$$R_{\gamma\phi}(v) \ge Q(v), \tag{2.9}$$

$$R_{\gamma\phi}(\phi) = R_0(\phi) \le c_1\varepsilon^{26/5}L^{16/5} + c_2(1 - \varepsilon^2)\varepsilon^4 L^3. \tag{2.10}$$

Note that the last term, containing $(1 - \varepsilon^2)$, vanishes if $\varepsilon = 1$, yielding the results of Collet *et al.* [CEES93a, Prop. 2.1].

We shall prove this proposition by constructing a suitable comparison function ϕ below. Following the order of the cited papers, we use Prop. 1 to obtain the theorem with bounds on $\int v^2 = \|v\|^2$, exactly as in [CEES93a, Zie95]. Letting the K_i be global constants, we compute from (2.5) and using (2.6)–(2.8),

$$\frac{1}{2}\partial_t\|v\|^2 \le -(v, v)_{\phi/2} + \frac{\epsilon}{2}(v, v)_\phi + \frac{1}{2\epsilon}(\phi, \phi)_\phi$$

$$\le \ldots$$

$$\le -K_1 Q(v) + K_2 R_\phi(\phi)$$

$$\le -K_1\frac{\varepsilon^2}{4}\|v\|^2 + K_2 R_0(\phi).$$

[†]Observe that we distinguish between the damping parameter ε and the arbitrary constant ϵ.

[‡]Our use of a factor $1/4$ in $Q(u)$, instead of the $1/2$ used by Ziegra [Zie95], allows the correct reduction to the results of [CEES93a] in the limit $\varepsilon^2 \to 1$.

Now we may use Gronwall's inequality and (2.10) to obtain

$$\|v(t)\|^2 \leq e^{-K_1\varepsilon^2 t/2}\|v_0\|^2 + \frac{1}{K_1}\left(1 - e^{-K_1\varepsilon^2 t/2}\right)\left(K_3\varepsilon^{16/5}L^{16/5} + K_4(1-\varepsilon^2)\varepsilon^2 L^3\right).$$

Since we get a similar estimate for $\|\phi\|^2 \leq (4/\varepsilon^2)Q(\phi) \leq (4/\varepsilon^2)R_0(\phi)$, and using $\|u\|^2 = \|v+\phi\|^2 \leq 2(\|v\|^2 + \|\phi\|^2)$, we obtain the theorem [Zie95, Thm. 2.3]:

Theorem 2 *If the initial data $u_0(x) = u(x,0)$ of the DKS equation (2.2) with $\varepsilon^2 \leq 1$ is in $\mathcal{A}_L \cap L^2(-L/2, L/2)$, then the solution is attracted to a bounded ball in $\mathcal{A}_L \cap L^2(-L/2, L/2)$. Specifically, there is a constant K, independent of L, u_0 and ε, so that*

$$\limsup_{t\to\infty}\|u(\cdot,t)\|^2 \leq K\left(\varepsilon^{16/5}L^{16/5} + (1-\varepsilon^2)\varepsilon^2 L^3\right). \tag{2.11}$$

Note that this result reduces for $\varepsilon = 1$ to that of Collet *et al.* [CEES93a, Thm. 2.2]: $\limsup_{t\to\infty}\|u\|_2 \leq K \cdot L^{8/5}$.

Comments on the proof of Proposition 1

The proof and construction of the comparison function ϕ proceeds exactly as in Ziegra's thesis [Zie95]; he in turn only slightly modified the proof of Collet *et al.* Here we primarily point out where modifications from the above references have been made. Note that throughout this computation, as in [CEES93a], it is possible to sharpen many numerical factors and coefficients. However, we shall not pursue this, as it does not affect the overall scaling of the bounds.

Construction of ϕ We begin with the Fourier decomposition

$$v(x) = \mathrm{i}\sum_n v_n e^{\mathrm{i}n\bar{q}x}, \qquad \phi'(x) = \frac{d\phi}{dx} = -\sum_n \psi_n e^{\mathrm{i}n\bar{q}x},$$

where $\bar{q} = 2\pi/L$, $L > 0$ fixed, and v, ϕ odd implies $v_n = -v_{-n}$, $\psi_n = \psi_{-n}$, and $v_0 = \psi_0 = 0$. The construction of the comparison function ϕ will require an appropriate choice of the Fourier coefficients ψ_n, obtained through careful estimates in Fourier space.

After substitution of these Fourier expansions and some manipulation, (2.9) can be shown to be equivalent to

$$\sum_{n>0}(E_n + \gamma\psi_{2n})v_n^2 + 2\gamma\sum_{k>m>0}v_k v_m\left(\psi_{|k+m|} - \psi_{|k-m|}\right) \geq \frac{\varepsilon^2}{4}\sum_{n>0}v_n^2\left((n\bar{q})^4 + 1\right), \tag{2.12}$$

where $E_n \overset{\text{def}}{=} (n\bar{q})^4 - 2(n\bar{q})^2 + 1 - \varepsilon^2$. If we set $\psi_{2n} = 16\varepsilon^2$, then for $\gamma \in [1/4, 1]$,

$$E_n + \gamma\psi_{2n} \geq \frac{\varepsilon^2}{2}\left((n\bar{q})^4 + 1\right) \tag{2.13}$$

holds for all n and $\varepsilon^2 \leq 1$. However, in order to have $\phi \in L^2$ the high Fourier coefficients of ϕ' must decay. If, instead, we assume only $\psi_{2n} \geq 0$, then (2.13) is valid uniformly for $\varepsilon^2 \leq 1$, provided $(n\bar{q})^2 \geq 2 + \sqrt{5}$; in fact, in this case,

$$E_n + \gamma\psi_{2n} \geq E_n \geq \frac{1}{2}\left((n\bar{q})^4 + 1\right).$$

Let us define $n_0 \geq \sqrt{2 + \sqrt{5}}/\bar{q}$ so that we set $\psi_n = 16\varepsilon^2$ for $n < n_0$ and use (2.13), but only require $\psi_n \geq 0$ for $n \geq n_0$; for example, $n_0 = 4/\bar{q}$ is more than sufficient.

Now define

$$\tau_n^2 \overset{\text{def}}{=} \begin{cases} \frac{\varepsilon^2}{2}((n\bar{q})^4 + 1) & \text{when } n < n_0, \\ \frac{1}{2}((n\bar{q})^4 + 1) & \text{when } n \geq n_0. \end{cases}$$

Combining the previous two conditions, we thus see that if we let $\psi_{2n} \geq 0$, and $\psi_{2n} = 16\varepsilon^2$ for n satisfying $(n\bar{q})^2 < 2 + \sqrt{5}$, then by the above estimates

$$E_n + \gamma\psi_{2n} \geq \tau_n^2$$

holds for all $\gamma \in [1/4, 1]$ and $\varepsilon^2 \leq 1$.

Defining $w_n \overset{\text{def}}{=} \tau_n v_n$, the left-hand-side of (2.12) is then bounded below by

$$\sum_{n>0} w_n^2 + 2\gamma \sum_{k>m>0} w_k \left| \frac{\psi_{|k+m|} - \psi_{|k-m|}}{\tau_k \tau_m} \right| w_m \overset{\text{def}}{=} (w, (\mathrm{Id} + 2\gamma\Gamma)w),$$

whereas the right-hand-side of (2.12) is smaller than $\frac{1}{2}\sum_{n>0} w_n^2 = \frac{1}{2}(w,w)$. As in [CEES93a, Zie95], (2.12) and hence (2.9) thus follows if we can define ψ_n suitably, so that the Hilbert-Schmidt norm of $2\gamma\Gamma$ is less than $\frac{1}{2}$ for all $\gamma \in [1/4, 1]$, or

$$\|\Gamma\|_{HS}^2 \overset{\text{def}}{=} \sum_{k>m>0} \left| \frac{\psi_{|k+m|} - \psi_{|k-m|}}{\tau_k \tau_m} \right|^2 < \frac{1}{16}. \tag{2.14}$$

This condition (2.14) clarifies the two conflicting requirements on the ψ_n. On the one hand, smaller and more rapidly decaying ψ_n implies a smaller norm of ϕ, and hence a better bound. On the other hand, since in (2.14) we have *differences* between Fourier coefficients, in order to have $\|\Gamma\|_{HS}$ sufficiently small, ψ_n should be slowly varying as a function of n. Following [CEES93a], we choose $\psi_{2n+1} = 0$ for all n, $\psi_0 = 0$ (derivative of a periodic function), and for n even,

$$\psi_n = \begin{cases} 16\varepsilon^2 & \text{when } 1 \leq |n| \leq 4M; \\ 16\varepsilon^2 f\left(\frac{|n|}{4M} - 1\right) & \text{when } |n| \geq 4M, \end{cases} \tag{2.15}$$

where $f(0) = 1$, $f'(0) = 0$, $\sup|f'| < 1$, and $\int_0^\infty (1 + k^2)|f^2(k)| \, dk < \infty$. (Note: this last integral is the Sobolev condition, expressed in Fourier space, that $\phi' \in H^1$, or $\phi \in H^2$, which is exactly the class of functions for which weak solutions of the DKS equation are defined.) We also impose the condition that $2M > n_0$; then there is no contribution to the sum for $\|\Gamma\|_{HS}^2$ for which both τ_k and τ_m contain a factor of ε^2. From the definition (2.15), we deduce, for $k > m > 0$, that

$$|\psi_{k+m} - \psi_{k-m}| \begin{cases} = 0 & \text{when } k + m \leq 4M; \\ \leq 8\varepsilon^2 \frac{m}{M} & \text{when } k > m. \end{cases}$$

We observe that a monotonically decaying f satisfying the above conditions is not too difficult to find, and that it does not appear that one choice is significantly superior to another; only the constant in front of the bound is changed. Some possibilities for f are $f(k) = (1 + k^2)^{-1}$, $f(k) = \mathrm{sech}(k)$ or the Gaussian, $f(k) = \exp(-k^2)$. For any of these f (and given M), we have been unable to obtain a full analytic expression for ϕ' from its Fourier series, although numerical approximations are possible. From the large flat part of the spectrum of ϕ', we see that it is an approximation to the Dirichlet kernel, or (negative) delta function.

The estimation of the Hilbert-Schmidt norm of Γ proceeds as in [CEES93a, Zie95] (see also [Joh98]), with minor modifications; thus we shall not repeat the somewhat lengthy and tedious derivation here. Carrying through the calculation, and weakening the final estimates slightly in order to obtain more pleasant-looking bounds than the best available (again, only affecting constants in the estimates, not their scaling), we find that the condition (2.14) is definitely satisfied if we choose M as the smallest integer larger than $\max\left\{4\varepsilon^{2/5}\bar{q}^{-7/5}, 2\bar{q}^{-1}\right\}$. The specification of M completes the definition of ψ_{2n}, and thus the construction of the comparison function ϕ (subject to a suitably chosen f). This is all that is needed to show the first part (2.9) of Prop. 1.

Estimate of bounds The second part of Prop. 1 involves the estimation of $R_0(\phi)$, again performed in Fourier space. Compared with the KS equation, the additional term in (2.1′) for $\varepsilon \neq 1$ contributes a constant to E_n and hence a term proportional to $1/n^2$ in the sum evaluated in the estimation of $R_0(\phi)$; however, this is not a problem, as $\sum_n 1/n^2 = \pi^2/6$ is finite (although it cannot be approximated by an integral; $\int 1/k^2$ diverges).

$$
\begin{aligned}
R_0(\phi) &= 2L \sum_{n=1}^{\infty} E_n (n\bar{q})^{-2} \psi_n^2 \\
&= \frac{4\pi}{\bar{q}} \sum_{n=1}^{\infty} \left((2n\bar{q})^2 - 2 + \frac{1-\varepsilon^2}{(2n\bar{q})^2} \right) \psi_{2n}^2 \\
&= \frac{4\pi}{q} \left[\sum_{n=1}^{2M} (4n^2\bar{q}^2 - 2)(16\varepsilon^2)^2 + \sum_{n=2M+1}^{\infty} (4n^2\bar{q}^2 - 2)(16\varepsilon^2)^2 f^2\left(\frac{2n}{4M} - 1\right) \right. \\
&\quad \left. + \sum_{n=1}^{\infty} \frac{1-\varepsilon^2}{4\bar{q}^2} \frac{1}{n^2} \psi_{2n}^2 \right] \\
&\leq \frac{1024\pi\varepsilon^4}{\bar{q}} \left[\frac{32\bar{q}^2 M^3}{3} + 64\bar{q}^2 M^3 \int_0^{\infty} (v^2+1) f^2(v)\, dv + (1-\varepsilon^2)\frac{1}{2\bar{q}^2} \right] \\
&= c_3 \varepsilon^4 \bar{q} M^3 + c_4 (1-\varepsilon^2) \bar{q}^{-3} \varepsilon^4,
\end{aligned}
\tag{2.16}
$$

where we have used $\sum_1^{\infty} 1/n^2 = \pi^2/6 < 2$. For εL large enough (see Sec. 2.3.2 below for discussion), $M \sim \varepsilon^{2/5}\bar{q}^{-7/5}$, and we can substitute for M to obtain

$$
R_0(\phi) \leq c_5 \varepsilon^{26/5} \bar{q}^{-16/5} + c_6 (1-\varepsilon^2) \varepsilon^4 \bar{q}^{-3},
$$

or with $\bar{q} = 2\pi/L$,

$$
R_0(\phi) \leq c_1 \varepsilon^{26/5} L^{16/5} + c_2 (1-\varepsilon^2) \varepsilon^4 L^3,
$$

giving the estimate (2.10). This completes the proof of Theorem 2 [Zie95]. We shall remark on these bounds, discussing various asymptotic limits, in Sec. 2.3.2 below, after completing the proofs for all the cases.

2.1.2 The destabilized odd case, $\varepsilon^2 \geq 1$

We next look at the unstable case, $\varepsilon^2 \geq 1$, and recall that we consider only solutions of (2.2) in the zero-mean space $\mathcal{P}_L^0$, since the mean would otherwise diverge (compare (2.4)).

We only briefly point out the differences in the estimates from the previous case: It turns out that to obtain estimates uniformly valid for large ε, we need to define, as in [CEES93a],

$$
Q(u) = \frac{1}{4} \left(\int (u'')^2 + \int u^2 \right)
$$

28

and

$$\tau_n^2 = \frac{1}{2}\left((n\bar{q})^4 + 1\right).$$

Again, ψ_n is defined as in (2.15), with f as before; this time, the bound $E_n + \gamma\psi_{2n} \geq \tau_n^2$ ($\gamma \in [1/4, 1]$) is guaranteed uniformly for all $\varepsilon^2 \geq 1$ if $M\bar{q} \geq \varepsilon^{1/2}$. The estimate $\|\Gamma\|_{HS}^2 < 1/16$ is satisfied if M is chosen as the smallest integer $\geq 4\varepsilon^{4/5}\bar{q}^{-7/5}$. The condition that the domain be long enough to permit nontrivial dynamics, by having at least one Fourier mode in the band of unstable wave numbers, is $\bar{q} < \sqrt{1 + \varepsilon} < \sqrt{2\varepsilon}$. With such $\bar{q}$, our choice of M certainly satisfies the condition $M\bar{q} \geq \varepsilon^{1/2}$ for $\varepsilon^2 \geq 1$. Finally, we estimate $R_0(\phi)$ as before, to give again

$$R_0(\phi) \leq \frac{1024\pi\varepsilon^4}{\bar{q}}\left[\frac{32\bar{q}^2 M^3}{3} + 64\bar{q}^2 M^3 \int_0^\infty (v^2 + 1)f^2(v)\,dv + (1 - \varepsilon^2)\frac{1}{2\bar{q}^2}\right],$$

and substitute the expression for M.

Hence we obtain a proposition very similar to Proposition 1, which we shall not state here; as before, it implies a result corresponding to Theorem 2, as follows:

Theorem 3 *If the initial data $u_0(x) = u(x, 0)$ of the DKS equation (2.2) with $\varepsilon^2 \geq 1$ is in $\mathcal{A}_L \cap L^2(-L/2, L/2)$, then the solution is attracted to a bounded ball in $\mathcal{A}_L \cap L^2(-L/2, L/2)$. Specifically, there is a constant K, independent of L, u_0 and ε, so that*

$$\limsup_{t\to\infty} \|u(\cdot, t)\|^2 \leq K\left(\varepsilon^{32/5} L^{16/5} + (1 - \varepsilon^2)\varepsilon^4 L^3\right)$$
$$\leq K\varepsilon^{32/5} L^{16/5}. \tag{2.17}$$

The last simplification occurs both because $(1 - \varepsilon^2) \leq 0$, and because for $\varepsilon^2 L \geq 1$ the first term in the bound always dominates. This result again reduces to that of [CEES93a] for $\varepsilon^2 = 1$. It is interesting to observe that we have shown that, as long as the mean is held at zero, the strength of the linear instability can be increased arbitrarily without destroying the L^2 dissipativity of (2.2). We shall comment further on this bound in Sec. 2.3.3 below, in the context of deriving an interesting special case, an explicit shock-like solution.

2.2 Dissipativity for general periodic initial data

In the original demonstration of dissipativity and a global L^2 bound for the KS equation by Nicolaenko *et al.* [NST85], only odd initial data was considered, as above. One of the major contributions of Collet *et al.* [CEES93a] (also achieved previously by Il'yashenko [Il'92] and independently by Goodman [Goo94]) was to extend the proof of dissipativity to general periodic initial data.

Motivated by this work, and essentially transferring the techniques of [CEES93a], we now extend the above results, obtained for odd solutions $u \in \mathcal{A}_L$, to general periodic (mean-zero) solutions of (2.2) $u \in \mathcal{P}_L^0$.

It turns out that the cases $\varepsilon^2 \leq 1$ and $\varepsilon^2 \geq 1$ must be treated somewhat differently. In fact, for $\varepsilon^2 \geq 1$ we may carry over the method of Collet *et al.* [CEES93a] to the result of Theorem 3 in the obvious way, while for $\varepsilon^2 \leq 1$, this fails, and a minor modification is needed. In this Section, we will again follow [CEES93a] and merely outline the proofs.

First, we assume that the antisymmetric case has been dealt with, as in the previous Section. That is, for each L and ε, a function $\tilde{\phi}$ has been constructed,[†] satisfying estimates of the form

$$R_{\gamma\tilde{\phi}}(v) \geq Q(v), \qquad R_0(\tilde{\phi}) \leq F(\varepsilon, L)$$

[†]We shall find later that we can sometimes, but not always, take $\tilde{\phi} = \phi$.

as in Proposition 1, for $v \in \mathcal{A}_L$; where the bound F is some function of ε and L, reducing to $F = K \cdot L^{8/5}$ for $\varepsilon^2 = 1$. The essential idea of the generalization to arbitrary periodic data [CEES93a, Goo94] is to use the given $\tilde{\phi}$ to construct a *family* of comparison functions by translation, and at each time, to choose the translation in such a way that the distance between u and this set is minimized.

Definitions   Consider general functions $u \in \mathcal{P}^0_{L/2}$; the reduction to a domain of length $L/2$ will be useful later. We introduce the family of comparison functions $\tilde{\phi}_b(x) \overset{\text{def}}{=} \tilde{\phi}(x + b)$; the evolution equation for $b = b(t)$ will be given below, in (2.20). Let $v(x,t) = u(x,t) - \tilde{\phi}_{b(t)}(x)$; as before, we will calculate the evolution equation for the norm of v. The comparison function ϕ constructed previously in (2.15) has only even Fourier coefficients, and is thus actually $L/2$-periodic; we shall see that this property carries over to $\tilde{\phi}$, so that also $v \in \mathcal{P}^0_{L/2}$. It is important to note that all integrals in this section are taken over $[-L/2, L/2]$, that is, twice the period of u (or v), so that

$$\int v^2 \overset{\text{def}}{=} \int_{-L/2}^{L/2} v^2 \, dx = 2 \int_{-L/4}^{L/4} v^2 \, dx = 2\|v\|^2_{L^2([-L/4,L/4])} \overset{\text{def}}{=} 2\|v\|^2.$$

Lastly, we define the bilinear form

$$B_{\gamma\tilde{\phi}_b}(v_1, v_2) \overset{\text{def}}{=} (v_1, v_2)_{\gamma\tilde{\phi}_b} + \frac{4\gamma^2}{\varepsilon^2 L} \int_{-L/2}^{L/2} v_1 \tilde{\phi}'_b \int_{-L/2}^{L/2} v_2 \tilde{\phi}'_b$$

$$= -\int v_1 \mathcal{L}_0 v_2 + (1 - \varepsilon^2) \int v_1 v_2 + \gamma \int v_1 v_2 \tilde{\phi}'_b + \frac{4\gamma^2}{\varepsilon^2 L} \int v_1 \tilde{\phi}'_b \int v_2 \tilde{\phi}'_b;$$

that is,

$$B_{\gamma\tilde{\phi}_b}(v, v) = R_{\gamma\tilde{\phi}_b}(v) + \frac{4\gamma^2}{\varepsilon^2 L} \left(\int v \tilde{\phi}'_b \right)^2. \tag{2.18}$$

In order to obtain our final estimates, we need a result analogous to Proposition 4.3 of [CEES93a], namely

$$B_{\gamma\tilde{\phi}_b}(v, v) \geq Q(v) \tag{2.19}$$

for all $v \in \mathcal{P}^0_{L/2}$ and $\gamma \in [1/4, 1]$. It is straightforward to establish that this inequality is independent of b, due to the periodicity of v; so that it is sufficient to prove the result for $b = 0$, that is, $B_{\gamma\tilde{\phi}}(v, v) \geq Q(v)$.

General evolution for $\|v\|$ Given the estimate (2.19), which we will show below separately for $\varepsilon^2 \leq 1$ and $\varepsilon^2 \geq 1$, we may estimate the norm of v. By exact analogy with the antisymmetric case, and with [CEES93a], we find

$$\frac{1}{2}\partial_t \int v^2 = -(v, v)_{\frac{1}{2}\tilde{\phi}_b} - (v, \tilde{\phi}_b)_{\tilde{\phi}_b} - (\partial_t b) \int v \tilde{\phi}'_b$$

$$\leq -(v, v)_{\frac{1}{2}\tilde{\phi}_b} + \frac{\epsilon}{2}(v, v)_{\tilde{\phi}_b} + \frac{1}{2\epsilon}(\tilde{\phi}_b, \tilde{\phi}_b)_{\tilde{\phi}_b} - (\partial_t b) \int v \tilde{\phi}'_b$$

$$= -\left(1 - \frac{\epsilon}{2}\right) B_{\gamma\tilde{\phi}_b}(v, v) + \left(1 - \frac{\epsilon}{2}\right) \frac{4\gamma^2}{\varepsilon^2 L} \left(\int v \tilde{\phi}'_b \right)^2$$

$$+ \frac{1}{2\epsilon} R_0(\tilde{\phi}_b) - (\partial_t b) \int v \tilde{\phi}'_b$$

30

$$\leq -\left(1 - \frac{\epsilon}{2}\right) Q(v) + \frac{1}{2\epsilon} R_0(\tilde{\phi}_b)$$
$$+ \left(1 - \frac{\epsilon}{2}\right) 4 \frac{(1-\epsilon)^2}{(2-\epsilon)^2} \frac{1}{\varepsilon^2 L} \left(\int v \tilde{\phi}_b'\right)^2 - (\partial_t b) \int v \tilde{\phi}_b'.$$

Here we have defined $\gamma \overset{\text{def}}{=} (1-\epsilon)/(2-\epsilon)$, and the above inequalities hold for $1/4 \leq \gamma \leq 1$, that is, for $\epsilon \leq 2/3$. The last two terms cancel if

$$\frac{(1-\epsilon)^2}{1-\epsilon/2} \frac{1}{\varepsilon^2 L} \left(\int v \tilde{\phi}_b'\right)^2 = (\partial_t b) \int v \tilde{\phi}_b',$$

that is,

$$\partial_t b(t) = \frac{c}{\varepsilon^2 L} \int v \tilde{\phi}_b' , \qquad c \overset{\text{def}}{=} \frac{(1-\epsilon)^2}{1-\epsilon/2}. \tag{2.20}$$

This gives us the desired evolution condition on $b(t)$. For instance, we could choose $\epsilon = 2/3$ ($\gamma = 1/4$) to obtain $c = 1/6$. Using this value, we find an inequality for $\|v\|$,

$$\partial_t \|v\|^2 \leq -\frac{2}{3} Q(v) + \frac{3}{4} R_0(\tilde{\phi}), \tag{2.21}$$

where we have used $R_0(\tilde{\phi}_b) = R_0(\tilde{\phi})$ by periodicity. The succeeding estimates, especially the demonstration of (2.19), differ for $\varepsilon^2 \leq 1$ and $\varepsilon^2 \geq 1$, so we treat them separately, considering the latter, simpler case first.

2.2.1 The destabilized general case, $\varepsilon^2 \geq 1$

In the unstable case (mean zero), we may directly adapt the method of Collet et $al.$ [CEES93a]: We define

$$Q(u) = \frac{1}{4} \left(\int (u'')^2 + \int u^2\right),$$

and construct $\phi(x)$ as in Sec. 2.1.2; in the notation of the above discussion, we then choose the basic function $\tilde{\phi}$ for our family to equal the previously constructed ϕ. The estimates of Section 2.1.2 then all hold for general antisymmetric functions.

Estimate for $B_{\gamma\tilde{\phi}}(v,v)$

We may decompose a general periodic function $v \in \mathcal{P}_{L/2}^0$ into its even and odd parts, plus a constant, via $v = v_a + v_s + v(0)$, where $v_a(-x) = -v_a(x)$, $v_s(-x) = v_s(x)$, and $v_s(0) = 0$. We find from the results on odd functions of Section 2.1.2 that

$$R_{\gamma\tilde{\phi}}(v_a) \geq Q(v_a), \qquad \text{and} \qquad R_{\gamma\tilde{\phi}}(v_s) \geq Q(v_s),$$

where the latter estimate follows from considering an antisymmetric $\tilde{v}_s$ (defined to equal v_s for positive x, and $-v_s$ for negative x), and from noticing that replacing v_s by $\tilde{v}_s$ in the integral definitions changes neither $R_{\gamma\tilde{\phi}}(v_s)$ nor $Q(v_s)$. By substitution into the relevant definitions, and eliminating all integrals with odd integrand by symmetry, we can confirm

$$Q(v_a) + Q(v_s) = Q(v) + \frac{1}{4} L v(0)^2,$$
$$\int v \mathcal{L} v = \int v_s \mathcal{L} v_s + \int v_a \mathcal{L} v_a + L(1-\varepsilon^2) v(0)^2.$$

31

Hence, in exact analogy with [CEES93a], we find

$$-R_{\gamma\tilde{\phi}}(v) \leq -Q(v_s) - Q(v_a) - 2\gamma v(0) \int v\tilde{\phi}' + (1-\varepsilon^2)Lv(0)^2$$

$$= -Q(v) - 2\gamma v(0) \int v\tilde{\phi}' + \frac{1}{4}(3 - 4\varepsilon^2)Lv(0)^2. \tag{2.22}$$

In this case, $\varepsilon^2 \geq 1$, so the coefficient of $Lv(0)^2$ is negative, and we can complete the square as in [CEES93a]; in fact, it is convenient to use $3 - 4\varepsilon^2 \leq -\varepsilon^2$ for $\varepsilon^2 \geq 1$, together with

$$-\frac{\varepsilon^2}{4}Lv(0)^2 - 2\gamma v(0) \int v\tilde{\phi}' \leq \frac{4\gamma^2}{\varepsilon^2 L}\left(\int v\tilde{\phi}'\right)^2.$$

Thus we find

$$Q(v) \leq R_{\gamma\tilde{\phi}}(v) + \frac{4\gamma^2}{\varepsilon^2 L}\left(\int v\tilde{\phi}'\right)^2$$

$$= B_{\gamma\tilde{\phi}}(v,v), \tag{2.23}$$

confirming the estimate (2.19), as in [CEES93a, Prop. 4.3].

Dissipativity—unstable case

Having established (2.19) and its consequences, we use (2.21) and the bound on $R_0(\tilde{\phi})$ from Thm. 3 to obtain

$$\partial_t\|v\|^2 \leq -\frac{2}{3}Q(v) + \frac{3}{4}R_0(\tilde{\phi})$$

$$\leq -\frac{1}{3}\|v\|^2 + \frac{3}{4}\tilde{c}_1\varepsilon^{32/5}L^{16/5},$$

or by Gronwall's lemma,

$$\|v(t)\|^2 \leq \|v_0\|^2 e^{-t/3} + \frac{9}{4}\tilde{c}_1\varepsilon^{32/5}L^{16/5}\left(1 - e^{-t/3}\right).$$

Since $\tilde{\phi}$ satisfies a similar bound, we obtain the final result, which coincides with that for odd solutions u, (2.17):

Theorem 4 *If the initial data u_0 of the DKS equation (2.2) is in $\mathcal{P}^0_{L/2}$, that is, $L/2$-periodic and of zero mean, there is a constant K, independent of L, u_0 and ε, so that*

$$\limsup_{t\to\infty}\|u(\cdot,t)\|^2 \leq K\varepsilon^{32/5}L^{16/5}, \tag{2.24}$$

for all $\varepsilon^2 \geq 1$ and all L.

2.2.2 The stabilized general case, $\varepsilon^2 \leq 1$

The damped case $\varepsilon^2 \leq 1$ is slightly more tricky; basically, the problem is that in the equivalent of (2.22), the last term is no longer negative for small ε, and we cannot complete the square to give a positive bound. We circumvent this difficulty by using a modified comparison function $\tilde{\phi}$.

Definitions Let us denote by a superscript ^{0} the quantities as they appear in [CEES93a], that is, for $\varepsilon^2 = 1$ (the "pure" KS equation)—by analogy with the relationship between $\mathcal{L}$ and $\mathcal{L}_0$ (the subscript $_0$ here forms the exception to this notation). In particular, let ϕ^0 be the comparison function Φ constructed in [CEES93a, Sec. 3]. For the proof in this Section, we will use the function

$$\tilde{\phi} \stackrel{\text{def}}{=} \varepsilon^2 \phi^0. \tag{2.25}$$

The only difference, in fact, between $\varepsilon^2 \phi^0$ and the ϕ constructed in Section 2.1.1 is the choice of M, the cutoff for the Fourier coefficients. The M^0 used for ϕ^0 has no dependence on ε, so $M^0 \geq M$, $\varepsilon^2 \phi^0 \geq \phi$, and in particular, for $v \in \mathcal{A}_L$,

$$R_{\gamma \varepsilon^2 \phi^0}(v) \geq R_{\gamma\phi}(v) \geq Q(v).$$

Estimate for $B_{\gamma\tilde{\phi}}(v, v)$

With this definition of $\tilde{\phi}$, it is straightforward to prove the estimate (2.19) for $B_{\gamma\tilde{\phi}}(v, v)$. From [CEES93a, Prop. 4.3] we know (for $v \in \mathcal{P}_{L/2}^0$, $\gamma \in [1/4, 1]$) that $B_{\gamma\phi^0} \geq Q^0(v)$, that is,

$$-\int v\mathcal{L}_0 v + \gamma \int v^2 \phi^{0\prime} + \frac{4\gamma^2}{L}\left(\int v\phi^{0\prime}\right)^2 \geq Q^0(v)$$

which implies

$$-\varepsilon^2 \int v\mathcal{L}_0 v + \gamma \int v^2 (\varepsilon^2 \phi^0)' + \frac{4\gamma^2}{\varepsilon^2 L}\left(\int v(\varepsilon^2 \phi^0)'\right)^2 \geq \varepsilon^2 Q^0(v).$$

Now, for general periodic functions, $(\mathcal{L}_0 - 1)$ is a negative definite operator—that is, for $v \in \mathcal{P}_{L/2}^0$,

$$-\int v(\mathcal{L}_0 - 1)v = \sum_n |v_n|^2 \left((n\bar{q})^2 - 1\right)^2 \geq 0;$$

thus

$$-\varepsilon^2 \int v\mathcal{L}_0 v \leq -\int v\mathcal{L}_0 v + (1 - \varepsilon^2)\int v^2 \qquad \text{for} \quad \varepsilon^2 \leq 1, \; v \in \mathcal{P}_{L/2}^0.$$

Hence the above inequalities imply

$$-\int v\mathcal{L}_0 v + (1 - \varepsilon^2)\int v^2 + \gamma \int v^2 (\varepsilon^2 \phi^0)' + \frac{4\gamma^2}{\varepsilon^2 L}\left(\int v(\varepsilon^2 \phi^0)'\right)^2 \geq \varepsilon^2 Q^0(v) = Q(v);$$

comparison with the definition of B in (2.18) and $\tilde{\phi}$ in (2.25) shows that this is equivalent to

$$B_{\gamma \varepsilon^2 \phi^0}(v, v) \geq Q(v), \qquad v \in \mathcal{P}_{L/2}^0. \tag{2.26}$$

This inequality, analogous to [CEES93a, Prop. 4.3], is the main new result we need.

Estimate for $R_0(\tilde\phi)$ We also need an estimate similar to (2.10) for $\tilde\phi = \varepsilon^2\phi^0$; this is obtained exactly as before, but noting that M^0 used in the definition for ϕ^0 is independent of ε; that is, we may take $M^0 = \max\{4\bar{q}^{-7/5}, 2\bar{q}^{-1}\} = 4\bar{q}^{-7/5}$, since $\bar{q} = 2\pi/L \leq \sqrt{1+\varepsilon} < \sqrt{2}$ in the only interesting case. By comparison with (2.16),

$$
\begin{aligned}
R_0(\tilde\phi) = R_0(\varepsilon^2\phi^0) &\leq \varepsilon^4\left[c_3\bar{q}(M^0)^3 + c_4(1-\varepsilon^2)\bar{q}^{-3}\right] \\
&\leq \varepsilon^4\left[c_5\bar{q}^{-16/5} + c_6(1-\varepsilon^2)\bar{q}^{-3}\right],
\end{aligned}
$$

that is,

$$
R_0(\tilde\phi) \leq \varepsilon^4\left[c_1 L^{16/5} + c_2(1-\varepsilon^2)L^3\right], \qquad \varepsilon^2 \leq 1. \tag{2.27}
$$

These bounds have a worse dependence on ε than (2.10), but they still reduce to previous results in the limit $\varepsilon^2 = 1$.

Dissipativity—stable case

The remainder of the computation is straightforward: From (2.21),

$$
\begin{aligned}
\partial_t\|v\|^2 &\leq -\frac{2}{3}Q(v) + \frac{3}{4}R_0(\tilde\phi) \\
&\leq -\frac{1}{3}\varepsilon^2\|v\|^2 + \frac{3}{4}\varepsilon^4\left[c_1 L^{16/5} + c_2(1-\varepsilon^2)L^3\right]
\end{aligned}
$$

(analogous to [CEES93a, Thm. 4.1]), so by Gronwall's Lemma,

$$
\|v(t)\|^2 \leq \|v_0\|^2 e^{-\varepsilon^2 t/3} + \frac{9}{4}\varepsilon^2\left(c_1 L^{16/5} + c_2(1-\varepsilon^2)L^3\right)\left(1 - e^{-\varepsilon^2 t/3}\right).
$$

This gives a long-time bound on v. Since $\tilde\phi_b = u - v$ satisfies a similar bound, we obtain the final theorem, asserting the existence of an absorbing ball in L^2 for general periodic initial data, analogous to the Main Theorem 4.2 of Collet *et al.* [CEES93a]:

Theorem 5 *If the initial data u_0 of the DKS equation (2.2) is in $\mathcal{P}^0_{L/2}$, that is, $L/2$-periodic and of zero mean, there is a constant K, independent of L, u_0 and ε, so that*

$$
\limsup_{t\to\infty}\|u(\cdot,t)\|^2 \leq K\varepsilon^2\left[L^{16/5} + (1-\varepsilon^2)L^3\right], \tag{2.28}
$$

for all $\varepsilon^2 \leq 1$ and all L.

Since in this Section we are considering only $L \geq 1$ and $(1-\varepsilon^2) \leq 1$, the first term in (2.28) is always dominant, so we obtain the final bound for solutions of the linearly damped KS equation:

$$
\limsup_{t\to\infty}\|u\|^2 \leq K\cdot\varepsilon^2 L^{16/5}, \qquad \text{for}\quad u \in \mathcal{P}^0_{L/2}. \tag{2.29}
$$

The ε-dependence in this estimate appears to be worse than that for odd solutions, (2.11); but see the discussion in Sec. 2.3.2 below.

2.3 Analyticity, special limits and a shock solution

2.3.1 Remarks on analyticity and related estimates

In the previous Sections, we demonstrated the dissipativity of the damped (and negatively damped) KS equation by estimating the radius of the absorbing ball in L^2. There were few surprises; we were able to adapt the methods of [CEES93a] almost completely. This success is not solely due to the simplicity of the additional term, however.

We are aware of two similar studies in which the effect of other perturbations of the KS equation were investigated. Duan and Ervin [DE98] considered the influence of a well-behaved nonlocal operator, a Hilbert transform term added to the KS equation, and estimated the asymptotic L^2 bound and the Hausdorff and fractal dimensions of the attractor, using the techniques of [CEES93a] and [NST85, Tem97]. Johnson [Joh98] performed similar calculations (for odd solutions only) for a KS equation (in the form (A.9)) in which the coefficient α is an even x-dependent function, and also estimated the dimension of the inertial manifold, following [CFNT89a, Tem97]. In both of these studies, as in ours, no essentially new ideas needed to be introduced. While this raises the interesting question of what it is about the KS equation that makes it so robust to perturbations, it also means that our success in Secs. 2.1–2.2 is unsurprising. Of course, part of the reason for the general applicability of the bounds of Collet *et al.* [CEES93a] is that they are "too crude"; their $\mathcal{O}(L^{8/5})$ scaling for the absorbing ball in the L^2 norm, while an improvement on earlier bounds, is still considerably larger than the optimal expected bound of $\mathcal{O}(L^{1/2})$ (see Sec. 1.2.2). In Sec. 2.3.3 we partially clarify this issue of excessively crude estimates by providing an explicit example, in the destabilized case $\varepsilon^2 \geq 1$, of a solution which satisfies the $\mathcal{O}(L^{8/5})$ bounds, but which does not have the extensive $\mathcal{O}(L^{1/2})$ scaling observed and conjectured for the pure KS equation.

Gevrey class regularity for the DKS equation

As we have remarked above, results on attractors and inertial manifolds valid for the pure KS equation have been readily transferable to modified equations, as observed in related studies [DE98, Joh98]. Here we briefly remark that, in a similar vein, one can derive the real analyticity of solutions u of (2.2) immediately by generalizing previous results.

Analyticity for the KS equation   Using techniques developed in [FT89], Collet *et al.* [CEES93b] established the analyticity of solutions of the KS equation. They did this by obtaining the boundedness of a suitably defined norm, the Gevrey norm, which allows one to deduce analyticity in a strip of finite width about the real axis from the exponential decay of Fourier modes. We quote the relevant theorems for reference:

Theorem 6 *[CEES93b, Thm. 3.1]*
If the initial condition u_0 of the KS equation (1.1) *with L-periodic boundary conditions satisfies* $\int_{-L/2}^{L/2} u_0^2(x)\, dx \leq R_L^2$, *then the solution $u(x,t)$ satisfies the bound*

$$\|e^{\alpha_L \min(t,t_L)A}u(\cdot,t)\|_2 \leq 2R_L, \tag{2.30}$$

where

$$A \stackrel{\text{def}}{=} \sqrt{-\partial_x^2}, \qquad \alpha_L \stackrel{\text{def}}{=} \alpha_0 R_L^{6/5}, \qquad t_L = t_0 R_L^{-8/5}.$$

Since we know that general initial data in L^2 is attracted to an absorbing ball, so that within finite time t' it enters a region of L^2 of radius $\rho_0 \sim \mathcal{O}(L^{8/5})$, we can shift the origin of time to t', and use the radius ρ_0 of the absorbing ball for R_L.

Theorem 7 *[CEES93b, Thm. 1.2]*
For large t, the function $u(x, t)$ satisfying (1.1) is analytic in x in a strip of width

$$\beta_L \geq \text{const.} \cdot R_L^{-2/5} \sim \text{const.} \cdot L^{-16/25} \qquad (2.31)$$

about the real axis.

Note that according to this estimate, the width of the strip of analyticity shrinks as $L \to \infty$. However, consistent with other numerical observations of extensivity (see Secs. 1.2.2 and 4.1.1), Collet *et al.* present strong numerical evidence that the width of the strip of analyticity is asymptotically independent of L.

Generalization to the DKS equation For the DKS equation (2.2) considered in this Chapter, Theorems 6 and 7 carry over immediately. The only modification to the KS equation we consider is to the linear operator $\mathcal{L}$, which does not affect the fundamental bounds of [CEES93b] on the nonlinear term, so the proofs carry over essentially line by line (some care must be taken for $\varepsilon^2 \geq 1$, but there is no serious difficulty). We shall therefore not give any details of the proofs here, referring the reader instead to Collet *et al.* [CEES93b]. The solutions to the DKS equation (2.2), for any ε, are thus also analytic, with exponentially decaying Fourier modes.

An estimate for the L^2 absorbing ball radius R_L, which implies the width of the strip of analyticity via (2.31), may be found for each of the four cases (odd or general initial data, $\varepsilon^2 \leq 1$ or $\varepsilon^2 \geq 1$) using Theorems 2–5. The scaling of R_L in some special limits is considered in the next Section.

Further estimates

Our experience in Secs. 2.1–2.2 with dissipativity, and that of [DE98, Joh98] with other bounds, suggests that we should not have too much difficulty extending other results on the KS equation to the DKS equation with linear damping or driving. In particular, we should be able to show the existence of an attractor [NST85] and inertial manifold [CFNT89a], and obtain bounds on their dimensions [Tem97, TW94], demonstrate time analyticity [JKT90, GK97] and the existence of four determining nodes [FK95], and bound the number of spatial oscillations [Kuk94], among several other properties of the KS equation. We plan to carry out some of these computations as an exercise. However, in this Chapter we prefer to explore the implications of the previously derived L^2 bounds a little further.

2.3.2   Some notes on the estimates

In this brief Section we comment on the scaling of the different bounds derived in Secs. 2.1–2.2, noting a few relevant limits; as usual, the c_i and K are appropriate constants. For each of the cases discussed, the L^2 bound $\rho_0 = R_L$ may be substituted into (2.31), to obtain an estimate for the width of the strip of analyticity. One observes that the domain of analyticity grows as $\varepsilon \to 0$; with more damping, the solution is smoother, as expected.

Bounds for $\varepsilon^2 \leq 1$

The first relevant observation for the stabilized KS equation is that the ε-dependence of the bounds appears to be worse for general periodic data than for odd solutions (compare (2.28) with (2.11)).

Specifically, provided the first term dominates, the radius of the absorbing ball is found to be $\rho_0 \sim \varepsilon L^{8/5}$ in general, compared with $\rho_0 \sim \varepsilon^{8/5} L^{8/5}$ for odd solutions. This effect arises because of the modified comparison function $\tilde{\phi} = \varepsilon^2 \phi^0$ we needed to introduce in Sec. 2.2.2: we found $\tilde{\phi} \geq \phi$, where ϕ is the comparison function for odd, damped solutions of Sec. 2.1.1. This does not seem to matter significantly: Interestingly, we shall see below that in situations where we may care about the ε-dependence (that is, in the scaling for $\varepsilon \to 0$), the odd and general cases have the same (correct) behavior in ε, but we have better L-dependence for the odd solutions.

Let us look at some limits. For fixed $\varepsilon^2 \leq 1$, we may look at the behavior as a function of L; in this case, the first term in (2.11) dominates, and we have the limits

$$\|u\| \leq K \cdot \varepsilon^{8/5} L^{8/5}, \qquad u \text{ odd}$$

$$\|u\| \leq K \cdot \varepsilon L^{8/5}, \qquad \text{general periodic } u$$

for $L \to \infty$ (fixed ε). By (2.28), the second bound is the only relevant scaling for asymmetric solutions, for $\varepsilon \leq 1$.

If we scale $L \sim \varepsilon^{-1}$ (that is, hold εL approximately constant as $L \to \infty$, $\varepsilon \to 0$), then $\varepsilon^2 L^3 = (\varepsilon L)^2 L$ is the dominant term in (2.11), and

$$\|u\| \leq K \cdot \varepsilon L^{3/2}, \qquad u \text{ odd.}$$

Scaling for small ε and the Ginzburg-Landau formalism In order to obtain the correct scaling for $\varepsilon \to 0$, we note that in the definition of ϕ in Sec. 2.1.1 (for odd solutions only), we encountered the condition

$$M \gtrsim \max \left\{ 4\varepsilon^{2/5} \bar{q}^{-7/5}, 2\bar{q}^{-1} \right\}, \tag{2.32}$$

which appeared in the bound for $\|u\|$ via (2.16). The first term in (2.32) dominates when $\bar{q}^{2/5} \lesssim 2\varepsilon^{2/5}$, or $\varepsilon L \gtrsim \pi/(2\sqrt{2}) \approx 1.11 \ldots$. In this case, we obtain all the above estimates. However, if this condition on εL does not hold, then the second term in (2.32) is the relevant one, so that $M \sim 2\bar{q}^{-1}$, and the estimate for $R_0(\phi)$ in (2.16) is replaced by

$$R_0(\phi) \leq c_7 \varepsilon^4 L^2 + c_8 (1 - \varepsilon^2) \varepsilon^4 L^3.$$

In this case, for sufficiently large L but small ε, the second term dominates. This is the appropriate limit for letting $\varepsilon \to 0$ in a way such that $\varepsilon L \to 0$—for instance, fixing L and letting $\varepsilon \to 0$—in which case we have

$$\|u\| \leq K \cdot \varepsilon L^{3/2}, \qquad u \text{ odd}, \quad \varepsilon \to 0.$$

In all cases, for odd and general periodic solutions, our estimate for the bounds for $\varepsilon \to 0$ is thus $\|u\| = \mathcal{O}(\varepsilon)$. This is reassuring, as it coincides with the scaling predicted via the Ginzburg-Landau formalism: for $\varepsilon \ll 1$, the only linearly unstable modes are located in a narrow band near $n\bar{q} = 1$, and one expects, and observes numerically, that the solution u to (2.2) in this limit is a perturbation of a purely sinusoidal solution; see Fig. 2.3(a). Formal multiple scale analysis indicates that in this case u may be written as

$$u = \varepsilon A(\varepsilon^2 t, \varepsilon x) e^{ix} + \text{c.c.} + \mathcal{O}(\varepsilon^2),$$

where the appropriate modulation equation governing the evolution of $A = \mathcal{O}(1)$ is the (real) Ginzburg-Landau (GL) equation. From this expression, it is clear that we expect $\|u\| \sim \varepsilon$.

The correspondence between u and A has recently been established rigorously; see for instance [MS95], where it is shown that for sufficiently small ε and for sufficiently "nice" initial data[†] the function u is uniformly bounded by a constant times ε. In fact, in this case we obtain the desired scaling $\|u\| \le K \cdot \varepsilon L^{1/2}$, establishing extensivity in this limit. However, we cannot extend this result to larger values of ε, let alone to the pure KS equation: firstly, rather strong conditions have been placed on the initial data, and secondly, the GL formalism in this form presupposes a rather narrow band of unstable modes; it breaks down at or before $\varepsilon = 3/5$, at which value there is a wave number q such that both q and $2q$ are in the band of instability.

Bounds for $\varepsilon^2 \ge 1$

In the destabilized case, the estimates for the absorbing ball, (2.17) for odd solutions and (2.24) for general periodic data, coincide, and we have

$$\|u\| \le K \cdot (\varepsilon^2 L)^{8/5}. \tag{2.33}$$

As before, the L-dependence is that previously obtained in [CEES93a]. It is not clear, however, that an $\varepsilon^2 L$ scaling is the expected one; the ε-dependence of these bounds does not seem very good.

For small ε, we were able to compare our bounds with rigorous results obtained through the Ginzburg-Landau formalism; where under more restricted conditions, one can also show extensivity. For large ε, we can find a steady solution, the asymptotics of which allow us to check the scaling in the opposite limit, with an interesting result.

2.3.3   An explicit "shock" solution

Numerical simulations of the DKS equation (2.2) for sufficiently large ε ($\varepsilon^2 \gtrsim 1.5$ seems large enough) indicate that arbitrary initial conditions rapidly converge to a stationary, shock-like solution; see Fig. 2.1(a). We may derive an asymptotic approximation of this solution, and compare its properties to our previous estimates. We remark that this shock solution has a similar shape to the comparison functions constructed in Secs. 2.1–2.2.

We note that similar oscillatory shock-like solutions have been observed in numerical simulations of the KS equation with homogeneous Neumann boundary conditions [Mic86], and in the simplified model for KS dynamics proposed and investigated in detail by Goren *et al.* [GEP98]; in the latter work, an analytic expression for the shock is given, similar to the one we obtain below. Our present aim is to extract some features of the shock pertinent to our other studies, not to investigate this solution in detail—we have not considered the stability of the shock, its basin of attraction or the rate of convergence to this state, nor have we sought detailed asymptotic rigor.

Asymptotic approximation to the shock

We obtain a lowest order approximation to the shock solution in the asymptotic limit $\varepsilon^2 \gg 1$, mainly in order to derive the relevant scalings.

The shock is antisymmetric about its center, so without loss of generality we may choose the center of the shock in the domain $x \in [-L/2, L/2]$ to lie at $x = 0$. We set $\nu \stackrel{\text{def}}{=} \varepsilon^2 - 1 \gg 1$, and

---

[†]Specifically, we need $u_0 \in H^1_{l,u}(\mathbb{R})$, where the "locally uniform" translationally invariant space $H^1_{l,u}$ contains functions with a finite Sobolev H^1_ρ norm with respect to a weight function $\rho(x)$ and all its translates; and we require $\|u_0\|_{H^1_{l,u}} \le K\varepsilon^{1/2}$; see [MS95].
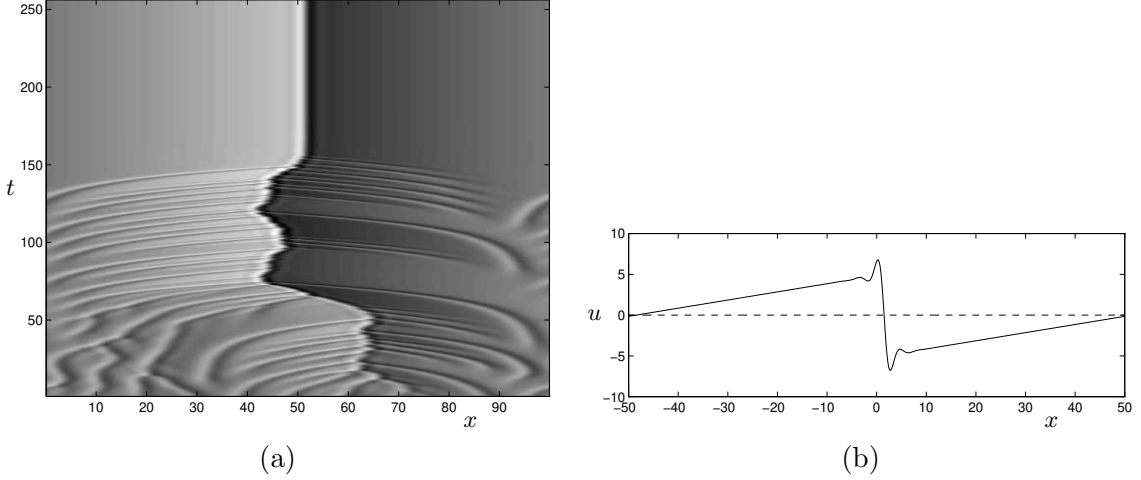
Figure 2.1: (a) Evolution of destabilized KS equation (2.2), with $\varepsilon^2 = 1.4$, showing the rapid convergence to a stable shock-like solution; notice that the gray-scale here ranges between $u = \pm 8.5$. (b) Cross-section of the asymmetric, stationary shock profile, showing the constant slope in the outer region and the narrow boundary layer; the x axis has been relabeled to $[-50, 50]$ for agreement with the notation in this Chapter.

seek an appropriate stationary solution ($u_t = 0$) to (2.2), satisfying

$$u_{xxxx} + 2u_{xx} - \nu u + uu_x = 0.$$

It is immediately apparent from the shock profile of Fig. 2.1(b) that there are two distinguished limits and a boundary layer of width $\sim \delta$, where we assume $\delta \ll 1$. The outer solution, valid for $|x| \gtrsim \delta$, is almost linear, and satisfies the asymptotic balance

$$uu_x \approx \nu u, \quad \text{or} \quad u_x \approx \nu, \qquad \nu \gg 1,$$

which implies

$$u_o(x) \approx \begin{cases} \nu(x - L/2), & x \in (\delta, L/2] \\ \nu(x + L/2), & x \in [-L/2, -\delta). \end{cases} \tag{2.34}$$

The maximum height of the outer solution at $x \approx \pm \delta$ is of the order $\pm \nu(L/2 - \delta) \approx \nu L/2$, and the change Δu across the boundary layer is $\sim \nu L$. Since $\nu \sim \varepsilon^2$ for $\varepsilon^2 \gg 1$, we see already that u is uniformly bounded in neither L nor ε for this shock solution.

The appropriate balance for the inner solution is $u_{xxxx} \approx -uu_x$. Within the boundary layer, $\partial_x \sim 1/\delta$, so that this balance gives $u/\delta^4 \sim u^2/\delta$, or

$$\delta \sim u^{-1/3} \sim (\nu L)^{-1/3} \sim (\varepsilon^2 L)^{-1/3}, \tag{2.35}$$

for $\varepsilon^2 \gg 1$, and $L \geq 2\pi$; in this limit, the width of the boundary layer is $\delta \sim (\varepsilon^2 L)^{-1/3} \ll 1$, and our Ansatz for the asymptotic balances is consistent.

The above results are sufficient to give us the scaling of the shock solution. We remark that we can approximate the inner solution to lowest order, and obtain via matching (in terms of the outer variables)

$$u(x) - \nu x - \text{const.} \approx \frac{1}{\mu \delta^3} \text{Si}\left(\frac{\mu x}{\delta}\right) = \frac{1}{\mu \delta^3} \int_0^{\mu x/\delta} \frac{\sin t}{t}\, dt,$$

39
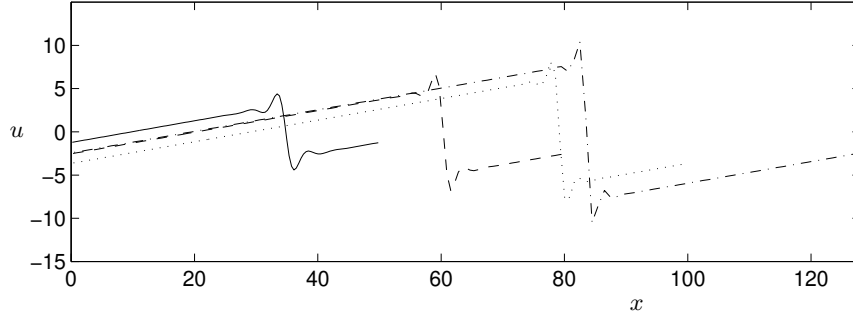
Figure 2.2: Stationary shock solutions for $\varepsilon^2 = 1.5$, and (from left to right, in increasing order of height) for $L = 50$, $L = 80$, $L = 100$ and $L = 128$.

where $\mu = 5^{-1/4}$; that is, the oscillatory shock front is well approximated by the sine integral function (see also [GEP98]). Our asymptotic approximations are all well supported by numerical simulations, which show a shock solution even when $\nu = \mathcal{O}(1)$, much smaller than the minimum required ν expected from the asymptotic analysis. Fig. 2.2 shows shock solutions for fixed $\varepsilon^2 = 1.5$ ($\nu = 0.5$) and varying L. The results of our asymptotic analysis—that the constant outer slope depends only on ν, the height of the shock increases linearly with L, and the width δ of the boundary layer decreases with L—are all clearly seen in the Figure.

Bounds for the shock solution

From the above scaling, we may read off bounds on the solutions. We have already seen that the amplitude, for a fixed ε^2, grows linearly in L: $\|u\|_\infty = \mathcal{O}(\nu L)$. This indicates that the dynamics of the destabilized KS equation are not extensive. A similar conclusion is deduced from consideration of the L^2 bound: The contribution of the outer layer to the energy is

$$\|u\|^2 = 2 \int_\delta^{L/2} u^2 \, dx \sim \int_0^{L/2} \left[\varepsilon^2 \left(x - \frac{L}{2} \right) \right]^2 dx = \frac{1}{12} \varepsilon^4 L^3.$$

The boundary layer contributes an amount $\mathcal{O}\big((\varepsilon^2 L)^{5/3}\big)$ to the energy, which is of lower order. Thus we find for the shock solution

$$\|u\| \sim \varepsilon^2 L^{3/2}. \tag{2.36}$$

This bound falls within the range given by Thm. 4, and is consistent with our previous results.

The scaling (2.36) is particularly interesting, since it shows that for sufficiently large, but fixed $\varepsilon^2 > 1$, there exists a solution to the DKS equation with $\|u\| \sim L^{3/2}$. For the KS equation with $\varepsilon^2 = 1$, the best bound conjectured is $\|u\| \sim L^{1/2}$ (corresponding to a global L-independent bound for $\|u\|_\infty$); this (counter)example shows that such extensive scaling no longer holds for the linearly unstable KS equation. It implies that while the $\mathcal{O}(\varepsilon^{16/5} L^{8/5})$ bound may be improved, it cannot be better than $\mathcal{O}(\varepsilon^2 L^{3/2})$ for $\varepsilon^2 > 1$.

Implications for proof of extensivity in the KS equation   Our shock example is instructive, as it sheds light on the failure to date of methods establishing dissipativity for the KS equation, to prove the conjectured extensivity, $\|u\| \sim L^{1/2}$. The methods in [NST85, CEES93a, Goo94] all involve the construction of comparison functions whose effect is an essentially uniform vertical

displacement in the linear dispersion relation. As we have shown in this chapter, any such methods also work for the DKS equation, including the case of a linear destabilizing term, simply by modifying the extent of the shift in the dispersion relation.

For any future proof to succeed in establishing extensivity for the KS equation (1.1), and a uniform L^∞ bound on the solutions, it must necessarily *fail* for the DKS equation with $\varepsilon^2 > 1$. We note that in the unstable DKS equation, we cannot achieve extensivity because as L increases, we have Fourier modes with positive linear growth rates arbitrarily close to $q = 0$. A successful demonstration of extensivity for the KS equation, $\varepsilon^2 \leq 1$, should probably make explicit use of the fact that the dispersion relation $\omega(q)$ satisfies $\lim_{q \to 0} \omega(q) \leq 0$. We speculate that one will need to study and estimate the nonlinear interactions between modes, especially for small q, in detail; and we continue to be interested in this problem.

2.3.4   General remarks on the DKS equation

As previously outlined in Sec. 1.1.2, the KS equation (1.1,1.3) has acquired the status of a paradigm describing dynamics and growth in dissipative systems subject to long wavelength instabilities [MV94]. As such, it is stripped down to the simplest necessary terms—large scale driving, small scale stability, and a nonlinear term—and many details specific to particular physical systems may have been neglected. When pertinent aspects of real systems are retained, other terms may appear in KS-type equations, and the basic "pure" KS equation forms the simplest member of a "cluster of models", each with slightly different characteristics (see [HR93]).

Generalizations of the KS equation   Among the large and growing class of modified KS equations which have been derived in various applications, and studied analytically and/or numerically, the additional terms considered include a KdV-type u_{xxx} dispersion term [CKTR76, TK78, CDK93, EMR93, AD94, BBIS96], an $h_x h_{xxx}$ term arising in a phase equation for a laser [MK96], integral operators [Siv77, CPS95] including a Hilbert transform $H(u_{xxx})$ term [GC96, DE98], and a noisy forcing term [CMTHS95, CL95]—the noisy KS equation is attracting recent interest for its application to the dynamics of surfaces eroded by ion sputtering. Other modifications to the KS equation include the use of a "regularizing" $\left[u_{xx}(1 + \alpha u_x^2)^{-3/2}\right]_{xx}$ term (instead of u_{xxxx}) arising from a surface tension effect in viscous fluids flowing down an incline [MR88, BKOR92, Bro92, HR93], and the consideration of time-dependent [CPS95] and space-dependent [Joh98] coefficients. This list is by no means comprehensive, and we have not considered multidimensional analogues of the KS equation at all.

Applications of the DKS equation

In general terms, it seems reasonable that the inclusion of an additive linear term to (1.1) to form (2.2) is the simplest modification to the KS equation. However, this form is also important in applications, with the linear term arising in several early derivations [LMRT75, CKTR76, Siv79]. For small ε^2, it was studied in the context of wave number selection as the "model b" variant of the Swift-Hohenberg model of convection [PM80, PZ81, CDHS83]. More recently, the DKS equation has become important in the study of directional solidification [NCS86, MMKT91] and the evolution of a terrace edge during step-flow growth [BMV93]. The DKS equation, with an additive noise term, has also been considered in the context of electrodeposition growth near equilibrium [BPRdlR97, BPRdlR98].

Like the "pure" KS equation (see Sec. 1.1.2), the stabilized KS equation is thus also a generic equation with a wide range of applicability [MV94]. Indeed, in the integrated form, with h in-

terpreted as a front position, we see that in the DKS equation the translational symmetry $(1.9'a)$ $h \to h + \delta h$ in the front direction no longer holds. This is as expected if there is an external field in the growth direction, which imposes a preferred front location; in the context of directional solidification, a thermal gradient provides this external driving force.

These numerous and diverse applications provide a motivation for establishing the mathematical properties of the DKS equation discussed in this Chapter. As far as we know, in all these applications the additive extra term has a damping effect, corresponding to $\varepsilon^2 \leq 1$ in our notation. However, the mathematical interest of the shock solution of Sec. 2.3.3 and its implications for proofs of bounds and extensivity in the KS equation, amply justifies our consideration of this "destabilized" case.

Summary of previous work on the DKS equation   We note that in addition to the question of wave number selection [PM80, PZ81, CDHS83], some other properties of the DKS equation have received attention. We have already noted recent rigorous work on the mathematical relation between the DKS equation for small ε, and the Ginzburg-Landau equation [MS95]. Between the cellular solutions for small ε, and the full spatiotemporal complexity of the KS equation for $\varepsilon = 1$, a transition takes place, which is still poorly understood. Chaté and Manneville [CM87] postulated a mechanism of "spatiotemporal intermittency", which does not appear to be well characterized; the fundamental question of the order of the transition was revisited recently [EGG97], but a general theory has not yet been forthcoming.

Understanding of the transition first requires a knowledge of the instabilities and bifurcations of the roll solutions, as ε increases and they become more spatiotemporally complex; see Fig. 2.3 for some short-time solutions for ε^2 increasing to one. Such understanding requires, in part, an extension of the stability theory for KS cellular solutions [FST86, EW96] to this more general case, in which (for the derivative DKS equation (2.2)) the Galilean invariance (1.9), fundamental to previous studies, is broken. An extensive analytical and numerical study of the DKS equation has been performed by Misbah and Valance [MV94], who report a multitude of states, including cellular, "breathing", "vacillating breathing", parity breaking and irregularly oscillating states (note also the study [PE97] for the two-dimensional DKS equation). It would be interesting to revisit and extend this work from the point of view of dynamical systems theory, and to consider the transition in the opposite direction, from the shock solution as $\varepsilon^2 \to 1$ from above.

Relation to remainder of thesis   In the remainder of this thesis, we do not consider any of these interesting issues. Instead, we return to the KS equation, and study its localized dynamics in space and scale using wavelet-based techniques. We have also not attempted to extend the computations and experiments of Chapters 4–6 to a range of values of $\varepsilon \neq 1$; as will become abundantly clear, even for the pure KS equation we have been unable to perform the large number of experiments needed for a full understanding of the dynamical structure.

Nevertheless, the results of this Chapter are relevant to the remainder of this thesis, especially to Ch. 5, as is apparent by comparison of Figs. 2.1(a) and 2.3 with some figures in that Chapter. We see this by noting that the main effect of the additive linear term in (2.2) is to damp the large scales (for $\varepsilon^2 < 1$) or to provide additional energy at long wavelengths ($\varepsilon^2 > 1$). In the experiments of Ch. 5 in which we manipulate the interactions of different wavelet levels, we frequently observe related effects due to energy imbalance at large scales; and similar solutions are observed as in this Chapter—shock-like solutions for excessive large-scale driving, and (perturbed) cellular solutions when large scales are removed or damped. In preparation for those experiments, we now introduce the wavelet formulation of the KS equation; and stress that for the remainder of this thesis, we consider only the pure KS equation $\varepsilon^2 = 1$.
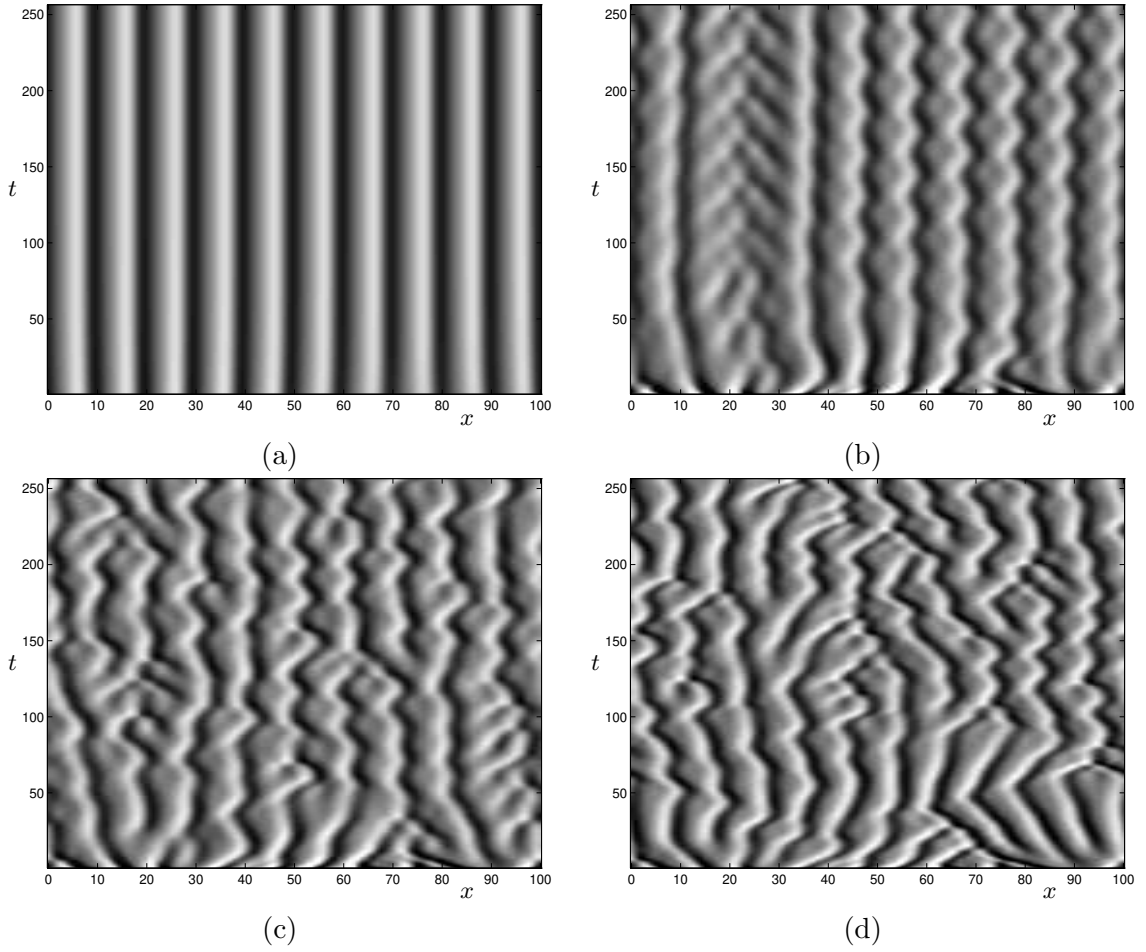
Figure 2.3: Short-time solutions for the DKS equation, for (a) $\varepsilon^2 = 0.3$; (b) $\varepsilon^2 = 0.5$; (c) $\varepsilon^2 = 0.7$; (d) $\varepsilon^2 = 0.9$. Note that the solutions in (b) and (c) appear to be transient; after longer time, they settle down to a cellular solution as in (a). Since the amplitudes increase with ε, the gray-scale is chosen appropriately to each plot.

Chapter 3

Wavelets and the KS Equation

In Sec. 1.4.1, we discussed several sets of basis functions designed to extract interesting features from the "pure" KS equation (1.1), and indicated some of their limitations. In this Chapter, we describe the projection of the KS equation onto the basis which we shall use for much of the remainder of this thesis: a periodic wavelet basis.

In contrast to a POD approach which seeks to extract the most energetic structures (see Sec. 1.4), the wavelet basis is not in any way optimized for the KS equation: the shapes of the basis functions do not approximate typical shapes of the coherent structures; they are neither concentrated in regions of high activity or small scales, nor do they move with the characteristic structures. Instead, we choose wavelets, in general, for their localization properties in space and scale, based on the observation that the spatiotemporally complex KS dynamics are characterized both by apparent "coherent structures", and by a definite peak in the power spectrum and a typical scale. In Ch. 4 we will see that a wavelet analysis allows a better understanding of scale and space localization in the STC regime than either real or Fourier space studies, and in Chs. 5 and 6 we find that wavelet-based models permit a remarkably detailed understanding of the components contributing to spatiotemporal complexity, especially with respect to the contributions of different scales. This Chapter provides the basis for the later studies.

There is, by now, a large and diverse literature on wavelets and their properties; see for instance [Dau92] among the many available introductions. As we shall need very few of their properties, and our use of wavelets is somewhat outside the usual context of their study, we shall forgo a discussion or review of the major themes of time-frequency analysis, a survey of some of the deep connections between diverse fields which have been discovered, or a glance at the many applications that have benefitted from orthogonal wavelets and their generalizations. We merely review those properties necessary for our investigations of the KS equation.

3.1 Some properties of the orthonormal wavelet basis

3.1.1 Multiresolution analysis and periodic spline wavelets

Our construction of an orthonormal wavelet basis begins with a function $\Psi(x)$, which is chosen to satisfy certain conditions [Dau92, Ch.5], which guarantee that the set of dyadically rescaled and translated functions, $\{\Psi_{j\,k}(y)\} \stackrel{\text{def}}{=} \{2^{j/2}\Psi(2^j y - k); j, k \in \mathbb{Z}\}$, forms an orthonormal basis of $L^2(\mathbb{R})$.

In particular, we require

$$\int_{-\infty}^{\infty} \Psi(y)\,dy = 0, \qquad \int_{-\infty}^{\infty} \Psi^2(y)\,dy = 1, \tag{3.1}$$

and that $\Psi(y)$ is orthogonal to its integer translates, that is,

$$\int_{-\infty}^{\infty} \Psi(y)\Psi(y+n)\,dy = \delta_{n,0}, \tag{3.2}$$

where $\delta_{n,0}$ is the Kronecker delta. Associated with the wavelet $\Psi(y)$ is a scaling function $\Phi(y)$, and a similarly defined family $\{\Phi_{j\,k}(y)\}$.

We can use the family $\{\Psi_{j\,k}(y)\}$ to construct an orthonormal basis of zero mean, 1-periodic functions on the unit interval, defining $\tilde{\psi}_{j\,k}(y) = \sum_{n\in\mathbb{Z}} \Psi_{j\,k}(y+n)$, or

$$\tilde{\psi}_{j\,k}(y) \stackrel{\text{def}}{=} 2^{j/2} \sum_{n\in\mathbb{Z}} \Psi\big(2^j(y+n) - k\big), \qquad y \in [0,1]. \tag{3.3}$$

A family of scaling functions $\tilde{\phi}_{j\,k}(y)$ is defined similarly from $\Phi(y)$.

Multiresolution analysis The family of wavelets defined in (3.3) is best understood in the context of a multiresolution (or multiscale) analysis of $L^2(\mathbb{T})$, where $\mathbb{T} = \mathbb{R}/\mathbb{Z}$ is the unit circle. The multiresolution analysis consists of a sequence of nested subspaces $\{V_j\}_{j\geq 0}$, permitting the increasingly close approximation of any given function, and including increasingly fine detail and oscillations. The definition here follows many sources, for instance [PB89, Dau92]; the spaces V_j satisfy

1. $V_0 \subset V_1 \subset V_2 \subset \ldots \subset V_j \subset \ldots \subset L^2(\mathbb{T})$,

2. $\overline{\bigcup_{j\geq 0} V_j} = L^2(\mathbb{T})$,

3. V_0 consists of constant functions,
   $f(y) \in V_j \Rightarrow f(2y) \in V_{j+1}$,
   $f(y) \in V_{j+1} \Rightarrow f(\frac{y}{2}) + f(\frac{y}{2} + \frac{1}{2}) \in V_j, \quad y \in [0,1]$,

4. $\dim V_j = 2^j$; for each j, there exists an orthonormal basis $\{\tilde{\phi}_{j\,k}(y)\} = \{\tilde{\phi}_{j\,0}(y - 2^{-j}k)\}$ of V_j.

If the multiresolution analysis on $L^2(\mathbb{T})$ is derived from one on $L^2(\mathbb{R})$, that is, if the functions $\tilde{\phi}_{j\,k}$ are obtained from the $\Phi_{j\,k}$ as above, then the spaces $V_j = \text{span}\{\tilde{\phi}_{j\,k}(y);\ k = 0\ldots 2^j - 1\}$ automatically satisfy the above conditions.

If we denote by W_j the orthogonal complement of V_j in V_{j+1},

$$V_{j+1} = V_j \oplus W_j, \qquad \text{(so that } L^2(\mathbb{T}) = V_0 \oplus W_0 \oplus W_1 \oplus W_2 \oplus \ldots \oplus W_j \oplus \ldots) \tag{3.4}$$

then $\dim W_j = 2^j$, and the functions $\{\tilde{\psi}_{j\,k}(y); k = 0\ldots 2^j - 1\}$ form an orthonormal basis for W_j. It follows that $\{\tilde{\psi}_{j\,k}(y); j \geq 0,\ k = 0\ldots 2^j - 1\} \cup \{1\}$ is a basis for $L^2(\mathbb{T})$, the finite energy periodic functions on $[0,1]$, as indicated previously. When we impose the zero mean condition, the space of constant functions becomes $V_0 = \{0\}$, and we only need the wavelets $\tilde{\psi}_{j\,k}$ as our basis.

Wavelets on $[0, L]_{per}$ We obtain an orthonormal basis of periodic functions on a domain of length L simply by rescaling:

$$\psi_{j\,k}^{L}(x) \stackrel{\text{def}}{=} L^{-1/2}\tilde{\psi}_{j\,k}\left(\frac{x}{L}\right) = L^{-1/2}2^{j/2}\sum_{n\in\mathbb{Z}}\Psi\left(2^j\left(\frac{x}{L}+n\right)-k\right), \qquad x\in[0,L]. \qquad (3.5)$$

We include the elementary demonstration that the $\psi_{j\,k}^{L}$ are correctly normalized, as an example of a typical computation with these rescaled and translated functions:[†]

$$\int_0^L [\psi_{j\,k}^{L}(x)]^2\,dx = L^{-1}2^j \int_0^L \sum_{n,n'\in\mathbb{Z}} \Psi\left(2^j\left(\frac{x}{L}+n\right)-k\right)\Psi\left(2^j\left(\frac{x}{L}+n'\right)-k\right)\,dx$$

$$= \int_0^{2^j} \sum_{n,n'\in\mathbb{Z}} \Psi\left(y+2^jn-k\right)\Psi\left(y+2^jn+2^j(n'-n)-k\right)\,dy$$

$$= \sum_{n\in\mathbb{Z}}\int_{n2^j}^{(n+1)2^j} \sum_{n''\in\mathbb{Z}}\Psi(y'-k)\Psi(y'-k+n''2^j)\,dy' \qquad (3.6)$$

$$= \sum_{n''\in\mathbb{Z}}\int_{-\infty}^{\infty}\Psi(y'')\Psi(y''+n''2^j)\,dy''$$

$$= \sum_{n''\in\mathbb{Z}}\delta_{n''2^j,0} \quad = 1.$$

In addition to straightforward changes of variables, we used (3.2) to obtain the last equality.

It follows from the above definitions that varying j, which implies compression or dilation of the wavelet, allows one to "zoom in" or "zoom out"; while changes in k correspond to horizontal translations. Throughout this thesis, we shall refer to the wavelets for a given j as a wavelet *level*. Thus a function $u(x)$, periodic on $[0, L]$ and with mean zero, can be expanded in the wavelet basis as

$$u(x) = \sum_{j\geq0}\sum_{k=0}^{2^j-1} a_{j\,k}\psi_{j\,k}(x); \qquad (3.7)$$

and the component of u at "level j" is the projection of $u(x)$ onto W_j, that is, $\sum_{k=0\ldots2^j} a_{j\,k}\psi_{j\,k}(x)$. By our choice of convention, $j = 0$ refers to the largest scale; more generally, small (positive) j implies large, or coarse, scales, while large j indicates small, or fine, scales.[‡] In practice, for numerical purposes a cutoff is needed at some finest scale J; if u has sufficiently rapid decay in Fourier space (for instance if u solves the KS equation (1.1)), such a cutoff can be readily justified.

Periodic spline wavelets

The usefulness of the wavelet decomposition follows from the relatively localized support of Ψ (and hence of the $\psi_{j\,k}$) in both real and Fourier space; of course, by the uncertainty principle, one

---

[†]In this computation, as in the remainder of this Chapter, we interchange the order of infinite sums and integrals without justification. The real space decay of the specific wavelets used below is exponential, validating the manipulations in (3.6); in later computations, the smoothness of u is assumed such that its wavelet coefficients $a_{j\,k}$ decay fast enough to allay any convergence fears. For our applications, these formal manipulations can all be justified rigorously, by checking convergence and using, when necessary, Fubini's theorem. Henceforth, we shall thus take the validity of exchanging the order of computations for granted and, without further comment, exchange sums and integrals with abandon.

[‡]Note that this convention is the opposite of that used in [Dau92].
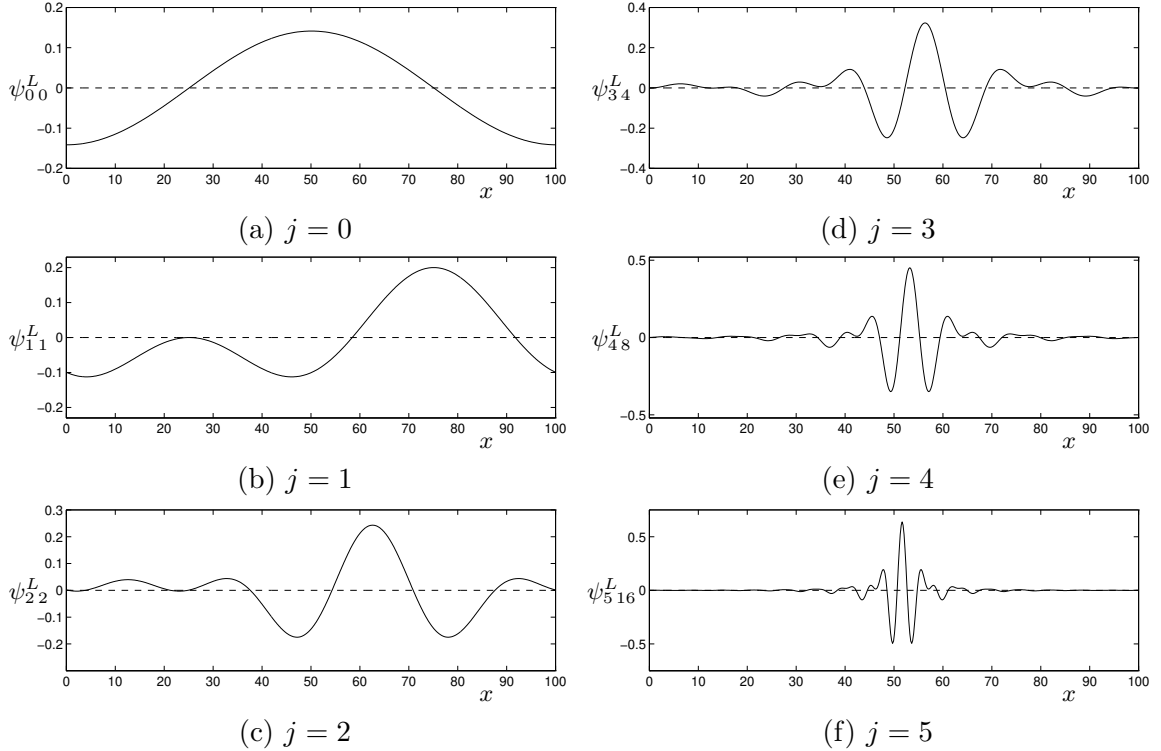
Figure 3.1: Elements $\psi^L_{jk}(x)$ of the $m = 8$ periodic spline wavelet basis, normalized on $L = 100$; wavelets at the lowest six levels $j = 0$–5, and centered near the middle of the domain: (a) $\psi^L_{00}(x)$; (b) $\psi^L_{11}(x)$; (c) $\psi^L_{22}(x)$; (d) $\psi^L_{34}(x)$; (e) $\psi^L_{48}(x)$; (f) $\psi^L_{516}(x)$.

cannot achieve complete localization in both x and q. Different wavelets have different localization properties, however, and for practical applications we need to choose a particular basis.

Following previous wavelet-based studies of the KS equation [BEH92, EBH93, MHEB95, EBH96], in this thesis we use an orthonormal, periodic spline wavelet basis, based on the Battle-Lemarié construction of m-th order spline wavelets. These wavelets are of class C^{m-2} (the subspaces V_j of the associated multiresolution analysis being spaces of piecewise polynomials of degree $m - 1$ between the grid points), and have the properties of $m - 1$ vanishing moments, exponential decay in x, and algebraic decay in q, with [BEH92]

$$|\hat{\psi}(q)| = o(|q|^{-m}), \quad |q| \to \infty; \qquad |\hat{\psi}(q)| = o(|q|^m), \quad |q| \to 0. \tag{3.8}$$

For more discussion of spline wavelets, their derivation and relevant formulae, see for instance [Dau92, Chu92, UA92]. Particularly useful for our purposes is the availability of a rapid wavelet transform algorithm to obtain the wavelet coefficients a_{jk} from a knowledge of grid values of $u(x_l)$, or *vice versa*; the rate-limiting step of the computation is the fast Fourier transform (FFT), so that the fast wavelet transform (FWT) requires $\mathcal{O}(N \log_2 N)$ steps, where $N = 2^{J+1}$ is the number of grid points. The algorithms we use in our computations, together with more relevant formulae, are given by Perrier and Basdevant [PB89], and much of our above discussion is based on their work.

Sample elements of the $m = 8$ periodic spline wavelet basis ψ_{jk} for different j are shown in Fig. 3.1. The wavelets of Fig. 3.1 represent the basis we use in this thesis; so we briefly describe some (numerically obtained) details of these functions. At level j, there are 2^j wavelets. For the $m = 8$ splines, these have real-space "support" (containing 99% of the energy) in intervals of length

$\sim 0.171 \cdot 2^{5-j}L$ (for j large enough that this result is unaffected by periodization). From the symmetry of $\Psi(y)$ about $y = \frac{1}{2}$, $\psi_{jk}(x)$ is centered about $x_{jk} \overset{\text{def}}{=} L2^{-j}(k + \frac{1}{2})$. In Fourier space, all wavelets at level j have the same support; the (overlapping) q-space intervals $q \in [0.62\,c_j, 1.4\,c_j]$ contain about 99% of the energy, where $q = c_j \approx 49 \cdot 2^{j-6}(2\pi/L)$ is the center of the support of the $\hat{\psi}_{jk}(q)$ (see Fig. 4.11(b), below).

The periodic spline wavelets appear well suited for our purpose of studying KS dynamics because of their smoothness, their good localization in x, and their relative simplicity. Since solutions of the KS equation (1.1) are analytic, we expect that smooth basis functions can represent them more faithfully; in particular, we expect to need at least four derivatives for Ψ to capture the behavior of the u_{xxxx} term in (1.1) satisfactorily. Increasing m improves the smoothness and localization in q, at the cost of increasing the spatial support; the results in this thesis all use $m = 8$ periodic orthonormal spline wavelets. However, while the details of the decomposition—in particular, the energy distribution among different wavelet levels, and hence the contributions of the levels to the overall dynamics—will depend on the particular choice of wavelet basis, we do not believe that the general conclusions drawn in this thesis are specific to our special choice of wavelet Ψ. The remaining theoretical discussion of this Chapter, for instance, is independent of the particular wavelets used. Having chosen a particular wavelet basis, therefore, for the remainder of the thesis we take this choice for granted and do not discuss it further.

3.1.2 The structure of the wavelet hierarchy

We now wish to examine the structure of the wavelet decomposition more closely. We revisit the decomposition (3.7) of a function $u(x)$ periodic on $[0, L]$:

$$u(x) = \sum_{j=0}^{J} \sum_{k=0}^{2^j-1} a_{jk} \psi_{jk}^L(x) \overset{\text{def}}{=} \sum_{\alpha} a_\alpha \psi_\alpha(x). \tag{3.9}$$

Here J is a small-scale cutoff, required to obtain a finite decomposition with $2^{J+1} - 1$ terms, and chosen high enough to give a suitably accurate representation of u. Of course, for a general function $u \in L^2([0, L]_{per})$, the first equality in (3.9) is only true in the limit $J \to \infty$, with convergence in the L^2 sense. For the theoretical discussion of this section, we shall typically ignore the cutoff J, which is equivalent to letting $J \to \infty$. For numerical computations, however, we need to impose a finite cutoff; and in Sec. 5.2.1 we investigate the effect of the smallest scales on obtaining a faithful representation of the KS dynamics.

In (3.5) and (3.9) we introduced the notation (with superscript ^{L}) ψ_{jk}^L for a wavelet periodized on $[0, L]$; this distinction will be important later. The wavelet coefficients a_{jk} are given by

$$a_{jk} = \int_0^L u(y)\psi_{jk}^L(y)\,dy \overset{\text{def}}{=} \left(u, \psi_{jk}^L\right)_L, \tag{3.10}$$

where this equation defines the inner product $(\cdot, \cdot)_L$ on $L^2([0, L])$.

We define $\mathbf{A}$ to be the set of indices in the decomposition (3.9),

$$\mathbf{A} = \{(j, k) | j = 0 \ldots J, \; k = 0 \ldots 2^j - 1\}.$$

It is frequently useful to identify the wavelet coefficients by a single index rather than two, both for simplicity (brevity) of notation, and because it is considerably easier, for numerical work and display of the results, to deal with a vector of coefficients rather than with a tensor. Thus we let α represent

Level number

$j = 0$ a_{00} Number of wavelets $2^j = 1$

1 a_{10} a_{11} 2

2 a_{20} a_{21} a_{22} a_{23} 4

3 a_{30} a_{31} a_{32} a_{33} a_{34} a_{35} a_{36} a_{37} 8

4 $a_{4\,8}$ 16

5 $a_{5\,16}$ 32

6 $a_{6\,32}$ 64

7 128

$x = 0$ $x = L$
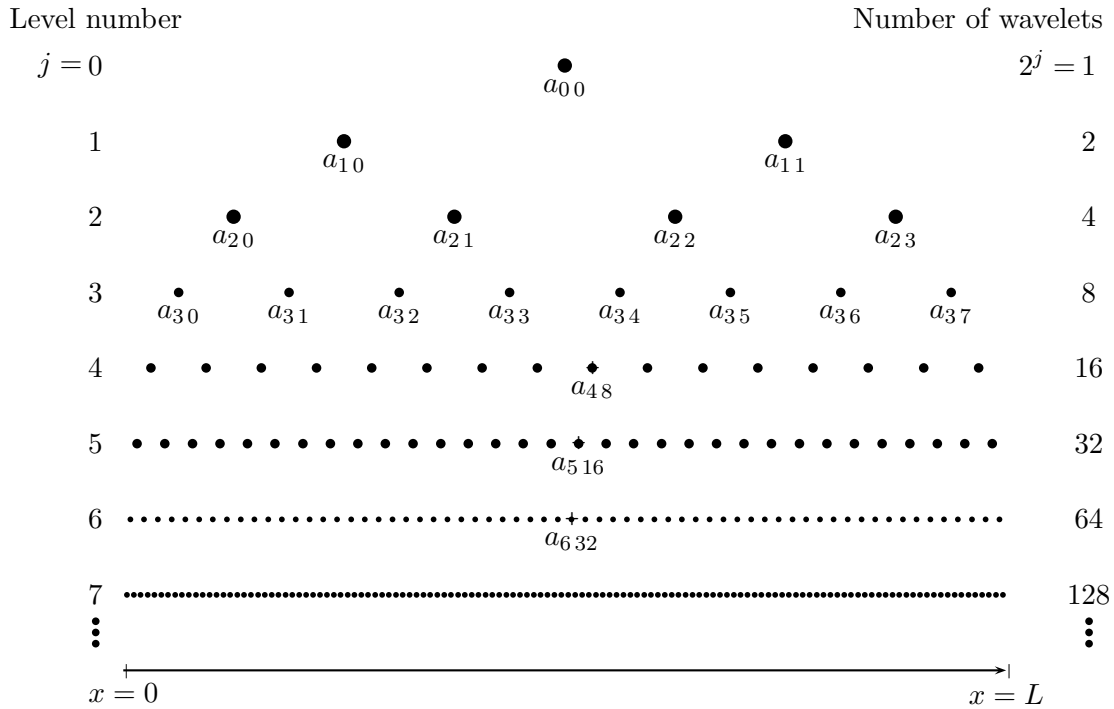
Figure 3.2: The wavelet pyramid, highlighting the hierarchical structure of the wavelet basis and its localization in space and scale; the locations of some representative wavelet coefficients are given.

the multi-index (j, k), and we shall use these two notations for the index interchangeably. (The specific numerical equivalence between these notations is straightforward: $\alpha = 2^j + k$. Conversely, $j = \lfloor \log_2 \alpha \rfloor$, $k = \alpha - 2^j$, where the floor $\lfloor y \rfloor$ denotes the largest integer $\leq y$.) Note that additional accents and superscripts in these notations will always correspond; thus for instance α' represents the pair (j', k').

The wavelet pyramid

The pyramid of Fig. 3.2 is very useful as an aid towards visualizing the structure of the wavelet hierarchy introduced in (3.9). In this representation, we can clearly see how the wavelets are ordered in scale, and how they are distributed in space for each scale. We have given the locations corresponding to some representative coefficients $a_\alpha \equiv a_{jk}$. This hierarchy applies, of course, to every orthonormal wavelet basis on an interval (satisfying specified boundary conditions), and most of this discussion holds generally, but for concreteness, one may think of the periodized spline wavelet basis introduced above in Sec. 3.1.1, since all numerical experiments were performed for this case.

The pyramidal representation of Fig. 3.2 particularly emphasizes the distinction between different wavelet levels j; for reference, we have included the level numbers, and the number 2^j of wavelets at each level j. In the horizontal direction, the points in Fig. 3.2 are placed at the centers $x_{jk} = L2^{-j}(k + \frac{1}{2})$ of the support of the wavelet ψ_{jk}.
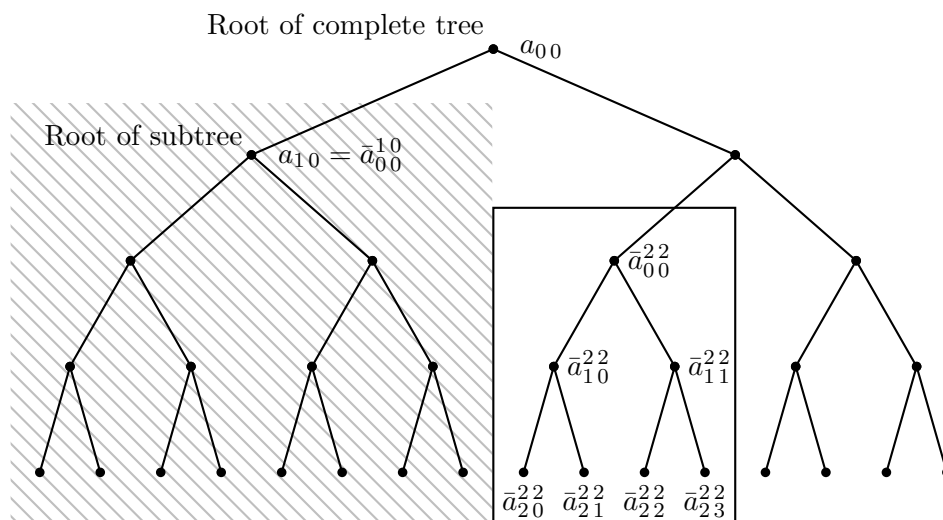
Figure 3.3: Binary tree of height 4, representing part of the full wavelet hierarchy. The hatched region marks the subtree rooted at the node n_{10}, with the two different notations for its root; the modes in this region belong to the box $\bar{\mathbf{B}}^{10}$. We have also indicated the box $\bar{\mathbf{B}}^{22}$ of length $L/4$, and the local coordinates for its internal modes.

Binary tree representation and local boxes   A useful way of thinking about the wavelet hierarchy is as a (complete) binary tree of height J, as in Fig. 3.3. We may identify the modes, or wavelet coefficients a_α (or, equivalently, simply the corresponding indices α) with nodes n_α of the tree; a_{00} is the root of the tree, while the modes at the highest (smallest scale) level J are the leaves. The depth of each node in the tree equals the wavelet level j of the corresponding mode.

In this picture, given a mode $a_{\alpha_0} = a_{j_0 k_0}$, it is straightforward to think of the subtree rooted at the corresponding node n_{α_0}, consisting of all the descendants of n_{α_0}. We define $\bar{\mathbf{B}}^{j_0 k_0}$ as the set of indices of the modes corresponding to this subtree; in terms of wavelet indices alone, $\alpha' = (j', k') \in \bar{\mathbf{B}}^{j_0 k_0}$ if $j' \geq j_0$ and $|x_{\alpha_0} - x_{\alpha'}| = L|k_0 2^{-j_0} - k' 2^{-j'}| \leq L 2^{-j_0}$. This $\bar{\mathbf{B}}^{j_0 k_0}$ corresponds to the "box" B_k of [EBH96] (where we use k_0 for their k, and j_0 for their $j_0 + 1$). Note that by this notation, the full index set $\mathbf{A} = \bar{\mathbf{B}}^{00}$. In some ways, such a subdivision of modes is artificial. For instance, the full system is spatially homogeneous, with no special points; in particular, there is nothing inherently different about $x = 0$ and $x = L/2$. The fact that, say, two wavelets centered on opposite sides of $x = L/2$ (for instance, a_{47} and a_{48}) are never both in the same resolved set $\bar{\mathbf{B}}^{j_0 k_0}$ (for $j_0 > 0$)—the only common ancestor of the corresponding nodes is the root of the entire tree—is an artifact of the wavelet decomposition; there is no inherent reason for the relation between a_{47} and a_{48} to be different from that between a_{48} and a_{49}, which are siblings in the tree, and such symmetry-breaking is the cause of some of our difficulties in constructing good wavelet-based local models for the KS equation (see Ch. 6).

Such extraction of modes corresponding to subtrees allows us to obtain spatially localized subsets of wavelet coefficients, since all the wavelets in $\bar{\mathbf{B}}^{j_0 k_0}$ are positioned in an interval I of width $L 2^{-j_0}$ centered on $L(k_0 + \frac{1}{2})2^{-j_0}$. Of course, due to the nonzero spatial support of the wavelets, this is not a perfectly localized set; the included wavelets "leak out" of the region I, while adjacent unresolved

wavelets also have support in I, as do the large-scale wavelets with $j < j_0$. However, the extraction of such subsets of resolved modes $\mathbf{B} = \bar{\mathbf{B}}^{j_0 \, k_0}$ provides a systematic way of obtaining fairly good spatial localization together with control over the behavior in scale.

It is useful to introduce an additional notation for the wavelets of a resolved set $\bar{\mathbf{B}}^{j_0 \, k_0}$, corresponding to nodes of a subtree. This notation identifies each mode by specifying the root of the subtree, and the position of the node relative to the root. Thus, for $a_{jk} \in \bar{\mathbf{B}}^{j_0 \, k_0}$, we write $a_{jk} = \bar{a}_{\bar{j}\bar{k}}^{j_0 \, k_0}$, where

$$j = j_0 + \bar{j}, \qquad k = k_0 2^{\bar{j}} + \bar{k}. \tag{3.11}$$

Conversely, given the "global" index (j, k), and the level j_0 of the root of the subtree, we can identify which box the mode belongs to (that is, the position k_0 of the root) and the "local" index (or "coordinate") relative to the box, from $\bar{j} = j - j_0$, $k_0 = \lfloor k/2^{\bar{j}} \rfloor$, and $\bar{k} = k - k_0 2^{\bar{j}}$. An example of this representation is shown in Fig. 3.3 for the box $\bar{\mathbf{B}}^{2\,2}$. Note that, ignoring questions of boundary conditions, the resolved modes $\{\bar{a}_{\bar{j}\bar{k}}^{j_0 k_0}\}$ in the box form a complete hierarchy $\bar{j} = 1 \ldots \bar{j}_{\max}$, $\bar{k} = 0 \ldots 2^{\bar{j}} - 1$, analogous to the full basis $\{a_{jk}\}$, on a smaller domain of length

$$\bar{L} \stackrel{\text{def}}{=} L 2^{-j_0}. \tag{3.12}$$

By appropriate rescaling and treatment of the boundary conditions, one can thus think of the box as a smaller model of a full system, which provides an approach to the construction of spatially localized models; this was a key idea in [EBH96].

The notation introduced in (3.11) and (3.12) will be used repeatedly throughout this Chapter, so we emphasize that coordinates $(\bar{j}, \bar{k})$ refer to the small subsystem, of length $\bar{L}$, while (j, k) refer to the full system of length L. Sometimes we will use (3.11) to express the full coordinates (and use $m \in [0, \ldots, 2^{j_0} - 1]$ instead of k_0 to denote a general box). As an example of this notation, we observe (and the reader may verify from the definition (3.5)):

$$\psi_{\bar{j}\,\bar{k}}^{L}(\bar{x}) = \psi_{\bar{j}\,\bar{k}+m2^{\bar{j}}}^{L}(\bar{x} + m\bar{L}), \qquad m \in [0, \ldots, 2^{j_0} - 1], \tag{3.13}$$

where, if necessary, we interpret this formula by periodization, that is, $\bar{k} + m2^{\bar{j}}$ is taken $(\mathrm{mod}\ 2^{j})$, and $\bar{x} + m\bar{L}$ is evaluated $(\mathrm{mod}\ L)$.

Periodized local subsystems

In the next Sections we shall outline the extraction of localized models for the KS equation, based on the boxes $\bar{\mathbf{B}}^{j_0 \, k_0}$ defined above; numerical experiments based on these ideas are described in Ch. 6. An important concept will be to apply periodic boundary conditions to the wavelets inside the boxes; then we can think of them either relative to the full system of length L, or to the shorter subsystem of length $\bar{L}$. We now make the relationship between these wavelets precise, deriving some of the consequences of periodizing.

First, we write down the relationship between wavelets periodized on the full system, and those periodized on the small box: For $\bar{x} \in [0, \bar{L}]$,

$$\psi^{\bar{L}}_{\bar{j}\bar{k}}(\bar{x}) = \bar{L}^{-1/2}2^{\bar{j}/2}\sum_{n\in\mathbb{Z}}\Psi\left(2^{\bar{j}}\left(\frac{\bar{x}}{\bar{L}}+n\right)-\bar{k}\right)$$

$$= \bar{L}^{-1/2}2^{\bar{j}/2}\sum_{n'\in\mathbb{Z}}\sum_{m=0}^{2^{j_0}-1}\Psi\left(2^{\bar{j}}\left(\frac{\bar{x}}{\bar{L}}+n'2^{j_0}-m\right)-\bar{k}\right)$$

$$= \sum_{m=0}^{2^{j_0}-1}L^{-1/2}2^{j/2}\sum_{n'\in\mathbb{Z}}\Psi\left(2^{j}\left(\frac{\bar{x}}{L}+n'\right)-\left(\bar{k}+m2^{\bar{j}}\right)\right)$$

$$= \sum_{m=0}^{2^{j_0}-1}\psi^{L}_{j\,\bar{k}+m2^{\bar{j}}}(\bar{x}) \tag{3.14}$$

$$= \sum_{m'=0}^{2^{j_0}-1}\psi^{L}_{j\bar{k}}(\bar{x}+m'\bar{L}). \tag{3.14'}$$

Here we used (3.5) (for both ψ^L and $\psi^{\bar{L}}$), (3.12) and (3.11); in particular, in the third line, we noted $L^{-1}2^j = \bar{L}^{-1}2^{\bar{j}}$. The second line depends on the fact that each $n \in \mathbb{Z}$ can be written as $n = m + n'2^{j_0}$, $0 \le m < 2^{j_0}$. Going from (3.14) to (3.14'), we used (3.13), $m' = 2^{j_0} - m$, and the L-periodicity of ψ^L. Note that (3.14) remains true on applying any linear operator, in particular a differential operator, to each side; no rescaling is necessary under differentiation.

This result—that wavelets for the short system can be expressed in terms of wavelets for the full system—is a straightforward consequence of the definition (3.5), and is equivalent to the fact that, say, the four wavelets at level 2 of Fig. 3.1, added together and rescaled, give the level 0 wavelet: $\tilde{\psi}_{2\,0}(y) + \tilde{\psi}_{2\,1}(y) + \tilde{\psi}_{2\,2}(y) + \tilde{\psi}_{2\,3}(y) = 2\tilde{\psi}_{0\,0}(4y)$. For our purposes, observe that except for small $\bar{j}$, the exponential decay of ψ^L means that the $m = 0$ term in (3.14) will make by far the dominant contribution to the sum, so that, for example for $j_0 = 2$, the $\bar{j} = 3$ wavelets of the short system look very much like the $j = 5$ wavelets of the full system. We shall see in Ch. 4, especially Sec. 4.2.5, that in the KS equation this relationship between short and full systems carries over to the statistical properties; see [EBH96].

For future reference, we also note the effect of summing large scale wavelets, $j < j_0$, in an analogous manner to (3.14'):

$$\sum_{m=0}^{2^{j_0}-1}\psi^{L}_{jk}(\bar{x}+m\bar{L}) = \sum_{m=0}^{2^{j_0}-1}L^{-1/2}2^{j/2}\sum_{n\in\mathbb{Z}}\Psi\left(2^{j}\left(\frac{\bar{x}+m\bar{L}}{L}+n\right)-k\right)$$

$$= L^{-1/2}2^{j/2}\sum_{n\in\mathbb{Z}}\sum_{m=0}^{2^{j_0}-1}\Psi\left(2^{j-j_0}\left(\frac{\bar{x}}{\bar{L}}+m+n2^{j_0}\right)-k\right) \tag{3.15}$$

$$= L^{-1/2}2^{j/2}\sum_{n'\in\mathbb{Z}}\Psi\left(2^{j-j_0}\left(\frac{\bar{x}}{\bar{L}}+n'\right)-k\right).$$

The form of this last expression is that of an $\bar{L}$-periodic wavelet at level $j - j_0 < 0$; but for a periodized wavelet basis, no negative-j levels are available, at a scale larger than $j = 0$, so the result must vanish. To show this more formally, in the final expression of (3.15), write $j_* \overset{\text{def}}{=} j_0 - j \ge 1$, $x' = 2^{-j_*}\bar{x}/\bar{L} - k$, and $n' = 2^{j_*-1}n'' + m'$ $(0 \le m' < 2^{j_*-1})$, to rewrite the sum as

$$\sum_{n'\in\mathbb{Z}}\Psi\left(2^{j-j_0}\left(\frac{\bar{x}}{\bar{L}}+n'\right)-k\right) = \sum_{m'=0}^{2^{j_*-1}-1}\sum_{n''\in\mathbb{Z}}\Psi(x'+n''/2).$$

The vanishing of the inner sum above is shown in [Dau92, Ch. 9, note 7]. In summary, we thus
have

$$\sum_{m=0}^{2^{j_0}-1} \psi^L_{j\,k}(\bar{x} + m\bar{L}) = 0, \qquad j < j_0. \tag{3.16}$$

3.2 Wavelet projections of the KS equation

Having established some of the general properties of wavelets which we need, we turn to the wavelet
formulation of the KS equation. Since a solution $u(x,t)$ of (1.1) is in $L^2[0,L]$, we can expand it in
terms of an orthogonal wavelet basis with time-dependent coefficients:

$$u(x,t) = \sum_{j=0}^{J} \sum_{k=0}^{2^j-1} a_{j\,k}(t)\psi^L_{j\,k}(x) \stackrel{\text{def}}{=} \sum_{\alpha} a_\alpha(t)\psi^L_\alpha(x). \tag{3.17}$$

The wavelet decomposition (3.17) can be used for the investigation of KS dynamics in two ways.
The first is *data analysis*: Given a solution $u(x,t)$ of (1.1) (with periodic boundary conditions),
obtained by our favorite numerical scheme—for instance the finite difference or Fourier methods
described in App. B—we can decompose the solution via a fast wavelet transform, to find the wavelet
coefficients $a_\alpha(t)$. This is sufficient to analyze the behavior at different scales, and in particular to
determine the energy per wavelet level, as well as the temporal behavior and coefficient distributions
at different levels. Such an analysis yields considerable information about the nature of the KS
dynamics, by decomposing it into its component scales; and is the subject of Sec. 4.2.

The full power of the wavelet approach to the study of such spatiotemporally complex dy-
namics is only realized, however, when we use wavelets as an *experimental tool*. That is, the KS
equation, rewritten in terms of the evolution of wavelet coefficients—which we derive and discuss
below—describes the interaction between modes localized in space and scale. By manipulating the
evolution, for instance through eliminating some modes or even complete levels, forcing at some
modes, or extracting a spatially localized set of modes and modifying its behavior, we can gain
considerable insight into "what makes the KS equation tick". Much of this thesis is devoted to
investigations of this type, and we are able to draw interesting conclusions on spatial localization
of interactions (Sec. 4.3.3), obtain detailed understanding of the contributions of different wavelet
levels to the overall characteristic dynamics (Ch. 5), and assess the picture of STC in a large domain
being composed of forced smaller, local subunits (Ch. 6).

3.2.1 Wavelet formulation of the KS equation

For the purposes of this section, notational convenience motivates our decision to write the KS
equation on $L^2[0,L]_{per}$ (or more correctly, on the Sobolev space H^2) as

$$u_t = \mathcal{L}u + u\mathcal{D}u \stackrel{\text{def}}{=} \mathcal{L}u + \mathcal{B}(u,u). \tag{3.18}$$

For the standard form (1.1) of the KS equation, the operators are defined by $\mathcal{L} \stackrel{\text{def}}{=} -\partial_x^4 - \partial_x^2$, and
$\mathcal{D} \stackrel{\text{def}}{=} -\partial_x$; and we note that $\mathcal{L}$ is a self-adjoint operator on our space.

The computations of this section do not depend on the specific form of $\mathcal{L}$, however. For instance,
they are equally valid for the damped KS equation discussed in Ch. 2, with $\mathcal{L} = -\partial_x^4 - 2\partial_x^2 - (1-\varepsilon^2)$,
or for more general self-adjoint (one-dimensional) linear differential operators. While we restrict
ourselves to the particular quadratic nonlinear operator $\mathcal{B}(u,u) = u\mathcal{D}u$, many results also hold

more generally; but we have not sought the most general possible results, choosing to explore the KS equation alone in more depth.

Galerkin projection onto a wavelet basis

To derive the wavelet coefficient evolution equations, we follow the standard Galerkin procedure, substituting (3.17) into (3.18), and then taking the inner product with a basis element ψ_α^L to obtain the evolution for $a_\alpha(t)$, exploiting the fact that the wavelets form an orthonormal basis. (This point and much of the following discussion are considered in greater depth in [MHEB95].) The ensuing KS equation for the evolution of the wavelet coefficients is

$$\dot{a}_\alpha = \sum_{\alpha' \in \mathbf{A}} l_{\alpha\alpha'} a_{\alpha'} + \sum_{\alpha',\alpha'' \in \mathbf{A}} n_{\alpha\alpha'\alpha''} a_{\alpha'} a_{\alpha''}, \tag{3.19}$$

for $\alpha \in \mathbf{A}$, where $\mathbf{A}$ is the complete set of modal indices, ideally infinite, but finite with an upper cutoff wavelet level in practice. The Galerkin coefficients $l_{\alpha\alpha'}$ and $n_{\alpha\alpha'\alpha''}$ are defined by

$$l_{\alpha\alpha'} \stackrel{\text{def}}{=} \left(\psi_\alpha^L, \mathcal{L}\psi_{\alpha'}^L\right)_L \qquad = -\int_0^L \psi_\alpha^L(y) \left(\partial_y^4 \psi_{\alpha'}^L(y) + \partial_y^2 \psi_{\alpha'}^L(y)\right) \, dy \tag{3.20}$$

$$n_{\alpha\alpha'\alpha''} \stackrel{\text{def}}{=} \left(\psi_\alpha^L, \mathcal{B}(\psi_{\alpha'}^L, \psi_{\alpha''}^L)\right)_L = -\int_0^L \psi_\alpha^L(y)\psi_{\alpha'}^L(y) \left(\partial_y \psi_{\alpha''}^L(y)\right) \, dy, \tag{3.21}$$

where the latter equations in each case are specific forms of the coefficients for the KS equation. Noting that for periodic boundary conditions, we can integrate by parts without picking up any boundary terms, we can also write (3.20) for the KS equation as

$$l_{\alpha\alpha'} = \left(\mathcal{D}\psi_\alpha^L, \mathcal{D}\psi_{\alpha'}^L\right)_L - \left(\mathcal{D}^2\psi_\alpha^L, \mathcal{D}^2\psi_{\alpha'}^L\right)_L$$

An important point here is that, in contrast to the Fourier Galerkin projection (1.5), the linear operator $\mathcal{L}$ is not diagonal in the wavelet basis. This complicates matters, as it means that different modes are interacting also through the linear term. Similarly, the nonlinear term does not enjoy a convolution form as in (1.5); there are no simple selection rules for coupling. These facts have considerable repercussions for the wavelet analysis; their implications for numerical solutions are discussed in App. B.2.2 and B.3.2.

Symmetries of the Galerkin coefficients The matrix representations $l_{\alpha\alpha'}$ and $n_{\alpha\alpha'\alpha''}$ of the linear and nonlinear operators have certain symmetries, which may be readily deduced from the definitions (3.20, 3.21), by appeal to periodicity, translational symmetry and integration by parts. In [MHEB95] these symmetries are discussed in detail, and thoroughly exploited, in the context of the wavelet structure of the KS equation for small systems. The most basic of these symmetries, independent of the wavelet basis, is

$$n_{\alpha\alpha'\alpha''} = n_{\alpha'\alpha\alpha''}; \tag{3.22}$$

and for any periodic basis, by integration by parts,

$$l_{\alpha\alpha'} = l_{\alpha'\alpha}, \qquad n_{\alpha\alpha'\alpha''} = -n_{\alpha''\alpha\alpha'} - n_{\alpha''\alpha'\alpha}. \tag{3.23}$$

From the second equation of (3.23), we can readily check the special cases

$$n_{\alpha\alpha\alpha'} = -2\, n_{\alpha'\alpha\alpha}, \qquad n_{\alpha\alpha\alpha} = 0,$$

and verify that each set of triad interactions, and hence the entire nonlinear term, conserves energy. Other symmetries are due to (discrete) translational invariance; in particular, since in $l_{\alpha\alpha'}$ only the relative position of modes α and α', not their absolute location, matters (and similarly for $n_{\alpha\alpha'\alpha''}$), the values of $l_{\alpha\alpha'}$ and $n_{\alpha\alpha'\alpha''}$ for any $\alpha = (j,k)$ can be computed provided all the values are known for $\alpha = (j,0)$. An important special case of this is the fact that the diagonal term $l_{\alpha\alpha} = l_{jk\,jk}$ depends only on the level j, not on the position k.

There are further relations, discussed in [MHEB95], which depend on the symmetry properties of Ψ, and thus do not hold for general wavelets; in our case, they arise from reflection symmetry of the periodic spline wavelets about their midpoints. One interesting consequence of this symmetry which is useful to keep in mind is $l_{00\,10} = l_{00\,11} = 0$; that is, there is no direct linear coupling between levels 0 and 1.

Extraction of models

In Chs. 5 and 6, we investigate the scale and space localization of KS dynamics by experimentally perturbing the system, and observing the effects. The basic approach is to construct wavelet-based "models", which are based on the evolution of an "internal" subset $\mathbf{B}$ of the full wavelet hierarchy $\mathbf{A}$. The model field $\tilde{u}$ is then reconstructed from the analogy of (3.17), using just the "resolved" internal coefficients,

$$\tilde{u}(x,t) = \sum_{\alpha \in \mathbf{B}} a_\alpha(t)\psi_\alpha^L(x). \tag{3.24}$$

Let us for now distinguish between resolved modes a_α for $\alpha \in \mathbf{B}$, and other modes $b_{\alpha'}$, $\alpha' \notin \mathbf{B}$ (we sometimes write $\mathbf{C} = \mathbf{A} \setminus \mathbf{B}$ for this set of "external" modes).[†] Separating the two sets of modes, the evolution (3.19) for the resolved modes becomes

$$\begin{aligned}
\dot{a}_\alpha = & \sum_{\alpha' \in \mathbf{B}} l_{\alpha\alpha'} a_{\alpha'} + \sum_{\alpha' \notin \mathbf{B}} l_{\alpha\alpha'} b_{\alpha'} \\
& + \sum_{\alpha',\alpha'' \in \mathbf{B}} n_{\alpha\alpha'\alpha''} a_{\alpha'} a_{\alpha''} + \sum_{\alpha' \in \mathbf{B},\ \alpha'' \notin \mathbf{B}} (n_{\alpha\alpha'\alpha''} + n_{\alpha\alpha''\alpha'}) a_{\alpha'} b_{\alpha''} \\
& + \sum_{\alpha',\alpha'' \notin \mathbf{B}} n_{\alpha\alpha'\alpha''} b_{\alpha'} b_{\alpha''}, \quad \alpha \in \mathbf{B}.
\end{aligned} \tag{3.25}$$

This is the general form for the evolution of a subset of the full set of modes, forced by the remaining modes in the wavelet Galerkin formulation (it corresponds to a splitting of the space, revisited in Sec. 5.3). The modes $b_{\alpha'}$ could evolve by an equation analogous to (3.25); but typically, the notation $b_{\alpha'}$ (instead of a_α, which denotes resolved modes) indicates that we consider the modes $b_{\alpha'}$ as external to the model.

In the implementation of our experiments, instead of integrating (3.25) directly, we integrate the full KS equation, but for $\alpha' \in \mathbf{A} \setminus \mathbf{B}$, at each time step we replace $a_{\alpha'}(t)$ by some $b_{\alpha'}(t)$, where $b_{\alpha'}$ is chosen according to the aspect of the overall dynamics we are testing in any given model. For instance, we might simply set $b_{\alpha'} = 0$ (usually for a complete level, in Ch. 5)—to determine whether a mode significantly affects the overall dynamics, we remove it and examine the effects. Or we might define the $b_{\alpha'}(t)$ to be a simple (constant or sinusoidal) forcing, obtain it from an autonomous KS computation or from an independent stochastic model, or derive it by periodizing the a_α, as explained below.

[†]A similar distinction between resolved and "other" modes is, of course, common in numerous related fields, among them the construction of center-unstable and inertial manifolds, and theoretical and numerical studies of turbulence.

Our distinction between two types of modes is similar in many ways to the approach of [EBH96] (for instance, (3.25) is equivalent to their Eq.(11) for the resolved modes $a^>$ with the identification $a^> = a_\alpha$, $a^< = b_\alpha$), but we do not *a priori* introduce a splitting between small and large scales; the resolved set $\mathbf{B}$ can, for now, be more general. Following [EBH96], we may define $\delta l_{\alpha\alpha'} \stackrel{\text{def}}{=} \sum_{\alpha''\notin\mathbf{B}}(n_{\alpha\alpha'\alpha''} + n_{\alpha\alpha''\alpha'})b_{\alpha''}$, $f_\alpha \stackrel{\text{def}}{=} \sum_{\alpha'\notin\mathbf{B}} l_{\alpha\alpha'}b_{\alpha'} + \sum_{\alpha',\alpha''\notin\mathbf{B}} n_{\alpha\alpha'\alpha''}b_{\alpha'}b_{\alpha''}$, and rewrite (3.25) as

$$\dot{a}_\alpha = \sum_{\alpha'\in\mathbf{B}}(l_{\alpha\alpha'} + \delta l_{\alpha\alpha'})a_{\alpha'} + \sum_{\alpha',\alpha''\in\mathbf{B}} n_{\alpha\alpha'\alpha''}a_{\alpha'}a_{\alpha''} + f_\alpha. \tag{3.26}$$

This representation distinguishes between two types of (time-dependent) forcing, the parametric perturbation of the linear term given by $\delta l_{\alpha\alpha'}$, and the additive forcing term f_α. This distinction is particularly interesting when the resolved modes in $\mathbf{B}$ are the large scales, for which the small scales provide an effective stochastic forcing f_α, as well as renormalizing the effective viscosity through $\delta l_{\alpha\alpha'}$. Indeed, the fact that the cutoff between the large and small scales could be chosen so that for all the resolved large-scale modes, the effective viscosity $\nu_{\alpha\alpha'} \stackrel{\text{def}}{=} -(l_{\alpha\alpha'} + \delta l_{\alpha\alpha'}) > 0$, was a major conclusion confirming the conjecture of Yakhot [Yak81] that the large-scale KS dynamics is in the same universality class as the forced Burgers equation (see [Zal89, HJJ93], and [EBH96] for the wavelet formulation discussed here; also refer to the next Section, and to Sec. 4.2.2). However, in this thesis, we concentrate on resolved modes at the active scales, and do not expect the distinction between the two types of forcing (additive and parametric) to be helpful for our interpretations, so we will not significantly pursue this issue further; see however Sec. 5.3.2.

3.2.2 Review of previous work, and preview of later Chapters

In Sec. 1.4 we reviewed some progress on the project of understanding (boundary-layer) turbulence through the extraction of low-dimensional Galerkin models, enabling the description of the local dynamics of energy-bearing coherent structures, which are identified through the proper orthogonal decomposition (POD)—see [HLB96]. This yielded the hope that highly complex spatiotemporal dynamics could be understood through description in terms of relatively low-dimensional models, accounting for spatially localized regions, which interact to give the full dynamics.

The study of the Navier-Stokes equations faces major analytical and numerical obstacles, however. Hence the Kuramoto-Sivashinsky equation has been popular as a test case for the study of spatiotemporal complexity, being a more tractable one-dimensional scalar PDE, rather than a multi-dimensional vector system. As already discussed in Sec. 1.4.1, however, owing to the periodic boundary conditions imposed on the KS equation, the POD method does not provide spatial localization, and related methods have so far not yielded convincing benefits. This line of thinking motivated Elezgaray, Berkooz, Holmes and coworkers [BEH92, EBH93, MHEB95, EBH96] to study wavelet-based models for the KS equation, with the goal of exploiting the good spatial and scale localization of wavelets, as described in Sec. 3.1.1 above. This thesis continues this line of inquiry.

Wavelets and turbulence Before reviewing previous work on wavelet-based studies of the KS equation, and the contribution of this thesis to the field, we note that there has recently been considerable activity in the study of fluid turbulence with the aid of wavelet techniques. This rapidly growing field has inspired several reviews (see for instance [Far92, FKPG96]) and at least one book ([Abr97]); and we do not attempt to cite or review the extensive literature, referring instead to the reviews for references and further discussion.

Multiresolution analysis and the wavelet decomposition enables one to localize simultaneously in space and scale, and to "zoom in" to fine scales for analysis or numerical simulation. Thus

wavelet-based techniques have been useful for the detection and characterization of singularities, and to analyze multifractal or self-similar structures. Analytical progress has benefited particularly from improved characterizations of function spaces such as Hölder, Sobolev and Besov spaces in terms of the wavelet transform, and from a rigorous basis for multifractality, believed to account for some features of turbulence (see [Fri95]). Wavelets have been used to analyze turbulent structures, local energy spectra and energy transfers, enabling decomposition of the turbulent velocity field into distinct regions: energetic regimes containing coherent structures, sheared and background regions. Various approaches to turbulence modeling and computation using wavelets have also shown promise recently.

The approach used for the study of the KS equation is quite different from that typically used in turbulence studies, however. Since KS solutions are analytic (see Secs. 1.2.2 and 2.3.1), and have strong decay in Fourier space (Fig. 1.4), there is no need to resolve small scales, or to resort to function spaces which support singularities. While rapid wavelet-based schemes are available for the KS equation (see App. B.2.2), and are heavily exploited in this thesis, for the full equation they offer no computational advantages over finite difference or Fourier methods. Our justification for using wavelets rests instead on their scale and space localization properties, as already indicated.

Traveling wavelets   Let us comment briefly on one wavelet-based approach which has been suggested for modeling localized structures, moving in space: the "traveling wavelet" method [BHP90]. In this Lagrangian approach, wavelets are treated as phase-space "atoms" whose time-dependent amplitude, scale and position evolve under ODEs derived from the governing PDE. This provides one way of letting coherent structures move around. This otherwise attractive idea is not appropriate for us, however: firstly, the shapes of the wavelets do not approximate our structures well, and secondly and more seriously, a major drawback to this method is the absence of a systematic and well-founded way of dealing with collisions between the "atoms"—as discussed in [PB91] in an application to the Burgers equation. We cannot hope to obtain a reasonable model for KS dynamics without being able to include the ubiquitous local creation and annihilation events (see [RK95] for a particle-based method of dealing with this problem).

Overview and critique of previous work as background for the following Chapters

In this thesis, we continue the program of seeking localized models, hopefully of relatively low dimension, for the essential features of STC in the KS equation. Motivations for this investigation include both the search for a small system which may be amenable to dynamical systems techniques, and an improved understanding of the nature of STC *per se*. In carrying out this investigation, we also revisit some of the earlier calculations, and renew our understanding of the results. In this Section, we review the previous work of Elezgaray, Berkooz, Holmes and others; a general overview of these results is also found in [EBDHM97], while [BEHLP93] gives an early review emphasizing the connection with low-dimensional modeling of coherent structures in fluids.

We have found that a necessary prerequisite for understanding models of the STC state is a more detailed characterization of this regime than has been previously available, for instance from [Pum85]. We thus compute improved statistics in real and Fourier space, as well as for wavelets, in Ch. 4. These calculations yield spectra, time constants and probability distributions for the full KS equation, which we use as benchmarks for the evaluation of our models, enabling a more careful determination of "success" of a model than has been possible previously [DHBE96, EBH96]. The wavelet statistics also enhance our understanding of scale localization, which is confirmed and extended through experiments on the contributions of complete wavelet levels.

Energy efficiency of wavelet basis   In the first wavelet-based study of the KS equation [BEH92], the energy efficiency of the wavelet basis was considered. This was because a major motivation for the use of the POD to extract coherent structures is its optimality, in the sense that on average, the first n POD eigenmodes contain at least as much energy as the first n modes of any other orthonormal basis. Since wavelets are not POD eigenmodes (these are Fourier modes for this homogeneous system), we expect that they will not capture as much of the energy in few modes. Berkooz *et al.* [BEH92] used the Fourier space decay of the periodic spline wavelets (3.8) to show that they do "almost as well" as Fourier modes in capturing the energy, and that the discrepancy decreases as the order m of the splines increases; although explicit representations of the difference are not given (and there is no indication that wavelets are in any way better than other orthonormal bases). Essentially, these results represent the fact that the wavelets are well localized in Fourier space, rather than a general result about wavelet approximation to the POD "best basis". The content of these results in the context of the KS equation is portrayed in Fig. 4.11(b).

Bifurcation analysis for short systems   As already discussed briefly in Sec. 1.2.3, the bifurcation behavior of the KS equation for short systems is understood in great detail, through studies of dynamical systems with a small number of Fourier modes, augmented by the use of a center-unstable manifold or approximate inertial manifold projection [AGH89, KNS90, JKT90]. The translation invariance of the KS equation, reflected in the $O(2)$ symmetry of the low-dimensional dynamical system, is typically essential to obtain the correct bifurcation behavior (see Sec. 1.2.1, and for instance [AGH88]). Since wavelets form an orthonormal basis, the full equation (3.19) must display all KS bifurcations; but what about a smaller system? A wavelet basis, being spatially localized, breaks the translation invariance (the continuous group $O(2)$ is replaced by the discrete dihedral group D_k, where $k = 2^{J+1}$ if wavelet levels up to J are included); thus the question arose whether the correct bifurcation behavior and "simple" solutions outlined in Sec. 1.2.3—in particular, the fundamental features of (modulated) traveling waves and heteroclinic cycles—are observed in a low-dimensional wavelet projection.

Using a 15-dimensional wavelet projection of the KS equation for $L \approx 4\pi$, Myers *et al.* [MHEB95], using previous results of [AGH88] and [CH92], showed that the breaking of symmetry was mild enough that the ensuing D_4-equivariant system preserved the basic features of the bifurcation picture, with some discrepancies. However, the demonstration of this result required a linear transformation into the combination of wavelets which best approximated Fourier modes. In a sense, it therefore showed that an "almost Fourier" basis gives "almost" the correct behavior.

In the context of understanding the nature of STC in the KS equation, it is unclear that the correct symmetry and bifurcation sequence are essential to the resulting STC regime. As shown in Ch. 4, the STC state is robust, persisting over a wide range of lengths L with little variation in its essential dynamical or statistical properties, while the number of active modes and the details of their interaction change considerably. The specific bifurcation diagram, containing the sequence and stability of the "simple" states and the transitions between them, is in some sense an accident of the particular constraints occurring in small systems; under small perturbations, the intricate interactions of bifurcation branches would be modified, the particular observed sequence of states would be disrupted, but the eventual spatiotemporally chaotic state, arising from the nonlinear interaction of many modes, would remain essentially unchanged. This conclusion is supported by the effect of changing the boundary conditions: For Dirichlet or mixed boundary conditions, the translation invariance and $O(2)$ symmetry is lost, the bifurcation sequence is completely different, but for a sufficiently large domain, the spatiotemporally complex dynamics in the interior is almost indistinguishable from that for periodic boundary conditions (see Sec. 4.3.1 and Fig. 4.18).

Localized models

Since the number of unstable modes grows linearly with the length of the system, in searching for low-dimensional models we seek a representation for small subsystems, of length $\bar{L}$. If $\bar{L}/L = 2^{-j_0}$ for some j_0 (for a given $\bar{L}$, we can choose L as a multiple of $\bar{L}$ by a power of two, to satisfy this condition, since in the STC regime, changes in L have little effect), then in the wavelet picture, such a subsystem corresponds to the extraction of a box $\bar{\mathbf{B}}^{j_0\,k_0}$, a subset of the full set $\mathbf{A}$ of wavelet modes, as discussed above in Sec. 3.1.2.

The crucial question is how to deal with unresolved modes, those outside the box $\bar{\mathbf{B}}^{j_0\,k_0}$. These include, firstly, wavelet levels outside the finite band retained. For the small scales, the use of a (computationally expensive) approximate inertial manifold technique is mentioned briefly in [EBH93]. As shown in Sec. 5.2.1, however, the effect of the small scales is sufficiently negligible that they can safely be ignored in many cases (except for pointwise tracking of solutions; see Sec. 5.3.1). The large scales, with $j < j_0$, were essentially ignored in the models discussed in [BEH92, EBH93] (although $\bar{L}$ was taken large enough that some large scales were retained), while in [EBH96], the interaction between the large and small scales was considered, largely through some statistics of energy transfer and the effective viscosity obtained in models coupling large scales and $\bar{L} = 50$ boxes. In Ch. 5 we discuss in detail the interactions between scales, and among other results, deduce the important contribution of the large scales to maintaining the spatiotemporal disorder.

Local models with external forcing More difficult is the issue of unresolved physical space, or of modes corresponding to physical locations outside the domain of length $\bar{L}$. One possibility— neither easy to implement in practice, nor to understand theoretically—is to model the external modes somehow, ideally through a stochastic model (as suggested in [BEH92]) which, one would expect, might need to respect the correct correlations, temporal behavior, and distributions of the modes that are being replaced, up to a certain "interaction distance". Results of this type have not yet been published; unpublished simulations of J. Elezgaray, in which forcing is via a few neighboring modes from a full simulation, show dynamics that tends to settle down to time-independent equilibria, or to constrained rigid states with little motion of peaks (see Sec. 6.1).

We have attempted to construct various different types of such localized, forced models; in Sec. 6.1 we review the results of several such experiments, and explain why our results do not seem promising for tracking or reasonable statistics. It seems that this approach fails because initially equivalent wavelet modes become inequivalent in an essential way in the localized box: the modes localized in the interior remain correlated with their neighbors, while those near the edge of the box lose some resolved neighbors, and are instead subject to adjacent forcing uncorrelated with the internal modes of the model.

This failure contrasts with the success of the boundary-layer turbulence model of Aubry *et al.* [AHLS88], where the pressure term was modeled by random forcing at the boundary. There, the original system is not homogeneous in the wall-normal direction, and the energy is concentrated near the wall, making a model of the wall region with external forcing is more plausible than in our case.

Periodized local models An alternative to non-periodic, forced models, is to "periodize" the model. That is, one postulates that the influence of missing neighboring modes at the boundary of the domain can be compensated for by interaction with distant, resolved modes, achieved through applying periodic boundary conditions to the subsystem. This approach is commonly used in fields such as computational fluid mechanics to reduce the size of the problem, and was

applied successfully in the streamwise and spanwise directions in [AHLS88]. This approach needs some assumptions (or results) on the distance across which modes interact, to avoid excessively constraining the system.

In the absence of interactions with the large scales, a periodized length $\bar{L}$ subsystem of a larger system is exactly equivalent to a KS equation on length $\bar{L}$, with periodic boundary conditions, as described in the next Sec. 3.3. This line of thought led to the study of the periodic, small-$\bar{L}$ KS equation on a wavelet basis, already mentioned above [MHEB95]. However, it also raises two points: Firstly, we have come full circle, back to the system we are seeking to understand, the periodic KS equation (though possibly on a smaller length); so what has been gained? Secondly, since our short system is exactly equivalent to (1.1), there is no need to use wavelet methods to study it; and as we already know, the Fourier projection, with a diagonal linear part, has proved more useful in understanding the bifurcation behavior for small lengths.

Fourier-based local models for periodic short systems   In view of the second point, Fourier projections of short periodic systems were studied by Dankowicz *et al.* [DHBE96] (see also [Dan95]). They observed short-term tracking relative to a large system, reflecting the fact that boundary influences propagate into the system at a finite rate. They also noted that some small systems, with a few unstable modes, can reproduce local "events" such as collisions and creation of peaks (see Sec. 1.3.2); and that some lengths are better than others at maintaining typical KS dynamics for a relatively long time, yielding approximately correct spectral properties (these lengths typically coincide with those known to have a chaotic attractor [HNZ86]). There was also evidence for a "resonance effect": that these lengths also provide superior tracking, on average, in experiments in which the state of the short system was repeatedly reset to the local state of a large system; this is a surprising and unexplained result about interaction between the influence of boundary conditions and internal unstable dynamics, if it withstands further extensive statistical scrutiny.

Dankowicz *et al.* also studied models in which the length is varied, either through following zeros of a run of a large system, or by an autonomous model for length variation via a quotient norm of the energy; and showed that under some conditions, this can keep the system "stirred up", though primarily for lengths in the vicinity of those which display a chaotic attractor or long transient for constant $\bar{L}$. It is unclear how the findings of [DHBE96] can be seen as modeling a large system, or accounting for the robust properties of the KS equation in the STC regime, rather than reflecting mainly the fact that the attractors for some small lengths $\bar{L}$ are chaotic.

A dynamic interaction length for periodic systems   In their original studies of wavelet-based localized models for the KS equation, Berkooz, Elezgaray and Holmes [BEH92, EBH93] periodized their model (extracted as a subsystem of a larger system, as described above), and conjectured the existence of a dynamically relevant interaction length l_c, so that within the box of length $\bar{L}$, only couplings $l_{\alpha\alpha'}$ and $n_{\alpha\alpha'\alpha''}$ between wavelets centered no more than l_c apart were retained in the model (their notation was L_C and L_B for our l_c and $\bar{L}$, respectively). In the simulations reported, for an $\bar{L} = 50$ system, an interaction length $l_c = 12.5$ led to rapid decay into a steady state, while $l_c = 18.75$ displayed a much longer transient of activity containing typical KS events. They regarded these simulations as evidence of the local nature of the interactions which underpin the STC state.

As noted previously, and shown rigorously below, in the absence of the large scales, such periodized models are equivalent to $\bar{L}$-periodic KS equations; this holds also when interactions are cut as described. In order to *quantify* the interaction length l_c postulated in [BEH92, EBH93], we perform an extensive series of experiments for various values of l_c, described in Sec. 4.3.3. While our results

are not statistically well-averaged, they provide strong evidence for the existence of such a *dynamical* interaction length, beyond which wavelets may be uncoupled with impunity with neglible effect on the STC dynamics, while the removal of interactions between wavelets too near each other typically has significant consequences, leading to blowup or decay into a stationary state. As discussed at length in Sec. 4.3, this interaction length conveys different information than do other, averaged measures of spatial correlation, and demonstrates the local nature of *instantaneous* dynamics, thus providing a further useful characterization of STC in the KS equation. However, the existence of l_c does not significantly promote the search for low-dimensional local models: compared with retaining all interactions, this approach does not reduce the number of modes, while considerably complicating the system (a PDE or Fourier mode description is no longer possible). Furthermore, since each mode interacts with a different subset of the full wavelet set, computing with this model is slow (see App. B.2.2), and it thus offers no computational advantage.[†]

Interactions of small subsystems with large scales   In order to obtain a model that truly describes a spatially localized domain as a subsystem of a larger system, we need to take account of the interactions with the large scales. This point was noted by Elezgaray *et al.* in [EBH96], whose main stated goal was to obtain a wavelet-based effective model for the large scale statistics. However, in doing so, they primarily computed active scale statistics[‡] for $L = 400$ and $\bar{L} = 50$, such as wavelet energy spectra and preliminary computations of wavelet coefficient distributions (which are improved and extended in Sec. 4.2), to show that their "short" periodic (sub)systems are minimally affected by the interactions with the large scales. They then argued that the statistics, in particular a "transfer" term between active and large scales, are little changed if a full KS equation is replaced by a set of $\bar{L}$-periodic subsystems, forced by time series of the large scales derived from the full system; although the agreement is worse if the large scales evolve under forcing from the periodized boxes.

While their idea of the STC state as an assembly of "short length subsystems, slowly driven via interactions with the large scales" is appealing, and informs the conceptual basis and motivation for much of this thesis, it is unclear to what extent they succeeded in validating this picture. In view of the fact that their "short" system has $\bar{L} = 50$, a length for which the attractor is chaotic [HNZ86], the "good" behavior of the coupled forced subsystems is hardly surprising; they are large enough to give complex behavior even in the absence of forcing. While [EBH96] did not aim to study local, low-dimensional models, it is not completely clear how they addressed the issue of an effective equation for large scales either: the most successful simulations required the large scales to be computed from the full KS equation, and the final "completely autonomous model" requires the solution of a high-dimensional system coupling the large scales to periodized subsystems and *vice versa*, a system that is no smaller, and is much more complicated, than the KS equation itself.

In this thesis we are not primarily concerned with the large scales; much work has been done in support of the idea of Yakhot [Yak81] that the large scales satisfy a forced Burgers equation, with the dynamically unstable active modes providing an effective stochastic forcing, and this work is reviewed in Sec. 4.2.2 and corroborated throughout this thesis. We are more interested in understanding the STC mechanisms functioning at the *active* scales, and in Sec. 6.2 we study periodized subsystems, forced from the large scales (so they are truly *sub*systems of a larger domain), for lengths $\bar{L}$ small enough that the unforced systems have a simple, nonchaotic attractor, providing a more stringent test of the effects of forcing than in [EBH96]. In the next Section we derive a theoretical basis for such periodized subsystems.

[†]This point was emphasized by an anonymous reviewer for the journal *Chaos*.

[‡]See Sec. 4.2 for definitions of large, active and small scales.

To conclude this Section, we include some cartoons in Fig. 3.4, giving a schematic summary, based on the wavelet pyramid, of the major themes of [EBH96] and of the experiments of Chs. 5 and 6.

3.3 Periodized models

Equivalence of periodized model on $[0, L]_{per}$ and KS equation on $[0, \bar{L}]_{per}$

In practice, we periodize from level j_0 (where $L = 2^{j_0} \bar{L}$) by equating corresponding wavelet coefficients from the 2^{j_0} boxes. That is, using the usual notation, we set a_{jk} equal to its 2^{j_0} translates at level j, obtained from $k \to k + m2^{\bar{j}} \pmod{2^j}$. More clearly perhaps, periodizing from level j_0 means that $\bar{a}_{\bar{j}\bar{k}}^{j_0 k_0}$ is independent of k_0; in this case, we simply denote the coefficients by $\bar{a}_{\bar{j}\bar{k}}^{j_0}$. We then also let $\bar{\mathbf{B}}^{j_0}$ be the set of all modes in a box, when the dependence on k_0 no longer matters. (For notational convenience, we will often assume the dependence on j_0 without making it explicit, writing $\bar{a}_{\bar{j}\bar{k}} = \bar{a}_{\bar{\alpha}}$ and $\bar{\mathbf{B}}$.)

We thus have two ways of solving the KS equation on an $\bar{L}$-periodic domain:

1. Solve the KS equation on an $\bar{L}$-periodic domain "directly"; that is, solve the evolution equations (3.19) for the wavelet coefficients of an $\bar{L}$-periodic $\bar{u}(x,t)$, where the coefficients in the Galerkin projection are obtained from wavelets periodized on $[0, \bar{L}]$:

$$\bar{l}_{\bar{j}\bar{k}\,\bar{j}'\bar{k}'} = \left(\psi_{\bar{j}\bar{k}}^{\bar{L}}, \mathcal{L}\psi_{\bar{j}'\bar{k}'}^{\bar{L}} \right)_{\bar{L}}, \qquad \bar{n}_{\bar{j}\bar{k}\,\bar{j}'\bar{k}'\,\bar{j}''\bar{k}''} = \left(\psi_{\bar{j}\bar{k}}^{\bar{L}}, \psi_{\bar{j}'\bar{k}'}^{\bar{L}} \mathcal{D}\psi_{\bar{j}''\bar{k}''}^{\bar{L}} \right)_{\bar{L}}.$$

2. Solve the KS equation (3.19) for wavelets defined on $[0, L]_{per}$, $L = 2^{j_0} \bar{L}$, where the coefficients a_{jk}, $j \geq j_0$ are, initially, periodized from level j_0 as described above, and $a_{jk}(0) = 0$ for $j < j_0$.

We need to confirm that these two approaches in fact give the same answers, so that we can in good conscience speak of the second method, a KS equation on $[0, L]_{per}$ periodized by initially equating the coefficients in the 2^{j_0} boxes, as a KS equation on $[0, \bar{L}]_{per}$. We need to demonstrate two things: that the system, if initially periodic, remains so, in particular that the symmetry-breaking large scales vanish for all t; and that the coefficients in the boxes, with $j \geq j_0$, obey the same evolution equations that they would in an $\bar{L}$-periodic system.

Invariance of periodic subspace The first condition is straightforward: A periodic initial state (invariant under the symmetry $x \to x + 2^{-j_0}L$) must remain periodic. In Sec. 1.2.1 we have already noted this invariance of the fixed point subspace of $\mathbb{Z}_{n_0}$ from the Fourier representation of the KS equation: the subspace $\{\hat{u}_q \neq 0 \text{ for } q = nq_0, n \in \mathbb{Z}; \hat{u}_q = 0 \text{ otherwise}\}$ is invariant under the evolution (1.5) for any $q_0 = (2\pi/L)n_0$, in particular for $n_0 = 2^{j_0}$. This result must carry over to the wavelet representation; and in particular, the symmetry-breaking large scales must remain zero. It is nevertheless illuminating to confirm this result directly from the wavelet evolution equations.

In writing the evolution equations for the modes a_{jk}, $j < j_0$ (which we denote also by a_α, $\alpha \in \mathbf{C} = \mathbf{A} \setminus \mathbf{B}$, where $\mathbf{B} = \{(j,k); j \geq j_0\}$), we can use a separation between internal (I) and external (E) modes as in (3.25) above to write

$$\dot{a}_\alpha = L_\alpha^I + N_\alpha^{II} + N_\alpha^{IE} + L_\alpha^E + N_\alpha^{EE}. \tag{3.27}$$

For any time at which $a_\alpha = 0$, $\alpha \in \mathbf{C}$, all the terms which contain internal modes with $j < j_0$ also vanish; thus, for instance, $N_\alpha^{IE} = \sum_{\alpha' \in \mathbf{B}} a_{\alpha'} \left[\sum_{\alpha'' \in \mathbf{C}} n_{\alpha\alpha'\alpha''} a_{\alpha''} \right] = 0$, and similarly $L_\alpha^I = N_\alpha^{II} = 0$.
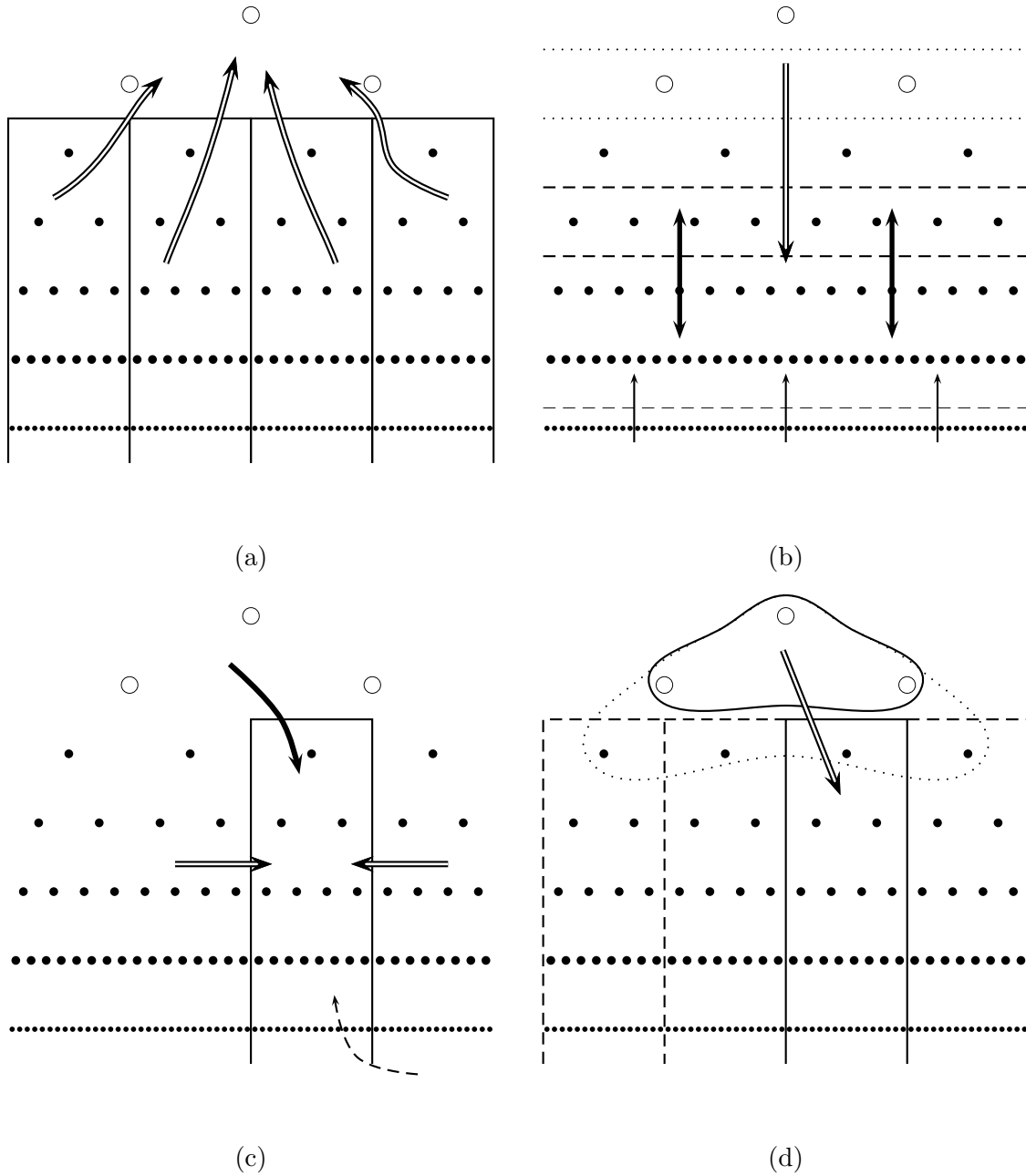
Figure 3.4: Schematic representation of the main themes of (a) Elezgaray *et al.* [EBH96], investigating the effect of the small and active scales on the large scales; (b) Ch. 5, studying the contributions and interactions of entire wavelet levels, especially of the large scales on the active scales; (c) Sec. 6.1, attempting to construct local models with external forcing from large and active scales; (d) Sec. 6.2, examining periodized local models forced from the large scales.

The remaining terms are those from the small, periodized scales, L_α^E and N_α^{EE}, which also vanish, as we show below.

For the linear term L_α^E, we compute

$$L_\alpha^E = \sum_{\alpha' \in \mathbf{B}} l_{\alpha\alpha'} a_{\alpha'} = \sum_{\alpha' \in \bar{\mathbf{B}}^{j_0}} a_{\alpha'} \sum_{m=0}^{2^{j_0}-1} l_{\alpha\alpha'}. \tag{3.28}$$

In writing down the second equation here, we performed a step which will recur in this Section. We can write the sum over all modes $a_{j'k'}$, $j' \geq j_0$ as the sum over all modes within one box $\bar{\mathbf{B}}^{j_0}$, then summed over the boxes. Since we have periodized, $a_{j'k'} = a_{j'\bar{k}'+m2^{\bar{j}'}}$ is independent of m, so that we can take it out of the sum $\sum_{m=0}^{2^{j_0}-1}$ over the boxes. The second sum in (3.28) is (with $j' = \bar{j}' + j_0$, $k' = \bar{k}' + m2^{\bar{j}'}$)

$$\sum_{m=0}^{2^{j_0}-1} l_{\alpha\alpha'} = \sum_{m=0}^{2^{j_0}-1} \left(\psi_{jk}^L, \mathcal{L}\psi_{j'k'}^L \right)_L$$

$$= \left(\psi_{jk}^L, \mathcal{L}\psi_{\bar{j}'\bar{k}'}^{\bar{L}} \right)_L \qquad = \int_0^L \psi_{jk}^L(y)\mathcal{L}\psi_{\bar{j}'\bar{k}'}^{\bar{L}}(y)\,dy$$

$$= \int_0^{\bar{L}} \left[\sum_{m'=0}^{2^{j_0}-1} \psi_{jk}^L(\bar{y} + m'\bar{L}) \right] \mathcal{L}\psi_{\bar{j}'\bar{k}'}^{\bar{L}}(\bar{y})\,d\bar{y}$$

$$= 0.$$

We have used the definitions of the Galerkin coefficients and inner products; the second equality uses (3.14), the fourth equality uses the $\bar{L}$-periodicity of $\psi^{\bar{L}}$, and the term $[\cdot]$ vanishes in the final step by (3.16), since $j < j_0$. Using this result in (3.28), we thus find that L_α^E vanishes in (3.27). A completely analogous computation for $N_\alpha^{EE} = \sum_{\alpha'\alpha'' \in \mathbf{B}} n_{\alpha\alpha'\alpha''} a_{\alpha'} a_{\alpha''}$ shows that this term also vanishes under the same conditions.

We have thus shown that if at any time, $a_{jk} = 0$ for $j < j_0$, and the modes for $j \geq j_0$ are periodized, then $\dot{a}_{jk} = 0$ for $j < j_0$; the symmetry-breaking large scales stay at zero. It is then quite straightforward to see that under these conditions, the vector field for $j \geq j_0$ is periodic (see below). We may conclude that the periodic subspace remains invariant under the KS evolution, as expected.

Equivalence of coefficient evolutions The second point we need to show is that the wavelet coefficients in this periodized system on $[0, L]$ (with vanishing large scales) obey the same evolution equations as they would as coefficients in an $\bar{L}$-periodic system. The main results we need here are that, for $k = \bar{k} + m2^{\bar{j}}$, and similarly for k' and k'',

$$\bar{l}_{\bar{j}\bar{k}\,\bar{j}'\bar{k}'} = \sum_{m=0}^{2^{j_0}-1} l_{jk\,j'k'} \tag{3.29}$$

$$\bar{n}_{\bar{j}\bar{k}\,\bar{j}'\bar{k}'\,\bar{j}''\bar{k}''} = \sum_{m=0}^{2^{j_0}-1} \sum_{m'=0}^{2^{j_0}-1} n_{jk\,j'k'\,j''k''}. \tag{3.30}$$

We recall that the $l_{jk\,j'k'} = \left(\psi_{jk}^L, \mathcal{L}\psi_{j'k'}^L \right)_L$ are the Galerkin coefficients of the linear term in the L-periodic KS equation, while $\bar{l}_{\bar{j}\bar{k}\,\bar{j}'\bar{k}'} = \left(\psi_{\bar{j}\bar{k}}^{\bar{L}}, \mathcal{L}\psi_{\bar{j}'\bar{k}'}^{\bar{L}} \right)_{\bar{L}}$ are the corresponding coefficients for the equation on $[0, \bar{L}]_{per}$; similarly for the nonlinear coefficients.

Due to the exponential decay of the wavelets in real space, for $\min(\bar{\jmath}, \bar{\jmath}', \bar{\jmath}'')$ sufficiently large, only the $m = 0$ (and $m' = 0$) terms contribute significantly to the sums in (3.29, 3.30), and we get approximate equality between the Galerkin coefficients of the full and short systems. This, in fact, is the content of Eq. (14) of [EBH96], for which (3.29, 3.30) are the exact statements.

We show the above results by multiple use of (3.14, 3.14′), in an analogous way to the demonstration that $L_\alpha^E = 0$ in (3.28). For instance, we obtain (3.29) by

$$
\sum_{m=0}^{2^{j_0}-1} l_{jk\,j'k'} = \sum_{m=0}^{2^{j_0}-1} \left(\psi^L_{j\,\bar{k}+m2^{\bar{\jmath}}}, \mathcal{L}\psi^L_{j'\,k'} \right)_L
$$

$$
= \int_0^L \psi^{\bar{L}}_{\bar{\jmath}\bar{k}}(y) \mathcal{L}\psi^L_{j'\,k'}(y)\, dy
$$

$$
= \int_0^{\bar{L}} \psi^{\bar{L}}_{\bar{\jmath}\bar{k}}(\bar{y}) \mathcal{L} \left[\sum_{m'=0}^{2^{j_0}-1} \psi^L_{j'\,k'}(\bar{y} + m'\bar{L}) \right] d\bar{y}
$$

$$
= \int_0^{\bar{L}} \psi^{\bar{L}}_{\bar{\jmath}\bar{k}}(\bar{y}) \mathcal{L}\psi^{\bar{L}}_{\bar{\jmath}'\,\bar{k}'}(\bar{y})\, d\bar{y} \qquad = \bar{l}_{\bar{\jmath}\bar{k}\,\bar{\jmath}'\bar{k}'}.
$$

The result (3.30) for the nonlinear term is derived in an exactly analogous manner.

We now write down the evolution equations for the periodized modes at levels $j \geq j_0$ (that is, for $\alpha \in \mathbf{B}$, where $\mathbf{B}$ and $\mathbf{C} = \mathbf{A} \setminus \mathbf{B}$ are as before):

$$
\dot{a}_\alpha = \sum_{\alpha' \in \mathbf{B}} l_{\alpha\alpha'} a_{\alpha'} + \sum_{\alpha' \in \mathbf{C}} l_{\alpha\alpha'} a_{\alpha'} + \sum_{\alpha',\alpha'' \in \mathbf{B}} n_{\alpha\alpha'\alpha''} a_{\alpha'} a_{\alpha''}
$$

$$
+ \sum_{\alpha' \in \mathbf{B}, \alpha'' \in \mathbf{C}} (n_{\alpha\alpha'\alpha''} + n_{\alpha\alpha''\alpha'}) a_{\alpha'} a_{\alpha''} + \sum_{\alpha',\alpha'' \in \mathbf{C}} n_{\alpha\alpha'\alpha''} a_{\alpha'} a_{\alpha''} \tag{3.31}
$$

$$
\stackrel{\text{def}}{=} L_\alpha^I + L_\alpha^E + N_\alpha^{II} + N_\alpha^{IE} + N_\alpha^{EE} \tag{3.32}
$$

$$
\stackrel{\text{def}}{=} h_\alpha^I(t) + h_\alpha^E(t) \stackrel{\text{def}}{=} h_\alpha(t).
$$

By the assumptions for this calculation, the large scale coefficients vanish, $a_{\alpha'} = 0$ for $\alpha' \in \mathbf{C}$, so $L_\alpha^E = N_\alpha^{IE} = N_\alpha^{EE} = 0$. Since we have periodized the modes for $\alpha \in \mathbf{B}$, we can take the coefficients $a_{\alpha'}$ and $a_{\alpha''}$ out of the sums over the boxes, as before, so that (3.31) becomes

$$
\dot{a}_\alpha = \sum_{\alpha' \in \bar{\mathbf{B}}^{j_0}} a_{\alpha'} \sum_{m=0}^{2^{j_0}-1} l_{\alpha\alpha'} + \sum_{\alpha',\alpha'' \in \bar{\mathbf{B}}^{j_0}} a_{\alpha'} a_{\alpha''} \sum_{m=0}^{2^{j_0}-1} \sum_{m'=0}^{2^{j_0}-1} n_{\alpha\alpha'\alpha''},
$$

where we are using the usual notational conventions, such as $\alpha' = (j', k') = (j', \bar{k}' + m2^{\bar{\jmath}'})$. Now we can evaluate the inner sums by using (3.29) and (3.30). The remaining sums are over a single short box; and we can rewrite the periodized coefficients as, for instance, $a_{\alpha'} = \bar{a}^{j_0}_{\bar{\jmath}'\bar{k}'}$, since they are independent of the box. We have thus shown that (3.31) is equivalent to

$$
\dot{\bar{a}}_{\bar{\jmath}\bar{k}} = \sum_{(\bar{\jmath}',\bar{k}') \in \bar{\mathbf{B}}} \bar{l}_{\bar{\jmath}\bar{k}\,\bar{\jmath}'\bar{k}'} \bar{a}_{\bar{\jmath}'\bar{k}'} + \sum_{(\bar{\jmath}',\bar{k}'),(\bar{\jmath}'',\bar{k}'') \in \bar{\mathbf{B}}} \bar{n}_{\bar{\jmath}\bar{k}\,\bar{\jmath}'\bar{k}'\,\bar{\jmath}''\bar{k}''} \bar{a}_{\bar{\jmath}'\bar{k}'} \bar{a}_{\bar{\jmath}''\bar{k}''}, \quad \bar{\jmath} \geq 0, \ \bar{k} = 0 \ldots 2^{\bar{\jmath}} - 1. \tag{3.33}
$$

But these are exactly the wavelet Galerkin projection equations for an $\bar{L}$-periodic KS equation. This concludes the verification that the full system defined on $[0, L]_{per}$, periodizing coefficients for $j \geq j_0$, and setting $a_{j\,k}$ for $j < j_0$ to zero, is exactly equivalent to a KS equation on $[0, \bar{L}]_{per}$.

65

For future reference, we observe that the above discussion can be restated in the following way: The $\bar{a}_{\bar{j}\bar{k}}^{j_0}$ are the wavelet coefficients of a function $\bar{u}(\bar{x}, t)$,

$$\bar{u}(\bar{x}, t) = \sum_{\bar{j}\geq 0}\sum_{\bar{k}=0}^{2^{\bar{j}}-1} \bar{a}_{\bar{j}\bar{k}}^{j_0}(t)\psi_{\bar{j}\bar{k}}^{\bar{L}}(\bar{x}) \stackrel{\mathrm{def}}{=} \sum_{\bar{\alpha}\in\bar{\mathbf{B}}} \bar{a}_{\bar{\alpha}}(t)\psi_{\bar{\alpha}}^{\bar{L}}(\bar{x}),$$

where $\bar{u}$ is periodic on $[0, \bar{L}]$, and satisfies the KS equation. In fact, we can "invert" the Galerkin projection equations to find the equation satisfied by $\bar{u}$. Since the $\{\psi_{\bar{\alpha}}^{\bar{L}}\}$ form an orthonormal basis on $L^2[0, \bar{L}]$, we have for $f \in L^2[0, \bar{L}]$ that

$$\sum_{\bar{\alpha}\in\bar{\mathbf{B}}} \left(\psi_{\bar{\alpha}}^{\bar{L}}, f\right)_{\bar{L}} \psi_{\bar{\alpha}}^{\bar{L}} = f. \tag{3.34}$$

Thus we can derive

$$\begin{aligned}
\bar{u}_t(\bar{x}, t) &= \sum_{\bar{\alpha}\in\bar{\mathbf{B}}} \frac{d}{dt}\bar{a}_{\bar{\alpha}}(t)\psi_{\bar{\alpha}}^{\bar{L}}(\bar{x}) \\
&= \sum_{\bar{\alpha}'\in\bar{\mathbf{B}}} \bar{a}_{\bar{\alpha}'} \sum_{\bar{\alpha}\in\bar{\mathbf{B}}} \left(\psi_{\bar{\alpha}}^{\bar{L}}, \mathcal{L}\psi_{\bar{\alpha}'}^{\bar{L}}\right)_{\bar{L}} \psi_{\bar{\alpha}}^{\bar{L}} + \sum_{\bar{\alpha}',\bar{\alpha}''\in\bar{\mathbf{B}}} \bar{a}_{\bar{\alpha}'}\bar{a}_{\bar{\alpha}''} \sum_{\bar{\alpha}\in\bar{\mathbf{B}}} \left(\psi_{\bar{\alpha}}^{\bar{L}}, \psi_{\bar{\alpha}'}^{\bar{L}}\mathcal{D}\psi_{\bar{\alpha}''}^{\bar{L}}\right)_{\bar{L}} \psi_{\bar{\alpha}}^{\bar{L}} \\
&= \sum_{\bar{\alpha}'\in\bar{\mathbf{B}}} \bar{a}_{\bar{\alpha}'}\mathcal{L}\psi_{\bar{\alpha}'}^{\bar{L}} + \left[\sum_{\bar{\alpha}'\in\bar{\mathbf{B}}} \bar{a}_{\bar{\alpha}'}\psi_{\bar{\alpha}'}^{\bar{L}}\right]\left[\sum_{\bar{\alpha}''\in\bar{\mathbf{B}}} \bar{a}_{\bar{\alpha}''}\mathcal{D}\psi_{\bar{\alpha}''}^{\bar{L}}\right] \\
&= \mathcal{L}\bar{u} + \bar{u}\mathcal{D}\bar{u},
\end{aligned} \tag{3.35}$$

which is the KS equation for $\bar{u}$, as required.

3.3.1 Periodic models forced from large scales

A general philosophy of parts of this thesis, especially Ch. 6, is to understand the spatiotemporally complex dynamics in the full system in terms of smaller, spatially localized subsystems, forced in some way as necessary to maintain dynamic activity. Since studies summarized above in Sec. 3.2.2 and reported in Sec. 6.1 imply that it is difficult to maintain reasonable behavior of the boundary wavelets for non-periodic models, we investigate the construction of periodized models for subsystems of a larger system.

In the last few pages, we have seen how a subsystem of length $\bar{L} = 2^{-j_0}L$ of a full system of length L, periodized by making 2^{j_0} copies of a box $\bar{\mathbf{B}}^{j_0}$ from level j_0, is precisely equivalent to a KS equation on length $\bar{L}$, when the large-scale coefficients a_α, $\alpha \in \mathbf{C}$ vanish. The evolution equations for the small-scale, periodized modes are given by (3.31), and the KS equation for $\bar{u}$, periodic on $[0, \bar{L}]$, is given by the terms L_α^I and N_α^{II}.

If we retain the large-scale modes a_α, $\alpha \in \mathbf{C}$, and their temporal evolution is externally specified, for instance from an independent run of the KS equation on $[0, L]$, then we can interpret (3.31) as representing a short system, forced by the large scales. This approach thus gives us a *systematic* way of deducing a forced KS equation, by assuming a small system to be a subsystem of a larger one.

General structure of forced periodic models

Let us look at the structure of (3.31), retaining the large scales, more closely. As discussed above, if we interpret the periodized modes as modes inside a box $\bar{\mathbf{B}}^{j_0}$, then the internal terms L_α^I and

N_α^{II} correspond to the terms in a KS equation for the short system,

$$L_\alpha^I = \sum_{\bar\alpha' \in \bar{\mathbf{B}}} \bar{l}_{\bar\alpha\bar\alpha'} \bar{a}_{\bar\alpha'} \qquad\qquad = \sum_{\bar\alpha' \in \bar{\mathbf{B}}} \left(\psi_{\bar\alpha}^{\bar{L}}, \mathcal{L}\psi_{\bar\alpha'}^{\bar{L}} \right)_{\bar{L}} \bar{a}_{\bar\alpha'},$$

$$N_\alpha^{II} = \sum_{\bar\alpha',\bar\alpha'' \in \bar{\mathbf{B}}} n_{\bar\alpha\bar\alpha'\bar\alpha''} \bar{a}_{\bar\alpha'} \bar{a}_{\bar\alpha''} \quad = \sum_{\bar\alpha',\bar\alpha'' \in \bar{\mathbf{B}}} \left(\psi_{\bar\alpha}^{\bar{L}}, \psi_{\bar\alpha'}^{\bar{L}} \mathcal{D}\psi_{\bar\alpha''}^{\bar{L}} \right)_{\bar{L}} \bar{a}_{\bar\alpha'} \bar{a}_{\bar\alpha''}. \tag{3.36}$$

The remaining terms fall into two types: L_α^E and N_α^{EE} are external forcing terms, while N_α^{IE} essentially plays the role of a parametric forcing of L_α^I. We can simplify these terms by combining the large scales into a single (L-periodic) function,

$$v(x,t) \stackrel{\text{def}}{=} \sum_{\alpha \in \mathbf{C}} a_\alpha(t)\psi_\alpha^L(x) = \sum_{j<j_0}\sum_{k=0}^{2^j-1} a_{jk}(t)\psi_{jk}^L(x). \tag{3.37}$$

In terms of v, the forcing terms become

$$L_\alpha^E = \sum_{\alpha' \in \mathbf{C}} \left(\psi_\alpha^L, \mathcal{L}\psi_{\alpha'}^L \right)_L a_{\alpha'} \qquad\qquad = \left(\psi_\alpha^L, \mathcal{L}v \right)_L,$$

$$N_\alpha^{EE} = \sum_{\alpha',\alpha'' \in \mathbf{C}} \left(\psi_\alpha^L, \psi_{\alpha'}^L \mathcal{D}\psi_{\alpha''}^L \right)_L a_{\alpha'} a_{\alpha''} \qquad = \left(\psi_\alpha^L, v\mathcal{D}v \right)_L, \tag{3.38}$$

$$N_\alpha^{IE} = \sum_{\alpha' \in \mathbf{B}, \alpha'' \in \mathbf{C}} \left(\psi_\alpha^L, \mathcal{D}\left(\psi_{\alpha'}^L \psi_{\alpha''}^L \right) \right)_L a_{\alpha'} a_{\alpha''} \quad = \sum_{\bar\alpha' \in \bar{\mathbf{B}}} \left(\psi_\alpha^L, \mathcal{D}\left(\psi_{\bar\alpha'}^{\bar{L}} v \right) \right)_L \bar{a}_{\bar\alpha'},$$

where in the formula for N_α^{IE} we also used (3.14). Together with the above definitions, (3.32) thus forms a complete system of equations for an $\bar{L}$-periodic KS system with large-scale forcing.

Asymmetric forcing In the above discussion, we have so far ignored the choice of α, or more specifically, the choice of box number k_0, where $\alpha \in \bar{\mathbf{B}}^{j_0 k_0}$. Whereas the coefficients $a_\alpha = a_{j\,\bar{k}+k_0 2^{\bar{j}}}$ inside the boxes are independent of k_0, the wavelet ψ_α^L, and hence the inner product $\left(\psi_\alpha^L, \cdot \right)_L$, are not. This is because the large-scale term is not $\bar{L}$-periodic. Thus as so far specified, the forcing is asymmetric at the scale of the boxes, the vector field $h_\alpha(t)$ depends on the choice of box, and if the coefficients in each box were allowed to evolve independently (as modes in the full system of length L), an initially periodized system would not remain so, being driven off the periodic subspace by the large-scale asymmetric forcing.

In the experiments of Sec. 6.2, therefore, we impose periodicity at each time step. That is, if at some time t we have a periodized full L-system with nonzero large scales, then we compute the vector field $h_\alpha(t)$ (or equivalently, the updated modal coefficients $a_\alpha(t+\delta t)$) only for a particular *distinguished* box $\bar{\mathbf{B}}^{j_0 k_0}$, chosen *a priori*. The coefficients in the other boxes $\bar{\mathbf{B}}^{j_0 m}$, $m \neq k_0$, are then overwritten by those in the distinguished box; that is, we set $a_{j\,\bar{k}+m 2^{\bar{j}}}(t+\delta t) = a_{j\,\bar{k}+k_0 2^{\bar{j}}}(t+\delta t)$.

The results of some such experiments with asymmetric forcing of a periodized system are discussed in Sec. 6.2. It appears that the asymmetry in the forcing occasionally leads to excessive energy of the low modes of the short subsystem, leading to atypical shock-like structures.

While the maintenance of periodicity in the time evolution for this model with asymmetric forcing requires "external intervention" in the context of the full system, (3.31) is a well-defined model *when considered as an $\bar{L}$-periodic system*. That is, we have a set of evolution equations for the coefficients $\bar{a}_{\bar\alpha}$, $\bar\alpha \in \bar{\mathbf{B}}$, forced externally. Note however that, since mode $\bar\alpha$ in the small box corresponds to 2^{j_0} different modes α in the full system (which have equal modal coefficients by

periodization, but different wavelets ψ_α^L), for a given large-scale forcing v, 2^{j_0} different evolutions for the small box are possible, depending upon from which box $\bar{\mathbf{B}}^{j_0\,k_0}$ the α are taken (assuming the forcing terms are all derived from the same box). Some consequences of the different asymmetric forcings for the small systems are demonstrated in Fig. 6.9(b).

Another disadvantage for this approach is that while this constitutes a model for the evolution of the wavelet coefficients, the asymmetry of the forcing v prevents the use of a formula such as (3.34) to "invert" the projected equations to obtain an effective equation for an $\bar{L}$-periodic function $\bar{u}$, as in (3.35). Such an effective PDE would greatly promote analysis of the model, in contrast to a Galerkin-type system for the wavelet coefficients (3.32) with (3.36, 3.38), which contains three separate forcing terms in the evolution equation for each mode.

Periodic forcing from the large scales

An effective PDE can be obtained, and the problems of atypical dynamics referred to above avoided, if the external forcing term is rendered $\bar{L}$-periodic. In that case, we are able to use (3.34), since for $f \in L^2[0, \bar{L}]_{per}$,

$$
\begin{aligned}
\left(\psi_\alpha^L, f\right)_L &= \int_0^L \psi_\alpha^L(y) f(y) \, dy \\
&= \int_0^{\bar{L}} \left[\sum_{m=0}^{2^{j_0}-1} \psi_\alpha^L(\bar{y} + m\bar{L}) \right] f(\bar{y}) \, d\bar{y} \\
&= \int_0^{\bar{L}} \psi_{\bar{\alpha}}^{\bar{L}}(\bar{y}) f(\bar{y}) \, d\bar{y} \\
&= \left(\psi_{\bar{\alpha}}^{\bar{L}}, f\right)_{\bar{L}}.
\end{aligned}
\tag{3.39}
$$

The obvious approach to satisfying the required condition is to periodize the forcing from the large scales, effectively averaging the vector field h_α over the boxes. Thus, define

$$
\bar{v}(\bar{x}, t) \stackrel{\text{def}}{=} 2^{-j_0} \sum_{m=0}^{2^{j_0}-1} v(\bar{x} + m\bar{L}, t)
\tag{3.40}
$$

$$
\bar{w}(\bar{x}, t) \stackrel{\text{def}}{=} 2^{-j_0} \sum_{m=0}^{2^{j_0}-1} v(\bar{x} + m\bar{L}, t) \mathcal{D}v(\bar{x} + m\bar{L}, t).
\tag{3.41}
$$

From the L-periodicity of v and the definitions, $\bar{v}$ and $\bar{w}$ are $\bar{L}$-periodic.

Now replacing v and $v\mathcal{D}v$ in (3.38) with their periodized forms $\bar{v}$ and $\bar{w}$, and using (3.39), the forcing terms become

$$
L_\alpha^E = \left(\psi_{\bar{\alpha}}^{\bar{L}}, \mathcal{L}\bar{v}\right)_{\bar{L}}, \qquad N_\alpha^{EE} = \left(\psi_{\bar{\alpha}}^{\bar{L}}, \bar{w}\right)_{\bar{L}}, \qquad N_\alpha^{IE} = \sum_{\bar{\alpha}' \in \mathbf{B}} \left(\psi_{\bar{\alpha}}^{\bar{L}}, \mathcal{D}(\psi_{\bar{\alpha}'}^{\bar{L}}\bar{v})\right)_{\bar{L}} \bar{a}_{\bar{\alpha}'}.
\tag{3.42}
$$

Thus (3.32), with the vector field defined by (3.36) and (3.42), forms a complete system of wavelet Galerkin equations for a short box, with periodized forcing from the large scales:

$$
\begin{aligned}
\dot{\bar{a}}_{\bar{\alpha}} = &\sum_{\bar{\alpha}' \in \bar{\mathbf{B}}} \left(\psi_{\bar{\alpha}}^{\bar{L}}, \mathcal{L}\psi_{\bar{\alpha}'}^{\bar{L}}\right)_{\bar{L}} \bar{a}_{\bar{\alpha}'} + \sum_{\bar{\alpha}', \bar{\alpha}'' \in \bar{\mathbf{B}}} \left(\psi_{\bar{\alpha}}^{\bar{L}}, \psi_{\bar{\alpha}'}^{\bar{L}} \mathcal{D}\psi_{\bar{\alpha}''}^{\bar{L}}\right)_{\bar{L}} \bar{a}_{\bar{\alpha}'} \bar{a}_{\bar{\alpha}''} \\
&+ \sum_{\bar{\alpha}' \in \mathbf{B}} \left(\psi_{\bar{\alpha}}^{\bar{L}}, \mathcal{D}(\psi_{\bar{\alpha}'}^{\bar{L}}\bar{v})\right)_{\bar{L}} \bar{a}_{\bar{\alpha}'} + \left(\psi_{\bar{\alpha}}^{\bar{L}}, \mathcal{L}\bar{v}\right)_{\bar{L}} + \left(\psi_{\bar{\alpha}}^{\bar{L}}, \bar{w}\right)_{\bar{L}}.
\end{aligned}
\tag{3.43}
$$

This system of evolution equations is again derived systematically for the short system as a subsystem of a larger one; but in contrast to the previously discussed models with asymmetric forcing, note that we no longer need to specify from which box $\bar{\mathbf{B}}^{j_0 k_0}$ of the full system we have extracted our subsystem. With $\bar{L}$-periodic forcing terms, the vector fields h_α are independent of the box containing mode α.

Effective equation for forced system

Since the inner products in (3.42) are now defined over $[0, \bar{L}]$, we can invert the Galerkin projection as in (3.34) to obtain an effective equation for the solution $\bar{u}(x,t) = \sum_{\bar{\alpha} \in \bar{\mathbf{B}}} \bar{a}_{\bar{\alpha}}(t) \psi_{\bar{\alpha}}^{\bar{L}}(x)$. Beginning with the evolution (3.43) for coefficients in the box subject to periodic forcing, multiplying by $\psi_{\bar{\alpha}}^{\bar{L}}(x)$ and summing over $\bar{\alpha} \in \bar{\mathbf{B}}$ (an orthonormal basis), and performing manipulations similar to those of (3.35), we find

$$\bar{u}_t = \mathcal{L}\bar{u} + \bar{u}\mathcal{D}\bar{u} + \mathcal{D}(\bar{v}\bar{u}) + \mathcal{L}\bar{v} + \bar{w}. \tag{3.44}$$

That is, $\bar{u}(\bar{x},t)$ obeys a KS equation on $[0,\bar{L}]_{per}$ with external forcing.

Let us look at the forcing terms $\bar{v}$ and $\bar{w}$ more closely. With some reflection, it is evident from our derivation that (in the context of the full system) $\bar{v}$ is just reconstructed from the large scales $j < j_0$, and then projected onto the scales $j \geq j_0$. Unsurprisingly, therefore (though unfortunately, in terms of our systematic derivation of a forced short KS equation as a subsystem of a larger system), $\bar{v}$ vanishes. Formally, we compute

$$\bar{v}(\bar{x},t) = 2^{-j_0} \sum_{m=0}^{2^{j_0}-1} \sum_{\alpha \in \mathbf{C}} a_\alpha(t) \psi_\alpha^L(\bar{x} + m\bar{L}) = 2^{-j_0} \sum_{\alpha \in \mathbf{C}} a_\alpha(t) \sum_{m=0}^{2^{j_0}-1} \psi_\alpha^L(\bar{x} + m\bar{L}) = 0, \tag{3.45}$$

since the inner sum vanishes for $j < j_0$ by (3.16).

Similarly, $\bar{w}$ is the projection of the nonlinear term reconstructed from the large scales, $v\mathcal{D}v$, onto the scales $j \geq j_0$. However, this term does not vanish in general. We motivate this by the observation that, for instance, the square $(\psi_{jk}^L)^2$ of a wavelet at level j has support at levels $j' > j$. Heuristically, we see this in Fourier space: if a wavelet ψ_{jk}^L is well localized near Fourier mode q, then its square has much of its support near mode $2q$, and hence at wavelet level $j+1$. Similarly, high-q components of ψ_{jk}^L are amplified by differentiation. The fact that $\bar{w}$ does not vanish, arises because the multiresolution subspaces W_j of (3.4) are not closed under multiplication or differentiation.

We learn more about $\bar{w}$ by decomposing it into its constituent contributions from pairs of large scale modes. Using the definitions (3.37) and (3.41), and writing $v\mathcal{D}v = \frac{1}{2}\mathcal{D}(v^2)$ in the latter definition, we may write

$$\bar{w}(x,t) = 2^{-j_0} \sum_{m=0}^{2^{j_0}-1} v(\bar{x} + m\bar{L}, t) \mathcal{D}v(\bar{x} + m\bar{L}, t)$$

$$= \sum_{\alpha,\alpha' \in \mathbf{C}} a_\alpha(t) a_{\alpha'}(t) \chi_{\alpha\alpha'}^{\bar{L}}(\bar{x}), \tag{3.46}$$

where for $\alpha, \alpha' \in \mathbf{C}$ we define (symmetric in α, α')

$$\chi_{\alpha\alpha'}^{\bar{L}}(\bar{x}) \overset{\text{def}}{=} \frac{1}{2}\mathcal{D}\bar{\chi}_{\alpha\alpha'}^{\bar{L}}(\bar{x}) \overset{\text{def}}{=} \frac{1}{2}\mathcal{D}\left[2^{-j_0} \sum_{m=0}^{2^{j_0}-1} \psi_\alpha^L(\bar{x} + m\bar{L})\psi_{\alpha'}^L(\bar{x} + m\bar{L})\right]. \tag{3.47}$$

69

This representation gives us a set of $\bar{L}$-periodic basis functions for the projection of $\psi_\alpha^L \mathcal{D} \psi_{\alpha'}^L$, where α, α' are large-scale modes, onto the scales $j \geq j_0$. It is straightforward to see that the functions $\bar{\chi}_{\alpha\alpha'}^L(\bar{x})$ do not vanish for general large-scale modes; in particular, when $\alpha = \alpha'$, $\bar{\chi}_{\alpha\alpha}^L(\bar{x})$ is a sum of squares and hence non-negative. We have verified numerically that the derivatives $\chi_{\alpha\alpha'}^L(\bar{x})$, which form the basis for $\bar{w}$ in (3.46), also do not vanish in general for the periodic spline wavelets (but see below), so that indeed, the large scales provide an external forcing to the periodized box.

An alternative representation for $\bar{w}$ comes from its projection onto the $\bar{L}$-periodic wavelet basis, that is, from its contribution to the evolution equation of the internal mode $\bar{a}_{\alpha'}$. Working either from the definition of N_α^{EE} from (3.32, 3.38), or by taking the inner product of $\chi_{\alpha'\alpha''}^{\bar{L}}$ with $\psi_{\bar{\alpha}}^{\bar{L}}$, we find that

$$
\bar{w} = \sum_{\bar{\alpha} \in \bar{\mathbf{B}}} \left(\psi_{\bar{\alpha}}^{\bar{L}}, \bar{w} \right)_{\bar{L}} \psi_{\bar{\alpha}}^{\bar{L}} = \sum_{\bar{\alpha} \in \bar{\mathbf{B}}} N_\alpha^{EE} \psi_{\bar{\alpha}}^{\bar{L}}
$$
$$
= \sum_{\alpha', \alpha'' \in \mathbf{C}} a_{\alpha'} a_{\alpha''} \left(\psi_{\bar{\alpha}}^{\bar{L}}, \chi_{\alpha'\alpha''}^{\bar{L}} \right)_{\bar{L}} \psi_{\bar{\alpha}}^{\bar{L}}, \tag{3.48}
$$

where by periodicity

$$
\left(\psi_{\bar{\alpha}}^{\bar{L}}, \chi_{\alpha'\alpha''}^{\bar{L}} \right)_{\bar{L}} = 2^{-j_0} \sum_{m=0}^{2^{j_0}-1} \tfrac{1}{2}(n_{\hat{\alpha}\alpha'\alpha''} + n_{\hat{\alpha}\alpha''\alpha'}), \qquad \hat{\alpha} \stackrel{\text{def}}{=} (j, \bar{k} + m2^{\bar{j}}). \tag{3.49}
$$

We have systematically obtained an effective equation for $\bar{u}$ on the small periodized subsystem, subject to nonzero additive forcing from the large scales:

$$
\bar{u}_t = \mathcal{L}\bar{u} + \bar{u}\mathcal{D}\bar{u} + \bar{w}, \tag{3.50}
$$

with $\bar{w}$ given as in (3.46) or (3.48). This describes a candidate local model for the origin of complex spatiotemporal dynamics.

Limitations of the effective forcing term We have implemented the program outlined above, of periodized models with periodic forcing from the large scales; this is described in Sec. 6.2.2. There we observe that retaining the large scales has a discernible effect, compared to setting them to zero; this confirms via numerical experiment that $\bar{w}$ does not vanish. However, it appears that the effect of the large-scale periodic forcing is rather small, insufficient to drive the periodic model into a spatiotemporally chaotic state (for $\bar{L} = 25$).

Our heuristic motivation above for why $\bar{w}$ should not be expected to vanish—because both multiplication and differentiation of wavelets typically shift the support to smaller scales and higher wavelet levels—also indicates that, due to the good (algebraic) localization of wavelets in Fourier space, $\bar{w}$ will be supported mainly in the lowest levels of the periodized box, for small $\bar{j}$. Thus we expect, *a priori*, that most of the effect of the large-scale forcing should be in the largest internal scales of the box, which according to our results of Ch. 5, are crucial for the excitation that leads to STC.

However, for symmetric wavelets such as the periodic spline wavelets we use in this thesis, there are some cancellations.[†] If α' and α'' belong to the same large-scale wavelet level, that is, $j' = j''$, then $\chi_{\alpha'\alpha''}^{\bar{L}}$ has no component at the lowest level within the box, $j = j_0$ or $\bar{j} = 0$. That is, interactions

---

[†]We have not studied the possibility of using nonsymmetric wavelets to avoid these cancellations; their use would impose a preferred x-direction that is not inherent to the KS equation, and which would greatly complicate interpretation of statistical and experimental results.

within a given large-scale level directly influence only internal modes at levels $\bar{j} \geq 1$. We see this by looking at the projection (3.49) for $\alpha = (j, k)$, $j = j_0$, that is, $\bar{j} = 0$. The large-scale wavelets $\psi^L_{\alpha'}$, $\alpha' = (j', k')$, and $\psi^L_{\alpha''}$, $\alpha'' = (j', k'')$ are symmetric, and are translates of each other, so their product is symmetric about their mutual center, $\hat{x}_{j'} \stackrel{\text{def}}{=} \frac{1}{2}(x_{j'\,k'} + x_{j'\,k''}) = L2^{-j'}\left(\frac{1}{2}(k' + k'') + \frac{1}{2}\right)$. We now compute

$$
\begin{aligned}
n_{jk\,j'k'\,j'k''} + n_{jk\,j'k''\,j'k'} &= \int_0^L \psi^L_{j\,k}(x) \mathcal{D}\big(\psi^L_{j'\,k'}(x)\psi^L_{j'\,k''}(x)\big)\, dx \\
&= \int_0^L \psi^L_{j\,k}(2\hat{x}_{j'} - y) \mathcal{D}\big(\psi^L_{j'\,k'}(2\hat{x}_{j'} - y)\psi^L_{j'\,k''}(2\hat{x}_{j'} - y)\big)\, dy \\
&= -\int_0^L \psi^L_{j\,k}(2\hat{x}_{j'} - y) \mathcal{D}\big(\psi^L_{j'\,k'}(y)\psi^L_{j'\,k''}(y)\big)\, dy \\
&= -\int_0^L \psi^L_{j\,\hat{k}}(y) \mathcal{D}\big(\psi^L_{j'\,k'}(y)\psi^L_{j'\,k''}(y)\big)\, dy \\
&= -\big(n_{j\hat{k}\,j'k'\,j'k''} + n_{j\hat{k}\,j'k''\,j'k'}\big); \quad\quad\quad\quad (3.51)
\end{aligned}
$$

where $\hat{k} \stackrel{\text{def}}{=} 2^{j-j'}(k' + k'' + 1) - k - 1$, in the second line we changed variables to $y = 2\hat{x}_{j'} - x$ and used periodicity, in the third line we used the symmetry of the large-scale wavelets about $\hat{x}_{j'}$, and the fourth line follows from the symmetry of $\psi^L_{j\,k}$ ($j \geq j_0$) about $x_{j\,k}$, and from (3.13) (generalized to shifts of arbitrary multiples of $L2^{-j}$ at level j). Now we see that if $j = j_0$, then in (3.49) the sum over the boxes includes all k values at level j_0, and by (3.51) the $n_{\hat{\alpha}\alpha'\alpha''}$ in the sum cancel pairwise, so that the sum vanishes: $\left(\psi^{\bar{L}}_{\bar{j}=0\,0}, \chi^{\bar{L}}_{j'k'\,j'k''}\right)_{\bar{L}} = 0$.

In the context of a length $\bar{L} = 25$ subsystems of a $L = 100$ system ($j_0 = 2$), this means that the level 0–0 and 1–1 interactions do not have an effect on the lowest level in the box, $j = j_0 = 2$ or $\bar{j} = 0$. However, the pairwise cancellations do not occur for higher internal levels, $\bar{j} \geq 1$, so that these interactions still influence higher internal levels, albeit relatively weakly.

There is another cancellation which is specific to the largest scales. We recall from Sec. 3.2 that there is no direct linear interaction between wavelet levels 0 and 1, by symmetry: $l_{\alpha\alpha'} = 0$ if $\alpha = (0, 0)$, $\alpha' = (1, 0)$ or $(1, 1)$ (or *vice versa*) [MHEB95]. Similarly, the product of wavelets between these levels vanishes, when projected onto smaller wavelet levels for $j_0 \geq 2$; that is, $\bar{\chi}^{\bar{L}}_{\alpha\alpha'} = 0$, and hence of course $\chi^{\bar{L}}_{\alpha\alpha'} = 0$.

Note that we can make use of the symmetry of ψ^L_{00} about $x = L/2$, and of ψ^L_{10} about $x = L/4$, their L-periodicity, and also of $\psi^L_{00}(x) + \psi^L_{00}(x + L/2) = 0$ (3.16), to find

$$
\sum_{m=0}^{3} \psi^L_{00}(x + mL/4)\psi^L_{10}(x + mL/4)
$$
$$
= \psi^L_{00}(x)\big(\psi^L_{10}(x) - \psi^L_{10}(-x)\big) + \psi^L_{00}(x + L/4)\big(\psi^L_{10}(x + L/4) - \psi^L_{10}(-x - L/4)\big).
$$

Now we can see the cancellation heuristically by observing that $\psi^L_{00}(x)$ is almost, up to a constant factor, $-\cos(2\pi x/L)$, while $\big(\psi^L_{10}(x) - \psi^L_{10}(-x)\big)$ is almost proportional to $\sin(2\pi x/L)$ [MHEB95]. Their product is therefore similar to $\sin(4\pi x/L)$, which has the desired property that $f(\cdot + L/4) = -f(\cdot)$.

This cancellation is somewhat unfortunate for our derivation of models with $j_0 = 2$: together with those previously mentioned, it implies that the periodized subsystem experiences no direct large-scale effects at level $\bar{j} = 0$. A possible remedy to this problem is to require $j_0 \geq 3$; this would

imply a full length $L = 200$ system to obtain a $\bar{L} = 25$ subsystem. In this case, the lowest internal level would be subject to cross-level couplings between the large scale modes at $j = 0$ and 2, and between $j = 1$ and 2. It would be interesting to consider such models within the present framework, but we have not pursued this possibility in this thesis.[†]

Discussion and further directions

In this Section we have described a systematic approach to the derivation of low-dimensional, periodized models subject to both asymmetric and periodized forcing from the large scales. The introduction of periodization both for the model and for the large scales is crucial in these small models, to prevent the occurrence of excessive amplitudes, which are observed in non-periodic models or for non-periodic forcing (Secs. 6.1 and 6.2).

However, while solving the problem of large amplitudes, it seems that by periodizing we have sacrificed too much. The term $\bar{v}$, which represents both the linear external forcing and the parametric driving of the small scales by the large in (3.44), averages away to zero. While the nonlinear term $\bar{w}$ remains, it is depleted by cancellations and has a relatively small effect. As described in Sec. 6.2.2, after periodizing, the remaining terms do not seem to be strong enough to "stir up" the local model to produce characteristic STC behavior.

We indicate some possible remedies, which do not follow directly from our approach, but are suggested by it:

- While the overall effect of the large scales on the small scales is symmetric, the local and instantaneous influence felt by individual active-scale modes from the large scales is definitely asymmetric. Within the above framework of (3.44), this could be modeled by an $\bar{L}$-periodic, but non-constant $\bar{v}$, designed to emulate the local parametric and linear effects of the large scales. This possibility is not studied in this thesis, but may be an avenue for future exploration.

- We shall see in Ch. 5 that the main contribution of the large scales is to provide the driving, which has Gaussian statistics and maintains the spatiotemporal complexity. In our model, much of this influence has been lost through periodization; but we can simulate the effect that the large scales should have on a subsystem by *explicitly driving* some internal modes (for instance, just the lowest level $j = j_0$, or $\bar{\jmath} = 0$) of the subsystem. In the formalism of (3.25), a driven mode such as $\bar{a}_{00}$ is now to be considered "external", although it lies inside the box. In Sec. 6.3 we have performed some promising experiments along these lines.

  The approach outlined here suggests the study of low-dimensional, non-autonomous models for the KS equation on small periodic domains, with or without large-scale forcing terms $\bar{v}$ and $\bar{w}$, with externally specified—possibly periodic or random—driving imposed on the largest-scale modes. The study of such low-dimensional driven models for the KS equation, and their potential relation to STC, is an interesting direction for further investigation. We note that, while this entire line of inquiry has been motivated by the wavelet interpretation, once we have formulated an effective PDE such as (3.44), we are no longer tied to a wavelet basis, so that it may be convenient to return to a Fourier representation to pursue the study of such driven spatiotemporally complex systems.

[†]We comment briefly that some of the cancellations depend on the particular form uu_x of the nonlinearity in (3.18). A quadratic nonlinearity even in x, such as $\mathcal{B}(u, u) = u^2$, would not suffer the pairwise cancellations in (3.51); while for a cubic nonlinearity, for instance u^3 as in the Swift-Hohenberg equation, both parametric and additive terms would remain in the equivalent of (3.50), obtained from the periodizations of $\bar{u}v^2$ and v^3, respectively. The implications of our approach to deriving periodized models for other systems may be worth further study.

In the remainder of the thesis, we implement via numerical computation and experimentation some of the ideas outlined and summarized in this Chapter. Before continuing to experiments, however, in the next Chapter we provide a detailed characterization of the spatiotemporally chaotic state of the KS equation, for comparison with our experiments.

Chapter 4

Scale and Space Localization

In Ch. 1, we reviewed some general analytical and bifurcation properties of the KS equation, and placed the study of its complex spatiotemporal dynamics in the context of other investigations of spatiotemporal chaos (STC) and turbulence. For the remainder of this thesis, we will attempt to gain a more detailed understanding of the nature of the spatiotemporally chaotic regime, primarily via the wavelet projections introduced in Ch. 3.

In this Chapter, we proceed by a careful characterization of the statistics well within the STC state. After reviewing and extending previous results on pointwise and Fourier statistics in Sec. 4.1, we examine various properties of the KS equation on a wavelet basis in Sec. 4.2, and show that this representation brings out the scale localization of the dynamics most clearly. A comparison with theories for the effective noisy dynamics at the large scales, reviewed in Sec. 4.2.2, motivates our introduction of a simple stochastic model to simulate the large scale dynamics, which we use in later experiments in Secs. 5.5.2 and 6.3. In the next Ch. 5, we use the separation of scales afforded by the wavelet representation to study scale localization in more detail, through several experiments designed to elucidate the contributions of different scales to the overall dynamics; and develop a fairly complete picture describing the distinct and complementary contributions of different scales to construct STC.

In Sec. 4.3 in the latter part of this Chapter, we show also that the dynamics in the STC regime is spatially localized, by describing and estimating various correlation lengths, and then introducing a novel numerical experiment, also wavelet-based, in which interactions between separated spatial domains are cut. This allows us to postulate a dynamic interaction length, somewhat larger than the estimated correlation lengths, which provides further support for the hypothesis of extensivity of the KS dynamics—that the large system behaves essentially as a union of smaller, spatially localized subsystems. We use some of these results on spatial localization in Ch. 6 to investigate the construction of low-dimensional, localized models.

4.1   Scale localization—statistics

Many statistical properties of the KS equation in real and Fourier space, especially the power spectrum $S(q)$, have frequently been computed and published—see for instance [Man81, PPP84, Pum85, ZL85, HNZ86, Zal89, LP92, HJJ93]. The most detailed study to date is that of Pumir [Pum85], who showed through various pointwise, temporal and Fourier statistics that the field u satisfying the KS equation (1.1) exhibits strongly nonequilibrium statistical behavior in the STC regime. We review and extend these results here for completeness, to build on the existing literature and to establish a comparison for the wavelet-based statistics of Sec. 4.2.

In a straightforward numerical integration of the KS equation, one needs at least $N_0 \approx 4L/2\pi$ equations for stability, as there are $N_0/2$ unstable modes (this is evident from the Fourier representation (1.5); see for instance [HLB96, Sec. 7.4]); however, the strong damping at small scales means that subject to the above constraint, a wide range of numerical schemes is feasible on a workstation. App. B outlines some of the finite difference, Fourier and wavelet algorithms available for the KS equation. Most of the long-time statistical computations presented here were performed using the $\mathcal{O}(N \log_2 N)$ Fourier pseudospectral method of App. B.2.1, keeping modes up to at least $q_{max} \geq 4$. Results were also obtained and checked with the $\mathcal{O}(N)$ combined Crank-Nicholson/Adams-Bashforth finite difference solver described in App. B.1, with a typical space step $\delta x = 100/256 \approx 0.39$. Typical time steps for all schemes were $\delta t = 0.0625$ and 0.03125, and temporal averaging was performed over samples separated by $\Delta t = 0.25$. The quantitative results were checked with smaller space and time steps, and more Fourier modes; the results presented are well-converged. In our experience, a large space step of $\delta x = 100/128$ (comparable to that used in much of the literature, for instance [SKJJB92, HJJ93]), while yielding the correct qualitative behavior, was insufficiently small for accurate statistical computations of active and small scale properties, and gave significant systematic errors, especially in temporal correlations; see the discussion of temporal statistics in Sec. 4.1.1 below.

4.1.1 Real space properties

Pointwise statistics

Pumir [Pum85] has studied higher order moments of the local velocity field $u(x,t)$ and its spatial derivatives to show its non-Gaussian behavior. The probability distribution functions (PDFs) for these local quantities demonstrate the deviation from Gaussianity most clearly, and are plotted in Fig. 4.1(a) for u (see [ZL85, HJJ93]) and its first four derivatives (from which the moments reported in [Pum85] may be computed). These PDFs, and others presented later in this chapter (see Figs. 4.14, 4.16, and 4.17(b)), are computed by binning the values obtained for a long-time integration (averaging was performed over at least 4×10^5 time steps, and for at least 80 bins). In Fig. 4.1(b,c) we also include typical spatial profiles for $\partial^j u/\partial x^j(\cdot, t)$ (all at the same time t) and time series for $\partial^j u/\partial x^j(x, \cdot)$ for $j = 0 \ldots 4$ (for the same time interval, evaluated at the same point x) for $L = 100$, for reference.

Note that by translation and parity invariance (restored in the statistical sense; see Sec. 1.2.1), the PDFs for u and its even derivatives are symmetric about 0, while the PDFs for the odd derivatives are strongly asymmetric. A simple explanation [Pum85] accounts for this: By analogy with the Burgers equation, the terms $u_t + u u_x$ in (1.1) tend to produce shocks; these are smoothed by the u_{xx} and u_{xxxx} terms, but are still evident in the asymmetric profile for $u(x, \cdot)$ (see Fig. 4.1(b)), and hence in the strongly skewed distributions for u_x and u_{xxx}.

In view of Sec. 1.3.1 and Fig. 1.2, a heuristic explanation for the shape of the PDF for u is as follows: The basic cellular structure is distorted through defects in the STC regime [CH95, Shr86], which is characterized by the creation and annihilation of peaks at the characteristic spatial scale l_m, corresponding to the peak at q_m near $q_0 = 2\pi/l_0 = 1/\sqrt{2}$ in the energy spectrum (Fig. 1.4; see Sec. 4.1.2). Compare the PDF for u with that expected for a simple cellular solution: a double-humped PDF, smoothed out by distortions in the wavelength or amplitude of the cells (for instance, a purely sinusoidal u has $\mathbb{P}(u \leq y) = \int_{-\infty}^{y} \rho(v) \, dv$, where $\rho(v) = 1/\pi\sqrt{1 - v^2}$ for $|v| < 1$, and $\rho(v) = 0$ otherwise). It appears that the characteristic shape (Fig. 4.1(a)) of the PDF for u thus corresponds to a field which remains near a typical cellular solution for part of its evolution, but also spends significant time near zero. Note also from the PDFs of Fig. 4.1 that the higher
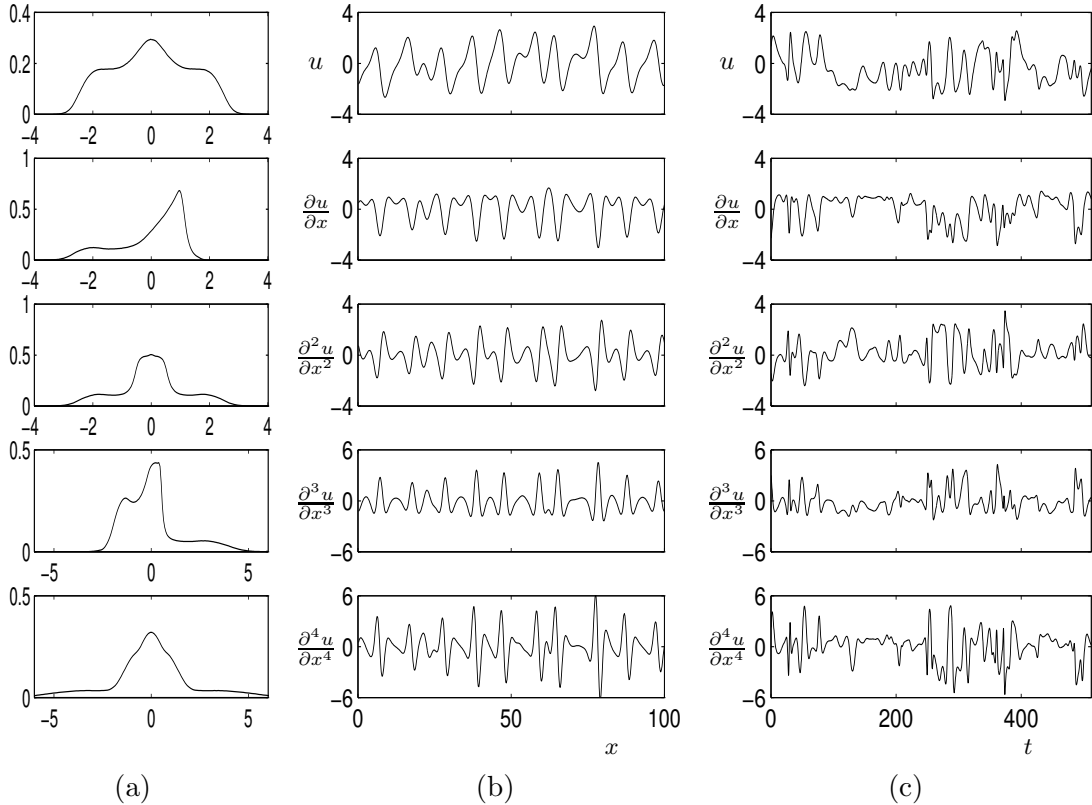
Figure 4.1: (a) Probability densities for u and its first four derivatives, for $L = 100$ and $L = 400$. (b) Typical spatial profiles, at the same time t, for u and its derivatives, for $L = 100$. (c) Typical time series at $x = 50$, for the same time interval, for u and its derivatives, for $L = 100$.

derivatives spend proportionately more of their evolution near zero, but have excursions to higher values. Since higher derivatives correspond to smaller scales, this is an indication of small-scale intermittency, which is confirmed by other results presented below; see Sec. 4.2.4. More discussion of different PDFs and models for them is contained in Sec. 4.2.

Temporal statistics

The local values of the field u, $s(t) \stackrel{\text{def}}{=} u(x_0, t)$ for a fixed x_0, give a time series whose temporal behavior may be investigated using spectral techniques [Zal89, Pum85, Man81]. In particular, the temporal correlations give an estimate of a characteristic time between "events". We shall later in Secs. 4.1.2 and 4.2.1 analyze the dynamics at different spatial scales, and see that these exhibit different characteristic times; the present pointwise results average over all scales. We compute the temporal spectrum $\langle|\hat{s}(\omega)|^2\rangle$ of $s(t)$ (Fig. 4.2(a)) using a periodogram estimate averaged over successive sequences of 1024 or 2048 points separated by $\Delta t = 0.25$, assuming stationarity in time and multiplying each string of data by a Bartlett window to reduce the effects of leakage due to non-periodicity of the signal [Pap84, Pum85, PTVF92]. The temporal statistics for $s(t) = u(x_0, t)$ are improved by averaging over space, using the statistical homogeneity of the attractor; spectra and correlation times calculated at individual values of x_0 agree with each other and with the spatial average (see Fig. 4.4(a) below).
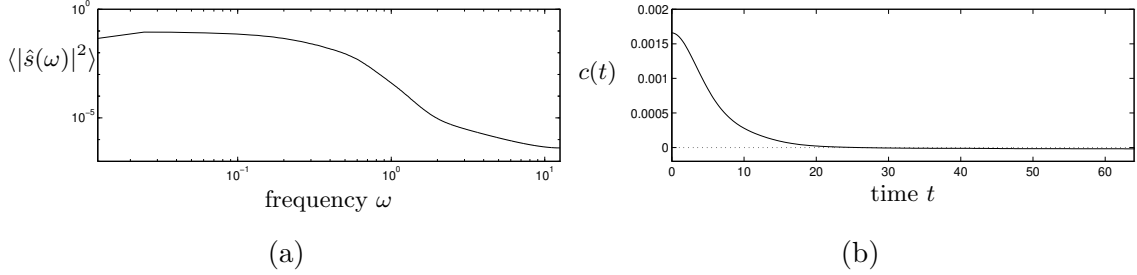
Figure 4.2: (a) Periodogram estimate of the temporal power spectrum of the local velocity field $s(t) = u(x_0, t)$, averaged over x_0 and over 500 successive segments of 2048 samples separated by $\Delta t = 0.25$. (b) Temporal autocorrelation function $c(t)$ corresponding to the spectrum of (a); the width of the peak at half maximum is $\tau_c \approx 10.15$.
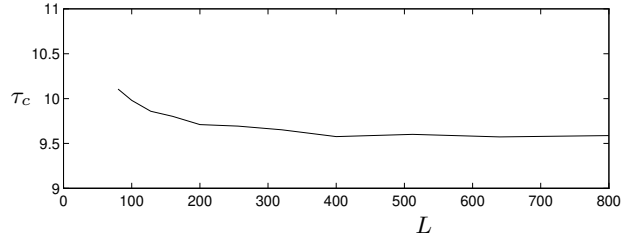
Figure 4.3: Width at half maximum autocorrelation times τ_c of the velocity field u, as a function of L.

The inverse Fourier transform of the periodogram gives an estimate of the autocorrelation function $c(t)$ (Fig. 4.2(b)), and we may compute an autocorrelation time τ_c from the width at half maximum of the peak of $c(t)$. We find $\tau_c \approx 10$ for $L = 100$, and τ_c remains essentially constant with increasing $L \gtrsim 400$ in the STC regime (Fig. 4.3), showing that it is an *intensive* property of the dynamics in the large-L limit; see Sec. 1.3.1. (As already noted, an insufficiently small spatial grid distorts the temporal dynamics; using $\delta x = 100/128$ gives $\tau_c \approx 7.5$, although the qualitative behavior, as in Fig. 1.2, looks similar.)

Computation of correlation times It is appropriate to remark here on the computation of correlation times and lengths, as this issue will reappear at several points in this chapter, especially in Sec. 4.3.2.[†] If a correlation function (such as, for definiteness, $c(t)$) is asymptotically decaying exponentially, then the standard definition of the correlation time τ is given by $c(t) \sim \exp(-t/\tau)$, $t \to \infty$. Different ways of computing τ, obtained for instance from the area under the peak of $c(t)$, the width at half maximum or root-mean-square width of the peak, all give equivalent results (up to an $\mathcal{O}(1)$ factor).

However, there is no obvious *a priori* correct way to define a robust correlation time τ if $c(t)$ is not exponentially decaying, as the correlation function is then not characterized by a unique length scale. Moreover, different plausible definitions of τ can give radically different results.

[†]I had useful comments from Henry Greenside and John Krommes on this point.
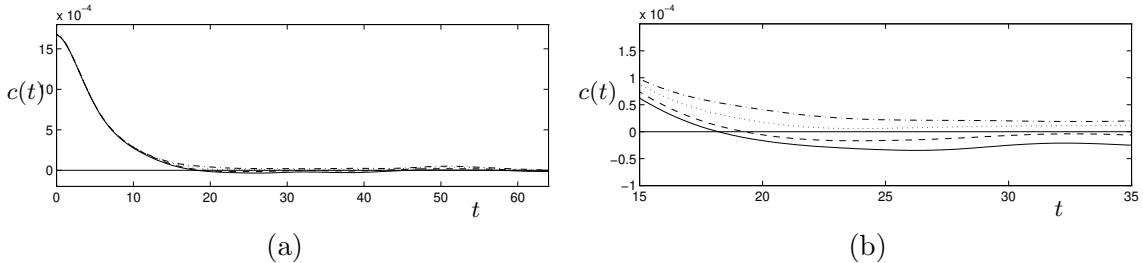
Figure 4.4: (a) Temporal autocorrelation functions $c(t; x)$, for four values of x near $x = 78$, for the KS equation with periodic boundary conditions (for the simulation discussed also in Fig. 4.5). (b) Blowup of (a); note the discontinuous jump in the first zero crossing $t_0(x)$.

As an example, consider the temporal autocorrelation functions $c(t; x)$ of Fig. 4.4(a), computed from the time series of $u(x, \cdot)$ for the KS equation for four nearby values of x. In Fig. 4.4(b) we see that, while these functions overlap strongly, the first two become negative near $t = 18$, while the others do not; that is, the position $t_0(x)$ of the first zero crossing jumps discontinuously. A definition of τ which depends on $t_0(x)$, for instance $\tau = t_0$, or the root-mean-square width of the peak,

$$\tau_{rms}^2 = 2 \int_0^{t_0} t^2 c(t) \, dt, \tag{4.1}$$

(this measure essentially computes the standard deviation, treating the positive part of $c(t)$ as a probability distribution) will thus undergo a jump where t_0 does.

It seems reasonable, however, that the temporal autocorrelation functions of Fig. 4.4 should have very similar correlation times, so that a definition of τ such as those above which depends largely on the outlying values near zero, rather than on the width of the main part of the peak, appears unsatisfactory. A correlation time defined by the width of the peak of $c(t)$ at half the maximum (or at some other fraction of the total height) is, we find, more robust to small variations such as those in Fig. 4.4, and hence seems more reasonable. Our preferred correlation time τ_c, obtained from the width at half maximum, is thus defined by the condition

$$c(\tau_c) = \frac{c(0)}{2}. \tag{4.2}$$

See also Sec. 4.3.2 for further discussion in situations when the autocorrelation function oscillates or decays exponentially.

Spatial dependence of correlation times We develop this point at some length in view of the paper of Egolf and Greenside [EG94b], who argue that in the KS equation for rigid (mixed) boundary conditions, correlation times are x-dependent, even far from the boundary. If this were true, it would contradict the results of Sec. 4.3 below, where we show that interactions are spatially localized, and the bulk spatiotemporally chaotic dynamics is asymptotically independent of boundary conditions. In attempting to reproduce the correlation times of [EG94b], however, we have found that their x-dependence is an artifact of the root-mean-square width method (4.1) they used to define the correlation time $\tau_{rms}(x)$.

In Fig. 4.5(a), we display the results of computing $\tau_{rms}(x)$ for a set of long-time simulations of (1.1) with different boundary conditions. Note the spatial variations, similar to those in [EG94b, Fig. 3]; for periodic boundary conditions, these contradict the expected spatial homogeneity (other
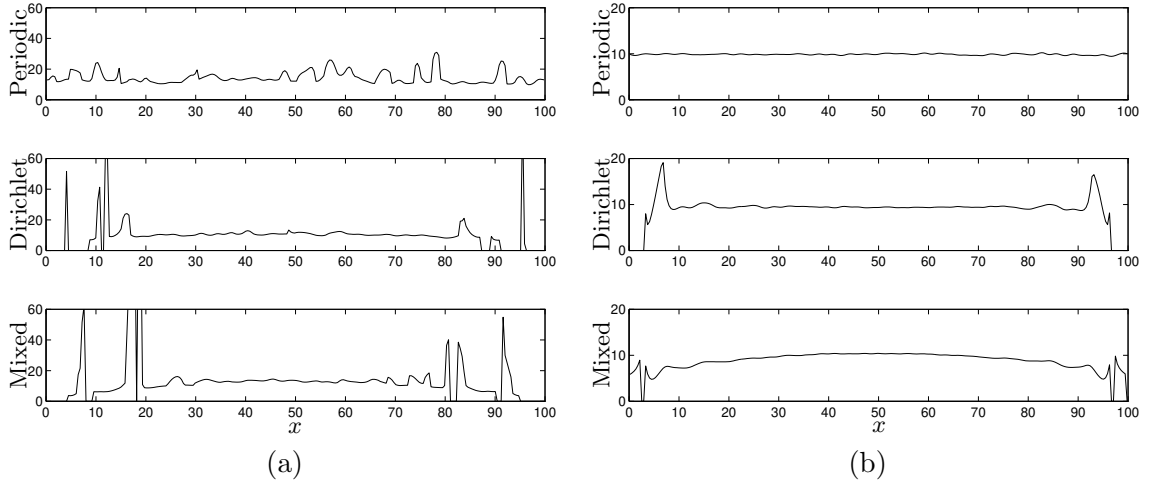
Figure 4.5: Spatial dependence of correlation times for the KS equation with various boundary conditions: (a) Root-mean-square computation of $\tau_{rms}(x)$ from (4.1); compare [EG94b]. (b) $\tau_c(x)$ computed using the width at half maximum (4.2), displaying the desired spatial homogeneity in the bulk.

computations, not shown, display even stronger spatial dependence). The origin of this effect is the discontinuous variation in the position of the first zero crossing which may occur for $c(t;x)$ varying smoothly and slowly with x, as discussed above; in fact, the autocorrelation functions $c(t;x)$ of Fig. 4.4 are those responsible for the jump in τ_{rms} near $x = 78$ in the top figure of Fig 4.5(a), for periodic boundary conditions. On recalculating $\tau_c(x)$ for the same simulations, using our preferred definition (4.2) of $\tau_c(x)$ as the width of $c(t;x)$ at half maximum, we find the curves of Fig. 4.5(b). Except for minor variations due to insufficient averaging, $\tau_c(x)$ is uniform for periodic boundary conditions, as expected; and sufficiently far from the boundary, the attractor is spatially homogeneous, and τ_c independent of x in the bulk, even for Dirichlet and mixed boundary conditions, contrary to the results reported in [EG94b] (see also Sec. 4.3.1).

Energy distribution

We briefly examine the statistics of the total energy,

$$E(t) = \|u(\cdot,t)\|^2 = \int_0^L u^2(x',t)\,dx' = L\sum_q |\hat{u}_q|^2 \approx L\frac{L}{2\pi}\int_0^\infty |\hat{u}_q|^2\,dq, \qquad (4.3)$$

and the energy density $\varepsilon(t) = E(t)/L$, with mean values $\bar{E}$ and $\bar{\varepsilon}$, respectively. The conjectured extensivity of E, or L-independence of ε (see Secs. 1.2.2 and 1.3.1), is equivalent to the L-invariance of the normalized power spectrum $S(q)$; since $\bar{\varepsilon} = (1/2\pi)\int_0^\infty S(q)\,dq$. Temporal fluctuations in u (or $\hat{u}$) lead to fluctuations in E, motivating the study of the distribution of values of E (Fig. 4.6(a)). In this situation, extensivity gives us definite predictions. Suppose the KS equation on length L can be considered as a union of independent subsystems of length l^*, perhaps of the order of a few correlation lengths ξ_2 or ξ_I of Sec. 4.3.2 (assume for simplicity that l^* divides L, $L/l^* = N$, say).
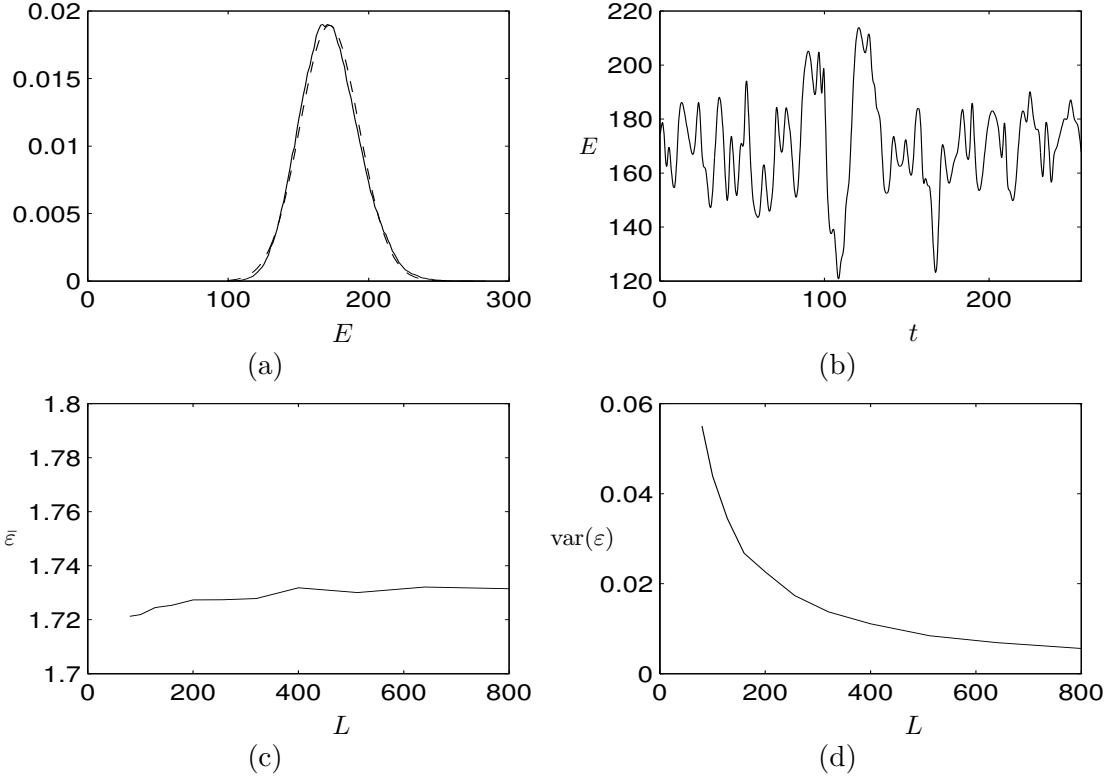
Figure 4.6: (a) PDF of the energy E, with a Gaussian fit superimposed (dashed line), for $L = 100$. (b) Sample time series of E. (c) Dependence of the mean energy density $\bar{\varepsilon}$ on L. (d) Dependence of the variance of ε on L.

Then

$$E^L(t) = \sum_{j=1}^{N} \int_{(j-1)l^*}^{jl^*} u^2(x',t)\,dx' \stackrel{\text{def}}{=} \sum_{j=1}^{N} E_j^{l^*}(t), \qquad (4.4)$$

or $\varepsilon^L(t) = (\sum_j \varepsilon_j^{l^*}(t))/N$. By the assumption of statistically identical, independent subunits, we can consider the $\{\varepsilon_j^{l^*}\}_{j=1\dots N}$ to be independent, identically distributed random variables, and ε^L is their mean. Then independently of the distributions of $\varepsilon_j^{l^*}$, as L increases we expect the distribution of ε to be Gaussian about its mean $\bar{\varepsilon} \approx 1.73$, with a variance $\langle(\varepsilon - \bar{\varepsilon})^2\rangle$ that is inversely proportional to L [Lau92] (by the Central Limit Theorem, since the number N of subunits is proportional to L. Observe that this argument is independent of the actual subunit length l^*; see also [LL80, Sec. 2]). This prediction of extensivity is confirmed in Fig. 4.6. Note that this implies that both the mean and variance of the total energy E increase proportionately to L. A typical correlation time for the evolution of the energy $E(t)$, as in Fig. 4.6(b), is approximately $\tau_E \approx 9.3$, which is comparable to the autocorrelation time $\tau_c \approx 10$ computed above (see Fig. 4.3), as expected.

4.1.2 Fourier space properties

The Fourier representation is a fundamental tool for the description of the behavior of different modes or scales of a spatially homogeneous system such as (1.1). Via the Wiener-Khinchin theorem, the mean energy spectrum $S(q)/L = \langle|\hat{u}_q|^2\rangle$ and the two-point correlation function

$C(x - x') = \langle u(x, \cdot)u(x', \cdot) \rangle$ form a Fourier transform pair; similarly, higher moments of $\hat{u}_q$ are related to multipoint correlation functions [Pum85]. (We discuss the two-point correlation function and the associated typical correlation length ξ_2 further in Sec. 4.3.2.)

The mean energy spectrum $S(q)$ (Fig. 1.4) is probably the most important statistic for the KS equation, as it summarizes the dynamics at different scales. (Our experience also indicates that it is the easiest statistic to compute and, except for low q, the fastest to approach its equilibrium value). We have already noted in Sec. 1.3.1 the three major distinct regions in the spectrum, whose origin is fairly well understood in qualitative terms [PPP84]: a region of approximate energy equipartition [FY77], a peak at q near $q_0 = 1/\sqrt{2}$, and an exponential decay region consistent with the analyticity of the solution.

The global energy balance gives us one constraint on the form of $S(q)$: The total energy $E(t) = \|u(\cdot, t)\|^2 = \int_0^L u^2(x, t)\, dx$ evolves under

$$\frac{1}{2}\frac{d}{dt}\|u\|^2 = \|u_x\|^2 - \|u_{xx}\|^2. \tag{4.5}$$

On average, we have therefore $\langle \|u_x\|^2 \rangle = \langle \|u_{xx}\|^2 \rangle$, which translates in Fourier space to the elementary condition on the power spectrum,

$$\sum_q (q^2 - q^4)S(q) = 0.$$

Toh [Toh87] has studied the averaged distribution $p(l)$ of peaks, or "coherent structures" (which he defined as maxima above some choice of cutoff amplitude) separated by distance l. By assuming the field to be a superposition of identically shaped structures, or "soliton-like pulses", and postulating that these are independently distributed on $[0, L]$ according to the distribution $p(l)$, he has been able to reproduce the general features of the spectrum $S(q)$, including the three distinct regions; but a rigorous *a priori* derivation of $S(q)$ from the KS equation (1.1) is still lacking.

Detailed characterization of power spectrum

Since the power spectrum is so important, we describe some of its features in more detail here. In this description, we can make a clear distinction between the large, active and small scales, which will be the focus of more attention when we use the wavelet transform to study the different ranges of scales in Sec. 4.2.

Large scales As discussed below in Sec. 4.2.2, in the large-scale limit, the asymptotic description in terms of the forced Burgers equation (4.11) predicts a flat spectrum: $S(q) \to$ const as $q \to 0$. However, the system lengths L in our calculations have not approached the crossover to KPZ scaling, and have been insufficiently long to observe this equipartition of energy among the large-scale Fourier modes cleanly; see [SKJJB92, Fig. 1(b)] or [LLPP93, Fig. 6] for simulations with larger L. There is a well-defined shoulder, also observed in [SKJJB92, LLPP93], in which the energy per Fourier mode increases slowly (Fig. 4.7(a)). We include this region among the large scales; it appears that $S(q) \approx 3.0\, q^{0.14}$, $0.06 \lesssim q \lesssim 0.37$ (although the data is not good enough to definitively exclude a linear scaling, $S(q) \approx 2.0 + 2.0\, q$).

Active scales The active scales, for $0.37 \lesssim q \lesssim 1.5$, contain most (about 90%) of the energy (Fig. 4.7(b)). Careful computations appear to indicate that the peak is at $q_m \approx 0.67 \pm 0.02$, or at slightly lower q than the most unstable mode, $q_0 = 1/\sqrt{2} \approx 0.7071$ (for $L = 800$, the observed
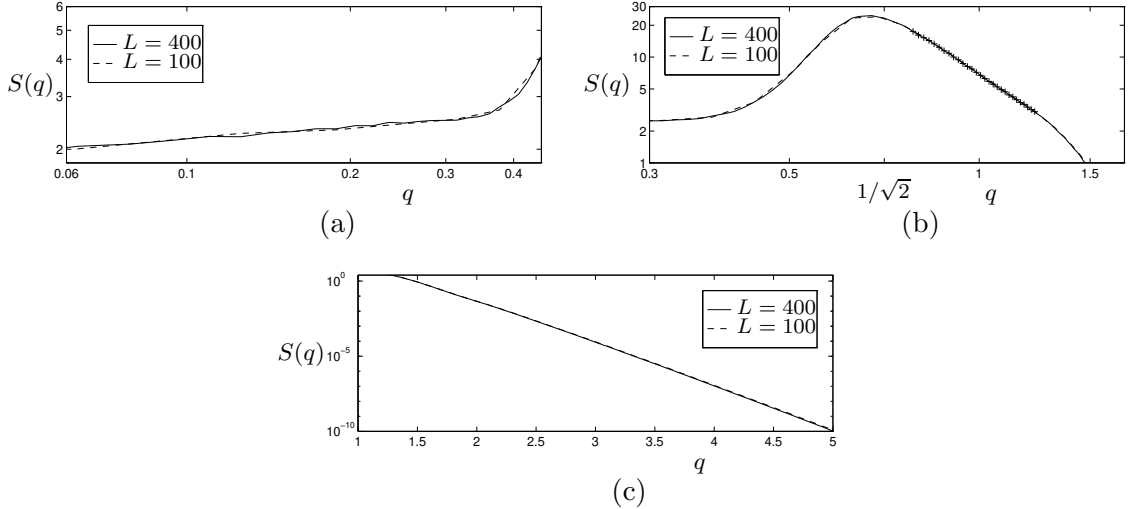
Figure 4.7: Enlargement of different regimes of the power spectrum $S(q)$; compare Fig. 1.4: —— $L = 400$, pseudospectral solution, 512 complex Fourier modes; − − $L = 100$, finite difference, 1024 points. (a) Large scales: Approximate equipartition of energy for modes at small q (log-log). (b) Active scales: peak at $q < \sqrt{2}$; +++ "inertial range", with q^{-4} decay (log-log). (c) Small scales: Exponential decay for large q (linear-log).

discrepancy is equivalent to about 5 Fourier modes; but the result $q_m \neq q_0$ should probably not yet be considered definite). In fact, there is no *a priori* reason why the most rapidly growing mode for the linear system should be the most energetic in the presence of nonlinear coupling, and the nonlinearity evidently induces a slight shift in the peak to larger scales (see also [Toh87]).

A remarkable feature of the power spectrum observed in Fig. 4.7(b) is the region $0.8 \lesssim q \lesssim 1.25$, in which there is a definite power law decay with an exponent experimentally indistinguishable from 4.0 (our numerically obtained slope is about 1% from 4.0, with larger error bars). By analogy with the inertial range in fluid turbulence, characterized by power law decay, it is tempting to think of this region $S(q) \sim q^{-4}$, where production and dissipation are almost balanced ($q^2 \approx q^4 \approx 1$), as an "inertial range" [PPP84]. In fact, this region, straddling the $q = 1$ transition from linear instability to stability, has the highest rate of energy transport. However, significant energy transport occurs for a far wider range of modes, and we do not expect this narrow band, spanning less than an octave in Fourier space, to have a determining role like the $k^{-5/3}$ range in turbulence; thus we have chosen to discuss this power law region as part of the larger "active region".

Small scales Above this range, the exponential decay at small scales due to the strong dissipation is readily observed (Fig. 4.7(c)), although the computed decay rate is significantly dependent on the accuracy of the numerical scheme. Using a Fourier pseudospectral scheme with $q_{max} \approx 8$, or a finite difference scheme with $\delta x = 100/1024$, we estimate $S(q) \sim e^{-6.5\,q} \sim 2^{-9.4\,q}$, for $q > 1.5$. Larger step sizes δx gave slower decay rates, indicating that for a given number of modes, the Fourier integrator is the most spectrally accurate.
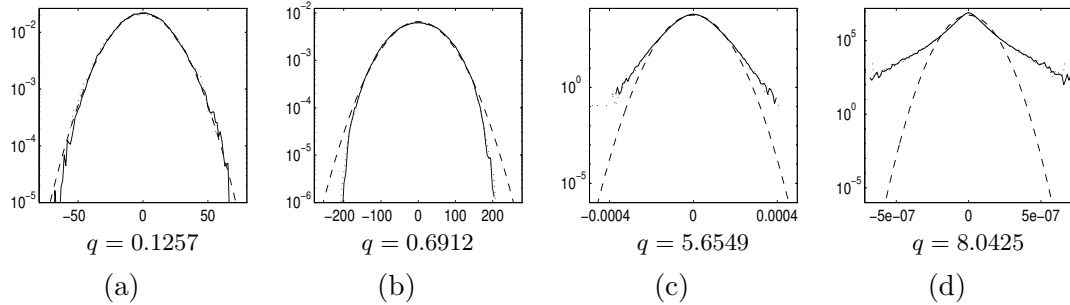
Figure 4.8: PDFs for some representative Fourier modes (both real and imaginary parts), for $L = 100$. $- -$ Gaussian fit to PDF. (a) Gaussian for large scales; (b) near-normal distribution at active scales; (c,d) increasingly long-tailed, exponential distributions for small scales.

Distributions of Fourier modes

The power spectrum gives only the lowest order statistics for the Fourier mode distributions, however; specifically, $S(q) = \langle |\hat{u}_q|^2 \rangle = 2\langle (\mathrm{Re}\ \hat{u}_q)^2 \rangle$ measures the variance of $\hat{u}_q = \mathrm{Re}\ \hat{u}_q + \mathrm{i}\,\mathrm{Im}\ \hat{u}_q$, where $\hat{u}_q$ has vanishing mean. Pumir [Pum85] has shown that the higher moments of the Fourier coefficients deviate markedly from Gaussian values for large q, and thus that the small-scale distributions are non-normal.

Before discussing Pumir's calculation further, we note that this effect is readily observed from the full Fourier mode probability distribution functions. At large scales, the PDFs are Gaussian, consistent with those observed for a forced Burgers equation (Fig. 4.8(a); see Sec. 4.2.2 below). At intermediate values of q near the peak of the power spectrum, there is some deviation from Gaussianity, including flattened, rapidly decaying distributions in this region of highest energy flux (Fig. 4.8(b)). The exponentially decaying PDFs at small scales (Fig. 4.8(c,d)) indicate the presence of small-scale intermittency [Fri95]. These features of the PDFs will reappear, more distinctly, in the wavelet analysis of Secs. 4.2.2–4.2.4.

Moments of distributions and scaling Instead of computing the full PDFs, however, Pumir [Pum85] studied moments of the distributions (and related them to multipoint correlation functions). If η is a centered (mean-zero) Gaussian-distributed random variable, with variance $\langle \eta^2 \rangle = \sigma^2$, then its even moments may readily be found:

$$\langle \eta^{2p} \rangle = (2p-1)!!\sigma^{2p} \quad \Rightarrow r_p \overset{\text{def}}{=} \frac{\langle \eta^{2p} \rangle}{\langle \eta^2 \rangle^p (2p-1)!!} = 1. \tag{4.6}$$

One can check also that if $\zeta = \eta_1 + \mathrm{i}\,\eta_2$, where η_1 and η_2 are independent, identically distributed real Gaussian random variables, then

$$\bar{r}_p \overset{\text{def}}{=} \frac{\langle |\zeta|^{2p} \rangle}{\langle |\zeta|^2 \rangle^p p!} = \frac{\langle \eta_1^{2p} \rangle}{\langle \eta_1^2 \rangle^p (2p-1)!!} = 1. \tag{4.7}$$

If η is exponentially distributed, on the other hand, then a straightforward computation confirms

$$\frac{\langle \eta^{2p} \rangle}{\langle \eta^2 \rangle^p (2p-1)!!} = p! \tag{4.8}$$

83
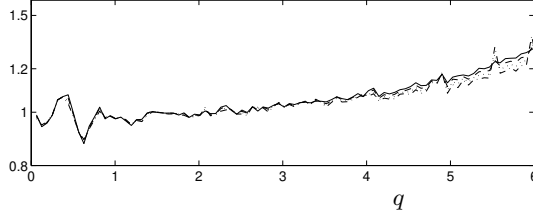
Figure 4.9: The flatness and its higher order analogues: $[r_p(q)]^{1/\beta_2(p)}$ (defined in the text) for $p = 2, 3, 4$ and 5, showing increasing deviations from Gaussianity for small scales [Pum85].

The idea of Pumir [Pum85] was, essentially, to plot the logarithms of $(r_p)^\gamma$ (or $\bar{r}_p^\gamma$; for any γ); the vanishing of these for all p would indicate Gaussianity by (4.6). Furthermore, this could be done as a function of the Fourier mode number q. Defining

$$r_p(q) \overset{\text{def}}{=} \frac{\langle (\text{Re } \hat{u}_q)^{2p} \rangle}{\langle (\text{Re } \hat{u}_q)^2 \rangle^p (2p-1)!!}, \quad \bar{r}_p(q) \overset{\text{def}}{=} \frac{\langle |\hat{u}_q|^{2p} \rangle}{\langle |\hat{u}_q|^2 \rangle^p p!}, \tag{4.9}$$

Pumir observed that the data appeared to obey a scaling law of the form

$$r_p(q) \simeq [\gamma(q)]^{\beta(p)}; \tag{4.10}$$

that is, the higher moments, when non-dimensionalized and rescaled appropriately, all fall on the same curve.[†] The definitions of $\gamma(q)$ and $\beta(p)$ can be modified, if necessary, so that $\beta(2) = 1$, and $\gamma(q) = r_2(q)$.

Such a scaling relation, if it could be shown definitively to hold, would present an interesting challenge for the theory of the Fourier mode distributions. On the basis of computations of $\bar{r}_p(q)$ for $p = 2, 3, 4$ and 5, Pumir suggested the empirical scaling exponent $\beta_1(p) = 2p - 3$. For the same values of p, we find that for low q, $\beta_2(p) = \frac{1}{2}p(p-1)$ seems to give better overlap of the curves. If the distributions of $\hat{u}_q$ tend to exponential for large q, this would imply a scaling exponent $\beta_3(p) = \log_2(p!)$. Our numerical data for the few values of p we have considered is insufficient to distinguish between these possibilities for $\beta(p)$ (although $\beta_2(p)$ appears to yield the best results). In fact, if the scaling hypothesis (4.10) is correct, it allows us to compute $\beta(p)$ from $\beta(p) = \log r_p(q)/\log r_2(q)$; in our computations, however, the right-hand-side of this expression oscillates strongly, especially for $1.5 < q < 3$, and then settles down to a weak q-dependence. At present, thus, the existence of scaling (which may only hold well for high q) does not seem to be established.

Given a functional form for $\beta(p)$, we plot $[r_p(q)]^{1/\beta(p)}$ to detect deviations from Gaussianity—compare Fig. 4.9 with [Pum85, Fig. 5]. The remarkable superposition of the curves for $p = 2, 3, 4$ and 5 is the basis for the scaling assumption which, as we have said, is not yet definitely established. However, there is no doubt that these curves do demonstrate the deviation from Gaussianity clearly, and corroborate the results of Fig. 4.8. As we have explained above, a Gaussian distribution for $\hat{u}_q$ would imply $r_p(q) = 1$ for each p. This is approximately satisfied for small q, and for q near 1. For large q (small scales) the moments increase well above the Gaussian values, indicating the long-tailed distributions which signal intermittency. The bump for $q \approx q_0$ (also seen in [Pum85, Fig.5]) is noteworthy, and indicates first a steepening, then a distinct broadening ($r_p(q) < 1$) of the distributions in the active scales. These features will all be confirmed and highlighted more clearly when we study the distributions of wavelet coefficients in Secs. 4.2.2–4.2.4 below.[‡]

[†]In fact, Pumir studied the moments of $|\hat{u}_q|$, that is, $\bar{r}_p(q)$, but the results are equivalent.

[‡]It is interesting to note that Pumir [Pum85] suggested that small-scale intermittency could more appropriately
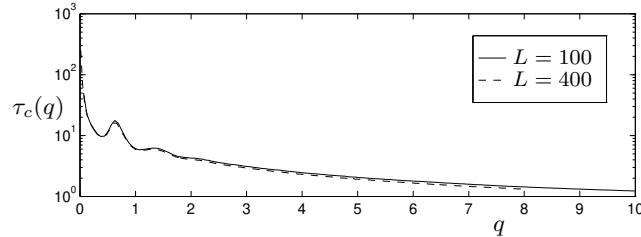
Figure 4.10: Correlation times $\tau_c(q)$ for different Fourier modes $\hat{u}_q(t)$.

Temporal behavior of Fourier modes

The temporal statistics of the (spatial) Fourier modes $\hat{u}_q(t)$ yield insight into the temporal behavior at different scales. We report here the lowest-order statistic, an autocorrelation time $\tau_c(q)$, which we may compute as before using (4.2), from the temporal power spectrum of each $\hat{u}_q(t)$ (Fig. 4.10).

The large scales have slow dynamics; in fact, from temporal scaling of the KPZ equation [KS91] (see Sec. 4.2.2), we may deduce that the correlation time diverges as $q \to 0$ at a rate $\tau_c(q) \sim q^{-3/2}$ (although our computed power law, which does not extend to q in the KPZ range, shows a slower divergence). The small-scale dynamics are rapid, with a characteristic time that appears to decrease with q as a power law. From calculations for $L = 100$ and $L = 400$, we estimate scaling of the form $\tau_c(q) \approx 7.3 \, q^{-0.78}$ for $q \geq 2.5$.

Near the peak of the power spectrum, the temporal behavior is somewhat different. There is a pronounced local maximum in $\tau_c(q)$ for q slightly below the peak of the power spectrum at $q_m \approx q_0$, with a correlation time $\tau_c(q_m) \approx 17.8$, somewhat larger than the characteristic time τ_c for the field u as a whole. In this active region, a faster linear growth rate is correlated with slower dynamics. We believe that the longer time scales for the excited modes arise from the metastability of the cellular solutions (stable for small L) undergoing continuous creation and annihilation events ("space-time defects") [CH95].

Note in Fig. 4.10 the adjacent local maximum in $\tau_c(q)$ for q near $2 \, q_m$, and to a lesser extent near $3 \, q_m$; that is, near the low-order harmonics of the most energetic mode q_m. These smaller maxima can be understood in terms of the slower dynamics for q near q_m. For instance, mode q is directly coupled to its second harmonic, as the Fourier evolution equation (1.5) for $\hat{u}_{2q}$ contains a term proportional to $\hat{u}_q^2$. Thus, for $q \approx q_m$, the slower dynamics of $\hat{u}_q$ has a direct effect in slowing down the dynamics of the mode $\hat{u}_{2q}$ (which of course also has its own internal dynamics). The effect is similar, but considerably less pronounced, for the higher harmonics.

4.2 Wavelet space properties and scale localization

The power spectrum, and the distributions and temporal behavior of the Fourier modes, provide much insight into the dynamics in the spatiotemporally complex regime, beyond that attainable through investigation of the field $u(x, t)$ alone. However, each Fourier basis function is distributed over the entire spatial domain. Thus the Fourier approach cannot provide information on spatially *localized* features of the dynamics in a subdomain. The phase relationships between different Fourier modes, which give rise to spatially local features in the superposition, are lost in the averaging which gives the power spectrum and statistics.

be investigated using a high pass filter; the wavelet approach provides just such a filter—see Sec. 4.2.4.

Furthermore, all Fourier-based properties (such as the energy spectrum and time correlations) are continuous in q; there is no separation of scales. We might sometimes prefer to group ranges of Fourier modes to separate and distinguish properties local to these ranges; this is particularly useful for an investigation such as that of Ch. 5, in which the dynamical contributions of different scales to the overall spatiotemporal chaos are obtained. This motivates the use of a spatially localized basis, which may be able to detect dynamical features arising from spatially localized events while providing a separation of scales.

In Sec. 3.1, we have given an overview of the orthogonal wavelet decomposition and the periodic spline wavelet basis used in this thesis. Given a solution $u(x,t)$ of the KS equation, we may obtain its time-dependent coefficients $a_\alpha(t)$ with respect to a wavelet basis via the decomposition (3.17). For the purposes of this Section, we need only these coefficients $a_\alpha(t) = a_{jk}(t)$, which reveal the behavior of $u(x,t)$ at wavelet level j and position k. These coefficients are obtained via a fast wavelet transform of a solution found by finite difference or Fourier pseudospectral techniques (see App. B.1–B.2). That is, we only perform wavelet *analysis* on the solution; we do not require the particular form of the wavelet Galerkin projection of the KS equation (3.19) until Sec. 4.3.3 and the following Chapters.

4.2.1 Spectrum, temporal behavior and PDFs of wavelet coefficients

In this Section, we will present results for the KS evolution for $L = 100$, a typical length well within the STC regime, but still short enough to allow sufficiently fast calculations and well-converged statistics; in Sec. 4.2.5, the dependence of the results on L will be considered. For $L = 100$, the peak of the Fourier spectrum is at $q_m \approx q_0 = 1/\sqrt{2}$, or at $n_m = \lfloor q_m L/2\pi \rfloor = 11$, and the highest unstable mode is at $L/2\pi \approx 15.92$. That is, there are 16 complex, or 32 real linearly unstable or marginal (Fourier) modes, and the energy is concentrated in the neighborhood of the 22nd real mode. Hence the peak is located in wavelet level 4 (levels 0-3 contain a total of $\sum_{j=0}^{3} 2^j = 15$ modes).

We remark that since wavelets, unlike Fourier modes, are not eigenmodes of the linear operator, they cannot clearly be said to be "stable" or "unstable". In the wavelet Galerkin representation of the KS equation (3.19), in the evolution for a wavelet mode a_α the diagonal linear term $l_{\alpha\alpha}a_\alpha = l_{jk\,jk}a_{j\,k}$ is particularly relevant; for instance, it plays a special role in designing efficient numerical schemes (App. B.3.2), and in determining stability when a single mode evolves freely, driven by all others obtained from a control KS integration (Sec. 5.3.2). In this thesis, a wavelet mode for which $l_{\alpha\alpha} > 0$ will thus be said to be *unstable*, while it is *stable* if $l_{\alpha\alpha} < 0$. For $L = 100$, the unstable levels are $j \leq 4$, while levels $j \geq 5$ are stable. This is consistent with the Fourier dispersion relation, taking into account the support of the wavelets in Fourier space.

Energy distribution among wavelet levels

We first compute the energy in each wavelet level (since ψ_{jk} is an orthonormal basis, this is simply found from $e_j(t) = \sum_k a_{j\,k}^2(t)$). Figure 4.11 shows the time averaged energy per wavelet level, as well as the energy for each individual wavelet at that level, given that there are 2^j wavelets at level j (by translational invariance, all wavelets at a given level have identical statistics). In Fig. 4.11(b), the comparison with the power spectrum of Fig. 1.4 shows a similar distribution of energy per mode, confirming that the wavelets are well-localized in Fourier space. In the dissipative range, the wavelet energies decay more slowly than $S(q)$, however; this arises largely because each wavelet level overlaps a range of Fourier modes, and with exponentially decaying power spectrum,
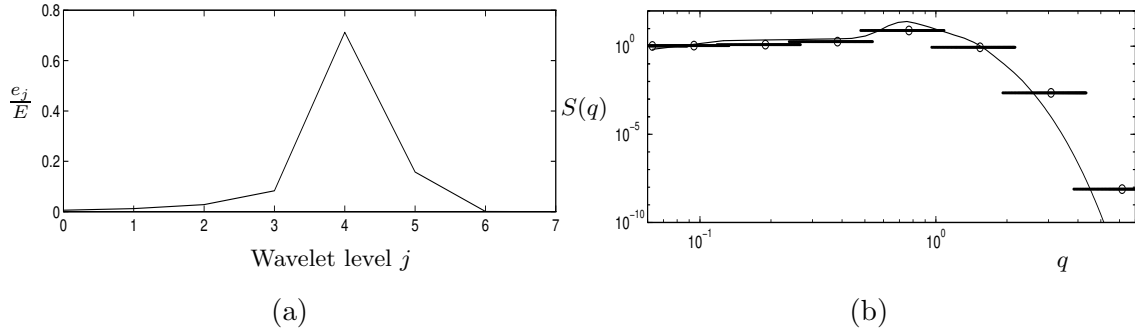
Figure 4.11: (a) Fraction of time-averaged total energy, $\langle e_j(\cdot)/E(\cdot)\rangle$, as a function of wavelet level j, for $L = 100$. (b) Power spectrum $S(q)$ (Fig. 1.4), compared to the energy per individual wavelet at each level j. The wavelet distribution is plotted with the approximate center and range of the support (containing 99% of the energy) in Fourier space.

the wavelet energies are strongly weighted by the low-q end of the range. We shall frequently refer to this energy distribution for comparison with experiments.

Identification of distinct ranges   From Fig. 4.11(a), we can identify the levels with distinct behaviors: Wavelet levels 0, 1 and 2 correspond to *large* scales, containing little energy in total (due especially to the small numbers of wavelets at these scales)—this corresponds to the nearly flat region of the Fourier spectrum. Levels 3, 4 and 5 contain the *active*, energetic modes near the peak of the Fourier spectrum. The *small* scales, levels 6, 7 and any higher (smaller scale) levels are strongly damped, with exponentially decreasing energy in the dissipative range. This terminology for the different scales (large, active and small), already introduced in discussing the Fourier space results, will be important for the remainder of this thesis. A visual distinction between the wavelets at large, active and small scales for $L = 100$ is provided by the sizes of the dots in the wavelet pyramid of Fig. 3.2.

Temporal behavior of wavelet coefficients

Typical time series for wavelet coefficients at each level (for wavelets at each scale centered near $x = L/2$, taken for the same time interval) are shown in Fig. 4.12. From this, we can clearly see the differences in time scales, distributions and dynamics at the different scales. Characteristic times τ_j for each level j are shown in Fig. 4.13 (compare Fig. 4.10). The (approximate) wavelet energy distributions of Fig. 4.11(a) and time scales of Fig. 4.13 for the full KS equation are summarized in Table 4.1 for ready reference.

PDFs of wavelet coefficients

In Fig. 4.14 we show the PDFs for the wavelet coefficients at each level, averaged over time, and over the 2^j wavelets at each level j; computed by binning from a long-time integration to $t > 10^5$ (compare [EBH96, Fig. 1]). This Figure clearly shows how the wavelet representation captures both scale and spatially localized information (*cf.* Figs. 4.1(a), 4.8). Along with the wavelet energy distributions and characteristic times, we will use these PDFs as the basis for discussing the different ranges of scales observed in KS spatiotemporally chaotic dynamics; the following Sections should be read in conjunction with the Fourier space results.
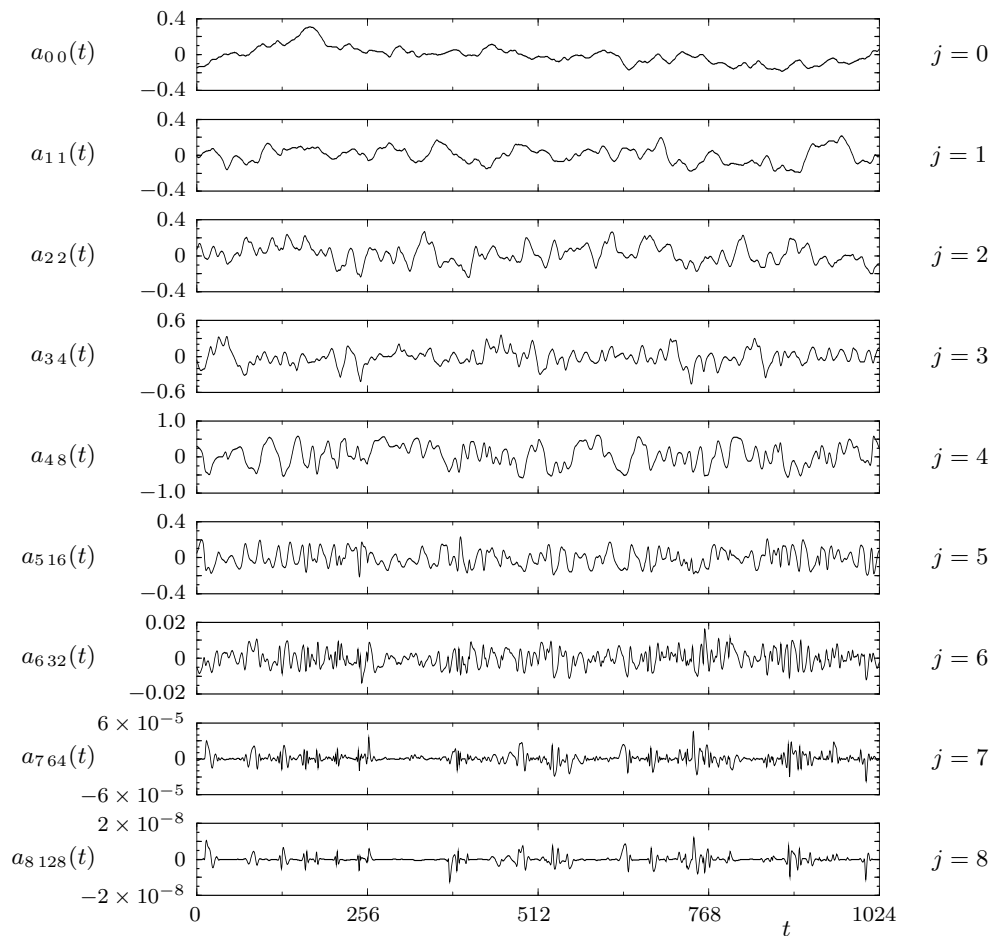
Figure 4.12: Sample time series for one wavelet coefficient $a_{jk}(t)$ at each level j, for $k = 2^j/2$, that is, centered near the middle of the domain of length $L = 100$.
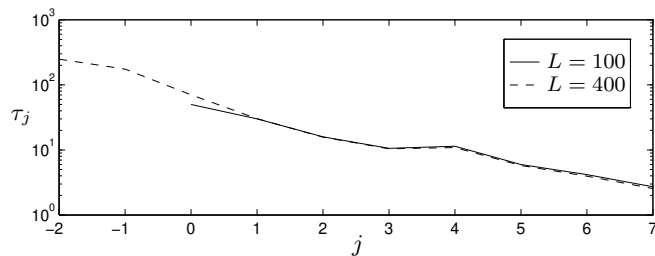
Figure 4.13: Width at half maximum autocorrelation times τ_j for the time series of wavelet coefficients at different scales j. Note that the values for $L = 400$ are shifted by two wavelet levels (we plot, in fact, τ_j against j–2)—see Sec. 4.2.5. Compare Fig. 4.10, noting that the horizontal axes are logarithmically related to each other ($j \propto \log q$).

Wavelet level	Fraction of energy	Autocorrelation time
j	e_j/E	τ_j
0	$5.9 \cdot 10^{-3}$	45
1	$1.2 \cdot 10^{-2}$	29
2	$2.8 \cdot 10^{-2}$	16
3	$8.4 \cdot 10^{-2}$	10
4	$7.1 \cdot 10^{-1}$	11
5	$1.6 \cdot 10^{-1}$	5.9
6	$8.2 \cdot 10^{-4}$	4.2
7	$4.1 \cdot 10^{-9}$	2.7

Table 4.1: Estimates for the fraction of energy per wavelet level, and the autocorrelation time at each level j, for $L = 100$. The total energy is $E \approx 172$, and the overall correlation time $\tau_c \approx 10$. Accurate values, especially at the small scales and for large scale correlation times, are difficult to obtain.

4.2.2 Large scales and effective dynamics

For large scales, the distribution is Gaussian. At these scales, the support of each wavelet includes several characteristic wavelengths. Due to spatial decorrelation and independence of sufficiently separated positions (Sec. 4.3.2), the averaging over several characteristic structures inherent in the large-scale wavelet coefficients may thus be expected to lead to the normal distribution. At the coarsest scales, therefore, the dynamics resembles slow noise. Note that the PDFs for the lowest j values are less well converged; this is both due to the fact that there are fewer wavelets at these j, over which to average; and also because the dynamics at the large scales is slow, requiring more time for statistical equilibration (see Figs. 4.12, 4.13).

In order to place these results in the broader context of the literature, in this Section we review the understanding of the large scale dynamics, following the literature and the reviews in [KS91, HHZ95], with a view to constructing a stochastic model for the large scales in Sec. 4.2.3. There has been considerable effort devoted to understanding the slow coarse-grained effective dynamics, that is, the large-scale, long-time behavior of the KS equation. This is of particular interest because (as suggested by the Gaussian statistics at large scales for Fourier and wavelet coefficients) at large scales, the system appears to obey an effective stochastic, Langevin-type dynamics, whereas the KS equation is completely deterministic. That is, the inherent instabilities and fluctuations of the chaotic dynamics at the small and intermediate scales simulate the effect of a random forcing on the large scales.

Forced Burgers and KPZ equations Efforts at making this notion more precise have focused on validating the early conjecture of Yakhot [Yak81], that the large scale behavior can be described by a noise-driven Burgers equation [FNS77],

$$u_t = \nu u_{xx} + \lambda u u_x + f; \qquad \nu > 0. \tag{4.11}$$

The form of this effective equation is motivated by symmetry principles, in particular, by the requirement of Galilean invariance [BS95] (see Sec. 1.2.1). For this description to be valid, the effect of the chaotic small scales on the large scales must be not only to mimic a stochastic forcing term $f(x,t)$, but also to renormalize the coefficient of u_{xx} to give a positive effective viscosity ν
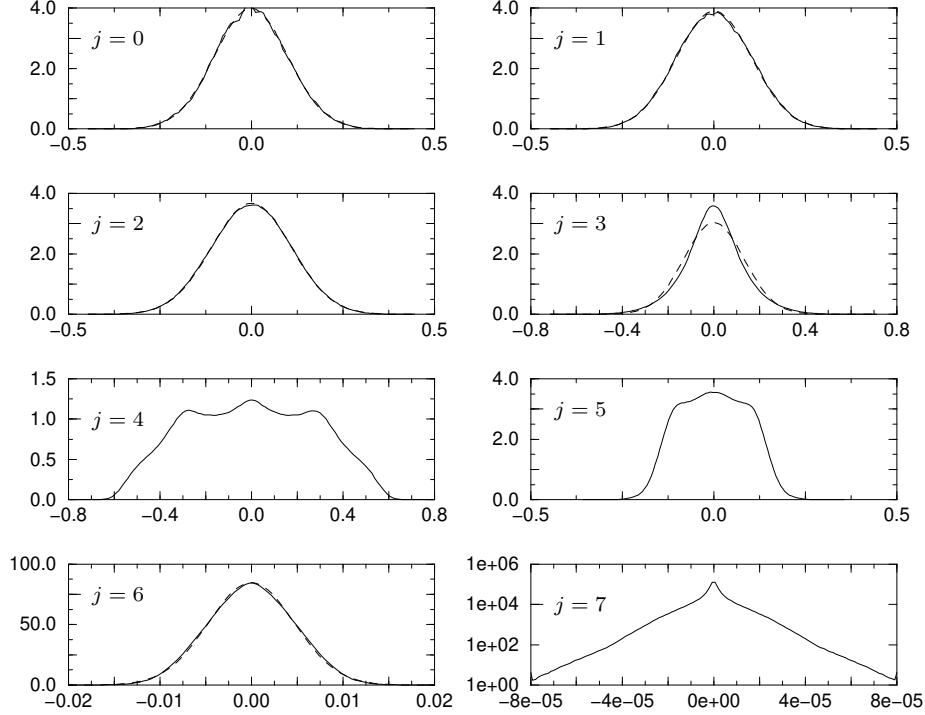
Figure 4.14: Probability density functions for the wavelet coefficients at each level $j = 0 \ldots 7$, for $L = 100$. For $j = 0$–3 and 6, a best-fit Gaussian distribution is superposed. Note the logarithmic axis at $j = 7$, denoting a near-exponential distribution.

(the effect of this is to render the fourth derivative term irrelevant, in the renormalization group sense, since $q^2 \gg q^4$ for $q \ll 1$).

There has been an explosion of interest in the effective equation (4.11) since Kardar, Parisi and Zhang (KPZ) [KPZ86] showed that its integral form,

$$h_t = \nu h_{xx} + \tfrac{1}{2}\lambda h_x^2 + \eta, \tag{4.12}$$

is the simplest equation describing the kinetic roughening of growing interfaces with stochastic local dynamics [KS91, BS95, HHZ95]. This equation has subsequently been shown to be applicable to a wide range of growth phenomena. In the idealized equation (4.12), the forcing $\eta(x, t)$ (where "$f = \eta_x$" in an appropriate mathematical interpretation, for example in Fourier space) is delta-correlated Gaussian white noise with covariance $\langle \eta(x, t)\eta(x', t')\rangle = D\delta(x - x')\delta(t - t')$, or in Fourier space, $\langle \hat{\eta}_q(t)\hat{\eta}_{q'}(t')\rangle = (D/L)\delta_{q+q',0}\delta(t - t')$, $\langle \hat{f}_q(t)\hat{f}_{q'}(t')\rangle = (D/L)q^2\delta_{q+q',0}\delta(t - t')$.

The equations (4.11, 4.12) are well-understood in one space dimension, $d = 1$. A scaling form for the growth and structure of the interface may be found; in particular, for the transient growth of an initially flat interface, the Fourier components satisfy

$$\langle |\hat{h}_q(t)|^2\rangle = \frac{A}{Lq^2}g_{\text{tr}}(q^z t), \tag{4.13}$$

where z is the dynamic scaling exponent, and the (universal) transient scaling function g_{tr} satisfies $g_{\text{tr}}(0) = 0$, $\lim_{s \to \infty} g_{\text{tr}}(s) = 1$. Here $z = 2$ (diffusive scaling) is relevant for the linear (Edwards-Wilkinson—EW) equation ((4.12) with $\lambda = 0$) while a perturbative renormalization group approach

[FNS77, BS95] reveals that the KPZ equation exhibits anomalous scaling, $z = 3/2$. Noting that $|\hat{u}_q| = |q\hat{h}_q|$, this scaling predicts the autocorrelation times $\tau_c(q) \sim q^{-3/2}$ in the KPZ limit, as mentioned in Sec. 4.1.2. It also follows that the power spectrum of u is flat: $\langle |\hat{u}_q(\cdot)|^2 \rangle = A/L$.

Scaling of the width and crossover   One can also look at the scaling of the interface width (the ideas here are also most readily understood in terms of the integrated equation for h; see [BS95, HHZ95]). Consider again an initially flat interface, with the height $h(x,t)$ growing according to (4.12). Then the width, defined by

$$w^2(t) \stackrel{\text{def}}{=} \frac{1}{L} \int_0^L (h(x,t) - \bar{h}(t))^2 \, dx, \qquad \bar{h}(t) \stackrel{\text{def}}{=} \frac{1}{L} \int_0^L h(x,t) \, dx,$$

scales as $w^2(t) \sim t^{2\beta}$. For a finite system of length L, eventually the width saturates, with a power law scaling $\lim_{t\to\infty} w(t) = w_{\text{sat}} \sim L^\alpha$. The three scaling exponents α, β and z are always related by $z = \alpha/\beta$, and in dimension $d = 1$ we have $\alpha = 1/2$ from the fluctuation-dissipation theorem discussed below. Lastly, for the linear EW equation, $z = 2$ and $\beta = 1/4$, while for the KPZ equation, the relation $\alpha + z = 2$ determines $z = 3/2$, as stated above. More careful analysis (see [HHZ95]) computes the evolution of the width for the linear and nonlinear equations as

$$w_{\lambda=0}^2(t) = \frac{D}{\sqrt{2\pi\nu}} t^{1/2}, \qquad w_{KPZ}^2(t) = c_2 (A^2 \lambda t)^{2/3}, \quad c_2 \approx 0.40. \tag{4.14}$$

Now consider an interface, growing from a flat state $h(x,0) = 0$. For short times (small h), the nonlinear term in (4.12) is negligible relative to the other terms, so that the linear EW scaling dominates and the width grows according to the first equation of (4.14). Eventually, h becomes large enough that the nonlinear term becomes relevant, and there is a crossover to the asymptotic nonlinear KPZ scaling. By equating the two expressions for $w(t)$ in (4.14), we can compute the crossover time t_c, and hence the width $w(t_c)$ at crossover. If the length L of the system is so small that the width has saturated before time t_c, $w_{\text{sat}} < w(t_c)$, then the crossover will not be observed and the system remains in the intermediate linear scaling regime. The saturation width w_{sat} can be computed by summing over the Fourier modes in the long time limit of (4.13); consequently, the critical length L_c for accessibility of the asymptotic regime may be estimated. The results of these calculations are [SKJJB92]

$$t_c = \frac{2^5}{\pi^3 c_2^6} \frac{\nu^5}{D^2 \lambda^4} \approx \frac{252}{\nu g^2}, \qquad w_{\text{sat}}^2(L) = \frac{AL}{12}, \qquad L_c \approx \frac{152}{g},$$

where $g \stackrel{\text{def}}{=} \lambda^2 D/\nu^3$ is the KPZ coupling constant.

Gaussian distribution for u   An alternative approach to the KPZ dynamics is to consider the Fokker-Planck equation corresponding to (4.11), describing the evolution of the distribution functional $\Pi[u(x);t]$ of the field u [BS95, HHZ95]:

$$\frac{\partial \Pi}{\partial t} = -\int \frac{\delta}{\delta u} \left[\left(\nu u_{xx} + \tfrac{1}{2}\lambda u u_x \right) \Pi \right] \, dx + D \int \frac{\partial^2 \Pi}{\partial u^2} \, dx.$$

For $d = 1$ (only), this equation has a stationary solution

$$\Pi = \exp \left(-\frac{\nu}{2D} \int u^2 \, dx \right), \tag{4.15}$$

which also solves the linear equation with $\lambda = 0$. This result, which follows from a fluctuation-dissipation theorem for the one-dimensional forced Burgers equation [FNS77, HHF85], determines the constant A in (4.13) above by $A = D/2\nu$. More importantly, it gives the full steady-state distribution of u satisfying (4.11): the local values of $u(x, \cdot)$ have a *Gaussian distribution*, that is, they are *random and uncorrelated* in x. It follows that the Fourier and wavelet coefficients of u also obey a Gaussian distribution.

Relationship between KS and KPZ equations

As already indicated from symmetry considerations, the forced Burgers equation is an appropriate model for the long wavelength dynamics of the KS equation. Furthermore, the properties discussed above for the forced Burgers equation agree with our observations at the large scales, including the power law growth in correlation times as $q \to 0$ and especially the Gaussian distributions in Fourier and wavelet coefficients at large scales. We have not observed the predicted flat power spectrum at large scales (see Fig. 4.7 and accompanying discussion); as described below, the lengths L we have considered do not approach the crossover to KPZ scaling.

While the motivation for wishing to relate the large-scale KS behavior to the KPZ equation is straightforward, a convincing demonstration that these models are equivalent as $q \to 0$ is not. Indeed, early investigations [Man81, ZL85, HNZ86] only detected the linear scaling regime. More recently, however, various groups have shown the desired equivalence using different methods.

Using a diagrammatic renormalization group technique, L'vov *et al.* [LLPP93] have shown to all orders in their perturbation scheme that the (one-dimensional) KS and KPZ equations have the same asymptotic scaling in the limit $q \to 0$. This confirms that these models are in the same universality class, but does not make quantitative predictions for finite L. Note that the situation is much less clear in higher dimensions [LP92]; especially for $d = 2$, there has been some controversy about whether the KPZ and KS equation are in the same universality class [PJLSZ92, JHP93].

Parameters in the effective equation   Sneppen *et al.* [SKJJB92] provided the definitive confirmation that the KPZ equation is valid for sufficiently large scales of the KS equation, and also accounted for the failure of previous attempts to observe KPZ scaling. They numerically simulated the (integrated) KS equation, for large L and long times, and measured the saturated width, the time evolution of the width, and (by imposing an overall tilt through the boundary conditions) the growth rate at a given macroscopic inclination, to measure the parameters $\nu = 10.5 \pm 0.6$, $D = 3.2 \pm 0.1$ and $\lambda = 4.65 \pm 0.15$ in the effective equation (4.12). By arguments given above, they then computed the coupling constant $g \approx 0.060 \pm 0.016$, and the crossover time and length. They were able to observe the expected KPZ scaling; but also estimated that system sizes $L \gg L_c \approx 2500$ (and times $t > t_c \approx 7000$) would be needed to see the asymptotic scaling regime. Li and Sander [LS95] have implemented a different method to compute the effective parameters.

The large value of L_c (associated with a large effective viscosity $\nu \approx 10.5$) explains the difficulties in observing asymptotic scaling; lengths far into the STC regime are required. Note that the lengths L considered in this thesis do not approach the crossover L_c, so we are, strictly speaking, not in the "large L limit". However, we are most interested in the STC dynamics in the active regime, with $q = \mathcal{O}(1)$. Since, as we have shown in this Section, the large, active intermediate, and damped small scales are well separated, and may be characterized independently, we do not believe that the crossover in the dynamic scaling at very large scales and low q significantly affects the properties of STC at the $\mathcal{O}(1)$ scale of the characteristic cellular structures.

Constructive approach to deriving the effective equation The approaches described so far do not address the origin of the stochastic forcing, or of the viscosity renormalization. The first demonstration that the forced Burgers equation (4.11) gives a good large-scale description for the KS equation was provided by Zaleski [Zal89]. He explicitly constructed the effective equation in Fourier space,

$$\frac{d}{dt}\hat{u}_q(t) = -\nu q^2 \hat{u}_q(t) + \sum_{\substack{q' \leq \Lambda \\ q-q' \leq \Lambda}} \hat{u}_{q'}(t)\hat{u}_{q-q'}(t) + \hat{f}_q(t), \tag{4.16}$$

by integrating out the short wavelength degrees of freedom in the equations for the large scale modes. That is, working in Fourier space, for a chosen cutoff Λ he separated the modes for $q < \Lambda$ and $q > \Lambda$, in an approach similar to the extraction of subsets of wavelet coefficients described in Sec. 3.2.1 (see (3.25, 3.26)). All terms containing modes $\hat{u}_{q'}$ for $q' > \Lambda$ contribute to the forcing term $\hat{f}_q$ in (4.16); the effective viscosity ν is determined by the requirement that $\hat{f}_{q'}(t')$ be a true stochastic force, that is, it should be uncorrelated with $\hat{u}_q(t)$ for $t < t'$.

Zaleski [Zal89] was able to carry out this program, and show that the small scales contributed to a (large) positive effective viscosity $\nu \approx 10$ in the coarse-grained system. Since in the KS equation, the "stochastic" forcing term f arises from deterministic dynamics, it cannot be delta-correlated as postulated in the ideal theory of (4.11, 4.12). However, the effective description is approximately valid if the correlations of the force $\hat{f}_q$ are much faster than those of $\hat{u}_q$. It was found [Zal89] that the autocorrelation time of the constructed f is of order $\tau_f \approx 10$, similar to that of the active scales and of the field u as a whole (Table 4.1). The effective equation (4.16) is thus plausible for small enough q (with long correlation time $\tau_c(q)$—see Fig. 4.10).

This approach was pursued further by Hayot *et al.* [HJJ93], who determined the effective parameters via an integration for longer L. Thus they were able to observe the crossover to asymptotic scaling (not seen in [Zal89]), and estimate crossover lengths and times even higher than those discussed above [SKJJB92]. The wavelet-based method of Elezgaray *et al.* [EBH96], discussed in more depth in Sec. 3.2.2, employs a similar idea of integrating out the small scales.

Mechanism for large scale stabilization While the preceding studies clarify the relation between the KS and KPZ equations, the mechanism by which one gets from the KS equation (1.1) to (4.11) is poorly understood [RK95]. That is, *how* do the small and active scales act on the large scales through the nonlinearity, thereby providing stabilization by renormalizing the viscosity? One would like a hydrodynamic theory to get from the local dynamics to the large scale properties. One approach is that of Elezgaray *et al.* [EBH96], who attempt to understand the energy transfer between different levels.

Chow and Hwa [CH95] have argued that the local KS dynamics is best understood in terms of cell interactions, in particular, the drifting of cells, and their creation and annihilation in response to local dilations and compressions. They construct an effective Langevin description of a coarse-grained local drift rate, which may be computed from the response of a *small* chaotic system, and which feeds back into the slow (large-scale) component of the field. They use the term "defect-mediated stability" for their mechanism.

Rost and Krug [RK95] have implemented the idea that the motion and interaction of cells is responsible for the spatiotemporally chaotic state by constructing a minimal model of interacting classical particles on the real line, obeying rules designed to mimic the cell defects. Their particle model shares many basic features of the KS equation, in particular, having large scale behavior of the KPZ-Burgers type.

4.2.3 A stochastic model for large scale modes

We have discussed the large-scale behavior of the KS equation at some length, to attempt to explain the origin of large-scale stochasticity. In this thesis, we are more concerned with understanding spatiotemporal chaos through the active scales. In the light of the above discussion, we can think of the large scales as supplying slow random noise to the active scales. In order to test this assumption in our experiments of later Chapters, we propose an autonomously generated stochastic process to reproduce the statistics of the large scales.

To model the large scales, we need a (mean-zero) Gaussian process with reasonable smoothness, variance and temporal correlations. The effective equation (4.11) discussed above provides a theoretical motivation for our model. Since the large scale wavelets are essentially linear combinations of few Fourier modes (see [MHEB95]), we restrict our discussion here to Fourier space.

A toy model for noisy large-scale behavior We greatly simplify our task by noting that we need only consider a linear model, derived from (4.11) with $\lambda = 0$. This is because, as already noted, the lengths we consider remain in the linear scaling EW regime, and do not approach the crossover to asymptotic KPZ scaling; also, by (4.15) the distributions for the linear and nonlinear forms of (4.11) coincide. Neglecting λ, (4.11) in Fourier space becomes

$$\frac{d}{dt}\hat{u}_q = -\nu q^2 \hat{u}_q + \hat{f}_q, \tag{4.17}$$

that is, just the linearization of (4.16). As discussed previously, the forcing term $\hat{f}_q$ obtained for the KS equation has finite correlation time τ_f, and is not delta-correlated in time as postulated for (4.11). From the point of view of modeling, letting $\hat{f}_q$ be white noise forcing is also undesirable, as $\hat{u}_q$ would then be non-differentiable with Hölder exponent $1/2$. The discussions following (4.12) and (4.16) imply that the forcing should satisfy $\langle \hat{f}_q(t)\hat{f}_{-q}(t+t')\rangle \simeq (Dq^2/2\tau_f L)\exp(-|t'|/\tau_f)$ [HJJ93] (which reduces to the delta-correlated case as $\tau_f \to 0$). The advantage of basing our model on (4.11) is that the effective parameters D, ν and τ_f have all been determined for the KS equation, as described previously.

It remains to choose a model for $\hat{f}_q$. Here we take the simplest form that gives exponential correlations (in the long-time limit), the Langevin equation

$$\frac{d}{dt}\hat{f}_q = -\nu_f \hat{f}_q + \sqrt{D_f}\,\hat{\eta}_q, \tag{4.18}$$

where now $\hat{\eta}_q$ is zero-mean, unit-variance, Gaussian white noise, with covariance $\langle \hat{\eta}_q(t)\hat{\eta}_{q'}(t')\rangle = \delta_{q+q',0}\delta(t-t')$.[†]

Correlations in the simple model Since η_q is a Gaussian process, so are $\hat{f}_q$ and $\hat{u}_q$, since (4.17) and (4.18) are linear. Note that in this model, $\hat{u}_q$ turns out to be Hölder $3/2$; not very smooth, but, we feel, adequate for our purposes. By explicit integration we can find the means $\langle \hat{f}_q \rangle$ and

---

[†]The notation and terminology we use for convenience throughout this Section are common in physics; but the results can be formalized in the language of stochastic differential equations and the Itô integral. For instance, strictly speaking $\hat{\eta}_q$ is the (formal) derivative of a Wiener process, and (4.18) describes the Ornstein-Uhlenbeck process via

$$dX_t = -\nu_f\, X_t\, dt + \sqrt{D_f}\, dW_t,$$

where $X_t = \hat{f}_q(t)$, and W_t is a standard Brownian motion (Wiener process).

$\langle \hat{u}_q \rangle$ (which vanish for zero initial data), and the covariances. For the Ornstein-Uhlenbeck process $\hat{f}_q$, by integrating (4.18) and averaging, one obtains the standard result (see for instance [Gar85])

$$\langle \hat{f}_q(t)\hat{f}_{-q}(t') \rangle = \frac{D_f}{2\nu_f} \mathrm{e}^{-\nu_f |t-t'|}\big(1 - \mathrm{e}^{-2\nu_f t'}\big), \qquad t \geq t', \tag{4.19}$$

which becomes stationary and has the desired exponential correlations as $t, t' \to \infty$. To obtain the correct forcing strength and time constant indicated above, we thus require $\nu_f = 1/\tau_f$, and $D_f = Dq^2/L\tau_f^2$.

By a calculation similar to that used to derive (4.19), though requiring somewhat more algebra, we find (writing temporarily $\nu_q \overset{\text{def}}{=} \nu q^2$, and assuming $\nu_f \neq \nu_q$)

$$\begin{aligned}
\langle \hat{u}_q(t)\hat{u}_{-q}(t') \rangle =& \frac{D_f}{2\nu_f \nu_q(\nu_q + \nu_f)(\nu_q - \nu_f)^2} \Big\{ (\nu_q - \nu_f)\big(\nu_q \mathrm{e}^{-\nu_f |t-t'|} - \nu_f \mathrm{e}^{-\nu_q |t-t'|}\big) \\
&- (\nu_q + \nu_f)\big(\nu_q \mathrm{e}^{-\nu_f(t+t')} + \nu_f \mathrm{e}^{-\nu_q(t+t')}\big) \\
&+ 2\nu_f \nu_q \big(\mathrm{e}^{-\nu_q t - \nu_f t'} + \mathrm{e}^{-\nu_f t - \nu_q t'}\big) \Big\},
\end{aligned} \tag{4.20}$$

symmetric in ν_f and ν_q. In the long time limit $t, t' \to \infty$ (or if we begin the process at $-\infty$) the terms on the second line of (4.20) vanish, and $\hat{u}_q$ becomes stationary. Substituting for D_f and ν_f, the equal-time correlation function takes the simple form (see [HJJ93])

$$\langle \hat{u}_q(t)\hat{u}_{-q}(t) \rangle = \frac{D}{2\nu L} \frac{1}{1 + \tau_f \nu q^2}. \tag{4.21}$$

From (4.21), we see that our toy model (4.17) with (4.18) reproduces the results stated above for the forced Burgers/KPZ equation—in particular, the flat power spectrum with $S(q) = L\langle |\hat{u}_q|^2 \rangle = D/2\nu$—in the limit $\tau_f \ll \tau_q \overset{\text{def}}{=} (\nu q^2)^{-1}$. That is, they are valid if $\hat{f}_q$ is delta-correlated ($\tau_f = 0$), as postulated in the idealized model (4.11). For forcing with finite time correlations, according to this model the effective KPZ description holds in the asymptotic limit $q \to 0$ [HJJ93]; this is all consistent with the theory presented previously. Note that spatial or temporal noise correlations—both of which would be expected to arise in a deterministic process such as the KS equation—considerably complicate the study of KPZ-type systems via numerical simulation and the renormalization group, and the theory is less complete than for delta-correlated noise [HHZ95, BS95].

For the effective description of the KS equation, ν and τ_f are both of order 10. The condition for a flat spectrum, $\tau_f \nu q^2 \ll 1$, thus implies $q \ll 0.1$. Since for a length $L = 100$, the lowest Fourier mode has $q = 2\pi/L \approx 0.06$, we now see why, at least in this simplified description, lengths of order a few hundred are insufficient to attain the flat power spectrum regime, and that much larger L is needed to approach KPZ scaling.

Simulation of toy model We have simulated (4.17) and (4.18) by standard methods [KPS94], using Euler stepping (with $\delta t = 0.01$) and the Polar Marsaglia method for generating Gaussian random variables. We used the effective parameters $D = 17.9$, $\nu = 7.5$, $\tau_f = 7.0$ given in [HJJ93],[†] and set $L = 100$ and $q = 2\pi/100$ corresponding to the lowest Fourier mode. A sample time history

---

[†]For our stochastic model, we use the effective parameters obtained by Hayot *et al.* [HJJ93] for the KS equation (1.1); the corresponding predictions for the flat part of the power spectrum, $\lim_{q \to 0} S(q) = D/2\nu$, agree well with our calculations. These parameters differ from those computed by Sneppen *et al.* [SKJJB92] and quoted in Sec. 4.2.2 above, which were obtained for the integrated form (1.3), and whose predictions for $D/2\nu$ differ from ours and those of [HJJ93] by approximately a factor of 2π, possibly due to the choice of scaling in the Fourier transform.
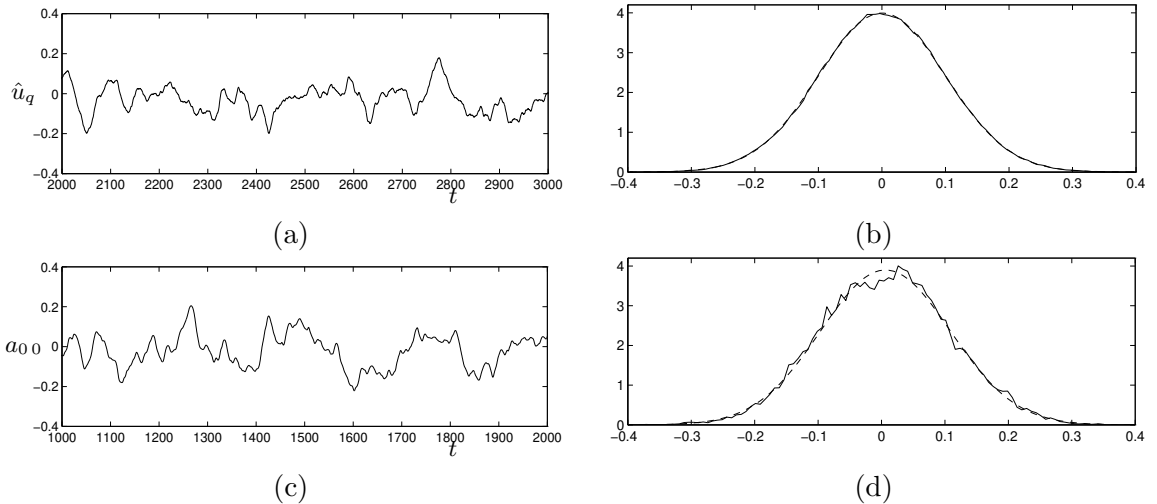
Figure 4.15: Simulation of autonomous stochastic process (4.17, 4.18) reproducing large scale behavior: (a) Sample time series; (b) PDF for long time simulation, with best-fit Gaussian superimposed. (c) For comparison, time series for the wavelet coefficient $a_{0\,0}(t)$ for $L = 100$, for the same simulation as in Fig. 4.12; (d) PDF for level $j = 0$ wavelet for $L = 100$, with superimposed Gaussian best fit, as in Fig. 4.14.

is shown in Fig. 4.15(a); for comparison, a time series for the $j = 0$ mode in an $L = 100$ KS integration is shown in (c) (*cf.* Fig. 4.12). Simulation of our stochastic model appears to reproduce the correct qualitative behavior of the large scales extremely well; in particular, note the Gaussian PDF for our simulation, shown in Fig. 4.15(b) from an integration to $t = 10^6$, which reproduces the correct amplitudes, compared with the large scale PDFs in Fig. 4.14, also shown in Fig. 4.15(d).

We will use this autonomous model for the large scales as random forcing in some experiments of Secs. 5.5.2 and 6.3. In these experiments, we simulate wavelet levels $j = 0$–2 for $L = 100$; the modes at these levels have the same amplitudes and PDFs, but different time scales (see Fig. 4.14 and Table 4.1). If necessary, we can readily obtain more rapid dynamics by modifying some parameters, notably τ_f and q. However, the experiments of Sec. 5.4.2 indicate that the time scales of the large-scale forcing terms have little effect on the overall dynamics (whereas the amplitudes are crucial), so that reproducing the correct time scales may not be essential for our modeling.

4.2.4 Active and small scales

Active scales

In studying the spatiotemporally chaotic dynamics of the KS equation, we are less interested in the large-scale randomness *per se*, than in its effect on the most active and energetic scales. At the active levels $j = 3$, 4 and 5, the support of the wavelets is comparable to the characteristic intrinsic wavelength $l_m = 2\pi/q_m$, and the PDFs are quite different, displaying features unlike any observed in the Fourier representation; see Fig. 4.14.

For $L = 100$, the $j = 3$ level, although still largely in the flat part of the Fourier spectrum, shows a distinct steepening of the distribution relative to a Gaussian. (See Sec. 4.2.5 for the effect of L variations.)

Levels 4 and 5 show the most striking, nonequilibrium PDFs which, unlike the Fourier coefficient

distributions, are comparable to the local distributions for u (see Fig. 4.1(a)): a broad, triple-humped distribution, superposing a peak at 0 and a double-humped peak reminiscent of the cellular (sinusoidal-like) solutions. This is most striking at $j = 4$, which contains the most energetic modes and characteristic length l_m, but $j = 5$ also shows this behavior. Such distributions may be observed, for instance, for a particle moving in a double-well potential subject to random forcing, as we have found in preliminary simulations; and further analysis of these observed nonequilibrium PDFs, leading to a more detailed explanation or model for them, would be an interesting topic for future study. The wavelet coefficients thus appear to capture on average the spatially local structures and events at the active scales.

Small scales

The wavelet PDF for level $j = 6$ (Fig. 4.14) is again well fitted by a Gaussian; it is interesting that such an equilibrium distribution should appear well within the dissipative range, possibly via some balance between the energy fed in from adjacent active scales, and the dissipation. Indeed, computation of the Fourier global energy flux confirms that there is fairly significant energy transfer over the range of scales covered by $j = 6$.

At the smaller scales, $j \geq 7$, the effects of strong dissipation are apparent. The amplitudes of a_{jk} decay exponentially with j in this regime, while the distributions have super-Gaussian tails. That is, the small scale coefficients remain near zero most of the time, with occasional (intermittent) excursions of relatively large amplitude driven by events at larger scales; for instance, note the "event" beginning near $t = 256$ at level $j = 7$, one of several visible in Fig. 4.12, which appears to be driven by activity in levels $j = 5$ and 6, and entrains a similar, though smaller, excursion in an adjacent $j = 8$ wavelet.

One view of the small-scale PDF derives from the properties of the wavelets: if at the scale of the analyzing wavelet, the field u is locally linear, or more generally a low-order polynomial, then by the low-order moment cancellation property of these smooth wavelets [Dau92], the corresponding wavelet coefficient vanishes. Thus the small-scale wavelets will have non-negligible coefficients only where $u(x, \cdot)$ has large curvature, that is, where there is a peak or trough of the field u. That is, the small-scale dynamics tracks the positions of the "coherent structures".

Small-scale intermittency   The near-exponential PDF is also reminiscent of those observed for velocity increments and gradients, which signal intermittency in turbulence [Fri95]; good fits to such turbulent PDFs have been obtained in some models [Kra90, BBPVV91]. In fact, recalling that the wavelet transform at small scales acts as a high pass filter, our observed small-scale behavior is closely related to turbulent dissipation-range intermittency, seen when the velocity field is filtered at a frequency associated with a scale comparable to the Kolmogorov dissipation scale [Fri95]; Frisch and Morf [FM81] showed that infrequent bursts leading to intermittency are associated with singularities at complex times of time-analytic functions u (such functions include solutions of the KS equation [GK97]).

The analytical and numerical study of small-scale intermittency is an active research field; Frisch [Fri95] provides an introduction to some of the issues in the context of turbulence, while the Burgers equation with random forcing or random initial data is frequently investigated as a model problem. Since the small scales do not contribute significantly to the observed spatiotemporal chaos which is our primary interest (see Sec. 5.2.1), we do not discuss aspects of intermittency further in this thesis.

In summary, the wavelet decomposition clearly distinguishes among the dynamics of different

wavelet levels, separating large-scale randomness, small-scale intermittency, and distributions reminiscent of characteristic events (creation and annihilation of peaks, and traveling waves with a typical intermediate wavelength). We have provided heuristic justifications for these PDFs, and hope for a theoretical derivation of some of these results from the underlying KS equation.

4.2.5   Invariance under length variations

All the aforegoing results were presented for $L = 100$. In this Section, we show that, in the regime of complex spatiotemporal dynamics, this length is not special; in particular, the "large-L" statistics are well-converged for $L = 100$, and the separation among scales is maintained for larger L.

Wavelet and intrinsic length scales   To see the effect of varying L, we first need to understand the interplay between length scales of wavelet levels, and characteristic lengths of the dynamics (see also Sec. 4.3.3). The scales associated with the dyadic wavelet decomposition are $l_j = L2^{-j}$, the distance between the centers of adjacent wavelets at level j. Clearly, this length depends on L. The length scales of the internal KS dynamics, on the other hand, are L-independent for sufficiently large L; in particular, the typical wavelength of the cellular structures, corresponding to the peak of the power spectrum, is $l_m = 2\pi/q_m \approx 9.4$. Hence the particular distribution of energy between levels, and the corresponding wavelet coefficient PDFs at different j, depends on the particular relationship between the lengths l_j of the dyadic wavelet decomposition and l_m of the intrinsic dynamics.

Invariance under increased length L

The most straightforward consequence of the dyadic wavelet hierarchy relative to the internal dynamics, is that a change in the length by a power of two corresponds to a complete shift in the wavelet levels, in terms of the dynamics of the respective wavelet coefficients. Specifically, suppose $L' = 2^{j'}L$. Then the distance l_j between wavelets at level j for length L is $L2^{-j} = L'2^{-(j+j')} = l'_{j+j'}$. We thus expect similar dynamics and statistics at level $j + j'$ for $L' = 2^{j'}L$, compared to level j for L, which correspond to the same spatial scale; *if* the dynamics for length L is intrinsic.

This prediction is confirmed for the PDFs in Fig. 4.16, where we compare the wavelet level PDFs for $L = 100$ and $L' = 400$ ($j' = 2$) [EBH96]. Of course, the longer $L' = 400$ system (see Fig. 1.3) contains additional large scale levels 0 and 1 absent in the short system, which display slow (poorly equilibrated) Gaussian dynamics. At all other scales, though, the statistics are essentially identical. Compare also Fig. 4.13 for the same scale-invariance in the wavelet level correlation times τ_j. This confirms that $L = 100$ is clearly in the STC regime, and that the distribution of properties among different, separated wavelet levels is *intrinsic* to the KS equation.

Distributions for lengths $L' \neq 2^{j'}L$

A confirmation of the general validity of our PDF results for lengths other than dyadic multiples of $L = 100$ is given in Fig. 4.17, where lengths $L = 80$, $L = 100$ and $L = 128$ are compared. As the total length L decreases, the distance $2^{-j}L$ between wavelets at a given level j decreases, so that a given physical distance such as l_m, reflected in the intrinsic KS dynamics, corresponds to a lower j level. Thus as expected, compared to $L = 100$, for $L = 80$ the wavelet level energy distribution shifts towards lower j; and correspondingly, for $L = 128$ toward higher j (Fig. 4.17(a)). The wavelet coefficient PDFs at the different scales display a similar effect (Fig. 4.17(b)). While there is little change at large and smallest scales, we note the variation in the shapes of the PDFs at the active
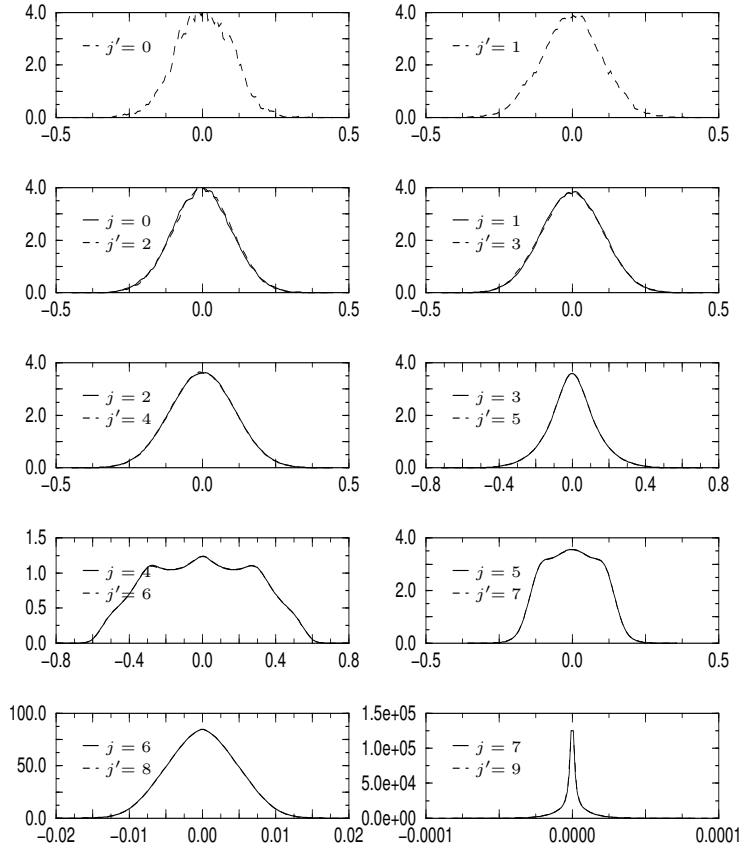
Figure 4.16: Comparison of PDFs for wavelet coefficients at level j for $L = 100$ with PDFs at level j' for $L' = 400$.

scales. That is, the details of the mixing among the behaviors at different scales is different, and thus produces different shapes of the PDFs. For instance, the $j = 4$ PDF for $L = 80$ appears to interpolate between the $L = 100$ PDFs for $j = 4$ and 5, as does the $j = 5$ PDF for $L = 128$.

In fact, $L = 100$ is a somewhat special case, in the sense that there is a marked peak in the energy distribution at $j = 4$; thus the characteristic behavior at the active scale is more pronounced. For L values at which two levels share the bulk of the energy more evenly, the PDFs are not quite as "clean". However, the general separation of scales, and distinction between the large, active and small scales is still clearly visible. It is plausible that there is a continuous distribution of density functions, interpolating between those shown, so that for each L, a discrete subset is selected.

4.3 Space localization

In the attempt to characterize homogeneous STC, much attention has been focussed on finding relevant measures of spatial localization (see [CH93, pp. 945ff] or [Gre98]), as part of the search for generally useful characteristics of the sustained complex dynamics of a nonequilibrium, spatially extended system, by analogy with the diagnostics that have proved useful in thermodynamics and

(a)

(b)
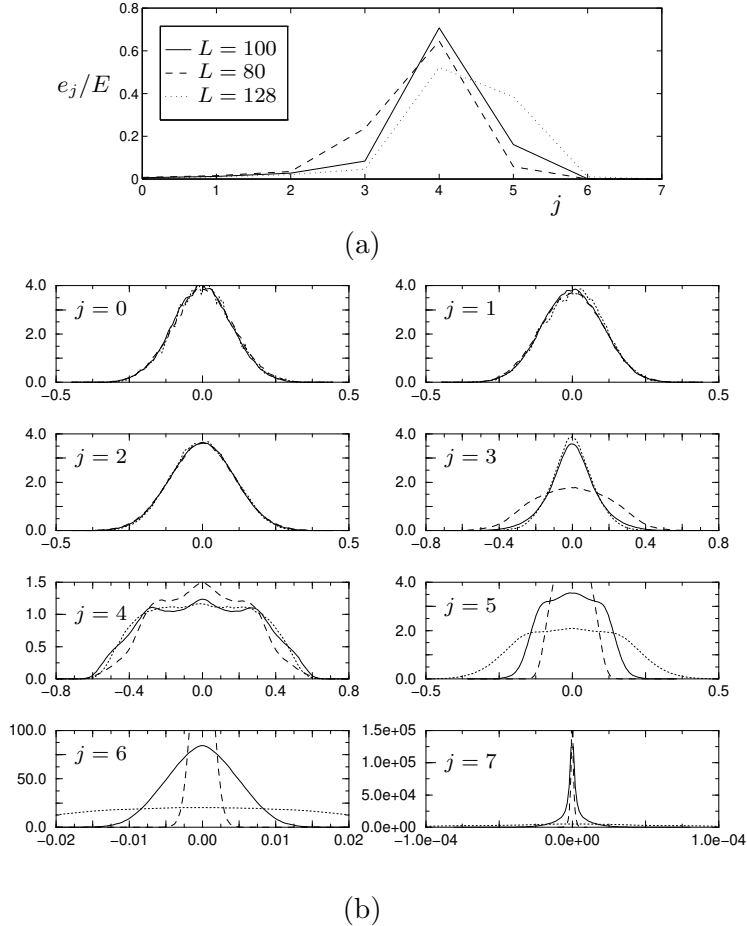
Figure 4.17: (a) Fraction of energy per wavelet level, for lengths $L = 100$, $L = 128$ and $L = 80$. (b) PDFs for wavelet coefficients for the same L values; we have retained the scaling of the axes appropriate to $L = 100$, for comparison with Figs. 4.14 and 4.16.

low-dimensional chaos; see Sec. 1.3. Heuristically, we may interpret localization as follows: in practice, we can capture the "correct" dynamics or statistics for the short time evolution of u at some x_0 by knowing only the instantaneous values of $u(x)$ for some interval $x \in [x_0 - l_c, x_0 + l_c]$, where l_c is a finite spatial interaction length, independent of system size L for large L. The existence of intrinsic correlation lengths is fundamental to the concept of "extensive chaos" and a thermodynamic limit—if interactions are spatially localized, then in the interpretation of the "very large" system in terms of coupled, sufficiently large subsystems, we do not expect "new" global collective effects to emerge as the number of these coupled subsystems increases as $L \to \infty$.

From the point of view of (instantaneous) dynamics, we are interested in the role of spatial localization in determining the "typical events" of Fig. 1.2, such as local stretching and compression of cells, and creation and annihilation of peaks (see Sec. 1.3.2). The goal of constructing low-dimensional models representing the dynamics of a few localized modes in a short system, would be unattainable in the absence of spatial localization; while a typical length scale would give an indication of the size of small system needed for successful modeling. Furthermore, of course, if dynamics are not locally determined, one would be unable to study an unbounded system numerically by replacement with a finite one with periodic or other boundary conditions.

For all these reasons, in this Section we study different length scales for the KS equation, both for better characterization of the STC state, and to guide the modeling of Ch. 6. Let us recall before continuing the basic length scale $l_0 = 2\pi\sqrt{2} \approx 8.886$, corresponding to the fastest growing mode.

4.3.1 Boundary conditions

For almost all of this thesis we consider the translationally invariant KS equation (1.1) with periodic boundary conditions. This ensures that the dynamics observed are *intrinsic* to the KS equation (hence expected to persist in the thermodynamic limit), and not driven or influenced by the boundary.

In the present context of spatial localization, however, one way of thinking about this is that bulk dynamics should be independent of boundary conditions. This gives rise to a boundary layer and finite size effects—frequently observed in experiments on patterning and complex dynamics—and the width l_b of the boundary layer gives an estimate of an interaction distance. Thus in this brief Section only, we consider the effects of fixed, non-periodic boundary conditions; in which case the behavior, at least near the walls, is strongly constrained by the boundary.

We have solved the KS equation with zero Dirichlet boundary conditions ($u = u_{xx} = 0$ at $x = 0, L$) and zero mixed (rigid) boundary conditions ($u = u_x = 0$ at $x = 0, L$); the finite difference numerical algorithms are given, with some more discussion, in App. B.1.3. As we see in Fig. 4.18 (compare Fig. 1.2), for sufficiently large L the characteristic spatiotemporally chaotic KS dynamics are observed in the bulk of the domain, sufficiently far from the boundaries—the system "forgets" its boundary conditions.

Mean spatial profile   The decay of boundary influences may be observed by visual inspection of space-time plots (Fig. 4.18(a,b)), as well as in other statistics. Of particular interest is the time-averaged profile $m(x) \stackrel{\text{def}}{=} \langle u(x, \cdot) \rangle_t$, shown in Fig. 4.18(c,d), which displays an ordered, inhomogeneous pattern with characteristic oscillations near the boundaries [Pum85, ZL85], similar to experimentally observed mean profiles (see the discussion and references in [EG94b, EAHGP98]). Note that $m(x)$, while breaking translational symmetry, still satisfies invariance under parity $u(x, t) \to -u(-x, t)$. Some other features of these averaged shapes have been discussed recently by Eguíluz *et al.* [EAHGP98] (for relatively small systems, for which the boundary influences have not fully decayed in the interior). A basic feature of these time-averaged patterns, and of other statistics, is that the spatial dependence is greatest near the boundary, with oscillations decaying in the interior (the internal oscillations observed in Fig. 1 of [ZL85] are due to imperfect averaging; compare Fig. 4.18(c)). The amplitude and shape of the mean spatial profile also appear to be invariant as the length L increases, confirming that the profile is a boundary effect, restricted to a boundary layer of width $l_b \sim 20$.

At this point, we make several related observations:

1. The length scale l_b, while depending on the KS dynamics, is also a function of the boundary conditions and is thus in principle independent of the intrinsic length scales l_c of the bulk, homogeneous dynamics discussed in the following Sections. In particular, the width l_b of the boundary layer varies with the amplitude of nonhomogeneous boundary conditions; this has been observed in unpublished computations of S. M. Zoldi.[†]

[†]Henry Greenside, personal communication.
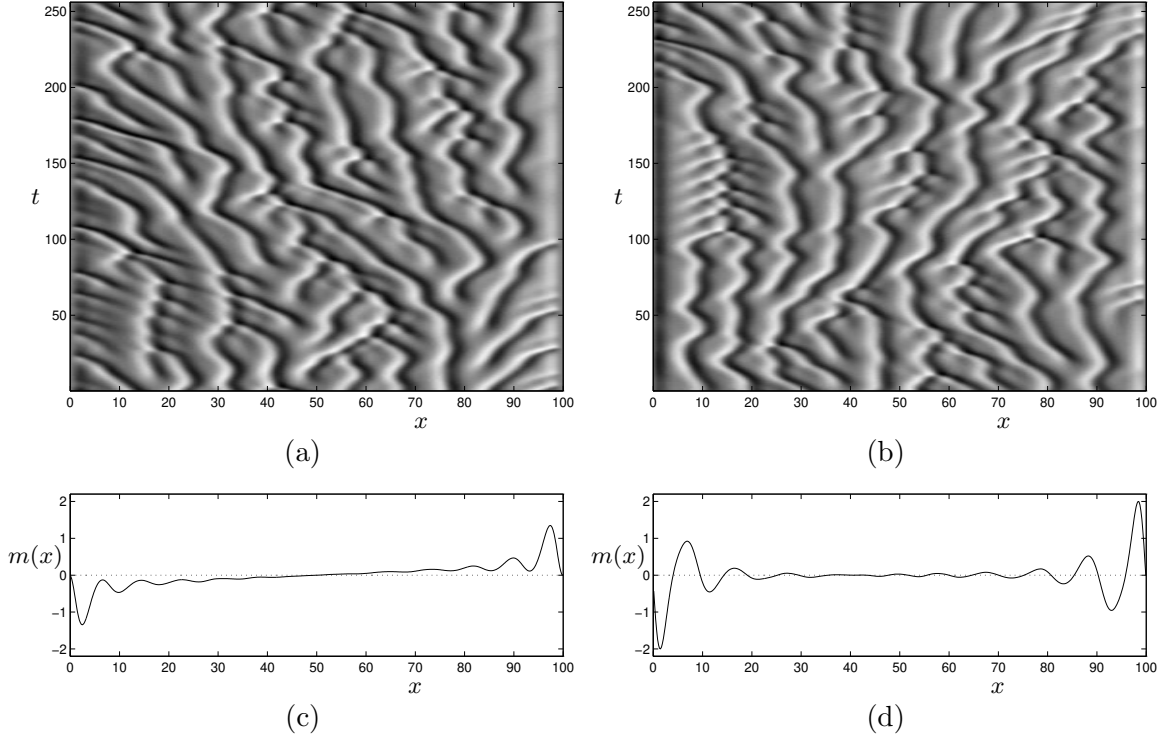
Figure 4.18: Effect of boundary condition variations: (a) Mixed (rigid) boundary conditions $u = u_x = 0$; (b) Dirichlet boundary conditions $u = u_{xx} = 0$; Time-averaged, space-dependent mean profiles $m(x) = \langle u(x, \cdot) \rangle$ for (c) mixed, (d) Dirichlet boundary conditions.

2. Zoldi and Greenside [ZG98] have computed many (unstable) periodic orbits for the KS equation with mixed boundary conditions, for a relatively small length $L = 50$. They find that for many of the periodic solutions, most of the time variation occurs away from the ends, and that an average over the orbits approximately reproduces the mean profile for a chaotic solution. The constraints imposed by the boundary layers are such that these results seem fairly unsurprising; especially if one interprets the spatiotemporally chaotic dynamics as sampling the attractor in phase space, moving from one unstable fixed or periodic solution to another and spending more time in the vicinity of the less unstable solutions, so that averages on the attractor can be computed via an appropriate weighting over unstable periodic orbits [AAC90, CCP97].

3. As already observed in [ZL85], for mixed boundary conditions $u = u_x = 0$ there is a slight overall tilt on the mean profile $m(x)$, or positive mean slope (corresponding to a parabolic profile for the mean front $\langle h(x) \rangle$). By the correspondence (1.9) between (local) mean and drift (see Sec. 1.2.1), this implies a net preferred drift to the left (negative x) for $x < L/2$, and to the right for $x > L/2$.

The presence of a boundary layer is apparent not only in the mean profile $m(x)$, but also in higher order statistics, such as the moments of pointwise distributions of $u(x, \cdot)$ as a function of distance from the boundary [Pum85]. It has been claimed [EG94b] that some averaged properties (in particular, a spatially-dependent correlation time $\tau_c(x)$) do not become homogeneous away from the boundary, which would contradict spatial localization. However, as discussed in detail in

102
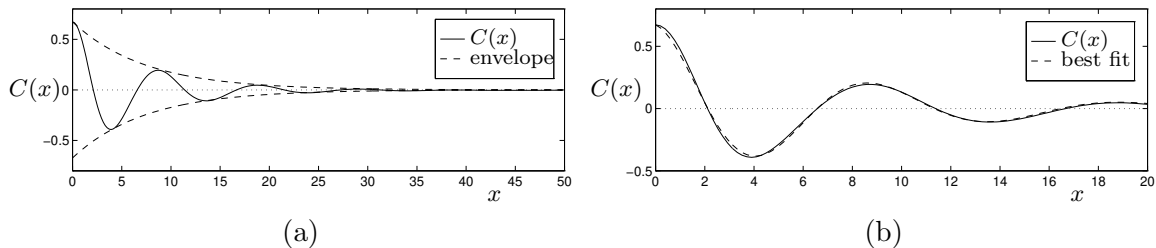
Figure 4.19: (a) Spatial autocorrelation function $C(x)$ for $L = 100$, with exponential envelope $C(0)\exp(-x/\xi_2)$. (b) Enlargement of (a), with best fit $C(0)\cos(q(x))\exp(-x/\xi_2)$, taking $q(x)$ to quadratic order.

Sec. 4.1.1 above, these published results are an artifact of insufficient averaging and of their method (4.1) used to define the correlation time τ_c, and a more careful study shows that $\tau_c(x)$ is indeed homogeneous in the bulk (with again a weak overall profile for mixed boundary conditions); see Fig. 4.5. Experiments with non-periodic boundary conditions thus confirm that the KS dynamics is spatially localized, with the influence of the boundary restricted to a region of finite width $\sim l_b$.

4.3.2 Correlation lengths

Returning to periodic boundary conditions, there are many possible choices for an appropriate correlation length for STC [CH93, Gre98], and it is not yet clear which are the most relevant. In this Section we discuss some of the candidate length scales for our system, before introducing an experiment designed to identify a *dynamic* interaction length. Any correlation length should, *a priori*, be constructed from the two lengths in our equation, the system length L and the most excited Fourier wavelength $l_0 = 2\pi/q_0$; and we expect that, through localization, correlation lengths are asymptotically independent of L.

Two-point correlation length

Two of the simplest length scales which measure spatial disorder and localization are the two-point correlation length ξ_2 and the mutual information correlation length ξ_I. We compute the spatial single-time autocorrelation function $C(x) = \langle u(x', \cdot)u(x'+x, \cdot)\rangle$ (independent of x' by spatial homogeneity) from the inverse Fourier transform of the power spectrum of Fig. 1.4, as mentioned in Sec. 4.1.2; its invariance under L variations follows from that of the power spectrum $S(q)$. As shown in Fig. 4.19, the correlation function is well modeled by the functional form $C(x) \approx C(0)\cos(q(x))\exp(-x/\xi_2)$, where to lowest order $q(x) \approx \tilde{q}x$, with $\tilde{q}$ near the peak of the power spectrum. The correlation function thus captures both the underlying oscillatory, cellular spatial structure of the KS dynamics, and the rapid spatial decorrelation reflecting the spatial disorder in the STC regime. An improved fit to $C(x)$ for reasonably small x, shown in Fig. 4.19(b), is given to quadratic order by $q(x) \approx 0.75x - 0.005x^2$; the resulting two-point correlation length is $\xi_2 \approx 7.4$. As measured by the two-point correlations, spatial coupling becomes negligible beyond a few multiples of ξ_2.

Mutual information length

The autocorrelation function $C(x)$ depends only on $\langle|\hat{u}_q|^2\rangle$, and as such is a linear measure of interactions; we might expect a quantity which depends nonlinearly on the dynamics to capture
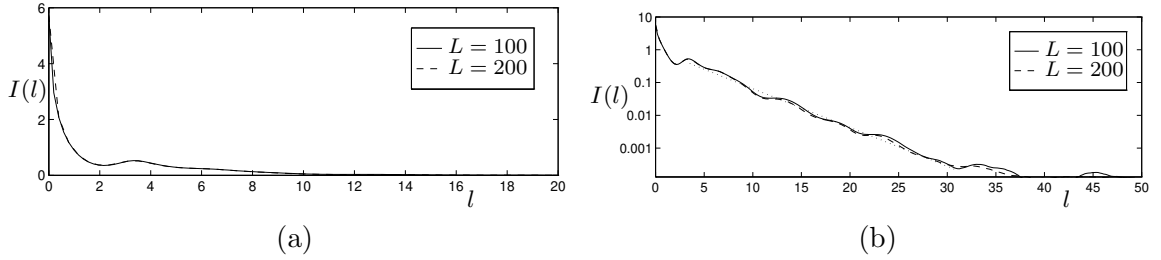
Figure 4.20: The mutual information $I(l)$, on linear and logarithmic axes; the dotted line in (b) is a fit to the $L = 200$ data, showing the exponential decay over a correlation length $\xi_I \approx 3.8$.

additional features [OEG96]. The independence of two spatial locations in the KS equation, or of two time series $s_1(t)$ and $s_2(t)$ more generally, may be quantified by the mutual information I [Pap84, Fra86], which measures the average amount of information about s_1 contained in s_2, or more specifically, the average reduction in the entropy of $s_1(\cdot)$, given knowledge of $s_2(\cdot)$. Given a discrete partition $\{S_i\}$ of the state space for $s_1(\cdot)$, with probabilities p_i, and similarly, probabilities q_i for $s_2(\cdot)$ and a joint probability distribution r_{ij} for s_1 and s_2, the mutual information may be estimated by

$$I(s_1(\cdot), s_2(\cdot)) = \sum_{i,j} r_{ij} \log_2 \frac{r_{ij}}{p_i q_j};$$ (4.22)

a similar definition holds for a continuous state space [Fra86]. In the context of chaotic dynamics, a mutual information correlation time was proposed by Fraser and Swinney [FS86, VS88, Fra89] as an optimal estimate for the choice of delay time for the reconstruction of attractors from time series.

For our application, to test the asymptotic independence of two spatial locations separated by l, we compute $I(l) \stackrel{\text{def}}{=} I(u(x, \cdot), u(x + l, \cdot))$ (averaged over x, by appeal to homogeneity). In this case, the distributions p_i of $u(x, \cdot)$ and q_i of $u(x + l, \cdot)$ are the same, and are just the single point distributions (*cf.* Fig. 4.1(a)); and simple binning seemed adequate to compute the joint distribution r_{ij}, so more sophisticated procedures [FS86, Fra89] were not employed. Note that when $s_1 = s_2$, the mutual information reduces to the single-point entropy, $I(0) = -\sum_i p_i \log_2 p_i$, while I vanishes if s_1 and s_2 are independent; that is, spatial localization implies that $I(l) \to 0$ as l becomes large.

The computed mutual information (independent of L) is shown in Fig. 4.20. Again, there is exponential decay, $I(l) \approx I(0) \exp(-l/\xi_I)$, where the mutual information correlation length $\xi_I \approx 3.8$. That is, the nonlinear correlations measured by the mutual information fall off more rapidly than the linear dependence captured by the autocorrelation function $C(x)$. The approximate relation $\xi_2 \approx 2\xi_I$ has been previously observed [OEG96] for the two-dimensional coupled map lattice Miller-Huse model [MH93].

Dimension density correlation length

As Greenside [Gre98] has pointed out, both ξ_2 and ξ_I may be unsatisfactory measures of STC, as they measure only spatial disorder, and are not dependent on time correlations of the spatial fields; changing the temporal ordering of the snapshots used to compute these correlation lengths would not affect $C(x)$ or $I(l)$. On dimensional grounds, a dimension correlation length ξ_δ has been proposed [CH93] as a more direct measure of dynamical complexity (see [Gre98]).

On the basis of computations for the KS equation with *mixed* boundary conditions $u = u_x = 0$

(see Sec. 4.3.1 above) for $L = 50$, 100, 200 and 400, Manneville [Man85] estimated that the number of non-negative Lyapunov exponents $N_{\geq}$ grows according to $N_{\geq} \approx L/7.63 - 1.30$. Finding the spectrum of Lyapunov exponents and using the Kaplan-Yorke formula, he estimated the fractal (Kaplan-Yorke, or Lyapunov) dimension as (see [CH93, p.951])[†]

$$D_F \approx L/4.35 - 2.70. \tag{4.23}$$

Similar results for the homogeneous KS equation, with periodic boundary conditions, have not been reported; but if (as argued in Sec. 4.3.1 above) the bulk dynamics are indeed independent of boundary conditions, then the fixed boundary values contribute only the additive term in (4.23) above, and $D_F \approx L/4.35$ for periodic boundary conditions. Thus we have the numerical observation for the KS equation and some other mathematical models (not yet supported by rigorous estimates in general) that the fractal dimension D_F of the STC attractor is extensive; that is, $D_F \propto L$. Motivated by this result, Cross and Hohenberg [CH93, p.945] have proposed extensivity of D_F as a general defining feature of STC.

This suggests the definition of a length by the inverse dimension density: $\xi_\delta \stackrel{\text{def}}{=} \lim_{L \to \infty} L/D_F(L)$ (alternatively, one could use the density of positive Lyapunov exponents). The relationship between ξ_δ and other correlation lengths ξ_2 and ξ_I has been discussed in the context of phase transitions in the Ginzburg-Landau [EG94a, EG95] and Miller-Huse [OEG96] models. For the KS equation, from Manneville's results (4.23) [Man85] we find $\xi_\delta \approx 4.35$. Note however that a quantity such as ξ_δ defined on purely dimensional considerations, does not unambiguously imply a characteristic physical length. Moreover, the definition of ξ_δ depends on extensivity and spatial localization, and thus does not provide independent support for these concepts.

Karhunen-Loève correlation length

Since a fractal dimension for a high-dimensional system is generally very difficult to compute, Zoldi and Greenside [ZG97] have proposed replacing D_F by a Karhunen-Loève (or POD) dimension $D_{\text{KLD}}(f)$, defined by the number of eigenmodes in the proper orthogonal decomposition (see Sec. 1.4) required to capture a given fraction f of the total energy; and have consequently defined a Karhunen-Loève correlation length ξ_{KLD}. This has a strongly nonlinear dependence on the fraction f, however, so that it is not quantitatively well-defined and has no direct physical meaning in the absence of an *a priori* choice for f.

For a nonhomogeneous system, this approach can speed up the computation of a dimension correlation length, and verify the presence of extensive chaos, by calculating ξ_{KLD} for small subsystems of various sizes [ZG97]. However, for a translationally invariant system such as the *periodic* KS equation (1.1), the Karhunen-Loève eigenmodes are Fourier modes ([HLB96]; see Sec. 1.4.1), so that ξ_{KLD} for any f can be computed directly from the power spectrum $S(q)$ of Fig. 1.4.

Computation of ξ_{KLD} from the power spectrum   The simplest way to see this is to construct the (symmetric-decreasing) rearrangement [LL96] of $S(q)$, normalized to have unit integral, $s^*(q) \stackrel{\text{def}}{=}$

[†]A quick count of the number of unstable modes indicates that the unstable manifold of the trivial zero solution for periodic boundary conditions has dimension $2(L/2\pi) > L/4.35$, which appears to contradict (4.23). It may be that the dynamical trajectories in the STC regime used in the numerical computation of the Lyapunov spectrum do not pass near all unstable equilibria, in particular, near the zero state. More generally, a candidate definition suggested by finite-dimensional dynamical systems theory [GH83], is that an attractor is a set containing, *inter alia*, all steady and periodic solutions and their unstable manifolds. Such a definition of "attractor" may be inappropriate for our extended system, if the invariant measure of the dynamics in the STC regime is supported on a set of lower dimension.
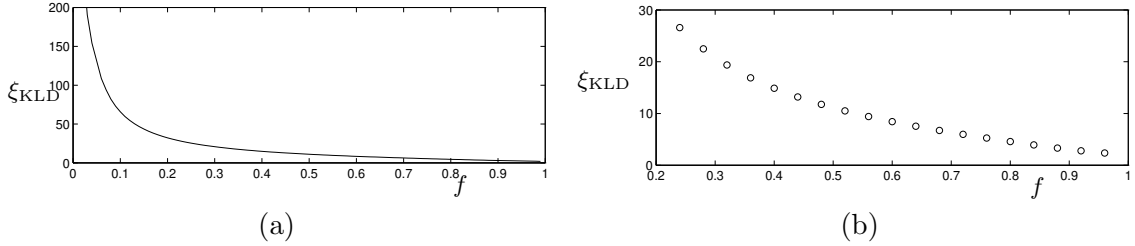
Figure 4.21: (a) KLD correlation length ξ_{KLD} as a function of fraction f, computed from the power spectrum $S(q)$ via (4.24). (b) Blowup of (a); compare with [ZG97, Fig. 2].

$S^*(q)/\int_0^\infty S(q)\,dq$. For finite L (discrete Fourier modes) this just corresponds to rearranging the modes in order of decreasing energy. Next, find q_* so that

$$\int_0^{q_*} s^*(q)\,dq = f;$$

that is, invert the indefinite integral $I^*(q') \stackrel{\text{def}}{=} \int_0^{q'} s^*(q)\,dq$, so that $q_* = (I^*)^{-1}(f)$. For finite length L, with Fourier modes discretely spaced at intervals $2\pi/L$, the POD dimension is then just the number of modes with wave number $\leq q_*$, that is, $D_{\text{KLD}}(f) = \lfloor 2q_*L/2\pi \rfloor$ (the extra factor of 2 arises because Fourier modes are complex); and the dimension density is the corresponding number of modes per unit length, well-defined in the extensive limit. The correlation length (inverse dimension density) is then immediately

$$\xi_{\text{KLD}} = \lim_{L\to\infty} \frac{L}{D_{\text{KLD}}} = \frac{\pi}{q_*}. \tag{4.24}$$

Fig. 4.21 shows the result of computing ξ_{KLD} for the KS equation via (4.24); compare Fig. 4.21(b) with Fig. 2 of [ZG97], obtained by a more complicated calculation requiring the extraction, ordering and counting of POD eigenmodes. The strongly nonlinear dependence of ξ_{KLD} on f is apparent; we find $\xi_{\text{KLD}} \approx 12.23$ for $f = 0.5$. Note that since ξ_{KLD} is computed using nothing more than the invariant power spectrum $S(q)$, it contains no more dynamical information than ξ_2.

Correlation lengths: Averaged and instantaneous   We have thus demonstrated spatial localization of the spatiotemporally chaotic KS dynamics, through the calculation of various correlation lengths. The lengths discussed are all statistical averages, however, and might not capture short-time or rare events. Moreover (with the possible exception of ξ_δ), they are measures only of spatial disorder, without capturing any information on the temporally complex dynamics responsible for the disorder. In order to investigate the local nature of *instantaneous* spatiotemporal dynamics, we now propose an experiment to test the range of influences relevant to the short-time interactions—with the hope of gaining understanding of the "microscopic" basis of STC, and to aid in the construction of models. To do so, we manipulate instantaneous couplings by solving the KS equation on a localized wavelet basis.

4.3.3   A dynamical interaction distance: An experiment

In Sec. 4.2, the wavelet decomposition of $u(x,t)$ was used to study scale and space localization through the temporal dynamics and distributions of wavelet coefficients $a_\alpha(t)$. For these calculations, we needed only perform a wavelet decomposition on solutions obtained from pseudospectral

and finite difference integrations of the KS equation, thereby using the wavelet formalism purely for data analysis. We now exploit the narrow spatial support of wavelets to investigate spatial localization of the KS dynamics more directly, and in doing so, make explicit use of the wavelet Galerkin projection of the KS equation (3.19).

Motivation: Exploiting wavelet localization

We first summarize the relevant facts from Ch. 3, where much more background and motivation for these experiments is given. The linear part of the wavelet Galerkin projection (3.19) is not diagonal, in contrast to the Fourier representation (1.5), as there is overlap of wavelets both within a scale and across scales. However, due to the scale and space localization of the wavelet basis, this overlap is limited. For instance, $l_{\alpha\alpha'} = l_{jk\,j'k'}$ couples wavelets at scales j and j'; but due to the power law decrease of ψ in Fourier space, this decays with the scale separation $|j - j'|$. More importantly for the present purpose, since each wavelet ψ_α is centered at a position x_α, we can define a distance between the centers of wavelets, $d_{\alpha\alpha'} \stackrel{\text{def}}{=} |x_\alpha - x_{\alpha'}|$; for wavelets at the same level, $d_{jk\,jk'} = L2^{-j}|k - k'|$. The linear term $l_{\alpha\alpha'}$ thus measures the overlap between wavelets (and their derivatives) centered a distance $d_{\alpha\alpha'}$ apart. Due to the spatial exponential decay of $\psi(x)$, this quantity falls off exponentially from the diagonal [EBH96, BEH92]; similarly for the nonlinear term $n_{\alpha\alpha'\alpha''}$. That is, the evolution of a particular wavelet coefficient is affected primarily by those modes $a_{\alpha'}$ for which $(l_{\alpha\alpha'} + \sum_{\alpha''} n_{\alpha\alpha'\alpha''} a_{\alpha''}) a_{\alpha'}$ is appreciable: those centered near a_α in space.

We may use these considerations to manipulate the KS dynamics and probe spatial localization. Since the coefficients $l_{\alpha\alpha'}$ and $n_{\alpha\alpha'\alpha''}$ in the Galerkin projection represent coupling between wavelets localized a distance $d_{\alpha\alpha'}$ or $d_{\alpha\alpha''}$ apart, we can cut all interactions beyond a certain length l_c by setting the corresponding coefficients to zero, leading to a localized model

$$\dot{a}_\alpha = \sum_{\alpha'} \tilde{l}_{\alpha\alpha'} a_{\alpha'} + \sum_{\alpha',\alpha''} \tilde{n}_{\alpha\alpha'\alpha''} a_{\alpha'} a_{\alpha''}, \tag{4.25}$$

where $\tilde{l}_{\alpha\alpha'} = l_{\alpha\alpha'}$ if $d_{\alpha\alpha'} \leq l_c$, $\tilde{l}_{\alpha\alpha'} = 0$ otherwise, and similarly for the nonlinear term; see (B.45). This allows us to quantify the *instantaneous* dynamical significance of the interaction length l_c. Note that, as discussed in more detail in Sec. 3.2.2, a few related experiments have been described in [BEH92, EBH93], though the motivation for these was slightly different.

Computational aspects   The algorithms used for these calculations are outlined in App. B.2.2, where we emphasize their computational cost: In contrast to the rapid finite difference and Fourier pseudospectral schemes (see App. B.1, B.2.1), the wavelet Galerkin method for (4.25) on N modes requires $\mathcal{O}(N^3)$ steps (and the storage of the N^3 terms of $n_{\alpha\alpha'\alpha''}$), while an enhancement using the fast wavelet transform still requires $\mathcal{O}(N^2 \log_2 N)$ computations per time step. A consequence of this is that long-time calculations, for a range of values of l_c, are prohibitively expensive; whereas for short times, we cannot hope to obtain well-converged statistics for many of the quantities discussed in Secs. 4.1–4.2.

We performed over 50 computations to time $t_{\max} \approx 1000$ with a range of interaction lengths l_c, for several different initial conditions and systems lengths L. Since the dynamics are so sensitive to initial conditions, we would need to perform many runs with different initial data for each set of parameter values to obtain conclusive results; thus our experiments should be regarded as preliminary.

Experimental observations

In general, we find that if l_c is large enough, we recover the essential KS dynamics, while small l_c results in significant disruption: a departure from the typical events, and changes in space and time scales, and in the form of the coherent structures observed. Among the features seen when the interaction length is sufficiently reduced are break-up into apparently independent subdomains, the presence of localized peaks, and fast local traveling pulses colliding with the peaks. As discussed in more detail in Sec. 5.4, such rapidly traveling dynamics are associated with excessive large-scale energy, due to variations in the local mean; see also Secs. 1.2.1 and 2.3.3.

Indeed, we find that frequently there is an energy buildup at large scales, which are disproportionately excited relative to the full KS equation. This large-scale excitation often results in a rapid, spatially localized transfer of energy to the small scales, leading to numerical blowup; with decreasing l_c such blowup becomes more likely and typically occurs sooner. To counteract such rapid transfer across scales, we have also performed some experiments in which we cut couplings across more than 3 wavelet scales, that is, for $|j - j'| > 3$; this measure seems to prevent or delay numerical blowup. The disruption does not decrease monotonically with increasing l_c: we also encountered some relatively large values of l_c for which there was an unusual likelihood of blowup, or capture into a steady state; this is reminiscent of a "resonance" effect encountered when solving the KS equation on short length subdomains [DHBE96].

Some representative results for system length $L = 100$ and different coupling lengths l_c are shown in Fig. 4.22. Observe that $l_c = L/2 = 50$ is the maximum distance between two points in an $L = 100$ periodic system, and thus corresponds to retaining all interactions; thus we have confirmed that our $l_c = 50$ wavelet calculation (not shown) reproduces the full KS dynamics. Figure 4.22(a) shows that for large enough l_c, we retain the characteristic KS dynamics (see Fig. 1.2). As we decrease l_c, many typical features remain, but the dynamics become increasingly disrupted, with rigid peaks, traveling pulses and excitation of the large scales (Figs. 4.22(b,c)). Numerical blowup becomes increasingly likely for sufficiently small l_c (Fig. 4.22(d)).

The conclusions of visual inspections are supported by the energy distributions across wavelet levels (Fig. 4.23), for the same values of l_c, compared to the spectrum for the full KS equation (Fig. 4.11). As l_c decreases, the energy shifts increasingly to larger scales (lower j). In this light, we can consider a (phenomenological) measure of the extent of disruption of the dynamics, the energy transfer to large scales. Specifically, in Fig. 4.24(a) we plot e_2/e_4, where $j = 4$ is the most active wavelet level for the full KS equation.

These results and others lead us to estimate a typical interaction length $\bar{l}_c$, beyond which cutting interactions significantly disrupts the KS dynamics; from Fig. 4.24, this is $\bar{l}_c \approx 25$. We interpret this length so that for $l_c > \bar{l}_c$, we typically obtain characteristic KS dynamics, improving as l_c approaches $L/2$, while the dynamics are increasingly disrupted as l_c decreases below $\bar{l}_c$. To our knowledge, this is the first attempt to quantify the *dynamical* significance of a coupling distance, in terms of its effect on the temporal evolution.

Dyadic wavelet hierarchy and length variations We note that the effect of cutting interactions is strongly dependent on the dyadic structure of the wavelet decomposition (Sec. 3.1.2). That is, which modes interact for a given l_c depends discontinuously on l_c. For instance, for $L = 100$, $l_c \geq 25$, adjacent wavelets at level $j = 2$ are coupled, while they cease to interact for $l_c < 25$. This experiment is therefore a rather crude measure of interaction length, since it depends on the decomposition as well as the dynamics.

To confirm that l_c is indeed a relevant interaction length, we performed some experiments for

(a) : $l_c = 30$
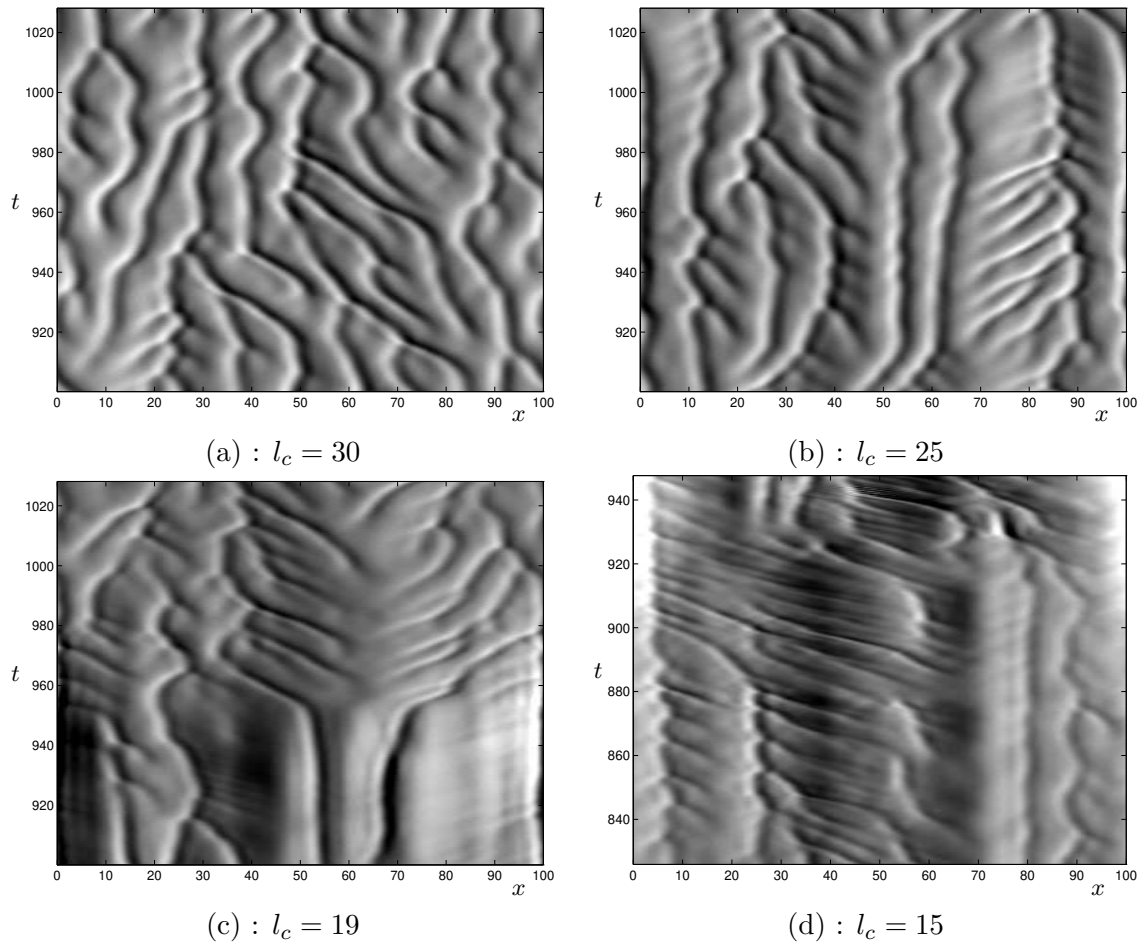
(b) : $l_c = 25$

(c) : $l_c = 19$

(d) : $l_c = 15$

Figure 4.22: Modified KS equation (4.25), coupling only wavelets nearer than l_c apart, for $L = 100$, and $N = 127$ wavelets; note the increasing disruption of KS dynamics as l_c decreases: (a) $l_c = 30$; (b) $l_c = 25$; (c) $l_c = 19$; (d) $l_c = 15$, shown just before the blowup at $t \approx 950$. Note: vertical scales are expanded in comparison with Fig. 1.2.
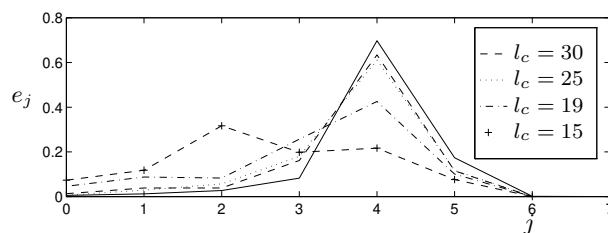
Figure 4.23: Wavelet energy distributions, for $L = 100$ and coupling lengths l_c as in Fig. 4.22; the solid line is the distribution for the full KS equation (or $l_c = 50$), from Fig. 4.11.

109
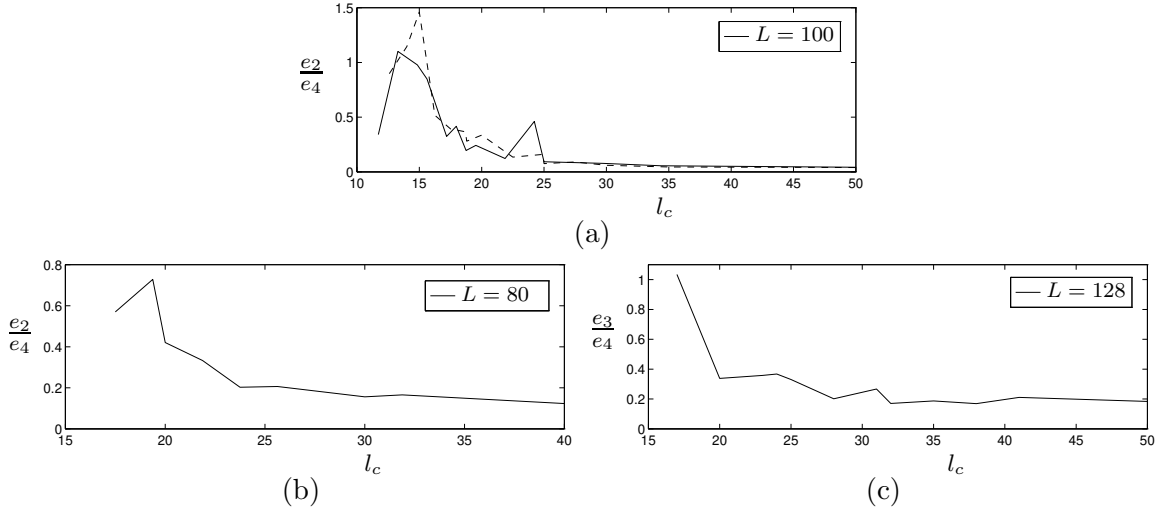
Figure 4.24: Energy ratio, a diagnostic for energy transfer as a function of interaction length l_c: (a) e_2/e_4 for $L = 100$: computations for two different initial conditions; (b) e_2/e_4 for $L = 80$; (c) e_3/e_4 for $L = 128$. The ratios appear to settle down to their asymptotic values for $l_c \geq \bar{l}_c \approx 25$. The data exclude computations for which blowup occurred before $t = 128$.

$L = 200$ (recall that this effectively corresponds to a shift by one wavelet level; see Sec. 4.2.5): even though many more wavelet interactions are cut, the results for a given l_c agree with those for $L = 100$. Similarly, we repeated the calculations for $L = 80$ and $L = 128$, which have a different relationship of intrinsic length to the dyadic decomposition, and we confirmed that although the distribution of energy among the wavelet levels influences the experimental results, $\bar{l}_c \approx 25$ still appears to be a relevant interaction length; see Figs. 4.24(b,c), and compare with the discussion in Sec. 4.2.5.

Some comments

- The interaction distance we have defined measures the distance between the *centers* of wavelets. Due to the significant non-compact support of $\psi(x)$, the value of $\bar{l}_c$ is only an approximation to the spatial range of interactions: there may be appreciable overlap between wavelets centered more than l_c apart. For this reason, the wavelet approach only yields a fairly rough estimate of spatial localization. However, the wavelets we use are exponentially localized in x, so the effect of noncompact wavelets is limited.

- The dynamical interaction distance $\bar{l}_c$ estimated by this technique, appears to be considerably larger than the mutual information distance $\xi_I \approx 3.8$, or the autocorrelation distance $\xi_2 \approx 7.4$. These other lengths are obtained from time averaging over the dynamics. The result $\bar{l}_c > \xi_I$, for instance, may indicate that the dynamics is strongly influenced by rare events which couple relatively distant spatial locations (separated by more than one cell). Thus, statistically averaged lengths such as ξ_I may be underestimates of the dynamically relevant coupling distance; *the asymptotic mutual statistical independence of two points is insufficient to imply their instantaneous dynamical independence.*

- This work also helps us to understand the transition to STC in the KS equation: For $L \leq 2\bar{l}_c \approx 50$, spatial locations are "doubly" coupled (due to periodicity); that is, for a given x_0

and interaction distance $l \leq \bar{l}_c$, x_0 is coupled to $x_0 + l$ and $x_0 - l$ (mod L), which could be the same point. Small systems are thus excessively constrained through their interactions, and consequently solutions frequently approach a "simple" attractor. For systems of length greater than about 50 or 60, on the other hand, x_0 is asymptotically and dynamically independent of $x_0 \pm L/2$, there are fewer constraints, and the system can sustain STC behavior.

In this Chapter, we have thus confirmed and extended some known statistics, and contributed new results, especially related to the wavelet decomposition; together, these conclusively demonstrate the local nature of spatiotemporal chaos, at least with respect to the dynamics of the KS equation. These results are used in the next two Chapters to design and interpret numerous experiments. In Ch. 5, we refine our understanding of scale localization by deducing, not only statistics, but the contributions of the different scales to the overall dynamics. The following Ch. 6 uses those results as a basis for the development and study of spatially localized models. Concerning such models, the experiments on the spatial localization of instantaneous interactions indicate that in a successful low-dimensional "short" model for the KS dynamics, wavelets should be coupled, either to other modes or to external forcing, up to at least a distance $\sim \bar{l}_c$, to ensure sufficient interactions.

Chapter 5

Scale-by-scale Structure of the Dynamics

In Ch. 3 we described the wavelet decomposition, and some facts about the KS equation projected on a wavelet basis. We analyzed the statistics at different wavelet levels in Ch. 4, and found remarkable distinctions between the coefficient distributions and temporal behaviors at the different levels; while suggestive, however, these statistics do not directly reveal the *dynamical relevance* of the different scales.

In this Chapter, we obtain a detailed understanding of the spatiotemporally chaotic dynamics viewed as arising from interactions of distinct and complementary contributions of different scales. We elucidate the respective functions of the different scales through a wide range of experiments, in which we actively intervene in the system, manipulating different wavelet levels by forcing, eliminating or otherwise modifying them, and observe the results. In particular, whereas in [EBH96] a major theme was the influence of the active scales on the large scales, we shall here be mainly concerned with the effect of the large scales on the active scales—after ascertaining that the small scales are essentially dynamically insignificant. The major results of the central Sections are summarized in Secs. 5.2.4, 5.3.3 and 5.4.3.

5.1 Experimental parameters and initial conditions

In this Chapter there is no spatial localization; all "horizontal" interactions in the wavelet pyramid are included. The set of internal modes $\mathbf{B}$ for the models almost always contains complete wavelet levels, and is often defined by a large-scale cutoff j_l and a small-scale cutoff j_s; the indices of the resolved modes are then given by

$$\mathbf{B} = \{(j,k) \,|\, j_l \leq j \leq j_s\}.$$

For some experiments, we study the dynamics of a non-contiguous set of modes, so the above representation for $\mathbf{B}$ does not apply.

To facilitate comparison of different computations (especially short-time comparison, or "tracking"; *cf.* [DHBE96]), in the face of the intrinsic chaotic dynamics, we maintain the same parameters and initial data for most of the numerical experiments. We summarize these data below.

Parameters Unless otherwise specified, the simulations of this and the next chapter have been performed for $L = 100$. In addition to the advantage of consistency enabling ready comparison

of results, there are several reasons for this choice, which we may infer from the statistical results of Ch. 4: For this length, the wavelet energy distribution is strongly peaked at level $j = 4$ (see Fig. 4.11), so that the active scales are readily isolated. The experiments on localization of Sec. 4.3.3 indicate that $\bar{l}_c \approx 25$ is a typical interaction distance, and hence we might expect length $\bar{L} = 25$ to be a good candidate length for a local model which retains sufficient internal interactions (see Ch. 6); $L = 100$ contains four $\bar{L} = 25$ subsystems (here L refers to the length of the full system, from which a subsystem of length $\bar{L}$ is cut). The KS equation for $L = 100$ also has several wavelet levels, 0, 1 and 2, with noisy Gaussian behavior (see Fig. 4.14)—enough that we can separate these from the active scales to study their relevance for the dynamics, and their role in driving the smaller scales.

Smaller total lengths L will have fewer large scales with dynamics well-separated from the active scales; once we go to L below about 50, the dynamics frequently approaches and, for most L values, is attracted to a "simple" low-dimensional state such as those described in Sec. 1.2.3. On the other hand, one does not gain much by going to L values significantly larger than $L = 100$, since the main effect is to add more levels of slow noise at the large scales; the additional subsystems of length $\bar{L}$ will be effectively independent.

In contrast to the computations of Sec. 4.3.3, in the runs of this and the next Chapter we do not explicitly enforce an interaction distance. Consequently, since we do not have to compute the vector field for each wavelet coefficient separately, we can use the fast wavelet integrator described in App. B.2.2. A typical time step used is $\delta t = 1/32 = 0.03125$ (compare Figs. 5.1(b)(iii) and 5.12(a,b)(i) below to see the effects of changing δt), we retain solutions separated usually by $\Delta t = 0.5$ (that is, every 16th time step), and spatial reconstruction is performed on 256 points, that is, with $\delta x = 100/256$. Most computations have been performed on 7 wavelet levels, $j = 0 \ldots 6 = J$, that is, with $2^{J+1} - 1 = 127$ wavelets; this corresponds to $q_{\max} \approx 2$; the difference between this choice and $J = 7$ is discussed in Sec. 5.2.1. For these parameters, an integration of the KS equation to $t = 256$ with post-processing, computing various relevant statistics as in Sec. 4.1, typically takes between 2 and 3 minutes on a 150 MHz Silicon Graphics workstation. Variations from these integration parameters are noted as necessary.

Initial conditions and reference computations

We rely mainly on two sets of initial conditions, both obtained as the final states of (different) integrations of the KS equation; that is, both corresponding to solutions essentially on the attractor. These initial conditions, which we shall denote by **a** and **b**, are shown in Fig. 5.1(i,ii), in wavelet coefficient and real space. Fig. 5.1(iii) shows space-time plots obtained by integrating these two initial conditions, with the above integration parameters, to time $t = 256$. In these plots, as in all others in this Chapter, the gray-scale is uniformly set for the range $|u(x, t)| \leq 3.5$ (see Fig. 5.2(d)); where white represents the most positive values, $u = +3.5$, and black the most negative values. Fig. 5.2 shows the wavelet energy distribution, the power spectrum, and the PDF for u, for both initial conditions **a** and **b**, obtained from the computation to $t = 4096$, to confirm that the wavelet computations indeed give (statistically) accurate solutions of the KS equation, when compared to the real space and Fourier results reported in Sec. 4.1. In fact, the results are compared in Fig. 5.2(a)–(c) to a longer-time Fourier integration, and in (d) to a real space integration of Section 4.1. Note that the energy in the small scales is significantly too low in the wavelet computation; this may be due to some form of aliasing, but is probably related to inaccurate computation of the spatial derivatives (especially u_{xxxx}) at the highest wavelet levels, as discussed briefly in App. B.2.2. Since the energies in the large and active scales are captured faithfully, we will not be too concerned with this discrepancy.
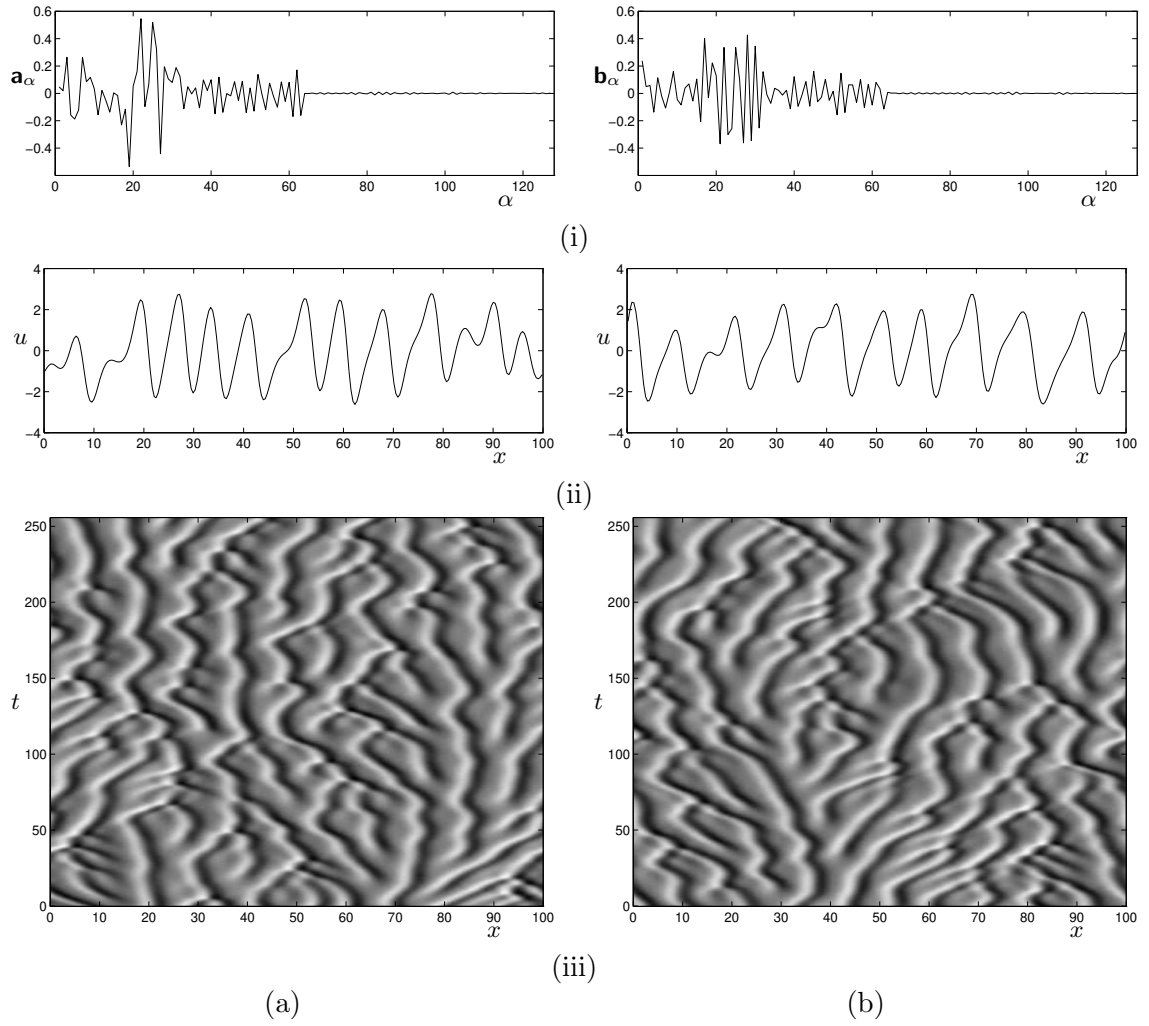
Figure 5.1: Reference computations: Initial conditions (a) **a**, (b) **b**; plotted in (i) wavelet space, and (ii) real space, for the reference computations. (iii) Space-time plot of integration to $t = 256$.
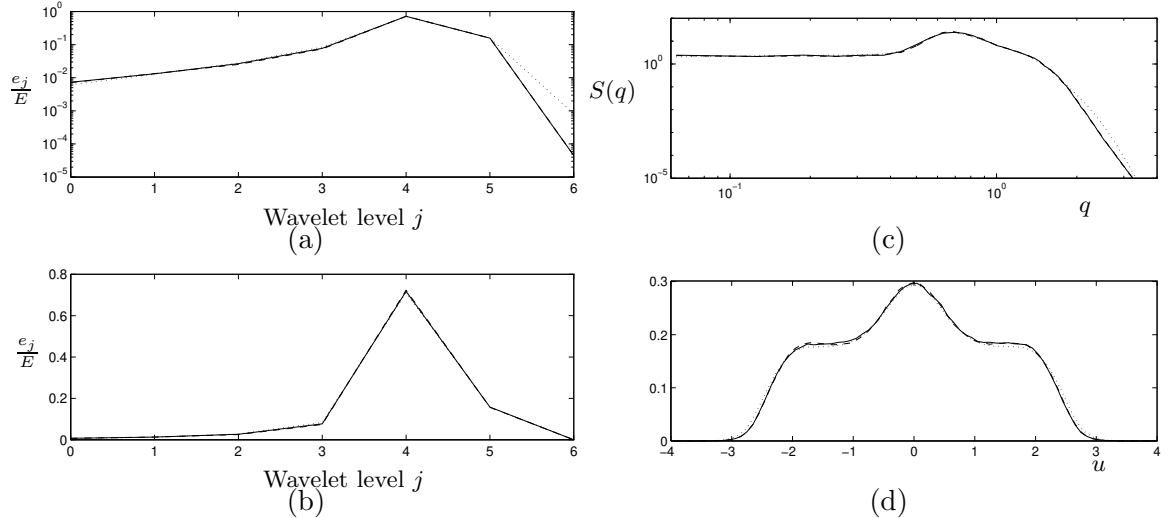
Figure 5.2: Comparison of statistics of reference wavelet computations, to $t = 4096$, with the results of Section 4.1; in each case, the statistics from initial data **a** (solid line) and **b** (dashed line) are essentially indistinguishable in the figures. (a), (b) Fraction of energy per wavelet level, on a linear and logarithmic scale, compared with a Fourier computation (dotted); see Figure 4.11. (c) Power spectrum, compared with Fourier computation; see Figure 1.4. (d) PDF for u, compared with a real space (finite difference) computation; see Figure 4.1(a).

We will use the computations shown in Fig. 5.1 for comparison for most of the experiments reported in this chapter. Typically, we will use the initial conditions **a** for our model computations; that is, for the resolved modes a_α, where $\alpha \in \mathbf{B}$ is in some subset of the full index set $\mathbf{A}$, we use $a_\alpha(0) = \mathbf{a}_\alpha$. We need to model the excluded modes $b_{\alpha'}$, $\alpha' \notin \mathbf{B}$ somehow. Sometimes these modes are set to zero or a constant, to undergo sinusoidal oscillations, or to be specified by the autonomous stochastic process of Sec. 4.2.3. Otherwise we shall frequently take the $b_{\alpha'}$ from an independent simulation of the KS equation (3.19), denoted the *reference* or *control run*, in which case we usually take $b_{\alpha'}(0) = \mathbf{b}_{\alpha'}$, that is, the $b_{\alpha'}(t)$ are the wavelet coefficients corresponding to the right-hand solution of Fig. 5.1.

Summary of experimental approach

Let us clarify how we perform the numerical experiments, integrating for the resolved modes a_α satisfying (3.25): We first compute the forcing (external) coefficients $b_{\alpha'}$, integrating, if necessary, a full KS equation. To perform a single time step of the model, we do not substitute the $b_{\alpha'}$ into the Galerkin projection (3.25), and integrate that system of M equations, which would be an $\mathcal{O}(N^2 M)$ algorithm, where $N = |\mathbf{A}|$ is the total number of wavelets, and $M = |\mathbf{B}|$ is the number of internal modes in the model. Rather, we take a full set of coefficients for $\alpha \in \mathbf{A}$, and at each time step overwrite the excluded coefficients $a_{\alpha'}$, $\alpha' \in \mathbf{A} \setminus \mathbf{B}$ by the forcing modes $b_{\alpha'}$. We then perform a time step for the full KS equation, using the wavelet pseudospectral algorithm of App. B.2.2, in $\mathcal{O}(N \log_2 N)$ steps. This gives us the new values of the resolved modes a_α.[†] The combination

---

[†]The integration also provides new values for the unresolved coefficients $a_{\alpha'}$, which are for our purposes meaningless and are at the next time step replaced by the updated $b_{\alpha'}$. Strictly speaking, we do not need to update the $a_{\alpha'}$ values for the model. However, eliminating this would not change the order of the integration algorithm, but would provide only a small speed-up in its efficiency. The advantage of the current approach is that we can use the same

of full pseudospectral KS time-stepping and replacement of coefficients at each time step, yields a method which is both computationally efficient, and straightforward to code and adapt for the different experiments.

We are aware of only one other study that uses a similar approach to the understanding of spatiotemporally complex dynamics, introducing various types of perturbations and carrying out numerical experiments to test the system's response by comparison with a control run. This is the recent investigation of the two-dimensional incompressible Navier-Stokes equations by Browning, Henshaw and Kreiss [BHK98]. They performed a direct numerical simulation of freely evolving turbulent flow in a periodic box, and studied the interaction between large and small scales by modifying the system in various ways, including changing the viscosity or the nature of the viscous operator, adding noise to small scales and testing whether low modes determine the high modes.

Browning *et al.* [BHK98] also used our method of overwriting modal coefficients at each time step; however, they performed their control run first, saved the time series of coefficients, and then reused those coefficients for each of their experiments. In our investigation, which was initially performed independently of theirs, we repeatedly recompute the forcing coefficients, which may seem inefficient. However, our computations are sufficiently fast (in contrast to their two-dimensional Navier-Stokes simulations) that the relatively small additional time investment is more than compensated for by increased flexibility, being able to change initial conditions, integration parameters or the length of computation "on the fly" without needing to recompute and save a modified control run each time.

5.2 Omitting scales

When we studied the spatial localization of KS dynamics in the previous chapter, a key set of experiments (Sec. 4.3.3) involved cutting spatial interactions in order to discern a spatial coupling length. In an analogous fashion, the first ingredient towards investigating the dynamical effects of different scales, involves removing particular scales from the system, and observing the changes in the dynamics.

5.2.1 Small scales

We first report on the small scales—in order to justify their exclusion. Fig. 5.3(a) shows a simulation, with initial conditions **a**, in which we omit the small-scale level $j = 6$. (As a reminder, for the implementation, we integrate the full KS equation for $j = 0$–6, on 127 modes, and set all the $a_{6\,k}$ to zero after every time step.) The qualitative dynamics look indistinguishable from those of a full KS simulation, and in fact, the short-time tracking is good as well: compare Fig. 5.1(a)(iii), and note how close the space-time plots are until about $t = 40$, but that, for instance, the peak beginning at $t = 0$, $x \approx 60$ deviates completely.

To the accuracy of these experiments, the statistics agree almost entirely with those from the full KS simulations, except that there is no energy in wavelet level $j = 6$ and in the corresponding regions of the Fourier power spectrum. This indicates very little backward influence from the small scales to the larger scales; compare also Fig. 5.34 and the corresponding discussion below. Indeed, the absence of meaningful small-scale effects, in a statistical sense, accounts for the previously discussed fact that, while the full wavelet pseudospectral integrator on 127 modes fails to treat

---

time-stepping scheme for the full KS equation and for the model, instead of having to design a new integrator for each experiment. In our approach, the only coding modification needed for each experiment is the choice of which modes to replace at each time step.

(a)   (b)
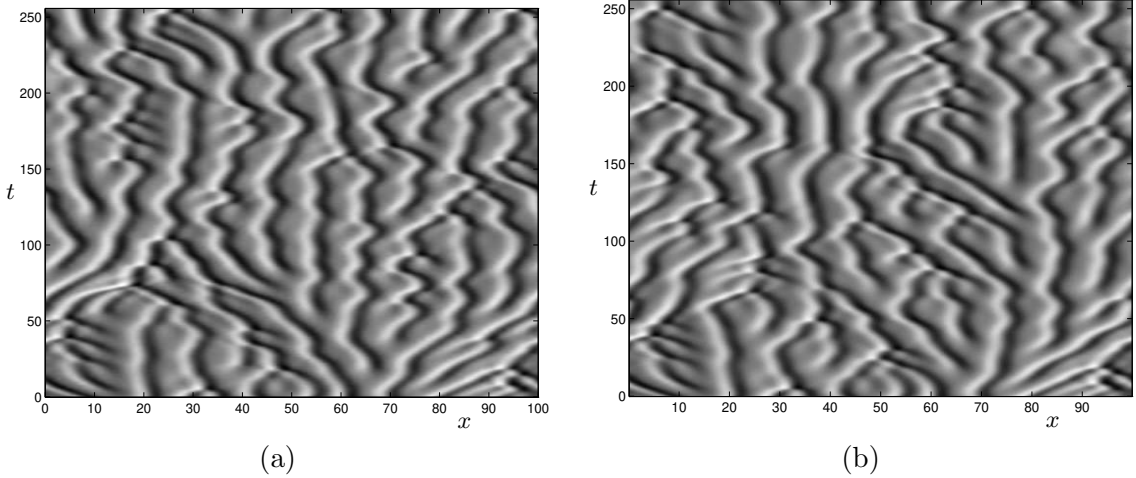
Figure 5.3: The negligible dynamical effects of small scales, displayed by experiments omitting them; compare Fig. 5.1(a)(iii): (a) **a**, setting level $j = 6$ to zero. (b) KS integration on 255 modes, including level $j = 7$.

level $j = 6$ accurately (see Fig. 5.2(a)), the energies, power spectra and PDFs for the large and active scales are all sufficiently accurate, and this scheme meets our need for a fast, adequate wavelet integrator. However, *tracking* only occurs for a finite time; the presence or absence of small scales (introducing small perturbations) influences the detailed dynamics, as one might reasonably expect in a system displaying sensitive dependence on initial conditions. That is, there is some small information transfer from small scales to large scales, inducing perturbations that eventually grow to yield $\mathcal{O}(1)$ deviations from the reference simulation, as also observed in [BHK98].

As a further check on the importance of small scales, we have integrated the KS equation, with initial conditions **a**, with an additional wavelet level; that is, on 255 wavelet modes, with $J = 7$ and $q_{\max} \approx 4$ (Fig. 5.3(b)). There is again little qualitative distinction from Fig. 5.1(a)(iii), and tracking is very good to $t \approx 90$. Comparison of Fig. 5.1(b)(iii) with a $J = 7$ computation on 255 modes and initial conditions **b** demonstrates similar tracking. Including one extra wavelet level in the simulations, while improving faithfulness to the "correct" solution (which we cannot hope to attain for long times due to the inherent instability of the chaotic dynamics) yields no significant benefits in terms of noticeably improved large- or active-scale statistics, and for reasons of computational speed, we have restricted ourselves to 127 wavelet modes, that is, $J = 6$, for the remainder of this Chapter.

For the purposes of obtaining low-dimensional models, the small scales, slaved to the active modes, are best represented as a graph over the modes retained in the model, using a center-unstable manifold or (approximate) inertial manifold reduction. However, since setting modes at levels 6 and higher to zero has so little effect, and such a reduction would be computationally expensive, we choose just to omit these levels when later constructing low-dimensional models. For the experiments discussed in the remainder of this Chapter, we retain the highest level $j = 6$, in the knowledge that omitting it would affect our results at best marginally.

Active scales: essential to dynamics and energy transfer

Whereas the linear term in the KS equation (1.1) pumps energy into the large scales and damps the small scales, the nonlinear term provides energy transfer between scales. If the field u is split

117

into low and high modes, $u = u^< + u^>$ (see Sec. 5.3.1 below), then heuristically, we expect the energy to be transferred from the low to the high modes largely via an interaction such as $u_t^> = \ldots + \mathcal{P}^> \mathcal{B}(u^<, u^<)$. In this thesis we have not explicitly studied the energy transfer mechanisms of the KS equation, but we are able to infer some of their features from our experiments.

Since small-scale levels $j \geq 6$ clearly feed back little information to the larger scales, their major influence in acting as an energy sink must be in receiving energy through nonlinear interactions *between* active-scale modes, rather than through interactions of the form $\mathcal{B}(u^<, u^>)$ between active and small scales. The important levels for the dissipation of energy are the active levels 4 and 5. This is readily demonstrated by experiments in which levels $j = 4$ and/or $j = 5$ are set to zero (not shown here); such simulations rapidly blow up, diverging to infinity in finite time. The energy build-up in the large-scale, linearly unstable modes cannot be dissipated through nonlinear interactions with the active modes, and the modal amplitudes grow exponentially up to the threshold imposed for numerical divergence. Computations of the scale-by-scale energy flux confirm that the maximal flux is at the active scales, verifying their essential role in the nonlinear energy transfer mechanism.

5.2.2 Large scales

Let us now consider the effects of the large scales, in particular, $j = 0$, 1 and 2. Recalling the results of Sec. 4.2.2, the Gaussian PDFs at these scales suggest that their influence is largely to contribute slow, large-scale noise, possibly to keep the dynamics "stirred up", without being essential to the detailed dynamics at the active scales. This idea, for which we shall find considerable supporting evidence, is basic to much of this and the next Chapter.

Successively omitting the largest scales   Fig. 5.4 shows the results of experiments in which the largest scales are successively "turned off", from excluding level 0 in (a) (which means, simply, $a_{00} \equiv 0$), to omitting the four largest-scale levels in (d); this implies successively increasing the large-scale cutoff j_l from 1 to 4. Omitting the largest scale clearly has minimal influence on the overall dynamics; there is little to distinguish Fig. 5.4(a) from a full KS simulation, although there is no tracking.

Leaving out $j = 0$ and 1 also seems to matter little; the generation, annihilation through collision, and dynamic behavior of the "coherent structures" appear to proceed unhindered in the absence of the largest two scales. However, the structures seem more "rigid" than usual; the mean-square velocity of the peaks has decreased, that is, there are fewer peaks traveling rapidly through the domain, observable as diagonal lines in the gray-scale space-time plots. Furthermore, statistics computed for a longer-time simulation, to $t = 4096$, reveal some differences from the full KS equation (Fig. 5.5).[†] While confirming that in this simulation there is indeed no energy in levels

---

[†]To compare our models with the full KS equation (1.1) using measures beyond mere visual inspection of space-time plots, we use the format of Fig. 5.5 repeatedly throughout this and the next Chapter for consistency of presentation and ease of use. Together with a gray-scale space-time plot and a typical spatial cross-section, we have chosen the quantities from Ch. 4 that seem most fundamental and important: namely the total energy of the model E_m and power spectrum, wavelet energy distribution, PDFs of values of u and of the wavelet coefficients at levels $j = 4$ and $j = 5$, and the width-at-half-maximum autocorrelation time τ_c (4.2); see also the caption to Fig. 5.5. Our statistics are obtained for integrations to a final time $t = 4096$, chosen to make the computation of statistics for a large number of distinct experiments feasible. This computation time is some orders of magnitude higher than the characteristic time scale of the dynamics $\tau \sim \mathcal{O}(10)$, but is too short to obtain well-converged statistics (as is most apparent from the $j = 4$ PDFs) and is much shorter than that used for the statistical characterization of the full KS equation in Ch. 4. However, while error bars should be expected to be fairly large, we feel that the integration times are sufficiently long to give an accurate qualitative indication of trends in the distributions, energies and correlation times of our models, relative to the full KS equation.

(a)

(b)

(c)

(d)
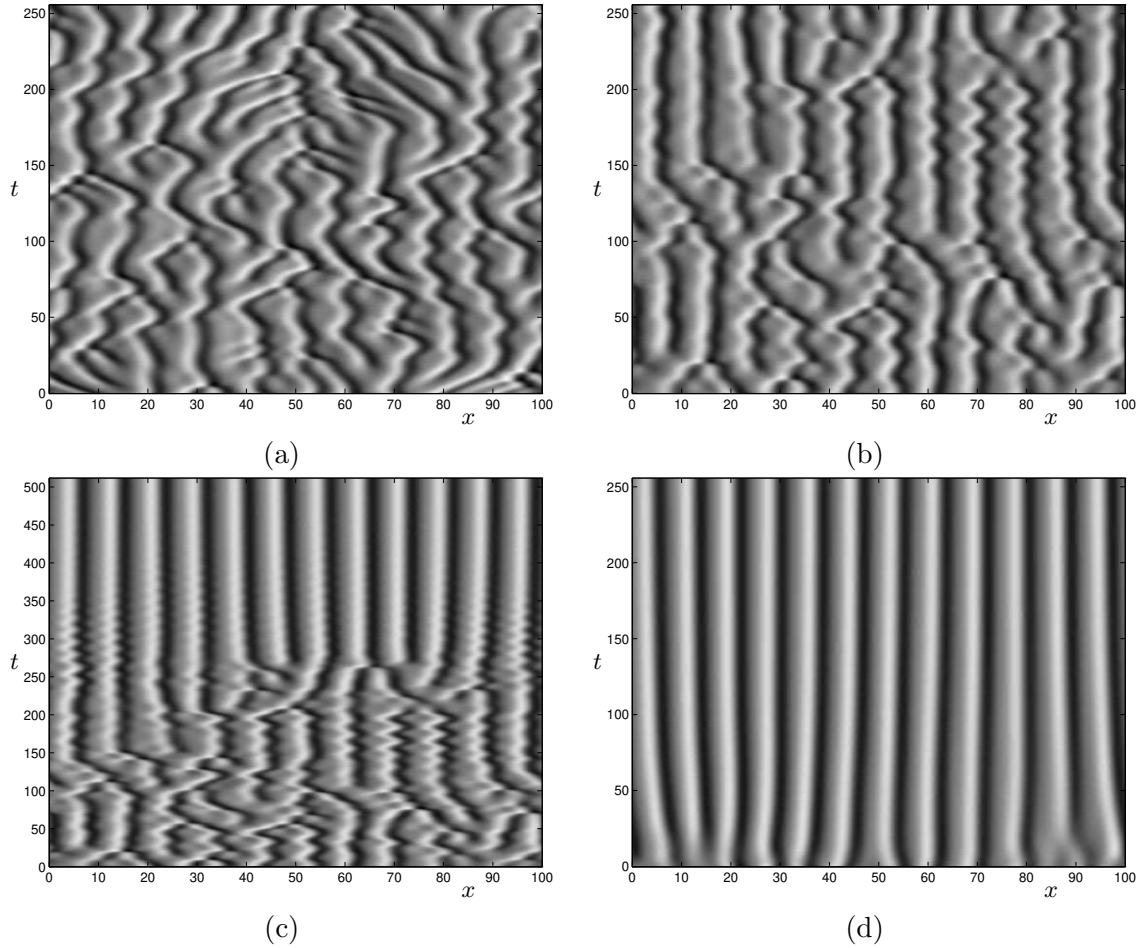
Figure 5.4: Setting successively more large-scale wavelet levels to zero. Levels eliminated: (a) $j = 0$; (b) $j = 0$ and 1; (c) $j = 0$, 1 and 2 (note the change of time scale); (d) $j = 0$–3.

0 and 1, the statistics indicate enhanced energy in level 4, and a slightly shifted distribution of u, and of wavelet coefficients $a_{4\,k}$ and $a_{5\,k}$, towards higher values, relative to the KS equation. This indicates that the attractor, while still dynamically active, is closer to a cellular state than the KS equation; and that the largest scales contribute to maintaining the disorder and keeping the system away from a pure cellular state.[†]

Returning to Fig. 5.4, we see from (c) (showing a longer time run, to $t = 512$) that in the absence of $j = 0$, 1 *and* 2, there is some (transient) dynamical activity, including cell creation and annihilation, though with rapid temporal oscillations and somewhat more rigidity than before. Eventually, however, the solution settles down to a stationary cellular state; in the absence of these largest scales, there is insufficient "excitation" to keep the dynamics "alive". Based on this experiment, the result of the following one, shown in Fig. 5.4(d), is predictable: when levels $j = 0$–3 are set to zero, removing all large-scale perturbations, the system settles down to a stationary cellular state very rapidly.

[†]In this Chapter, the *cellular state* refers to a state of or approaching rigid or stationary rolls, reminiscent of that seen for some small L values (Sec. 1.2.3 and Fig. 1.1(a)) or for small ε^2 (Fig. 2.3(a)).
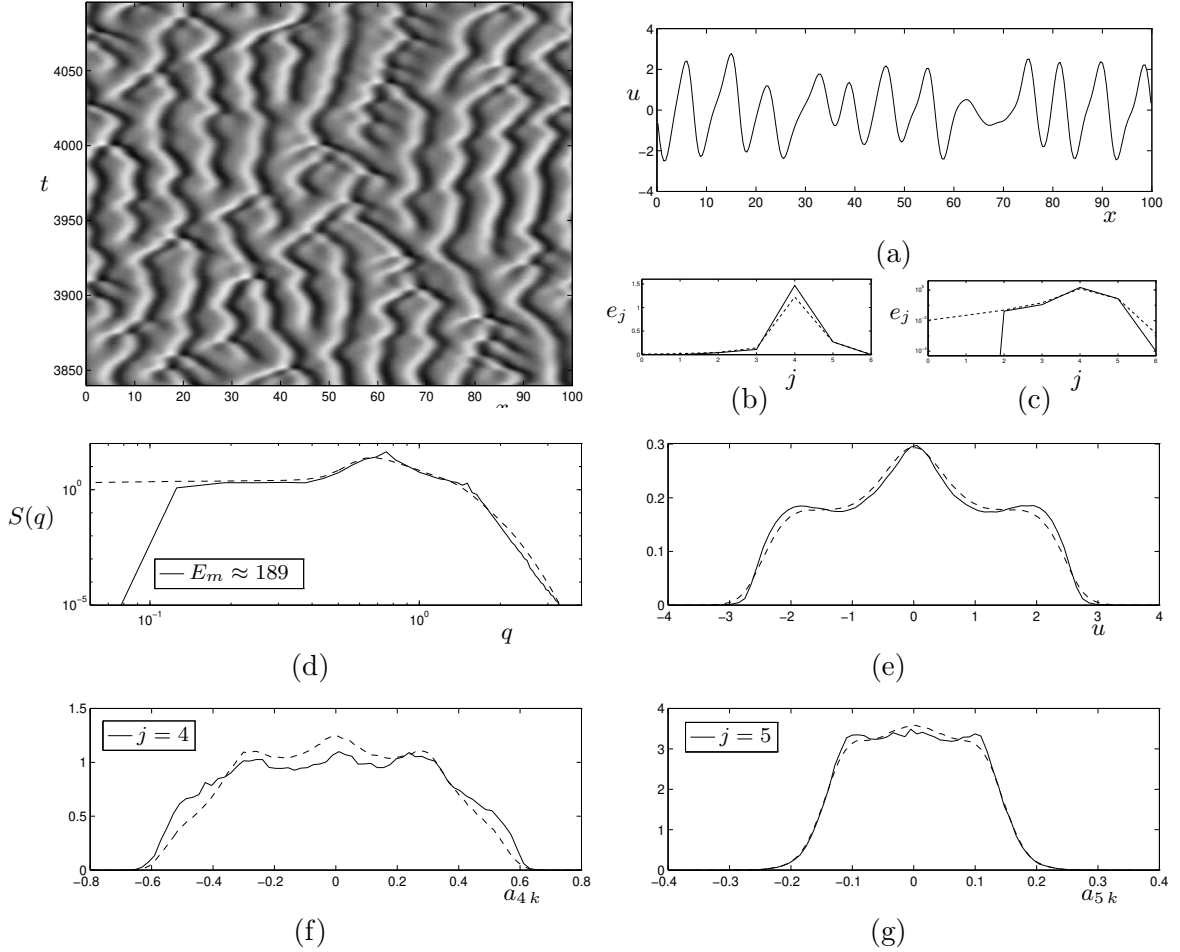
Figure 5.5: Comparison of model statistics with full KS equation: Eliminating levels $j = 0$ and 1. "Long-time" runs to compute statistics are performed to $t = 4096$, and compared, in (b)–(g), with well-averaged results for the KS equation on $L = 100$, as described in Ch. 4; full KS results are shown with dashed lines, and comparisons are with a Fourier-based integration, except with a finite difference integration in (e)). For detailed comparisons, we retain this format throughout this and the next Chapter, for consistency. Top left: space-time plot, for the last interval of length $t = 256$ of our model computation. (a) Spatial cross-section at $t = 4096$. (b), (c) Total energy per wavelet level, on linear and logarithmic axes. (d) Power spectrum, and total model energy E_m (KS equation: $E \approx 173$). (e) PDF of u. (f), (g) PDFs of wavelet coefficients, for the active wavelet levels $j = 4$ and 5. The width-at-half-maximum autocorrelation time for this model is $\tau_c \approx 13$ (KS equation: $\tau_c \approx 10$).

Figure 5.6: Comparison of model statistics with full KS equation: Eliminating level $j = 2$. See caption of Fig. 5.5 for description. Autocorrelation time $\tau_c \approx 12$.

Eliminating level 2 It might seem, from these results, that it is the function of level $j = 2$ to maintain the disorder, and that $j = 0$ and 1 are effectively redundant for this purpose. That this is not the case is shown in Fig. 5.6, in which we present a simulation with level 2 set to zero, and the corresponding long-time statistics. Clearly, in the absence of $j = 2$ modes, levels 0 and 1 can assume the function of maintaining disorder. In this simulation, the PDFs again imply that the attractor is slightly closer to a cellular state than the reference KS system, although with different characteristics; this system seems to display more local traveling wave structures, with fewer collisions and births of peaks.

It appears that both levels 0 and 1 are required for this continuing disorder; that level 1 by itself, freely evolving within the model, is insufficient is suggested by a simulation (not shown) with levels 0 and 2 set to zero. This system displays KS-like dynamics for a long time, beyond $t = 1000$, but eventually, by $t = 4000$, settles down to a state of weak irregular oscillations about a cellular-like state, driven by low-amplitude noisy dynamics at level 1. We will discuss later the somewhat similar effects of retaining just level 0, and eliminating levels 1 and 2.

In summary, a good heuristic description of the effect of the Gaussian noise due to the large scales seems to be given by a thermodynamic analogy: The driving noise acts as a "heat bath", keeping the system at a "finite temperature" with persistent disorder, while the cellular state

is akin to a "zero temperature" state. We further confirm this picture in Sec. 5.5.2, where the deterministic large scales of the KS equation are replaced by a Gaussian stochastic process, and in our model for driven short systems in Sec. 6.3. A more quantitative formulation of such an analogy to thermodynamics or statistical mechanics would possibly be of interest (see [HS89]).

5.2.3   The role of level $j = 3$

For the KS equation with $L = 100$, we have tended to include the wavelet level $j = 3$ among the active, energetic scales—see Secs. 4.2.1 and 4.2.4. However, the contribution of this, linearly unstable, level is somewhat different from those of $j = 4$ and 5. It contains a lower fraction of the total energy than those levels, and whereas the PDFs of the wavelet coefficients $a_{4\,k}$ and $a_{5\,k}$ are broad and reminiscent of the cellular state, the PDFs of the $a_{3\,k}$ are more strongly peaked at zero than a Gaussian (positive kurtosis). This suggests that the dynamic influence of level $j = 3$ has less to do with the cellular state and characteristic spatial structure than with fostering a tendency to drive u and the wavelet coefficients towards zero. That this level, in contrast to the other active levels 4 and 5, is not an essential component of the nonlinear energy transfer mechanism which ensures the dissipativity of the KS dynamics is seen in Fig. 5.4(d); the energy remains finite in the absence of level 3.

Level $j = 3$ thus appears to play a different dynamical role than both the large scales $j = 0$–2, which supply Gaussian excitation to prevent the system from settling down, and the most active scales $j = 4$–5, which are crucial for facilitating the nonlinear energy transfer, and which "live" at the scale of and construct the characteristic spatial structure. As before, we probe the dynamical significance of level 3, testing the expectations outlined above, by eliminating it from the system; our experiment is summarized in Fig. 5.7.

Maintenance of typical "events"   As is clear from the simulation, in the absence of level 3, most of the typical dynamical interactions of coherent structures are eliminated; few creation and collision events remain (see Sec. 1.3.2). Instead, the characteristic separation of peaks is more pronounced, and the dynamics are dominated by local traveling wave structures, as groups of a few approximately evenly spaced peaks move together. The relative enhancement of cellular structures is indicated by the marked increase in energy at level 4 (Fig. 5.7(b)), and the shift of the u distribution toward large amplitudes at the expense of remaining near zero (Fig. 5.7(e)). The most striking statistical effect of removing level 3 is in the wavelet PDFs for levels 4 and 5, shown in Figs. 5.7(f) and (g). The peak in the distribution at zero has disappeared, in favor of a significant enhancement at the wings. While the overall amplitudes of u and wavelet coefficients remain unchanged, the absence of level 3 results in a marked shift in the distributions toward the larger values characteristic of the cellular state. We may thus deduce the function of level $j = 3$ to be related to a tendency to drive the dynamics near zero, and to maintain the local events, the creation and annihilation of defects, characteristic of the spatiotemporally chaotic regime (Sec. 1.3.2).

Eliminating levels 2 and 3   The above conclusions are confirmed by an experiment in which both levels 2 and 3 are set to zero; see Fig. 5.8, which should be compared with the two previous experiments. While the largest scales $j = 0$ and 1 still provide enough excitation to keep the system from settling down into a steady or periodic state, we essentially have a cellular state with few defects, driven by the large scales to move about irregularly with little change in shape. Note in Fig. 5.8 that the peak contours appear smoother than in the presence of level 2 (Fig. 5.7). This is straightforwardly understood, since dynamics at level 2 are considerably faster than at the larger
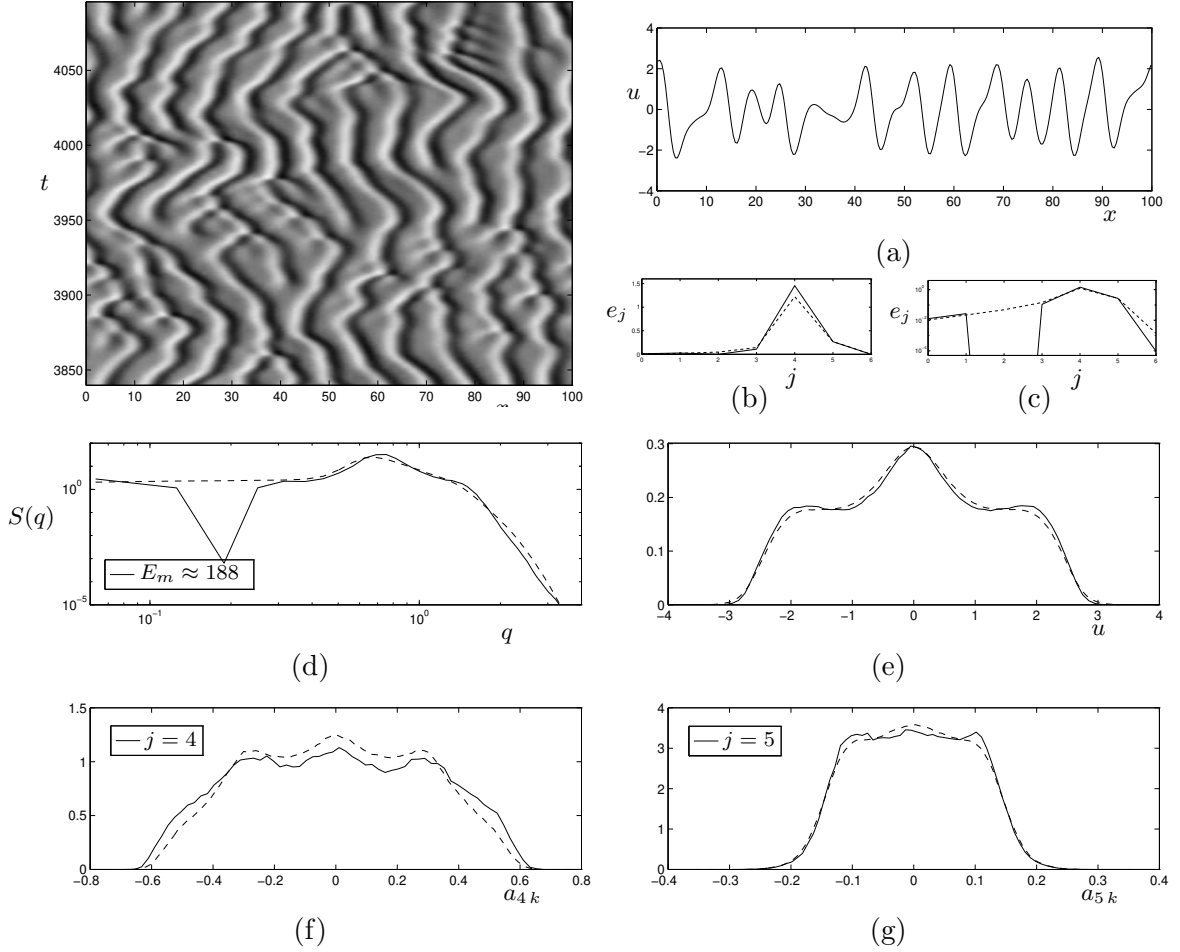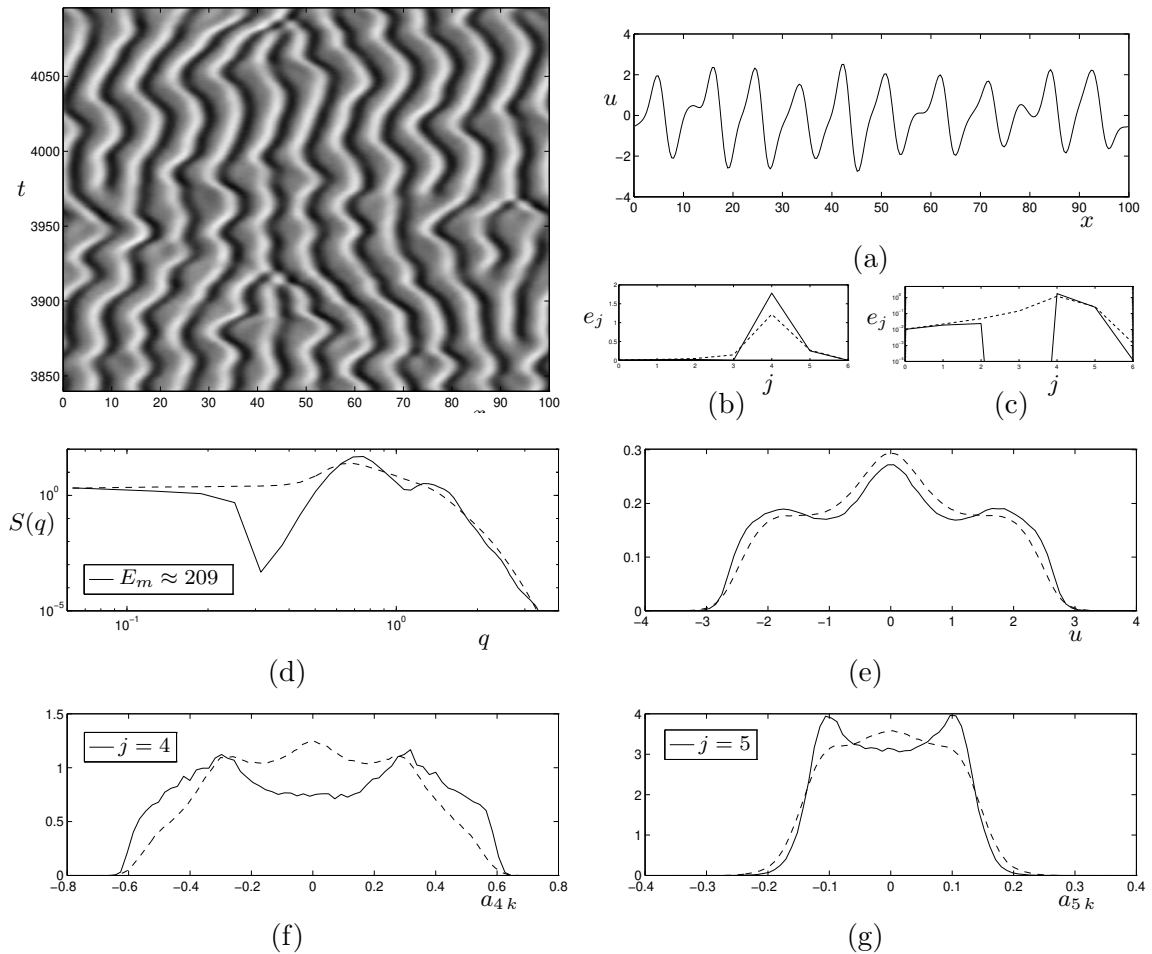
Figure 5.7: Comparison of model statistics with full KS equation: Eliminating level $j = 3$. See caption of Fig. 5.5 for description. Autocorrelation time $\tau_c \approx 14$.

scales $j = 0$ and 1 (see Fig. 4.13 and Table 4.1) and thus tend to roughen the space-time plot. Looking at the distributions, we see that the PDFs, especially for u, are further shifted away from zero towards large amplitudes; also interesting is the appearance of a pair of local maxima, near the maximum amplitude, in the PDFs for a_{4k} at level 4, confirming the dominance of the cellular structure in this system.

It is interesting to observe from (d) of Figs. 5.5, 5.6, 5.7 and 5.8 that the total energy E_m (and the energy e_4 of the most active level 4) increases as more levels, and more active levels, are deleted from the system, indicating a role for all these levels to participate in the energy transfer process. In particular, the nonlinear stabilization mechanism is such that, seemingly counterintuitively, the energy decreases in the presence of more linearly unstable modes.

Nonlocal information transfer

In the last few experiments discussed, the set of resolved modes **B** has not contained a contiguous range of wavelet levels; so that the action of the noisy large scales in driving the active-scale dynamics away from the cellular equilibrium state, and the influence of the active scales in providing damping for the unstable large scales, has required information to "jump" across missing scales.
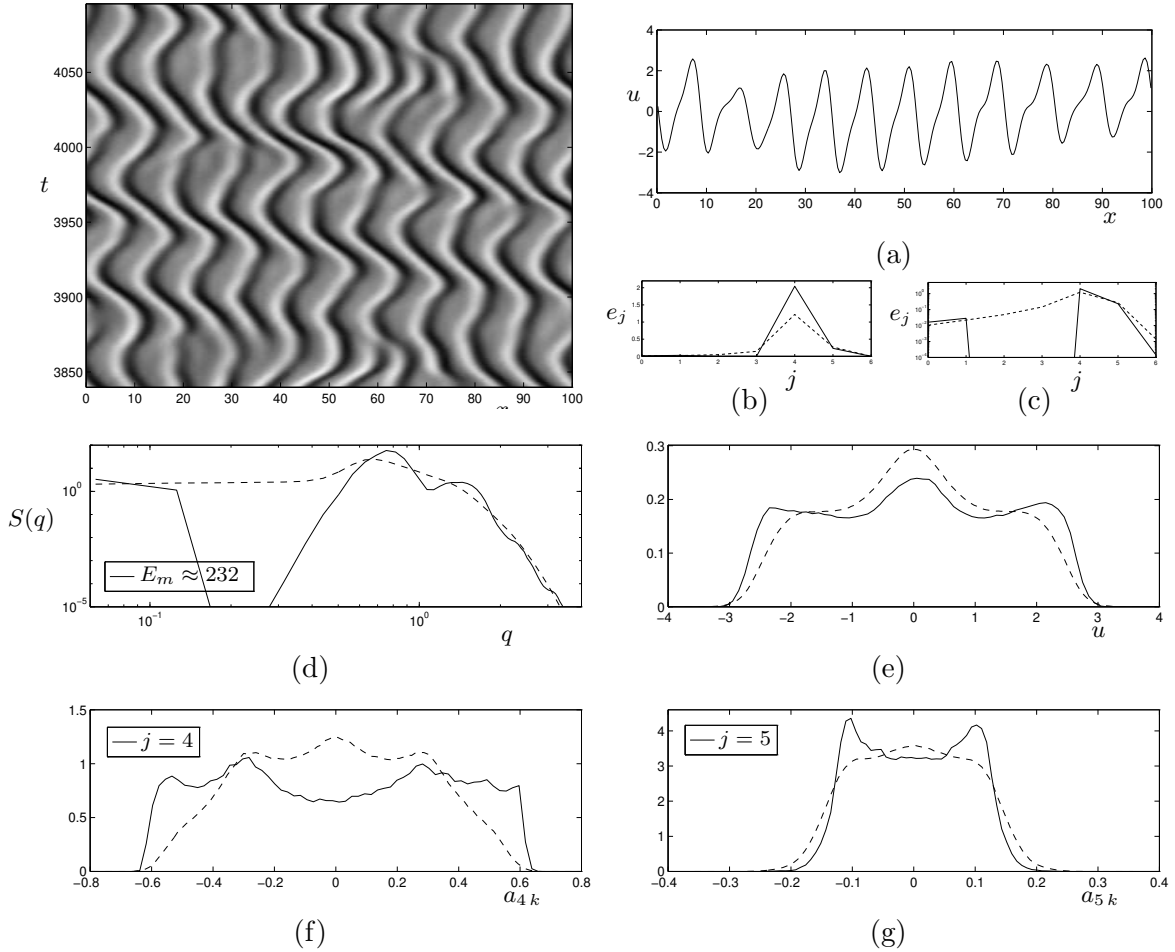
Figure 5.8: Comparison of model statistics with full KS equation: Eliminating levels $j = 2$ and 3. See caption of Fig. 5.5 for description. Autocorrelation time $\tau_c \approx 14$.

The nonlinear uu_x term in the KS equation enables significant interaction between scales that are relatively far apart. Two further experiments to conclude this Section also demonstrate this effect, and corroborate previous results on the roles of the different levels.

We recall from Fig. 5.4(d) that in the absence of levels 0–3, the system almost immediately settles down to a steady cellular state. If the largest scale, level 0, is retained, however, the solution remains "alive" for quite a long time; in fact, the coefficient $a_{0\,0}$ undergoes regular oscillations and drives the scales at levels $j \geq 4$, as shown in Fig. 5.9(a). Note that the peaks are essentially stationary near the (spatial) zeroes of the level 0 wavelet $\psi_0(x) \approx -\cos(2\pi x/L)$; this effect will be discussed in more detail in Sec. 5.4.1 below. After a long transient of oscillations of increasing amplitude, this system eventually does collapse to a stationary cellular state, as seen in Fig. 5.9(b), which continues this simulation to $t = 2048$. However, this experiment is significant in showing that information may be transferred nonlocally in scale, directly from $j = 0$ to $j = 4$, when the three intermediate levels are set to zero.

Eliminating levels 1 and 2   A less severe test is provided by enforcing the vanishing of levels 1 and 2. In the absence of the other large-scale modes but coupled to the active scales, level 0 can perform the task of maintaining disorder for a relatively long time, just like levels 1 and
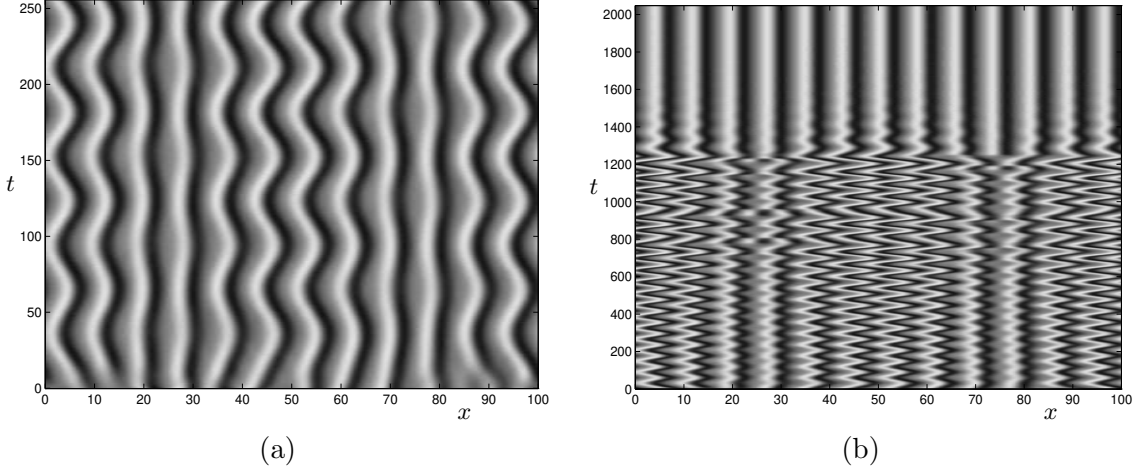
Figure 5.9: Eliminating levels $j = 1$–3, showing information transfer across missing scales: (a) Early-time oscillatory state, with level $j = 0$ driving the active scales. (b) Longer-time integration: after transient growth of oscillations, system finally settles in a stationary cellular attractor.

2 individually, as discussed previously; see Fig. 5.10(a). It appears that this system alternates between such a spatiotemporally disordered state, and a "standing wave" oscillatory state such as Fig. 5.10(b), in which a_{00} periodically drives levels $j \geq 3$, in spite of the absence of two intermediate levels. Once the system is in the standing wave state, oscillations steadily grow, presumably ejecting the system along the unstable manifold of this state either to another standing wave state, related to the first by a symmetry, or to a disordered state, from which the evolution eventually approaches the standing wave state again. These possibilities are shown in Figs. 5.10(c) and (d), showing two (consecutive) sequences of the simulation, each of length $t = 2048$. Fig. 5.10(e) shows the time evolution of the mode a_{00} over the interval spanned in (c,d), showing that the oscillatory and disordered states of the full system coincide with those of the large-scale driving mode. Note that the stationary cellular state previously observed in Fig. 5.4(d) is certainly present in this system, though unstable; it corresponds to $a_{00} \equiv 0$. In our simulations the residence time in the irregular and oscillatory states seems to be increasing; this is strongly suggestive of heteroclinic connections between the disordered state and the cellular state. The cellular state appears to be a saddle point; the standing wave states lie on its unstable manifold, and are observed as the system spirals away from the cellular state.

5.2.4 Discussion

We summarize the conclusions of this Section in a series of observations; the assignment to particular wavelet levels j is appropriate to $L = 100$, although the qualitative results hold, we believe, more generally:

- The smallest scales, $j \geq 6$, appear essentially irrelevant to the dynamics, and may be neglected at little cost except to detailed tracking.

- The most active scales, $j = 4$ and 5, are crucial for both the characteristic spatial structure and the energy transfer mechanism.

- The largest scales, $j = 0$, 1 and 2, collectively and to some extent individually (especially level 2) contribute the excitation that maintains the spatiotemporal disorder, though no one of these levels itself is vital to this purpose.

125
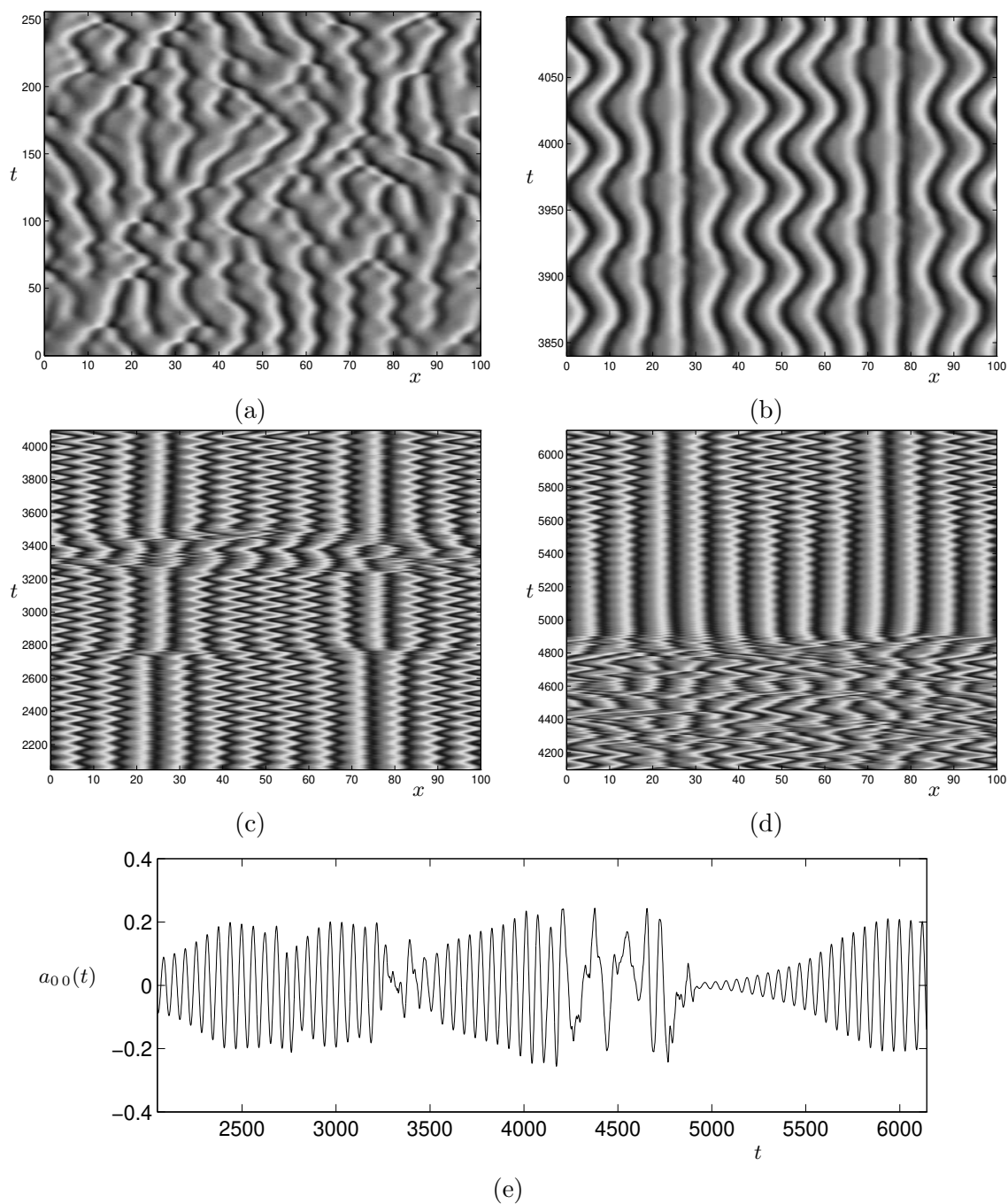
Figure 5.10: Eliminating levels $j = 1$ and 2: Heteroclinic connection between spatiotemporally chaotic and cellular states. (a) Chaotic dynamics; (b) Oscillatory dynamics. (c),(d) Successive long-time integrations, showing jumps between states of growing oscillations (on the unstable manifold of the cellular state), and between oscillatory and chaotic states. (e) Time series of mode $a_{00}(t)$, which drives the active scales, for the time interval shown in (c) and (d).

- Level $j = 3$, intermediate between the large and most active scales, plays a major role in sustaining the typical "events", the creation and annihilation of defects, and in driving the distributions away from the cellular structure and towards zero.

- Nonlocal transfer in scale occurs; information may be transferred even in the absence of bands of wavelet levels from the system.

We have reported on a *particular* series of experiments here, keeping integration parameters and initial conditions **a** fixed for ready comparisons. For more general applicability, these experiments, and those discussed in later Sections, should be repeated for different parameters and for a range of initial conditions; or even for a different choice of wavelet basis. In particular, the relative contributions of different wavelet levels vary with the choice of total length L. It is not clear that the benefits of these additional experiments, allowing one to corroborate the above observations and modify them slightly for different situations, would justify the effort involved.

A major conclusion of this section is that, *with the aid of the wavelet decomposition, we may identify and discriminate between the contributions of different ranges of scales to the overall spatiotemporally complex dynamics.* In the following Sections, instead of merely removing levels from our system, we confirm and extend these conclusions by various types of forcing at different wavelet levels.

5.3 Forcing from an independent run

Having investigated the effect of eliminating wavelet levels, we now force them from an independent integration of the KS equation. Specifically, the set **B** of modes resolved in the model is again defined by a set of complete wavelet levels. Unless otherwise specified, the retained model coefficients a_α, $\alpha \in \mathbf{B}$ are given initial conditions **a**; and their evolution is forced by the time series $b_{\alpha'}(t)$, $\alpha' \in \mathbf{A} \backslash \mathbf{B}$, which are wavelet coefficients obtained from a control run of the KS equation with initial conditions **b**.

Since we are forcing by modes having the correct KS statistics, we expect the models to display qualitative agreement with the KS equation. Indeed, this is the case, as demonstrated by the simulations displayed in Fig. 5.11, in which (a) the lowest mode $a_{0\,0}$, and (b) the lowest three levels, $j = 0$–2, are forced. While these are not actually solutions of the KS equation—the forcing low modes are not coupled to the higher levels—and do not look in detail like either of the reference computations in Fig. 5.1 from which they were derived, they certainly "look right". A study of their statistical properties, such as energy distributions and PDFs (not shown), also shows no marked divergence from those for the true KS equation. This is unsurprising: the "correct" kind of forcing leads to the "correct" dynamics. However, it does show that the low modes need not be correlated with the high modes, nor respond to them, to provide driving which stimulates reasonable dynamics; this point will be emphasized in Sec. 5.5.2 below.

5.3.1 Tracking: Small scales are slaved to large scales

External forcing at the large scales from an independent KS run can reproduce qualitatively plausible dynamics. However, the interest in the experiments reported in this Section goes beyond just trying to get a model that "looks right". Motivated by the results of preliminary experiments in which we forced more wavelet levels than just $j = 0$–2, we pose the question which was also stated
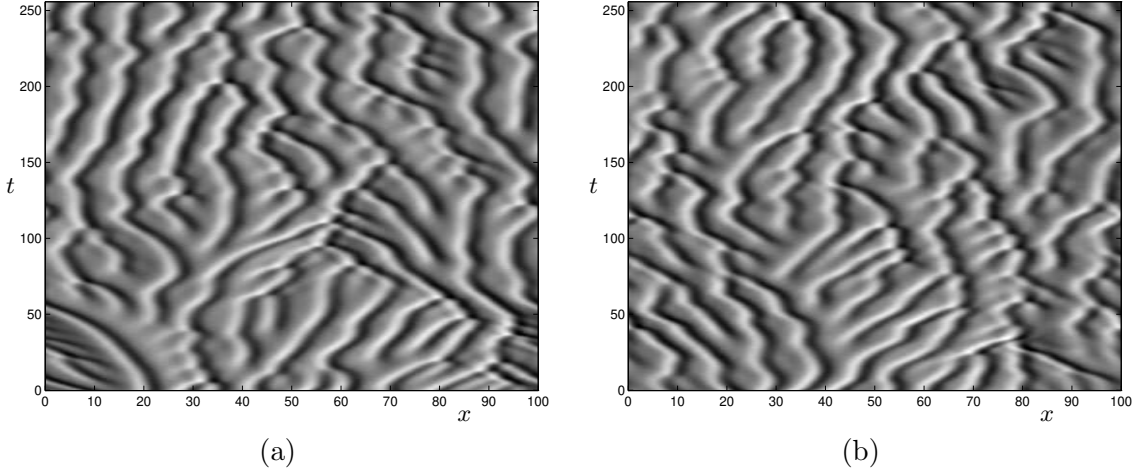
Figure 5.11: Forcing from independent KS integration, at (a) level $j = 0$, and (b) levels $j = 0$–2.

by Browning *et al.* [BHK98]: Do low modes determine the high modes? A related question is the issue of where to distinguish between "low" and "high" modes: how many low modes are needed?[†]

Theory of tracking: Sufficiently many low modes determine the dynamics

The fact that dissipative evolution equations such as the KS equation possess finite-dimensional inertial manifolds and attractors indicates that a finite set of modes determines the dynamics in an appropriate Hilbert space $\mathcal{H}$, for instance in L^2 or in the Sobolev space H^2; see Sec. 1.2.2. That is, there is a finite-dimensional projection $\mathcal{PH}$ of the full phase space $\mathcal{H}$ which contains the determining modes, collectively labeled by $\mathbf{p}$; the other modes $\mathbf{q}$ may be found in terms of $\mathbf{p}$ through a map $\mathbf{q} = \Phi(\mathbf{p})$. This is equivalent to saying that the inertial manifold $\mathcal{M}$ is given in the form of a graph $\{\mathbf{p}, \Phi(\mathbf{p})\}$; see [Tem97, Sec. VIII.2]. In some sense, this is related to a center-unstable manifold reduction, and is what is intuitively meant by saying that the high modes are "slaved" to the low modes.

The results on dissipativity (see Secs. 2.1–2.2) and finite-dimensional attractors and inertial manifolds for the KS equation do not immediately apply here, however, since we are *externally* specifying the low modes, without feedback from the high modes. A separate tracking theorem is needed for this case, and a fairly simple result of this type is given here. Much more general tracking results for a wide class of dissipative PDEs, including the Navier-Stokes equations, some reaction-diffusion equations and the KS equation, have recently been obtained by Mattingly, who discusses the situation for the two-dimensional Navier-Stokes equations in his thesis [Mat98].

Consider a decomposition of the Hilbert space $\mathcal{H}$ into "low" and "high" modes via $\mathcal{H} = \mathcal{H}^< \oplus \mathcal{H}^>$, where our notation is chosen because we will usually think of large and small scales, although for now, the splitting can be more general. The subspaces $\mathcal{H}^<$ and $\mathcal{H}^>$ could, for instance, be spanned by complementary subsets of the full Fourier mode basis, or could be obtained from a multiresolution

---

[†]Some of the investigations of this and the next Section, and of Sec. 6.1, are related to the problem of tracking and synchronization in chaotic systems [PC90], which has recently attracted considerable interest. While we do not actively pursue this connection or relate our work to the vast existing literature, we have commented on implications for synchronization where appropriate. In particular, our analytical approach here and in Sec. 5.3.2 is related to Lyapunov function methods which have been employed successfully to demonstrate the potential for synchronization in the Lorenz system and elsewhere; an introduction is given in [Str94, Sec. 9.6].

analysis of $\mathcal{H}$. We denote the projections onto these subspaces by $\mathcal{P}^<$ and $\mathcal{P}^>$, and for $u \in \mathcal{H}$ we define $u^< = \mathcal{P}^< u$, $u^> = \mathcal{P}^> u$. Observe that since $\mathcal{P}^<$ and $\mathcal{P}^>$ are projections, the inner product between low and high modes vanishes,[†]

$$\left(u_1^<, u_2^>\right) = 0 \quad \text{for any } u_1, u_2 \in \mathcal{H}. \tag{5.1}$$

Suppose $v \in \mathcal{H}$ solves the KS equation (1.1). Then the projection $v^>$ onto $\mathcal{P}^> \mathcal{H}$ satisfies

$$v_t^> = -(v_{xx})^> - (v_{xxxx})^> - (vv_x)^>. \tag{5.2}$$

(We do not need to assume that the projection commutes with differentiation, that is, for instance that $(v_{xx})^> = (v^>)_{xx} \overset{\text{def}}{=} v_{xx}^>$. This is true if we are splitting between low and high Fourier modes, but not, for instance, for a wavelet decomposition.)

Let $u \in \mathcal{H}$, $u \not\equiv v$ be such that its high modes also satisfy (5.2),

$$u_t^> = -(u_{xx})^> - (u_{xxxx})^> - (uu_x)^>. \tag{5.3}$$

At this point, we make the important assumption that $u^< = v^<$. Note that this implies that $u = v^< + u^>$ does not, in general, solve the KS equation (that is, we cannot remove the projection operators from (5.3)), as the low modes of u are externally specified, and unaffected by its high modes. In fact, this type of forcing, in the wavelet formulation, corresponds exactly to the model (3.25), and hence to many experiments of this Chapter.

We define the difference $w \overset{\text{def}}{=} u - v$, and observe that fixing the low modes implies $w^< = 0$, so that $w = w^>$. We have the evolution

$$\begin{aligned} w_t^> &= -(w_{xx})^> - (w_{xxxx})^> - [(v + w)(v_x + w_x)]^> + (vv_x)^> \\ &= -(w_{xx})^> - (w_{xxxx})^> - [ww_x + vw_x + wv_x]^>. \end{aligned} \tag{5.4}$$

On taking the inner product with $w = w^>$, we may drop the projection operators $\mathcal{P}^>(\cdot) = (\cdot)^>$, as any low mode components vanish due to (5.1) (for this reason, we do not need $\mathcal{P}^>$ and ∂_x to commute). Thus, integrating by parts, and using the fact that boundary terms at 0 and L vanish by periodicity, we have

$$\begin{aligned} \tfrac{1}{2}\frac{d}{dt}\|w\|^2 &= -\int ww_{xx} - \int ww_{xxxx} - \int w^2 w_x - \int vww_x - \int w^2 v_x \\ &= \|w_x\|^2 - \|w_{xx}\|^2 + 0 - \tfrac{1}{2}\int w^2 v_x. \end{aligned} \tag{5.5}$$

We can bound the final term, due to the nonlinearity, using

$$\left|\int w^2 v_x\right| \le |v_x|_\infty \|w\|^2 \le \rho_1 \|w\|^2. \tag{5.6}$$

Here we use an L^∞ bound for the derivative of a solution v of the KS equation; this bound appears to be constant independent of L—see Fig. 4.1 —but can in general only rigorously be bounded in terms of the L-dependent L^2 bounds for $\|v_x\|$ and $\|v_{xx}\|$; see Sec. 1.2.2. Using (5.6) in (5.5), we thus have

$$\tfrac{1}{2}\frac{d}{dt}\|w\|^2 \le \|w_x\|^2 - \|w_{xx}\|^2 + \tfrac{1}{2}\rho_1\|w\|^2. \tag{5.7}$$

[†]The decomposition and projection operators $\mathcal{P}^<$ and $\mathcal{P}^>$ are defined on the larger space $L^2[0, L]_{per}$, which contains $\mathcal{H}$; hence (5.1) is generally valid for $u_1, u_2 \in L^2$.

So far, nothing about this derivation differs from the usual estimates for the difference between two solutions of the KS equation; and in general, we cannot make much progress beyond this point. However, to derive tracking results, we now (explicitly) assume that the splitting $\mathcal{H} = \mathcal{H}^< \oplus \mathcal{H}^>$ is indeed between large and small scales, and that on $\mathcal{H}^>$, a Poincaré inequality holds of the form

$$\|w\|^2 \leq \lambda_K^2 \|w_x\|^2 \leq \lambda_K^4 \|w_{xx}\|^2. \tag{5.8}$$

For instance, if $\mathcal{P}^<$ is the projection onto the first $2(K-1)$ Fourier modes, and $\mathcal{P}^> = \mathcal{I} - \mathcal{P}^<$, then defining for present convenience $q_k \overset{\text{def}}{=} 2\pi k/L$,

$$w = \mathcal{P}^> w = \mathrm{i} \sum_{|k| \geq K} \hat{w}_{q_k} \mathrm{e}^{\mathrm{i} q_k x}, \quad w_x = - \sum_{|k| \geq K} q_k \hat{w}_{q_k} \mathrm{e}^{\mathrm{i} q_k x},$$

so that

$$\|w\|^2 = \sum_{|k| \geq K} |\hat{w}_{q_k}|^2 = \left(\frac{L}{2\pi K}\right)^2 \sum_{|k| \geq K} |\hat{w}_{q_k}|^2 q_K^2$$

$$\leq \left(\frac{L}{2\pi K}\right)^2 \sum_{|k| \geq K} |\hat{w}_{q_k}|^2 q_k^2 = \left(\frac{L}{2\pi K}\right)^2 \|w_x\|^2,$$

and similarly for the second inequality of (5.8). In this case, $\lambda_K = L/2\pi K = q_K^{-1}$.

Using (5.8) in (5.7), we obtain the desired Gronwall inequality,

$$\tfrac{1}{2}\frac{d}{dt}\|w\|^2 \leq \left(\tfrac{1}{2}\rho_1 \lambda_K^4 + \lambda_K^2 - 1\right)\|w_{xx}\|^2. \tag{5.9}$$

To obtain a tracking result, it remains to choose the splitting so that the coefficient in (5.9) is negative; that is, λ_K must be chosen sufficiently small (for example, the Fourier mode cutoff K must be sufficiently large) that $\tfrac{1}{2}\rho_1 \lambda_K^4 + \lambda_K^2 - 1 < 0$. Then, using (5.8) again,

$$\tfrac{1}{2}\frac{d}{dt}\|w\|^2 \leq -\gamma \|w\|^2, \qquad \text{where} \quad \gamma \overset{\text{def}}{=} \frac{1 - \lambda_K^2 - \tfrac{1}{2}\rho_1 \lambda_K^4}{\lambda_K^4} > 0, \tag{5.10}$$

so that

$$\|w(t)\| \leq \|w(0)\| \mathrm{e}^{-\gamma t}. \tag{5.11}$$

This exponential decay of the difference in high modes $w = w^>$ indicates *tracking*; the high modes $u^>$ forced by $v^<$ at the low modes, are asymptotically entrained to the phase space trajectory v.

Some comments are in order:

- According to the range of validity of these estimates, one can in general only entrain stable modes; all linearly unstable modes must be included in $\mathcal{H}^<$.

- These estimates are very crude, especially through the use of (5.6) and (5.8). That is, the fine balances and phase relationships responsible for the interesting KS dynamics are replaced by very coarse global bounds. Thus the cutoff in the splitting (mode K in the Fourier picture) is expected to be far from optimal; it gives only a sufficient condition for tracking, which may not be necessary for the KS equation. Also, these estimates say nothing about the effects of forcing from an incomplete wavelet level, in which case we expect local spatial interactions to contribute to entrainment; see the discussion of experiments below.

- There is little in this discussion that is specific to the KS equation. The derivation goes through essentially unchanged with a general linear operator $\mathcal{L}$—a necessary condition is that it is negative definite on $\mathcal{H}^>$—a bound on the nonlinear term, and a Poincaré inequality obtained from the splitting with a sufficiently small constant λ that the linear damping dominates the nonlinearity. In this way the result may be extended to other systems—see [Mat98].

Tracking: Experiments

Forcing at levels 0–3   The result above indicates that tracking occurs if sufficiently many modes are specified; however, the crude estimates on the nonlinear term mean that the bounds derived for the number of modes required are not sharp. The experiments reported here are designed to investigate the number of determining modes.

In our simulations we initially detected tracking while forcing at the lowest 15 modes, levels 0–3, with time step $\delta t = 1/8$, giving results similar to Figs. 5.12(a). In this case, the set of resolved modes is $\mathbf{B} = \{(j,k)|j \geq 4\}$, and we obtained time series of the modes $b_{j'\,k'}$, for $j' \leq 3$, from a control run $v(x,t)$ with initial conditions $\mathbf{b}$, as shown in Fig. 5.12(a)(i). The $b_{j'\,k'}$ were fed into the evolution equations (3.25) for the model coefficients $a_{j\,k}$, $j \geq 4$, which had initial conditions $\mathbf{a}$. The reconstructed field for the model, from both the resolved and forced coefficients, $u(x,t) = \sum_{\alpha \in \mathbf{B}} a_\alpha(t)\psi_\alpha(x) + \sum_{\alpha' \notin \mathbf{B}} b_{\alpha'}(t)\psi_{\alpha'}(x)$ is shown in Fig. 5.12(a)(ii). One can observe apparent tracking by careful comparison of (i) and (ii); but it is more readily seen by plotting the difference $v(x,t) - u(x,t) = \sum_{\alpha \in \mathbf{B}}(b_\alpha(t) - a_\alpha(t))\psi_\alpha(x)$, which has nonzero components only at the high modes $j = 4$–6. As shown in Fig. 5.12(a)(iii), there is definite tracking beyond about $t = 150$. Similar and even more rapid convergence to tracking was observed when the initial conditions were reversed (that is, the control run had initial state $\mathbf{a}$, and the model coefficients were initialized with $\mathbf{b}$).

When this experiment was repeated (not shown) with the time step reduced to $\delta t = 1/32$, the value used for most simulations of this Chapter, such rapid convergence of the model to the control was no longer observed, however; although for much longer time, $t > 1024$, the model seemed to settle down towards the control run. To clarify matters, we used a much smaller step size, $\delta t = 1/200$; the results, which are similar to those with $\delta t = 1/32$, are shown in Fig. 5.12(b). In this case the model in (ii) fails to agree with the control run in (i) over the time interval shown. From the difference, plotted in (iii) over a longer time period, we see that the model sometimes approaches the control, only to diverge again. For times well above $t = 1024$, the model again seems to follow the control, however. (Note that if at least one of the modes at or below level 3 is left to evolve independently, instead of being forced, then in numerical simulations the model never approaches the control run at any time step; this is understandable in view of our results of Sec. 5.3.2 below.)

These observations, in particular the rapid convergence to the control for large time step, suggest that what is observed here is not tracking in the sense above, in which the high modes exponentially approach the control, but numerical dissipation, due to the inevitable small but compounding errors of any integration scheme. Supporting evidence for this conclusion is found in Fig. 5.13, in which $\rho(t)$, defined as the L^2 norm (squared) of the difference, $\rho(t) \overset{\text{def}}{=} \|v - u\|^2(t)$, is plotted for various time steps. In (a), the difference for $\delta t = 1/8$ falls off rapidly, showing the exponential decay suggested by Figs. 5.12(a). For smaller time steps (b), however, the difference remains large, and nearly constant, for a long time before finally decreasing, which is inconsistent with the exponential convergence of trajectories which would be implied by tracking of the type (5.11).
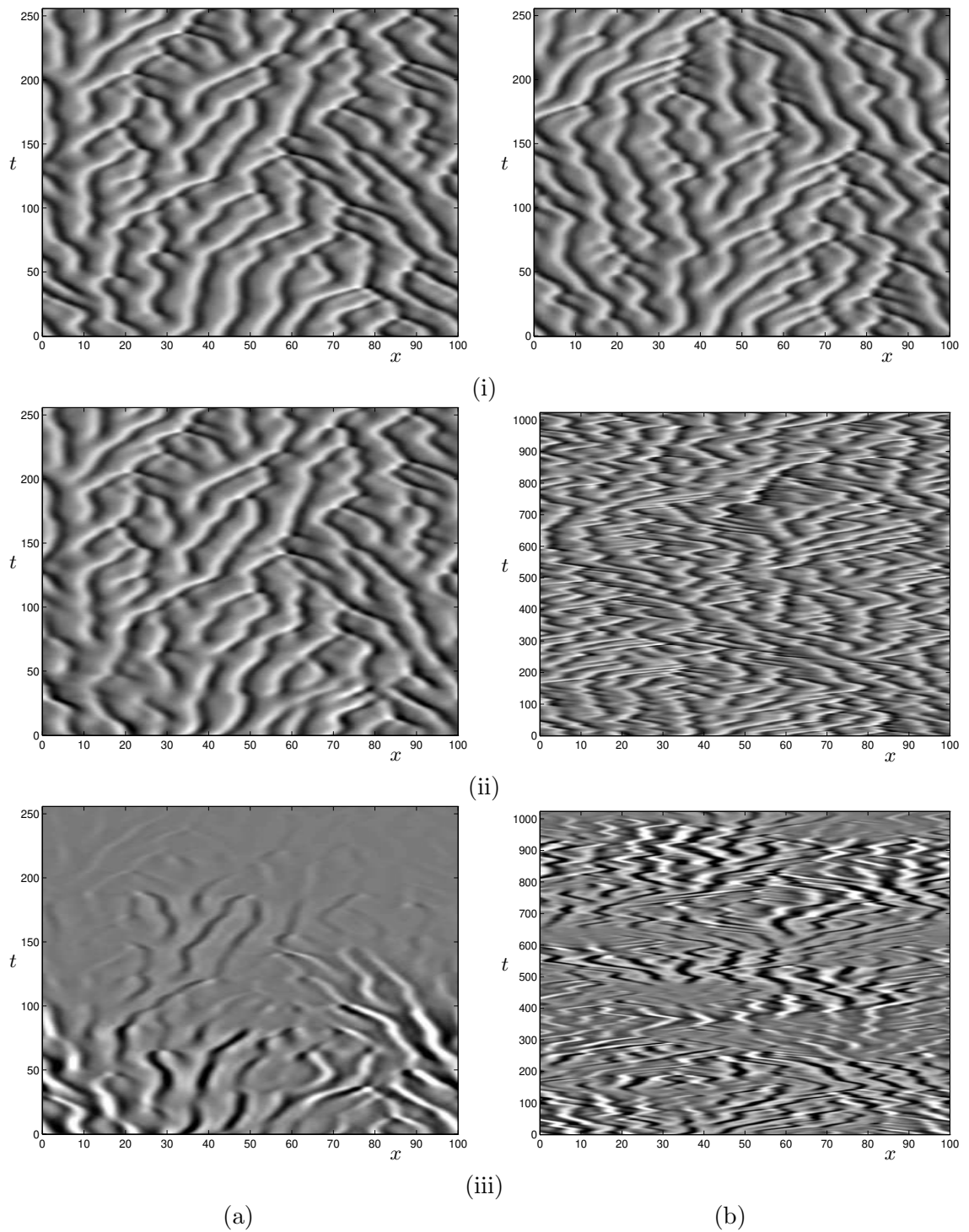
Figure 5.12: Forcing at levels $j = 0$–3 from an independent control run, with time steps (a) $\delta t = 1/8$, and (b) $\delta t = 1/200$. (i) Reference computation, with initial conditions **b**; compare with Fig. 5.1(b)(iii) to see the sensitivity of the detailed dynamics to varying δt. (ii) Model run, forced at low modes, high modes evolving independently (over longer time interval in (b)). (iii) Difference (at levels $j \geq 4$) between model and reference run, showing more rapid convergence to reference solution for large δt.
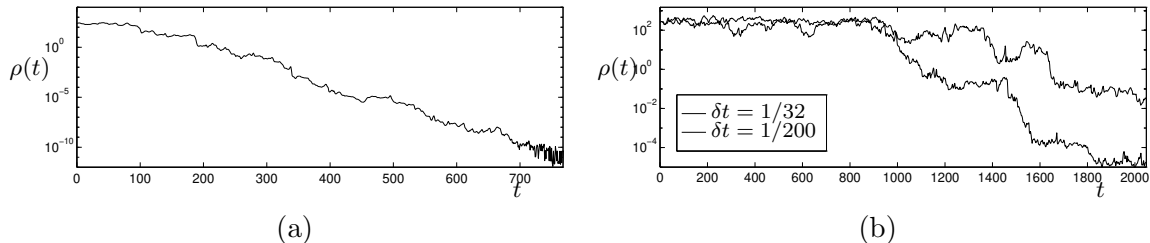
Figure 5.13: Forcing at levels $j = 0$–3: L^2 norms (squared) of differences between model and reference run, $\rho(t) = \|v - u\|^2(t)$. (a) Exponential decay for large time step $\delta t = 1/8$; (b) independent evolution of model, and apparent tracking at later times, for $\delta t = 1/32$ and $\delta t = 1/200$.

Note that if, on average, the high modes at levels $j \geq 4$ of the model and the control run are independent—that is, there is no tracking at all—then we expect $\langle \rho \rangle = \langle \|v - u\|^2 \rangle = \langle \|v^> - u^>\|^2 \rangle = \langle \|v^>\|^2 + \|u^>\|^2 + 2(v^>, u^>) \rangle \approx \langle 2\|v^>\|^2 \rangle = 2\sum_{j \geq 4}\langle e_j \rangle$, since the inner product $(v^>, u^>)$ vanishes on average, and the energy in the high modes for the model is similar to that of the control run. The averaged norms of the differences shown in Fig. 5.13(b), especially for $\delta t = 1/32$, satisfy this relation fairly well for t less than about 1000, before the model begins to approach the control.

Incidentally, the full control runs in Fig. 5.12(i), compared to each other and to Fig. 5.1(b)(iii), demonstrate the sensitivity of the chaotic KS system to the integration scheme and parameters. These computations all have the same initial conditions **b** and integrator, and differ only in the time step size δt employed. All the simulations "look correct", and display all characteristic events and statistical behavior—in this sense, they are all adequate computations of the KS dynamics—but they differ in their detailed time histories, such as the paths of local extrema. As can be seen, the large step size $\delta t = 1/8$ computation rapidly diverges from the others, while the run for $\delta t = 1/32$ tracks that for $\delta t = 1/200$ up to about $t = 30$ before their trajectories separate. This sensitive dependence on the time step, together with that on other parameters such as the number of modes retained (see Fig. 5.3), reminds us that for long times it is impossible to get an *exact* numerical solution for given initial conditions. However, shadowing results assure us that for a "sufficiently good" integrator, the numerically obtained trajectory will for finite times be close to *some* trajectory in the attractor, and we thus feel confident that the numerical simulations and statistics extensively discussed in this, the previous and next Chapters correctly describe the qualitative behavior of the system, even if not the detailed path in phase space. It is thus important to remember that, for the purpose of numerical simulations, discussions of tracking are only meaningful when the integrator and parameters are held *fixed* for a given experiment, as done in this Section.

Forcing all unstable modes   It is not surprising that forcing only levels 0–3 fails to produce tracking, since level 4 contains the most linearly unstable modes. However, when we force at this level as well, then we do expect tracking, and this is indeed observed. If we force at all the unstable levels $j = 0$–4 (so that only modes a_{jk}, $j \geq 5$ evolve independently in the model), the convergence of the model to the reference run is sufficiently fast that a plot of the difference $v - u$, which rapidly approaches zero, is unenlightening. Fig. 5.14(a) shows the exponential decay of $\rho(t)$, the L^2 norm of the difference, obeying the estimate (5.11). This simulation, and others not shown here with different initial conditions and time steps, confirms the theoretical result that tracking is possible if sufficiently many low modes are specified; in particular, if the set of "low modes" includes all linearly unstable large-scale modes.
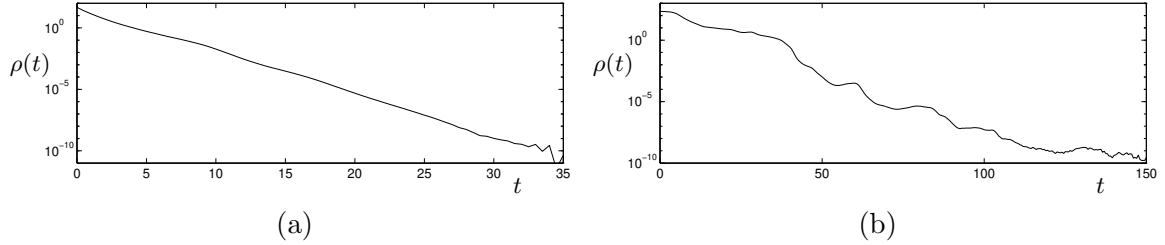
Figure 5.14: Tracking and exponential decay of norm of differences, for forcing from independent run at (a) levels $j = 0$–4; and (b) levels $j = 0$–3, and alternate modes $a_{4\,2k'}$ at level 4.

Forcing part of level 4   Must we force at all of level 4 (together with $j = 0$–3) to achieve tracking; or is driving only some of the most active modes sufficient to entrain the others? Because this is the appropriate place to investigate such tracking-related issues, the experiments discussed here are an exception to the rest of this Ch. 5, in that the set of resolved modes of our models contains some partially filled wavelet levels.

Fig. 5.14(b) shows the decay of the norm of the difference for a simulation in which alternate modes at level 4 are forced (as well as all lower levels). That is, we set $a_{j\,k}(t) = b_{j\,k}(t)$ if $j \leq 3$, or $j = 4$ and $k = 2k', k' = 0 \ldots 7$, leaving the odd modes at level 4 to evolve independently. While the convergence to the control is not as fast as if the entire level is forced (Fig. 5.14(a)), it is clear that the odd modes are rapidly entrained by their neighbors and the lower levels.

A related experiment concerns whether forcing in one region of space will eventually enforce tracking throughout the domain. Fig. 5.15 shows the evolution of differences and their norms for two such experiments. For the simulation of (a) and (c), the left half of the domain is forced to level 4, the right half to level 3; that is, we force modes $a_{j\,k}$ for $j \leq 3$, and $j = 4, k \leq 7$ (or in alternative notation, $\alpha \leq 23$). We see that tracking is established quite rapidly. If we only force the left-most quarter at level 4, as shown in Fig. 5.15(b) and (d), convergence of the model to the control is somewhat slower, but eventually tracking occurs. In fact, our simulations suggest that forcing only a single wavelet coefficient at level 4, in conjunction with all lower levels, may be sufficient to entrain all others—see Fig. 5.16— though we have not established this with confidence. If this result or related ones requiring forcing at only a few $j = 4$ modes were indeed to be true, then it could have interesting implications for detection and control: The long time history of a system can be completely determined from measurements or forcing of all the low modes, but only some of the most active ones, which could be localized in space. This is related to, but not as strong as, results which show that the complete time history at a few spatial determining *nodes* is sufficient to specify the system [FT91, FK95].

We emphasize that these results are only tentative, however, and are somewhat ambiguous in the light of the discussion of the next Section, since some of the retained modes in the model are linearly unstable. Our discussion implies mainly that spatial interactions play a role in synchronization which is not taken into account by a scale-by-scale analysis.

5.3.2   Independent evolution of low modes

A question related to the above discussion on tracking and control is whether *all* large-scale modes must be specified for tracking, or whether forcing most large-scale and/or active modes is sufficient to entrain some independently evolving slow large-scale modes. Since the direction of overall energy
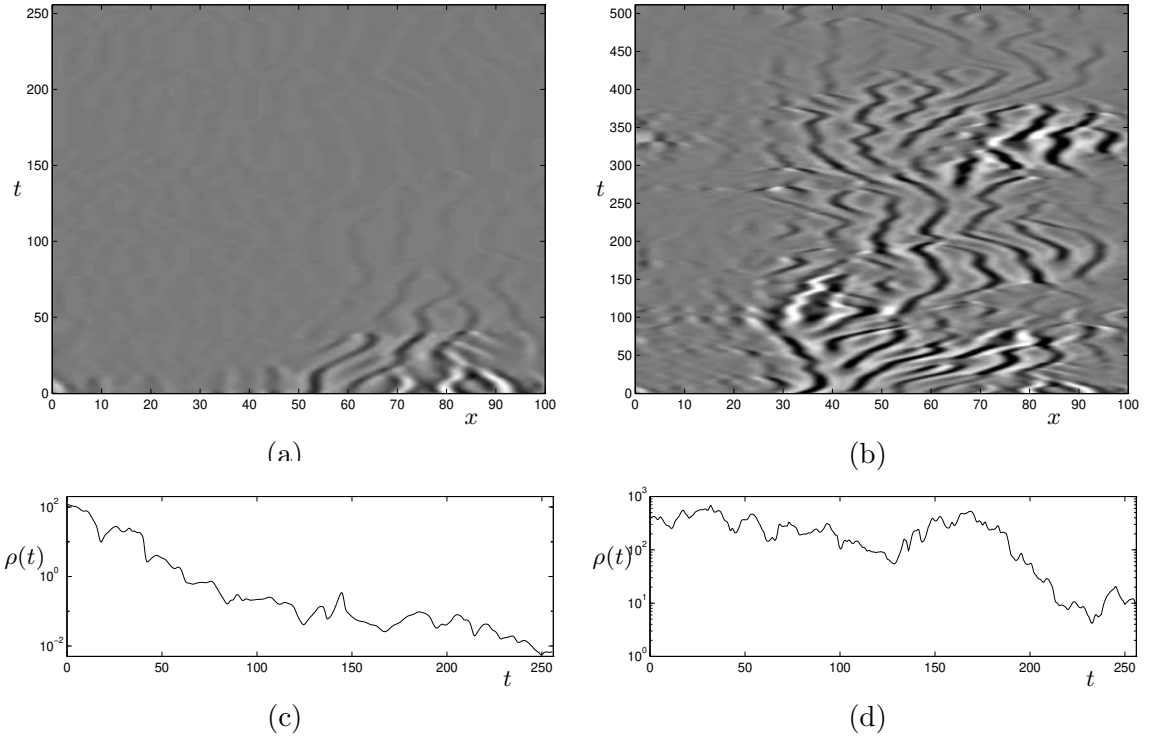
Figure 5.15: Space-time evolution of difference $v - u$, and evolution of difference norms $\rho(t) = \|v - u\|^2(t)$, between reference run v and model u, with low-mode forcing and localized forcing at active scales: (a,c) Forcing at $j = 0$–3, and at $a_{4\,k}$, $k = 0\ldots 7$; (b,d) Forcing at $j = 0$–3, and at $a_{4\,k}$, $k = 0\ldots 3$.

flow is from large to small scales, and the results of Sec. 5.2 imply that it is the function of the large scales to drive the active scales, not *vice versa*, tracking seems unlikely if the large scales are free.

Visual comparison of Fig. 5.17(a,b) with the control run Fig. 5.1(b)(iii), and the evolution of norms of differences $\rho(t)$ in Fig. 5.17(c,d), confirm that the lowest wavelet levels, especially $j = 0$, are not entrained by the other modes. In these experiments, various combinations of large and active scales are forced, while the lowest levels remain in the set **B** of model coefficients and evolve freely within the model. The difference $v - u$ for these models does not decay asymptotically, and there is no tracking.

Forcing all modes except one

We derive some results, similar in spirit to those of the previous Section, relevant to this situation. Before discussing the general case, we first treat an interesting special case obtained if there is forcing at all large and active scales except at a single mode a_α; that is, a_α is left to evolve in response to the forcing $b_{\alpha'}$, $\alpha' \neq \alpha$. If the "free" mode $a_{j\,k}$ is linearly unstable ($j \leq 4$ for our $L = 100$ KS model), then in such a situation, tracking never occurs; instead, as seen in the plots of Fig. 5.18 in which the lowest mode $a_{0\,0}$ evolves freely, the single mode that is forced from an independent run diverges exponentially from the control run, growing without bound.

The cause of this behavior is readily apparent from the evolution equations for the free mode,
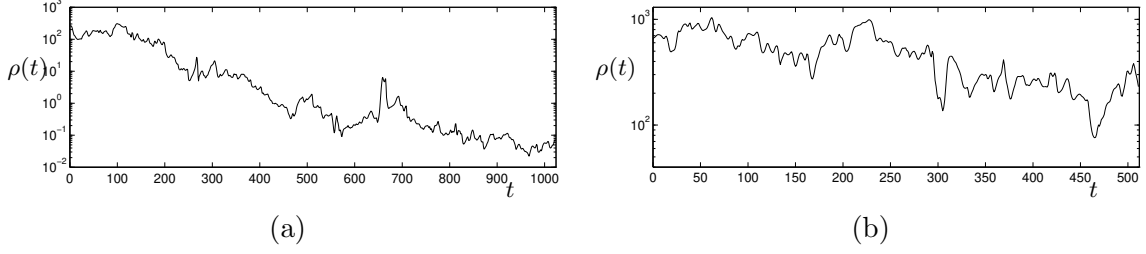
Figure 5.16: Forcing all modes at levels $j = 0$–3, and a single mode at level 4; the difference norm evolution $\rho(t) = \|v - u\|^2(t)$ indicates possible tracking. (a) Forcing at mode $a_{4\,0}$; (b) forcing at mode $a_{4\,9}$.

when forced by all the other wavelet coefficients (in fact, this discussion holds for any orthonormal basis, not just wavelets). In this case, the set of resolved coefficients $\mathbf{B}$ contains just one element α, which we will treat as a fixed and distinguished index below, and (3.25) may be written as

$$\dot{a}_\alpha = l_{\alpha\alpha}a_\alpha + \sum_{\alpha' \neq \alpha} l_{\alpha\alpha'}b_{\alpha'} + \tfrac{1}{2}a_\alpha \sum_{\alpha' \neq \alpha} n_{\alpha\alpha\alpha'}b_{\alpha'} + \sum_{\alpha',\alpha'' \neq \alpha} n_{\alpha\alpha'\alpha''}b_{\alpha'}b_{\alpha''}. \tag{5.12}$$

Here we have used the identity for the wavelet Galerkin coefficients (obtained by integration by parts; see (3.23)) $n_{\alpha\alpha'\alpha} = -\tfrac{1}{2}n_{\alpha\alpha\alpha'}$, and its special case $n_{\alpha\alpha\alpha} = 0$, which prohibits the quadratic a_α^2 term from the evolution equation for a_α. Defining the forcing terms

$$f_\alpha(t) \stackrel{\text{def}}{=} \sum_{\alpha' \neq \alpha} l_{\alpha\alpha'}b_{\alpha'} + \sum_{\alpha',\alpha'' \neq \alpha} n_{\alpha\alpha'\alpha''}b_{\alpha'}b_{\alpha''}, \qquad g_\alpha(t) \stackrel{\text{def}}{=} \tfrac{1}{2}\sum_{\alpha' \neq \alpha} n_{\alpha\alpha\alpha'}b_{\alpha'},$$

we find that the mode a_α undergoes the (linear) evolution

$$\dot{a}_\alpha = \big(l_{\alpha\alpha} + g_\alpha(t)\big)a_\alpha + f_\alpha(t). \tag{5.13}$$

In fact, the same equation holds for any (distinguished) mode in the KS equation, in particular for the mode b_α of the control run, which has an identical evolution equation (5.13) to a_α, but with a different initial value. However, b_α feeds back to the evolution equations for the other $b_{\alpha'}$, and since the entire system is dissipative, $\|v\|^2 = \sum_{\alpha'} b_{\alpha'}^2 \leq \text{const.}$, and thus $|b_\alpha|$ is bounded. The free mode a_α, on the other hand, does not influence the evolution of the $b_{\alpha'}$, and $f_\alpha(t)$ and $g_\alpha(t)$ are just externally imposed additive and parametric forcing terms, respectively.

We may readily deduce from the above equations that, while a_α may increase or decrease (depending on the signs and magnitudes of f_α and g_α, which are expected to fluctuate), on average, if α corresponds to a small scale (linearly stable) mode, tracking occurs, while for linearly unstable modes, the magnitude of a_α increases without bound.

Let us define, as usual, the difference $d_\alpha \stackrel{\text{def}}{=} a_\alpha - b_\alpha$. Then d_α evolves by

$$\dot{d}_\alpha = \big(l_{\alpha\alpha} + g_\alpha(t)\big)d_\alpha; \tag{5.14}$$

this equation is equivalent to (5.5) when the space $\mathcal{H}^>$ contains a single forced mode, $u^> = a_\alpha\psi_\alpha$. The above equation is easily integrated to give

$$d_\alpha(t) = d_\alpha(0)e^{l_{\alpha\alpha}t}e^{G_\alpha(t)t}, \tag{5.15}$$

136
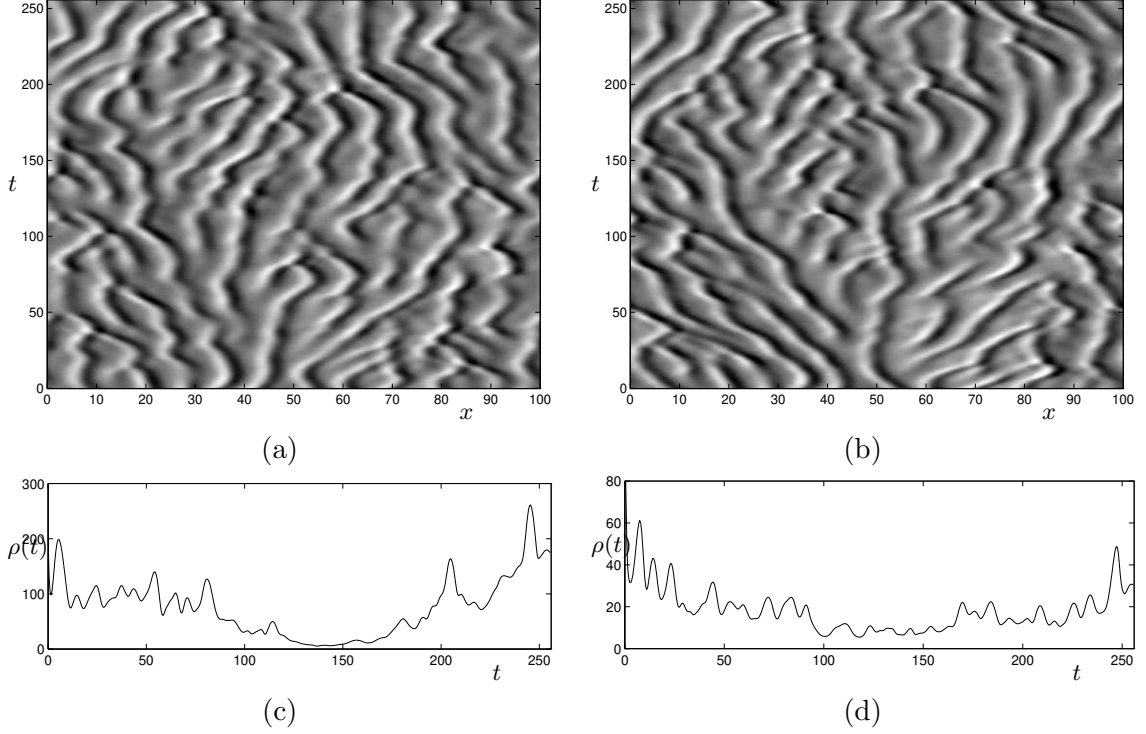
Figure 5.17: Absence of tracking when forcing at some, but not all, active and large-scale modes from a control run. Model run, for forcing at (a) levels $j = 1$–3; (b) levels $j = 1$ and 2. If we force at the active scales $j = 3$ and 4, visual inspection will reveal few discrepancies, but the lack of tracking is apparent in the difference norms $\|v - u\|^2$: forcing at (c) levels $j = 3$ and 4; (d) levels $j = 2$–4.

where we define

$$G_\alpha(t) \stackrel{\text{def}}{=} \frac{1}{t} \int_0^t g_\alpha(s) \, ds,$$

the time average of $g_\alpha(t) = \frac{1}{2} \sum_{\alpha'} n_{\alpha\alpha\alpha'} b_{\alpha'}(t)$ (we may include the $\alpha' = \alpha$ term in the sum since $n_{\alpha\alpha\alpha} = 0$). We can rewrite the formula (5.15) as

$$\frac{1}{t} \log \left(\frac{d_\alpha(t)}{d_\alpha(0)} \right) = l_{\alpha\alpha} + G_\alpha(t). \tag{5.16}$$

Our extensive numerical results of Sec. 4.2.1 (see the PDFs for the wavelet coefficients in Fig. 4.14) indicate that all the $b_{\alpha'}(t)$ have zero time average in the spatiotemporally chaotic state, so that $\lim_{t\to\infty} G_\alpha(t) = 0$. Asymptotically, we therefore expect

$$\frac{d_\alpha(t)}{d_\alpha(0)} \sim e^{l_{\alpha\alpha} t}, \quad t \to \infty. \tag{5.17}$$

If α corresponds to a small (linearly stable) scale, then asymptotically, we therefore expect tracking to occur, with exponential decay of the difference, since then $l_{\alpha\alpha} < 0$. For the linearly unstable modes, on the other hand, the magnitude of $d_\alpha(t)$ and hence of $a_\alpha(t)$ grows without bound. This is observed in Fig. 5.18, in which the growth rate for $d_{00}(t)$ shows good agreement with the prediction of (5.17).
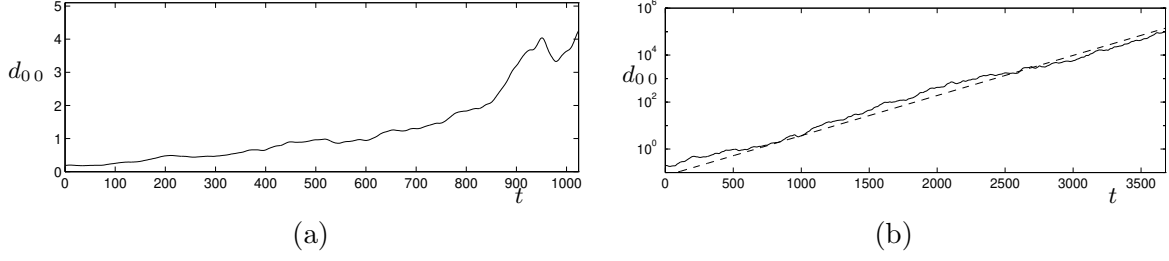
Figure 5.18: Evolution of the difference $d_{0\,0}(t) = b_{0\,0}(t) - a_{0\,0}(t)$, when $a_{0\,0}$ is the only freely evolving mode in the model; all other modes are forced from the independent run. (a) Growth for short times; (b) Exponential growth of $d_{0\,0}(t)$; the dashed line corresponds to const..$e^{l_{0\,0}t}$, $l_{0\,0} = 3.93 \cdot 10^{-3}$, in excellent agreement with (5.17).

Some comments on this result   The argument leading to (5.17) is fairly heuristic. If we were to be a bit more careful, we could argue by an approach akin to a law of large numbers that $G_\alpha(T) < \epsilon$ for some sufficiently large $T = T(\epsilon)$, so that the asymptotic growth rate is greater than $\sim \exp\big[(l_{\alpha\alpha} - \epsilon)t\big]$ for each $\epsilon > 0$; we could also use the distribution of the $b_\alpha(t)$ to say more about the distribution of $G_\alpha(t)$, and hence of $d_\alpha(t)$. An obstacle to such attempts at rigor is the fact that the wavelet coefficients $b_{\alpha'}$ are not all Gaussian; more seriously, we do not know their distributions theoretically, only numerically (see Fig. 4.14). To prove even that $\langle b_{\alpha'}(t) \rangle_t = \langle \int v(x,t)\psi_\alpha(x)\,dx \rangle_t = 0$ requires a type of ergodic result, related to the equivalence of space and time averages for this system in the STC state, which is not (yet) available. Indeed, the above result on the evolution of d_α is not, *a priori*, correct in a KS regime with a simpler (symmetry-breaking) attractor, such as a stationary state, for which the $b_{\alpha'}(t) \neq 0$ are constant.

However, note that

$$
\begin{aligned}
G_\alpha(t) &= \frac{1}{t}\int_0^t g_\alpha(s)\,ds = \frac{1}{t}\int_0^t \sum_{\alpha'} \tfrac{1}{2}n_{\alpha\alpha\alpha'}b_{\alpha'}(s)\,ds \\
&= -\frac{1}{2t}\int_0^t \sum_{\alpha'} b_{\alpha'}(s)\int_0^L \psi_\alpha^2(x)\frac{d}{dx}\psi_{\alpha'}(x)\,dx\,ds \\
&= \frac{1}{2t}\int_0^t \int_0^L \Big(\frac{d}{dx}\psi_\alpha^2(x)\Big)\Big[\sum_{\alpha'} b_{\alpha'}(s)\psi_{\alpha'}(x)\Big]\,dx\,ds \\
&= \int_0^L \frac{1}{2}\Big(\frac{d}{dx}\psi_\alpha^2(x)\Big)\Big[\frac{1}{t}\int_0^t v(x,s)\,ds\Big]\,dx,
\end{aligned}
\tag{5.18}
$$

where we have used the definitions of $g_\alpha(s)$ and $n_{\alpha\alpha\alpha'}$, integration by parts and the wavelet decomposition for $v(x,s)$, and where interchange of summation and integration, and the order of integration by Fubini's theorem, are permitted because all series are convergent and integrands are continuous as needed. This equation (5.18) allows us to reformulate the hypotheses required to establish (5.17); a sufficient condition is that the time average of v vanishes pointwise, or that the time average equals the space average in the STC regime.

Several resolved modes driven by the control run

The aforementioned formalism may readily be generalized to the case in which more than one mode is permitted to evolve freely under the action of the external forcing. As usual, we let a_α, $\alpha \in \mathbf{B}$ be

138

driven by the modes $b_{\alpha'}$, $\alpha' \notin \mathbf{B}$, the wavelet coefficients of the solution $v(x,t)$ of the control run. We shall write down the relevant equations for the differences $d_\alpha \stackrel{\text{def}}{=} a_\alpha - b_\alpha$ in terms of the wavelet coefficients; the equivalent formulation for the reconstructed field, $w(x,t) = \sum_{\alpha \in \mathbf{B}} d_\alpha(t)\psi_\alpha(x)$, is exactly as in the derivation in Sec. 5.3.1 leading to (5.4), except for the interpretation: in the present case, in contrast to the calculation in Sec. 5.3.1, we typically assume that the resolved subspace (denoted there by $\mathcal{H}^>$) contains some linearly unstable large-scale modes.

The main difference from the previous case of a single freely evolving mode is that quadratic interactions between resolved modes are no longer forbidden; this leads to an additional nonlinear term. The modes a_α, $\alpha \in \mathbf{B}$ evolve according to (3.25), while the driving coefficients $b_{\alpha'}$ satisfy the KS equation (3.19). Hence the differences d_α solve the equation

$$\dot{d}_\alpha = \sum_{\alpha' \in \mathbf{B}} l_{\alpha\alpha'}d_{\alpha'} + \sum_{\alpha',\alpha'' \in \mathbf{B}} n_{\alpha\alpha'\alpha''}(d_{\alpha'}b_{\alpha''} + d_{\alpha''}b_{\alpha'} + d_{\alpha'}d_{\alpha''})$$
$$+ \sum_{\alpha' \in \mathbf{B},\ \alpha'' \notin \mathbf{B}} (n_{\alpha\alpha'\alpha''} + n_{\alpha\alpha''\alpha'})d_{\alpha'}b_{\alpha''}.$$

After the usual manipulations using (3.23), we can write this as

$$\dot{d}_\alpha = \sum_{\alpha' \in \mathbf{B}} \left[l_{\alpha\alpha'} + g^I_{\alpha\alpha'}(t) + g^E_{\alpha\alpha'}(t) \right] d_{\alpha'} - \tfrac{1}{2} \sum_{\alpha,\alpha' \in \mathbf{B}} n_{\alpha'\alpha''\alpha}d_{\alpha'}d_{\alpha''}, \tag{5.19}$$

where

$$g^I_{\alpha\alpha'}(t) \stackrel{\text{def}}{=} - \sum_{\alpha'' \in \mathbf{B}} n_{\alpha'\alpha''\alpha}b_{\alpha''}(t)$$

arises from "internal" interactions between resolved modes, and

$$g^E_{\alpha\alpha'}(t) \stackrel{\text{def}}{=} - \sum_{\alpha'' \in \mathbf{A}\setminus\mathbf{B}} n_{\alpha'\alpha''\alpha}b_{\alpha''}(t)$$

is due to "external" interactions between resolved modes in the model and the driving modes. We may combine these two parametric driving terms as

$$g_{\alpha\alpha'}(t) \stackrel{\text{def}}{=} g^I_{\alpha\alpha'}(t) + g^E_{\alpha\alpha'}(t)$$
$$= - \sum_{\alpha'' \in \mathbf{A}} n_{\alpha'\alpha''\alpha}b_{\alpha''}(t). \tag{5.20}$$

By substituting the definitions for $n_{\alpha'\alpha''\alpha}$ and $b_{\alpha''}$, we find via calculations similar to those of (5.18) that

$$g_{\alpha\alpha'}(t) = \int_0^L v(x,t)\psi_{\alpha'}(x)\frac{d}{dx}\psi_\alpha(x)\,dx.$$

In particular, if the driving solution $v(x,t)$ is a spatiotemporally chaotic state, then we expect that the mean of each of the $b_{\alpha''}(t)$, and hence of $g_{\alpha\alpha'}(t)$, vanishes. Note that g_α of the previous derivation is just $g_{\alpha\alpha}$ in this notation.

The evolution of the differences d_α for $\alpha \in \mathbf{B}$ is thus

$$\dot{d}_\alpha = \sum_{\alpha' \in \mathbf{B}} \left[l_{\alpha\alpha'} + g_{\alpha\alpha'}(t) \right] d_{\alpha'} - \tfrac{1}{2} \sum_{\alpha',\alpha'' \in \mathbf{B}} n_{\alpha'\alpha''\alpha}d_{\alpha'}d_{\alpha''}. \tag{5.21}$$

Reconstructing the field $w(x,t)$ from its wavelet coefficients d_α, $\alpha \in \mathbf{B}$, we may see that (5.21) is just (5.4) written in wavelet space, and we can similarly obtain the evolution of the norm as in (5.5). Furthermore, (5.14) is just the special case of (5.21) in which $\mathbf{B}$ contains a single mode.

From Sec. 5.3.1 we know that if $\mathbf{B}$ contains only sufficiently small-scale modes, then tracking occurs; previously we have seen that if $\mathbf{B}$ contains a single large-scale mode, then the difference grows exponentially. The general case is much more difficult, even if we only consider the *linear* stability of the synchronization subspace: for small differences d_α, we can linearize (5.21) to give

$$\dot{d}_\alpha \approx \sum_{\alpha' \in \mathbf{B}} \left[l_{\alpha\alpha'} + g_{\alpha\alpha'}(t) \right] d_{\alpha'} \quad \stackrel{\text{def}}{=} \quad \sum_{\alpha' \in \mathbf{B}} A_{\alpha\alpha'}(t) d_{\alpha'}. \tag{5.22}$$

For driving by a spatiotemporally chaotic solution v, we expect that $g_{\alpha\alpha'}(t)$ has mean zero for α, $\alpha' \in \mathbf{B}$, so that the time average of $A_{\alpha\alpha'}(t)$ is just $l_{\alpha\alpha'}$. Whereas in the case of a single equation (5.14), we could conclude exponential growth or decay according to the sign of the constant term $l_{\alpha\alpha}$, for a system of parametrically forced equations we cannot reach such general conclusions.

It is tempting to suppose that the matrix $A_{\alpha\alpha'}$ also, on average, inherits the eigenvalues of $l_{\alpha\alpha'}$, which would be the Lyapunov exponents for the growth or decay of differences d_α. However, the example of Mathieu's equation shows that the stability of the constant linear operator does not, in general, carry over to a parametrically driven system, even with mean-zero driving; in the present notation, by this example resonant instability is possible under sinusoidal forcing even if $l_{\alpha\alpha'}$ restricted to the model has only negative eigenvalues.

In our KS equation studies, the parametric driving term $g_{\alpha\alpha'}(t)$ is chaotic; while this may eliminate resonance effects, it is analytically less tractable. If the possibility of synchronization— that is, $d_\alpha(t) \to 0$ for all resolved modes α—depends only on the eigenvalues of the constant matrix $l_{\alpha\alpha'}$ restricted to the freely evolving modes, then in the experiments of Sec. 5.3.1 in which we left some or all of level $j = 4$ to evolve freely within the model, driven by the lower modes $j = 0$–3 and the remainder of level 4, we would never expect tracking, contrary to our experimental observations. While the simulations of Figs. 5.12, 5.15 and 5.16 are admittedly inconclusive, in Fig. 5.14(b) there does seem to be definite exponential decay to tracking when alternate modes of level 4 (and all modes of levels $j = 0$–3) are driven by the remainder. This suggests that spatial effects, which are not transparent in (5.22), can play a role in synchronization, and indicates that the stability of $l_{\alpha\alpha'}$ is in general insufficient to determine the average behavior under the linearized matrix $A_{\alpha\alpha'}(t)$. Making any statement about the stability of the "synchronization subspace" $d_\alpha = 0$, $\alpha \in \mathbf{B}$ more precise would be a difficult problem, especially as the matrices $l_{\alpha\alpha'}$ and $g_{\alpha\alpha'}(t)$ do not commute, and we do not attempt to pursue this issue further here.

Energy evolution under external driving   In the case of a single freely evolving mode, the linear stability completely determines the evolution and energy growth due to the absence of a nonlinear term in (5.14). In the general case, we expect that the quadratic terms in (5.21) provide energy transfer among the modes of the model. However, these terms do not affect the overall energy balance of the internal modes:

$$\sum_{\alpha,\alpha',\alpha'' \in \mathbf{B}} n_{\alpha\alpha'\alpha''} d_\alpha d_{\alpha'} d_{\alpha''} = 0;$$

in terms of the reconstructed $w(x,t)$, this is equivalent to the fact that the ww_x term conserves energy (see (5.5)). The "internal" energy of the model $\|w\|^2 = \sum_{\alpha \in \mathbf{B}} d_\alpha^2$ thus evolves as

$$\tfrac{1}{2} \frac{d}{dt} \sum_{\alpha \in \mathbf{B}} d_\alpha^2 = \sum_{\alpha,\alpha' \in \mathbf{B}} \left[l_{\alpha\alpha'} + g_{\alpha\alpha'}(t) \right] d_\alpha d_{\alpha'}. \tag{5.23}$$
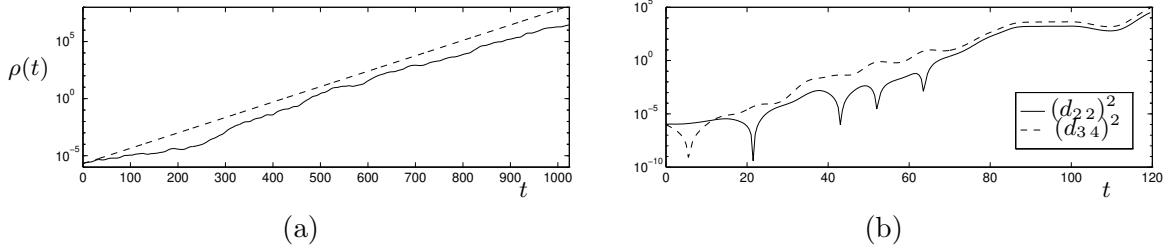
Figure 5.19: (a) Exponential growth of energy when the large-scale modes at level $j = 1$ are driven by the control run; the dashed line corresponds to growth at the largest eigenvalue of $l_{\alpha\alpha'}$ restricted to level 1. (b) Growth of two unstable modes a_{22} and a_{34} driven externally, with a single stable mode a_{53} supplying insufficient damping.

If all the resolved modes a_α, $\alpha \in \mathbf{B}$ are linearly unstable, and all stable modes participate in the driving, we thus expect that (on average) the operator $A_{\alpha\alpha'}$ is positive definite, and hence that the total energy grows exponentially, just as in the case of a single free unstable mode. This is corroborated for a particular example in Fig. 5.19(a), where the two modes of level $j = 1$ (with small initial discrepancy from the control: $|d_{1k}(0)| = 0.001$) are driven by the control run; both a_{10} and a_{11} grow exponentially, as does their energy, at a rate which is well approximated by the largest eigenvalue of $l_{\alpha\alpha'}$ restricted to level 1. We have observed similar exponential growth when the seven wavelet modes of levels $j = 0$–2 are driven by all the rest (not shown).

If some of the modes retained in the model are damped by the linear operator, then the quadratic term can facilitate energy transfer from unstable to stable modes and forestall exponential growth of the solutions; this is the case in Fig. 5.17. Such damping is not guaranteed, however; the interaction between the retained stable and unstable modes should be sufficiently strong. The simulation of Fig. 5.19(b) shows what may occur otherwise: the (arbitrarily chosen) damped a_{53} mode—admittedly distant from the other two modes in space and scale—is unable to prevent blowup of the unstable a_{22} and a_{34} modes when these three modes are driven by the control run. Even when enough stable modes are retained within the model to permit sufficient energy transfer and damping, it is possible that the unstable modes grow to unusually large amplitudes before the damping takes over; this effect is observed in several experiments of Sec. 6.1.

Summary   A heuristic expectation based on (5.22) would thus be that if the set $\mathbf{B}$ contains one or more large-scale, linearly unstable modes, so that $l_{\alpha\alpha'}$ for α, $\alpha' \in \mathbf{B}$ has positive eigenvalues, then the synchronization subspace is, on average, linearly unstable and tracking does not occur. Furthermore, if $\mathbf{B}$ contains only unstable modes, or if the interactions with resolved stable modes are too weak, then the model undergoes exponential growth. This is borne out by the experiments of this Section, as well as ones described in Sec. 6.1 below. However, the simulations of Sec. 5.3.1 appear to contradict our simple expectations based on the eigenvalues of $l_{\alpha\alpha'}$ on the resolved subspace, as they seem to indicate that one can achieve tracking without forcing at all the modes of level $j = 4$. This interesting issue of synchronization and tracking is thus presently unresolved and should be investigated further elsewhere.

141

5.3.3   Discussion

We review our results and observations of this Section concerning theory and experiments in which some wavelet levels or modes are driven by time series obtained from an independent control run of the KS equation, and none are eliminated:

- Driving at a contiguous band of (large-scale) wavelet levels $j = 0$–$\tilde{j}$, for any $\tilde{j}$, with time series obtained from a KS integration yields the "correct" qualitative dynamics and statistics; the interesting issue here is the possibility of tracking.

- Provided sufficiently many large-scale modes in a continuous band are externally specified from an independent KS integration, the small scales are entrained at an exponential rate to a unique trajectory specified by these low modes.

- Numerical experiments indicate that driving at levels $j = 0$–3 for $L = 100$ is insufficient for the previous result to hold. Although preliminary computations with a large time step δt indicated tracking, more accurate simulations with smaller δt failed to confirm this.

- Forcing up to and including all of level $j = 4$ certainly gives exponential decay to the control run; and it appears that driving only some of the level 4 modes, together with $j = 0$–3, may be sufficient to entrain the other modes.

- Entrainment does not occur in the opposite direction: Active- and small-scale modes do not enslave the large scales; on the contrary, the "synchronization subspace" appears to be, on average, linearly unstable.

- A special case of the previous statement is that if one or several large-scale, unstable modes evolve independently, being driven by all the other modes—in particular, no linearly stable modes remain in the model to evolve freely and respond to the growth of the unstable modes— there is exponential growth and divergence.
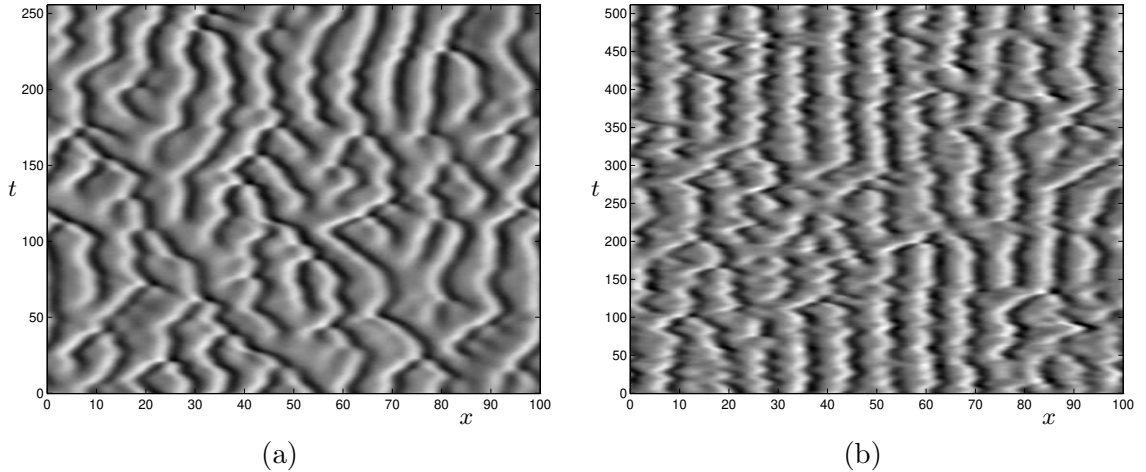
Figure 5.20: (a) Forcing at level $j = 2$ from an independent KS integration, and eliminating levels $j = 0$ and 1; (b) forcing at $j = 3$, eliminating $j = 0$–2.

5.4 Forcing from an independent run: Variations on a theme

In Sec. 5.2, we studied the dynamical significance of different scales by sequentially removing them from the system; while in the previous Sec. 5.3, we showed that retaining all levels, and applying statistically correct forcing from an autonomous run to some of them, almost always led to qualitatively accurate KS dynamics, so that the main question of interest was whether and when tracking and synchronization occurred. With the experimental apparatus we have developed, a much wider variety of interventions is accessible to us. In this Section, we manipulate the forcing modes and interactions in various ways, on the basis that we can best complete our understanding of the full spatiotemporally complex KS dynamics by learning what "goes wrong" in modified systems, obtained in a manner akin to "surgical intervention". The study most closely related to this philosophy of which we are aware, though for a more complicated system and not as wide-ranging as the present work, is that of Browning *et al.* [BHK98] mentioned previously.

5.4.1 Eliminating some levels, and forcing others

In Sec. 5.2 we looked at the effect of removing complete wavelet levels, and found that frequently the retained scales are capable of maintaining many aspects of the characteristic KS dynamics, with large scales keeping the system "alive" even in the absence of intervening levels. However, sometimes the system settles into a simple attractor because the retained large scales, evolving with the model, decay into a stationary or oscillatory state, and are thus incapable of successfully driving the active scales. By instead forcing the large scales from an independent KS simulation, we are better able to evaluate their contribution to maintaining the overall complex dynamics.

Forcing at levels 2 and 3 To begin this Section, we recall from Fig. 5.5 that removing levels $j = 0$ and 1 has little effect on the overall dynamics; clearly level 2 remains sufficiently active. Forcing level 2, instead of letting it evolve as part of the model, hardly seems necessary then, and the result is reminiscent of normal KS behavior (Fig. 5.20(a)). We include this simulation for comparison, and as a reminder of how to place these experiments in the general framework of Sec. 5.1: We force at level 2, and set levels 0 and 1 to zero; the internal modes $a_\alpha = a_{jk}$ ($\alpha \in \mathbf{B}$)

143
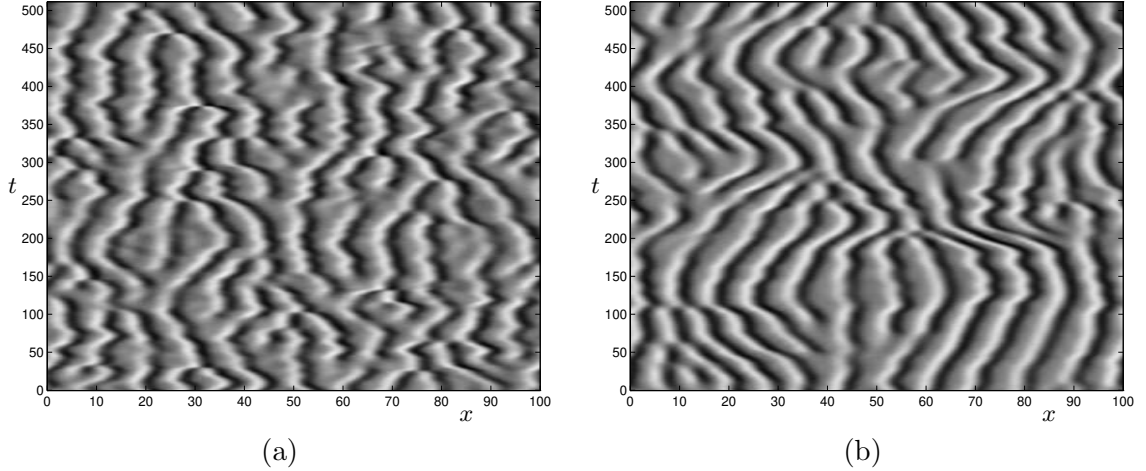
Figure 5.21: (a) Forcing from an independent run at level $j = 2$, and eliminating levels $j = 0, 1$ and 3; (b) forcing at level $j = 1$, eliminating $j = 0, 2$ and 3.

evolving within the model thus have $j \geq 3$, and initial conditions **a**. For the other modes, we set $a_{jk}(t) = 0$ for $j = 0, 1$, and $a_{jk}(t) = b_{jk}(t)$ for $j = 2$, where the $b_{\alpha'}$ are wavelet coefficients from a control integration of the KS equation with initial conditions **b**.

As shown in Fig. 5.4(c), when the lowest three levels $j = 0$–2 are eliminated, the system settles down to a more rigid state, and eventually falls into a stationary cellular state, in which levels $j \geq 3$ take time-independent values. Fig. 5.20(b) shows, to $t = 512$, a simulation where level $j = 3$ is forced externally instead of remaining in the model. As we observed for early times in Fig. 5.4(c), the dynamics appears rigid. While characteristic defect creation and annihilation events still occur—we have previously shown that level 3 plays the major role in facilitating these events— the local maxima remain largely stationary, with few traveling wave-like structures familiar from the true KS equation. This experiment thus confirms that while level 3 is responsible for most local coherent structure interactions, one or more of the large scales $j = 0$–2 is needed to establish and maintain more global, traveling dynamics.

Local events in the absence of level 3 While level 3 appears to be most important for generating local events—witness the effect of removing this level, in Fig. 5.7—it need not necessarily be present for such events to occur. In Fig. 5.21(a), we show a simulation in which level 2 is forced from an independent run, while levels 0, 1 and 3 are set to zero. The dynamics are reminiscent of normal KS dynamics; peak collisions and creation occur as usual. Even though level 3 is not present in this model, the level 2 forcing derives from a full KS run in which level 2 is properly interacting with level 3. Thus it seems that one way in which level 3 ensures the presence of the typical events is via its interactions with the larger scales to generate the correct dynamics and statistics at those levels. Once the behavior of level 2, say, is consistent with the generation of local events, level 3 is no longer required to be present in the model in order for those events to occur. Note however that the events in Fig. 5.21(a) occur on a somewhat slower timescale than usual (the plot extends to $t = 512$), as they are driven by level 2, instead of directly by the more rapidly varying level 3.

A similar effect is observed in Fig. 5.21(b), in which the model is driven by level 1, with levels 0, 2 and 3 eliminated. By comparison with Fig. 5.8, there are still dynamical events, since the

144
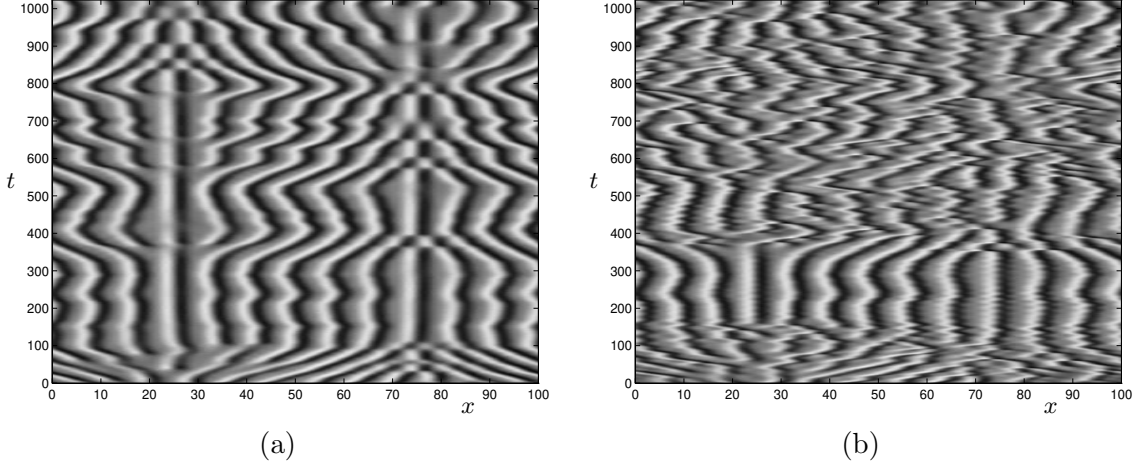
Figure 5.22: Nonlocal information transfer to the active scales across missing levels, shown by forcing a_{00} at level $j = 0$, and removing intervening levels: (a) eliminating $j = 1$–3; (b) eliminating $j = 1$ and 2.

forcing level 1 has the correct behavior; however, they occur at the much longer time and larger space scales consonant with level 1. Similar dynamics is observed if the model is forced at levels 0 and 1, still setting $j = 2$ and 3 to zero (not shown).

Note that it appears that level $j = 3$ needs mainly to induce the "correct" Gaussian noise at the larger scales. In Sec. 5.5.2 we check this by replacing the deterministically generated large scale modes from the control run, as studied here, by a stochastic process; and we obtain remarkably similar results.

Information transfer past missing modes

In the last-mentioned simulations, the lowest modes drive the most active scales, in spite of the absence of the intervening levels 2 and 3. This is an appropriate place to revisit the issue of nonlocal (in scale) energy transfer, which we previously encountered at the end of Sec. 5.2. We saw there that information could be directly transferred from level 0 to 4, when the intermediate levels were missing; although in the experiment reported in Fig. 5.9, when level 0 was allowed to evolve as part of the model, the solution was eventually absorbed into the cellular state.

This immediately suggests the question of whether the system can "stay alive" if level 0 is externally specified and remains active. In Fig 5.22(a), we see that this is indeed the case; level 0 can force the active scales, and there is nonlocal energy transfer.

The dynamics of this model, however, apart from being very slow (note the time axis), are somewhat peculiar. There is an apparent symmetry about the lines $x = L/4$ and $x = 3L/4$, which are the zeros of the largest scale wavelet $\psi_0(x)$. All events reminiscent of collisions or creation of peaks occur in the vicinity of these lines; in the intervening regions there is only bulk traveling wave motion. For the typical annihilation and creation events, we need to break the symmetry, and clearly, level 1 or preferably level(s) 2 and/or 3 needs to be present.

The behavior observed in Fig. 5.22(a) is completely determined by the time history of the forcing mode at level 0, that is, $b_{00}(t)$ from the KS simulation with initial conditions **b**, which is plotted in Fig. 5.23. For instance, note that the velocity of the traveling peaks depends on the amplitude of b_{00}, and the direction of motion on the sign of the forcing; when $b_{00} > 0$, the waves in the
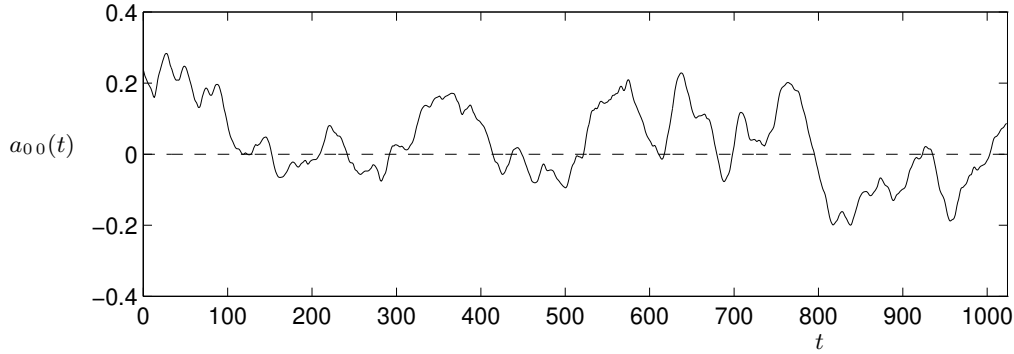
Figure 5.23: Time history of the large scale forcing mode at level 0, $a_{00}(t) = b_{00}(t)$, obtained from a KS simulation with initial data **b** and used to drive the experiments in Fig. 5.22.

middle of the domain ($30 \leq x \leq 70$) travel to the right, and *vice versa*. We will account for these observations below by discussing more carefully the effect of large-scale forcing on KS dynamics.

The fact that level 0 completely determines the behavior at levels $j \geq 4$ in this experiment should not be surprising. We have completely specified the time histories for the lowest 4 levels, $j = 0$–3 (here by fixing levels 1–3 to vanish)—as indeed we also did in the previously discussed simulations shown in Figs. 5.20(b) and 5.21(a,b). We already know from our previous tracking experiments of Sec. 5.3.1 that in certain situations, specifying all wavelet levels up to $j = 3$ appeared to suffice for tracking. For general forcing, this seemed to be a numerical artifact without at least some specification of level 4 modes, but it may be unsurprising that if we, for instance, remove levels 1–3 altogether, level 4 rapidly locks into a unique trajectory determined by the lowest mode.

Complex spatiotemporal dynamics in the absence of levels 1 and 2   The experiment of Fig. 5.22(a) has shown that level 0 can transfer information to distant wavelet levels and maintain activity in the system, but that the ensuing dynamics is unusual and uniquely determined by $b_{00}(t)$. If we retain level 3 in the model, complex spatiotemporal dynamics are possible, as shown in Fig. 5.22(b). We recall from Fig. 5.4(c) that if all of levels 0–2 are removed, the system settles to a cellular state; levels $j \geq 3$ will not independently maintain active dynamics. This accounts for the behavior in the range $150 \leq t \leq 350$ in Fig. 5.22(b), which remains close to a cellular state because the forcing mode is near zero (see Fig. 5.23). As shown in Fig. 5.10, on the other hand, level 0 can communicate across the missing levels 1 and 2 and, in the absence of these levels, maintain disorder in the system. However, in that simulation, a_{00} evolved independently, and frequently fell into an oscillation, presumably on the unstable manifold of the cellular state.

By forcing the lowest mode with a time series from an independent KS simulation,[†] we forestall the oscillations, and the system remains in a spatiotemporally disordered state. Inspection of the statistics for this model (Fig. 5.24) indicates that the properties of this state are somewhat different from the ordinary KS equation, however. In particular, the relative enhancement of large-amplitude values in the PDFs for u and the wavelet coefficients shows that this model, in the absence of the noisy levels 1 and 2, is closer to a cellular state than the KS equation, a feature we already observed in other experiments in Sec. 5.2 in which entire levels were eliminated.

[†]We obtain similar results, in fact, on forcing with a stochastic process; see Sec. 5.5.2 and Figs. 5.43(b) and 5.44 below.
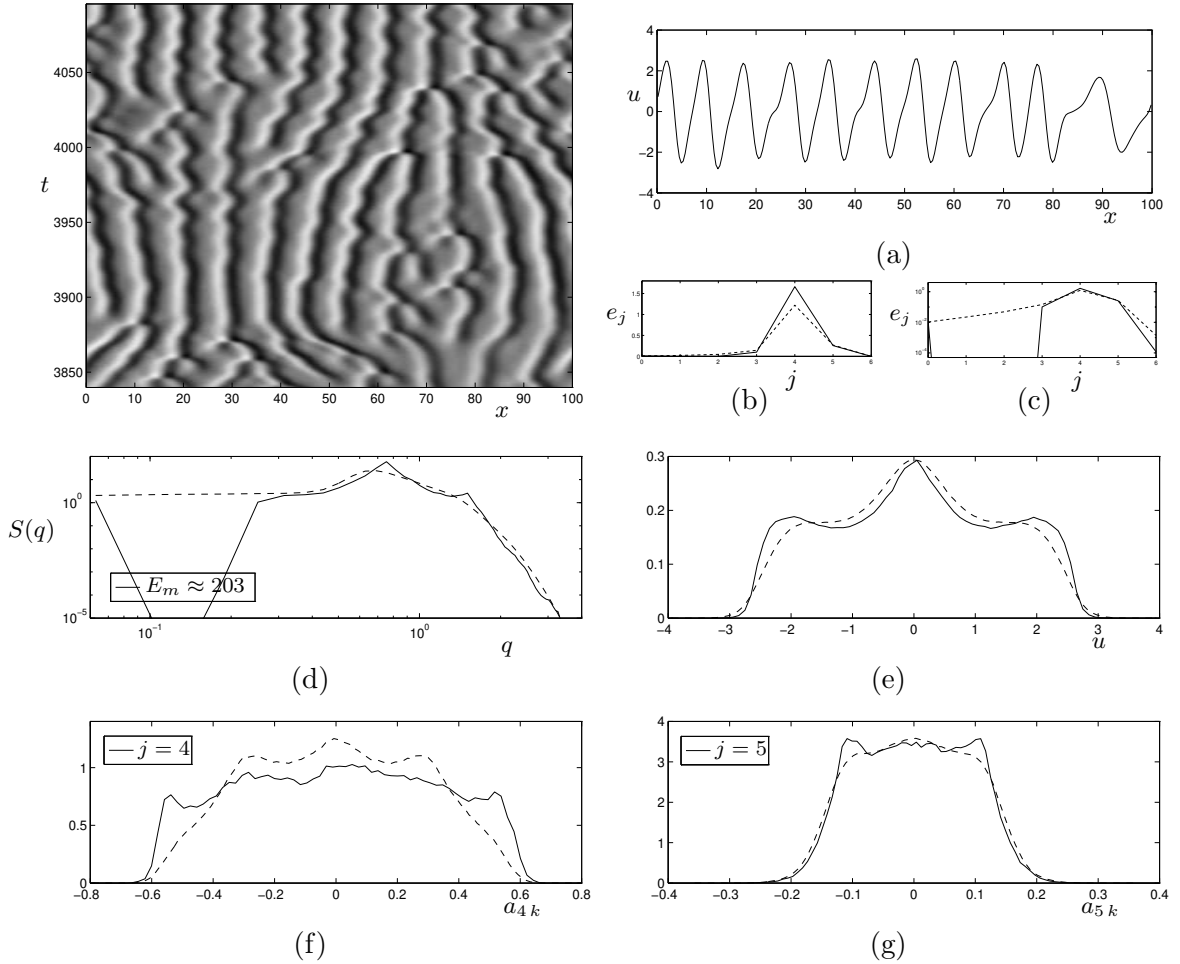
Figure 5.24: Comparison of model statistics with full KS equation: Forcing at level $j = 0$ from autonomous run, setting levels 1 and 2 to zero, as in Fig. 5.22(b). See caption of Fig. 5.5 for description. Autocorrelation time $\tau_c \approx 17$.

Summary   As long as there is some means of ensuring that the large scale mode retains the correct amplitude and temporal behavior, and doesn't fall into a near-zero or oscillatory state (for levels 0 and 1, the modes may need to be forced externally), then any of the large scales $j = 0, 1$ and 2 is able to drive the active scales and maintain spatiotemporal disorder, even in the absence of the other two.

Drift induced by the large scales

In Sec. 1.2.1 we have already seen that a solution to the KS equation with nonzero mean can be constructed from a zero mean solution and a drift; see (1.9). Specifically, a positive mean value m corresponds to motion to the right, or positive x values, with velocity m. Since the KS equation dynamics are spatially localized (see Sec. 4.3), it seems plausible that if a sufficiently large local mean were to occur over a relatively large distance, say on the order of a few characteristic wavelengths, then this would induce a local drift.

This simple explanation accounts for the behavior of Fig. 5.22(a), in which the model dynamics follows the large-scale mode at level 0. We recall that the lowest level wavelet $\psi_0(x) \approx -\cos(2\pi x/L)$

(a)   (b)
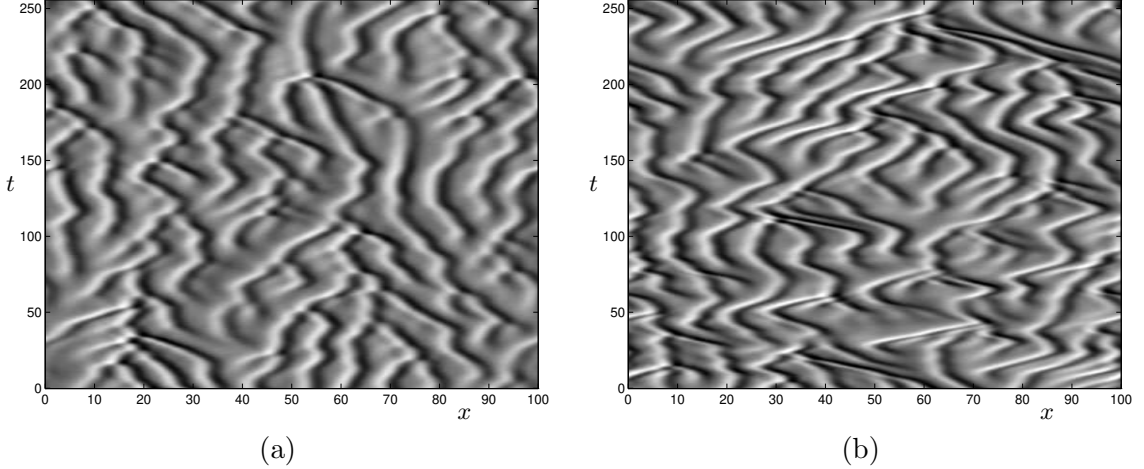
Figure 5.25: Mixing modes: (a) Forcing from an independent run at levels $j = 0$–2, with modes permuted, as described in the text. (b) Forcing at levels $j = 0$ and 1 with modes taken from $j = 4$ of the reference run.

has zeros at $x = L/4$ and $3L/4$, and is positive for $L/4 < x < 3L/4$ and negative outside this region. Its local mean is thus positive and largest near $x = L/2$, falling off away from the center and reaching a minimum at $x = 0$ (which is the same point as $x = L$, by periodicity). The magnitude of the drift velocity of the peaks is readily seen to decay away from the extrema of $\psi_0(x)$, while the dynamics is stationary at the zeros of $\psi_0(x)$. The direction of drift is given by the sign of $b_{0\,0}(t)\psi_0(x)$: if the coefficient $b_{0\,0}(t)$ of this mode is positive, the peaks near $x = L/2$ move to the right, and *vice versa*.

We can use this account to understand heuristically many other cases of rapidly traveling peaks in this thesis. In the experiments of Sec. 4.3.3, for example, in which we investigated the effects of cutting spatial interactions, we observed that an excess of energy in the low, large-scale modes was correlated with a rapid small-scale drift. In the remainder of this Section, we will encounter other related examples.

5.4.2 Forcing with incorrect statistics

We established in Sec. 5.3 that forcing with the "correct" statistics results in the "correct" KS-like dynamics. This invites the question: What if we do not force with the correct statistics?

There are arbitrarily many ways in which one can manipulate the forcing, even if using only the time series from the control run with initial conditions **b**. As we hope to extract some general principles in addition to those we have previously obtained, we rather perform a few more focussed experiments, than attempt to be exhaustive.

Mixing the forcing coefficients

The two experiments shown in Fig. 5.25 demonstrate some examples in which inappropriate forcing is applied at the lowest wavelet levels. In Fig. 5.25(a), we force at levels $j = 0$, 1 and 2, permuting some coefficients. (Specifically, for the computation shown, we arbitrarily set $a_{0\,0} = b_{2\,0}$, $a_{1\,0} = b_{2\,3}$, $a_{1\,1} = b_{1\,0}$, $a_{2\,0} = b_{0\,0}$, $a_{2\,1} = b_{2\,2}$, $a_{2\,2} = b_{1\,1}$, and $a_{2\,3} = b_{2\,1}$.) Recalling the wavelet distributions of Fig. 4.14 and characteristic times τ_j of Fig. 4.13 and Table 4.1, we note that in this manipulation the forcing coefficients have incorrect time scales, though their distributions appear correct (levels
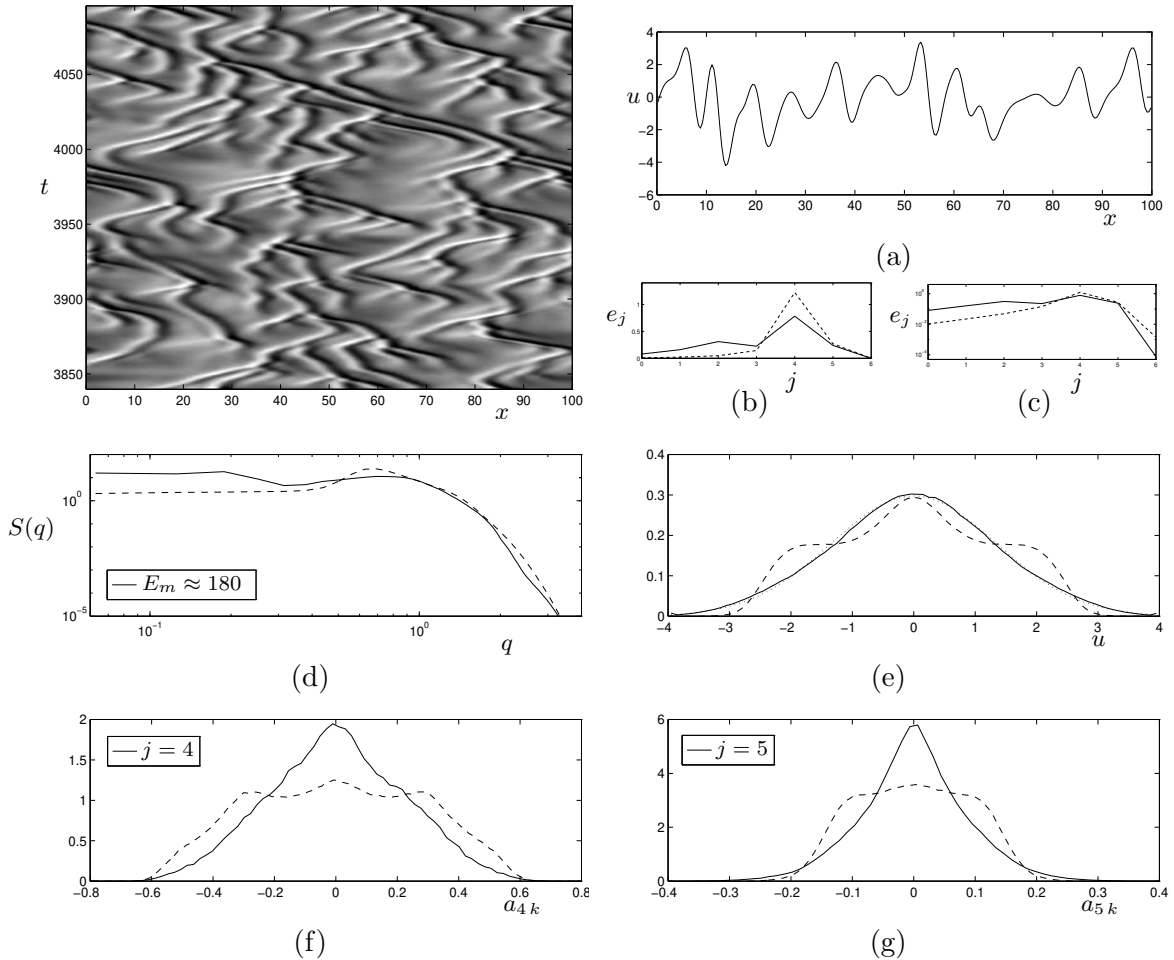
Figure 5.26: Comparison of model statistics with full KS equation: Forcing at levels $j = 0$, 1 and 2 with modes taken from level 4 of autonomous run. See caption of Fig. 5.5 for description; in (e) a Gaussian distribution is superimposed on the PDF for u. Autocorrelation time $\tau_c \approx 5.3$.

$j = 0$, 1 and 2 have Gaussian PDFs with the same amplitude). Also, through our scrambling we have undone the correlations between adjacent wavelet coefficients in the forcing terms. These manipulations do not appear to have harmed the modes a_{jk}, $j \geq 3$ much: the dynamics of Fig. 5.25(a) look qualitatively correct.

The same is not true of the simulation of Fig. 5.25(b), however. In this experiment, we forced at levels 0 and 1, replacing the (correct) coefficients with some taken from level 4. Recalling again the typical wavelet coefficient distributions, amplitudes and time scales, in this case the forcing is both too rapid, and too strong (amplitudes are too large). These manipulations yield a system which apparently has the typical KS dynamics, but occurring too rapidly. In fact, the ensuing distributions for u and the wavelet coefficients (not shown) also deviate from their typical KS forms; an effect which is even more pronounced in the next experiment.

In Fig. 5.26 we see a simulation, with corresponding statistics, for a run in which levels 0–2 are forced by cofficients from level 4. (The actual prescription for the experiment, chosen arbitrarily, was $a_{00} = b_{47}$, $a_{10} = b_{410}$, $a_{11} = b_{42}$, $a_{20} = b_{40}$, $a_{21} = b_{45}$, $a_{22} = b_{414}$, and $a_{23} = b_{46}$.) Observe how much the system has been "deformed": While typical events still occur, they are more rapid (note the low correlation time τ_c) and there are regions which are free of peaks altogether. Meanwhile, the

149

u and wavelet distributions are strongly peaked at zero: In fact, the field u has an almost Gaussian distribution, while the level 4 and 5 wavelets spend a disproportionate time near zero, implying the localized absence of structure and the low energy in level 4. Note how the large-amplitude forcing is reflected in the unusually high energy in the low modes; remarkably, the total model energy E_m is very close to that of the KS equation.

As we have noted, when we force at the lowest levels from level 4 (we expect that forcing from levels 3 and 5 would give similar results) we are forcing with time scales and amplitudes inconsistent with the usual KS equation (in fact, the PDFs of these forcing terms are also "wrong", but we will not pursue this point further). While Fig. 5.25(a) already indicates that changing the time scales may be less important, these "mixing" experiments do not permit the effects of amplitude to be studied independently of time scales of forcing. Keeping these experiments on the effects of forcing from the "wrong" levels in mind, we therefore proceed to isolate the two perturbations, of *amplitude* and *time scales* of forcing.

Varying the time scale of forcing

We have performed several experiments in which the time series of the forcing coefficients are speeded up or slowed down by a factor of 2 or 4, qualitatively inspected the resulting simulations, and computed the usual statistics. In practice, we achieve the discrepancy in time scales by, as always, computing the model and the control run simultaneously, and replacing model coefficients by forcing at each integration step; but the size of the time step δt for the driving control run with initial data **b** is changed by the appropriate factor (taking care that it remains small enough to give a statistically accurate KS solution), which has the effect of increasing or decreasing the forcing rate.

Some representative results are shown in Fig. 5.27. We have forced at level 0 (a), and at level 1 in the absence of level 0 (b); speeding up the forcing by factors of $\frac{1}{2}$, 2 and 4. For these runs, we might expect that the remaining large scale level 2, which also keeps the system disordered, might counteract the effect of varied time scales at the lowest levels; so we have also performed experiments in which we force at levels 0, 1 and 2 (c), and in which we force at level 0, eliminating levels 1 and 2 (d). We have only shown results for a few of the permutations.

While the simulations often look qualitatively slightly different from the usual KS equation, as evidenced by the results presented, the statistical properties of the solutions are essentially indistinguishable from the "correct" values; energy distributions, PDFs and also the overall autocorrelation times τ_c are as usual. (For the experiments in which we forced at level 0 with varying speeds, in the absence of levels 1 and 2, the statistics are in fact different from those of the KS equation, but in this case agree with each other and with those of Fig. 5.24 above, showing that the determining effect here is the missing levels, not the varying time scales of forcing.)

We demonstrate this robustness of KS dynamics by a fairly extreme example in Fig. 5.28. For this experiment, we speed up the forcing coefficients at the lowest three levels $j = 0$, 1 and 2 to a rate ten times their usual speed; that is, we use $a_{jk}(t) = b_{jk}(10\,t)$ for $j \leq 2$. The effect of this rapid forcing is seen in the fine scale temporal structure in the peaks of the simulation, and in the evolution of the wavelet coefficients in the model. Ignoring these rapid oscillations superimposed on the time evolution, however, the characteristic KS dynamics is again observed: the spatial structure is unaffected, the PDFs appear correct, and the typical events occur at the usual time scales. More significantly, not only is the overall time constant τ_c accurate, but the time scales τ_j for $j \geq 3$ all agree closely with the standard KS values of Table 4.1.
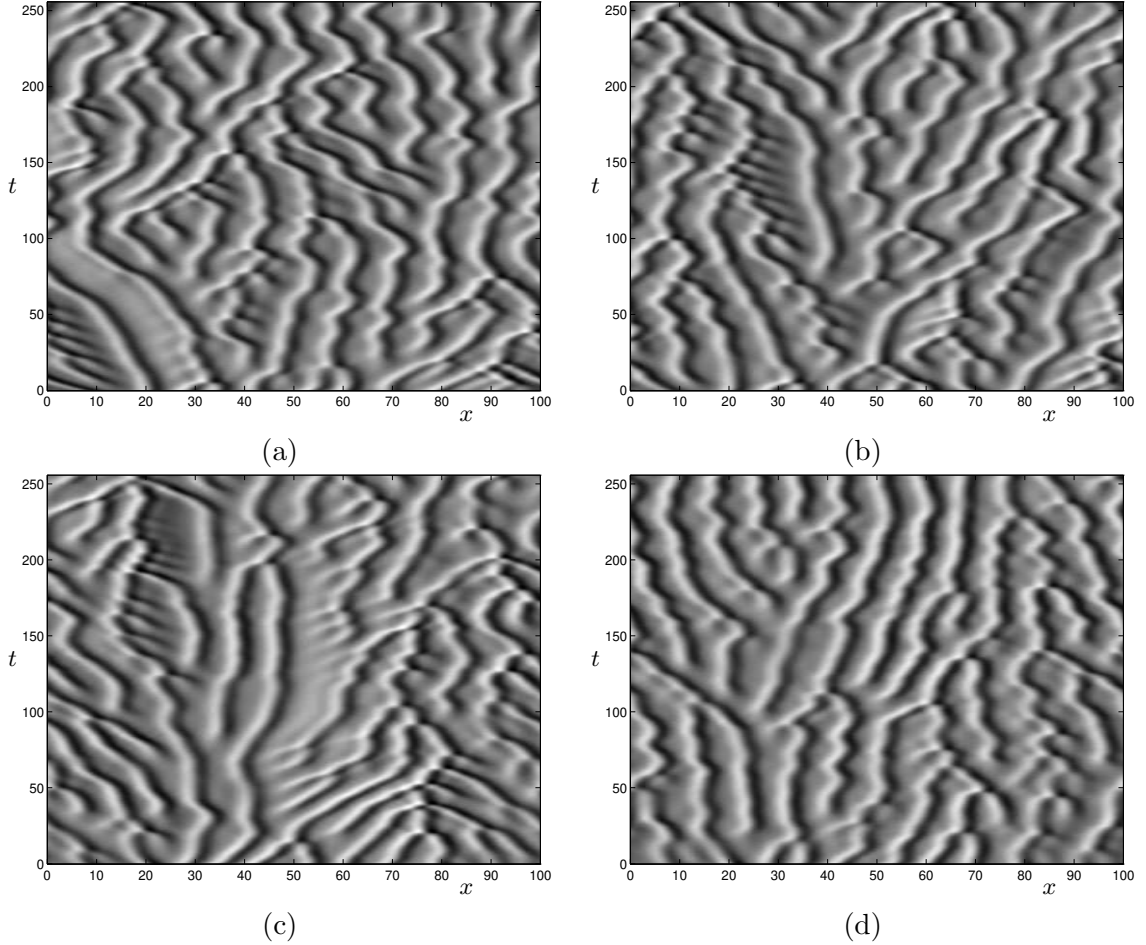
Figure 5.27: Varying the time scale of the forcing: (a) Forcing at level $j = 0$, from an independent run speeded up by a factor of two; that is, $a_{0\,0}(t) = b_{0\,0}(2t)$; (b) slowing down level $j = 1$, eliminating $j = 0$, that is, $a_{0\,0}(t) \equiv 0$, $a_{1\,k}(t) = b_{1\,k}(t/2)$; (c) slowing down levels $j = 0\text{--}2$, $a_{j\,k}(t) = b_{j\,k}(t/2)$, $j = 0\text{--}2$; (d) speeding up level $j = 0$, $a_{0\,0}(t) = b_{0\,0}(4t)$, and eliminating $j = 1$ and 2.

These experiments thus indicate a remarkable *robustness* of the temporal dynamics of the active scales of the KS equation. We already know that the large scales $j = 0\text{--}2$ are necessary to maintain the spatiotemporal disorder, and keep the system "alive"; but given forcing of the correct amplitude, the active scales are able to compensate and respond at their intrinsic time scales, largely independent of the large scale forcing rate over some range. If, indeed, the sole purpose of the large scales is to provide Gaussian excitation, then the effect of these experiments is merely to vary the rate at which we are sampling the Gaussian distribution; in this interpretation, it is fairly unsurprising that temporal variations in the driving have little effect (see also Secs. 5.5.1 and 5.5.2).

Varying the amplitude of forcing

Since it is now apparent that the *temporal* characteristics of the time series derived from level $j = 4$ are innocent of causing the disruption in the dynamics observed in Fig. 5.26, we might surmise that it is the larger *amplitudes* of these forcing coefficients that are the culprits. To test this deduction, we experiment with varying the amplitude of the forcing, while retaining the correct temporal behavior and distributions.
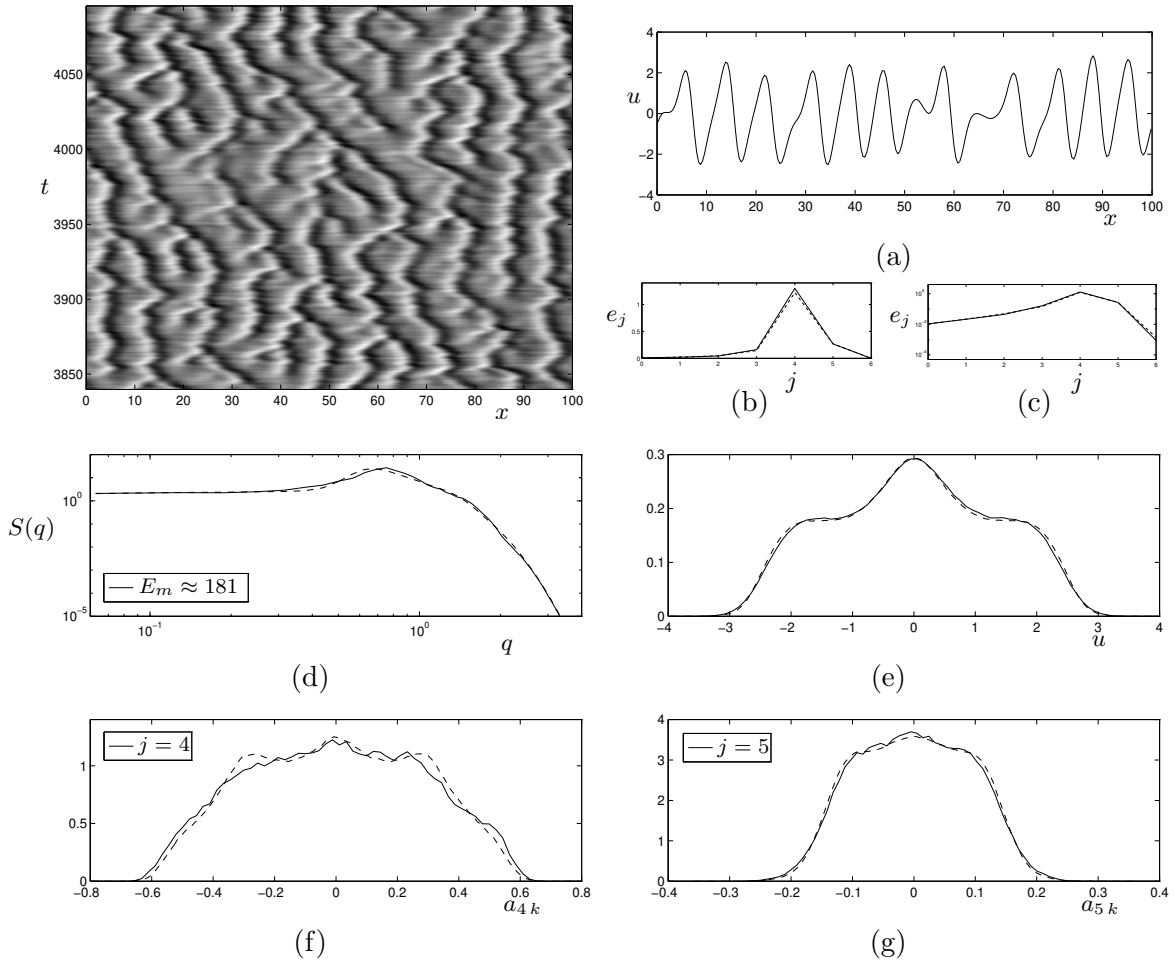
Figure 5.28: Comparison of model statistics with full KS equation: Forcing at levels $j = 0$–2 from an autonomous run, speeded up by a factor of 10. See caption of Fig. 5.5 for description. Autocorrelation time $\tau_c \approx 10$.

Excessive low-mode forcing In Fig. 5.29 we see some of the consequences of applying excessive amplitudes. In each case, as usual, the forcing is derived from the control run with initial conditions **b**. For (a), we force at the lowest two levels with double strength: $a_{jk} = 2\,b_{jk}$ for $j = 0, 1$. Typical dynamical events occur, but they appear to be speeded up (something accelerating the forcing could not accomplish). In fact, the statistics of this solution turn out to be quite similar to that of Fig. 5.25(b). Similar reasonable-looking, but slightly altered and more rapid dynamics occur if we double the amplitude at level 1, and eliminate level 0, as in Fig. 5.29(b), or if we force at double strength at $j = 2$, setting $j = 0$ and 1 to zero, as in (c).

The statistical effects of these manipulations are clearer and more pronounced when we double the amplitude of forcing at the lowest three levels, $j = 0$–2, as shown in Fig. 5.30. Both this simulation and the accompanying statistics look very similar to those of Fig. 5.26, indicating that excessive amplitude was indeed the cause of the altered dynamics in that case. On studying Fig. 5.30, it is interesting to note that (as in Fig. 5.26) the energy E_m is hardly changed from the full KS equation: firstly, the large scales only contain a small fraction of the energy (see Table 4.1) so that quadrupling the energy in these levels has little overall impact; and secondly, in the presence of all wavelet levels, the system is able to compensate for the extra energy at low modes by reducing

152
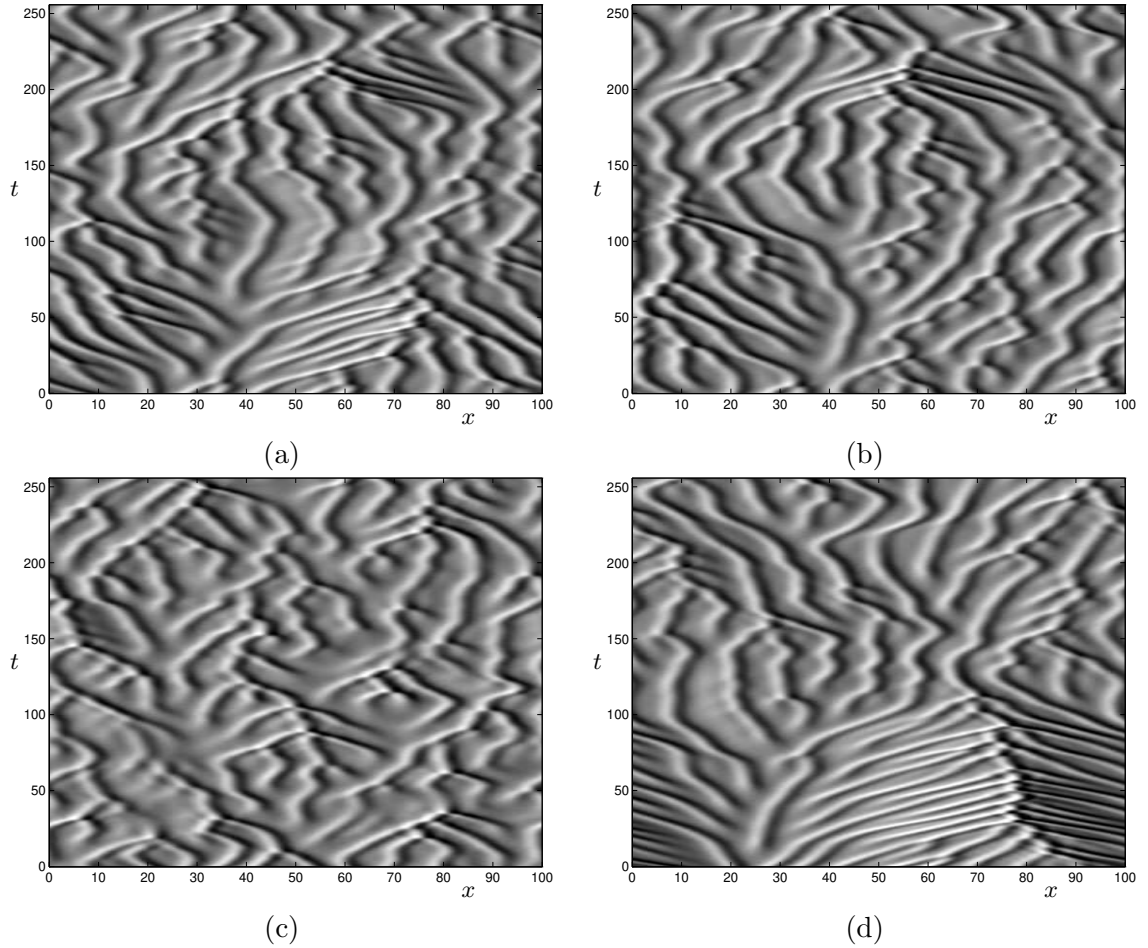
Figure 5.29: Large-amplitude forcing at the low modes from an independent run: (a) Doubling the amplitude at levels $j = 0$ and 1, $a_{jk} = 2b_{jk}$, $j = 0$, 1; (b) eliminating level $j = 0$, $a_{00} \equiv 0$, and doubling the amplitude at $j = 1$, $a_{1k} = 2b_{1k}$; (c) eliminating levels $j = 0$ and 1, and double strength forcing at $j = 2$, $a_{2k} = 2b_{2k}$; (d) quadrupling the amplitude of forcing at level $j = 0$, $a_{00} = 4b_{00}$.

it at the active scales (see Fig. 5.30(b)). This is achieved because the system is driven away from the perturbed cellular state to a more generally disordered state; the distributions for u and the wavelet coefficients are closer to Gaussians, spending a greater fraction of the time near zero. Note the smaller overall characteristic time τ_c, confirming that the dynamics has speeded up.

Rapidly traveling peaks due to varying local mean   We have already encountered two basic features of the KS equation:

- Under normal circumstances, a local (distorted) cellular structure dominates, maintaining the local mean near zero.

- A nonzero local mean on a scale of several characteristic wavelengths l_0 induces a drift, with peaks traveling rapidly with a speed and direction determined by the amplitude and sign of the local mean; this leads to what we shall call a *"ridge state"*.

153
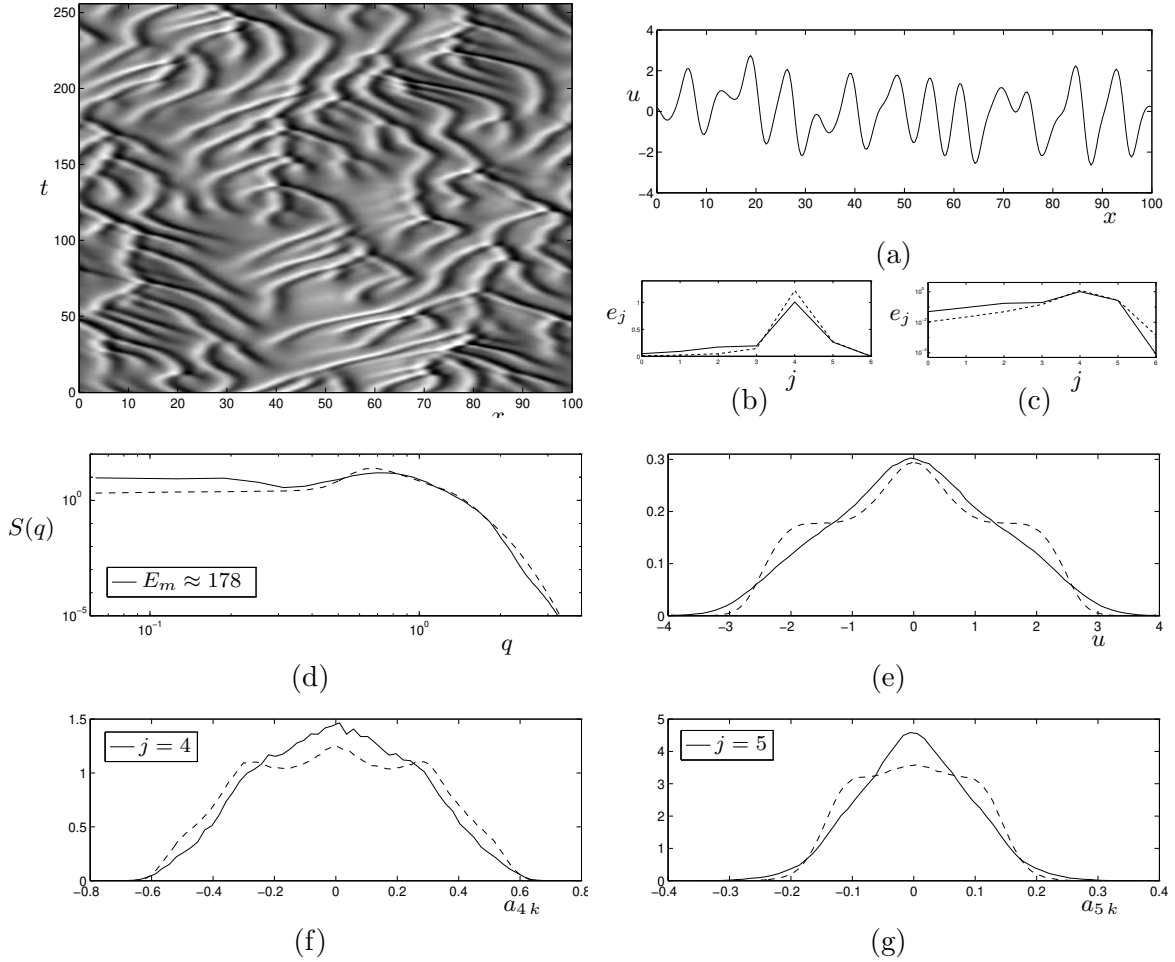
Figure 5.30: Comparison of model statistics with full KS equation: Forcing at levels $j = 0$–2 from an autonomous run, doubling the amplitude. See caption of Fig. 5.5 for description. Autocorrelation time $\tau_c \approx 6.1$.

These two elements combine transparently in Fig. 5.29(d), in which level $j = 0$ is forced at four times the usual amplitude, $a_{00} = 4\,b_{00}$; the time series $b_{00}(t)$, given in Fig. 5.23, can be used to predict the essential features of the simulation. For early times, the large-amplitude forcing is equivalent to a global underlying inhomogeneity of shape $\psi_0(x) \approx -\cos(2\pi x/L)$, and the direction of drift, to the right near $x = L/2$, follows since $4\,b_{00}(t) > 0$. The ensuing observed state, caused by excessive large-scale amplitudes relative to the usual distribution, is a quintessential example of what we term a *ridge state*. For $130 < t < 250$ in Fig. 5.29(d), on the other hand, $4\,b_{00}(t)$ is small enough to fall in the normal range (see the PDF for level 0 in Fig. 4.14), and the usual KS dynamics return.

Fig. 5.31(a) shows a later part of the same simulation as Fig. 5.29(d), over a longer time interval of length 512. Again, we can compare with the forcing time series of Fig. 5.23 and observe the alternating usual disordered KS dynamics and ridge states, including a change in direction of the drift as $4b_{00}(t)$ takes a large negative value, as occurs for instance near $t = 880$.

If we further increase the forcing amplitude, to ten times its regular value, we obtain Fig. 5.31(b) for the same time interval as (a). Here, of course, the amplitude is unusually large for a greater fraction of the time, with the ridge state predominating, but still with short intervals of normal
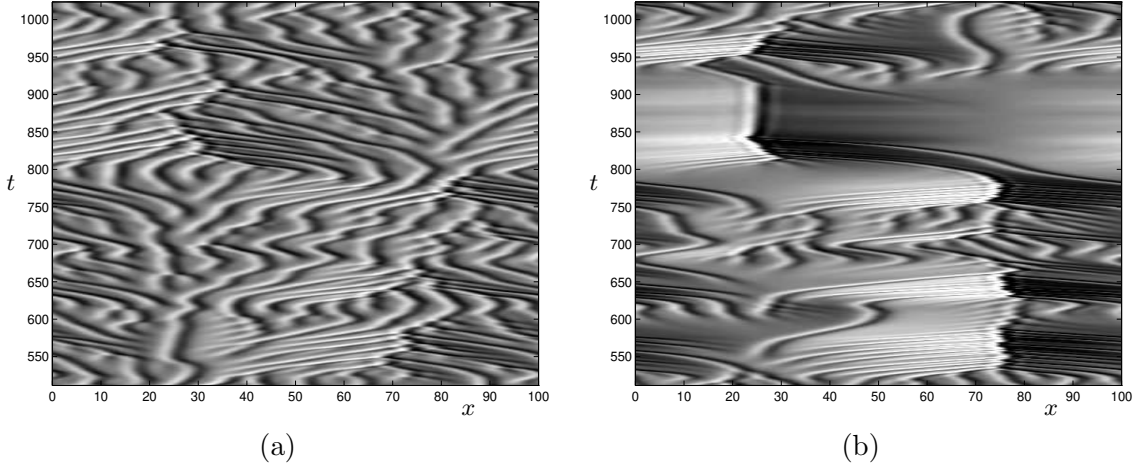
Figure 5.31: Rapidly traveling peaks and shocks due to excessive forcing at the low modes, level $j = 0$: (a) $a_{00}(t) = 4b_{00}(t)$; (b) $a_{00}(t) = 10b_{00}(t)$. The time series of the forcing $b_{00}(t)$ is shown in Fig. 5.23.
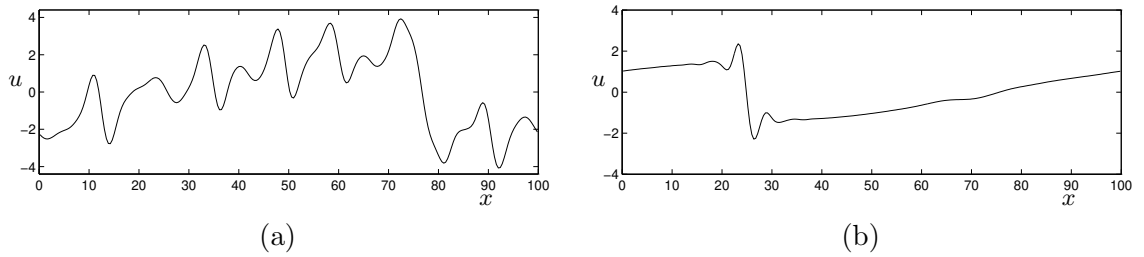
Figure 5.32: Spatial cross-sections of Fig. 5.31(b), showing (a) a ridge state at $t = 550$, and (b) a shock at $t = 880$; compare Fig. 2.1(b).

dynamics when $b_{00}(t)$ is near zero. In the ridge state, the velocity of the peaks is more rapid than before, commensurate with the increased local mean. Fig. 5.32(a) shows a cross-section at $t = 550$, showing an instantaneous configuration of peaks traveling up the slope in the ridge state. In the presence of even stronger forcing, as for $t = 850$–900, the temporal dynamics are washed out entirely, and a shock develops, as shown for $t = 880$ in Fig. 5.32(b). This is remarkably similar to the solution which we observed for the linearly destabilized KS equation in Sec. 2.3.3— see Fig. 2.1. This confirms that ultimately, these two techniques of pumping excess energy into the low modes, a global negative damping term or external forcing with large amplitude, have fundamentally equivalent effects.

We will return later to large-amplitude forcing at the low modes, in a more controlled manner, after discussing manipulation of the forcing at the active and small scales.

Forcing at the active scales We have seen that excessive forcing at the large scales can have a significant impact on the KS dynamics. At the active scales, we are not so interested in increasing the external forcing; after all, these are the levels we wish to include in any model for the spatiotemporally complex dynamics, possibly forced at the large scales. Thus our question here is slightly different.
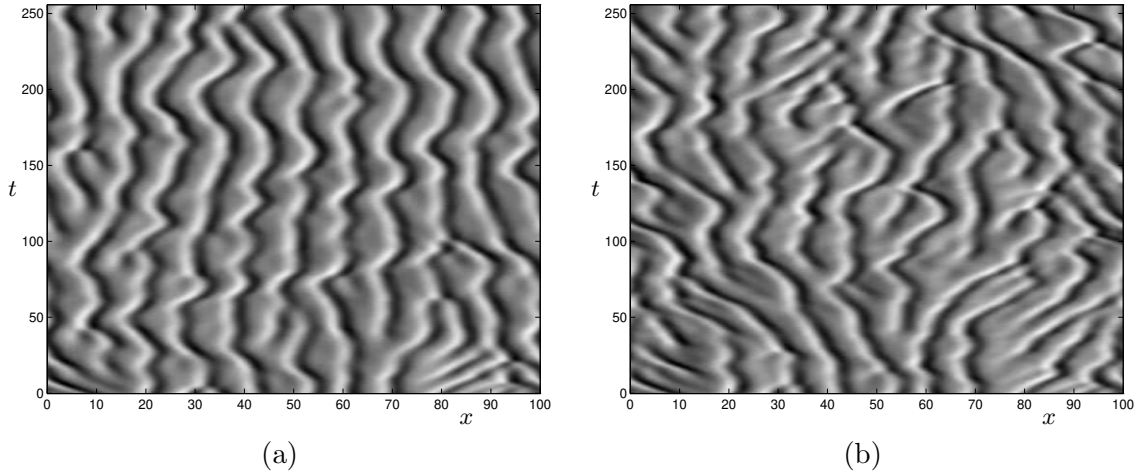
Figure 5.33: Low-amplitude forcing at level $j = 3$ from an independent run: (a) $a_{3\,k} = 0.25\,b_{3\,k}$; (b) $a_{3\,k} = 0.75\,b_{3\,k}$.

In Sec. 5.2 we have noted the effects of eliminating the active scales; in brief, level $j = 3$ can be removed at the cost of losing most of the typical events, while the penalty for setting levels 4 and/or 5 to zero is divergence of the solution, as the energy transfer mechanism is disrupted. What happens if we include the active levels, but at somewhat lower amplitude?

We have performed only a few exploratory experiments for levels 3, 4 and 5, and some results are displayed in Fig. 5.33. As seen in (a) of this Figure, forcing at level 3 with low amplitude (that is, $a_{3\,k} = 0.25\,b_{3\,k}$) still results in a dearth of defect annihilation and creation events (*cf.* Sec. 5.2.3). However, forcing at a larger fraction 0.75 of the usual amplitude appears to restore the events (Fig. 5.33(b)). We have not attempted to determine a transition between these two types of behavior.

Small-amplitude forcing at levels 4 and/or 5, on the other hand, still leads to blowup; but so does forcing at these levels from a control run with their full magnitude, that is, $a_{j\,k} = b_{j\,k}$ for $j = 4$ and/or $j = 5$. It seems that the energy transfer mechanism requires not only the presence of modes at these most active levels, but also the correct phase relationships. Modes at these levels should thus be retained as internal modes of any model for it to be "well-posed".

Forcing at the small scales   We already know from experiments in which the smallest scales ($j \geq 6$ for $L = 100$) are eliminated, that they are essentially irrelevant to the dynamics—see Fig. 5.3. This conclusion is reinforced by a simulation in which the small scales are "overexpressed" by a factor of ten, setting $a_{6\,k} = 10\,b_{6\,k}$. Fig. 5.34 shows the consequences, or rather, the lack thereof. As expected, there is an excess of energy at $j = 6$ and in the small scales of the power spectrum, and a discernible fine structure in the spatial cross-section in (a) and in the gray-scale plot. It is remarkable that these are the only effects; the rest of the energy spectra, and the PDFs, are apparently unaffected by the extra small-scale energy. It seems that there is negligible backwards propagation of energy from the small scale level $j = 6$ to the active and large scales.

5.4.3   Discussion

In the experiments of this Section, we have confirmed and extended our interpretation of the contributions of the different levels to the overall dynamics, and obtained some results about the
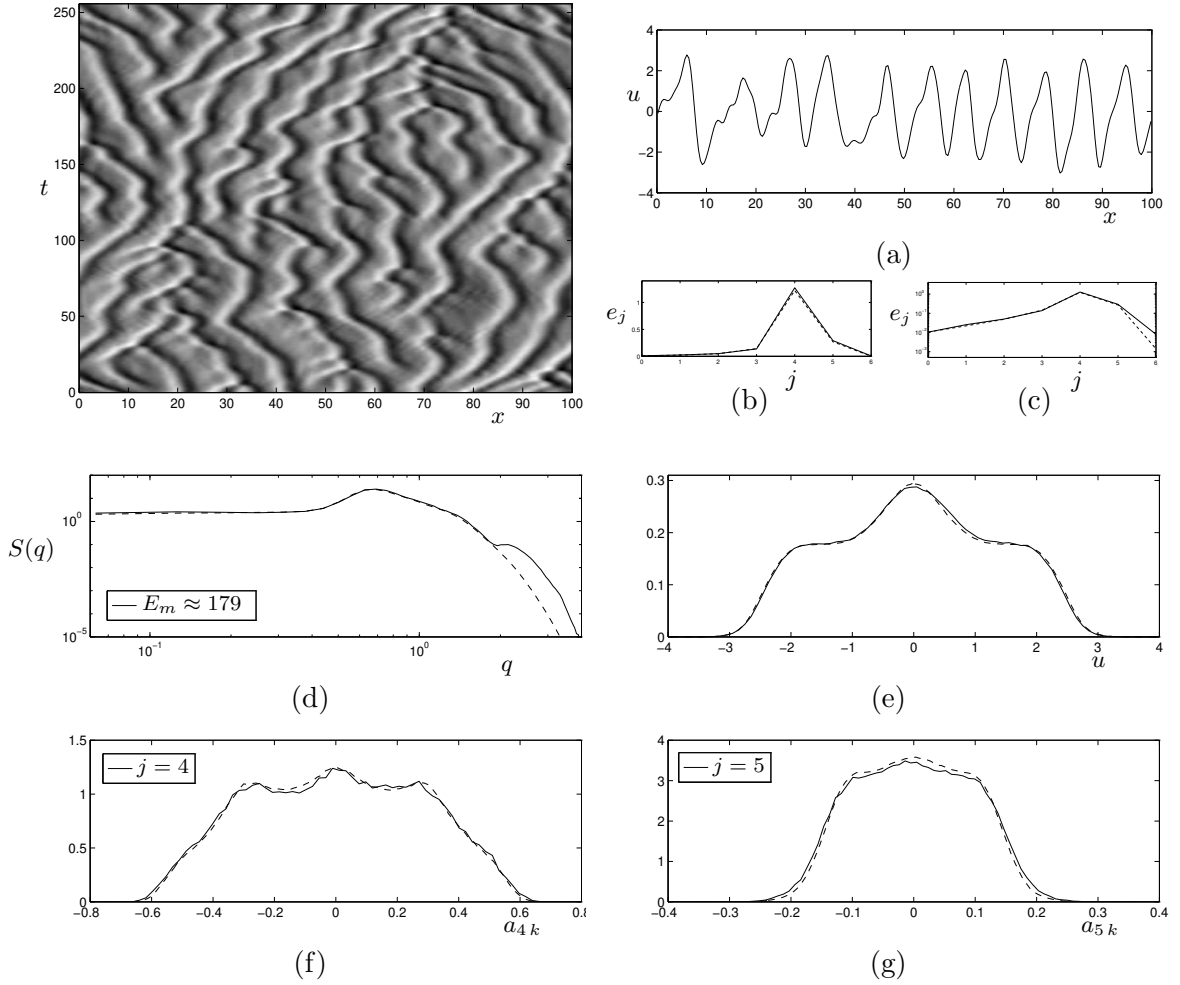
Figure 5.34: Comparison of model statistics with full KS equation: Forcing at level $j = 6$ with time series taken from autonomous run, and amplified by a factor of 10. See caption of Fig. 5.5 for description. Autocorrelation time $\tau_c \approx 9.6$.

robustness of the KS dynamics to amplitude and time perturbations. We summarize our observations, the assignment to particular wavelet levels j again being specific to $L = 100$:

- Provided they have the correct statistics, the large-scale modes $j = 0$–2, especially at level 2, can generate typical local events even in the absence of level $j = 3$, albeit at a slower rate.

- Information can be transferred nonlocally in scale, past missing levels; in particular, level $j = 0$ can maintain disordered behavior at the active scales in the absence of levels 1 and 2.

- Variations in the rate of the large-scale forcing have little effect on the active-scale dynamics.

- The dynamics are sensitive to the driving amplitude; in particular, excessive energy at large scales induces a ridge state with drifting peaks due to variations in the local mean, while even larger amplitudes lead to shock-like behavior.

- The system cannot respond to the disruption of phase relationships arising from manipulation of or forcing at the active scales $j = 4$ and 5, and solutions blow up in finite time.

- Driving at the small scales $j \geq 6$ has a negligible effect on the dynamics.

5.5 Externally prescribed forcing at the large scales

By manipulating the amplitude and rate of forcing from a control integration of the KS equation at the large scales, we have learnt much about the functions of these levels, and especially about the effect of a nonzero local mean leading to traveling peaks. However, we have so far been dependent on the chaotic KS dynamics to generate the forcing time series such as $b_{00}(t)$ of Fig. 5.23. For the purposes of obtaining relatively simple models and understanding the effects of the large scales, we wish to model them without requiring the full solution of a KS equation. Thus we study the effects of large scales prescribed by simple deterministic rules or by an independent stochastic process. Furthermore, by imposing an *a priori* determined external forcing, we have more control over the experiments. These simulations do not yield many new results, but rather largely confirm the existing ones (and in some cases also give strikingly attractive patterns...)

5.5.1 Deterministic forcing

Constant forcing

We corroborate the results on excessive energy in the lowest modes by applying a constant forcing; specifically, we set $a_{00}(t) = \text{const.} \overset{\text{def}}{=} C$. In Fig. 5.35 we show some effects of such constant forcing, while retaining all other levels. On the basis of our earlier experiments, we can readily predict the results of these manipulations, and we need to recall only a few things to understand these pictures:

1. If level 0 is forced with its characteristic energy or not much more, then it will have little effect on the KS dynamics, especially in the presence of levels 1–3 which maintain the disorder and typical events; the mean energy at level 0 (see Table 4.1) is 0.010, which is supplied by a constant forcing $C = 0.1$ (Fig. 5.35(a)).

2. As the energy supplied to level 0 increases, the imposed variations in the local mean induce a drift. For relatively little excess forcing, characteristic dynamics are superimposed on the drift (b); as the forcing amplitude C increases, it increasingly entrains the system, giving a ridge state with minor perturbations (c,d).

3. The speed of drift increases with the local mean, and hence with the amplitude of the forcing term (b,c,d).

4. The direction of drift depends on the sign of the local mean; compare the situation with $C < 0$ (Fig. 5.35(c)) to that of $C > 0$ (d).

If levels $j = 1$–3 are eliminated, while retaining constant forcing at level 0, then the lowest mode completely determines the system. Without the other large scales to promote disorder, after the decay of initial transients the system is in a regular ridge state, with the speed of the traveling peaks again determined by the amplitude of forcing; see Fig. 5.36 for some examples.
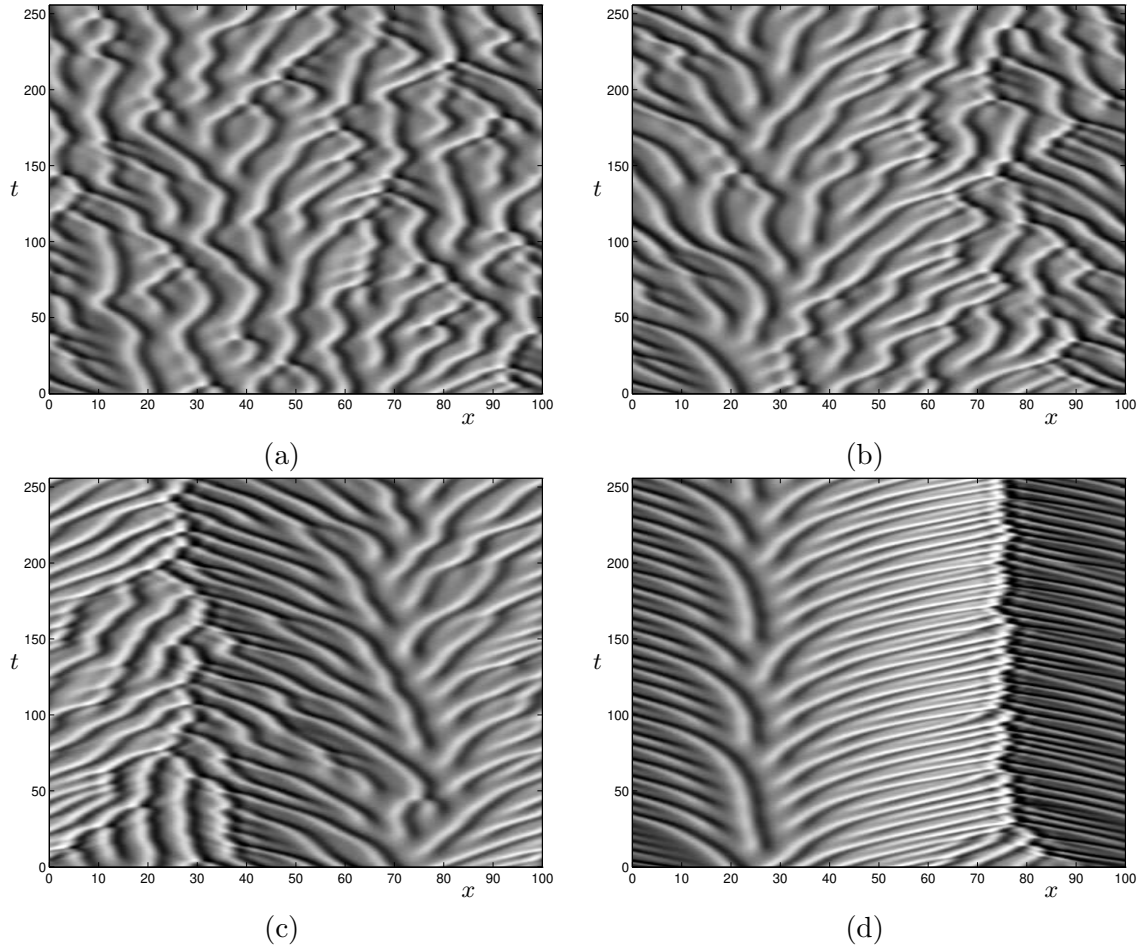
Figure 5.35: Imposing a constant amplitude at level $j = 0$, retaining all other wavelet levels, showing the effect of a varying local mean: (a) $a_{00} \equiv 0.1$; (b) $a_{00} \equiv 0.3$; (c) $a_{00} \equiv -0.5$ (the change in sign causes a change in direction of the traveling peaks); (d) $a_{00} \equiv 1.0$.
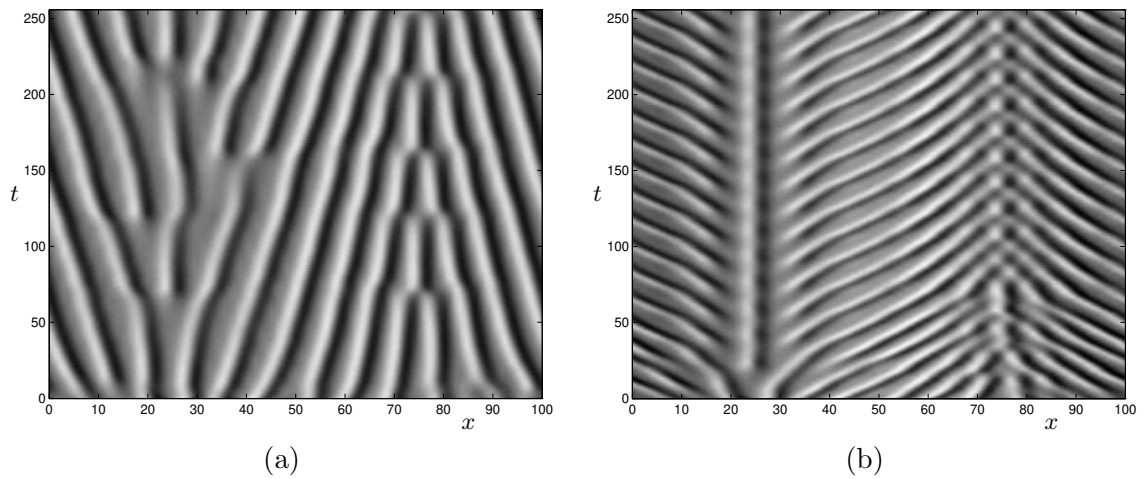
Figure 5.36: In the absence of levels $j = 1$–3, level 0 completely determines the system. Eliminating $j = 1$–3, and holding $j = 0$ constant: (a) $a_{00} \equiv 0.1$; (b) $a_{00} \equiv 0.5$.
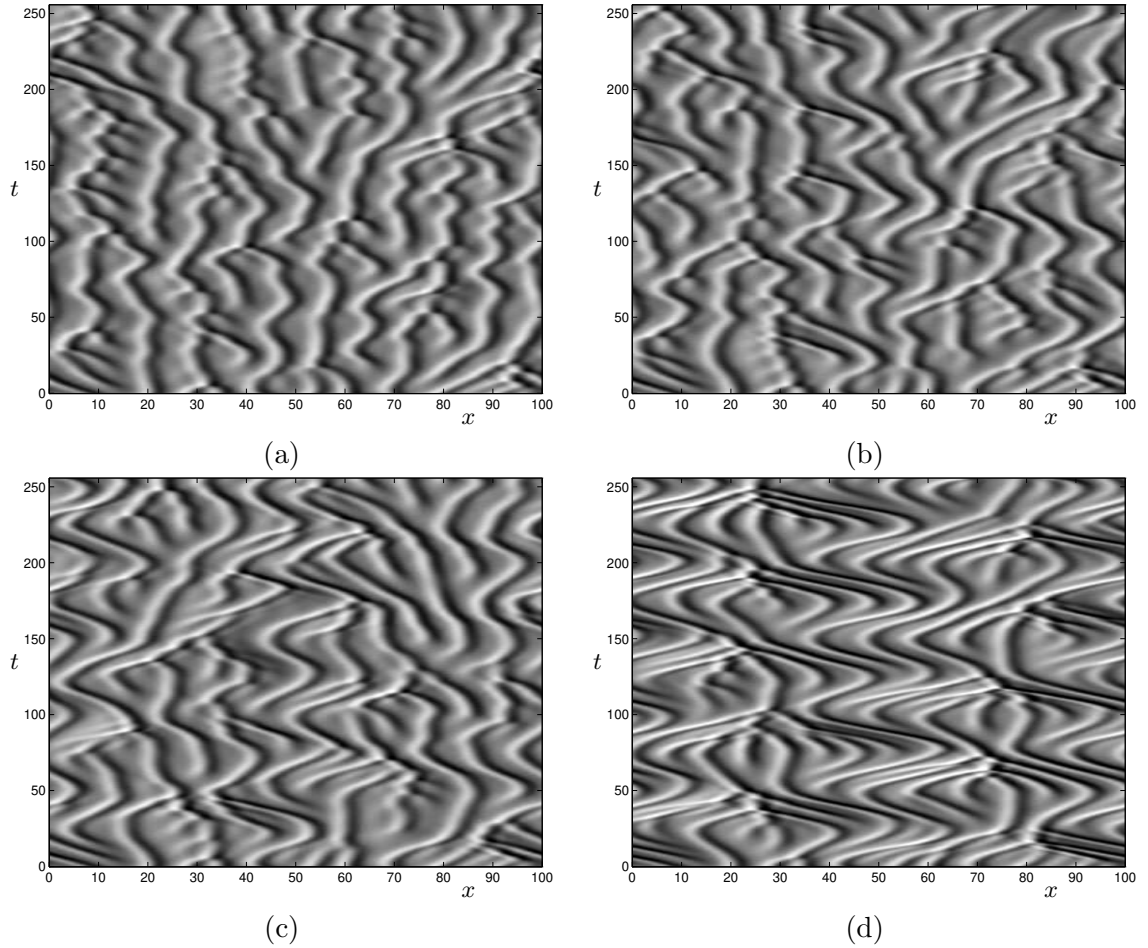
Figure 5.37: Oscillatory forcing with period $T = 50$ at level $j = 0$, $a_{0\,0}(t) = C\sin(2\pi t/T)$, retaining other wavelet levels: (a) amplitude $C = 0.1$; (b) $C = 0.3$; (c) $C = 0.5$; (d) $C = 1.0$.

Oscillatory forcing

We briefly present some simulations in which level 0 is periodically driven; we do not show here similar experiments with driving at level $j = 1$. These results can be understood in the same way as those for constant forcing, with the main change being that the direction of overall drift oscillates with the sign of the forcing term, for large-amplitude driving.

In Fig. 5.37 we see several simulations in which level 0 undergoes sinusoidal forcing, and all other levels are retained. The forcing is specified by $a_{0\,0}(t) = C\sin(2\pi t/T)$, where $T = 50$ is fixed and C is varied for the simulations of Fig. 5.37. We should recall from Table 4.1 that $\tau_0 \approx 45$–50 is a characteristic time for level 0, compared with $\tau_1 \approx 30$ and $\tau_2 \approx 16$; and that (since the average of $\sin^2(\cdot)$ over a period is 0.5) the amplitude C which would deliver the correct mean energy at levels 0–2 is $C = 0.2$. Keeping in mind these points and the discussion above for constant forcing, the results of Fig. 5.37 are unsurprising, ranging from the typical KS dynamics for low forcing in (a), through typical events superimposed on a local drift in (b) and (c), to near-entrainment for large oscillatory forcing in (d).

When levels 1–3 are eliminated from the system, then as before the dynamics are completely entrained to the level 0 driving, and there are oscillations away from the zeros of $\psi_0(x)$. All previous
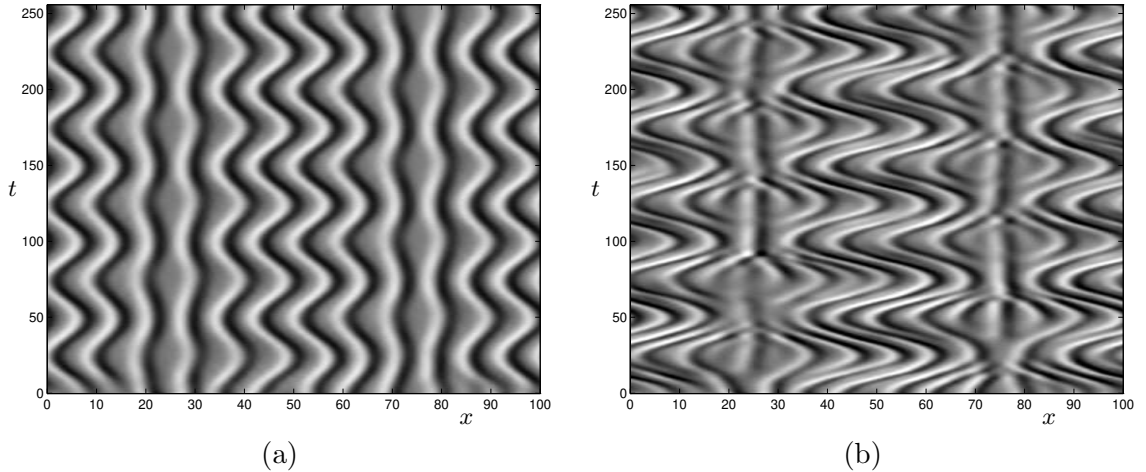
Figure 5.38: Oscillatory forcing at level $j = 0$, $a_{00}(t) = C\sin(2\pi t/T)$, with period $T = 50$, completely entrains a system in which levels $j = 1$–3 are eliminated. (a) Amplitude $C = 0.3$; (b) $C = 1.0$.

principles hold here—in particular, the speed of drift and hence the extent of oscillations in x, increases with the amplitude of the forcing. The dependence on the period T is also straightforward: For larger T, peaks drift further before having to turn around and change direction, so the extent of the oscillations in x is larger. In Fig. 5.38 and Fig. 5.39 we show several experiments of this kind; the results are fairly predictable, but the plots are included largely for aesthetic reasons, their symmetries being visually pleasing. Note the similarities of Fig. 5.38(a) with Fig. 5.9, in which level 0 was allowed to evolve independently in the absence of levels 1–3 (and eventually settled down to $a_{00} = 0$). The Figures here reconfirm that nonlocal information transfer in scale is possible, with level 0 driving the active scales in the absence of intervening levels.

5.5.2 Random forcing

We conclude the Chapter with a brief discussion of nondeterministic effects. We have already repeatedly encountered the notion, motivated by Gaussian PDFs, that the dynamical function of the modes at the large scales is to supply an effective noisy forcing to drive the active scales. In Sec. 5.3, this idea received partial validation, when we found that driving from an independent KS integration, in which the large scales did not respond to the active scales of the model, reproduced the correct behavior. Here we take this idea one step further, testing whether any correlations at all between the large scale modes are needed. That is, we test the hypothesis that the contributions of the large scales to the overall dynamics derive solely from their Gaussian nature, and leave no trace of their deterministic origins (in the full system).

In Sec. 4.2.3 we proposed a "toy" stochastic model (4.17, 4.18) for the large scale dynamics, and showed that with a suitable choice of parameter values such as those quoted by Hayot *et al.* [HJJ93], we can obtain excellent agreement with the distributions and temporal statistics of large-scale modes of the KS equation. In this Section we use this model to probe the effective randomness of the large-scale modes.

Large-scale random excitation   Fig. 5.40(a) shows a simulation in which the lowest three levels of an $L = 100$ system, $j = 0$–2, are driven by time series generated by the stochastic model. In

161
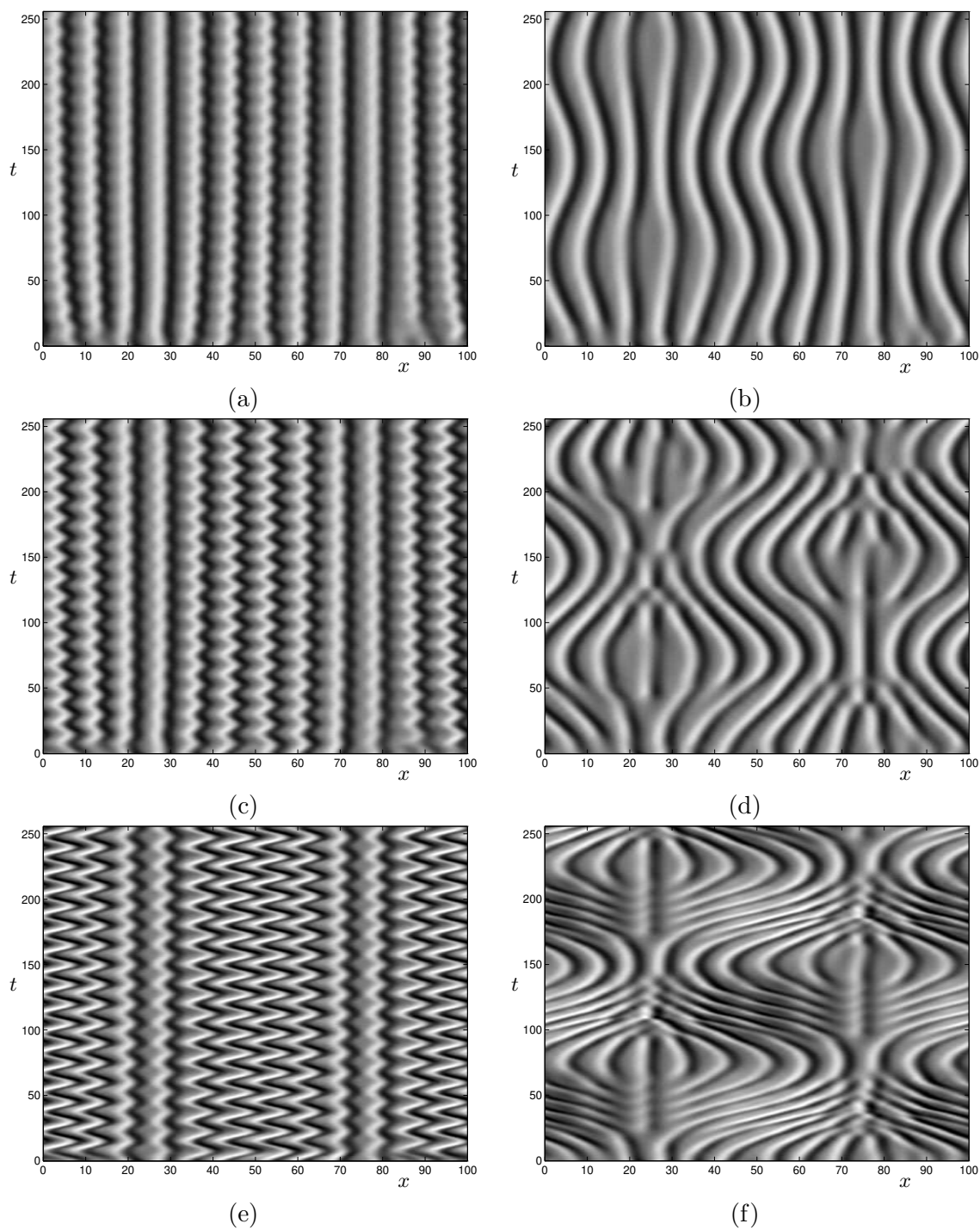
Figure 5.39: Oscillatory forcing at level $j = 0$, $a_{0\,0}(t) = C\sin(2\pi t/T)$, and eliminating levels $j = 1$–3, showing the effects of varying amplitude C and period T. Left-hand-side, (a,c,e) period $T = 15$; right-hand-side, (b,d,f) period $T = 150$. (a,b) amplitude $C = 0.1$; (c,d) $C = 0.3$, (e,f) $C = 1.0$.
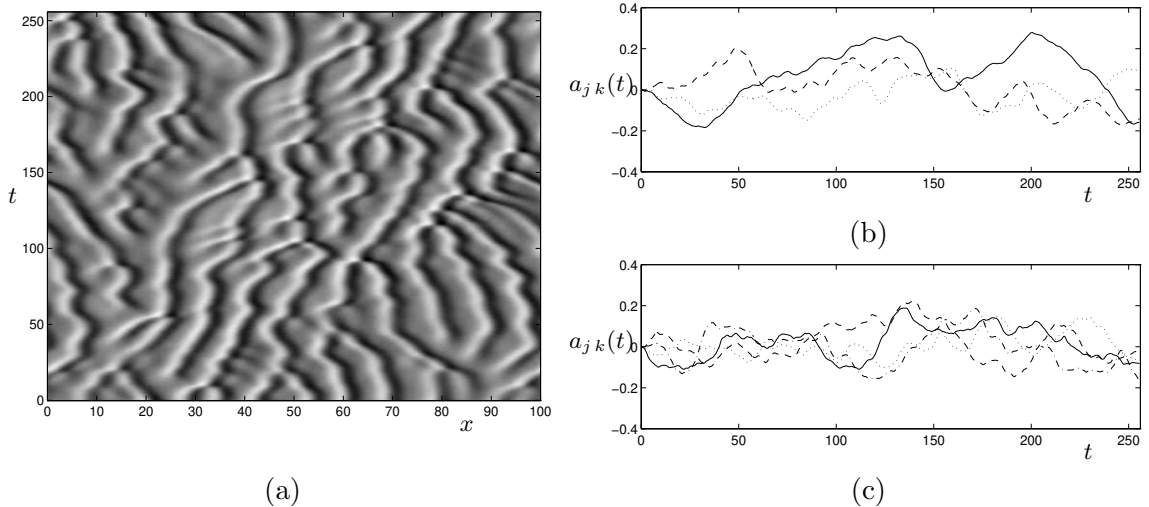
Figure 5.40: Random forcing reproduces the effects of the large scales: (a) Wavelet levels $j = 0, 1$ and 2 driven by the stochastic process described in Sec. 4.2.2; (b) driving time series at $j = 0$ and 1 generated by the random process; (c) the corresponding time series for $j = 2$ forcing.

this Section we do not investigate the effects of varying amplitudes or time scales, having already studied these at some depth in this Chapter. Thus the parameters $D = 17.9$, $\nu = 7.5$ and $\tau_f = 7.0$ [HJJ93] are fixed at the values already found in Sec. 4.2.3 to yield good results (see Fig. 4.15). Time scales depend on the choice of q in (4.17): The value $q = 2\pi n/L$, $n = 1$ gives good results for level $j = 0$ of an $L = 100$ system, and we might expect $n \approx 2$ and $n \approx 4$ to be appropriate to wavelet levels $j = 1$ and $j = 2$, respectively. However, these values correspond to the scaling $\tau_q \sim q^{-2}$, which is inappropriate for these relatively large q values, near the active scales (see Figs. 4.10 and 4.13); and we find that they yield excessively rapid temporal behavior. A scaling of $\tau_q \sim q^{-1}$ appears more reasonable in this range of scales (*cf.* Table 4.1). To simulate the higher wavelet levels $j \geq 1$ in our experiment, we thus use (4.17, 4.18) with $q = 2\pi\sqrt{2}/100$ for $j = 1$, $q = 2\pi \cdot 2/100$ for $j = 2$. Fig. 5.40(b,c) shows the generated time series used to drive the model at $j = 0$–2; comparison with wavelet coefficient time series of Fig. 4.12 confirms that our stochastic model gives reasonable results. The robustness of the KS dynamics to changes in time scale of the forcing (see Figs. 5.27 and 5.28) also implies that it is unnecessary to get the time scales "exactly right".

Fig. 5.40(a) shows that this model, with stochastically generated large scales according to the above prescription, displays good qualitative agreement with the full KS equation and with a model in which we drive the low modes from an independent KS run, Fig. 5.11(b). Unsurprisingly, we get similarly good qualitative agreement if we force only levels $j = 0$ and 1 (not shown). In Fig. 5.41 we show that the statistics of this stochastically forced model also correspond very well with the STC regime of the KS equation.

The random processes generated by our stochastic model are mutually independent. The contribution of the large scales to the STC regime is thus effectively just that of uncorrelated, Gaussian noise; their "memory" of their deterministic origins, including correlations with other large-scale modes, appears to be irrelevant to their interactions with the active scales.
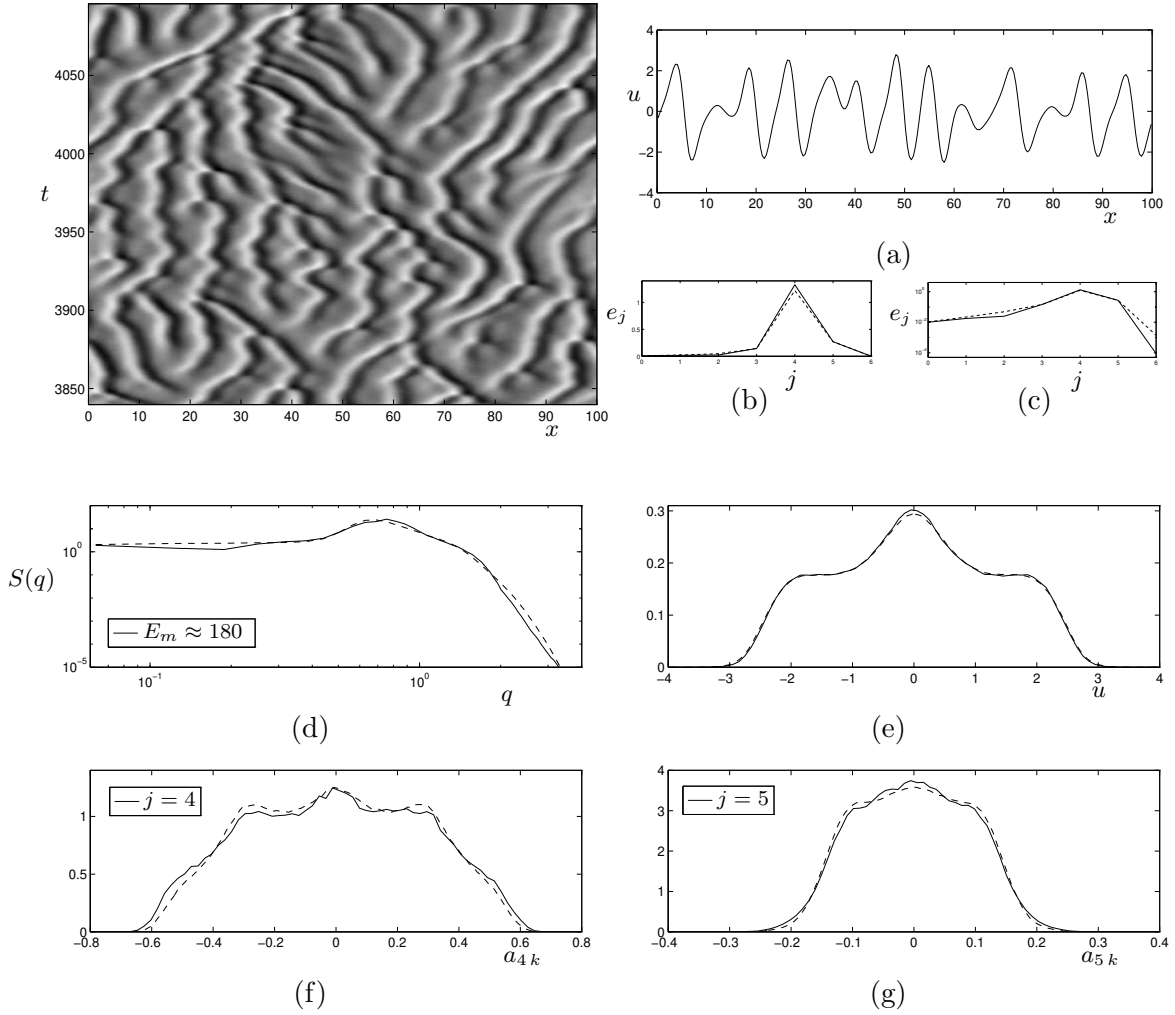
Figure 5.41: Comparison of model statistics with full KS equation: Random forcing at the large-scale levels $j = 0$, 1 and 2, as in Fig. 5.40. See caption of Fig. 5.5 for description. Autocorrelation time $\tau_c \approx 11$.

Random forcing with elimination of some levels To ascertain whether our general conclusions about the essential stochasticity of the large-scale modes hold true also for individual wavelet levels, we have performed some experiments similar to those of Secs. 5.2 and 5.4.1, in which we force at some levels and eliminate others. Again, the agreement with results obtained from the "correct" forcing is excellent. Consider for instance Fig. 5.42. In (a), we stochastically force at levels $j = 0$ and 1, and eliminate level 2; the qualitative behavior, as well as the statistics (not shown), closely agree with those of Fig. 5.6. The slightly more rigid dynamics observed in Fig. 5.42(b), in which we remove levels $j = 0$ and 1, and force at $j = 2$, also correspond well both qualitatively and statistically with the corresponding experiments of Figs. 5.4(b), 5.5 and 5.20(a).

The slightly more stringent tests of Fig. 5.43 are also passed successfully. In (a), we drive level 2 with the time series shown in (c), and remove $j = 0$, 1 and 3 from the model. The longer time scales for typical events in the absence of $j = 3$ have been observed previously for the analogous experiment with driving from an independent KS run, in Fig. 5.21(a).
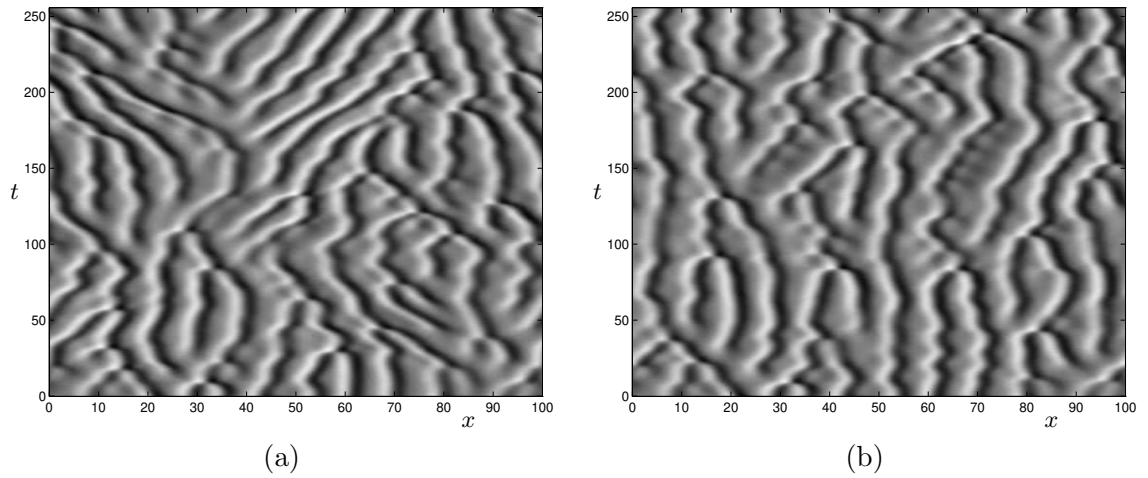
Figure 5.42: (a) Random forcing at levels $j = 0$ and 1, and eliminating level $j = 2$; (b) random forcing at $j = 2$, eliminating $j = 0$ and 1.
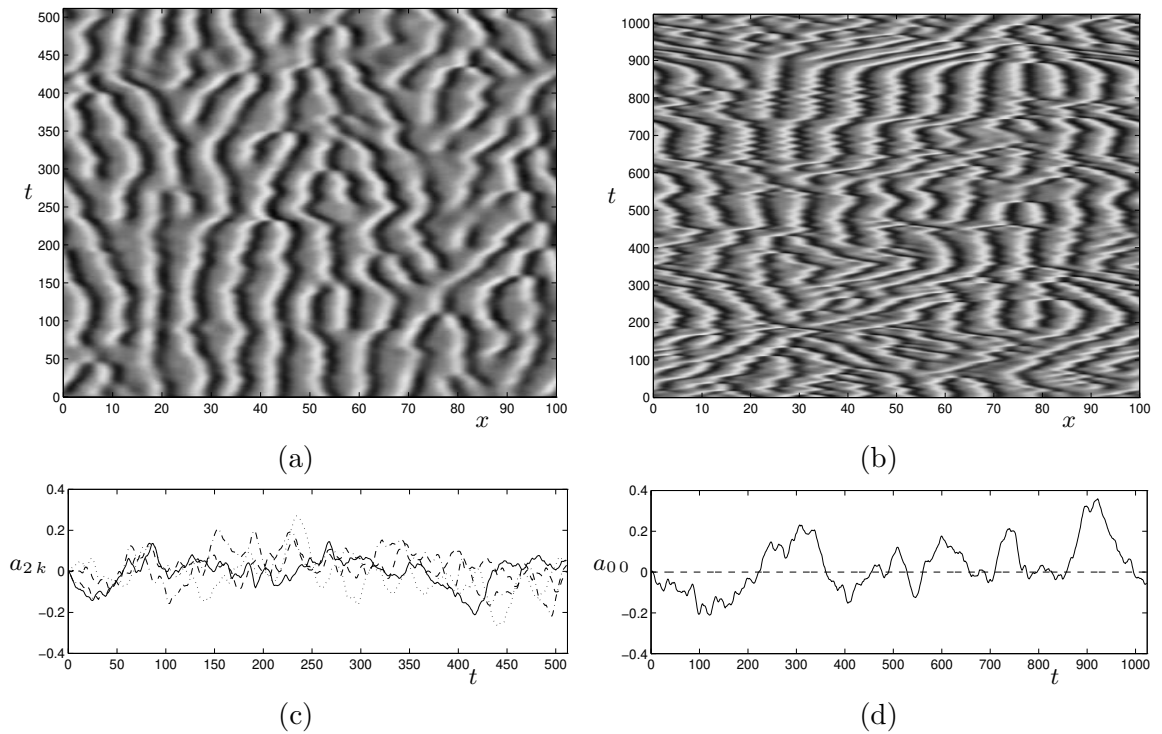
Figure 5.43: (a) Random forcing at level $j = 2$, and eliminating levels $j = 0$, 1 and 3 (compare Fig. 5.21(a)); (b) random forcing at level $j = 0$, and eliminating $j = 1$ and 2 (compare Fig. 5.22(b)). (c) Time series of random forcing $a_{2\,k}(t)$ for the run (a); (d) random forcing coefficient $a_{0\,0}(t)$ for the simulation in (b).
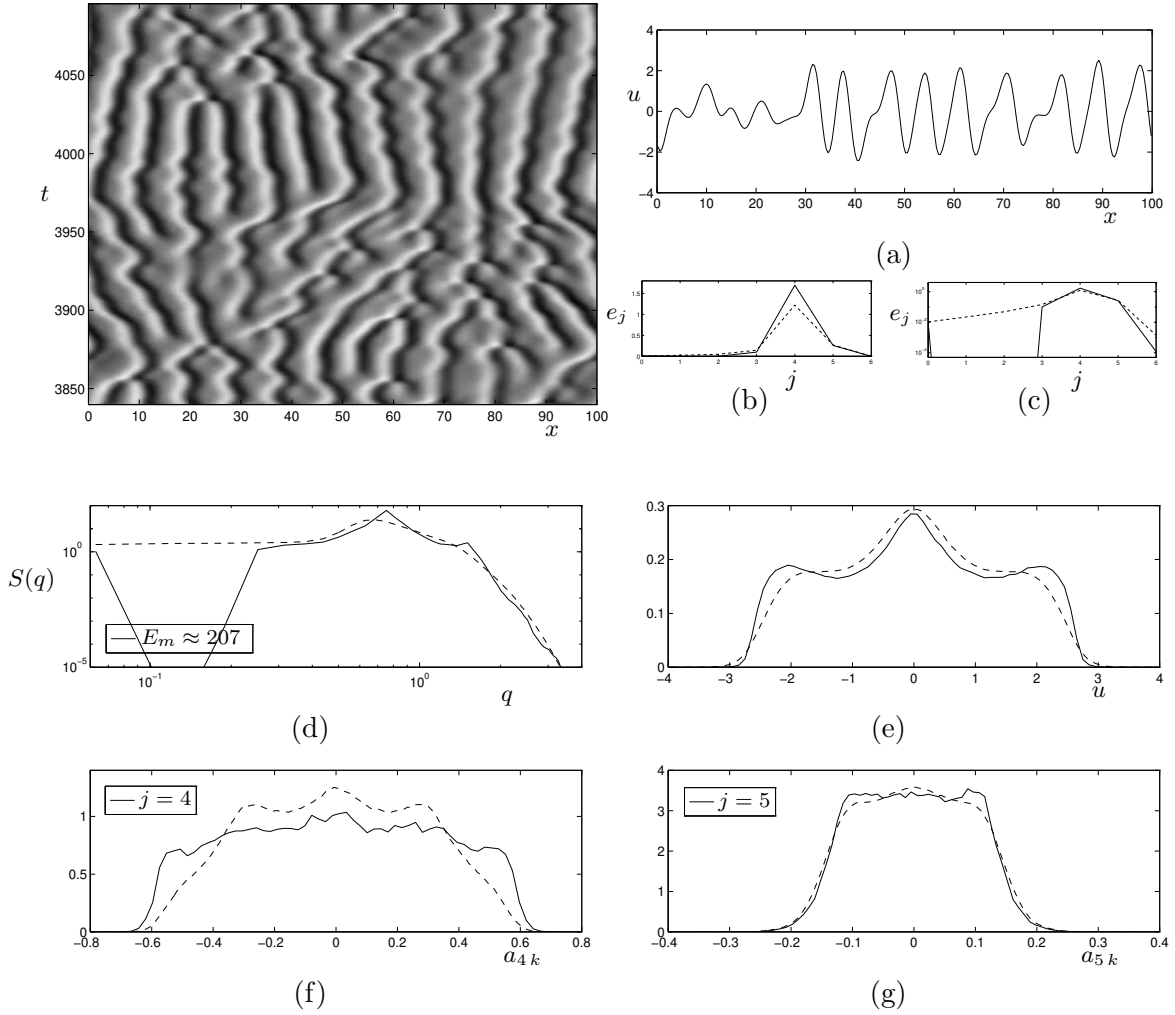
Figure 5.44: Comparison of model statistics with full KS equation: Random forcing at level $j = 0$, setting levels 1 and 2 to zero, as in Fig. 5.43(b). See caption of Fig. 5.5 for description. Autocorrelation time $\tau_c \approx 18$.

In Fig. 5.43(b), we repeat our previous experiments on information transfer from $j = 0$ past the missing levels $j = 1$ and 2, this time with the randomly generated time series of (d). The agreement with Fig. 5.22(b) is again convincing, including the decay towards the cellular state when the forcing amplitude is small; also compare again the autonomously generated time series of Fig. 5.43(d) with that for the KS wavelet coefficient $a_{00}(t)$ in Fig. 5.23. The statistics for a long-time integration of this model with random forcing at $j = 0$, without levels 1 and 2, are shown in Fig. 5.44. The comparison with Fig. 5.24 demonstrates that the dynamical effect of even a single stochastically forced mode at the largest scale is closely comparable to that of its deterministically generated counterpart from the full KS equation. Our results for random forcing of the lowest mode should also be contrasted with the case in which it was allowed to evolve independently, in Fig. 5.9, in which case we observed heteroclinic transitions between cellular and spatiotemporally chaotic states.

The experiments of this last Section have thus confirmed that the essentially random nature of the large scale dynamics carries over to its interactions with the active scales. We return to the study of models with autonomously generated large-scale stochasticity in Sec. 6.3 of the next Chapter.

166

In this Chapter, we have discussed a selection from a wide range of different numerical experiments, which we have designed to elucidate the internal workings of the spatiotemporally chaotic KS dynamics. Let us be clear what a small fraction of the total number of possible experiments we have been able to perform. Specifically, we have kept two parameters constant: the length of the system $L = 100$, and the damping $\varepsilon^2 = 1$. In the previous Chapter we have carefully argued that, once we are in the STC regime, the length L essentially does not matter; but of course the relative distribution of energy among wavelet levels, and hence the relative contributions of these levels, is affected by L, or rather by the relation between the characteristic dyadic wavelet lengths $2^{-j}L$ and the characteristic length of the system l_0. However, the study presented in this Chapter, discussing the relative functions of different levels, will certainly be representative of the STC regime.

The other parameter we have held fixed is the damping. For the full transition to STC, we would need to redo all the above experiments for a range of ε^2 values (see Sec. 2.3.4). That is a study for a different occasion; while the machinery now exists to do this, this would clearly be a lengthy investigation. In addition to these two major points, virtually all the above experiments have been performed for a given set of integration parameters (time step δt, and total length of run), for fixed initial conditions for the model **a** and for the control run **b**. For truly reliable results, we should average over initial conditions, and compute longer-time statistics with different integration parameters. For these reasons, the results discussed here should probably not be taken as definitive. However, the robustness of the STC exhibited by the KS equation, and its apparent ergodicity, means that we are fairly confident that the qualitative results are reliable, even if the quantitative statistics may not yet be well-converged.

Chapter 6

Spatially Localized Models

In the previous Chapter, we have discussed the results of experiments in which entire wavelet levels are eliminated, forced or otherwise manipulated, thereby obtaining a fairly detailed understanding of the contributions of different scales to the overall dynamics. In this Chapter, we return to the question of spatial localization, and investigate the ability of spatially localized models to reproduce the dynamics of the full system. As described in Secs. 1.3 and 3.2.2, we wish to critically examine the idea, prevalent in thermodynamics, of a large chaotic system being composed of smaller, weakly interacting subsystems of relatively low dimension, the dynamics of which, in isolation, might be analyzed and understood (see Sec. 1.4).

Choice of parameters   For the experiments in this Chapter, we retain the parameters and initial conditions **a** and **b** described in Sec. 5.1, unless otherwise stated; recall that **a** is used to initialize the local model, while **b** provides the initial data for the independent full KS run used to force the model. In particular, our local models will usually be based on a subsystem of length $\bar{L} = 25$ of the full $L = 100$ system.[†] We choose this for various reasons:

- We can exploit the extensive statistical results of Ch. 4 for the $L = 100$ KS system, as well as the insights of Ch. 5 on the contributions of different wavelet levels to its overall dynamics; these results on separation of scales carry over to multiples of $L = 100$ by powers of two (see Sec. 4.2.5).

- We know that $\bar{l}_c \approx 25$ is a good estimate for a characteristic dynamic interaction length (Sec. 4.3.3), so $\bar{L} = 25$ seems a reasonable length for a localized model.

- Larger choices of $\bar{L}$ both require higher-dimensional models, and imply more complex internal dynamics; for large enough $\bar{L}$, no external forcing is needed to reproduce spatiotemporally chaotic behavior. In contrast, for the range $L \in [20, 30]$, various types of "simple" attractors exist for the KS equation, including fixed points, standing and traveling waves and heteroclinic cycles; see Sec. 1.2.3.

- For given $\bar{L}$, a larger "full system" length L just adds more large-scale levels, providing slow Gaussian forcing, and contains additional boxes which do not significantly interact with the subsystem we are interested in, being separated from it by a distance greater than $\bar{l}_c$.

The wavelet coefficients for the length $\bar{L} = 25$ subsystem of the $L = 100$ full system are those corresponding to a box $\bar{\mathbf{B}}^{2\,k}$ in the notation of Sec. 3.1.2, that is, a subtree with root at level 2. In

---

[†]In Sec. 6.3 we extend our study to short L-periodic systems for a range of L.

particular, we shall usually focus on the box $\bar{\mathbf{B}}^{22}$, highlighted in Fig. 3.3; so that the coefficients a_α, $\alpha \in \bar{\mathbf{B}}^{22}$ are the internal modes of the model, forced by coefficients $b_{\alpha'}$ for $\alpha' \in \mathbf{C} = \mathbf{A} \setminus \bar{\mathbf{B}}^{22}$ (see (3.25)) usually obtained from an independent integration of the full KS equation.

6.1   Localized models with forcing

In the full KS equation, each local "box" of wavelet modes interacts with its neighbors and with the large scales, which act as external forcing. Provided L is sufficiently larger than $2\bar{l}_c$, the system is locally unaware of the global periodicity (the bulk dynamics is independent of boundary conditions, Sec. 4.3.1). Thus it seems reasonable to seek models in which the local box is forced from the large scales and external adjacent modes, without imposing the constraint of periodicity; see the schematic depiction of this idea in Fig. 3.4(c).

The successful construction of such models was originally sought as the culmination of previous investigations of the KS equation in the STC regime [BEH92], and also motivated much of the work in this thesis; in particular, we studied the statistics of different wavelet levels carefully (Ch. 4) in the expectation that success would depend on feeding in the "correct" statistics for the $b_{\alpha'}$ modes. However, preliminary investigations (J. Elezgaray, unpublished, 1994; referred to in [MHEB95]) suggested that in such models, the symmetry is broken too drastically, leading to relatively "rigid" dynamics. In this Section, we revisit such calculations, and reach broadly similar conclusions.

6.1.1   Fundamental features of external forcing

The basic features of these experiments are shown in Fig. 6.1. In practice, we integrate a full KS equation, but at every time step overwrite the amplitudes for the modes $\alpha' \in \mathbf{C}$ by their externally specified values $b_{\alpha'}$, usually obtained from an independent full KS integration, or set to zero. In (a), we have integrated a local, unforced system ($b_{\alpha'} = 0$ for all external $\alpha' \in \mathbf{C}$). This system rapidly settles down to a steady state, with fixed peaks; a cross-section is shown in Fig. 6.1(c). In the absence of both forcing and periodic boundary conditions, the dynamics of this 15-dimensional system, containing 4 wavelet levels 2–5, thus remains rigid. A similar rigidity, with more internal peaks, was observed in an unforced, non-periodized integration of a longer, $\bar{L} = 50$ subsystem, obtained by integrating modes in the larger box $\bar{\mathbf{B}}^{11}$ (not shown).

Local model with full external forcing

Fig. 6.1(b) shows a local model (with initial conditions $\mathbf{a}$ for modes $\alpha \in \bar{\mathbf{B}}^{22}$), forced from the outside by all modes $b_{\alpha'}$, from levels 0 to 5. Here the $b_{\alpha'}$ are obtained from an integration of the KS equation with initial conditions $\mathbf{b}$ (see Fig. 5.1(b)). The Figure is reconstructed from the internal modes of the model as well as the forcing terms, so that the response of the model to the external driving is readily apparent; this will be done throughout this Section. The wavelets ψ_α^L, $\alpha \in \bar{\mathbf{B}}^{22}$ comprising the model are centered in the region bounded by two lines, $L/2 < x < 3L/4$. Apart from effects due to the fact that some of the support of the internal wavelets overlaps the external region, the reconstructed solution for $x < L/2$ and $x > 3L/4$ is exactly that of the KS equation with initial conditions $\mathbf{b}$, Fig. 5.1(b). As before, the gray-scale is set so that white corresponds to $u = +3.5$, black to $u = -3.5$.

To interpret the results of Fig. 6.1(b) and later results of this Section, we recall some important observations of Sec. 5.3: Forcing at all wavelet levels up to and including level 3, together with some forcing at level 4, may induce tracking, so that modes with $j > 4$ are slaved to the larger
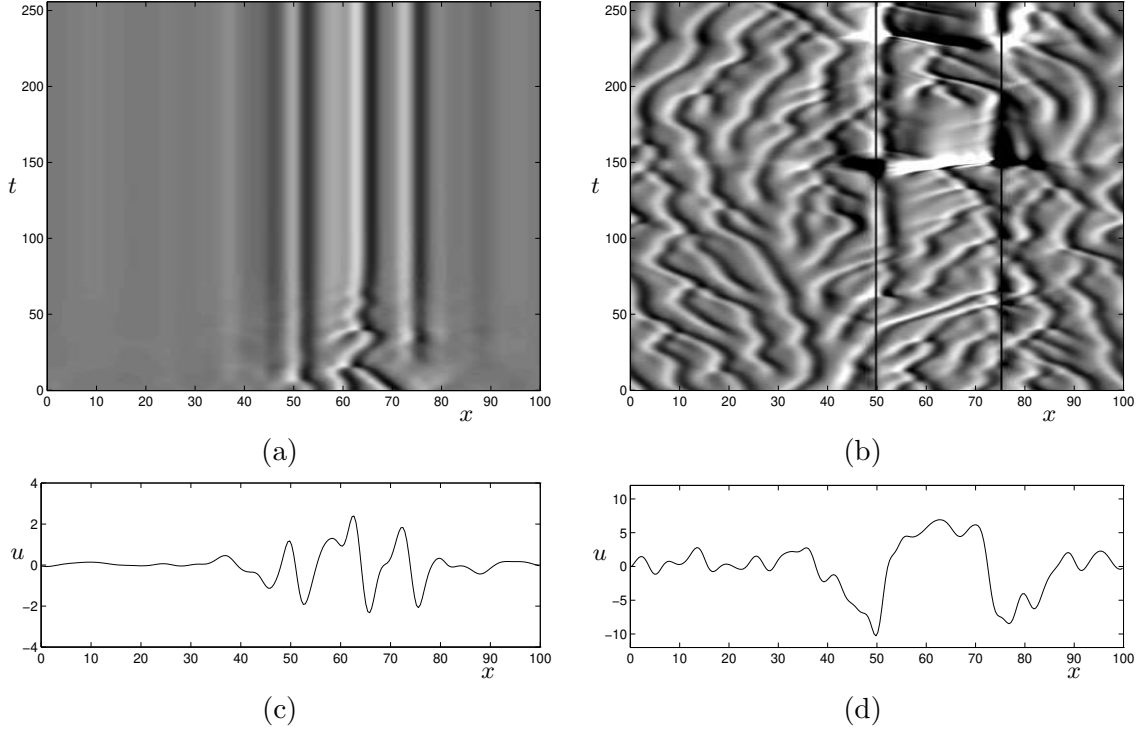
Figure 6.1: (a) Local, non-periodized model with modes in $\bar{\mathbf{B}}^{22}$, unforced; with $t = 150$ cross-section shown in (c). (b) Local model, forced from levels 0–5; with $t = 150$ cross-section shown in (d).

scales. However, the large-scale, linearly unstable levels $j \leq 3$ are not entrained under any forcing from an independent integration. Furthermore, if the only modes left to evolve independently, driven by the control run, are linearly unstable large-scale modes, then their amplitudes grow exponentially (see Sec. 5.3.2, especially Figs. 5.18 and 5.19). If sufficiently many stable modes are retained in the model, the energy transfer between internal modes provides damping, but does not necessarily restrict modal amplitudes to the values they would attain in the full system; the large-scale wavelet coefficients subject to driving may grow abnormally before they are damped. The abnormal behavior in the presence of driving is due to disruption of the feedback mechanism: the evolution of the external modes $b_{\alpha'}$ is independent of the a_α, so the $b_{\alpha'}$ cannot provide the normal compensation for growth in the internal modes, sometimes serving rather to reinforce unusually large amplitudes.

In Fig. 6.1(b), the internal modes evolving as part of our model include the linearly unstable large-scale modes a_{22}, a_{34} and a_{35}, as well as some modes at levels $j \geq 4$. By the previous discussion, subject to external forcing these may undergo excessive growth; and such effects are indeed observed, near $t \approx 150$ and again from $t \approx 230$. Fig. 6.1(d) shows a cross-section for $t = 150$. Observe the large amplitudes in the region $L/2 < x < 3L/4$; a glance at the wavelet coefficients confirms that, indeed, the level 2 and 3 coefficients are too large. The local model does retain stable modes, however, and nonlinear interactions and energy transfer among the internal modes ensure damping; thus the solution does not blow up, but eventually returns to reasonable amplitudes (this is in contrast with cases in which we evolve only unstable modes driven by all the rest, as in Sec. 5.3.2).

It is also interesting to note the recurrence of an important theme of Sec. 5.4: the relation between local mean and drift. Once again, excessive large-scale amplitudes lead to rapidly traveling fronts, which move in the positive (near $t \approx 50$ and $t \approx 150$) or negative (near $t \approx 240$) x direction, depending on the sign of the local mean; that is, according to the sign of a_{22}. A simulation in which we retain a larger set of internal modes, $\alpha \in \bar{\mathbf{B}}^{11}$, and force from an independent run, gives similar results (not shown) with even larger amplitudes and more rapid fronts, in which the internal mode a_{11} is unduly excited.

Implications for the construction of local models and synchronization The excessive growth of low modes in the presence of external, independently generated excitations is the concept we need to understand the results of Fig. 6.1(b). However, it also implies that whenever some large-scale modes, subject to external forcing, are retained in a model of this type, unusual amplitudes accompanied by rapidly traveling structures are likely to occur. Moreover, we expect that if such undesirable results are obtained even if the forcing is from a full KS integration—that is, if the driving necessarily has all the "correct" statistical properties—then we can hardly expect better results from more simplified types of external random fluctuation. This bodes ill for the program of constructing localized non-periodic models with external forcing; for the problem of excessive growth seems destined to occur whenever our model is able to support its own dynamics, without being slaved to the forcing, that is, whenever it is large enough to contain modes at levels $j \leq 3$.

We observe as an aside that these conclusions do not necessarily depend on our wavelet formulation, or even on the KS equation. They may apply more generally to synchronization of a localized model through boundary forcing, whenever the system is large enough to contain one or more (sufficiently) unstable modes.

6.1.2 Related experiments

Local models with "correct" initial conditions

The lack of synchronization in the presence of external forcing persists even if the initial conditions for the model are those appropriate for the forcing terms; that is, if both the modes a_α of the model and $b_{\alpha'}$ of the independent KS run have the same initial data, in our experiments **b**. This statement obviously needs qualification: if the integration of the model is performed with all the same parameters as the full system, and with the same initial values, then at each time step, the internal modes a_α are subject to the same vector field as the corresponding modes b_α of the full system, and their evolutions are identical. We checked our algorithm for the forced, non-periodized model by confirming that we indeed observed this correct behavior in our simulation (not shown).

Consider, however, the simulation shown in Fig. 6.2(a). In this case, the reference (external) computation is the integration shown in Fig. 5.1(b), with initial data **b** and retaining all modes to $j = 6$. The local model (evolving modes $\alpha \in \bar{\mathbf{B}}^{22}$), on the other hand, has the same initial data, but only retains, and is forced by, wavelet levels to $j = 5$.

From Sec. 5.2.1 we know that the small scale levels $j \geq 6$ have a negligible effect on the typical dynamics and statistics of the KS equation, and that their evolution is completely determined by that of the larger scales—see Sec. 5.3.1. However (see Fig. 5.3) we also know that the presence or absence of small scales can disrupt the system sufficiently that, due to the intrinsic sensitivity of the large-scale dynamics to perturbations, detailed tracking is lost even while all relevant statistical properties are retained. This is observed in Fig. 6.2(a): There is apparent tracking for fairly long time, to $t \approx 70$, by which time perturbations due to the absence of level $j = 6$ have been amplified to $\mathcal{O}(1)$ errors. Beyond this point, we are in the same situation as in Fig. 6.1(b); the linearly
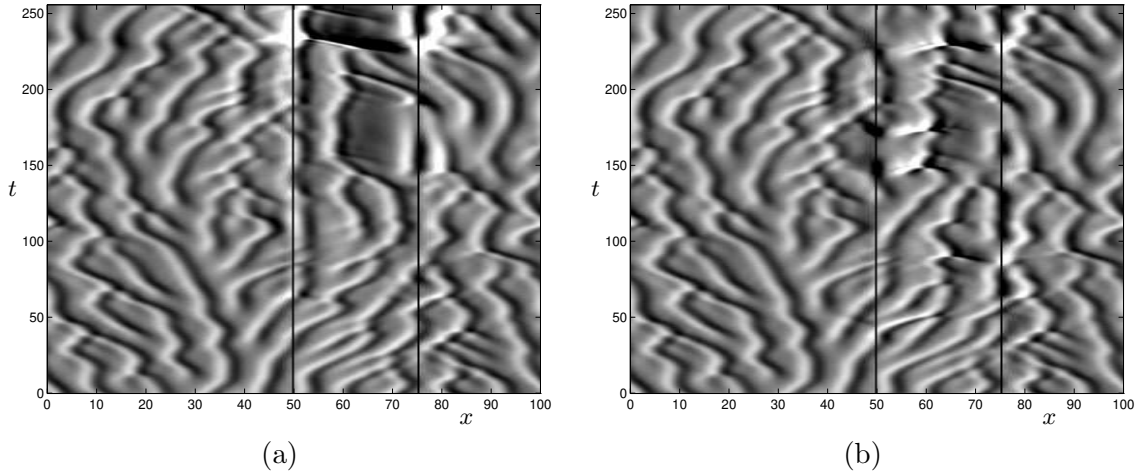
Figure 6.2: Local, non-periodized model with external forcing from an independent KS integration; both the model and the external run have initial data **b**. (a) Forcing externally up to level $j = 5$. (b) As in (a), but the internal mode a_{22} is also forced.

unstable internal modes for $j = 2$ and 3 may be unusually excited, and large-amplitude events occur.

It is interesting to note that in Figs. 6.1(b) and 6.2(a), which experience identical forcing but with different initial conditions, the dynamics beyond about $t \approx 220$ follow the same trajectory. This suggests that the external forcing may in fact completely determine the long-time evolution of the system, though yielding a somewhat pathological trajectory rather than that of the control run. This agrees with some observations of Sec. 5.4, especially Fig. 5.35, where we saw that sufficiently large amplitudes in the lowest modes of our model can entrain higher modes which would otherwise evolve independently. In the present case, the large-amplitude events drive the model to the attractor determined by the time history of the forcing.

The results of Fig. 6.2(a) are important, as they demonstrate that forcing with external modes cannot even hold a (slightly perturbed) model system with "correct" initial data on or near the "correct" trajectory for arbitrarily long times, let alone synchronize a model initialized elsewhere in phase space.

Forcing at all external modes: Lack of synchronization One might object that the afore-going results are not directly relevant to the problem of synchronization: While we have driven the box with all the determining large- and active-scale modes, to which the small scales are slaved, the external forcing in Figs. 6.1(b) and 6.2(a) does not include all modes of the control run. Hence the completely synchronized state (the state $d_\alpha = a_\alpha - b_\alpha = 0$ for all internal modes $\alpha \in \mathbf{B}$, in the notation of Sec. 5.3.2) is not an exact solution of our evolution equations (3.25).[†]

To reassure ourselves that the lack of synchronization is due to the internal instability of the

---

[†]There has been recent interest in the synchronization of chaos because of the potential for secure communications [CO93], whereby a message $m(t)$ is masked by a chaotic signal $u(t) \gg m(t)$ from a transmitter, and the superposition of the two signals $u(t) + m(t)$ is used to drive a receiver. The receiver dynamics are synchronized to those of the transmitter, and regenerate the original chaotic time series $u(t)$, which may then be subtracted off from the masked signal to yield the message; see [Str94, Sec. 9.6] for an introduction. Of relevance to our present question of slightly "wrong" or "incomplete" driving is that in the above scenario for encoding and decoding a signal using chaos, synchronization is achieved with a *perturbation* of the original chaotic time series [COS93].
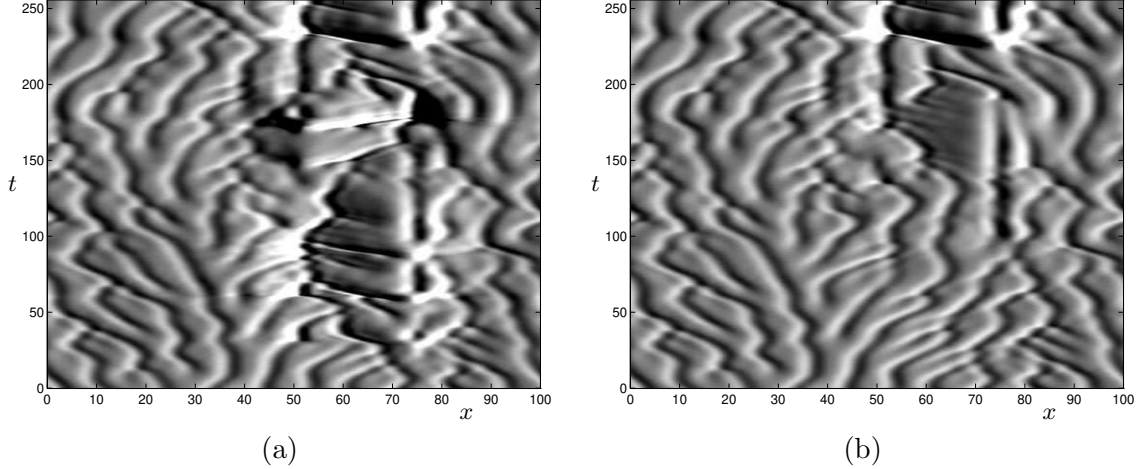
Figure 6.3: Local, non-periodized model with external forcing from the control run at all levels (to $j = 6$), showing the instability of the synchronized state: The control run has initial data $\mathbf{b}$, while the initial conditions for the model are perturbed slightly from $\mathbf{b}$ at (a) the largest internal mode a_{22}; (b) the smallest-scale modes at level $j = 6$.

dynamics, rather than being due to slight errors in the boundary forcing at small scales, we have performed the simulations of Fig. 6.3, in which the external driving includes all modes. As a test of the linear stability of the synchronized state and of the theory of Sec. 5.3.2, the initial data for the resolved internal modes in the box are taken to be a slight perturbation of the values $\mathbf{b}$ for the control run. In Fig. 6.3(a), the initial conditions have a discrepancy only at the lowest internal mode: $a_{jk}(0) = \mathbf{b}_{jk}$ for $j \geq 3$, $a_{22}(0) = \mathbf{b}_{22} + 0.001$. As is apparent in the Figure, there is rapid growth of this small large-scale perturbation. For the simulation of (b), the initial data inside the box $\bar{\mathbf{B}}^{22}$ are taken from $\mathbf{b}$ except at the smallest-scale modes a_{6k}, which initially vanish. Though these $j = 6$ modes are rapidly enslaved to the larger scales, their initial deviation from the control perturbs the remaining internal modes of the model sufficiently that the solution eventually diverges from the synchronized state, although discernible $\mathcal{O}(1)$ differences are only seen for $t > 100$. In both (a) and (b), the norm of the difference between the model and the control run grows exponentially for short times, consistent with linear instability of the $\{d_\alpha = 0\}$ subspace as given by (5.22). In each of these simulations, we also observe large-amplitude events and rapidly traveling peaks, as before. The lack of synchronization may thus clearly be traced to the intrinsic instability of the large-scale internal dynamics, rather than to our choice of the small-scale cutoff of the boundary forcing.

Driving lowest internal modes If, in addition to the external forcing, we also specify the time series of some internal modes, then the dynamics more realistically approximates the "correct" KS behavior. Fig. 6.2(b) shows a simulation in which the largest internal scale, the mode a_{22}, is specified, as are all external modes (again, up to level $j = 5$, as in Fig. 6.2(a)). In this case, the unstable level 3 remains free and occasionally subject to excessive excitation; the resulting events, while still too large, have smaller amplitude than in (a), and are also more spatially localized, consistent with the smaller spatial support of the wavelets ψ_{3k}^L. We have also performed simulations (not shown) in which the internal levels $j = 2$ and 3 are both specified, together with full external forcing. That these simulations closely reproduce the dynamics of the full system is unsurprising, since we already know (Sec. 5.3.1) that specifying levels 0–3 and part of level 4 is generally sufficient
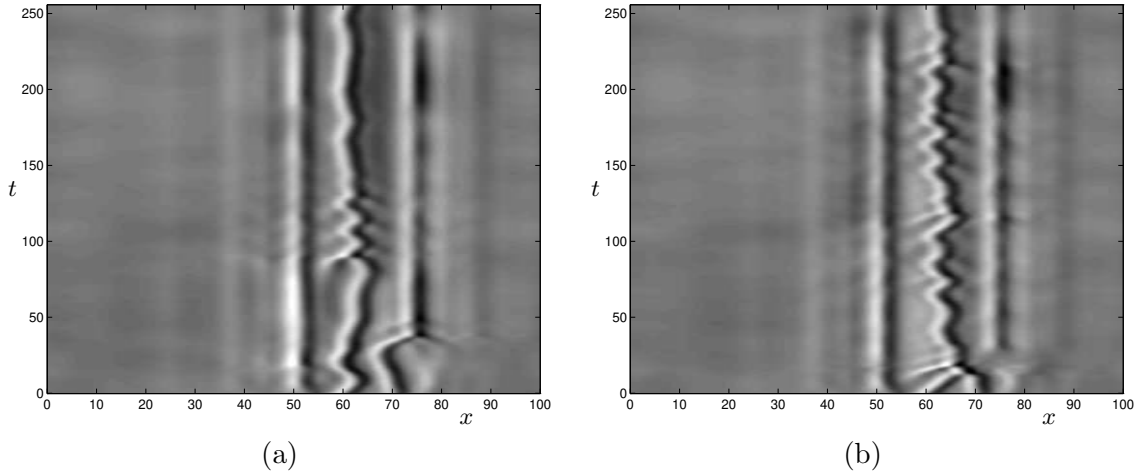
Figure 6.4: Non-periodized model, with modes in the box $\bar{\mathbf{B}}^{2\,2}$, forced from the large scales of an independent KS run: (a) Forcing only at levels 0 and 1. (b) As in (a), but mode $a_{2\,2}$ inside the box is also specified.

to induce tracking. Note that for these simulations, the qualitative conclusions again depend little on the initial data for the internal modes of the model.

Forcing at individual wavelet levels

We investigate driving by various subsets of the external modes to see whether we can obtain a model with less rigid dynamics than in Fig. 6.1(a), with more typical events and traveling behavior, while avoiding the excessive amplitudes of Fig. 6.1(b). Consider first the effect of forcing only from certain external wavelet levels.

Large-scale forcing Fig. 6.4 shows that the large scales have little effect on rigid dynamics within the model. In Fig. 6.4(a) we force the modes a_α, $\alpha \in \bar{\mathbf{B}}^{2\,2}$ only by levels 0 and 1 from the independent simulation (which, as we know already, is tantamount to supplying Gaussian noise to the system). We see that this is a small perturbation of Fig. 6.1(a). The internal peak is agitated back and forth; sometimes a second peak is created, only to collide rapidly with the first; but the peaks at the boundaries remain stationary and repel the internal structure, constraining it to remain near the center of the model domain.

With only large-scale forcing, the potential dynamical activity of the model is very limited. We have observed this to be the case also if the model is forced externally at levels $j = 0$, 1 and 2. In Fig. 6.4(b) we see a related experiment: in addition to forcing at levels 0 and 1, we also specify the internal mode $a_{2\,2}$ from a full simulation. The "correct" dynamics for the largest scale inside the box appears to do little to stimulate more varied behavior within the system.

Active-scale forcing In Fig. 6.5, we demonstrate the effect of restricting the external forcing to the active scales. One naturally hypothesizes that relative to large-scale stimuli, active-scale driving should have a greater effect; this turns out to be true. Indeed, the internal peak appears to enjoy more freedom to move back and forth, especially for forcing at levels 3 or 4. However, the boundary dynamics is still fairly rigid, and there is no "communication" with the exterior of the model in the

(a)

(b)

(c)

(d)
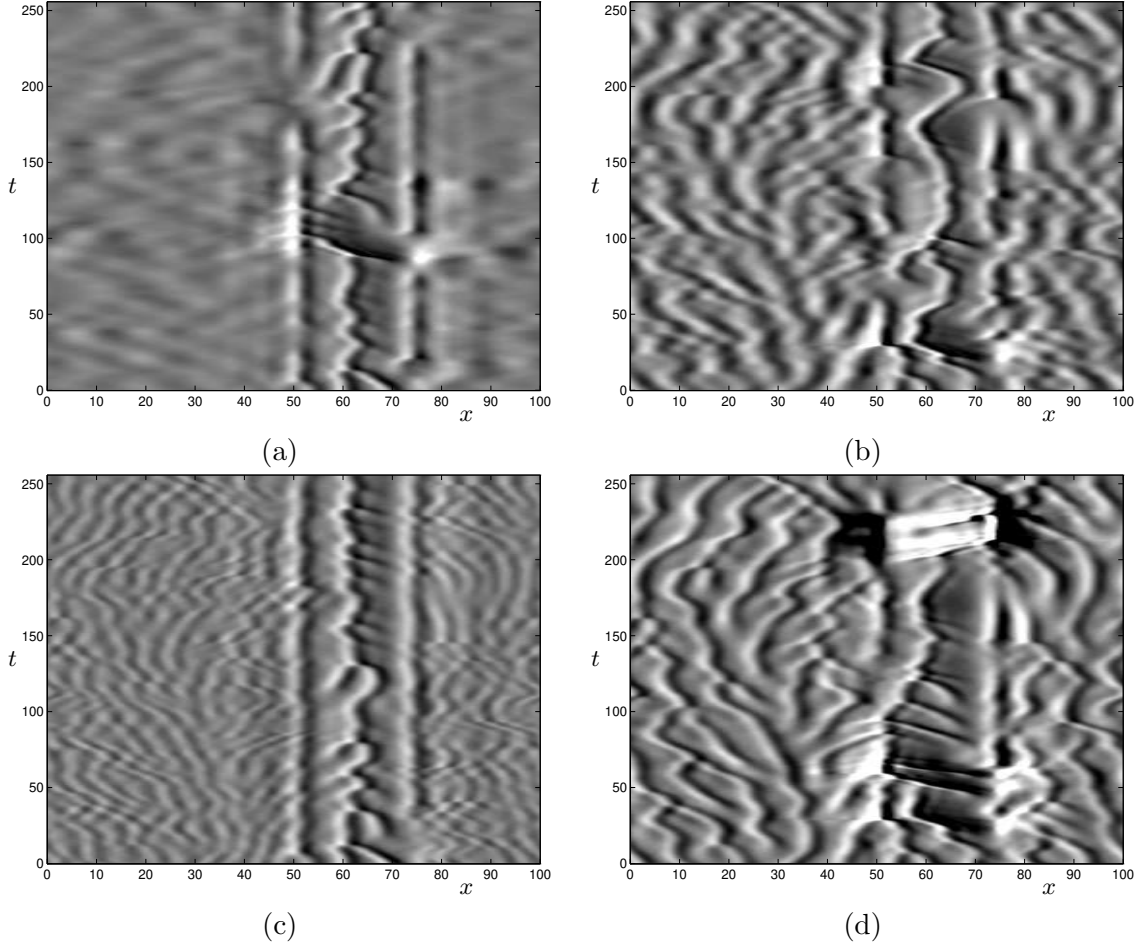
Figure 6.5: Non-periodized model, with modes in the box $\bar{\mathbf{B}}^{22}$ forced from the active scales of the control run: Forcing at level (a) $j = 3$; (b) $j = 4$; (c) $j = 5$; (d) $j = 4$ and 5. Note that the external region, especially for $x \leq 40$, illustrates the decomposition of the KS dynamics of Fig. 5.1(b)(iii) onto active-scale wavelet levels.

sense of passage of coherent structures across the boundaries. Furthermore, especially for forcing at both levels 4 and 5, there is a tendency towards the large-amplitude events previously described for Fig. 6.1(b). More active internal dynamics of the model, and more typical events such as collisions and traveling structures, thus come at the price of a greater likelihood of excessive excitation of the large scales.

Incidentally, we have taken the opportunity to display all four figures of Fig. 6.5 for another reason. Observe that we also reconstruct the external driving field; in this case this corresponds, for x outside and well away from the box, to reconstructing the projection of the full KS field u onto a particular wavelet level. The gray-scale representation we have chosen implies that in Fig. 6.4, we see that the large scales make hardly any contribution to the magnitude of u. By comparison with Fig. 5.1(b), we can see in Fig. 6.5(a)–(c) how the field is constructed out of the superposition of levels $j = 3$, 4 and 5. In particular, it is apparent from Fig. 6.5(d) that $j = 4$ and 5 together constitute almost the entire field. Of course, we know this already from the energy distribution displayed in Fig. 4.11 and Table 4.1, for instance, but the wavelet decomposition is more visually explicit in Fig. 6.5.
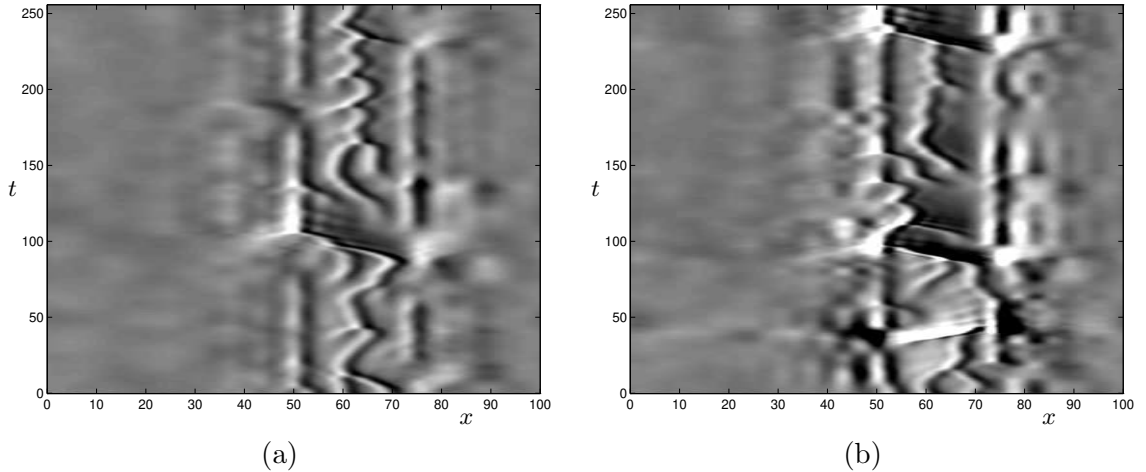
Figure 6.6: Non-periodized local model, in which modes in the box $\bar{\mathbf{B}}^{22}$ are forced by adjacent modes (from full KS integration) at levels (a) $j = 2$ and 3; (b) $j = 2$, 3 and 4.

Forcing from nearest neighbors

In the unpublished experiments of J. Elezgaray (1994), local non-periodized models forced only by the nearest active-scale wavelets were studied. We obtain similar results: either the local system remains too rigid, with stationary boundaries and a fluctuating internal peak, or large scales are amplified excessively, leading to large amplitudes (or both).

In Fig. 6.6 we include two representative results chosen from a range of experiments performed, in which we force with the nearest, or the nearest two, wavelet modes at the active scales. In (a), the local model is driven by adjacent wavelets at levels $j = 2$ and 3. This is best visualized via the wavelet pyramid of Fig. 3.2: We set all external modes $b_{\alpha'}$, $\alpha' \in \mathbf{C}$ to vanish except for b_{21}, b_{23}, b_{33} and b_{36}, which are taken from the independent full KS simulation. The effect of this driving is to give a slightly active, but rigid system, with the internal peak constrained between the stationary boundary peaks most of the time, and otherwise leading to large amplitudes associated with collisions of the internal peak with the boundary. Similar behavior is observed when we force with the two nearest neighbors at levels 2 and 3.

The addition of forcing also from adjacent modes at level 4 (Fig. 6.6(b)) generates more activity, including large-amplitude events due to excess low-mode energy such as those we have already frequently encountered. Similar effects are observed when we include adjacent coefficients at level 5, or add the next-nearest neighbor at these levels; in fact, forcing with adjacent level $j = 4$ coefficients, b_{47} and b_{412} alone, leads to similar large-amplitude excursions (not shown).

6.1.3 Discussion

In summary, we find that for a non-periodized model subject to external forcing, one of two possibilities tends to occur; these broadly correspond to the two extreme cases (a) and (b) of Fig. 6.1:

- The first situation arises when the excitation of the internal modes is weak; for instance, when it arises from the large scales, or is due only to a few external modes. In this case, the model dynamics is rigid; a peak in the interior may move around and undergo some typical "events", but peaks at the boundaries of the model are stationary and excessively constrain the internal dynamics.

176

- In the alternative case, the internal modes are influenced more strongly by exterior modes, usually when forcing is at the active-scale levels $j = 4$ and/or 5. In this situation, more realistic dynamics can occur, including motion of the peaks; but large-scale internal modes tend to be excited excessively due to failure of the standard damping mechanisms, leading to large amplitudes and rapid fronts.

In some experiments, the conditions for both of these anomalies are satisfied, leading to even more disrupted model dynamics. It is apparent from the space-time plots of the solutions that their statistics will not compare well with those of the full KS equation, so we exclude them.

The search for local, *non-periodized* models, reproducing the essential dynamics of the KS equation when subject to large-scale and/or external forcing, must thus be deemed unsucessful. Either the dynamics remains rigid at the boundaries, indicating that the effect of the symmetry-breaking is too drastic; or excessively excited structures result when active-scale forcing of large-scale modes, unable to compensate for growing amplitudes, leads to a mismatch.

6.2 Periodized models

The above considerations lead us again to consider periodic local models. As indicated in Sec. 3.2.2, a common motivation for imposing periodicity is to replace the influence of missing adjacent "external" modes by distant "internal" modes. This approach has the advantage, by contrast with the models of the previous Section, that the drastic inequivalence between modes in the center and at the boundaries of the model is eliminated, and the infinitesimal translation symmetry of the KS equation (1.1) is better approximated.

The notation and theoretical basis for the construction of periodized models are discussed in Ch. 3, where we also review previous studies on periodic models for the KS equation on small subdomains, including [DHBE96] using a Fourier basis, and [BEH92, MHEB95] from a wavelet perspective; see Sec. 3.2.2. We now build on these preliminary studies. In brief, the wavelet formulation restricts us to obtaining periodized subsystems of lengths $\bar{L} = 2^{-j_0} L$, for $j_0 > 0$, where L is the full domain length. We do this by equating corresponding modes in the 2^{j_0} boxes $\bar{\mathbf{B}}^{j_0 m}$, $m = 0, \ldots, 2^{j_0} - 1$. That is, choose a distinguished box $\bar{\mathbf{B}}^{j_0 k_0}$; say, $\bar{\mathbf{B}}^{2\,2}$ as above, for $j_0 = 2$. Every mode $a_{j\,k'}$ for $j \geq j_0$ has a *corresponding* mode $a_{j\,k}$ in the distinguished box, where the centers of the wavelets $\psi^L_{j\,k}$ and $\psi^L_{j\,k'}$ are separated by a multiple of $\bar{L}$. We integrate a periodized model by setting, at each time step, the values of all modes $a_{j\,k'}$ for $j \geq j_0$ to those of the corresponding modes in the distinguished box $\bar{\mathbf{B}}^{j_0\,k_0}$, and then evolving only the modes $a_{j\,k}$ within that box.

Unforced periodized subsystems

Let us first suppose that the large-scale modes, at level $j < j_0$, are set to zero. In Sec. 3.3 we prove that under these conditions, a length L system, periodized from level j_0, is exactly equivalent to a length $\bar{L}$ periodic KS equation.

We illustrate this result in Fig. 6.7, for $L = 100$, $\bar{L} = 25$. For our experiments, as usual we periodize from level $j_0 = 2$, and in Fig. 6.7(a) the distinguished box is $\bar{\mathbf{B}}^{2\,2}$ (see Fig. 3.3); the values of all other modes are equated to the corresponding values inside this box. The four boxes $\bar{\mathbf{B}}^{2\,m}$ are thus identical by construction, as is clearly seen in the Figure. As expected, the dynamics approaches a trimodal (on length $\bar{L}$) fixed point, known to be the attractor for $\bar{L} = 25$ [HNZ86].

We include Fig. 6.7(b) to observe that with this approach, we can perform $2^{j_0} = 4$ numerical experiments simultaneously, via different choices of k_0 for the distinguished box $\bar{\mathbf{B}}^{j_0\,k_0}$. In the
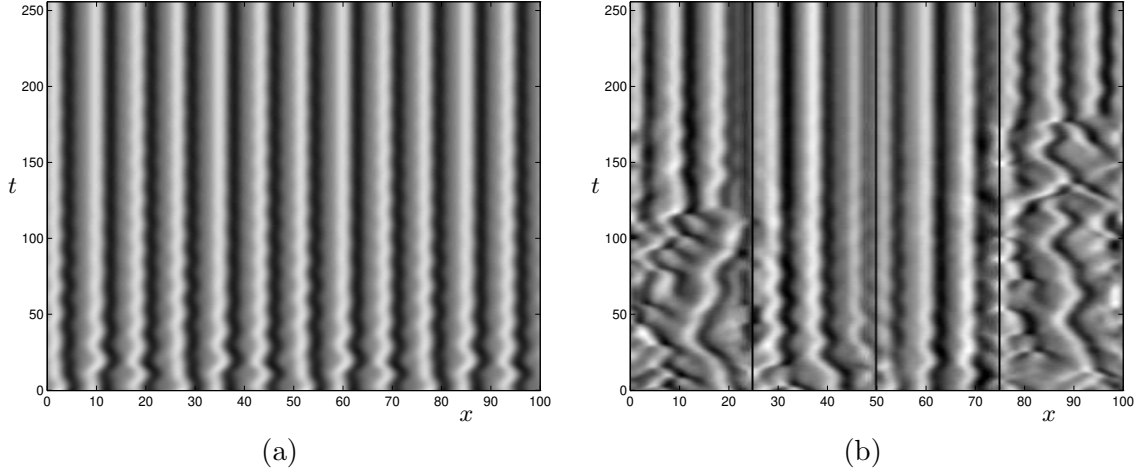
Figure 6.7: (a) An unforced $L = 100$ full system, periodized from level $j_0 = 2$ and with $\bar{L}$-periodized initial data, demonstrates dynamics appropriate to $\bar{L} = 25$, converging to the trimodal fixed point attractor. (b) As in (a), showing four simultaneous runs corresponding to the adjacent boxes $\bar{\mathbf{B}}^{2\,m}$ started with non-periodized initial data $\mathbf{a}$.

absence of large scales, the modes in these boxes of course satisfy identical evolution equations, but with different initial data (the initial conditions $\mathbf{a}$ are not $\bar{L}$-periodic); and thus exhibit different transient times before convergence to the trimodal attractor. We shall see below that if we retain (non-periodized) large-scale forcing, the dynamics in the boxes remain inequivalent.

We confirm briefly that these results are valid for other lengths L by showing some of the other small-$\bar{L}$ attractors [HNZ86], as discussed in Sec. 1.2.3, which arise when we periodize from level $j_0 = 2$ for $L \neq 100$. The representations of Fig. 6.8 show four adjacent copies of some simple attractors, including (a) traveling waves ($\bar{L} = 12.5$), (b) standing waves ($\bar{L} = 17.5$), (c) heteroclinic cycles ($\bar{L} = 20$) and (d) modulated traveling waves associated with the "strange fixed point" (giant state [HNZ86, GK88]) for $\bar{L} = 30$; compare Fig. 1.1. We have also observed, among other low-dimensional attractors, the 2-cell (bimodal) state for $\bar{L} = 15$, and the 4-cell state for $\bar{L} = 32$. Note that in some cases a very small time step is required for the integrator to settle down on these attractors with the correct amplitudes.

6.2.1 Periodized models with aperiodic forcing

To this point, periodization from a large L-periodic system has not yielded anything different than an $\bar{L}$-periodic system. However, if we retain the large scales (that is, the wavelet levels $j' < j_0$), this approach provides a systematic way of forcing the periodized boxes, and of interpreting a smaller periodic system as a subsystem of a larger one.

Introduction to experiments with large-scale forcing The structure of the equations for the modes of a small subsystem, forced by the large scales, is discussed in Sec. 3.3.1. Observe that the large scale wavelets are not $\bar{L}$-periodic. Due to the differing relative positions of the boxes $\bar{\mathbf{B}}^{j_0\,m}$ to the large scale wavelets, modes within one box experience the large-scale driving differently than do corresponding modes in another box. Consequently, without intervention initially $\bar{L}$-periodic data (for $j \geq j_0$) will not remain so.
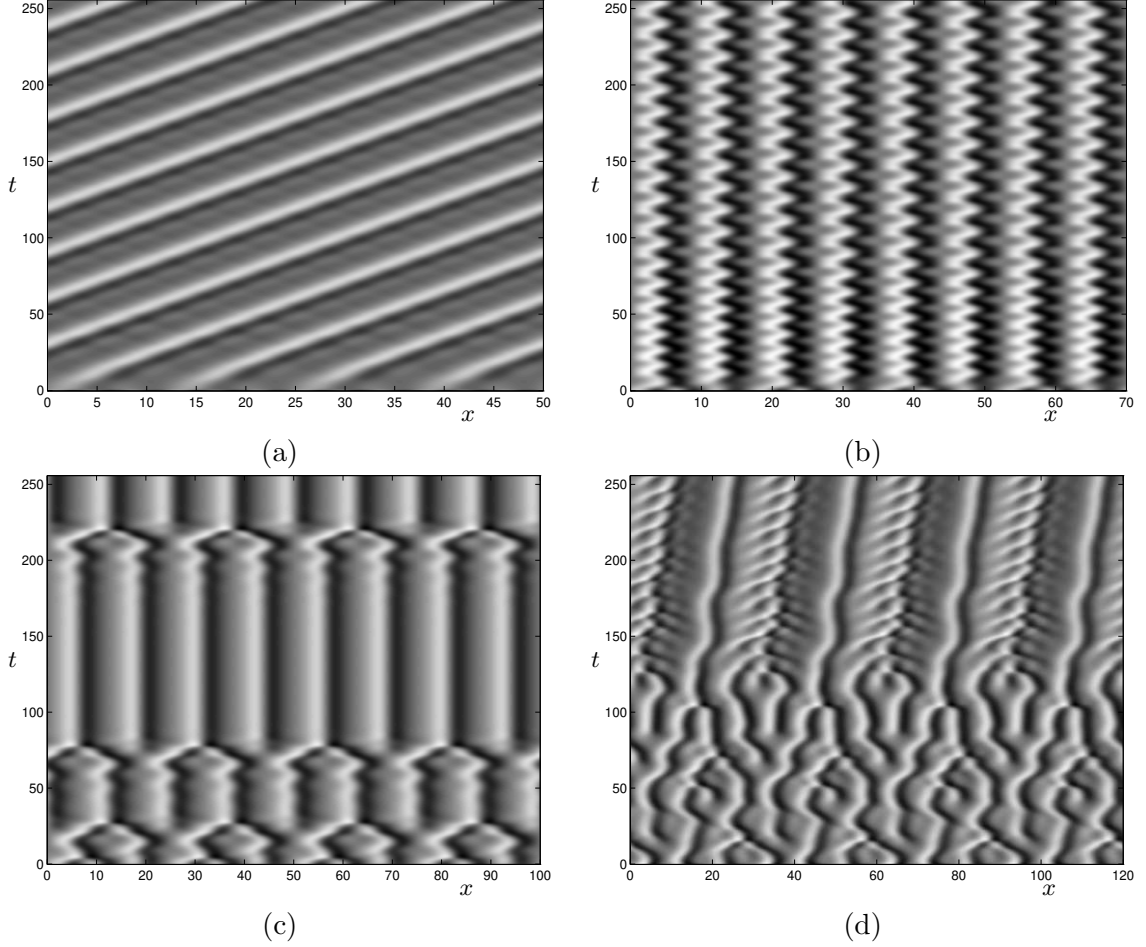
Figure 6.8: Simple attractors in unforced systems periodized at level $j_0 = 2$. (a) Traveling wave, $L = 50$, $\bar{L} = 12.5$; (b) Standing wave, $L = 70$, $\bar{L} = 17.5$; (c) Heteroclinic cycle, $L = 80$, $\bar{L} = 20$; (d) Modulated traveling waves, $L = 120$, $\bar{L} = 30$.

For experiments reported here, therefore, we evolve the modes within a distinguished box $\bar{\mathbf{B}}^{j_0 \, k_0}$, subject to periodicity and large-scale forcing. The time series for the large scale modes $b_{j' \, k'}$ are obtained from a full KS simulation with initial conditions $\mathbf{b}$. Periodicity is enforced by overwriting the values in the other boxes $\bar{\mathbf{B}}^{j_0 \, m}$ by the corresponding values from the distinguished box, at each time step.

Related experiments were reported in [EBH96], in which the Galerkin projection equations for periodized $\bar{L} = 50$ subsystems of a $L = 400$ system were integrated, subject to large-scale forcing. However, the reasonable agreement cited in [EBH96] with the statistical behavior of the full equation is hardly surprising, since an unforced $\bar{L} = 50$ KS system is by itself capable of sustaining STC. The experiments to follow provide a more severe test of the effect of forcing, since the unforced model for $\bar{L} = 25$ decays to a steady state.

Forcing from levels $j = 0$ and 1

For the experiment shown in Fig. 6.9(a), we periodize from the distinguished box $\bar{\mathbf{B}}^{2 \, 2}$. That is, the contribution of the large scales $j = 0$ and 1 to the evolution of the modes in the boxes is

179
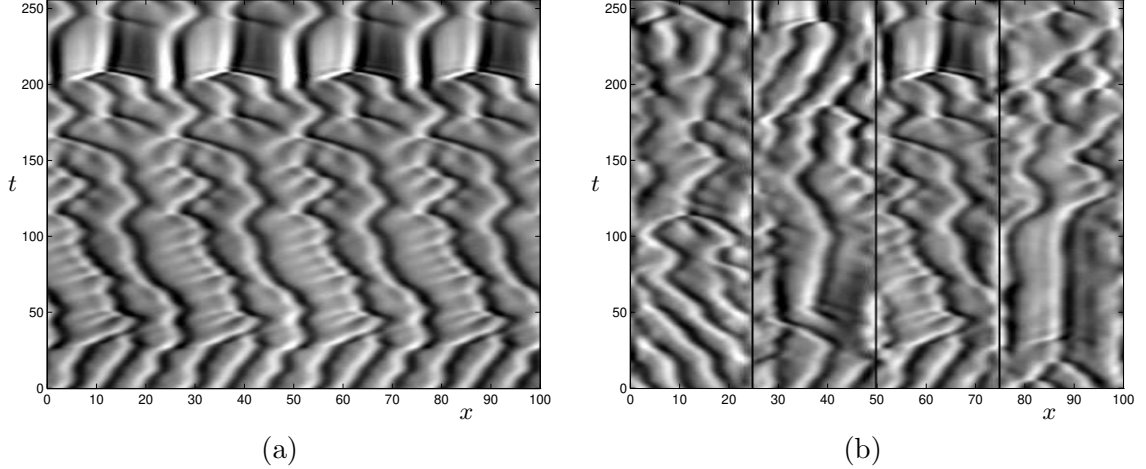
Figure 6.9: Periodized model with forcing: (a) Integration of modes in the distinguished box $\bar{\mathbf{B}}^{2\,2}$, periodized and forced by levels $j = 0$ and 1 of an independent KS integration with initial data $\mathbf{b}$. (b) Four simultaneous simulations, for boxes $\bar{\mathbf{B}}^{2\,m}$ with identical initial data, displaying the effects of aperiodicity of the forcing.

that which would be experienced by the modes in $\bar{\mathbf{B}}^{2\,2}$. The asymmetric influence of the large-scale forcing on the different boxes is apparent in Fig. 6.9(b), where we have performed four simultaneous experiments, treating each of the four boxes $\bar{\mathbf{B}}^{2\,m}$ in turn as distinguished. The initial data in (b) was chosen to be periodic, specifically, to be the data appropriate to $\bar{\mathbf{B}}^{2\,2}$ (so that (a) simply shows four copies of the third subsystem of (b)). The differences between the four boxes in Fig. 6.9(b) are thus solely due to the large-scale aperiodicity.

The first important point to note in Fig. 6.9 is that the large scale driving (which is essentially equivalent to Gaussian noise) maintains the periodized subsystem away from the steady state. Furthermore, local "events" reminiscent of the STC state, such as traveling structures and creation and collision of peaks, occur persistently. That is, the large-scale forcing is responsible for keeping the system "alive"; we also reached this conclusion in Sec. 5.2.2. However, visual inspection indicates that the dynamics of these forced models is somewhat unusual, a conclusion supported by the long-time statistical calculations reported in Fig. 6.10. In particular, the distribution of u, and of the $j = 5$ wavelet coefficients, is broader than for the full KS equation and approaches a Gaussian distribution, indicating a degradation of the characteristic spatial structure; while there is excess energy in wavelet levels 2, 5 and especially 3, which clearly shows up in the power spectrum.

Anomalous shock-like events   The statistical discrepancies may be related to occasional anomalous events, one of which is seen clearly beyond $t \approx 205$ in Fig. 6.9(a). Fig. 6.11(a) shows a cross-section of this structure at $t = 225$. From its shock-like shape, reminiscent of the shock discussed in the context of the destabilized KS equation (2.2) for $\varepsilon^2 > 1$, in Sec. 2.3.3 (compare Fig. 2.1), we may associate this structure with excessive energy in the largest scales of our model, that is, at wavelet levels 2 and 3. A glance at the wavelet coefficients (see Fig. 6.11(c)) indicates that the amplitudes of $a_{3\,4}$ and $a_{3\,5}$ are too large. Similar localized shocks are seen on following the solution in Fig. 6.9(a) further, for instance near $t \approx 450$. For convenience, in this Section we shall refer to these structures as *level 3 shocks*, as they are associated with too much energy in level 3; in the length $\bar{L}$ subdomain, they consist of a shock-like structure and a single adjacent spatial oscillation. More rarely, this model also supports *level 2 shocks*, in which the mode at level 2, the largest scale

180
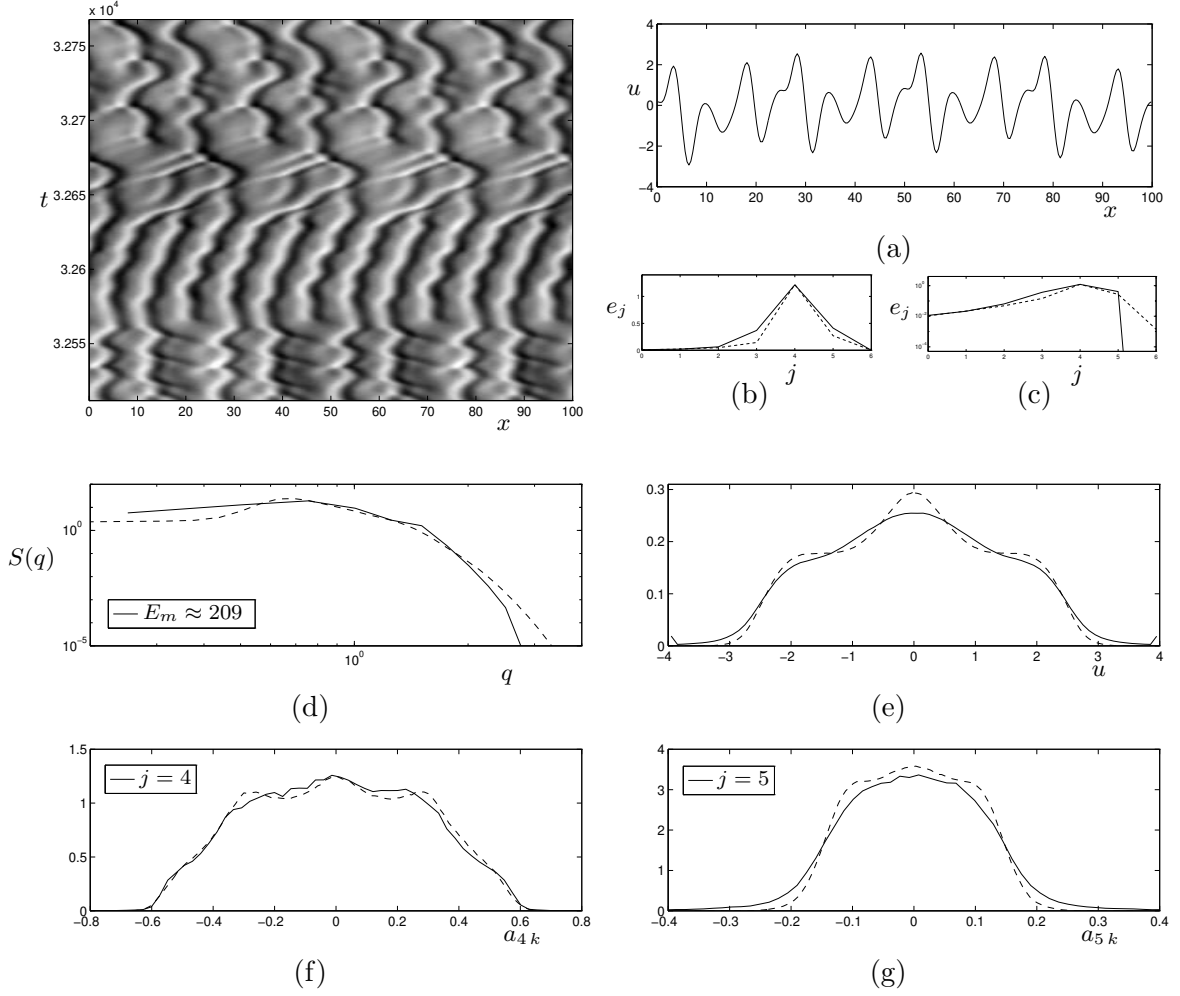
Figure 6.10: Comparison of model statistics with full KS equation: Forcing the periodized box $\bar{\mathbf{B}}^{2\,2}$ from levels $j = 0$ and 1 of autonomous run, as in Fig. 6.9(a). See caption of Fig. 5.5 for description. Autocorrelation time $\tau_c \approx 12$.

of the subsystem, is unduly excited. This single $\bar{L}$-periodic shock structure more closely resembles that of Fig. 2.1 in Sec. 2.3.3; an example for $t = 1200$ is shown in Fig. 6.11(b).

Fig. 6.11(c) shows the time history of the lowest three wavelet coefficients in the box, $a_{2\,2}$, $a_{3\,4}$ and $a_{3\,5}$, to $t = 512$. We can clearly see the large amplitudes in the level 3 wavelets responsible for the level 3 shocks near $t = 225$ (also seen in Fig. 6.9(a) and Fig. 6.11(a)) and near $t = 450$; in fact, for these two events, most of the energy is in $a_{3\,4}$, while $a_{2\,2}$ retains normal values. In Fig. 6.11(d) we show the evolution of the coefficients $b_{0\,0}$, $b_{1\,0}$ and $b_{1\,1}$, obtained from an independent run, which provide the large-scale driving. The level 3 shock beginning after $t \approx 205$ appears to be correlated with a large excursion in $b_{1\,1}$; however, the trigger for the event near $t \approx 450$ is not readily apparent from the forcing. Furthermore, one observes that the level 3 shock near $t = 225$ occurs only in box $\bar{\mathbf{B}}^{2\,2}$; none of the other boxes display this event, though they are all subject to the same forcing history (Fig. 6.9(b)). Instead, similar shock-like events occur within the other boxes at different times. We conclude that excess energy fed into the low internal modes can cause a level 2 or level 3 shock only when particular internal mode dynamics conspires with the large-scale excitations. The time series of the forcing alone is insufficient to predict such atypical events.
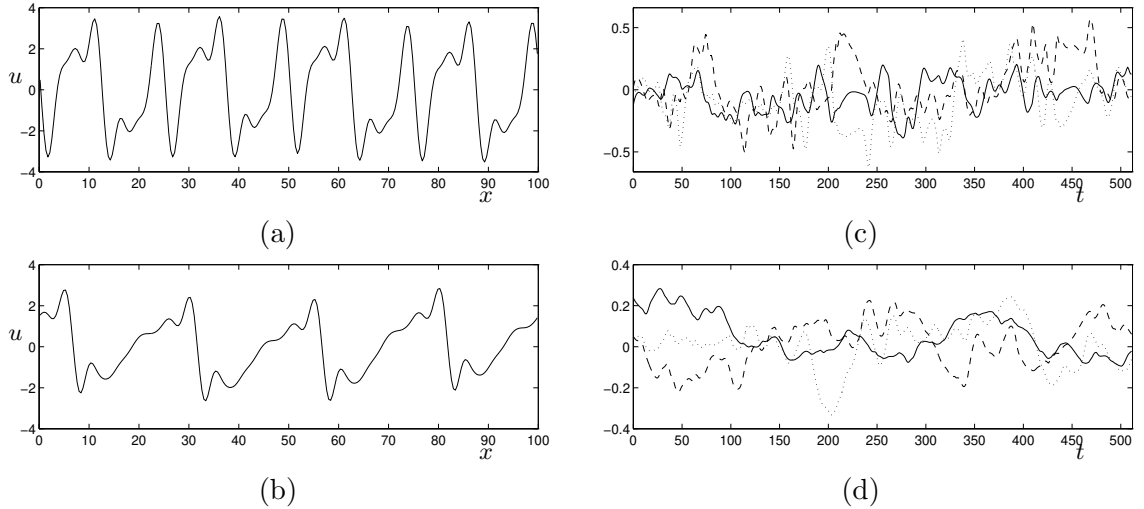
Figure 6.11: A closer look at the shock-like events for the simulation of Figs. 6.9(a) and 6.10. (a) Cross-section of level 3 shock at $t = 225$. (b) Cross-section of level 2 shock at $t = 1200$. (c) Time history to $t = 512$ for the lowest modes in the box: The solid, dashed and dotted lines are, respectively, $a_{2\,2}(t)$, $a_{3\,4}(t)$ and $a_{3\,5}(t)$. (d) Time series, for the same interval as in (c), of the large scale forcing modes from an independent KS run: respectively, $b_{0\,0}(t)$, $b_{1\,0}(t)$ and $b_{1\,1}(t)$.

Note that contrary to the case of the non-periodized, forced boxes of Sec. 6.1, the energy dissipation mechanism in these periodized subsystems is intact. Hence the actual amplitudes of u in these models rarely exceed those for the full KS equation. Instead, the energy distribution among the different wavelet levels within the model is distorted, leading to atypical structures. These observations are similar to those of Sec. 5.4.2, in which too much energy at the large scales led to shock-like structures, including the ridge states.

While the disruption relative to typical KS dynamics is less severe than for non-periodic models, the small $\bar{L}$-symmetric periodized models with asymmetric large-scale forcing still fail to capture successfully the main features of the STC state.

Related experiments

We have investigated some variations on the above-mentioned forcing approach. Large-scale forcing at level 0 alone (not shown) has a weaker effect on the active-scale models: while level 2 or 3 shocks appear less frequently, the system (with $L = 100$) is more likely to settle down into a mild perturbation of the trimodal attractor for an unforced $\bar{L} = 25$ periodic system.

Forcing at the lowest internal mode We have also considered experiments in which we specify the lowest mode internal to the boxes, $a_{2\,m}$, from the independent full KS integration, rather than letting it evolve within the model; see Fig. 6.12(a). This precludes the formation of level 2 shocks, since the modes for $j = 2$ are externally determined and thus cannot absorb excess energy within the model. However, level 3 shocks still occur. Visual inspection of space-time plots, as well as statistical analysis (not shown) similar to that of Fig. 6.10 indicates that this modified model has rather similar dynamics to that of Fig. 6.9 in which only levels 0 and 1 are externally forced.
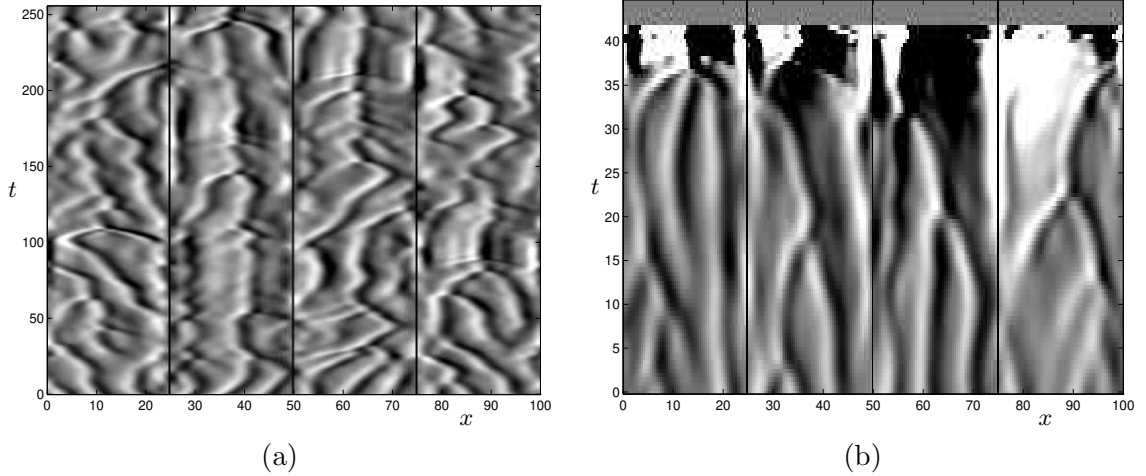
Figure 6.12: (a) Periodized models with periodic initial data. Levels $j = 0$ and 1, and internal modes at $j = 2$, are specified from an independent KS run with initial conditions **b**. (b) Self-consistent model: Modes in the periodized boxes $\bar{\mathbf{B}}^{2\,m}$ are forced from $j = 0$ and 1; those large-scale modes, in turn, are driven by the boxes. Note the different time scales, and observe the blowup before $t = 50$.

Varying the total length L Simulations (not shown) of periodized models with aperiodic large-scale forcing (at levels $j = 0$ and 1, or $j = 0$, 1 and 2) with different total lengths $L \neq 100$ indicate results largely similar to those discussed above. In fact, in our computations for $L = 50$, 60, 70 and 80, level 2 and 3 shocks appear more prevalent than they do for $L = 100$, and the dynamics has even less resemblance to the usual STC regime.

Self-consistent models A motivation for the creation of periodized subsystems of a full system is the construction of a *fully self-consistent* model for the KS dynamics: (periodized) subsystems are forced by the large scales, and in turn drive the large scale evolution. Such simulations were reported in [EBH96]. In such a model, the 2^{j_0} boxes $\bar{\mathbf{B}}^{j_0\,m}$ are periodized as before, and forced asymmetrically from the large scales. The modes $a_{j\,k}$ for $j < j_0$, however, instead of being obtained from an independent KS run, satisfy equations derived from the Galerkin projection in which the modal amplitudes for $j \geq j_0$ are obtained from the periodized boxes.

One of our simulations is shown in Fig. 6.12(b). The system blows up before $t = 50$, due to growth in the large-scale modes. We have encountered similar growth in Sec. 5.3.2 and Sec. 6.1. It appears that the energy transfer mechanism is again disrupted; in particular, we lose the correct phase relationships between active scale wavelets, which are adjacent from the point of view of the large scales (in the full system), but which belong to different boxes.

Observations

We have constructed localized periodic models with aperiodic forcing from the large scales, which is a natural choice in the light of the locations of the wavelets in the boxes relative to the large scale wavelets. The forcing, generated from an independent KS integration, can maintain the system in an active state away from the simple attractor, and can promote some typical KS events (Sec. 1.3.2). However, there are also atypical structures, such as the level 2 and level 3 shocks associated with excessive forcing of the lowest wavelet levels inside the boxes. The statistical behavior also does

183

not well approximate that of the STC regime of the KS equation. The discrepancies appear to be due to the asymmetry of the forcing terms.

As discussed more carefully in Sec. 3.3, the aperiodic forcing is also less desirable for the purposes of deriving a tractable effective equation. The experiments discussed here correspond to relatively low-dimensional models; there are 15 internal modes for levels $j = 2$–5, forced by a few modes at the large scales (three modes for forcing at $j = 0$ and 1). However, these forcing terms, being derived from a Galerkin projection of the full system, appear in the evolution equations for each internal mode in a rather complicated and opaque way.

From the point of view of deriving a tractable low-dimensional model, $\bar{L}$-periodic forcing is more desirable, in which the large scales are averaged over the boxes. Furthermore, there is promise that the atypical events observed previously will disappear under periodic forcing. Following the theoretical development of Sec. 3.3.1 and the motivation of this and the previous Sections, we now turn to periodized subsystems with periodized forcing.

6.2.2   Periodized models with periodic forcing

In our implementation of periodic forcing from the large scales, instead of explicit spatial averaging over the wavelets for low j, we average the vector field over the boxes; this permits us to remain within the framework of manipulating the wavelet coefficients at each time step, while retaining our fast wavelet transform KS integrator of App. B.2.2. In practice, this is equivalent to performing a time step with aperiodic large scale influences, as in Sec. 6.2.1, and then replacing each model wavelet coefficient by the average over the boxes of corresponding modes. As usual, we periodize from level $j_0 = 2$; here there are no distinguished boxes, all boxes $\bar{\mathbf{B}}^{2\,m}$ being equivalent.

External forcing from the large scales

For the experiment reported in Fig. 6.13(a), we periodize the forcing from levels $j = 0$ and 1; as usual, the driving time series is obtained from a concurrently running, independent full KS integration with initial data **b**.

By comparison with Fig. 6.7(a), with the same initial conditions, we see that the periodized forcing has a noticeable effect, maintaining some dynamical activity until beyond $t = 50$; however, ultimately this model settles down into the trimodal attractor. Relative to Fig. 6.9(a), in which the same large-scale driving was applied without periodization, the imposition of periodicity has greatly reduced the effects of the forcing term, and appears to have severely diminished its capability to keep the model dynamics "alive" and away from a simple attractor.

We have considered the effective evolution equation for this model at some length in Sec. 3.3.1; see (3.44, 3.50). There we have observed that $\bar{v}$ defined in (3.40) vanishes (see (3.45)); the periodization removes linear and parametric influences of the large scales. The fact that Fig. 6.13(a) and Fig. 6.7(a) are distinct provides empirical confirmation that the nonlinear contribution $\bar{w}$ of the large scales remains nonzero (see (3.41, 3.46, 3.48)). But these results also corroborate the discussion of Sec. 3.3.1 in which we find that $\bar{w}$ is small, and that there are numerous cancellations, including the vanishing of the nonlinear interaction between levels $j = 0$ and 1. In particular, there is no direct influence of $\bar{w}$ on the lowest internal level $j_0 = 2$, to provide the driving necessary to stir up the model. The elimination of excessive amplitudes and atypical dynamics which caused difficulties in Secs. 6.1 and 6.2.1 has come at the cost of reducing the large-scale influence below the threshold needed to drive the short system out of the basin of attraction of the trimodal cellular state; at least for the parameter values we are considering, the effective equation obtained via
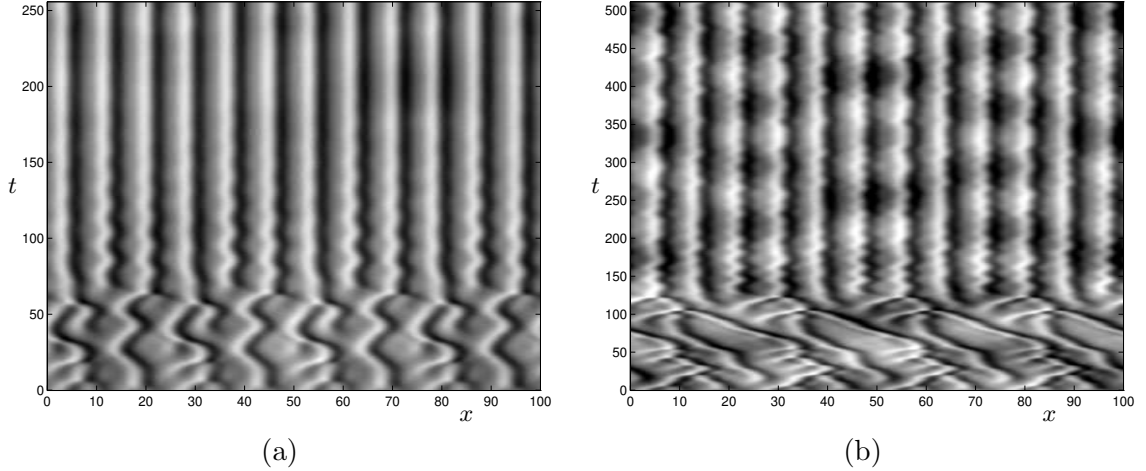
Figure 6.13: Periodized model with periodized forcing: Driving the large-scale levels $j = 0$ and 1, from (a) an independent KS integration with initial data **b**; (b) sinusoidal forcing, as specified in the text. The vector field is averaged over the boxes $\bar{\mathbf{B}}^{2\,m}$, equivalent to imposing $\bar{L}$-periodicity on the large-scale excitation.

periodic forcing does not seem to be sufficient to account for spatiotemporal chaos at the active scales.

We have performed several other experiments with controlled forcing at the large scales (compare Sec. 5.5), to confirm these results. Fig. 6.13(b) shows one of these experiments, a run in which the strength of the large-scale forcing is increased: the driving at levels $j = 0$ and 1 is sinusoidal, with slow period and large amplitude compared to the characteristic values at those levels in the KS equation (the actual, arbitrarily chosen specification of the experiment is $a_{0\,0}(t) = 0.5\sin(2\pi t/T)$, $a_{1\,0}(t) = 0.5\sin(1.9 \cdot 2\pi t/T)$, $a_{1\,1}(t) = 0.55\sin(1.87 \cdot 2\pi t/T + 0.87)$, with $T = 150$). As seen in the Figure (note the time axis), the transient time before decay into the attractor is increased, and the forcing from the large scales induces oscillations of the peaks at a rate higher than the driving frequency; but even this enhanced forcing amplitude is insufficient to maintain complex dynamics. In experiments (not shown) in which the (periodized) modes at levels 0 and 1 are held constant with sufficiently large amplitude, the dynamics do not appear to settle down to the trimodal state over the time of our simulation, but this is an excessively unrealistic and artificial situation which brings us no closer to a reasonable local model for reproducing STC.

More general large-scale periodic forcing

Periodization of the large-scale forcing to obtain an effective local model thus seems to eliminate too much of the desirable driving, as envisaged in Sec. 3.3.1. However, as indicated there, we can use these ideas to suggest extensions of this model, in which the forcing is periodic and thus does not incur the undesirable effects of symmetry-breaking, but there is still a strong direct influence on the active scale modes.

One possibility suggested in Sec. 3.3.1 is the introduction of a nonzero function $\bar{v}$ into (3.44), to simulate the effects of parametric and linear large-scale driving. In the remainder of this Chapter, we shall take a different approach, and consider direct forcing of the largest scale(s) of the model, by externally specifying the mode at the internal level $\bar{j} = 0$.

(a)   (b)
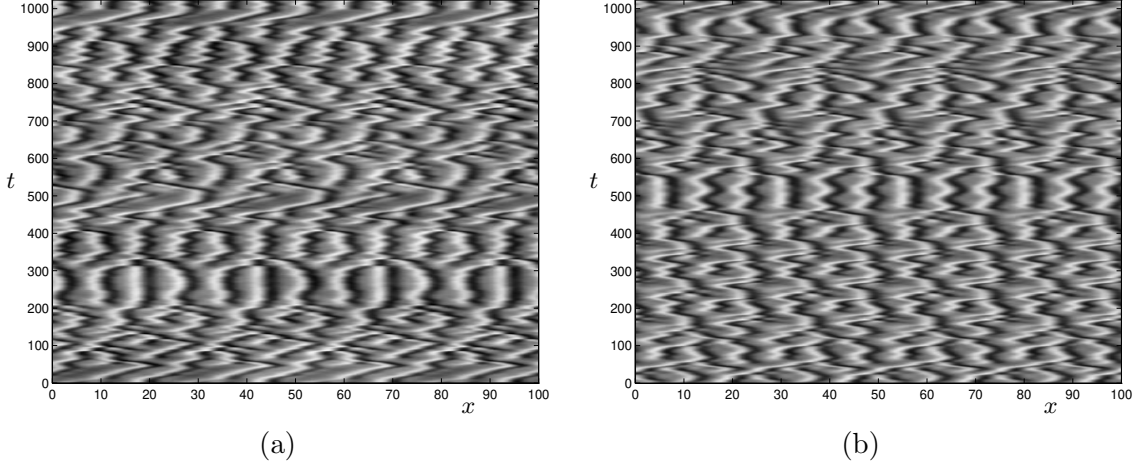
Figure 6.14: Periodized model with periodic forcing: (a) Periodized forcing of the box $\bar{\mathbf{B}}^{22}$ from levels $j = 0$ and 1, and driving of the lowest internal mode at level $j = 2$, obtained from an independent KS integration with initial data **b**. (b) Sinusoidal forcing, only at the largest scale internal mode at $j = 2$ ($\bar{\jmath} = 0$) of the local periodic model.

Periodized model with driving at lowest internal mode   Fig. 6.14(a) shows a plot, over a long time interval, of spatiotemporally complex dynamics which arises when, in addition to periodized forcing from levels $j = 0$ and 1, the lowest internal mode at level 2 (or at level $\bar{\jmath} = 0$ in terms of the local coordinates of the box) is also driven: $a_{2k} = b_{22}$, where b_{22} is obtained as usual from an independent KS run (compare Fig. 6.12(a), where the external large scale forcing is not periodized). The dynamics look remarkably like the complex dynamics of the KS equation; it is readily confirmed that the windows (for instance for $t \approx 200$–300 in Fig. 6.14(a)) in which the solution remains near the trimodal state, are those in which the driving amplitude $|b_{22}(t)|$ is unusually small. A glance at long-time statistics for this model (Fig. 6.15) also indicates excellent agreement with typical STC for the KS equation.

Let us recap what we are doing here. We have a periodized, local model for a subsystem of length $\bar{L} = 25$ of an $L = 100$ system, which is subject to external, periodized driving from the large scale levels $j = 0$ and 1 outside the model, and in which the lowest internal mode is explicitly forced. The latter is crucial, in view of our observation that the external force $\bar{w}$ is small and relatively ineffectual. It is the Gaussian excitation at the largest scale of the model, $j = 2$, which provides the stimulus for the typical events of STC, in full accord with our conclusions of Ch. 5.

Since, by the comparison between Fig. 6.13(a) and Fig. 6.14(a) the level $j = 2$ excitation clearly plays such a powerful determining role, relative to the periodized forcing from levels $j = 0$ and 1, it is reasonable to ask whether the external forcing $\bar{w}$ from $j = 0$ and 1 is necessary at all; what happens if we just drive at level 2?

Our simulations have confirmed that, as expected, forcing the periodized model at level $j = 2$ from the control run is sufficient to maintain complex dynamics and good statistics. The results, not shown here, are very similar to those of Figs. 6.14(a) and 6.15; levels 0 and 1, once periodized, do not have much influence. In Fig. 6.14(b) we show a similar simulation, in which we drive at level $j = 2$ not from an independent control run, but with sinusoidal forcing, $a_{2k}(t) = 0.1 \sin(2\pi t/T)$, $T = 50$. Though neither the amplitude (too low) nor the period (somewhat too long) are exactly as would be expected for level 2 of the STC state, this forcing is sufficient to maintain very convincing spatiotemporally complex KS dynamics, for which the statistics are also accurate (not shown).

186
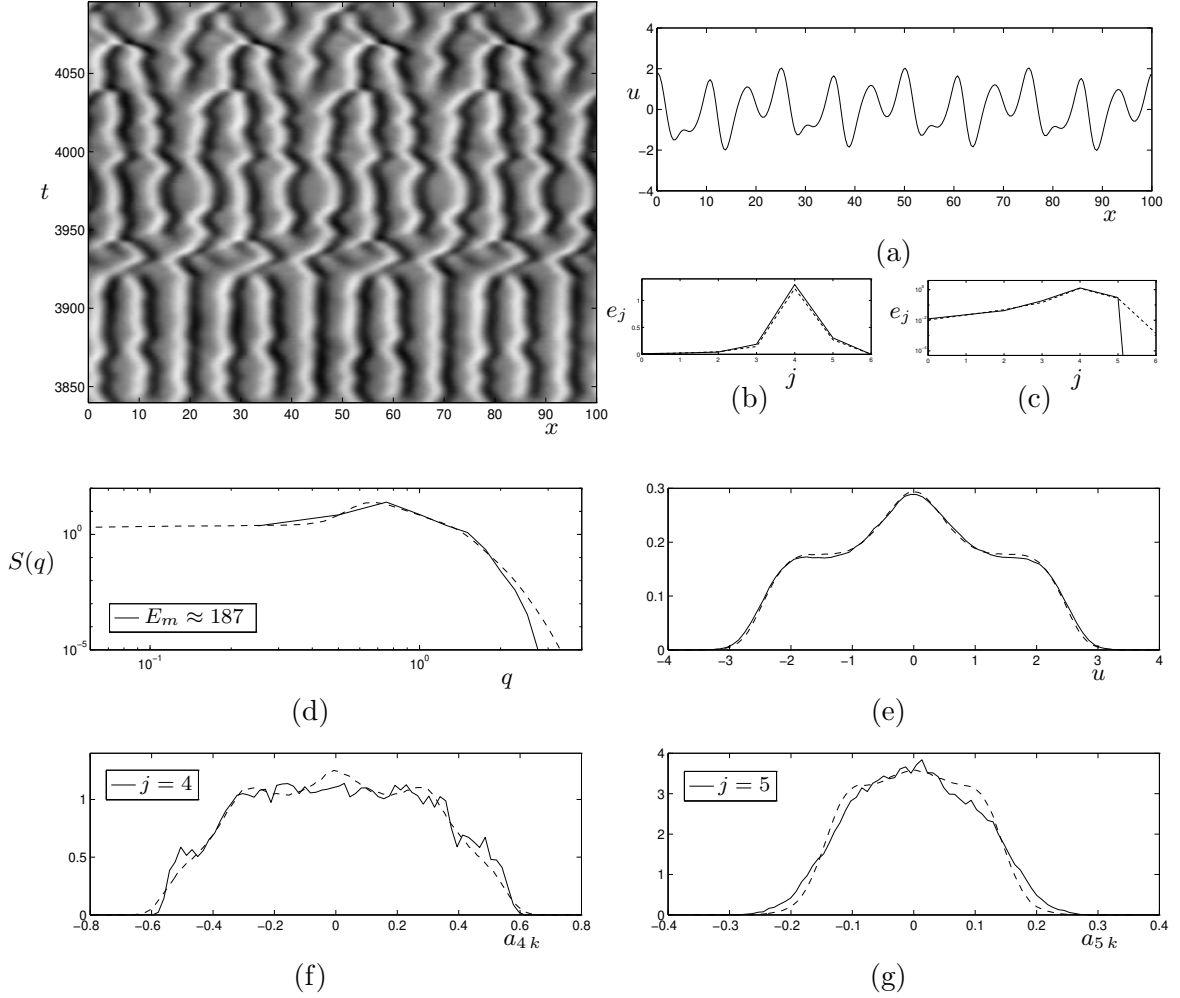
Figure 6.15: Comparison of model statistics with full KS equation: Periodized model with periodic forcing at levels $j = 0$–2, as in Fig. 6.14(a). See caption of Fig. 5.5 for description. Autocorrelation time $\tau_c \approx 13$.

6.2.3 Discussion

Of all the models considered so far in this Chapter, those of Fig. 6.14 have given the best results, in terms of reproducing the dynamics of the full system. Retaining the symmetries of the system by requiring periodized local models and periodic driving has removed the problem of excessive growth, as well as permitting typical events and traveling structures, while we allow external specification of the lowest internal mode of the box in order to obtain sufficient excitation.

We have now come full circle. A moment's reflection will convince the reader that Fig. 6.14(b), in which the only forcing is at the lowest internal mode, is nothing more or less than a full KS equation (1.1) on a short $\bar{L}$-periodic domain, in which the lowest level is externally specified. This is due to the equivalence between $\bar{L}$-periodized subsystems of large systems, and KS equations on $[0, \bar{L}]$, which is shown in Sec. 3.3.

To this point in this Chapter, we have treated the length $\bar{L}$ ($= 25$) models as subsystems of larger systems. However, in the light of our observations regarding Fig. 6.14, it is reasonable to consider small $\bar{L}$-periodic independent KS systems, with forcing. In our quest for localized models

reproducing STC in the KS equation, we are led naturally to study such small systems forced at their large scales, which are the subject of the final set of experiments.

6.3   Short models with spatiotemporally complex dynamics

Within the framework of short, forced systems, there is of course a wide range of possible models, encompassing different amplitudes, time scales and temporal characteristics of the driving; these may include (simple or chaotic) deterministic or random forcing time series. Furthermore, the length of the model domain—encompassing different elementary attractors in the absence of forcing—the treatment of small scales, and the number and location of modes at which the system is forced, may vary. A comprehensive set of experiments covering variations in several of these parameters could form the basis for another study, and we have not attempted to assess the effects of changes in the forcing. Our goal is simply to demonstrate that such short systems with forcing form a reasonable model for STC in the KS equation, by presenting the results of two kinds of simulations for a range of (short) values of L.[†]

To motivate these experiments further, let us briefly recap some of our previous conclusions:

- Within the STC regime, the dynamics are spatially localized, but interactions up to a length $l \sim \bar{l}_c \approx 25$ are dynamically relevant.

- The typical interactions of coherent structures occur at the active scale levels, but the large scales provide the excitation essential to sustain the complex spatiotemporal dynamics.

- The strength of the large-scale driving plays an important role; forcing that is too weak may lead to collapse into a cellular state, while unduly large amplitudes lead to ridge states and rapidly traveling peaks, or even to a shock-like solution.

- The temporal structure and correlation time of the driving has a relatively small influence.

- To avoid excessive growth, the forcing should be spatially L-periodic; but it should be sufficiently strong at the largest scales within the model to drive the characteristic spatiotemporal behavior.

On the basis of these observations, we now perform two final kinds of experiments, in which the forcing amplitude is "correct", but with different temporal characteristics; specifically, we look respectively at deterministic and random forcing.

Time-periodic forcing

In Fig. 6.16 we show the space-time evolution, for an interval of length $\Delta t = 256$ beyond the expected decay of transients, of short L-periodic KS systems of various lengths L driven at the lowest wavelet level with a deterministic sinusoidal signal. The forcing is specified as $a_{0\,0}(t) = C \sin(2\pi t/T)$. Here we fix $C = 0.2$ to give the correct mean square value $\langle a_{0\,0}^2 \rangle^{1/2} = 0.1$ for the wavelet coefficient in the STC regime (compare the PDFs in Fig. 4.14 for the large scales $j = 0$–2, recalling that level 0 for a length 25 system corresponds to level 2 for a length 100 domain). We have chosen the period of the forcing $T = 50$. This is somewhat slower than the characteristic time $\tau_2 \approx 16$ (see Table 4.1)—although the correct relation between correlation time and the period of

---

[†]We write L rather than $\bar{L}$ to emphasize that these short KS systems are not necessarily subsystems of larger ones.
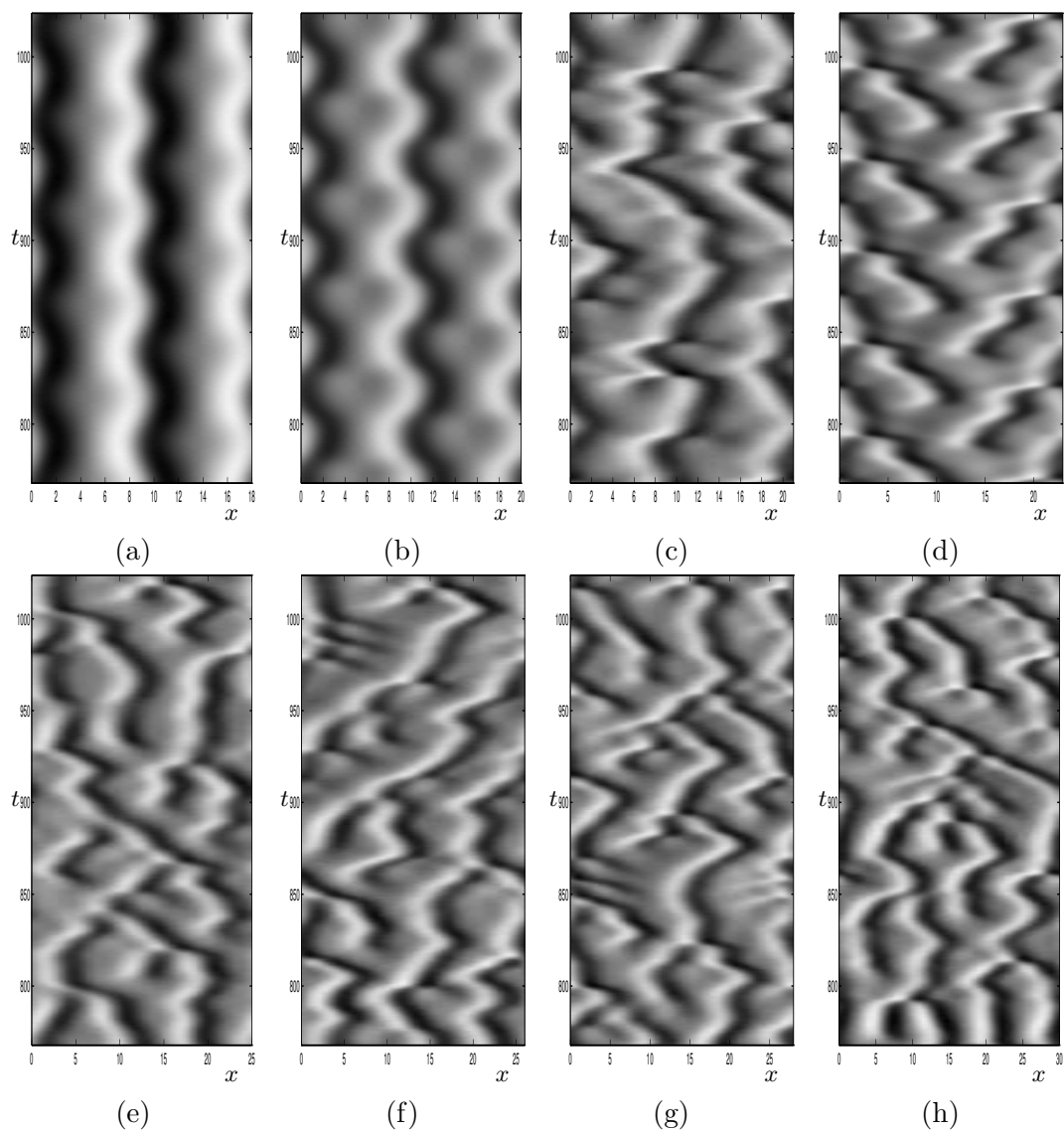
Figure 6.16: Short systems for a range of lengths L, sinusoidally driven at their lowest wavelet level, via $a_{0\,0}(t) = 0.2 \sin(2\pi t/T)$, $T = 50$: (a) $L = 18$, (b) $L = 20$, (c) $L = 21$, (d) $L = 23$, (e) $L = 25$, (f) $L = 26$, (g) $L = 28$, and (h) $L = 30$.

a sinusoid is unclear—but the slower driving is consistent with forcing that ultimately derives from low levels of a larger system well within the STC regime. In preliminary experiments (not shown) with sinusoidal driving with period $T = 15 \approx \tau_2$ and $L = 25$, the model underwent standing wave oscillations at the driving frequency about the trimodal state, whereas a slower $T = 50$-periodic signal facilitates sustained disorder (Figs. 6.16(e) and 6.17); this has motivated our experiments with the longer driving period.

As we see in Fig. 6.16, the large-scale forcing is generally sufficient to sustain complex dynamics in short systems, provided they are not too short. In (a) and (b), the systems oscillate about a cellular state; for $L = 18$ and $L = 20$, the domain appears to be simply too short and highly constrained to generate the typical events necessary for STC. This is consistent with our finding in Sec. 4.3.3 that $\bar{l}_c \approx 25$ is a characteristic dynamical interaction length in the STC regime, which implies that models successful at capturing the complex dynamics should have length $L \gtrsim \bar{l}_c$. We also observe in Fig. 6.16(d) that the $L = 23$ system is entrained by the sinusoidal driving, undergoing periodic motion with a complicated spatial structure at the driving frequency.

For the other lengths depicted, however—for $L = 21$, and for $L \geq 25$, seen in Fig. 6.16(c,e–h)—the large-scale oscillatory forcing stirs up the model sufficiently to yield sustained complex spatiotemporal dynamics; we have also observed this on continuing to larger $L > 30$. While for some lengths in this range, the attractor is chaotic in the absence of forcing—for instance, a Šil'nikov connection leads to chaos in the vicinity of $L \approx 26$—we recall that for most such L values, the unforced KS equations are attracted to relatively simple states, including cellular equilibria, the strange fixed point and their associated traveling or modulated traveling waves (see [HNZ86] and Fig. 1.1(a,c)). We deduce that the low-mode driving within the model is responsible for maintaining STC in these experiments.

The qualitative dynamics look convincingly similar to those typical in the full KS equation in the STC regime (see Sec. 1.4.1). For further confirmation of the success of our model, we perform a statistical comparison, as we have done throughout this and the previous Chapter. Fig. 6.17 compares, as usual, the distributions and spectra of a long time integration of a sinusoidally forced $L = 25$ system (Fig. 6.16(e)) with those of a full $L = 100$ KS equation.[†] The agreement is excellent; our short forced model simulates the STC of the full system. We have also compared the statistics of $L = 21$ and $L = 30$ sinusoidally forced models with the full $L = 100$ KS equation (not shown), and find a similarly convincing correspondence, although in the short $L = 21$ case the model remains somewhat nearer a cellular state. Note that in these latter situations, the comparisons in wavelet energy spectra and PDFs are complicated by the varying distribution of energy among wavelet levels; see Sec. 4.2.5 and Fig. 4.17.

A deterministic, sinusoidal driving force applied at the lowest wavelet mode thus appears to suffice for the generation of sustained spatiotemporal activity, with local events and statistical properties reminiscent of those in the STC state for large systems. However, instead of this artificial periodic forcing, we would prefer to work with an excitation that more closely approximates the Gaussian statistics of the true KS equation.

[†]On interpreting the statistics of Fig. 6.17 comparing $L = 25$ and $L = 100$, one should take into account that the smaller system has two fewer large-scale wavelet levels, and is expected to have 1/4 of the total energy.

Figure 6.17: Comparison of model statistics with full KS equation: Sinusoidal forcing at the lowest level of a short $L = 25$ system. The two space-time plots represent the first and last intervals of duration $\Delta t = 256$ of the integration to time $t = 32768$. Note that by comparison with an $L = 100$ system, the lowest two wavelet levels are missing, corresponding PDFs are shifted by two wavelet levels (so that (f) and (g) display the $j = 2$ and 3 wavelet level PDFs for the model, compared with levels $j = 4$ and 5 for $L = 100$, respectively), and the total energy E_m is proportional to the length. See caption of Fig. 5.5 for further description. Autocorrelation time $\tau_c \approx 14$.

Forcing generated via a stochastic model

We have performed experiments analogous to those described above, in which the excitation at the mode $a_{0\,0}$ is derived from the stochastic process (4.17, 4.18) described in Sec. 4.2.3. As in the similar simulations of Sec. 5.5.2, we have chosen to retain the values given in [HJJ93] for the parameters D, ν and τ_f, which reproduce the correct amplitudes corresponding to equipartition of energy at the large scales. The choice of q in (4.17) only affects the time scales, $\tau_q \sim q^{-2}$. Ostensibly, for the largest scale mode of a length L system, we should use $q = 2\pi/L$; however, the ensuing temporal dynamics is too rapid, as we have already observed in Sec. 5.5.2 for level $j = 2$ of an $L = 100$ system. In trying to imitate STC in these short systems, we wish to simulate the effects of slow Gaussian noise which arises in much longer domains. We have found that an effective way to achieve this, and to reduce the time scales of forcing appropriately, is to choose $q = 2\pi/2L$ in the model (4.17, 4.18) for the forcing at the lowest mode.

Using this stochastic model with the given parameters, we have performed experiments with Gaussian forcing for the same range of lengths L as previously; some results are shown in Fig. 6.18. As in the case of sinusoidal forcing, the $L = 18$ and $L = 20$ systems are too short to sustain interesting spatiotemporal dynamics, and settle into an apparent heteroclinic cycle in which the random excitation drives them from one bimodal state to the other and back. The longer systems with $L \geq 21$ in Fig. 6.18(c–h), however, all display sustained chaotic behavior closely reminiscent of the STC state for long KS systems, a fact which is borne out by a comparison of the statistics between the $L = 25$ model of (e) and the full equation (Fig. 6.19). Similar statistical agreement, not shown, was displayed by the $L = 21$ and $L = 30$ experiments.

A minor caveat to the above discussion is that the statistics of Fig. 6.19, especially the PDFs of u and the level 2 wavelets in (e) and (f), display a trend towards the cellular state; this is also apparent in the space-time plots of Fig. 6.18(d,e,f). This effect is readily understood by recalling that for lengths including $L = 25$ the system will tend to the attracting cellular state in the absence of forcing, and will thus temporarily approach such a state over time intervals during which the stochastic forcing $a_{0\,0}$ has small amplitude; compare for instance Figs. 5.22(b) and 5.23. The occasional decay to a cellular state and away from STC is thus a consequence of the fact that we are forcing with a single time series. One observes a similar effect for the full KS equation for a length such as $L = 50$, which has a chaotic attractor but occasionally approaches simpler cellular states. For large L well within the STC regime, there are sufficiently many Gaussian modes that the likelihood of their almost vanishing simultaneously is negligible, leading to the observed persistent disorder.

Taking this comment into account, our short system with randomly generated forcing well reproduces the spatiotemporally chaotic state observed for larger lengths L. Both deterministic and stochastic forcing at the lowest wavelet level of a short KS system are capable of driving the system sufficiently that it generates complex dynamics similar to those observed in the large-L thermodynamic limit.

192
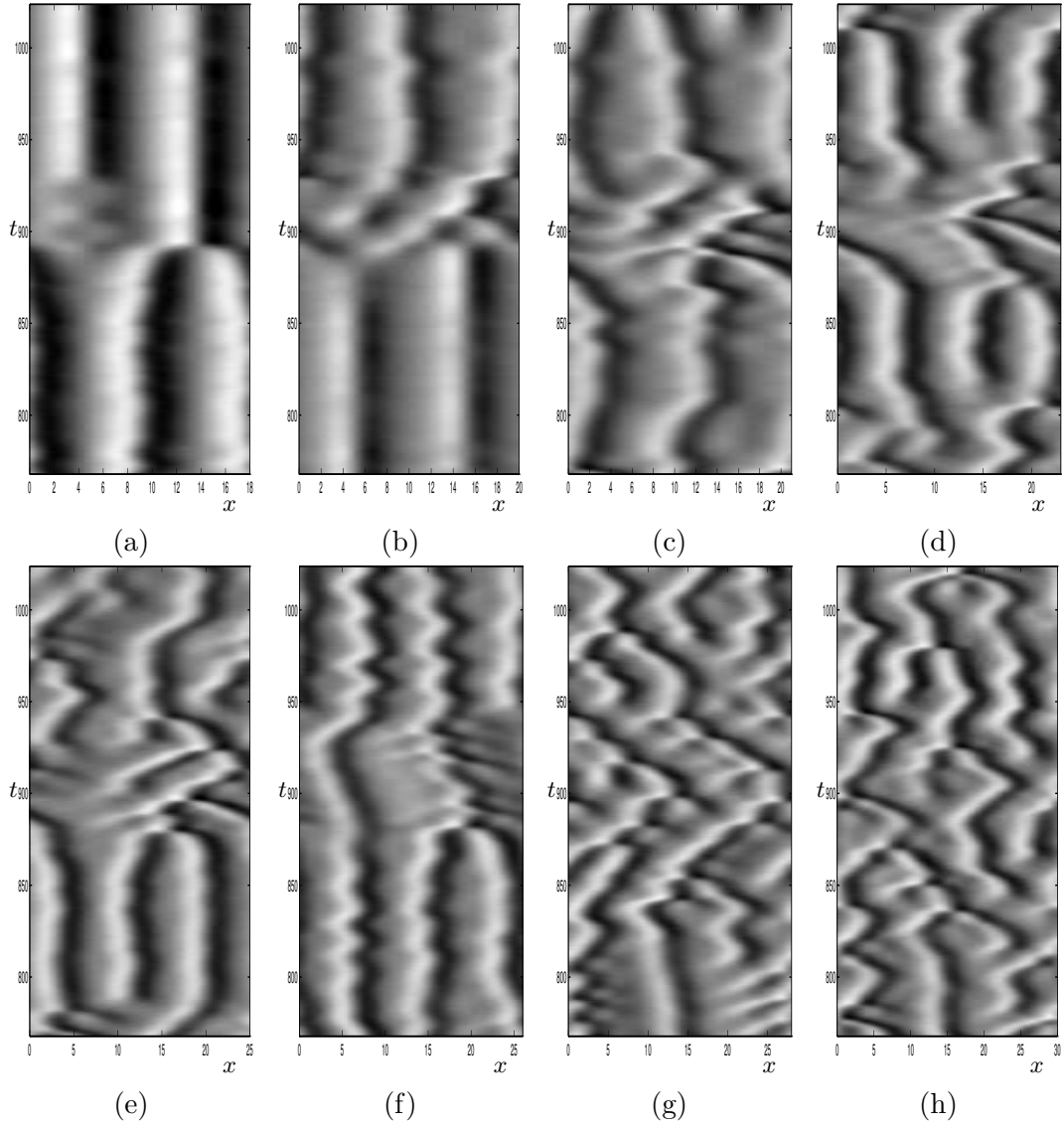
Figure 6.18: Short systems for a range of L, randomly driven at their lowest wavelet level according to the stochastic model of Sec. 4.2.2: (a) $L = 18$, (b) $L = 20$, (c) $L = 21$, (d) $L = 23$, (e) $L = 25$, (f) $L = 26$, (g) $L = 28$, and (h) $L = 30$.
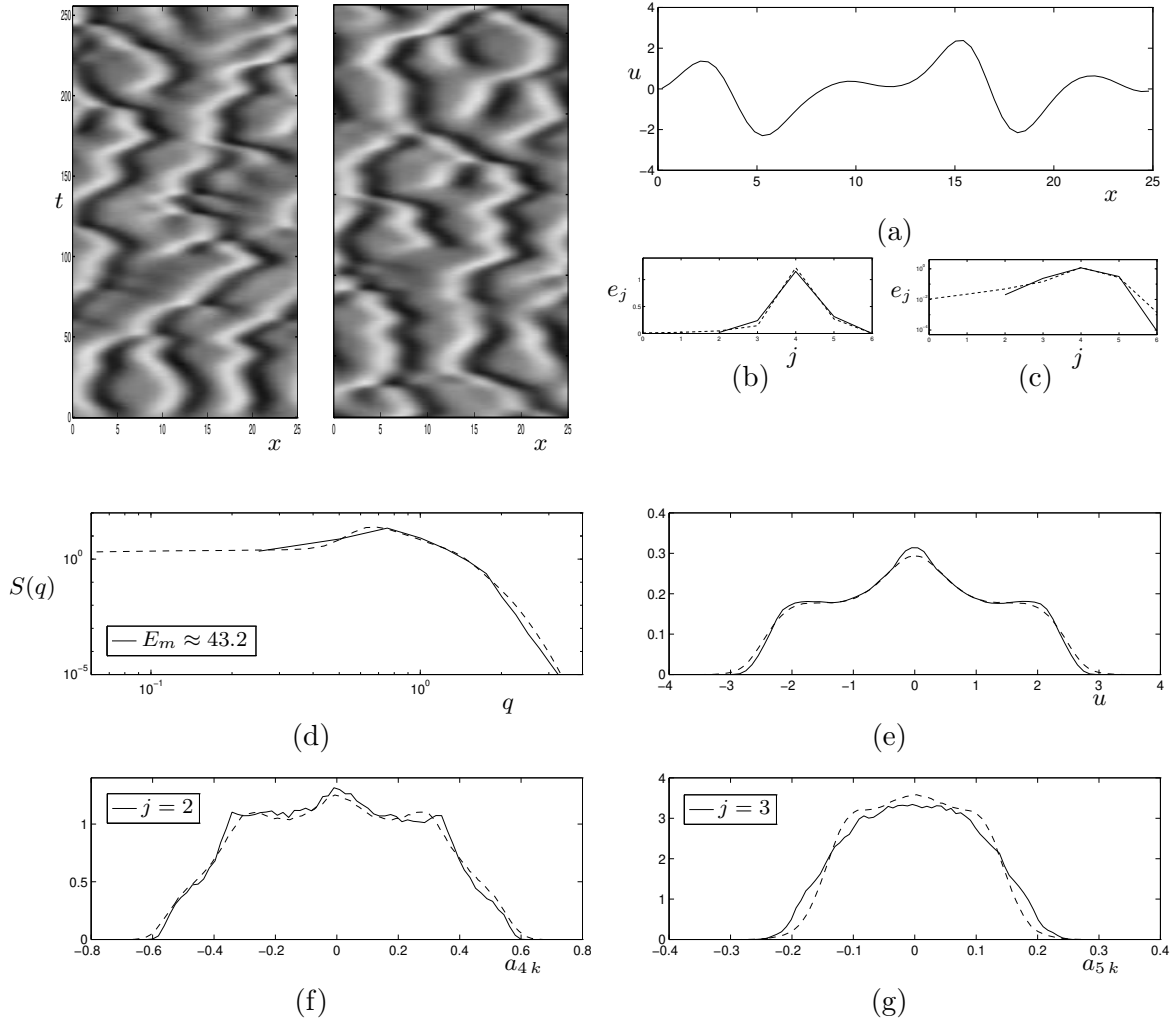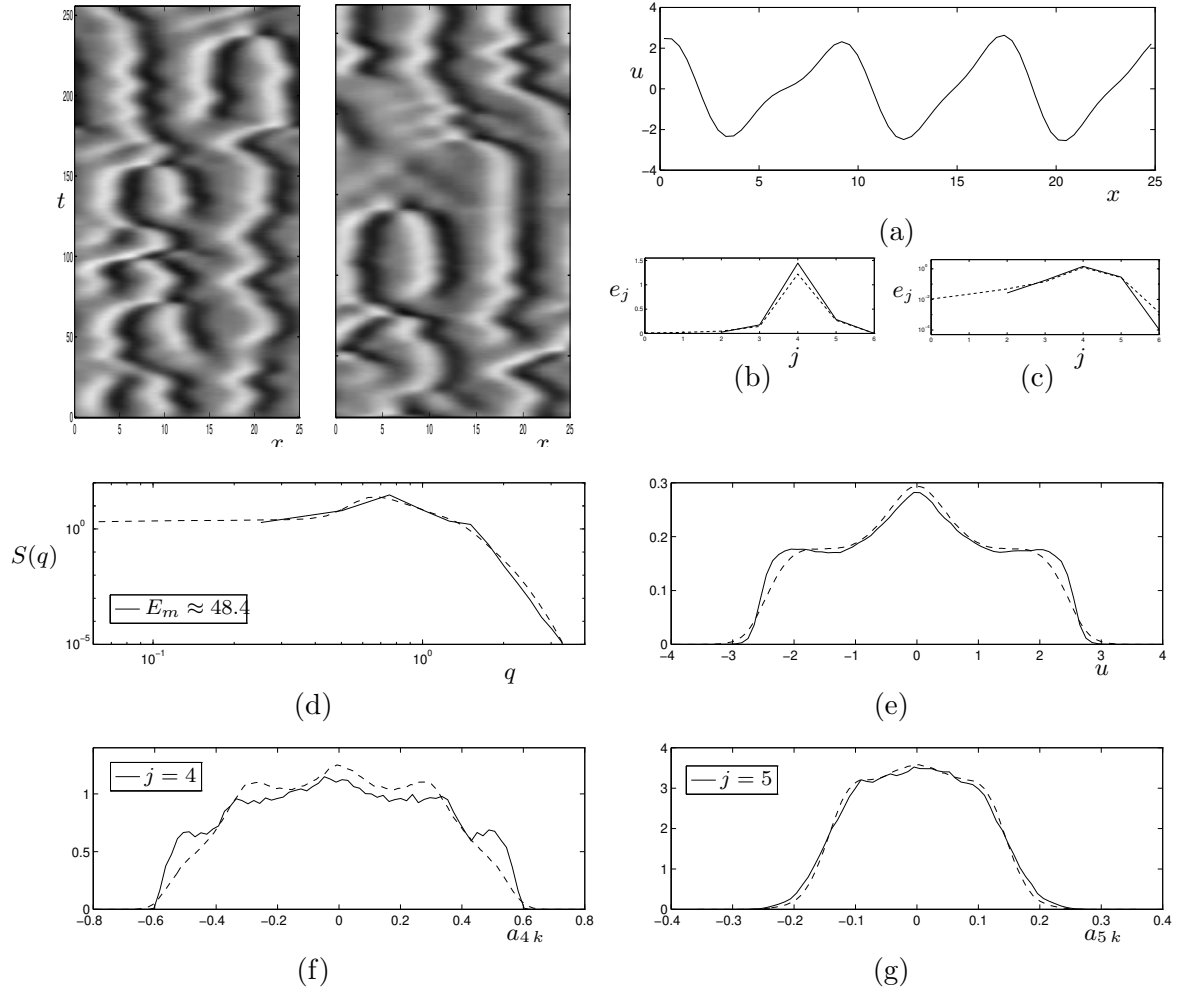
Figure 6.19: Comparison of model statistics with full KS equation: Random forcing at the lowest level of a short $L = 25$ system. See caption of Figs. 5.5 and 6.17 for description. Autocorrelation time $\tau_c \approx 18$.

194

6.4 Discussion and conclusions

It is remarkable that such small systems, when forced at their largest scales, appear to maintain spatiotemporally complex behavior so robustly; and this certainly merits further investigation. While both aperiodic forced systems and periodic models with aperiodic forcing display undesirable features, from the point of view of simulating the full STC state, our short systems with periodic forcing at the low modes seem to have all the "right" dynamics. We appear to have discovered a "minimal box" containing the ingredients for spatiotemporal chaos in the Kuramoto-Sivashinsky equation.

Such short systems are particularly attractive as they may be described by relatively low-dimensional dynamical systems, obtained via Galerkin projection, and using center-unstable or inertial manifold truncation to provide appropriate modeling of small scales. In a wavelet framework, for instance, with simple truncation of small scales, we can get a good representation for an $L \leq 25$ KS equation with levels $j = 0$–4, that is, with a 31-dimensional system of ODEs; and a suitable choice of inertial manifold projection or, possibly, further truncation may allow us to remove another level, to give a 15-dimensional system. These dimensionalities approach those that may be tractable by standard dynamical systems techniques, and the investigation of relatively low-dimensional systems, externally driven at one or more of the largest scales, is an interesting project for further exploration suggested by the results of this thesis, especially of Sec. 6.3.

The wavelet decomposition and pyramidal hierarchy has been very useful to us, forming the basis for the experiments of this and the previous Chapter in which we have thoroughly explored STC in the KS equation. However, at this point there is no *a priori* reason not to return to a Fourier description and force at the largest scale Fourier modes, especially as such models may be analytically more tractable. While we have restricted ourselves here to the simplest case of forcing at a single mode, the extension to more general forcing may also be interesting, although of course no longer as appealing on the grounds of simplicity.

In this thesis, we do not pursue the analysis of such finite-dimensional systems further. One possible interesting direction, which may facilitate a more quantitative understanding than that possible in our experiments, may involve a bifurcation analysis for a small system, as the forcing strength (either deterministic or stochastic) is increased, to attempt to detect a qualitative change signaling a transition to STC.

We have obtained strong support for the idea that KS dynamics is localized in space and scale. We achieved this first through the extensive statistical characterizations of Ch. 4, and by ascertaining the existence of finite averaged and instantaneous interaction lengths. We continued in Ch. 5 by introducing a novel series of experiments, in which numerous manipulations allowed us to identify distinctive dynamical contributions from different wavelet levels. Lastly, the successes in the present Chapter on obtaining spatially localized models verify that the spatiotemporally chaotic behavior is locally determined.

In all these investigations, the use of wavelets, introduced in Ch. 3, has been very helpful. The spatial localization of the basis functions allowed us to extract models on a restricted subdomain. Furthermore, wavelets group different blocks of scales, and provide a relatively coarse-grained description. This was crucial to the experiments of Ch. 5, since as the length L increases, the number of wavelet levels spanning the active scales remains constant, and in manipulating wavelet levels, there is a finite number of possible permutations. In a Fourier description, on the other hand, the modes asymptotically become a continuum, severely hampering efforts to distinguish distinct contributions. We have utilized few properties of wavelets other than their pyramidal hierarchy and that they form an orthonormal basis, however; in particular, we make no claim that

the periodic spline wavelets are best suited to the KS equation, and we would welcome studies with other wavelet families.

In the light of our experiences in this investigation, we suggest the use of similar techniques for the study of other spatiotemporally complex systems; the methods of Ch. 5, in particular, could have more general applicability. An obvious candidate for such analyses is of course the damped KS equation of Ch. 2 for a range of damping parameters ε^2, or other extensions of the KS equation [DE98, Joh98]. However, one may be able to shed new light on other complex systems in this or related ways.

To complement the investigations of this thesis, especially of Ch. 5, we are studying the energy transfer mechanism more thoroughly. It appears that with the use of a wavelet basis, the analysis of time- and space-dependent correlations between modes confirms that the flow of energy is localized in space and scale.

From the results of Sec. 6.3, we deduce that short systems, provided they have length at least of order the dynamical interaction length, can sustain spatiotemporal complexity. In this view, the attractor for the appropriately forced short systems is in some sense similar to that in the extensive limit. We can give an, as yet purely heuristic, description for this idea that the large system may be fully understood in terms of the dynamics of smaller subsystems, by writing

$$\text{``}\mathcal{A}_L \approx \oplus \mathcal{A}_{\bar{L}}\text{''},$$

where $\mathcal{A}_L$ represents the attractor for a length L system; of course, this representation presupposes the as yet unproven extensivity of the KS equation. This picture deduced from our experiments of Sec. 6.3 allows us to speculate that the main difference between "large" and "small" systems is the noisy dynamics at the lowest modes which drives the typical events. This noise arises due to the collective interactions of the subsystems; and the threshold to sustained STC occurs when sufficiently many subsystems interact to maintain the Gaussian large-scale dynamics, which in turn feeds into the subsystems and maintains activity within them, in a similar way to our latest experiments.

This suggests seeking a simple model for the self-consistent interaction between subsystems and one or a few large-scale modes, in which each perturbs the others away from simple attracting states. The preliminary Fourier-based work on coupled local models reported in the thesis of Dankowicz, which encompasses external driving at the largest scales (see [Dan95, Fig. 6.10]), may be a step in this direction.

In summary, by a combination of theory, analysis of long-time computations, experimental manipulation of interactions and modeling, we have achieved a detailed understanding of the spatiotemporally chaotic regime in the Kuramoto-Sivashinsky equation, one that is highly suggestive concerning features of localization and extensivity of the dynamics. Placing our results on a rigorous mathematical footing is a next important, and quite nontrivial, challenge.

Appendix A

Alternative Formulations of the KS Equation

The literature on the Kuramoto-Sivashinsky equation is slightly confused by the multiplicity of alternative forms and scalings in which the equation is written. The following "dictionary" may ease translation of results from one form to another (see also the Appendix of [Joh98]).

Basic form of the KS equation

"Derivative" form   For our fundamental, preferred formulation of the KS equation, we will take (1.1):

$$\boxed{u_t + u_{xxxx} + u_{xx} + uu_x = 0,}$$ (A.1)

where $x \in [0, L]$, and we impose periodic boundary conditions. The L^2 norm (squared) is

$$\|u\|^2 \stackrel{\text{def}}{=} \int_0^L u^2 \, dx.$$

Here the bifurcation parameter L is the domain length, not a parameter in the PDE itself (see [JKT90]). Also, L is here assumed constant (independent of x and t). Of course, (A.1) on $[0, L]$ is equivalent to the same equation on $[-L/2, L/2]$. This is the form used for instance by [CEES93a].

The formulation (A.1) is the one used throughout this thesis, unless noted otherwise. The major exception is Ch. 2, where we use the form (A.11) described below (with $L/\sqrt{2} \to L$) for easy correspondence with the more general damped KS equation (2.2). In this Appendix we relate, with occasional references, many of the other formulations encountered in the literature to the basic form (A.1).

Note that u may be thought of as the derivative of a periodic function w (see (A.2) below); thus we always require u to have mean zero; that is,

$$\int_0^L u \, dx = \int_{-L/2}^{L/2} u \, dx = 0.$$

197

"Integral" form   Writing $u = w_x$,[†] and integrating once with respect to x, we find the integrated form (1.3)

$$w_t + w_{xxxx} + w_{xx} + \frac{1}{2}w_x^2 + K = 0, \quad x \in [0, L],$$

(A.2)

where K is a constant of integration, often assumed to vanish. The evolution of the mean, $m \stackrel{\text{def}}{=} (1/L)\int_0^L w\, dx$, satisfies the drift equation (see [KNS90])

$$\frac{dm}{dt} = -\frac{1}{2L}\int_0^L w_x^2\, dx - K.$$

Thus, if we ignore the constant of integration K, in general the magnitude of the mean will grow without bound. This is desirable for interpretations of w as a growing interface height (see Sec. 4.2.2), but less suitable for numerical simulations; by choosing K appropriately, we may subtract off the drift, so that (A.2) becomes

$$w_t + w_{xxxx} + w_{xx} + \frac{1}{2}w_x^2 - \frac{1}{2L}\int_0^L w_x^2\, dx = 0, \quad x \in [0, L].$$

(A.3)

The L^2 norms of u and w_x are related by

$$\|u\|^2 = \int_0^L u^2\, dx = \int_0^L (w_x)^2\, dx = \|w_x\|^2.$$

Alternative formulations obtained via constant rescalings

1. The general linear rescaling of the KS equation (in the "derivative" form)[‡] is

$$y = ax, \ \tau = bt, \ v = cu \ \text{ (use } a, b, c > 0) \quad \Rightarrow \quad \frac{\partial u}{\partial t} = \frac{b}{c}\frac{\partial v}{\partial \tau}, \ \frac{\partial u}{\partial x} = \frac{a}{c}\frac{\partial v}{\partial y}.$$

On multiplying through by c/b, we obtain

$$v_\tau + \frac{a^4}{b}v_{yyyy} + \frac{a^2}{b}v_{yy} + \frac{a}{bc}vv_y = 0, \quad y \in [0, aL],$$

(A.4)

where

$$\|u\|^2 = \int_0^{aL}\left(\frac{v}{c}\right)^2 d\left(\frac{y}{a}\right) = \frac{1}{ac^2}\int_0^{aL} v^2\, dy.$$

This is the most general form, *provided* the rescaling is constant in space and time; it contains four parameters, of which three may be arbitrarily chosen. As already noted, due to our focus in this thesis on the comparison between long and short systems, the most appropriate form for our purposes (A.1) retains the bifurcation parameter in the length of the domain: $a = b = c = 1$.

[†]In the remainder of this thesis, we write $h \stackrel{\text{def}}{=} \int u\, dx$, interpreting it as an interface height. However, in this Appendix, h is used as a length scaling parameter, so instead we use w for the solution of the integrated equation (A.2).

[‡]The rescaled versions of the KS equation, given in this Appendix for the derivative form (A.1), may all be translated to the integral form (A.2) or (A.3).

A related scaling, with $a = b = 1$, $c = 1/2$, appears in the thesis of Dankowicz [Dan95], and in [Man81, ZL85, DHBE96, EAHGP98]; it is frequently obtained by differentiating an integral form similar to (A.2) without the factor $1/2$ multiplying the nonlinear term.

The scalings discussed below are all special cases of the general form (A.4) which have arisen in the literature.

2. Simple rescaling of the domain:

$$y = \frac{x}{h} \quad \Rightarrow \quad u_x = \frac{1}{h}u_y,$$

so (with $v = u$, $\tau = t$)

$$v_\tau + \frac{1}{h^4}v_{yyyy} + \frac{1}{h^2}v_{yy} + \frac{1}{h}vv_y = 0, \quad y \in [0, L/h];$$

and the norm is

$$\|u\|^2 = h\int_0^{L/h} v^2\,dy.$$

Choosing $h = L$, this gives the equation on the unit interval

$$\boxed{v_\tau + \frac{1}{L^4}v_{yyyy} + \frac{1}{L^2}v_{yy} + \frac{1}{L}vv_y = 0, \quad y \in [0, 1]} \tag{A.5}$$

where

$$y = \frac{x}{L}, \quad v = u, \quad \tau = t; \quad \text{and} \quad \|u\|^2 = L\int_0^1 v^2\,dy.$$

Choosing $h = L/(2\pi)$, we get

$$\boxed{v_\tau + \frac{(2\pi)^4}{L^4}v_{yyyy} + \frac{(2\pi)^2}{L^2}v_{yy} + \frac{2\pi}{L}vv_y = 0, \quad y \in [0, 2\pi]} \tag{A.6}$$

where

$$y = \frac{2\pi x}{L}, \quad v = u, \quad \tau = t; \quad \text{and} \quad \|u\|^2 = \frac{L}{2\pi}\int_0^{2\pi} v^2\,dy.$$

These forms are useful for numerical simulation of (A.1); in particular, we use (A.6) for a Fourier pseudospectral implementation, as our fast Fourier transform assumes 2π-periodicity (see App. B.2.1), while (A.5) is appropriate for wavelet-based routines, with standard wavelet transforms defined for a basis periodic on the unit interval $[0, 1]$ (see App. B.2.2).

3. More generally, one can write

$$y = \frac{x}{h}, \quad \tau = \frac{1}{\nu h^4}t, \quad v = hu.$$

Then

$$\frac{\partial u}{\partial t} = \frac{1}{\nu h^5}\frac{\partial v}{\partial \tau}, \quad \frac{\partial u}{\partial x} = \frac{1}{h^2}\frac{\partial v}{\partial y},$$

and (A.1) becomes (on multiplying through by νh^5)

$$v_\tau + \nu v_{yyyy} + \nu h^2(v_{yy} + vv_y) = 0, \quad y \in [0, L/h].$$

199

One typically removes one of the superfluous parameters by taking $h = L/2\pi$, as we shall assume below; $h = L$ is of course another simple case, in which case the domain becomes $[0, 1]$.

In the case $h = L/2\pi$, we can write the previous equation as

$$\boxed{v_\tau + \nu v_{yyyy} + \alpha(v_{yy} + vv_y) = 0, \quad y \in [0, 2\pi],}$$
(A.7)

where

$$\alpha = \nu h^2 = \nu \left(\frac{L}{2\pi}\right)^2, \quad \text{or} \quad \frac{L}{2\pi} = \sqrt{\frac{\alpha}{\nu}},$$

and

$$\|u\|^2 = \int_0^{L/h} \left(\frac{v}{h}\right)^2 d(yh) = \frac{2\pi}{L} \int_0^{2\pi} v^2 \, dy = \sqrt{\frac{\nu}{\alpha}} \int_0^{2\pi} v^2 \, dy;$$

α and ν are the parameters in the system, one of which may still be fixed arbitrarily.

One of the forms given originally by Sivashinsky [Siv79] used $\nu = 4$, to give

$$\boxed{v_\tau + 4v_{yyyy} + \alpha(v_{yy} + vv_y) = 0, \quad y \in [0, 2\pi], \ \alpha = 4h^2.}$$
(A.8)

In the integrated form (often with the mean explicitly subtracted off) this scaling has been very popular; see for instance [HNZ86, GK88, SKN88, KNS90, BJKT90, AGL92, KA92, SK93, ALT93, BK96], and other works by these authors and their coworkers; in [SC96a, CS97] the form analogous to (A.8) is studied with the choice $h = L$, on a unit length domain.

Alternatively, one can set $\nu = 1$, which yields

$$\boxed{v_\tau + v_{yyyy} + \alpha(v_{yy} + vv_y) = 0, \quad y \in [0, 2\pi],}$$
(A.9)

where

$$\alpha = h^2 = \left(\frac{L}{2\pi}\right)^2, \quad \text{or} \quad L = 2\pi\alpha^{1/2};$$

in the thesis of Johnson [Joh98] this form was studied, as well as the extension where $\alpha = \alpha(x)$ was assumed to be spatially varying.

A further possibility is to retain the viscosity ν, and eliminate α, by setting $\alpha = 1$, or $\nu = h^{-2}$ —see [SP91, SP96, CCP97]:

$$\boxed{v_\tau + \nu v_{yyyy} + v_{yy} + vv_y = 0, \quad y \in [0, 2\pi],}$$
(A.10)

where

$$\nu = \frac{1}{h^2} = \left(\frac{2\pi}{L}\right)^2, \quad \text{or } L = 2\pi\nu^{-1/2}.$$

In the integrated equation, this scaling was used for instance by [HN86, AGH89].

4. A particular rescaling that is useful when relating the KS equation to other amplitude equations, or when including damping, is

$$y = \frac{1}{\sqrt{2}}x, \ \tau = \frac{1}{4}t, \ v = 2\sqrt{2}u \quad \Rightarrow \quad \frac{\partial u}{\partial t} = \frac{1}{8\sqrt{2}}\frac{\partial v}{\partial \tau}, \ \frac{\partial u}{\partial x} = \frac{1}{4}\frac{\partial v}{\partial y}.$$

Then (A.1) is equivalent to

$$v_\tau + v_{yyyy} + 2v_{yy} + vv_y = 0, \quad y \in [0, L/\sqrt{2}]; \qquad (A.11)$$

and

$$\|u\|^2 = \int_0^{L/\sqrt{2}} \left(\frac{v}{2\sqrt{2}}\right)^2 d(\sqrt{2}y) = \frac{1}{4\sqrt{2}} \int_0^{L/\sqrt{2}} v^2 \, dy.$$

A reason this formulation is interesting is that it may be written as

$$v_t = -(\partial_y^2 + 1)^2 v + v - vv_y,$$

in which the negative definite part of the linear operator has been isolated, and which is in a similar form to the Swift-Hohenberg equation. Replacing the v term on the right-hand-side by $\varepsilon^2 v$ leads to the "damped" KS equation (2.2) (see [PM80, PZ81, Zie95, MS95]), which is the subject of Ch. 2.

Appendix B

Numerical Algorithms

B.1 Finite difference methods

B.1.1 Inversion of 5-diagonal matrix

A second order finite difference discretization of the fourth derivative term u_{xxxx} of the KS equation is based on a five point stencil. Since all implicit integration schemes require inversion of the discrete differentiation matrix, we begin the discussion of finite difference schemes by describing a fast algorithm for inversion of a 5-diagonal matrix.

The inversion algorithm is a straightforward modification of a well-known algorithm for inversion of a tridiagonal matrix (sometimes referred to as the Thomas algorithm), and may be derived easily from a LU decomposition for any band-diagonal matrix—see for instance [IK66, Sec. 2.3], [PTVF92, Sec. 2.4] or [Tho95, Sec. 2.6.3]; the 5-diagonal matrix is a special case of a band- or block-diagonal matrix, for which standard inversion routines exist. Nevertheless, we derive and write out the routine explicitly for later reference.

The general 5-diagonal matrix, with constant entries a_i, b_i, c_i, d_i, e_i, has the form

$$\mathsf{D} = \begin{pmatrix} \mathsf{c}_1 & \mathsf{d}_1 & \mathsf{e}_1 & 0 & 0 & \dots & & & & \\ \mathsf{b}_2 & \mathsf{c}_2 & \mathsf{d}_2 & \mathsf{e}_2 & 0 & \dots & & & 0 & \\ \mathsf{a}_3 & \mathsf{b}_3 & \mathsf{c}_3 & \mathsf{d}_3 & \mathsf{e}_3 & \dots & & & & \\ & & & & & \ddots & & & & \\ & & & & \dots & \mathsf{a}_{N-2} & \mathsf{b}_{N-2} & \mathsf{c}_{N-2} & \mathsf{d}_{N-2} & \mathsf{e}_{N-2} \\ & 0 & & & \dots & 0 & \mathsf{a}_{N-1} & \mathsf{b}_{N-1} & \mathsf{c}_{N-1} & \mathsf{d}_{N-1} \\ & & & & \dots & 0 & 0 & \mathsf{a}_N & \mathsf{b}_N & \mathsf{c}_N \end{pmatrix} \tag{B.1}$$

LU decomposition of 5-diagonal matrix

The solution of the 5-diagonal system of equations $\mathsf{D}\mathbf{x} = \mathbf{f}$, for a given right-hand-side $\mathbf{f} = (f_1, f_2, \dots, f_N)^T$ and a vector of unknowns $\mathbf{x} = (x_1, x_2, \dots, x_N)^T$, begins with a factorization $\mathsf{D} = \mathsf{LU}$ into lower and upper triangular matrices. We can then solve $\mathsf{L}(\mathsf{U}\mathbf{x}) = \mathbf{f}$ by successively solving $\mathsf{L}\mathbf{z} = \mathbf{f}$, $\mathsf{U}\mathbf{x} = \mathbf{z}$. The algorithms for all these steps are derived by straightforwardly carrying out the relevant matrix multiplications.

In the first step, we seek a factorization of the form

$$D = LU$$

$$
\begin{pmatrix}
\gamma_1 & 0 & \cdots \\
\beta_2 & \gamma_2 & 0 & \cdots \\
\alpha_3 & \beta_3 & \gamma_3 & \cdots \\
& & & \ddots \\
& & \cdots & \gamma_{N-3} & 0 & 0 \\
& & \cdots & \beta_{N-2} & \gamma_{N-2} & 0 & 0 \\
& \ddots & & \cdots & \alpha_{N-1} & \beta_{N-1} & \gamma_{N-1} & 0 \\
& & & \cdots & 0 & \alpha_N & \beta_N & \gamma_N
\end{pmatrix}
\begin{pmatrix}
1 & \delta_1 & \varepsilon_1 & 0 & \cdots \\
0 & 1 & \delta_2 & \varepsilon_2 & \cdots \\
0 & 0 & 1 & \delta_3 & \cdots \\
0 & 0 & 1 & \cdots \\
& & & \ddots \\
& & \cdots & 1 & \delta_{N-2} & \varepsilon_{N-2} \\
& \ddots & & \cdots & 0 & 1 & \delta_{N-1} \\
& & & \cdots & & 0 & 1
\end{pmatrix}
\tag{B.2}
$$

By carrying out the matrix multiplication explicitly, and identifying corresponding terms with (B.1), we derive the algorithm to find $\alpha_i, \beta_i, \gamma_i, \delta_i$, and ε_i (in practice, this algorithm needs only to be carried out once at the beginning of our finite difference integration of the PDE, since the entries of D and hence of L and U are constant for given parameter values):

$$
\begin{aligned}
\gamma_1 &= \mathsf{c}_1, \\
\delta_1 &= \mathsf{d}_1/\gamma_1, \\
\varepsilon_1 &= \mathsf{e}_1/\gamma_1,
\end{aligned}
\qquad
\begin{aligned}
\beta_2 &= \mathsf{b}_2, \\
\gamma_2 &= \mathsf{c}_2 - \beta_2\,\delta_1, \\
\delta_2 &= (\mathsf{d}_2 - \beta_2\,\varepsilon_1)/\gamma_2, \\
\varepsilon_2 &= \mathsf{e}_2/\gamma_2,
\end{aligned}
$$

For $i = 3, \ldots, N-2$

$$
\begin{aligned}
\alpha_i &= \mathsf{a}_i, \\
\beta_i &= \mathsf{b}_i - \alpha_i\,\delta_{i-2}, \\
\gamma_i &= \mathsf{c}_i - \alpha_i\,\varepsilon_{i-2} - \beta_i\,\delta_{i-1}, \\
\delta_i &= (\mathsf{d}_i - \beta_i\,\varepsilon_{i-1})/\gamma_i, \\
\varepsilon_i &= \mathsf{e}_i/\gamma_i,
\end{aligned}
\tag{B.3}
$$

$$
\begin{aligned}
\alpha_{N-1} &= \mathsf{a}_{N-1}, \\
\beta_{N-1} &= \mathsf{b}_{N-1} - \alpha_{N-1}\,\delta_{N-3}, \\
\gamma_{N-1} &= \mathsf{c}_{N-1} - \alpha_{N-1}\,\varepsilon_{N-3} - \beta_{N-1}\,\delta_{N-2}, \\
\delta_{N-1} &= (\mathsf{d}_{N-1} - \beta_{N-1}\,\varepsilon_{N-2})/\gamma_{N-1},
\end{aligned}
\qquad
\begin{aligned}
\alpha_N &= \mathsf{a}_N, \\
\beta_N &= \mathsf{b}_N - \alpha_N\,\delta_{N-2}, \\
\gamma_N &= \mathsf{c}_N - \alpha_N\,\varepsilon_{N-2} - \beta_N\,\delta_{N-1}.
\end{aligned}
$$

Solution of 5-diagonal system

At each time step of the finite difference integration, we need to solve $D\mathbf{x} = \mathbf{f}$. As already mentioned, this involves two steps:

1. Forward pass—solve $L\mathbf{z} = \mathbf{f}$:

$$
\begin{aligned}
z_1 &= f_1/\gamma_1 \\
z_2 &= (f_2 - \beta_2\,z_1)/\gamma_2
\end{aligned}
\tag{B.4}
$$

$$\text{For } i = 3, \ldots, N$$

$$z_i = (f_i - \alpha_i\,z_{i-2} - \beta_i\,z_{i-1})/\gamma_i$$

2. Back substitution—solve $\mathsf{U}\mathbf{x} = \mathbf{z}$:

$$x_N = z_N$$
$$x_{N-1} = z_{N-1} - \delta_{N-1}\, x_N \qquad \text{(B.5)}$$
$$\text{For } i = N-2, \ldots, 1$$
$$x_i = z_i - \delta_i\, x_{i+1} - \varepsilon_i\, x_{i+2}$$

After the initial calculation of the coefficients $\alpha_i, \ldots, \varepsilon_i$ (an $\mathcal{O}(N)$ calculation), the complete matrix inversion requires $5N - 6$ multiplications and divisions (or a total of $11N - 12$ binary operations); being $\mathcal{O}(N)$, it is a very efficient algorithm.

The factorization and solution algorithms can be shown to be numerically stable if D is diagonally dominant, and are, in practice, also stable for the (non-diagonally dominant) 5-diagonal matrices which arise from finite difference discretizations of a PDE (as in this thesis)—see [PTVF92].

B.1.2   Finite difference schemes—discretization and time integration

In discussing finite difference schemes, we use as example the damped KS equation (2.2),

$$u_t = -u_{xxxx} - 2u_{xx} - (1 - \varepsilon^2)u - uu_x \overset{\text{def}}{=} -\mathcal{A}u - \mathcal{G}(u); \qquad \text{(B.6)}$$

since we can easily specialize to the usual KS equation.[†] Most of the ideas discussed here are quite standard; for general discussions of finite difference schemes, see for instance [IK66, PTVF92, Tho95].

Spatial discretization   We subdivide the one-dimensional domain $[0, L]$ into N (or $N + 1$, depending on the boundary conditions) equal intervals, and will ultimately evaluate our solution on a uniform space and time grid,

$$u_i^j \overset{\text{def}}{=} u(i\delta x, j\delta t), \qquad i = 1, \ldots, N, \quad j = 0, 1, \ldots$$

Discretizing only in space for now, we employ standard second-order finite differencing for the second and fourth derivatives; the linear differencing operator acts as a matrix on the vector of grid values $\mathbf{u} \overset{\text{def}}{=} (u_1, \ldots, u_N)^T$, by

$$(\mathsf{A}\mathbf{u})_i \overset{\text{def}}{=} \frac{u_{i+2} - 4\,u_{i+1} + 6\,u_i - 4\,u_{i-1} + u_{i-2}}{\delta x^4} + 2\frac{u_{i+1} - 2\,u_i + u_{i-1}}{\delta x^2} + (1 - \varepsilon^2)u_i \qquad \text{(B.7)}$$
$$= (\mathcal{A}u)_i + \mathcal{O}(\delta x^2).$$

A variety of discretizations is possible for the nonlinear term

$$G(\mathbf{u})_i = (uu_x)_i.$$

The strong linear dissipation inhibits Burgers-like shock formation, and upwind differencing does not seem to affect the results, so provided the space step is small enough to include sufficiently many grid points in each cell of size $\approx 2\pi\sqrt{2}$ (we typically used at least 20 points per wavelength), in our experience several different difference schemes for the nonlinear term appear to yield approximately

---

[†]We confess here to excessive notation: in Ch. 3 we used $\mathcal{L}$ for $-\mathcal{A}$, $\mathcal{B}$ for $-\mathcal{G}$. In mitigation, we cite a preference for avoiding minus signs in Ch. 3, and retaining them here.

equivalent results. Among the second-order schemes we employ (with error $\mathcal{O}(\delta x^2)$) are centered differencing for u_x,

$$G(\mathbf{u})_i = u_i \frac{u_{i+1} - u_{i-1}}{2\,\delta x};$$

(B.8)

centered differencing for $uu_x = \frac{1}{2}(u^2)_x$,

$$G(\mathbf{u})_i = \frac{1}{2}\frac{u_{i+1}^2 - u_{i-1}^2}{2\,\delta x} = \frac{1}{2}\big(u_{i+1} + u_{i-1}\big)\frac{u_{i+1} - u_{i-1}}{2\,\delta x};$$

(B.9)

and a scheme for $uu_x = \frac{1}{3}\big(uu_x + (u^2)_x\big)$, energy preserving in the nonlinear term,

$$G(\mathbf{u})_i = \frac{1}{3}\big(u_{i+1} + u_i + u_{i-1}\big)\frac{u_{i+1} - u_{i-1}}{2\,\delta x}.$$

(B.10)

After space discretization, we thus have an ODE for the vector of grid values $\mathbf{u}$,

$$\frac{d\mathbf{u}}{dt} = -\mathsf{A}\mathbf{u} - G(\mathbf{u}),$$

(B.11)

where $\mathsf{A}\mathbf{u}$ and $G(\mathbf{u})$ are given as above, and we ignore boundary conditions for now.

The linear term: Time-stepping

Provided we have a rapid inversion algorithm for the matrix representation of the linear operator, such as that presented in Sec. B.1.1, we can treat the linear term implicitly. Thus we may follow the common approach to parabolic PDEs (such as the diffusion equation), and use the stable, second-order in time, Crank-Nicholson (CN) scheme, discretizing the linear equation $\mathbf{u}_t = -\mathsf{A}\mathbf{u}$ in time as

$$\frac{\mathbf{u}^{j+1} - \mathbf{u}^j}{\delta t} = -\frac{1}{2}\left[(\mathsf{A}\mathbf{u})^{j+1} + (\mathsf{A}\mathbf{u})^j\right],$$

which can be rewritten as

$$\left[(\mathsf{I} + \tfrac{1}{2}\delta t\,\mathsf{A})\mathbf{u}\right]^{j+1} = \left[(\mathsf{I} - \tfrac{1}{2}\delta t\,\mathsf{A})\mathbf{u}\right]^j$$

(where I is the identity matrix), or as

$$\mathbf{u}^{j+1} = (\mathsf{I} + \tfrac{1}{2}\delta t\,\mathsf{A})^{-1}(\mathsf{I} - \tfrac{1}{2}\delta t\,\mathsf{A})\mathbf{u}^j \overset{\text{def}}{=} \mathsf{M}\mathbf{u}^j.$$

(B.12)

We may write the eigenvectors of A as $\mathbf{a}_n$, with corresponding eigenvalues λ_n. The action of the linearized operator $\mathsf{M} = (\mathsf{I} + \tfrac{1}{2}\delta t\,\mathsf{A})^{-1}(\mathsf{I} - \tfrac{1}{2}\delta t\,\mathsf{A})$ on the eigenvectors of A is then

$$\mathsf{M}\mathbf{a}_n = \frac{1 - \tfrac{1}{2}\delta t\,\lambda_n}{1 + \tfrac{1}{2}\delta t\,\lambda_n}\mathbf{a}_n \overset{\text{def}}{=} m_n\mathbf{a}_n.$$

Recalling the definition (B.6) of the linear operator, we have $\lambda_n < 0$ for the unstable large-scale modes, so that $m_n > 0$ as expected; note that we need

$$\delta t < \frac{2}{|\min_n \lambda_n|}$$

(B.13)

for stability of the numerical scheme. For $|\lambda\,\delta t| \ll 1$, $m_n = 1 - \lambda\,\delta t + \mathcal{O}(\delta t^2)$, confirming that this scheme gives the correct lowest-order behavior; a further simple calculation verifies its second-order accuracy in time.

Two alternative integration schemes, readily obtained by similar reasoning, are the explicit Euler method, which has

$$\mathsf{M}^E = \mathsf{I} - \delta t\,\mathsf{A},$$

and the fully implicit backward Euler (BE) scheme, with

$$\mathsf{M}^I = (\mathsf{I} + \delta t\,\mathsf{A})^{-1}.$$

We can easily confirm that these both have the correct linearization for $|\lambda\,\delta t| \ll 1$, but that they are both only first-order accurate in time. For this reason, we choose to use the CN scheme. Subject to the restriction (B.13), we do not need to limit the time step δt to ensure stability, so we choose it for an optimal combination of accuracy and speed. For our finite difference computations, we usually used $\delta t = 0.125 = 1/8$, and checked our results with $\delta t = 0.0625 = 1/16$.

Small scale behavior   An important aspect of our choice of integrator is its behavior at small scales. The linear operator

$$-\mathcal{A}u = -(\partial_x^2 - 1)^2 u + \varepsilon^2 u$$

is a smoothing operator, which strongly damps high Fourier modes, or small-scale structures. Indeed, as discussed in Sec. 1.2.2 and shown in Ch. 2, initial data in $L^2[0, L]$ are attracted to an absorbing ball in L^2, and solutions are analytic in x for any $t > 0$ (discontinuities in the initial data are immediately smoothed out by the KS time evolution).

In the spatial discretization employed for a finite difference scheme, discontinuities manifest themselves as structures on the scale of the mesh spacing, living in the smallest-scale eigenspace of the discretized operator A, where it has eigenvalue $\lambda_n \gg 1$. Unless we are prepared to make δt prohibitively small, the strong dissipation thus implies that $\lambda_n \delta t \gg 1$ for the small scales.

The explicit Euler scheme is unstable in this case, and becomes increasingly unstable as we go to smaller scales, with $m_n = 1 - \lambda_n \delta t \to -\infty$; which is why this is essentially a useless scheme except for very small δt. Both implicit methods, the CN and BE schemes, are stable as λ_n increases. For the fully implicit BE method, $m_n = (1 + \lambda_n \delta t)^{-1} \to 0$ as $\lambda_n \to \infty$, reproducing the damping behavior of the true operator. For the CN scheme, on the other hand,

$$m_n = \frac{1 - \frac{1}{2}\,\delta t\,\lambda_n}{1 + \frac{1}{2}\,\delta t\,\lambda_n} \to -1 \quad \text{as } \lambda_n \to \infty.$$

That is, structures on the scale of the mesh spacing are not damped, except very slowly, but rather oscillate. For this reason, the CN scheme performs poorly if the initial data contains small-scale structures or discontinuities, and we have experienced this effect in our numerical computations. In order to exploit the small-scale damping properties of the fully implicit BE scheme for non-smooth initial data, but still to preserve the superior time accuracy of the CN scheme, in practice we use the discretized operator M^I of the BE scheme for a few time steps, to smooth out the small scales (in our experience, even one such step was often sufficient), and then used the CN scheme for the remainder of the integration. See [CHQZ88, Sec. 4.3–4] for further discussion of this point.

Time-stepping for the nonlinear term

Treating the nonlinear term implicitly would require the slow solution of a system of nonlinear equations at each time step. Instead, we prefer an explicit integrator for $\mathbf{u}_t = -G(\mathbf{u})$, for which first-order Euler time-stepping,

$$\frac{\mathbf{u}^{j+1} - \mathbf{u}^j}{\delta t} = -G(\mathbf{u})^j,$$

and the second-order in time two-step Adams-Bashforth (AB) scheme,

$$\frac{\mathbf{u}^{j+1} - \mathbf{u}^j}{\delta t} = -\left[\tfrac{3}{2}G(\mathbf{u})^j - \tfrac{1}{2}G(\mathbf{u})^{j-1}\right],$$

are the simplest cases (we will discuss Adams-Bashforth methods in more depth in Sec. B.3.2, below).

In practice, for the nonlinear term we begin our integration with a single Euler step, and use Adams-Bashforth for subsequent steps, retaining the approximation for $G(\mathbf{u})$ at each time step for use in the next step; in fact, this is the approach used for the nonlinear term for all the numerical schemes described in this Appendix.

In sum, therefore, the mixed explicit-implicit ABCN finite difference scheme for the solution of the KS equation (B.6) is represented by

$$\frac{\mathbf{u}^{j+1} - \mathbf{u}^j}{\delta t} = -\tfrac{1}{2}\left[(\mathsf{A}\mathbf{u})^{j+1} + (\mathsf{A}\mathbf{u})^j\right] - \left[\tfrac{3}{2}G(\mathbf{u})^j - \tfrac{1}{2}G(\mathbf{u})^{j-1}\right]$$

or

$$\left[(\mathsf{I} + \tfrac{1}{2}\delta t\,\mathsf{A})\mathbf{u}\right]^{j+1} = \left[(\mathsf{I} - \tfrac{1}{2}\delta t\,\mathsf{A})\mathbf{u}\right]^j - \tfrac{1}{2}\delta t\left[3\,G(\mathbf{u})^j - G(\mathbf{u})^{j-1}\right]; \tag{B.14}$$

where

$$\left[(\mathsf{I} + \tfrac{1}{2}\delta t\,\mathsf{A})\mathbf{u}\right]_i = r_1\,u_{i+2} + (-4\,r_1 + r_2)\,u_{i+1} + (1 + 6\,r_1 - 2\,r_2 + r_3)\,u_i$$
$$+ (-4\,r_1 + r_2)\,u_{i-1} + r_1\,u_{i-2},$$

$$r_1 \stackrel{\text{def}}{=} \tfrac{1}{2}\frac{\delta t}{\delta x^4}, \qquad r_2 \stackrel{\text{def}}{=} \frac{\delta t}{\delta x^2}, \qquad r_3 \stackrel{\text{def}}{=} \tfrac{1}{2}\delta t(1 - \varepsilon^2),$$

and $\left[(\mathsf{I} - \tfrac{1}{2}\delta t\,\mathsf{A})\mathbf{u}\right]_i$ and $G(\mathbf{u})_i$ are defined similarly.

At each time step, the evaluation of the right-hand-side requires $\mathcal{O}(N)$ operations. Solving for $\mathbf{u}^{j+1}$ then involves inverting $(\mathsf{I} + \tfrac{1}{2}\delta t\,\mathsf{A})$, which (ignoring boundary conditions for now) is a 5-diagonal matrix. We may thus solve this system of equations using the algorithm of Sec. B.1.1, after precalculating the coefficients in the LU decomposition of $(\mathsf{I} + \tfrac{1}{2}\delta t\,\mathsf{A})$. In summary, this is an efficient algorithm, especially for large systems; the total operation count for the second-order in space and time finite difference ABCN integrator on N grid points is $\mathcal{O}(N)$ operations per time step.

B.1.3 Boundary conditions: Dirichlet and mixed

To this point, we have completely ignored boundary conditions while setting up the general finite difference integrator. In this Section and the next we turn to this important topic.

The first noteworthy point is that we need to specify four boundary conditions (BCs) for well-posedness of the fourth-order PDE. The most important possibilities for this initial-boundary value

problem are (1) periodic boundary conditions, and (2) specifying two BCs at each end, $x = 0$ and $x = L$. For the latter situation, which we discuss first, we will consider "Dirichlet" conditions, in which we specify u and u_{xx} at each end, and "mixed" conditions, where u and u_x at each boundary are fixed.

We do not consider the third plausible case, "Neumann" (free) boundary conditions, in which u_x and u_{xxx} are given; for the case of the usual KS equation ($\varepsilon^2 = 1$) and zero Neumann conditions, $u \equiv c$ is a solution for any constant c, and in our numerical simulations with these BCs, this constant solution seems to be attracting, so that the typical spatiotemporally chaotic KS dynamics which are the main focus of this thesis, do not appear to be sustained in this case.

Dirichlet boundary conditions

The BCs we term "Dirichlet" or stress-free, require the specification of u and u_{xx} at the boundaries:

$$u(0,t) = a(t), \qquad u(L,t) = b(t),$$
$$u_{xx}(0,t) = c(t), \qquad u_{xx}(L,t) = d(t). \tag{B.15}$$

In practice, the BCs are specified at discrete time intervals, for instance $a^j \overset{\text{def}}{=} a(j\delta t)$, $b^{j+1} \overset{\text{def}}{=} b((j+1)\delta t)$, etc.

The most commonly studied case is that of zero Dirichlet conditions, $u = u_{xx} = 0$ at the ends, and this is the only case that is mentioned in the body of this thesis (see Sec. 4.3.1); but for generality, we develop the numerical scheme for the general case (B.15).

There have been some analytical studies of the KS equation with these BCs; in particular, some of the early analytical results (see for instance, [NST85, Nic86]) were derived for this case, or equivalently, for Neumann BCs $h_x = h_{xxx} = 0$ for the integrated KS equation (1.3). Observe that if u solves the KS equation (B.6) with zero Dirichlet BCs on $[0, L]$, then

$$\bar{u}(x,t) = \begin{cases} u(x,t) & 0 \leq x \leq L, \\ -u(2L - x, t) & L \leq x \leq 2L \end{cases} \tag{B.16}$$

is a solution to (B.6) with periodic BCs on $[0, 2L]$. Thus the space of Dirichlet solutions is a (generally unstable) subspace of those for periodic BCs, and all analytical results for periodic BCs may be specialized to this case.

Approximation of boundary conditions For a finite difference solution on N internal grid-points, with fixed BCs, we write $\delta x = L/(N+1)$ (we derive everything at $x = 0$; the formulae at $x = L$ are analogous). The usual 5-point stencil for the fourth derivative operator at $x = \delta x$ ($i = 1$) requires values for u_0 and u_{-1}. The values for u_0 (and u_{N+1}) are obtained by using the boundary condition on u:

$$u_0 = a, \qquad u_{N+1} = b.$$

The exterior points u_{-1} (and u_{N+2}) are accounted for by applying the other BC, for u_{xx}.

We give first the most straightforward way to apply the other condition. We can approximate $u_{xx}(0) = c$ by

$$c = \frac{u_1 - 2\,u_0 + u_{-1}}{\delta x^2} = \frac{u_1 - 2\,a + u_{-1}}{\delta x^2} \quad \left(+\mathcal{O}(\delta x^2)\right)$$

which implies

$$u_{-1} = 2\,a - u_1 + c\,\delta x^2 \quad \left(+\mathcal{O}(\delta x^4)\,\right). \tag{B.17}$$

Hence the discretization of u_{xxxx} at $x = \delta x$ becomes

$$\left(u_{xxxx}\right)_1 = \frac{u_3 - 4\,u_2 + 6\,u_1 - 4\,u_0 + u_{-1}}{\delta x^4} = \frac{u_3 - 4\,u_2 + 6\,u_1 - 4\,a + (2\,a - u_1 + c\delta x^2)}{\delta x^4}$$
$$= \frac{u_3 - 4\,u_2 + 5\,u_1 - 2\,a}{\delta x^4} + \frac{c}{\delta x^2}. \tag{B.18}$$

Inserting $u_0 = a$ into the formula for $\left(u_{xxxx}\right)_2$, and deriving the analogous formulae at the other boundary $x = L$, we get a complete specification of the finite difference scheme with these Dirichlet BCs; which appears to give reasonable numerical results.

However, on closer examination this is not a consistent numerical scheme at the boundary. We check consistency by Taylor expanding about $x = \delta x$ and substituting the boundary conditions (see [Tho95, Sec. 2.3]); for the special case of zero BCs, $a = c = 0$, for instance, one computes

$$u_3 - 4\,u_2 + 5\,u_1 = \tfrac{11}{12}\,\delta x^4\,u_{xxxx}(\delta x) + \tfrac{1}{12}\,\delta x^5\,u_{xxxxx}(\delta x) + \mathcal{O}(\delta x^6);$$

that is, the right-hand-side of (B.18) is an approximation to $\frac{11}{12}u_{xxxx}$ evaluated at $x = \delta x$, not to u_{xxxx} (this is a boundary effect; the scheme is consistent and second-order accurate at interior points). An expedient approach to obtaining a consistent scheme is simply to multiply (B.18) by $\frac{12}{11}$; but one would prefer a numerical scheme derived from first principles.

The origin of the inconsistency can be traced to the errors in our approximations: the error in the formula (B.17) for u_{-1} is $\frac{1}{12}\,\delta x^4\,u_{xxxx}(0)$, which becomes $\mathcal{O}(1)$ in the approximation for $\left(u_{xxxx}\right)_1$ and accounts for the missing $\frac{1}{12}\,u_{xxxx}$ on the right-hand-side of (B.18). A second-order approximation to the second derivative is thus insufficient, and the problem can be remedied by a higher order approximation to $u_{xx}(0) = c$:

$$c = \frac{-u_3 + 4\,u_2 + 6\,u_1 - 20\,u_0 + 11\,u_{-1}}{12\,\delta x^2} \quad \left(+\mathcal{O}(\delta x^3)\,\right),$$

giving the approximation

$$u_{-1} = \tfrac{20}{11}\,a - \tfrac{6}{11}\,u_1 - \tfrac{4}{11}\,u_2 + \tfrac{1}{11}\,u_3 + \tfrac{12}{11}\,c\,\delta x^2 \quad \left(+\mathcal{O}(\delta x^5)\,\right). \tag{B.19}$$

On substituting for u_{-1} and u_0 into the formula for $\left(u_{xxxx}\right)_1$, this yields the consistent approximation

$$\left(u_{xxxx}\right)_1 = \frac{u_3 - 4\,u_2 + 6\,u_1 - 4\,a + \frac{1}{11}(20\,a - 6\,u_1 - 4\,u_2 + u_3 + 12\,c\,\delta x^2)}{\delta x^4}$$
$$= \frac{12}{11}\,\frac{u_3 - 4\,u_2 + 6\,u_1 - 2\,a + c\,\delta x^2}{\delta x^4}, \tag{B.20}$$

which is indeed just $\frac{12}{11}$ of the formula (B.18). The approximations to the boundary conditions at $x = L$ are obtained simply by replacing a with b, and c with d.

Summary: A finite difference scheme for Dirichlet boundary conditions   On substituting the discretizations and boundary conditions for the linear operator $\mathcal{A}$, we finally obtain a consistent scheme for finite difference solution of the KS equation with Dirichlet BCs:

$$\left[(\mathsf{I} + \tfrac{1}{2}\delta t\,\mathsf{A})\mathbf{u}\right]^{j+1} = \left[(\mathsf{I} - \tfrac{1}{2}\delta t\,\mathsf{A})\mathbf{u}\right]^{j} + \mathbf{b}^{j} - \tfrac{1}{2}\delta t\left[3\,G(\mathbf{u})^{j} - G(\mathbf{u})^{j-1}\right], \tag{B.21}$$

where we solve for the N-component vector $\mathbf{u} = (u_1, \ldots, u_N)^T$. Here $\mathbf{b}^j$ contains the nonhomogeneous boundary conditions, and has components

$$\mathbf{b}_1^j = \left(\tfrac{24}{11} r_1 - r_2\right)(a^{j+1} + a^j) - \tfrac{6}{11} r_2 (c^{j+1} + c^j),$$
$$\mathbf{b}_2^j = -r_1 (a^{j+1} + a^j),$$
$$\mathbf{b}_i^j = 0, \qquad 3 \leq i \leq N - 2 \tag{B.22}$$
$$\mathbf{b}_{N-1}^j = -r_1 (b^{j+1} + b^j),$$
$$\mathbf{b}_N^j = \left(\tfrac{24}{11} r_1 - r_2\right)(b^{j+1} + b^j) - \tfrac{6}{11} r_2 (d^{j+1} + d^j).$$

The matrix $(\mathsf{I} + \tfrac{1}{2}\delta t\, \mathsf{A})$ is 5-diagonal, of the form D of (B.1), with components:
For $3 \leq i \leq N - 2$,

$$\mathsf{c}_i = 1 + 6\,r_1 - 2\,r_2 + r_3,$$
$$\mathsf{b}_i = \mathsf{d}_i = -4\,r_1 + r_2,$$
$$\mathsf{a}_i = \mathsf{e}_i = r_1,$$

and boundary conditions are represented by

$$\mathsf{c}_1 = \mathsf{c}_N = 1 + \tfrac{60}{11} r_1 - 2\,r_2 + r_3,$$
$$\mathsf{d}_1 = \mathsf{b}_N = -\tfrac{48}{11} r_1 + r_2,$$
$$\mathsf{e}_1 = \mathsf{a}_N = \tfrac{12}{11} r_1,$$

$$\mathsf{b}_2 = \mathsf{b}_{N-1} = -4\,r_1 + r_2,$$
$$\mathsf{c}_2 = \mathsf{c}_{N-1} = 1 + 6\,r_1 - 2\,r_2 + r_3,$$
$$\mathsf{d}_2 = \mathsf{d}_{N-1} = -4\,r_1 + r_2,$$
$$\mathsf{e}_2 = \mathsf{a}_{N-1} = r_1.$$

The components of the matrix $(\mathsf{I} - \tfrac{1}{2}\delta t\, \mathsf{A})$ are found similarly. Several discretizations for $G(\mathbf{u})$ have previously been discussed; higher-order schemes have been used in some studies [EAHGP98], but a sufficiently small space step obviates the need for these.

Finally, the time evolution proceeds by solving the system of linear equations for $\mathbf{u}$ at each time step, using the algorithm discussed in Sec. B.1.1 to invert the 5-diagonal matrix.

Mixed boundary conditions

The "mixed", or "clamped" or "rigid", boundary conditions involve the specification of u and its first derivative u_x at the boundaries:

$$u(0, t) = a(t), \qquad u(L, t) = b(t),$$
$$u_x(0, t) = e(t), \qquad u_x(L, t) = f(t). \tag{B.23}$$

Unlike for the Dirichlet BCs, neither sine nor cosine functions individually satisfy these BCs, so that solutions of (B.6) with (B.23) are not necessarily a subset of solutions with periodic BCs (on some larger domain).

Approximation of boundary conditions The derivation of the finite difference scheme for mixed BCs proceeds in an analogous way to that for Dirichlet BCs, so we will just quote the results. In the most straightforward approach, the derivative boundary condition $u_x(0) = e$ at $x = 0$ is approximated by

$$e = \frac{u_1 - u_{-1}}{2\,\delta x} \quad \left(+\mathcal{O}(\delta x^2)\right)$$

implying

$$u_{-1} = u_1 - 2 e \delta x \quad \left(+\mathcal{O}(\delta x^3)\right). \tag{B.24}$$

However, as before, this does not yield a consistent scheme for $(u_{xxxx})_1$, and we need a higher order approximation of the derivative:

$$e = \frac{-u_2 + 6 u_1 - 3 u_0 - 2 u_{-1}}{6 \delta x} \quad \left(+\mathcal{O}(\delta x^3)\right), \tag{B.25}$$

yielding the approximation

$$u_{-1} = -\tfrac{1}{2} u_2 + 3 u_1 - \tfrac{3}{2} u_0 - 3 e \delta x \quad \left(+\mathcal{O}(\delta x^4)\right). \tag{B.26}$$

On substituting u_{-1} from (B.26), and $u_0 = a$, we obtain the formula for $(u_{xxxx})_1$:

$$\left(u_{xxxx}\right)_1 = \frac{\tfrac{4}{3} u_3 - 6 u_2 + 12 u_1 - \tfrac{22}{3} a - 4 e \delta x}{\delta x^4}. \tag{B.27}$$

The formulae at the other boundary, $x = L$, are found by replacing a with b, and e with $-f$.

A finite difference scheme for mixed boundary conditions   The finite difference scheme for mixed BCs proceeds as for the Dirichlet BCs. The basic formula is (B.21), as before; in this case, the nonhomogeneous BCs are contained in $\mathbf{b}^j$ via

$$
\begin{aligned}
\mathbf{b}_1^j &= \left(\tfrac{22}{3} r_1 - r_2\right)(a^{j+1} + a^j) + 4 r_1 \delta x (e^{j+1} + e^j), \\
\mathbf{b}_2^j &= -r_1 (a^{j+1} + a^j), \\
\mathbf{b}_i^j &= 0, \qquad 3 \le i \le N - 2 \\
\mathbf{b}_{N-1}^j &= -r_1 (b^{j+1} + b^j), \\
\mathbf{b}_N^j &= \left(\tfrac{22}{3} r_1 - r_2\right)(b^{j+1} + b^j) - 4 r_1 \delta x (f^{j+1} + f^j).
\end{aligned}
\tag{B.28}
$$

The components of the 5-diagonal matrix $(\mathsf{I} + \tfrac{1}{2}\delta t \mathsf{A})$ are:
For $3 \le i \le N - 2$,

$$
\begin{aligned}
\mathsf{c}_i &= 1 + 6 r_1 - 2 r_2 + r_3, \\
\mathsf{b}_i = \mathsf{d}_i &= -4 r_1 + r_2, \\
\mathsf{a}_i = \mathsf{e}_i &= r_1,
\end{aligned}
$$

with boundary values

$$
\begin{aligned}
\mathsf{c}_1 = \mathsf{c}_N &= 1 + 12 r_1 - 2 r_2 + r_3, \\
\mathsf{d}_1 = \mathsf{b}_N &= -6 r_1 + r_2, \\
\mathsf{e}_1 = \mathsf{a}_N &= \tfrac{4}{3} r_1,
\end{aligned}
\qquad
\begin{aligned}
\mathsf{b}_2 = \mathsf{b}_{N-1} &= -4 r_1 + r_2, \\
\mathsf{c}_2 = \mathsf{c}_{N-1} &= 1 + 6 r_1 - 2 r_2 + r_3, \\
\mathsf{d}_2 = \mathsf{d}_{N-1} &= -4 r_1 + r_2, \\
\mathsf{e}_2 = \mathsf{a}_{N-1} &= r_1.
\end{aligned}
$$

B.1.4 Periodic boundary conditions

For the case of periodic boundary conditions, which is by far the most important case for this thesis, we require that u and all its derivatives are periodic on $[0, L]$. For the KS equation (B.6), it is sufficient to enforce the four conditions

$$u(0,t) = u(L,t), \qquad u_x(0,t) = u_x(L,t),$$
$$u_{xx}(0,t) = u_{xx}(L,t), \qquad u_{xxx}(0,t) = u_{xxx}(L,t). \tag{B.29}$$

In the next Sec. B.2 of this Appendix, we discuss Fourier- and wavelet-based spectral techniques for the numerical solution of this problem; here we outline the finite difference approach.

The finite difference specification of periodic BCs is quite straightforward, with none of the previous issues of consistency of the approximation (Sec. B.1.3); we simply enforce

$$u_{-1} = u_{N-1}, \quad u_0 = u_N, \quad u_1 = u_{N+1}, \quad u_2 = u_{N+2}. \tag{B.30}$$

Notice that in contrast to the case of fixed BCs, here we have to solve for one of the endpoint values, say for u_N at $x = L$; thus the number of grid points N equals the number of intervals, and the space step is $\delta x = L/N$.

We obtain the finite difference approximations to the derivatives at the ends by substituting (B.30) into the standard discretizations; for instance,

$$\left(u_{xx}\right)_1 = \frac{u_2 - 2\,u_1 + u_N}{\delta x^2}, \quad \left(u_{xxxx}\right)_{N-1} = \frac{u_1 - 4\,u_N + 6\,u_{N-1} - 4\,u_{N-2} + u_{N-3}}{\delta x^4}, \quad \ldots$$

The integration scheme is, as usual, based on (B.21), where $\mathbf{b}^j = 0$ since the BCs are homogeneous.

Inversion of cyclic 5-diagonal matrix Compared to the previous cases, the main difficulty is that the matrix form A of the linear operator is no longer band diagonal; the periodization introduces nonzero terms in the "corners" of the matrix, leading to a *circulant* or *cyclic 5-diagonal* matrix. Specifically, A has the form[†]

$$\tilde{\mathsf{P}} = \begin{pmatrix}
c_1 & d_1 & e_1 & 0 & 0 & \ldots & & 0 & a_1 & b_1 \\
b_2 & c_2 & d_2 & e_2 & 0 & \ldots & & & * & a_2 \\
a_3 & b_3 & c_3 & d_3 & e_3 & \ldots & & 0 & & 0 \\
& & & & \ddots & & & & & \\
0 & & & 0 & \ldots & a_{N-2} & b_{N-2} & c_{N-2} & d_{N-2} & e_{N-2} \\
e_{N-1} & * & & & \ldots & 0 & a_{N-1} & b_{N-1} & c_{N-1} & d_{N-1} \\
d_N & e_N & 0 & & \ldots & 0 & 0 & a_N & b_N & c_N
\end{pmatrix} \tag{B.31}$$

Hence we cannot immediately apply the $\mathcal{O}(N)$ algorithm of Sec. B.1.1, valid for 5-diagonal matrices of the form D of (B.1). Fortunately, however, we need not resort to a slow $\mathcal{O}(N^3)$ inversion; the Sherman-Morrison formula allows us to exploit the fact that $\tilde{\mathsf{P}}$ is a perturbation of a 5-diagonal matrix, which itself is easily invertible.

Suppose we wish to invert the system of linear equations

$$\mathsf{C}\,\mathbf{x} = \mathbf{f}. \tag{B.32}$$

The Sherman-Morrison formula (see for instance [PTVF92, Sec. 2.7] or [Tho95, Sec. 5.6]) lets us solve for $\mathbf{x}$ if C has the form

$$\mathsf{C} = \mathsf{C}_0 - \mathbf{w}\,\mathbf{z}^T \tag{B.33}$$

[†]The terms marked $*$ in (B.31) vanish for the cyclic 5-diagonal matrix, but the inversion routine works even if they are nonzero; see below.

(where $\mathbf{w}\mathbf{z}^T = \mathbf{w} \otimes \mathbf{z}$ is the matrix whose i,jth element is $w_i z_j$), and if $\mathsf{C}_0^{-1}\mathbf{f}_0$ may be computed rapidly for any $\mathbf{f}_0$. By substitution, one readily confirms that

$$\mathsf{C}^{-1} = \mathsf{C}_0^{-1} + \frac{\mathsf{C}_0^{-1}\mathbf{w}\,\mathbf{z}^T\mathsf{C}_0^{-1}}{1 - \mathbf{z}^T\mathsf{C}_0^{-1}\mathbf{w}}$$

so that

$$\mathbf{x} = \mathsf{C}^{-1}\mathbf{f} = \mathsf{C}_0^{-1}\mathbf{f} + \frac{\left(\mathbf{z}^T\mathsf{C}_0^{-1}\mathbf{f}\right)\mathsf{C}_0^{-1}\mathbf{w}}{1 - \mathbf{z}^T\mathsf{C}_0^{-1}\mathbf{w}}. \tag{B.34}$$

Our matrix $\tilde{\mathsf{P}}$ cannot be written in the form (B.33), and ostensibly we may need to appeal to the Woodbury formula, which is the block-matrix form of (B.34) [PTVF92, Sec. 2.7], and requires the successive solution of several auxiliary problems to obtain the matrix inversion. However, for the symmetric cyclic 5-diagonal matrix obtained in the finite difference discretization for periodic BCs, and in fact under slightly more general conditions on $\tilde{\mathsf{P}}$ described below, we can derive a single formula, since it can be written in the form (B.35), similar to (B.33):

$$\mathsf{C} = \mathsf{C}_0 - \mathbf{w}_1\mathbf{z}_1^T - \mathbf{w}_2\mathbf{z}_2^T. \tag{B.35}$$

We can thus generalize the Sherman-Morrison formula, noting that $\mathsf{C} = \mathsf{C}_1 - \mathbf{w}_2\mathbf{z}_2^T$, where $\mathsf{C}_1 = \mathsf{C}_0 - \mathbf{w}_1\mathbf{z}_1^T$, so all that is needed are two successive applications of (B.34).

After a fair bit of algebra, we find that the solution to (B.32) with (B.35) is given by

$$\mathbf{x} = \mathsf{C}^{-1}\mathbf{f}$$

$$= \mathsf{C}_0^{-1}\mathbf{f} + \frac{\gamma_1(1 - \beta_{22}) + \gamma_2\beta_{12}}{(1 - \beta_{11})(1 - \beta_{22}) - \beta_{12}\beta_{21}}\mathsf{C}_0^{-1}\mathbf{w}_1 + \frac{\gamma_2(1 - \beta_{11}) + \gamma_1\beta_{21}}{(1 - \beta_{11})(1 - \beta_{22}) - \beta_{12}\beta_{21}}\mathsf{C}_0^{-1}\mathbf{w}_2, \tag{B.36}$$

which is symmetric under the interchange $1 \leftrightarrow 2$, as expected. Here

$$\beta_{ij} \stackrel{\text{def}}{=} \mathbf{z}_i^T\mathsf{C}_0^{-1}\mathbf{w}_j, \qquad \gamma_i \stackrel{\text{def}}{=} \mathbf{z}_i^T\mathsf{C}_0^{-1}\mathbf{f}, \qquad i = 1,2, \ j = 1,2. \tag{B.37}$$

(Compare $\mathbf{x} = \mathsf{C}_1^{-1}\mathbf{f} = \mathsf{C}_0^{-1}\mathbf{f} + (\gamma_1\mathsf{C}_0^{-1}\mathbf{w}_1)/(1 - \beta_{11})$, which is (B.34) rewritten in this notation.)

To find $\mathsf{C}^{-1}\mathbf{f}$, we must thus compute $\mathsf{C}_0^{-1}\mathbf{f}$, $\mathsf{C}_0^{-1}\mathbf{w}_1$ and $\mathsf{C}_0^{-1}\mathbf{w}_2$, all of which can be found rapidly. In particular, if C_0 is 5-diagonal, then each inversion can be performed in $\mathcal{O}(N)$ steps, and the overall complexity of the algorithm to compute $\mathsf{C}^{-1}\mathbf{f}$ remains linear, $\mathcal{O}(N)$. Note that extensions to the Sherman-Morrison formula for $\mathsf{C} = \mathsf{C}_0 + \sum_{i=1}^p \mathbf{w}_i\mathbf{z}_i^T$ rapidly become more complex as p increases—compare the results (B.34) for $p = 1$ and (B.36) for $p = 2$—and the formulae for higher p, while derivable, may be too complicated to be much use (one would then apply the Woodbury formula).

A finite difference scheme for periodic boundary conditions For the application of (B.36) to the finite difference integration of the KS equation with periodic BCs, it remains to show how the discretized operator $(\mathsf{I} + \frac{1}{2}\delta t\,\mathsf{A})$ can be written in the form (B.35). For simplicity we will consider

$$\mathsf{P} = \begin{pmatrix} c & b & a & 0 & 0 & \dots & & 0 & a & b \\ b & c & b & a & 0 & \dots & & & 0 & a \\ a & b & c & b & a & \dots & & 0 & & 0 \\ & & & \ddots & & & & & & \\ 0 & & 0 & & \dots & a & b & c & b & a \\ a & 0 & & & \dots & 0 & a & b & c & b \\ b & a & 0 & & \dots & 0 & 0 & a & b & c \end{pmatrix}, \tag{B.38}$$

although this method works for any symmetric matrices of the form $\tilde{\mathsf{P}}$, or more generally, for $\tilde{\mathsf{P}}$ under the condition $\mathsf{a}_1 = \mathsf{e}_N$, $\mathsf{a}_2 = \mathsf{e}_{N-1}$, $\mathsf{b}_1 = \mathsf{d}_{N-1}$, and the equality of the two entries marked $*$ (they do not need to vanish).

It is readily checked that if we choose

$$\mathbf{w}_1 = \begin{pmatrix} -\mathsf{b} \\ -\mathsf{a} \\ 0 \\ \vdots \\ 0 \\ -\mathsf{a} \\ -\mathsf{b} \end{pmatrix}, \quad \mathbf{z}_1 = \begin{pmatrix} 1 \\ 1 \\ 0 \\ \vdots \\ 0 \\ 1 \\ 1 \end{pmatrix}, \quad \mathbf{w}_2 = \begin{pmatrix} \mathsf{b} - \mathsf{a} \\ \mathsf{a} \\ 0 \\ \vdots \\ 0 \\ \mathsf{a} \\ \mathsf{b} - \mathsf{a} \end{pmatrix}, \quad \mathbf{z}_2 = \begin{pmatrix} 0 \\ 1 \\ 0 \\ \vdots \\ 0 \\ 1 \\ 0 \end{pmatrix}, \tag{B.39}$$

then P from (B.38) can be written in the form (B.35) as

$$\mathsf{P} = \tilde{\mathsf{D}} - \mathbf{w}_1 \mathbf{z}_1^T - \mathbf{w}_2 \mathbf{z}_2^T. \tag{B.40}$$

Here $\tilde{\mathsf{D}}$ is 5-diagonal, and has the form D of (B.1), with

$$\mathsf{c}_1 = \mathsf{c}_N = \mathsf{c} - \mathsf{b},$$
$$\mathsf{d}_1 = \mathsf{b}_2 = \mathsf{d}_{N-1} = \mathsf{b}_N = \mathsf{b} - \mathsf{a},$$
$$\mathsf{a}_i = \mathsf{a} \qquad (3 \le i \le N),$$
$$\mathsf{b}_i = \mathsf{b} \qquad (3 \le i \le N-1),$$
$$\mathsf{c}_i = \mathsf{c} \qquad (2 \le i \le N-1),$$
$$\mathsf{d}_i = \mathsf{b} \qquad (2 \le i \le N-2),$$
$$\mathsf{e}_i = \mathsf{a} \qquad (1 \le i \le N-2).$$

Observe that due to the simple forms for $\mathbf{z}_1$ and $\mathbf{z}_2$, the computation of the scalars β_{ij} and γ_i of (B.37) is very quick: for any $\mathbf{g}$,

$$\mathbf{z}_1^T \mathbf{g} = g_1 + g_2 + g_{N-1} + g_N, \qquad \mathbf{z}_2^T \mathbf{g} = g_2 + g_{N-1}.$$

Since the discretized operator $(\mathsf{I} + \frac{1}{2}\delta t\, \mathsf{A})$ for (B.6) with (B.29) has the form P of (B.38), with

$$\mathsf{a} = r_1, \qquad \mathsf{b} = -4\, r_1 + r_2, \qquad \mathsf{c} = 1 + 6\, r_1 - 2\, r_2 + r_3,$$

we can readily compute $\tilde{\mathsf{D}}$, $\mathbf{w}_1$ and $\mathbf{w}_2$ of (B.40). Repeated application of the Thomas inversion routine of Sec. B.1.1 and the Sherman-Morrison formula (B.36) thus allows us to solve for $\mathbf{u}^{j+1}$ in (B.21) in $\mathcal{O}(N)$ operations at each time step. In summary, this finite difference routine permits the rapid computation of the evolution of the KS equation with periodic BCs.

B.2 Fourier and wavelet methods

In this Section and the next, we look at Fourier and wavelet Galerkin and pseudospectral schemes. There are two issues to be considered: the evaluation of the vector field, and the time integration scheme. Since the time integrator we use is independent of the *particular* form of the vector field, depending only on its general structure, and since we use a similar approach for both the Fourier and wavelet schemes, we discuss the time-stepping algorithm in Sec. B.3, and concentrate in this Section on the evaluation of the vector field.

B.2.1 Fourier methods

The damped KS equation (B.6) in Fourier space is (compare (1.5))

$$\frac{d}{dt}\hat{u}_q = \left[-q^4 + 2\,q^2 - 1 + \varepsilon^2\right]\hat{u}_q + \sum_{q'} q'\hat{u}_{q'}\hat{u}_{q-q'}, \tag{B.41}$$

where $u(x,t) = \mathrm{i}\sum_q \hat{u}_q(t)\exp(\mathrm{i}qx)$, $q = 2\pi n/L$, $n \in \mathbb{Z}$. Implementing the reality condition $\hat{u}_q = -\hat{u}_{-q}^*$ for the Fourier coefficients, we need consider only Fourier modes $q \geq 0$. For numerical solution, we must restrict ourselves to a finite number N of equations (so that the highest Fourier mode included in the computation is $q_M = \frac{2\pi}{L}(\frac{N}{2} - 1)$). The fact that the modal coefficients $\hat{u}_q$ are complex introduces some complications into the numerical implementation of these equations— essentially, the real and imaginary parts must be treated separately—but we will not consider the implications of this issue here, assuming that the routine modifications needed for complex coefficients are introduced as appropriate.

For sufficiently small systems, the Galerkin projection equations (B.41) can be evaluated explicitly. However, because of the convolution structure of the nonlinear term, its evaluation requires $\mathcal{O}(N)$ steps for each equation, or $\mathcal{O}(N^2)$ computations in total, which is slow for large systems. The explicit Galerkin projection equations (and formulations derived from them through center-unstable manifold or inertial manifold projections) are thus mainly useful for theoretical considerations, and for studying the bifurcations in small systems [AGH89].

Considerably superior to the explicit Galerkin scheme, from a numerical point of view, is a pseudospectral approach (see for instance [CHQZ88]). This involves evaluating the nonlinear term in real space: noting that $\partial_x \to \mathrm{i}q\cdot$ in Fourier space, we take the inverse Fourier transforms of $\hat{u}_q$ and $\mathrm{i}q\hat{u}_q$ to give values u and u_x on a grid, multiply pointwise, then Fourier transform again to find the Fourier space representation of the nonlinear term, $\widehat{(uu_x)}_q$. With the aid of the fast Fourier transform ([PTVF92], for instance), the evaluation of the nonlinear term requires $\mathcal{O}(N\log_2 N)$ computations, which is the overall complexity of evaluation of the vector field.

To prevent the effects of aliasing in the implementation of the pseudospectral scheme, one typically needs to compute with at least $\frac{3}{2}M$ Fourier modes to get an M-mode accurate solution. For the KS equation, however, we are able to exploit the exponential decay of solutions in Fourier space to avoid aliasing problems by taking q_M well within the exponential decay regime, for instance, $q_M \gtrsim 4$, where modes $q > 1$ are stable and decaying.

Finally, we observe that (B.41) can be written in the general form

$$\frac{d}{dt}\hat{u}_q = \lambda_q\hat{u}_q + \mathcal{G}[\hat{u}]_q, \qquad \lambda_q = -q^4 + 2\,q^2 - 1 + \varepsilon^2, \tag{B.42}$$

clearly distinguishing between the (diagonal) linear term and the nonlinear term.

B.2.2 Wavelet methods

In Ch. 3 we have discussed some of the theory behind the wavelet Galerkin projection (3.19) of the KS equation,

$$\dot{a}_\alpha = \sum_{\alpha'} l_{\alpha\alpha'}a_{\alpha'} + \sum_{\alpha',\alpha''} n_{\alpha\alpha'\alpha''}a_{\alpha'}a_{\alpha''} \stackrel{\text{def}}{=} h_\alpha, \tag{B.43}$$

where $l_{\alpha\alpha'} = \int_0^L \psi_\alpha^L(y)\mathcal{L}\psi_{\alpha'}^L(y)\,dy$, $n_{\alpha\alpha'\alpha''} = \int_0^L \psi_\alpha^L(y)\psi_{\alpha'}^L(y)\mathcal{D}\psi_{\alpha''}^L(y)\,dy$, and the sums are over the full wavelet pyramid, α representing the multi-index (j,k). Here $\mathcal{D} = -\partial_x$, and the formalism holds

for the usual KS equation, for its extension to the damped case (Ch. 2) with $\mathcal{L} = -\partial_x^4 - 2\,\partial_x^2 - (1 - \varepsilon^2)$, or for any other (one-dimensional) linear differential operator $\mathcal{L}$. As before, we restrict ourselves to a finite number N modes, $N = 2^{J+1} - 1$, if we keep wavelet levels 0–J.

Explicit Galerkin evaluation   In contrast to the Fourier representation, the linear operator is not diagonal in the wavelet basis, nor does the nonlinear term have a simple convolution structure. Consequently, a direct evaluation of the vector field in (B.43) requires N computations for the linear term and N^2 for the nonlinear term for each mode α, for a total of $\mathcal{O}(N^3)$ computations at each time step.

This also assumes that the Galerkin coefficients $l_{\alpha\alpha'}$ and $n_{\alpha\alpha'\alpha''}$ have been precomputed. Such computation need only be done once, in advance of the time integration, and is speeded up through the use of the symmetries (3.22), (3.23) and translational invariance; but the memory requirements for storing the N^3 coefficients of $n_{\alpha\alpha'\alpha''}$ are large. All in all, this $\mathcal{O}(N^3)$ algorithm imposes very restrictive time and memory limitations.

Wavelet pseudospectral scheme   As for Fourier methods, a considerable speedup can be achieved by using pseudospectral methods, using a fast wavelet transform (FWT) algorithm, which allows one compute wavelet coefficients from real-space grid values or, alternatively, to reconstruct a solution in real space from its wavelet coefficients. As described in Sec. 3.1.1, we use periodic spline wavelets ψ_{jk}, and implement the algorithm described by Perrier and Basdevant [PB89], which performs the FWT via Fourier space, making use also of the FFT; its total operation count (including three FFTs per FWT) is also $\mathcal{O}(N \log_2 N)$. Since the terms on the right-hand side of (B.43) are just the wavelet coefficients of the linear $\mathcal{L}u$ and nonlinear $u\mathcal{D}u$ terms, respectively, we can evaluate the vector field h_α in $\mathcal{O}(N \log_2 N)$ steps: For the linear term $\mathcal{L}u$, we transform part of the way to Fourier space, evaluate the derivatives there, then transform back to wavelet space; the nonlinear term $u\mathcal{D}u$ is evaluated by performing the full FWT to real space, multiplying pointwise, then inverting the FWT to compute the wavelet coefficients.

Inexact evaluation at small scales   We should note here that when we retain a finite number of levels, the FWT evaluation of derivatives (especially the fourth derivative term) is inaccurate at the highest wavelet levels. This is because wavelets are not perfectly localized in Fourier space, and any high-q components of ψ are amplified by differentiation (since $\partial_x^4 \to q^4\cdot$). Thus, for instance, $\partial_x^4 \psi_{jk}(x)$ contains significant contributions at levels $j' > j$; for large j, these are not included in a model with cutoff at $j = J$. Similarly, $uu_x = (\frac{1}{2}u^2)_x$ tends to enhance small scales (for individual Fourier modes, $u \mapsto u^2$ implies $q \mapsto 2q$, so heuristically, the effect is a shift from j to $j+1$).

We expect that this might be a reason that the evolution is not very faithful, and the wavelet energy spectrum is not captured accurately, for high j near the cutoff (see Sec. 5.2.1). For accurate representation of the vector field up to level j, we should ideally compute up to level $j+1$, or even $j+2$. However, as also discussed in Sec. 5.2.1 (see also Fig. 5.34), the small scales contribute so negligibly to the overall dynamics that we gladly trade the small cost in accuracy for the gain in speed allowed by the use of fewer wavelet levels (of course, retaining at least one small-scale level in the strongly damped region, where the energy is exponentially decaying).

As in the Fourier case, we note finally that the wavelet algorithm can be written in the form

$$\frac{d}{dt}a_\alpha = \lambda_\alpha a_\alpha + f_\alpha(\{a_{\alpha'}\}) + g_\alpha(\{a_{\alpha'}\}), \tag{B.44}$$

separating the linear diagonal term from the others. Here g_α is the α component of the nonlinear

term, while f_α represents the linear term without the diagonal contribution, that is,

$$f_\alpha = \left(\mathcal{L}u\right)_\alpha - \lambda_\alpha a_\alpha,$$

where $\lambda_\alpha = l_{\alpha\alpha} = (\psi_\alpha, \mathcal{L}\psi_\alpha)$ can be precomputed once at the beginning of the integration scheme and is, of course, a function only of the wavelet level j, not of the position k, by translation invariance. The separation of the diagonal term from the remainder of the vector field will be fundamental to the time integration schemes discussed in the next Section B.3, while the separation of the linear (off-diagonal) f_α and nonlinear g_α terms will also be useful.

Manipulating interactions

Many of the experimental results of this thesis rest on attempts to understand KS dynamics by manipulating the components that contribute to it (for instance, through modifying complete wavelet levels, Ch. 5, or periodization or external forcing of a local model, Ch. 6). In most cases, these experiments are performed by integrating the usual KS vector field using the algorithms described above, but modifying the set of model wavelet coefficients $\{a_\alpha\} = \{a_{jk}\}$ at each time step—for instance setting modes at some levels j to zero, or replacing some modes by ones computed from an independent KS integration. The manipulations performed for the different experiments are outlined in their respective sections.

For the experiments of Sec. 4.3.3 designed to test the spatial localization of interactions, however, we retain all wavelet coefficients a_α in our model, but modify the form of the vector field h_α of (B.43). In particular, we perform one of the simplest of such manipulations, eliminating interactions between wavelets ψ_α and $\psi_{\alpha'}$ if the distance between their centers, $d_{\alpha\alpha'} = |x_\alpha - x_{\alpha'}|$ (see Sec. 3.1.1), is greater than some predefined interaction distance l_c.

Galerkin implementation: modify coupling coefficients In the explicit Galerkin algorithm of (B.43), this is straightforward to implement, by modifying the precomputed Galerkin coefficient matrices to vanish if the wavelets are too far apart. That is, we define

$$\tilde{l}_{\alpha\alpha'} \stackrel{\text{def}}{=} w_{\alpha\alpha'} l_{\alpha\alpha'}, \qquad \tilde{n}_{\alpha\alpha'\alpha''} \stackrel{\text{def}}{=} w_{\alpha\alpha'\alpha''} n_{\alpha\alpha'\alpha''}, \tag{B.45}$$

where we define the weight step function $w_{\alpha\alpha'}$ by

$$w_{\alpha\alpha'} \stackrel{\text{def}}{=} \begin{cases} 1 & \text{if } d_{\alpha\alpha'} \leq l_c, \\ 0 & \text{if } d_{\alpha\alpha'} > l_c; \end{cases}$$

or in terms of the Heaviside function $H = \chi_{[0,\infty)}$, as $w_{\alpha\alpha'} = H\left(l_c - d_{\alpha\alpha'}\right)$. Similarly, $w_{\alpha\alpha'\alpha''} = H\left(l_c - \max(d_{\alpha\alpha'}, d_{\alpha\alpha''})\right)$; that is, for the nonlinear term, both $\psi_{\alpha'}$ and $\psi_{\alpha''}$ should be centered within l_c of ψ_α for the three-mode interaction $n_{\alpha\alpha'\alpha''}$ to be included. With precomputed matrices $\tilde{l}_{\alpha\alpha'}$ and $\tilde{n}_{\alpha\alpha'\alpha''}$, this algorithm is implemented by direct summation in the same way as the explicit Galerkin method (B.43), with the same $\mathcal{O}(N^3)$ speed and memory limitations.

Pseudospectral implementation: restrict set of interacting modes As before, this algorithm can be improved by the use of the FWT. Here, in evaluating the vector field h_α for a *given* α, the restriction on the interaction distance is implemented by setting to zero all wavelet coefficients $a_{\alpha'}$ that are too distant from a_α, before the $\mathcal{O}(N \log_2 N)$ wavelet pseudospectral calculation of derivatives and the nonlinear term; in terms of the previous notation, this amounts to computation

of the vector field with wavelet coefficients $\tilde{a}_{\alpha'} = w_{\alpha\alpha'}a_{\alpha'}$ (one readily confirms the equivalence of this approach to the restriction of interactions to the previous one). Each mode a_α now interacts with a *different* subset of the total set of modes $\{a_{\alpha'}\}$, however, so that the vector field now must be computed separately for each α. A total of $\mathcal{O}(N^2 \log_2 N)$ computations is thus needed.

The prefactor in the above $\mathcal{O}(N^2 \log_2 N)$ is sufficiently large that the pseudospectral algorithm for restricting interactions only becomes competitive with the $\mathcal{O}(N^3)$ explicit Galerkin approach at about $N = 127$, or $J = 6$ (which is the number of levels we use for most $L = 100$ computations). However, as already noted, the pseudospectral approach has the additional advantage of not requiring storage of the N^3 matrix elements of $n_{\alpha\alpha'\alpha''}$. For this reason, most results on manipulating interactions reported in this thesis (Sec. 4.3.3) use the pseudospectral approach to evaluating the vector field.

B.3   Time integration schemes

In the last Section we have described the evaluation of the vector field, in both Fourier and wavelet bases; it remains to consider the time-stepping routine. These algorithms depend only on the general form of the vector field, so we will restrict our discussion to the simple scalar equation

$$\dot{a} = \lambda a + f(a). \tag{B.46}$$

As usual, we write the solutions for discretized time intervals $t_j = j\delta t$ as $a^j \stackrel{\text{def}}{=} a(j\delta t)$, and write $f(a^j)$ for $f(a)$ evaluated at $t = t_j$.

The evolution of individual modes in both the Fourier and wavelet representations can be written in this general form; see (B.42,B.44). In fact, in both cases we are solving for a vector $\mathbf{a} = \{a_i\}$ of modes, and $\mathbf{f}(\mathbf{a})$ is a function of all the modes; so that the general form should really read

$$\dot{a}_i = \lambda_i a_i + f_i(\mathbf{a}).$$

However, we will not assume anything about $\mathbf{f}$ except that it may be evaluated at each time step; so we discuss only the situation of a simple scalar equation (B.46), with the extension to the vector case for $\mathbf{a}$ being straightforward.

Numerous schemes for the integration of (B.46) are well known (see for instance [SB80, PTVF92]). For our applications, the evaluation of $f(a)$ is the most time-consuming step, as we have seen in Sec. B.2. The system is stiff: for unstable modes, $\lambda > 0$, while there are stable modes with very negative λ. Also, the intrinsic chaotic instability of the KS dynamics means that perfect tracking of a "true" solution is not a feasible goal. These considerations dictate our choice of integration scheme: we desire a sufficiently accurate scheme which is stable for reasonably large time steps, to enable long-time integrations and computation of statistics (where "sufficiently accurate" is checked by comparing qualitative dynamics and statistics for different integrators and smaller time steps). Instead of seeking highly accurate algorithms such as variable-order, variable-step methods, we prefer relatively simple schemes which do not require inversion of the vector field (except for the linear diagonal term), which minimize the number of vector field evaluations, and which are appropriate for stiff systems.

B.3.1   ABCN approach

A straightforward integrator, formally second-order accurate in time, is an "Adams-Bashforth-Crank-Nicholson" or ABCN scheme; in investigations related to ours, such an approach has been

used in [BEH92, EBH96]. The ABCN method has already been discussed in the finite difference context in Sec. B.1.2:

$$a^{j+1} = a^j + \tfrac{1}{2}\,\delta t\left(\lambda a^{j+1} + \lambda a^j\right) + \delta t\left(\tfrac{3}{2}\,f(a^j) - \tfrac{1}{2}\,f(a^{j-1})\right)$$

or

$$a^{j+1} = \frac{1 + \tfrac{1}{2}\lambda\,\delta t}{1 - \tfrac{1}{2}\lambda\,\delta t}a^j + \frac{\tfrac{1}{2}\,\delta t}{1 - \tfrac{1}{2}\lambda\,\delta t}\left(3\,f(a^j) - f(a^{j-1})\right) \tag{B.47}$$

(with a single Euler step for the nonlinear term $f(a)$ at the first time step). As already noted in Sec. B.1.2, this approach performs poorly for the strongly stable modes, with $\lambda < 0$, $|\lambda| \gg 1$, since as $\lambda\,\delta t \to -\infty$, $(1 + \tfrac{1}{2}\lambda\,\delta t)(1 - \tfrac{1}{2}\lambda\,\delta t)^{-1} \to -1$. While sufficiently stable, this method requires small time steps, and deteriorates instead of improving as more and more stable modes are included (see also [FST86]).

B.3.2   Integrating factor approach

An approach which circumvents this difficulty, and optimizes the treatment of the most stable modes, is one which exactly integrates the linear diagonal terms (see [CHQZ88, Sec. 4.4.2]).

   With the use of an integrating factor, the general system (B.46) can be integrated from $t = t_j = j\,\delta t$ to $t = t_{j+1}$ to give

$$e^{-\lambda t_{j+1}}a(t_{j+1}) - e^{-\lambda t_j}a(t_j) = \int_{t_j}^{t_{j+1}} e^{-\lambda s}f(a(s))\,ds,$$

or

$$a^{j+1} = e^{\lambda\,\delta t}a^j + e^{\lambda t_{j+1}}\int_{t_j}^{t_{j+1}} e^{-\lambda s}f(a(s))\,ds \tag{B.48}$$

$$\overset{\text{def}}{=} e^{\lambda\,\delta t}a^j + e^{\lambda t_{j+1}}\int_{t_j}^{t_{j+1}} g(s, a(s))\,ds. \tag{B.48$'$}$$

The integration scheme is then defined by the approximation chosen for the integral; given, in our case, knowledge of a and $f(a)$ at equally spaced times $t_j, t_{j-1}, t_{j-2}, \ldots$

General principles of Adams-Bashforth schemes   Consider the general equation

$$\dot{b} = h(b), \quad \text{or} \quad b^{j+1} = b^j + \int_{t_j}^{t_{j+1}} h(b(s))\,ds.$$

If we approximate the integral by polynomial interpolation of the integrand at the p times $t_j, t_{j-1}, t_{j-2}, \ldots, t_{j-(p-}$ (where $t_{j-i} = (j - i)\,\delta t = t_j - i\,\delta t$), we obtain the Adams-Bashforth methods (see [SB80, Sec. 7.2.6] or [CHQZ88, Sec. 4.3.1]). For instance, if we interpolate using only the value of h at $t = t_j$, that is, $h(b(s)) \approx h(b^j)$, we get exactly the explicit Euler method,

$$b^{j+1} = b^j + \delta t\,h(b^j);$$

which is thus a $p = 1$ Adams-Bashforth method.

   In our case (B.48), our integrand has a slightly different form, containing an exponential term, and there are two possibilities:

1. Interpolate the entire integrand $g(s, a(s)) = e^{-\lambda s} f(a(s))$; or

2. Interpolate only $f(a(s))$, and integrate the exponential exactly.

In the following discussion, we largely follow the approach and notation of Stoer and Bulirsch [SB80]; note that the second possibility has also been discussed and implemented by Zaleski [Zal89].

Interpolate the full integrand

The Lagrange polynomial interpolation formula for $g(s, a(s))$ is (see [IK66, SB80])

$$P_p(t) = \sum_{i=0}^{p-1} g(t_{j-i}, a^{j-i}) \prod_{\substack{l=0 \\ l \neq i}}^{p-1} \frac{t - t_{j-l}}{t_{j-i} - t_{j-l}} \quad \stackrel{\text{def}}{=} \quad \sum_{i=0}^{p-1} g(t_{j-i}, a^{j-i}) \, L_i(t), \tag{B.49}$$

where $L_i(t)$ are the Lagrange interpolation coefficients. Substituting this interpolation form into (B.48′), we find the approximation

$$a^{j+1} - e^{\lambda \, \delta t} a^j = e^{\lambda t_{j+1}} \sum_{i=0}^{p-1} e^{-\lambda t_{j-i}} f(a^{j-i}) \, \delta t \, \beta_{pi}$$

or

$$a^{j+1} = e^{\lambda \, \delta t} a^j + \delta t \, e^{\lambda \, \delta t} \sum_{i=0}^{p-1} \beta_{pi} \, e^{\lambda i \, \delta t} \, f(a^{j-i}) \tag{B.50}$$

where we obtain β_{pi} from

$$\delta t \, \beta_{pi} \stackrel{\text{def}}{=} \int_{t_j}^{t_{j+1}} L_i(t) \, dt \qquad = \int_{t_j}^{t_{j+1}} \prod_{\substack{l=0 \\ l \neq i}}^{p-1} \frac{t - t_{j-l}}{t_{j-i} - t_{j-l}} \, dt$$

$$= \int_0^1 \prod_{\substack{l=0 \\ l \neq i}}^{p-1} \frac{l+s}{l-i} \, ds \qquad i = 0, 1, \ldots, p-1. \tag{B.51}$$

We can readily compute that

$$
\begin{aligned}
(p=1): & \quad \beta_{10} = 1 \\
(p=2): & \quad \beta_{20} = \tfrac{3}{2}, \quad \beta_{21} = -\tfrac{1}{2} \\
(p=3): & \quad \beta_{30} = \tfrac{23}{12}, \quad \beta_{31} = -\tfrac{16}{12}, \quad \beta_{32} = \tfrac{5}{12}
\end{aligned}
$$

etc.

The above numbers look familiar as the coefficients in the ($p = 1$) Euler and ($p = 2$) second-order Adams-Bashforth schemes (see Sec. B.1.2). For $p = 3$, for the general equation $\dot{b} = h(b)$, the values for β_{3i} give the third-order AB scheme,

$$b^{j+1} = b^j + \delta t \left[\tfrac{23}{12} h(b^j) - \tfrac{4}{3} h(b^{j-1}) + \tfrac{5}{12} h(b^{j-2}) \right].$$

Substituting the values of β_{pi} into our formula (B.50) gives pth order accurate schemes for the evaluation of (B.48′), obtained by interpolating the full integrand. For reference, we record the $p = 1$ formula,

$$a^{j+1} = e^{\lambda \, \delta t} a^j + \delta t \, e^{\lambda \, \delta t} f(a^j). \tag{B.52}$$

Interpolate $f(a(s))$, with exact integration of exponential

Again using the Lagrange interpolation formula for f, we can approximate (B.48) by

$$a^{j+1} - e^{\lambda\,\delta t}a^j = e^{\lambda\,t_{j+1}} \sum_{i=0}^{p-1} f(a^{j-i}) \int_{t_j}^{t_{j+1}} e^{-\lambda t} L_i(t)\,dt$$

or

$$a^{j+1} = e^{\lambda\,\delta t}a^j + \delta t\,e^{\lambda\,\delta t} \sum_{i=0}^{p-1} \gamma_{pi}\, f(a^{j-i}), \tag{B.53}$$

where we define

$$e^{-\lambda\,t_j}\delta t\,\gamma_{pi} \stackrel{\text{def}}{=} \int_{t_j}^{t_{j+1}} e^{-\lambda t} L_i(t)\,dt,$$

and consequently derive

$$\gamma_{pi} = \int_0^1 e^{-\lambda\,s\,\delta t} \prod_{\substack{l=0 \\ l\neq i}}^{p-1} \frac{l+s}{l-i}\,ds. \tag{B.54}$$

We note that the two approaches should become equivalent in the limit $\lambda \to 0$ (when $e^{-\lambda s} \to 1$), so that $\gamma_{pi} \to \beta_{pi}$ in this limit. On evaluating the integrals in (B.54), we find

$$(p=1): \quad \gamma_{10} = \frac{1 - e^{-\lambda\,\delta t}}{\lambda\,\delta t}$$

$$(p=2): \quad \gamma_{20} = \frac{1}{\lambda\,\delta t}\left[1 - 2e^{-\lambda\,\delta t} + \frac{1 - e^{-\lambda\,\delta t}}{\lambda\,\delta t}\right]$$

$$\gamma_{21} = \frac{1}{\lambda\,\delta t}\left[e^{-\lambda\,\delta t} - \frac{1 - e^{-\lambda\,\delta t}}{\lambda\,\delta t}\right]$$

$$(p=3): \quad \gamma_{30} = \frac{1}{\lambda\,\delta t}\left[1 - 3\,e^{-\lambda\,\delta t} + \frac{3 - 5\,e^{-\lambda\,\delta t}}{2\,\lambda\,\delta t} + \frac{1 - e^{-\lambda\,\delta t}}{(\lambda\,\delta t)^2}\right]$$

$$\gamma_{31} = \frac{1}{\lambda\,\delta t}\left[3\,e^{-\lambda\,\delta t} + \frac{4\,e^{-\lambda\,\delta t} - 2}{\lambda\,\delta t} + \frac{2\,e^{-\lambda\,\delta t} - 2}{(\lambda\,\delta t)^2}\right]$$

$$\gamma_{32} = \frac{1}{\lambda\,\delta t}\left[-e^{-\lambda\,\delta t} + \frac{1 - 3\,e^{-\lambda\,\delta t}}{2\,\lambda\,\delta t} + \frac{1 - e^{-\lambda\,\delta t}}{(\lambda\,\delta t)^2}\right]$$

etc.

Taylor expansion and some algebraic manipulation confirms that in all cases, $\gamma_{pi} \to \beta_{pi}$ as $\lambda \to 0$. In this way, Adams-Bashforth schemes can be derived, with and without exact integration of the exponential term, to arbitrarily high order. For reference, the $p=1$ scheme for (B.53) is

$$a^{j+1} = e^{\lambda\,\delta t}a^j + \frac{e^{\lambda\,\delta t} - 1}{\lambda}f(a^j) \tag{B.55}$$

(a leap-frog version of this scheme, with the right-hand side replaced by $e^{2\,\lambda\,\delta t}a^{j-1} + (e^{2\,\lambda\,\delta t} - 1)f(a^j)/\lambda$ to give second order accuracy in time, has been discussed and implemented by Frisch *et al.* [FST86]).

Implementation

We thus have two families of integrators with the use of an integrating factor, exact for the linear diagonal terms, which we have implemented successfully for the pseudospectral schemes of Sec. B.2. In contrast to the ABCN method, small scales are rapidly damped in these schemes, so we can use much larger time steps δt; we find that the maximum possible δt giving a stable numerical scheme with reasonable dynamics is at least an order of magnitude higher than that possible for the ABCN scheme, allowing considerable speedup of the integration.

Small scales slaved to large scales The small scale modes (with very negative λ) adiabatically adjust to the input provided by $f(a)$ due to their rapid damping (see for instance Sec. 5.3.1), and a lowest order approximation to their evolution is

$$\dot{a} = -|\lambda|a + f(a) \approx 0, \quad \text{implying} \quad a \approx \frac{f(a)}{|\lambda|};$$

this quasi-equilibrium, valid if a varies on much faster time scales than f, is related to the existence of an inertial manifold. It is advantageous to choose a scheme which reproduces this behavior, with the strongly damped modes rapidly adapting to the forcing.

As pointed out by Frisch *et al.* [FST86] (see also [Zal89]), the second class of schemes (B.53), with interpolation of $f(a)$ and integration of the exponential, gives the desired behavior. We can see this most readily for the $p = 1$ schemes: In (B.52), $a^{j+1} \to 0$ exponentially as $\lambda \to -\infty$, while in (B.55), we get

$$a^{j+1} \to \frac{f(a^j)}{|\lambda|} \quad \text{as} \quad \lambda \to -\infty,$$

as needed; the results are similar for higher-order schemes, $p \geq 2$. The second class of algorithms thus gives not only the requisite small-scale damping (in contrast to ABCN), but also the slaving to the large scales.

For the Fourier pseudospectral methods described in Sec. B.2.1, our time integrator of choice has thus been (B.53) for $p = 2$. This is the technique used for the computation of many of the statistical results of Ch. 4, and in our experience gives the most spectrally accurate results of all the integration schemes described in this Appendix.[†]

Modifications required in the wavelet algorithms Straightforward implementation of (B.53) does not work for the wavelet pseudospectral method, however; when we did this, the integration diverged. The cause of this problem is the lack of diagonal dominance of the linear operator $l_{\alpha\alpha'}$, as we argue now.

As in (B.44), we can separate the nondiagonal terms of the vector field $f(a)$ into the linear off-diagonal, and nonlinear terms, to give the evolution

$$\dot{a}_\alpha = \lambda_\alpha a_\alpha + \sum_{\alpha' \neq \alpha} l_{\alpha\alpha'} a_{\alpha'} + g_\alpha(\{a_{\alpha'}\}),$$

where $\lambda_\alpha = l_{\alpha\alpha}$ (the wavelet pseudospectral scheme essentially amounts to this equation). Writing down the scheme (B.53) for this case (using, for convenience, $p = 1$), we have

$$a_\alpha^{j+1} = e^{\lambda_\alpha \, \delta t} a_\alpha^j + \left(e^{\lambda_\alpha \, \delta t} - 1\right) \frac{\sum_{\alpha' \neq \alpha} l_{\alpha\alpha'} a_{\alpha'}^j}{l_{\alpha\alpha}} + \frac{e^{\lambda_\alpha \, \delta t} - 1}{\lambda_\alpha} g_\alpha(\{a_{\alpha'}\}). \tag{B.56}$$

[†]Results do not appear much changed on using $p = 3$, which has also been implemented successfully.

One can verify, for instance numerically, that $l_{\alpha\alpha'}$ is not diagonally dominant for small scales:

$$\left| \sum_{\alpha' \neq \alpha} l_{\alpha\alpha'} \right| > |l_{\alpha\alpha}|, \quad \text{so that} \quad |k_\alpha| \overset{\text{def}}{=} \left| \frac{\sum_{\alpha' \neq \alpha} l_{\alpha\alpha'}}{\lambda_\alpha} \right| > 1.$$

The likelihood of blowup for small scales is thus apparent; for if $\lambda_\alpha < 0$, $|\lambda_\alpha| \gg 1$, $e^{\lambda_\alpha \, \delta t} \ll 1$, then

$$a_\alpha^{j+1} \approx -\frac{\sum_{\alpha' \neq \alpha} l_{\alpha\alpha'} a_{\alpha'}^j}{\lambda_\alpha} - \frac{g_\alpha(\{a_{\alpha'}\})}{\lambda_\alpha}. \tag{B.57}$$

Here the linear off-diagonal term gives problems: The scenario for blowup is most apparent if the coefficients $\{a_{\alpha'}\}$, or at least those for α' near α, for which $l_{\alpha\alpha'}$ is significant, are approximately equal; for then this scheme gives

$$a_\alpha^{j+1} \approx -k_\alpha a_\alpha^j, \quad \text{or} \quad |a_\alpha^{j+m}| \sim |k_\alpha|^m |a_\alpha^j| \xrightarrow[m \to \infty]{} \infty.$$

More realistically, the different modes reinforce each other with multipliers $k_\alpha > 1$, rendering the scheme (B.53) unstable for this case.[†]

The last (nonlinear) term in (B.57) does not contribute to this scenario for instability, remaining well-behaved as $\lambda_\alpha \to -\infty$; furthermore, as already discussed, the small-scale slaving properties of this scheme (B.53) are desirable. For the wavelet-based formulation of the KS equation (B.43), therefore, we employ a mixed time integrator: We treat the last two terms in (B.44) separately, using the scheme (B.50) for the off-diagonal linear term f_α (interpolating the full integrand, as in (B.48′) with (B.49)), and using (B.53) for the nonlinear term g_α (with exact integration of the exponential). This lets us retain the benefits of accuracy and large step size from the use of an integrating factor method, and the small-scale slaving to the nonlinear term, while avoiding the instability due to the off-diagonal linear terms.[‡]

Motivated by (B.44) and the above discussion, we summarize by formulating a time integrator for a general scalar equation of the form (B.46), in which the term $f(a)$ is separated into two parts:

$$\dot{a} = \lambda a + f_1(a) + f_2(a). \tag{B.58}$$

The mixed integration scheme for (B.58), stable and pth order accurate in time, is

$$a^{j+1} = e^{\lambda \, \delta t} a^j + \delta t \, e^{\lambda \, \delta t} \sum_{i=0}^{p-1} \beta_{pi} \, e^{\lambda i \, \delta t} f_1(a^{j-i}) + \delta t \, e^{\lambda \, \delta t} \sum_{i=0}^{p-1} \gamma_{pi} \, f_2(a^{j-i}), \tag{B.59}$$

where the β_{pi} and γ_{pi} have been given previously.

For the computations of Ch. 5 and Ch. 6, we used the $p = 2$ version of this integrator (initializing the integration with a single $p = 1$ Euler step):

$$a^{j+1} = e^{\lambda \, \delta t} a^j + \delta t \left[\tfrac{3}{2} e^{\lambda \, \delta t} f_1(a^j) - \tfrac{1}{2} e^{2\lambda \, \delta t} f_1(a^{j-1}) \right]$$

$$+ \left[e^{\lambda \, \delta t} - 2 + \frac{e^{\lambda \, \delta t} - 1}{\lambda \, \delta t} \right] \frac{f_2(a^j)}{\lambda} + \left[1 - \frac{e^{\lambda \, \delta t} - 1}{\lambda \, \delta t} \right] \frac{f_2(a^{j-1})}{\lambda}. \tag{B.60}$$

[†]Since for the Fourier scheme the linear part is diagonal and thus trivially diagonally dominant, this problem does not occur there.

[‡]In the light of the previous discussion, it seems prudent to choose the time step δt so that $\max_\alpha \delta t \, |(\sum_{\alpha' \neq \alpha} l_{\alpha\alpha'})/l_{\alpha\alpha}| < 1$.

Bibliography

[Abr97]   P. Abry. *Ondelettes et Turbulences: Multirésolutions, algorithmes de décomposition, invariance d'échelle et signaux de pression*. Nouveaux Essais. Diderot, Paris New York, 1997.

[AD94]   C. Alfaro and M. Depassier. A five-mode bifurcation analysis of a Kuramoto-Sivashinsky equation with dispersion. *Phys. Lett. A* **184**, 184–189 (1994).

[AGH88]   D. Armbruster, J. Guckenheimer, and P. Holmes. Heteroclinic cycles and modulated traveling waves in systems with $\mathbf{O}(2)$ symmetry. *Physica D* **29**, 257–282 (1988).

[AGH89]   D. Armbruster, J. Guckenheimer, and P. Holmes. Kuramoto-Sivashinsky dynamics on the center-unstable manifold. *SIAM J. Appl. Math.* **49**, 676–691 (1989).

[AAC90]   R. Artuso, E. Aurell, and P. Cvitanović. Recycling of strange sets: I. Cycle expansions. *Nonlinearity* **3**, 325–359 (1990).

[AGL92]   N. Aubry, R. Guyonnet, and R. Lima. Spatio-temporal symmetries and bifurcations via bi-orthogonal decompositions. *J. Nonlinear Sci.* **2**, 183–215 (1992).

[AHLS88]   N. Aubry, P. Holmes, J. L. Lumley, and E. Stone. The dynamics of coherent structures in the wall region of a turbulent boundary layer. *J. Fluid Mech.* **192**, 115–173 (1988).

[AL93]   N. Aubry and W.-Y. Lian. Exploiting and detecting space-time symmetries. In *Exploiting Symmetry in Applied and Numerical Analysis* (E. L. Allgower, K. Georg, and R. Miranda, eds.), Lectures in Applied Mathematics, vol. 29, American Mathematical Society, Providence, R.I., 1993, pp. 389–404.

[ALT93]   N. Aubry, W.-Y. Lian, and E. S. Titi. Preserving symmetries in the proper orthogonal decomposition. *SIAM J. Sci. Comput.* **14**, 483–505 (1993).

[BS95]   A.-L. Barabási and H. E. Stanley. *Fractal Concepts in Surface Growth*. Cambridge University Press, Cambridge, 1995.

[BCDGG90]   M. Bartuccelli, P. Constantin, C. Doering, J. D. Gibbon, and M. Gisselfält. On the possibility of soft and hard turbulence in the complex Ginzburg-Landau equation. *Physica D* **44**, 421–444 (1990).

[BHP90]   C. Basdevant, M. Holschneider, and V. Perrier. Méthode des ondelettes mobiles. *C. R. Acad. Sci. Paris, Série I* **310**, 647–652 (1990).

[BMV93]   I. Bena, C. Misbah, and A. Valance. Nonlinear evolution of a terrace edge during step-flow growth. *Phys. Rev. B* **47**, 7408–7419 (1993).

[Ben66]   D. Benney. Long waves on liquid films. *J. Math. and Phys.* **45**, 150–155 (1966).

[BBPVV91]   R. Benzi, L. Biferale, G. Paladin, A. Vulpiani, and M. Vergassola. Multifractality in the statistics of the velocity gradients in turbulence. *Phys. Rev. Lett.* **67**, 2299–2302 (1991).

[BEH92]   G. Berkooz, J. Elezgaray, and P. Holmes. Coherent structures in random media and wavelets. *Physica D* **61**, 47–58 (1992).

[BEHLP93]   G. Berkooz, J. Elezgaray, P. Holmes, J. Lumley, and A. Poje. The proper orthogonal decomposition, wavelets and modal approaches to the dynamics of coherent structures. In *Eddy Structure Identification in Free Turbulent Shear Flows* (J. P. Bonnet and M. N. Glauser, eds.), Kluwer Academic Publishers, 1993, pp. 295–309.

[BHL93]   G. Berkooz, P. Holmes, and J. L. Lumley. The proper orthogonal decomposition in the analysis of turbulent flows. *Ann. Rev. Fluid Mech.* **25**, 539–575 (1993).

[BBIS96]   H. A. Biagioni, J. L. Bona, R. J. Iorio, Jr., and M. Scialom. On the Korteweg-de Vries-Kuramoto-Sivashinsky equation. *Adv. Diff. Eqns.* **1**, 1–20 (1996).

[Bro92]   H. S. Brown. A computer assisted, nonlinear dynamic study of instabilities and pattern formation for interfacial waves. Ph.D. thesis, Princeton University, 1992.

[BJKT90]   H. S. Brown, M. S. Jolly, I. G. Kevrekidis, and E. S. Titi. Use of approximate inertial manifolds in bifurcation calculations. In *Continuation and Bifurcations: Numerical Techniques and Applications* (D. Roose, B. De Dier, and A. Spence, eds.), Kluwer Academic Publishers, Dordrecht, 1990, pp. 9–23.

[BK96]   H. S. Brown and I. G. Kevrekidis. Modulated traveling waves for the Kuramoto-Sivashinsky equation. In *Pattern Formation: Symmetry Methods and Applications* (J. Chadam, M. Golubitsky, W. Langford, and B. Wetton, eds.), American Mathematical Society, Providence, R.I., 1996, pp. 45–66.

[BKOR92]   H. S. Brown, I. G. Kevrekidis, A. Oron, and P. Rosenau. Bifurcations and pattern formation in the "regularized" Kuramoto-Sivashinsky equation. *Phys. Lett. A* **163**, 299–308 (1992).

[BHK98]   G. L. Browning, W. D. Henshaw, and H.-O. Kreiss. A numerical investigation of the interaction between the large and small scales of the two-dimensional incompressible Navier-Stokes equations, preprint, April 1998; UCLA CAM Report 98-23, 1998.

[BPRdlR97]   J. Buceta, J. M. Pastor, M. A. Rubio, and F. J. de la Rubia. The stochastic stabilized Kuramoto-Sivashinsky equation: a model for compact electrodeposition growth. *Phys. Lett. A* **235**, 464–468 (1997).

[BPRdlR98]   J. Buceta, J. M. Pastor, M. A. Rubio, and F. J. de la Rubia. Small scale properties of the stochastic stabilized Kuramoto-Sivashinsky equation. *Physica D* **113**, 166–171 (1998).

[CH92]   S. A. Campbell and P. Holmes. Heteroclinic cycles and modulated traveling waves in a system with $\mathbf{D}_4$ symmetry. *Physica D* **59**, 52–78 (1992).

[CHQZ88]   C. Canuto, M. Y. Hussaini, A. Quarteroni, and T. A. Zang. *Spectral Methods in Fluid Dynamics*. Springer Series in Computational Physics. Springer-Verlag, Berlin Heidelberg, 1988.

[Cha86]   H.-C. Chang. Nonlinear waves on liquid film surfaces—I. Flooding in a vertical tube. *Chem. Eng. Sci.* **41**, 2463–2476 (1986).

[CDK93]   H.-C. Chang, E. A. Demekhin, and D. I. Kopelevich. Laminarizing effects of dispersion in an active-dissipative nonlinear medium. *Physica D* **63**, 299–320 (1993).

[CM87]   H. Chaté and P. Manneville. Transition to turbulence via spatiotemporal intermittency. *Phys. Rev. Lett.* **58**, 112–115 (1987).

[CG88]   P. Chossat and M. Golubitsky. Symmetry-increasing bifurcation of chaotic attractors. *Physica D* **32**, 423–436 (1988).

[CH95]   C. C. Chow and T. Hwa. Defect-mediated stability: an effective hydrodynamic theory of spatiotemporal chaos. *Physica D* **84**, 494–512 (1995).

[CCP97]   F. Christiansen, P. Cvitanović, and V. Putkaradze. Spatiotemporal chaos in terms of unstable recurrent patterns. *Nonlinearity* **10**, 55–70 (1997).

[Chu92]   C. K. Chui. *An Introduction to Wavelets*. Wavelet Analysis and its Applications, vol. 1. Academic Press, San Diego, 1992.

[CKTR76]   B. Cohen, J. Krommes, W. Tang, and M. Rosenbluth. Nonlinear saturation of the dissipative trapped-ion mode by mode coupling. *Nucl. Fus.* **16**, 971–992 (1976).

[CEES93a]   P. Collet, J.-P. Eckmann, H. Epstein, and J. Stubbe. A global attracting set for the Kuramoto-Sivashinsky equation. *Commun. Math. Phys.* **152**, 203–214 (1993).

[CEES93b]   P. Collet, J.-P. Eckmann, H. Epstein, and J. Stubbe. Analyticity for the Kuramoto-Sivashinsky equation. *Physica D* **67**, 321–326 (1993).

[CFNT89a]   P. Constantin, C. Foias, B. Nicolaenko, and R. Témam. Spectral barriers and inertial manifolds for dissipative partial differential equations. *J. Dyn. Diff. Eq.* **1**, 45–73 (1989).

[CFNT89b]   P. Constantin, C. Foias, B. Nicolaenko, and R. Temam. *Integral Manifolds and Inertial Manifolds for Dissipative Partial Differential Equations*. Applied Mathematical Sciences, vol. 70. Springer-Verlag, New York, 1989.

[CPS95]   A. V. Coward, D. T. Papageorgiou, and Y. S. Smyrlis. Nonlinear stability of oscillatory core-annular flow: A generalized Kuramoto-Sivashinsky equation with time periodic coefficients. *Z. angew. Math. Phys. (ZAMP)* **46**, 1–39 (1995).

[CDHS83]   M. C. Cross, P. G. Daniels, P. C. Hohenberg, and E. D. Siggia. Phase-winding solutions in a finite container above the convective threshold. *J. Fluid Mech.* **127**, 155–183 (1983).

[CH93]   M. C. Cross and P. C. Hohenberg. Pattern formation outside of equilibrium. *Rev. Mod. Phys.* **65**, 851–1112 (1993).

[CL95]   R. Cuerno and K. B. Lauritsen. Renormalization group analysis of a noisy Kuramoto-Sivashinsky equation. *Phys. Rev. E* **52**, 4853–4859 (1995).

[CMTHS95] R. Cuerno, H. A. Makse, S. Tomassone, S. T. Harrington, and H. E. Stanley. Stochastic model for surface erosion via ion sputtering: Dynamical evolution from ripple morphology to rough morphology. *Phys. Rev. Lett.* **75**, 4464–4467 (1995).

[CO93]   K. M. Cuomo and A. V. Oppenheim. Circuit implementation of synchronized chaos, with applications to communications. *Phys. Rev. Lett.* **71**, 65–68 (1993).

[COS93]   K. M. Cuomo, A. V. Oppenheim, and S. H. Strogatz. Synchronization of Lorenz-based chaotic circuits, with applications to communications. *IEEE Trans. Circuits and Systems* **40**, 626–633 (1993).

[CS97]   A. Cutler and E. Stone. Moving archetypes. *Physica D* **107**, 1–16 (1997).

[CAMV98]   P. Cvitanović, R. Artuso, R. Mainieri, and G. Vattay. *Classical and Quantum Chaos: A Cyclist Treatise*, Webbook, `http://www.nbi.dk/ChaosBook/`, 1993–98.

[DHBE96]   H. Dankowicz, P. Holmes, G. Berkooz, and J. Elezgaray. Local models of spatio-temporally complex fields. *Physica D* **90**, 387–407 (1996).

[Dan95]   H. J. Dankowicz. Chaos in low- and high-dimensional systems. Ph.D. thesis, Cornell University, 1995.

[Dau92]   I. Daubechies. *Ten Lectures on Wavelets.* CBMS-NSF Regional Conference Series in Applied Mathematics, vol. 61. SIAM, Philadelphia, 1992.

[DGN94]   M. Dellnitz, M. Golubitsky, and M. Nicol. Symmetry of attractors and the Karhunen-Loève decomposition. In *Trends and Perspectives in Applied Mathematics* (L. Sirovich, ed.), Applied Mathematical Sciences, vol. 100, Springer-Verlag, New York, 1994, pp. 73–108.

[DE98]   J. Duan and V. J. Ervin. Dynamics of a nonlocal Kuramoto-Sivashinsky equation. *J. Differential Equations* **143**, 243–266 (1998).

[EG94a]   D. A. Egolf and H. S. Greenside. Relation between fractal dimension and spatial correlation length for extensive chaos. *Nature* **369**, 129–131 (1994).

[EG94b]   D. A. Egolf and H. S. Greenside. Spatial variation of correlation times for 1D phase turbulence. *Phys. Lett. A* **185**, 395–400 (1994).

[EG95]   D. A. Egolf and H. S. Greenside. Characterization of the transition from defect to phase turbulence. *Phys. Rev. Lett.* **74**, 1751–1754 (1995).

[EAHGP98] V. Eguíluz, P. Alstrøm, E. Hernández-García, and O. Piro. Average patterns of spatiotemporal chaos in the Kuramoto-Sivashinsky equation, preprint `chao-dyn/9805003`, 1998.

[EGG97]   K. Elder, J. Gunton, and N. Goldenfeld. Transition to spatiotemporal chaos in the damped Kuramoto-Sivashinsky equation. *Phys. Rev. E* **56**, 1631–1634 (1997).

[EBDHM97] J. Elezgaray, G. Berkooz, H. Dankowicz, P. Holmes, and M. Myers. Local models and large scale statistics of the Kuramoto-Sivashinsky equation. In *Multiscale Wavelet Methods for Partial Differential Equations* (W. Dahmen, A. J. Kurdila, and P. Oswald, eds.), Wavelet Analysis and Its Applications, vol. 6, Academic Press, San Diego, 1997, pp. 441–471.

[EBH93]   J. Elezgaray, G. Berkooz, and P. Holmes. Wavelet analysis of the motion of coherent structures. In *Progress in Wavelet Analysis and Applications* (Y. Meyer and S. Roques, eds.), Editions Frontieres, Gif-sur-Yvette, 1993, pp. 471–476.

[EBH96]   J. Elezgaray, G. Berkooz, and P. Holmes. Large-scale statistics of the Kuramoto-Sivashinsky equation: A wavelet-based approach. *Phys. Rev. E* **54**, 224–230 (1996).

[EW96]   J. N. Elgin and X. Wu. Stability of cellular states of the Kuramoto-Sivashinsky equation. *SIAM J. Appl. Math.* **56**, 1621–1638 (1996).

[EMR93]   N. M. Ercolani, D. W. McLaughlin, and H. Roitner. Attractors and transients for a perturbed periodic KdV equation: A nonlinear spectral analysis. *J. Nonlinear Sci.* **3**, 477–539 (1993).

[Far92]   M. Farge. Wavelet transforms and their applications to turbulence. *Ann. Rev. Fluid Mech.* **40**, 395–457 (1992).

[FKPG96]   M. Farge, N. Kevlahan, V. Perrier, and E. Goirand. Wavelets and turbulence. *Proc. IEEE* **84**, 639–669 (1996).

226

[FJ95]   C. Foias and M. S. Jolly. On the numerical algebraic approximation of global attractors. *Nonlinearity* **8**, 295–319 (1995).

[FJKT94]   C. Foias, M. S. Jolly, I. G. Kevrekidis, and E. S. Titi. On some dissipative fully discrete nonlinear Galerkin schemes for the Kuramoto-Sivashinsky equation. *Phys. Lett. A* **186**, 87–96 (1994).

[FK95]   C. Foias and I. Kukavica. Determining nodes for the Kuramoto-Sivashinsky equation. *J. Dyn. Diff. Eq.* **7**, 365–373 (1995).

[FNST85]   C. Foias, B. Nicolaenko, G. R. Sell, and R. Temam. Variétés inertielles pour l'équation de Kuramoto-Sivashinski. *C. R. Acad. Sc. Paris, Série I* **301**, 285–288 (1985).

[FNST88]   C. Foias, B. Nicolaenko, G. R. Sell, and R. Temam. Inertial manifolds for the Kuramoto-Sivashinsky equation and an estimate of their lowest dimension. *J. Math. pures et appl.* **67**, 197–226 (1988).

[FT89]   C. Foias and R. Temam. Gevrey class regularity for the solutions of the Navier-Stokes equations. *J. Funct. Anal.* **87**, 359–369 (1989).

[FT91]   C. Foias and E. S. Titi. Determining nodes, finite difference schemes and inertial manifolds. *Nonlinearity* **4**, 135–153 (1991).

[FNS77]   D. Forster, D. R. Nelson, and M. J. Stephen. Large-distance and long-time properties of a randomly stirred fluid. *Phys. Rev. A* **16**, 732–749 (1977).

[Fra86]   A. M. Fraser. Using mutual information to estimate metric entropy. In *Dimensions and Entropies in Chaotic Systems: Quantification of Complex Behavior* (G. Mayer-Kress, ed.), Springer Series in Synergetics, vol. 32, Springer-Verlag, Berlin Heidelberg, 1986, pp. 82–91.

[Fra89]   A. M. Fraser. Information and entropy in strange attractors. *IEEE Trans. Info. Theory* **35**, 245–262 (1989).

[FS86]   A. M. Fraser and H. L. Swinney. Independent coordinates for strange attractors from mutual information. *Phys. Rev. A* **33**, 1134–1140 (1986).

[Fri95]   U. Frisch. *Turbulence: The Legacy of A.N. Kolmogorov.* Cambridge University Press, Cambridge, 1995.

[FM81]   U. Frisch and R. Morf. Intermittency in nonlinear dynamics and singularities at complex times. *Phys. Rev. A* **23**, 2673–2705 (1981).

[FST86]   U. Frisch, Z. S. She, and O. Thual. Viscoelastic behaviour of cellular solutions to the Kuramoto-Sivashinsky model. *J. Fluid Mech.* **168**, 221–240 (1986).

[FY77]   H. Fujisaka and T. Yamada. Theoretical study of a chemical turbulence. *Prog. Theor. Phys.* **57**, 734–745 (1977).

[Gar85]   C. W. Gardiner. *Handbook of Stochastic Methods for Physics, Chemistry and the Natural Sciences*, 2nd ed. Springer Series in Synergetics, vol. 13. Springer-Verlag, Berlin Heidelberg, 1985.

[GC96]   A. González and A. Castellanos. Nonlinear electrohydrodynamic waves on films falling down an inclined plane. *Phys. Rev. E* **53**, 3573–3578 (1996).

[Goo94]   J. Goodman. Stability of the Kuramoto-Sivashinsky and related systems. *Commun. Pure Appl. Math.* **47**, 293–306 (1994).

[GEP98]   G. Goren, J.-P. Eckmann, and I. Procaccia. Scenario for the onset of space-time chaos. *Phys. Rev. E* **57**, 4106–4134 (1998).

[GK88]   J. M. Greene and J.-S. Kim. The steady states of the Kuramoto-Sivashinsky equation. *Physica D* **33**, 99–120 (1988).

[Gre98]   H. S. Greenside. Spatiotemporal Chaos in Large Systems: How Complexity Scales with Size. In *Semi-Analytic Methods for the Navier-Stokes Equations* (K. Coughlin, ed.), Proceedings of the CRM Workshop, Centre de Recherches Mathématiques, Montréal, 1998.

[Gru00]   Z. Grujić. Spatial analyticity on the global attractor for the Kuramoto-Sivashinsky equation. *J. Dynam. Diff. Eq.* **12**, 217–228 (2000).

[GK97]   Z. Grujić and I. Kukavica. A remark on time-analyticity for the Kuramoto-Sivashinsky equation, preprint, 1997.

[GK98]   Z. Grujić and I. Kukavica. Space analyticity for the Navier-Stokes and related equations with initial data in L^p. *J. Funct. Anal.* **152**, 447–466 (1998).

[GH83]   J. Guckenheimer and P. Holmes. *Nonlinear Oscillations, Dynamical Systems and Bifurcations of Vector Fields.* Applied Mathematical Sciences, vol. 42. Springer-Verlag, New York, 1983, Fifth revised and corrected printing 1997.

[HHZ95]   T. Halpin-Healy and Y.-C. Zhang. Kinetic roughening phenomena, stochastic growth, directed polymers and all that. *Phys. Rep.* **254**, 215–414 (1995).

[HJJ93]   F. Hayot, C. Jayaprakash, and C. Josserand. Long-wavelength properties of the Kuramoto-Sivashinsky equation. *Phys. Rev. E* **47**, 911–915 (1993).

[HR93]   T. Hocherman and P. Rosenau. On KS-type equations describing the evolution and rupture of a liquid interface. *Physica D* **67**, 113–125 (1993).

[HS89]   P. Hohenberg and B. I. Shraiman. Chaotic behavior of an extended system. *Physica D* **37**, 109–115 (1989).

[HLB96]   P. Holmes, J. L. Lumley, and G. Berkooz. *Turbulence, Coherent Structures, Dynamical Systems and Symmetry.* Cambridge University Press, Cambridge, 1996.

[HLBMW97]   P. J. Holmes, J. L. Lumley, G. Berkooz, J. C. Mattingly, and R. W. Wittenberg. Low-dimensional models of coherent structures in turbulence. *Phys. Rep.* **287**, 337–384 (1997).

[HG85]   A. P. Hooper and R. Grimshaw. Nonlinear instability at the interface between two viscous fluids. *Phys. Fluids* **28**, 37–45 (1985).

[HHF85]   D. A. Huse, C. L. Henley, and D. S. Fisher. Response. *Phys. Rev. Lett.* **55**, 2924 (1985).

[HN86]   J. M. Hyman and B. Nicolaenko. The Kuramoto-Sivashinsky equation: A bridge between PDEs and dynamical systems. *Physica D* **18**, 113–126 (1986).

[HNZ86]   J. M. Hyman, B. Nicolaenko, and S. Zaleski. Order and complexity in the Kuramoto-Sivashinsky model of weakly turbulent interfaces. *Physica D* **23**, 265–292 (1986).

[Il'92]   J. Il'yashenko. Global analysis of the phase portrait for the Kuramoto-Sivashinsky equation. *J. Dyn. Diff. Eq.* **4**, 585–615 (1992).

[IK66]   E. Isaacson and H. B. Keller. *Analysis of Numerical Methods.* John Wiley & Sons, New York, 1966, Dover edition 1994.

[JHP93]   C. Jayaprakash, F. Hayot, and R. Pandit. Universal properties of the two-dimensional Kuramoto-Sivashinsky equation. *Phys. Rev. Lett.* **71**, 12–15 (1993).

[Joh98]   M. E. Johnson. Computer-assisted studies and visualization of nonlinear phenomena: two-dimensional invariant manifolds, global bifurcations, and robustness of global attractors. Ph.D. thesis, Princeton University, 1998.

[JKT90]   M. Jolly, I. Kevrekidis, and E. Titi. Approximate inertial manifolds for the Kuramoto-Sivashinsky equation: Analysis and computation. *Physica D* **44**, 38–60 (1990).

[KPZ86]   M. Kardar, G. Parisi, and Y.-C. Zhang. Dynamic scaling of growing interfaces. *Phys. Rev. Lett.* **56**, 889–892 (1986).

[KE92]   P. Kent and J. Elgin. Travelling-waves of the Kuramoto-Sivashinsky equation: period-multiplying bifurcations. *Nonlinearity* **5**, 899–919 (1992).

[KNS90]   I. G. Kevrekidis, B. Nicolaenko, and J. C. Scovel. Back in the saddle again: A computer assisted study of the Kuramoto-Sivashinsky equation. *SIAM J. Appl. Math.* **50**, 760–790 (1990).

[Kir92]   M. Kirby. Minimal dynamical systems from PDEs using Sobolev eigenfunctions. *Physica D* **57**, 466–475 (1992).

[KA92]   M. Kirby and D. Armbruster. Reconstructing phase space from PDE simulations. *Z. angew. Math. Phys. (ZAMP)* **43**, 999–1022 (1992).

[KAG91]   M. Kirby, D. Armbruster, and W. Güttinger. An approach for the analysis of spacially localized oscillations. In *Bifurcation and Chaos: Analysis, Algorithms, Applications* (R. Seydel, F. W. Schneider, T. Küpper, and H. Troger, eds.), International Series of Numerical Mathematics, vol. 97, Birkhäuser Verlag, Basel, 1991, pp. 183–187.

[KPS94]   P. E. Kloeden, E. Platen, and H. Schurz. *Numerical Solution of SDE Through Computer Experiments.* Universitext. Springer-Verlag, Berlin Heidelberg, 1994.

[Kra90]   R. H. Kraichnan. Models of intermittency in hydrodynamic turbulence. *Phys. Rev. Lett.* **65**, 575–578 (1990).

[KS91]   J. Krug and H. Spohn. Kinetic roughening of growing interfaces. In *Solids far from Equilibrium* (C. Godrèche, ed.), Monographs and Texts in Statistical Physics, vol. 1, Cambridge University Press, Cambridge, 1991, pp. 479–582.

[Kuk94]   I. Kukavica. Oscillations of solutions of the Kuramoto-Sivashinsky equation. *Physica D* **76**, 369–374 (1994).

[Kur78]   Y. Kuramoto. Diffusion-induced chaos in reaction systems. *Suppl. Prog. Theor. Phys.* **64**, 346–367 (1978).

[Kur80]   Y. Kuramoto. Instability and turbulence of wavefronts in reaction-diffusion systems. *Prog. Theor. Phys.* **63**, 1885–1903 (1980).

[Kur84]   Y. Kuramoto. *Chemical Oscillations, Waves, and Turbulence.* Springer Series in Synergetics, vol. 19. Springer-Verlag, Berlin Heidelberg, 1984.

[KT75]   Y. Kuramoto and T. Tsuzuki. On the formation of dissipative structures in reaction-diffusion systems. *Prog. Theor. Phys.* **54**, 687–699 (1975).

[KT76]   Y. Kuramoto and T. Tsuzuki. Persistent propagation of concentration waves in dissipative media far from thermal equilibrium. *Prog. Theor. Phys.* **55**, 356–369 (1976).

[KY76]   Y. Kuramoto and T. Yamada. Turbulent state in chemical reactions. *Prog. Theor. Phys.* **56**, 679–681 (1976).

[LL80]   L. Landau and E. Lifshitz. *Statistical Physics, Part 1*, 3rd ed. Course of Theoretical Physics, vol. 5. Pergamon, Oxford, 1980.

[LMRT75]   R. LaQuey, S. Mahajan, P. Rutherford, and W. Tang. Nonlinear saturation of the trapped-ion mode. *Phys. Rev. Lett.* **34**, 391–394 (1975).

[Lau92]   Y.-T. Lau. Large-period turbulent solutions of the Kuramoto-Sivashinsky equation. *Phys. Lett. A* **169**, 329–334 (1992).

[LS95]   J. Li and L. M. Sander. Scaling properties of the Kuramoto-Sivashinsky equation. *Fractals* **3**, 507–514 (1995).

[LL96]   E. H. Lieb and M. Loss. *Analysis.* Graduate Studies in Mathematics, vol. 14. American Mathematical Society, Providence, RI, 1996.

[Liu91]   X. Liu. Gevrey class regularity and approximate inertial manifolds for the Kuramoto-Sivashinsky equation. *Physica D* **50**, 135–151 (1991).

[LLPP93]   V. S. L'vov, V. V. Lebedev, M. Paton, and I. Procaccia. Proof of scale invariant solutions in the Kardar-Parisi-Zhang and Kuramoto-Sivashinsky equations in 1+1 dimensions: analytical and numerical results. *Nonlinearity* **6**, 25–47 (1993).

[LP92]   V. S. L'vov and I. Procaccia. Comparison of the scale invariant solutions of the Kuramoto-Sivashinsky and Kardar-Parisi-Zhang equations in d dimensions. *Phys. Rev. Lett.* **69**, 3543–3546 (1992).

[Man81]   P. Manneville. Statistical properties of chaotic solutions of a one-dimensional model for phase turbulence. *Phys. Lett. A* **84**, 129–132 (1981).

[Man85]   P. Manneville. Liapounov exponents for the Kuramoto-Sivashinsky model. In *Macroscopic Modelling of Turbulent Flows* (U. Frisch, J. Keller, G. Papanicolaou, and O. Pironneau, eds.), Lecture Notes in Physics, vol. 230, Springer-Verlag, Berlin Heidelberg, 1985, pp. 319–326.

[Man90]   P. Manneville. *Dissipative Structures and Weak Turbulence.* Academic Press, San Diego, 1990.

[MR88]   M. Matalon and P. Rosenau. A regularized KS equation describing the formation of cellular flames. *Phys. Lett. A* **133**, 23–28 (1988).

[Mat98]   J. C. Mattingly. The stochastically forced Navier-Stokes equations: Energy estimates and phase space contraction. Ph.D. thesis, Princeton University, 1998.

[Mic86]   D. Michelson. Steady solutions of the Kuramoto-Sivashinsky equation. *Physica D* **19**, 89–111 (1986).

[MS77]   D. Michelson and G. Sivashinsky. Nonlinear analysis of hydrodynamic instability in laminar flames—II. Numerical experiments. *Acta Astron.* **4**, 1207–1221 (1977).

[MS95]   A. Mielke and G. Schneider. Attractors for modulation equations on unbounded domains—existence and comparison. *Nonlinearity* **8**, 743–768 (1995).

[MH93]   J. Miller and D. A. Huse. Macroscopic equilibrium from microscopic irreversibility in a chaotic coupled-map lattice. *Phys. Rev. E* **48**, 2528–2535 (1993).

[MMKT91]   C. Misbah, H. Müller-Krumbhaar, and D. E. Temkin. Interface structure at large supercooling. *J. Phys. I* **1**, 585–601 (1991).

[MV94]   C. Misbah and A. Valance. Secondary instabilities in the stabilized Kuramoto-Sivashinsky equation. *Phys. Rev. E* **49**, 166–183 (1994).

[MK96]   M. Münkel and F. Kaiser. An intermittency route to chaos via attractor merging in the Laser-Kuramoto-Sivashinsky equation. *Physica D* **98**, 156–170 (1996).

[MHEB95]   M. Myers, P. Holmes, J. Elezgaray, and G. Berkooz. Wavelet projections of the Kuramoto-Sivashinsky equation I. Heteroclinic cycles and modulated traveling waves for short systems. *Physica D* **86**, 396–427 (1995).

[Nic86]   B. Nicolaenko. Some mathematical aspects of flame chaos and flame multiplicity. *Physica D* **20**, 109–121 (1986).

[NS84]   B. Nicolaenko and B. Scheurer. Remarks on the Kuramoto-Sivashinsky equation. *Physica D* **12**, 391–395 (1984).

[NST84]   B. Nicolaenko, B. Scheurer, and R. Temam. Quelques propriétés des attracteurs pour l'équation de Kuramoto-Sivashinsky. *C. R. Acad. Sc. Paris, Série I* **298**, 23–25 (1984).

[NST85]   B. Nicolaenko, B. Scheurer, and R. Temam. Some global dynamical properties of the Kuramoto-Sivashinsky equations: Nonlinear stability and attractors. *Physica D* **16**, 155–183 (1985).

[NCS86]   A. Novick-Cohen and G. I. Sivashinsky. On the solidification front of a dilute binary alloy: Thermal diffusivity effects and breathing solutions. *Physica D* **20**, 237–258 (1986).

[OEG96]   C. S. O'Hern, D. A. Egolf, and H. S. Greenside. Lyapunov spectral analysis of a nonequilibrium Ising-like transition. *Phys. Rev. E* **53**, 3374–3386 (1996).

[PE97]   M. Paniconi and K. Elder. Stationary, dynamical, and chaotic states of the two-dimensional damped Kuramoto-Sivashinsky equation. *Phys. Rev. E* **56**, 2713–2721 (1997).

[Pap84]   A. Papoulis. *Probability, Random Variables, and Stochastic Processes*, 2nd ed. McGraw-Hill, New York, 1984.

[PC90]   L. M. Pecora and T. L. Carroll. Synchronization in chaotic systems. *Phys. Rev. Lett.* **64**, 821–824 (1990).

[PB89]   V. Perrier and C. Basdevant. Periodical wavelet analysis, a tool for inhomogeneous field investigation. Theory and algorithms. *Rech. Aérosp.* **1989-3**, 53–67 (1989).

[PB91]   V. Perrier and C. Basdevant. Travelling wavelets method, Proceedings of the USA-French "Wavelets and Turbulence" workshop, Princeton, 1991.

[PM80]   Y. Pomeau and P. Manneville. Wavelength selection in cellular flows. *Phys. Lett. A* **75**, 296–298 (1980).

[PPP84]   Y. Pomeau, A. Pumir, and P. Pelce. Intrinsic stochasticity with many degrees of freedom. *J. Stat. Phys.* **37**, 39–49 (1984).

[PZ81]   Y. Pomeau and S. Zaleski. Wavelength selection in one-dimensional cellular structures. *J. Physique* **42**, 515–528 (1981).

[PDM97]   S. Ponce Dawson and A. M. Mancho. Collections of heteroclinic cycles in the Kuramoto-Sivashinsky equation. *Physica D* **100**, 231–256 (1997).

[PTVF92]   W. H. Press, S. A. Teukolsky, W. T. Vetterling, and B. P. Flannery. *Numerical Recipes in C: The Art of Scientific Computing*, 2nd ed. Cambridge University Press, Cambridge, 1992.

[PJLSZ92]   I. Procaccia, M. H. Jensen, V. S. L'vov, K. Sneppen, and R. Zeitak. Surface roughening and the long-wavelength properties of the Kuramoto-Sivashinsky equation. *Phys. Rev. A* **46**, 3220–3224 (1992).

[Pum85]   A. Pumir. Statistical properties of an equation describing fluid interfaces. *J. Physique* **46**, 511–522 (1985).

[Rob94]   J. C. Robinson. Inertial manifolds for the Kuramoto-Sivashinsky equation. *Phys. Lett. A* **184**, 190–193 (1994).

[RK95]   M. Rost and J. Krug. A particle model for the Kuramoto-Sivashinsky equation. *Physica D* **88**, 1–13 (1995).

[SKN88]   C. Scovel, I. Kevrekidis, and B. Nicolaenko. Scaling laws and the prediction of bifurcations in systems modeling pattern formation. *Phys. Lett. A* **130**, 73–80 (1988).

[SFT85]   Z. S. She, U. Frisch, and O. Thual. Homogenization and visco-elasticity of turbulence. In *Macroscopic Modelling of Turbulent Flows* (U. Frisch, J. Keller, G. Papanicolaou, and O. Pironneau, eds.), Lecture Notes in Physics, vol. 230, Springer-Verlag, Berlin Heidelberg, 1985, pp. 1–13.

[Shr86]	B. I. Shraiman. Order, disorder and phase turbulence. *Phys. Rev. Lett.* **57**, 325–328 (1986).
[Siv77]	G. Sivashinsky. Nonlinear analysis of hydrodynamic instability in laminar flames—I. Derivation of basic equations. *Acta Astron.* **4**, 1177–1206 (1977).
[Siv79]	G. Sivashinsky. On self-turbulization of a laminar flame. *Acta Astron.* **6**, 569–591 (1979).
[SM80]	G. Sivashinsky and D. Michelson. On irregular wavy flow of a liquid film down a vertical plane. *Prog. Theor. Phys.* **63**, 2112–2114 (1980).
[SP91]	Y. S. Smyrlis and D. T. Papageorgiou. Predicting chaos for infinite dimensional dynamical systems: The Kuramoto-Sivashinsky equation, a case study. *Proc. Natl. Acad. Sci. USA* **88**, 11129–11132 (1991).
[SP96]	Y. S. Smyrlis and D. T. Papageorgiou. Computational study of chaotic and ordered solutions of the Kuramoto-Sivashinsky equation, preprint, 1996.
[SKJJB92]	K. Sneppen, J. Krug, M. Jensen, C. Jayaprakash, and T. Bohr. Dynamic scaling and crossover analysis for the Kuramoto-Sivashinsky equation. *Phys. Rev. A* **46**, R7351–R7354 (1992).
[SB80]	J. Stoer and R. Bulirsch. *Introduction to Numerical Analysis.* Springer-Verlag, New York, 1980.
[SC96a]	E. Stone and A. Cutler. Archetypal analysis of spatio-temporal dynamics. *Physica D* **90**, 209–224 (1996).
[SC96b]	E. Stone and A. Cutler. Introduction to archetypal analysis of spatio-temporal dynamics. *Physica D* **96**, 110–131 (1996).
[SK93]	E. Stone and M. Kirby. Dependence of bifurcation structures on the approximation of O(2) symmetry. In *Exploiting Symmetry in Applied and Numerical Analysis* (E. L. Allgower, K. Georg, and R. Miranda, eds.), Lectures in Applied Mathematics, vol. 29, American Mathematical Society, Providence, R.I., 1993, pp. 389–404.
[Str94]	S. H. Strogatz. *Nonlinear Dynamics and Chaos.* Addison-Wesley, Reading, MA, 1994.
[Tad86]	E. Tadmor. The well-posedness of the Kuramoto-Sivashinsky equation. *SIAM J. Math. Anal.* **17**, 884–893 (1986).
[Tem97]	R. Temam. *Infinite-Dimensional Dynamical Systems in Mechanics and Physics*, 2nd ed. Applied Mathematical Sciences, no. 68. Springer-Verlag, New York, 1997.
[TW94]	R. Temam and X. Wang. Estimates on the lowest dimension of inertial manifolds for the Kuramoto-Sivashinsky equation in the general case. *Diff. and Int. Eqns.* **7**, 1095–1108 (1994).
[Tho95]	J. Thomas. *Numerical Partial Differential Equations: Finite Difference Methods.* Texts in Applied Mathematics, vol. 22. Springer-Verlag, New York, 1995.
[Toh87]	S. Toh. Statistical model with localized structures describing the spatio-temporal chaos of Kuramoto-Sivashinsky equation. *J. Phys. Soc. Japan* **56**, 949–962 (1987).
[TK78]	J. Topper and T. Kawahara. Approximate equations for long nonlinear waves on a viscous fluid. *J. Phys. Soc. Japan* **44**, 663–666; 2003 (1978).
[UA92]	M. Unser and A. Aldroubi. Polynomial splines and wavelets—a signal processing perspective. In *Wavelets: A Tutorial in Theory and Applications* (C. K. Chui, ed.), Wavelet Analysis and its Applications, vol. 2, Academic Press, San Diego, 1992, pp. 91–122.
[VS88]	J. A. Vastano and H. L. Swinney. Information transport in spatiotemporal systems. *Phys. Rev. Lett.* **60**, 1773–1776 (1988).
[WS95]	R. Wallace and D. M. Sloan. Numerical solution of a nonlinear dissipative system using a pseudospectral method and inertial manifolds. *SIAM J. Sci. Comput.* **16**, 1049–1070 (1995).
[Yak81]	V. Yakhot. Large-scale properties of unstable systems governed by the Kuramoto-Sivashinski equation. *Phys. Rev. A* **24**, 642–644 (1981).
[YK76]	T. Yamada and Y. Kuramoto. A reduced model showing chemical turbulence. *Prog. Theor. Phys.* **56**, 681–683 (1976).
[Zal89]	S. Zaleski. A stochastic model for the large scale dynamics of some fluctuating interfaces. *Physica D* **34**, 427–438 (1989).
[ZL85]	S. Zaleski and P. Lallemand. Scaling laws and intermittency in phase turbulence. *J. Physique Lett.* **46**, L793–L797 (1985).
[Zie95]	A. Ziegra. A global attracting set for the weakly unstable Kuramoto-Sivashinsky equation. Master's thesis, University of Hannover, 1995.

[ZG97]   S. M. Zoldi and H. S. Greenside. Karhunen-Loève decomposition of extensive chaos. *Phys. Rev. Lett.* **78**, 1687–1690 (1997).

[ZG98]   S. M. Zoldi and H. S. Greenside. Spatially localized unstable periodic orbits of a high-dimensional chaotic system. *Phys. Rev. E* **57**, R2511–R2514 (1998).